



CIVIL ENGINEERING JOURNAL

Vol. 10 - No. 04
Apr 2024



E-ISSN: 2476-3055
P-ISSN: 2676-6957



Editor in Chief:

Prof. M. R. Kavianpour

K.N.Toosi University of Technology (Iran)

Executive Manager:

Dr. O. Aminoroayaie Yamini

K.N.Toosi University of Technology (Iran)

Dr. S. Hooman Mousavi

K.N.Toosi University of Technology (Iran)

Editorial Board Members:

Prof. Dintie S. Mahamah

St. Martin's University (USA)

Dr. Kartik Venkataraman

Tarleton State University (USA)

Dr. Tanya Igneva

University of ACEG (Bulgaria)

Dr. Daniele Bocchiol

Polytechnic University of Milan (Italy)

Dr. Michele Iervolino

Second University of Naples (Italy)

Dr. Rouzbeh Nazari

Rowan University (USA)

Prof. Marta Bottero

Polytechnic University of Turin (Italy)

Chris A. O'Riordan-Adjah (PhD Candidate)

University of Central Florida (USA)

Dr. Yasser Khodair

Bradley University (USA)

Dr. Weidong Wu

University of Tennessee - Chattanooga (USA)

Dr. Kaveh Saleh

University of Sherbrooke (Canada)

To view all editorial board members [Click Here](#).

Dr. Jiliang Li

Purdue University North Central (USA)

Dr. Yaqi Wanyan

Texas Southern University (USA)

Prof. M.M. Rashidi

Tongji University (China)

Dr. Sanjay Tewari

Louisiana Tech University (USA)

Prof. Nikolaos Eliou

University of Thessaly (Greece)

Dr. Mohammad Reza Najafi

University of Victoria (Canada)

Dr. Saeed Khorram

Eastern Mediterranean University (Cyprus)

Dr. Xinqun Zhu

University of Western Sydney (Australia)

Dr. Jalil Kianfar

St. Louis University (USA)

Dr. Luca Comegna

Second University of Naples (Italy)

Dr. Davide Dalmazzo

Polytechnic University of Turin (Italy)

Dr. Viviana Letelier González

University of the Frontera (Chile)

Dr. Paola Antonaci

Polytechnic University of Turin (Italy)

Dr. Davorin Penava

University of Osijek (Croatia)

Dr. Ali Behnood

Purdue University (USA)

Dr. Uğur Albayrak

Eskisehir Osmangazi University (Turkey)



Contents

Vol. 10, No. 04, April, 2024

■ Page 994-1011

Development of a Conservative Hamiltonian Dynamic System for the Early Detection of Leaks in Pressurized Pipelines

Edgar Orlando Ladino-Moreno, César Augusto García-Ubaque, Eduardo Zamudio-Huertas

■ Page 1012-1033

Corrosion Resistance of Reinforcing Steel in Concrete Using Natural Fibers Treated with Used Engine Oil

Alejandro Flores Nicolás, Elsa C. Menchaca Campos, Mario Flores Nicolás, Omar A. Gonzalez Noriega, Cesar A. García Pérez, Jorge Uruchurtu Chavarín

■ Page 1034-1050

Strength Assessment of Stiffened-Panel Structures against Buckling Loads: FE Benchmarking and Analysis

M. Sholikhah, R. Ridwan, A. R. Prabowo, T. Ghanbari-Ghazijahani, I. Yaningsih, N. Muhyat, D. D. D. P. Tjahjana, R. Adiputra, J. M. Sohn

■ Page 1051-1068

Stress Concentration Factors in KT-Joints Subjected to Complex Bending Loads Using Artificial Neural Networks

Mohsin Iqbal, Saravanan Karuppanan, Veeradasan Perumal, Mark Ovinis, Afzal Khan, Muhammad Faizan

■ Page 1069-1092

Optimizing Alkali-Concentration on Fresh and Durability Properties of Defected Sanitary Ware Porcelain based Geopolymer Concrete

Woratid Wongpattanawut, Borvorn Israngkura Na Ayudhya

■ Page 1093-1112

Innovative Method for Reinforcing Beams with Different Types of Concrete Using Cross-Rod Steel Bracing Under Pure Torsion

Adnan I. Abdullah, Assim M. Lateef

■ Page 1113-1124

An Empirical Formula for Assessing the Characteristic Strength of Unreinforced Laterite Stone Masonry

Hassane Seini Moussa, Decroly Djoubissié Denouwé, Abdou Lawane, Anne Pantet, Mamadou Diop, Koami Wisdom Boko

■ Page 1125-1144

Properties and Microstructure of Treated Coal Bottom Ash as Cement Concrete Replacement

Moad Alost, Ahmed Mamdouh, Hussein Al Mufargi, Farah N. A. Abd Aziz, Ahmed Rashid, Otman M. M. Elbasir, Husam Al Dughhaishi

■ Page 1145-1158

Unveiling Effectiveness of Lean Construction Practices: A Comprehensive Study through Surveys and Case Studies

Mughees Aslam, Edmund Baffoe-Twum, Muhammad Ahmed, Aman Ulhaq

■ Page 1159-1181

Valuation of Urban Green Open Spaces Using the Life Satisfaction Approach

Retno Setiowati, Raldi H. Koestoer



Contents

Vol. 10, No. 04, April, 2024

■ **Page 1182-1195**

Utilization of Sand Cushion for Stabilization of Peat Layer Considering Dynamic Response of Compaction

Ali Basha, Waseim Azzam, Mohamed Elsiragy

■ **Page 1196-1209**

Applying Harmony Degree Equation and TOPSIS Combined with Entropy Weights in Surface Water Classification

Kieu Diem Le, Giao Thanh Nguyen

■ **Page 1210-1220**

Highlighting Traffic Accidents on Roundabouts Using MRSS-AHP Expert System

Ghassan Suleiman, Mohammad K. Younes, Murat Ergun, M. F. Abushammala, Mohammad Aljaradin

■ **Page 1221-1231**

Monitoring Physiological State of Drivers Using In-Vehicle Sensing of Non-Invasive Signal

Siti Fatimah Abdul Razak, Sharifah N. M. Sayed Ismail, Bryan Hii Ben Bin, Sumendra Yogarayan, Mohd Fikri Azli Abdullah, Noor Hisham Kamis

■ **Page 1232-1253**

Investigating Barriers to the Adoption of Energy Management Practices for Sustainable Construction Projects: SEM and ANN Approaches

Yasir Alhammadi, Ahmed Farouk Kineber, Mohammad Alhusban

■ **Page 1254-1264**

Concrete Strength and Aggregate Properties: In-Depth Analysis of Four Sources

Kamal Hosen, Md Abdulla Al Maruf, Rayhan Howlader, Kripendra Chakma, Md Rezars Mia

■ **Page 1265-1291**

Examining Soil Microplastics: Prevalence and Consequences Across Varied Land Use Contexts

Muhammad A. Walenna, Zarah A. Hanami, Rachmat Hidayat, Annisa D. Damayanti, Suprihanto Notodarmojo, . Kurniaty, Lucky Caroles

■ **Page 1292-1309**

Mechanical and Microstructural Properties of Geopolymer Concrete Containing Fly Ash and Sugarcane Bagasse Ash

Mohammed Ali M. Rihan, Richard O. Onchiri, Naftary Gathimba, Bernadette Sabuni

■ **Page 1310-1335**

Seismic Resilience of Steel-Braced Frames Incorporating Steel Slit Dampers: A Review and Comparative Numerical Analysis

Zaid A. Al-Sadoon, M. Almohammad-albakkar

■ **Page 1336-1353**

Evaluating Recycled PET as an Alternative Material for the Construction Sector Towards Sustainability

Omar Albatayneh, Mohammad Nadeem Akhtar



Focus and Scope

Civil Engineering Journal (C.E.J) is a multidisciplinary, an open-access, internationally double-blind peer-reviewed journal concerned with all aspects of civil engineering, which include but are not necessarily restricted to:

- Building Materials and Structures
- Coastal and Harbor Engineering
- Constructions Technology
- Constructions Economy and Management
- Earthquake Engineering
- Environmental Engineering
- Renovation of Buildings
- Geotechnical Engineering
- Highway Engineering
- Hydraulic and Hydraulic Structures
- Road and Bridge Engineering
- Structural Engineering
- Surveying and Geo-Spatial Engineering
- Transportation Engineering
- Tunnel Engineering
- Urban Engineering and Economy
- Water Resources Engineering
- Urban Drainage

Special Issues

Special Issues deal with more focused topics with high current interest falling within the scope of the journal in which they are published. Special Issue proposals are welcome at any time during the year.

For most of the civil engineering conferences it is possible to submit papers presented at the conference for subsequent publication in special issues of the C.E.J.

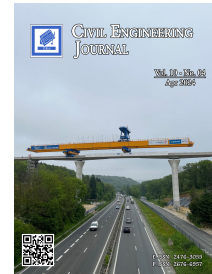
- Civil Engineering Journal (C.E.J) is published monthly.
- Civil Engineering Journal (C.E.J) has fast peer review process (3-4 weeks).

Civil Engineering Journal (C.E.J) Indexing & Abstracting



- This is an open access journal under the CC-BY license (<https://creativecommons.org/licenses/by/4.0/>).





Development of a Conservative Hamiltonian Dynamic System for the Early Detection of Leaks in Pressurized Pipelines

Edgar Orlando Ladino-Moreno ¹, César Augusto García-Ubaque ^{1*},
Eduardo Zamudio-Huertas ¹

¹ Department of Civil Engineering, Universidad Distrital Francisco José de Caldas, Bogotá, Colombia.

Received 27 December 2023; Revised 09 March 2024; Accepted 14 March 2024; Published 01 April 2024

Abstract

In this study, we propose an innovative approach for real-time leakage detection in pipelines by integrating conservative Hamiltonian equations and experimental Internet of Things (IoT) technologies. The proposed method combines a hybrid model that utilizes sensors and IoT devices to acquire real-time data and solves the coupled system of Hamiltonian equations using the ODE45 numerical integration method. Spectral frequency analysis is an essential part of this method, as it reveals specific patterns in the pressure and flow signals. The findings highlighted 95% accuracy in leak detection, which was validated through a comparison of the theoretical and experimental data. The novelty of this approach lies in its ability to maintain constant total system energy, thereby enabling continuous monitoring for early leak detection. As an improvement, the proper handling of sensor signals is emphasized, underscoring its contribution to the efficient management of water resources in potable water distribution systems.

Keywords: @Arduino; Conservative Systems; Hamiltonian System; IoT; Leaks; ODE45, Real-Time; Pipelines.

1. Introduction

The primary objective of early leakage detection in pipelines is to reduce the amount of water lost from potable water distribution systems. However, the existing methods for leak localization and quantification have significant limitations in terms of accuracy and detection capability. Leak detection and localization are challenging because of the spatiotemporal dynamics of the process variables [1]. The current instrumentation of potable water distribution networks is marked by deficiencies, contributing to a loss of approximately 40% of the treated water at water treatment plants. For example, Speziali et al. (2021) [2] indicated that water loss rates due to leaks remain exceedingly high for service providers. Additionally, the strategic placement of sensors is crucial for monitoring and preventing failure events in water distribution networks (WDNs).

Verde & Torres (2016) [3] mentioned that each leak in a hydraulic system introduces three unknown fluid-related parameters: leak position, flow loss, and friction factor. These parameters play a crucial role in understanding and characterizing the impact of leaks on a system. An unstable or transient flow is characterized by physical conditions, including liquid compression and the resistance of the pipe material to deformations caused by a wavefront. This phenomenon can result in elastic or inelastic transients. In elastic situations, the method based on characteristics is effective for addressing transient scenarios. Similarly, in inelastic systems, such as those with rigid column pipes for nonstationary flows, the liquid flowing through the pipe is incompressible, and the pipe material does not undergo

* Corresponding author: cagarcaiu@udistrital.edu.co

<http://dx.doi.org/10.28991/CEJ-2024-010-04-01>



© 2024 by the authors. Licensee C.E.J, Tehran, Iran. This article is an open access article distributed under the terms and conditions of the Creative Commons Attribution (CC-BY) license (<http://creativecommons.org/licenses/by/4.0/>).

deformation. In this case, the system is affected only by inertia and friction. In addition, because the liquid density and pipe cross-sectional area remain constant, the instantaneous velocity remains the same throughout the control volume. The solution for both systems is based on the continuity and momentum equations, allowing the determination of the velocity and piezometric head along the pipe under a one-dimensional flow configuration. Numerical model validation is carried out by comparison with measurements of real transients and depends on pre-established boundary conditions in terms of algebraic and/or differential equations based on the physical properties of the fluid and pipe material. It is important to highlight that the transient itself is not a problem; the issue lies in the speed of change generated by the closing velocity of the control valves. In other words, the transient state originates between the two steady states. Rodríguez Calderón & Pallares Muñoz (2007) [4] suggested that a transient state can be induced through the instantaneous closure of a downstream valve, generating a wavefront that oscillates through the fluid.

This effect can be reduced or even prevented by gradually activating the flow control devices. Firouzi et al. (2020) [5] asserted that a water hammer can manifest when sudden disturbances occur under stable flow conditions at a specific point in the pipeline owing to instantaneous events. Disturbances originating from leaks in the pipeline can be detected by considering the flow in a pipeline as a conservative Hamiltonian dynamic system. These leaks cause significant changes in the energy within the system. Sánchez-Jiménez et al. (2020) [6] indicated that these changes can be detected through the real-time monitoring of state variables. For instance, the Euler–Lagrange approach has been employed to model pipes conveying water and experiencing leaks under the theory of a rigid column of water. Macias & Kooktae (2022) [7] asserted that it is possible to pinpoint the source of a leak in a gas pipeline using a Hamiltonian approach with the utilization of a backtracking horizon. Similarly, Schneider et al. (2002) [8] studied the transient chaos variations when changing the orientation of a major leak within a chaotic region in closed Hamiltonian systems. On the other hand, Torres and Besancon (2019) [9] described the dynamics of incompressible flow in rigid pipes with leaks and partial obstructions using port-Hamiltonian (pH) models, where interconnected modules are established. Consequently, it is possible to study the behavior of leaks in a hydraulic system based on a Hamiltonian dynamic model derived from the state variables. Perryman et al. (2022) [10] designed controllers for a nonlinear model of a Water WDN, demonstrating that the system led to a pH system while preserving system stability. The energy behavior in the system can be monitored by coupling Hamiltonian differential equations with mathematical functions determined for each leak in terms of flow and pressure. The equations of motion describe the evolution of the generalized coordinates and their conjugate moments over time. On the other hand, the energy conservation equation indicates the total energy in the system over time.

Owing to the occurrence of a leak in a hydraulic system, which generates a pressure differential and mass outflow, it is possible to represent the fluid behavior in a pipeline in terms of energy and determine the changes caused by disturbances inherent to leaks in the system. The Hamiltonian model allows the simulation and analysis of different leak scenarios, enabling the assessment of the impact of these conditions on the dynamic variables of the system. Lopezlena (2014) [11] proposed the development of a computer system for the detection and localization of leaks in pipelines based on a real-time transient model (RTTM), inspired by the pH algorithm. This algorithm is an optimization technique that is used to model distributed pH fluids (DPHFs). Rashad et al. (2021) [12] demonstrated that the pH model corresponds solely to the kinetic energy of a fluid to represent a variety of fluid dynamic systems. The pH algorithm establishes a series of ports to form a physical system to determine the aim of finding optimal control conditions. These port-controlled Hamiltonian models were derived from a theoretical systems approach based on energy modeling. These models are square, indicating that they have an equal number of state variables and control inputs.

Beattie et al. (2018) [13] suggested that these models are passive, suggesting that they do not generate energy internally and can only dissipate or store energy. The configuration of the Hamiltonian system and the flow rate and pressure differential functions yield a set of differential equations that can be solved using the ODE45 algorithm. This algorithm can find a numerical solution for the proposed system of differential equations, thereby allowing for analysis and an understanding of the system's behavior over time. For example, Zi Li et al. (2019) [14] used the built-in ODE45 function in Matlab® to calculate the movement of pipeline inspection gauges conveying petroleum and the motion of the Solghar and Nieckele models. Consequently, the main challenge in establishing a Hamiltonian model for leak detection is determining suitable functions that can accurately represent the flow rate and pressure in the system. Furthermore, the choice and application of appropriate filters for processing the signals emitted by the sensors significantly affect the final model results. It is crucial to select suitable filters to eliminate noise and unwanted disturbances from signals to obtain more accurate measurements for leak detection in a hydraulic system.

In contrast, Bendimerad et al. (2024) [15] studied 1D pH systems with dissipation, such as the Dzekster model for water filtration and viscous nanorods. Equations and implicit representations in Stokes–Lagrange subspaces are derived, addressing pH formulations for Timoshenko and Euler–Bernoulli beams. They explored transformations between explicit and implicit representations. Zhang et al. (2024) [16] observed dynamics with noise in observational data through Hamiltonian mechanics and proposed the Hamiltonian neuron Koopman operator (HNKO), which incorporates mathematical knowledge to automatically discover and maintain conservation laws. Eidnes et al. (2023) [17] proposed a hybrid machine-learning approach using Hamiltonian formulations for mechanical systems, whether conservative or non-conservative. Additionally, they introduced pseudo-Hamiltonian algorithms as a generalization of the Hamiltonian formulation through a pH formulation.

Therefore, the proposed approach to fill this research gap focuses on comprehensively addressing the early detection of leaks in hydraulic systems by combining mathematical models with synchronous flow and pressure signal detection. The proposed model integrates Internet of Things (IoT) technologies and mathematical modeling, structuring a hybrid model based on Hamiltonian equations and signal monitoring to describe the dynamics of the hydraulic system. The experimental model involves the installation of pressure and flow sensors at strategic points in the hydraulic system. Sensors such as USP-G41-1.2 and YF-S201 measure pressure and flow at different locations. The acquired data were filtered to eliminate the inherent sensor signal noise. Once the noise was removed, a mathematical model based on the conservative Hamiltonian equations was incorporated. These equations describe energy conservation in the hydraulic system and allow for the representation of interactions between variables, including disturbances caused by leaks, thereby providing a crucial analytical tool for understanding system dynamics.

To solve the coupled system of Hamiltonian equations and regression functions derived from the sensor data, the numerical integration method ODE45 (Runge–Kutta method) was employed. Finally, different scenarios were generated for the two simultaneous leaks. The Hamiltonian model allows for the analysis of the energy impact on the system generated by the two leaks (energy balance). Different leakage scenarios with temporal variations were considered, which contributed to the applicability of the proposed approach.

1.1. Hamiltonian Conservative System

The development of a Hamiltonian conservative system for leak detection in a simple pipeline begins with the kinetic energy associated with the flow, the potential energy represented by pressure, and a function that determines the energy derived from leaks. The kinetic energy is linked to the flow passing through the pipeline. This energy depends on the velocity and mass of the fluid and can be calculated using the kinetic energy equation. Potential energy is related to the fluid pressure in the pipeline. Sultana & Rahman (2013) [18] indicated that these forms of energy involve a function that represents the energy associated with leaks. This function captures the effect of leaks on the system and can vary depending on the location and magnitude of the leaks and is used to model and quantify the hydraulic head loss owing to leaks in the pipeline. The Hamiltonian conservative approach aims to develop a system of differential equations that describes the evolution of these different forms of energy over time. This allows for the detection and quantification of leaks based on changes in flow, pressure, and energy associated with the leaks. To develop this system, the following equations are considered:

$$H = \int \frac{Q^2}{2A} dx + \int \frac{P}{A^2} dx + Perturbation_1(t) + Perturbation_2(t) \quad (1)$$

where the first integral represents the kinetic energy of the system, the second integral represents the potential energy, $Perturbation_1(t)$ and $Perturbation_2(t)$ are functions that model the perturbations associated with leaks over time in terms of pressure. These perturbations were obtained from the proposed experimental system based on a mathematical function generated from the pressure data at each leak location over time. For the data obtained from the USP–G41–1.2 sensor, a statistical analysis was performed, determining the mathematical function that best fits the observed data and obtaining measurements of the perturbation generated by the leak at different moments. The Bernoulli equation is used to develop the system.

$$P + \frac{Q^2}{2A} = Constant + Perturbation_1 + Perturbation_2 \quad (2)$$

where P represents the pressure in the pipeline, A is the cross-sectional area of the pipe, and $Perturbation_1$ and $Perturbation_2$ are the perturbations at each leak in terms of pressure. Subsequently, by applying the mass-conservation equation, we obtain:

$$\frac{\partial Q}{\partial t} + \frac{\partial(Q^2/2)}{\partial x} = Leak_1 + Leak_2 \quad (3)$$

In this context, Q represents the flow rate in the pipeline, $Leak_1$ and $Leak_2$ the leak rates in terms of the flow. From the Hamiltonian, the corresponding equations can be derived using partial derivatives concerning flow rate Q and pressure P variables:

$$\frac{\partial P}{\partial t} = - \frac{\partial H}{\partial Q} \quad (4)$$

where $\frac{\partial P}{\partial t}$ represents the partial derivative of pressure concerning time, $\frac{\partial H}{\partial Q}$ represents the partial derivative of the Hamiltonian function H concerning the flow:

$$\frac{\partial Q}{\partial t} = \frac{\partial H}{\partial P} \quad (5)$$

where $\frac{\partial Q}{\partial t}$ represents the partial derivative of flow concerning time and $\frac{\partial H}{\partial P}$ represents the partial derivative of the Hamiltonian function H concerning pressure P . From this approach, it is possible to describe the temporal evolution of the flow and pressure in the experimental model considering the conservation of energy and the influence of leaks on the system. To determine the flow rate at each leak, the flow data were collected from the YF-S201 sensor at the location of each leak over time. These data allowed us to obtain measurements of the flow rate at different times and find a mathematical function that models the behavior. Thus, it is possible to implement an energy-conservative approach in the system that can contribute to the detection of abnormal changes in flow and pressure caused by simultaneous leaks in the pipes. Consequently, the Hamiltonian model allows the prediction of how the variables of the hydraulic system evolve over time. Disturbances caused by possible leaks in the pipeline were identified by monitoring the changes in pressure and flow in real-time.

This was achieved by comparing the sensor measurements with a theoretical model comprising Hamiltonian differential equations. Therefore, the state variables for this study are defined as follows: $-q(x, t)$ represent the flow rate at position x and time t and $-p(x, t)$ represent the pressure at position x and time t . Thus, the coupling of the Hamiltonian equations is given by:

$$H(q, p, x, t) = \int \left[p(x, t) + \frac{1}{2} q^2(x, t) \right] dx \quad (6)$$

Therefore,

$$\frac{\partial q}{\partial t} = -\frac{\partial H}{\partial p} = -\frac{\partial p}{\partial x} \quad (7)$$

For leaks 1 and 2, we have

$$\frac{\partial p}{\partial t} = -\frac{\partial H}{\partial q} = -\frac{\partial (q^2/2)}{\partial x} + Leak_1 + Leak_2 \quad (8)$$

The energy contributions to the hydraulic system are represented by $(Leak_1, Leak_2)$. In this way, the boundary conditions for the initial flow rate are given by: $-q(x, 0) = q_0(x)$. In terms of the initial system pressure, we have: $-p(x, 0) = p_0(x)$. These boundary conditions directly depend on the configuration of the hydraulic system. Once a Hamiltonian system is established to detect the two leaks in the system, it is important to process the signals emitted by the sensors. Hence, various filters, statistical analyses, noise-detection tests, and transformations must be implemented. For example, the fast Fourier transform (FFT) allows the decomposition of pressure and flow signals into their frequency components, transitioning from the time domain to the real-time frequency domain. The FFT identifies patterns and establishes unwanted frequencies in the signal, whether high or low. For example, Przystupa et al. (2020) [19] used the standard FFT algorithm to analyze the dynamic responses of a hydraulic pump within a low range of operating frequencies. Consequently, the spectral power behavior of the pressure and flow signals was determined for each leak, displaying the energy distribution at different frequencies. The application of filters, such as low-pass, high-pass, or moving average filters, involves a detailed study of the moment at which the leak occurs. This is crucial because the leak generates a pressure differential that may be confused with noise in the signal. Ji'e et al. (2022) [20] state that the dynamic behaviors linked to various parameters can be identified from the Lyapunov exponent.

2. Materials and Methods

2.1. Experimental Method

The design adopted a hybrid approach that combined conservative Hamiltonian equations and Internet of Things (IoT) technologies for real-time leak detection in pipelines. The execution was carried out by real-time data acquisition using USP-G41-1.2 pressure sensors and YF-S201 flow sensors, positioned at distances of 0.3 and 0.9 m, respectively. These data were incorporated into a mathematical model that solved a coupled system of Hamiltonian equations using the ODE45 numerical integration method. For data analysis, FFT was applied to the signals, allowing for the identification of patterns and subpeaks in the frequency spectrum. The findings, highlighting 95% accuracy in leak detection, were validated by comparing the theoretical and experimental data. This comprehensive approach, from design to data analysis, reveals a robust methodology for addressing the issue of leaks in hydraulic systems by leveraging both mathematical models and advanced real-time monitoring technologies. Figure 1 illustrates the methodological phases that determined the development of the study, including data acquisition using sensors, noise detection in signals, application of filters, spectrogram analysis, coupling of Hamiltonian equations, and prediction of flow and pressure signals over time and along the pipeline.

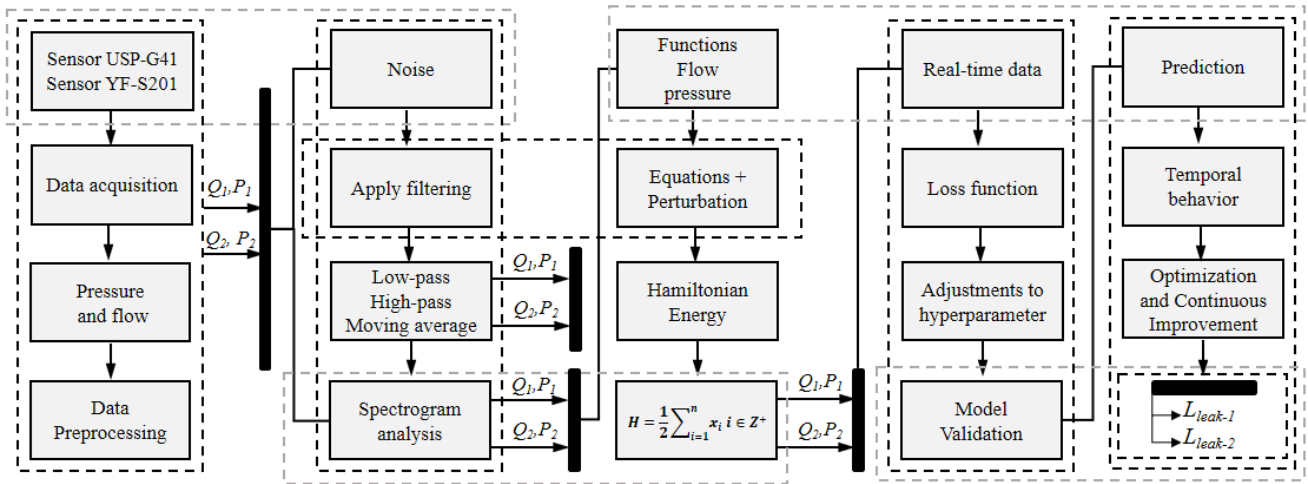


Figure 1. Flow Diagram (Modeling)

Table 1 presents the parameters used to formulate the PDE system of partial differential equations that describe the dynamics of the hydraulic system affected by leaks. The application of the conservative Hamiltonian method in this context aims to conserve the energy in the system as it evolves over time.

Table 1. Table 1. Hydraulic model parameters

Parameter	Value	Unit
Pressure (P)	8-14.5	psi
Flow (Q)	4-12	L/min
Pipe diameter	1/2"	inch
Pipe length	1.5	meters
Location leak ₁	0.3	meters
Location leak ₂	0.9	meters

Information on the physical constants of the fluid (water) is provided in Table 2.

Table 2. Physical parameters

Parameter	Value	Unit
Temperature	18	°C
Viscosity	0.001002	Pa·s

The Hamiltonian model for leak detection in hydraulic systems is significantly influenced by several key parameters. The pipe length (L) determines the temporal propagation of disturbances, such as leaks, throughout the system. The division of the pipe into intervals (N) and the spatial step (Δx) influence the ability of the model to accurately represent the distribution of these perturbations caused by leaks along the pipe. The time step (Δt) affects the temporal resolution of the model, being essential for capturing instantaneous events in the system. The initial and boundary conditions define the initial state of the system and the conservation of pressure at the ends of the pipe, respectively, thus shaping its temporal evolution. Similarly, the physical constants of a fluid, such as the density and viscosity of water, introduce fundamental properties that determine the response of the system to perturbations. The proper choice and precise configuration of these parameters are essential for constructing a Hamiltonian model. Consequently, sampling datasets of the flow and pressure signals were created for different time points ($t = 5\text{ s}, t = 15\text{ s}, t = 10\text{ s}, t = 20\text{ s}$), establishing the dataset necessary to validate and fit the model. Table 3 lists the temporal conditions and initial and boundary conditions that were applied in this analysis.

Table 3. Temporal parameters

$\Delta x = L/N$	N	Δt	Initial condition (Flow)	Initial condition (Pressure)	Temporal iteration	Spatial condition
0.1	15	0.1	$Q(x, 0) = 0$	$P(x, 0) = 1$	$0, \Delta t, 2t, \dots, T$	$P(L, t) = 1$

2.2. IoT Experimental Hydraulic Design

Figure 2 represents the experimental design implemented, which is based on a 1.5-m-long pipe, with two regulating valves driven by a centrifugal pump: 0.37 KW, 30 – 80 L/min. Four holes were created in the pipe, located at distances of 0.3 and 0.9 m from the beginning of the pipe, with a hole diameter of 2 mm in each one. Eight sensors were used to monitor the system. Electronics Hobby (2018) [21] proposed a precision flow meter; therefore, a YF-S201 flow meter was used, which was calibrated using a LUXQ flow meter with a two-wire 4–20-mA output. On the other hand, to capture the pressure signals, the USP-G41-1.2 sensor was implemented, which was calibrated using a SCJN-series pressure gauge with a precision of $\pm 0.5\%$ FS. The sensors were connected to an ESP8266 board, which acted as a microcontroller and captured the signals from the sensors. These signals are transmitted via WiFi to the Matlab® server using ThingSpeak, with a 1 s delay between each transmission. Graphs of the behavior of the pressure and flow upstream, downstream, and on the abscissa of the leaks are shown in real-time through the website.



Figure 2. Experimental design (Hydraulics Laboratory, Universidad Distrital Francisco José de Caldas)

2.3. Signal Processing

After calibrating the sensors, the signals from the USP-G41-1.2 and YF-S201 sensors were processed. First, the signals from both sensors were captured. Once connected to the ESP8266 microcontroller, the pressure sensor transmits its signal through pin A0 as it emits an analog signal that is proportional to the measured pressure in the form of a current. On the other hand, the sensor communicates through pin D4 using a digital signal. Second, the signals are encoded using the Arduino development environment. A control panel is established in Matlab®, where the data obtained from the time series with a sampling frequency of one second are stored. The analysis was performed using two approaches. The first is a stationary approach in which the flow rate in the system does not vary; that is, it remains constant. In this case, the pressure and flow were monitored and recorded as functions of time to obtain information on

the behavior of the system under stable conditions. The second approach is nonstationary or transient, where the flow rate varies as a function of time. Urbanowicz et al. (2020) [22] noted that a new simplified model was applied to simulate viscoelastic transient pipe flows and a method of characteristic (MOC) numerical scheme was implemented. By observing the signal in real-time, the reaction of the system to variations in flow can be examined, as well as how the pressure is affected when both leaks occur simultaneously. Figure 3 shows the electronic layout of the proposed prototype, where the corresponding pins are assigned to each sensor.

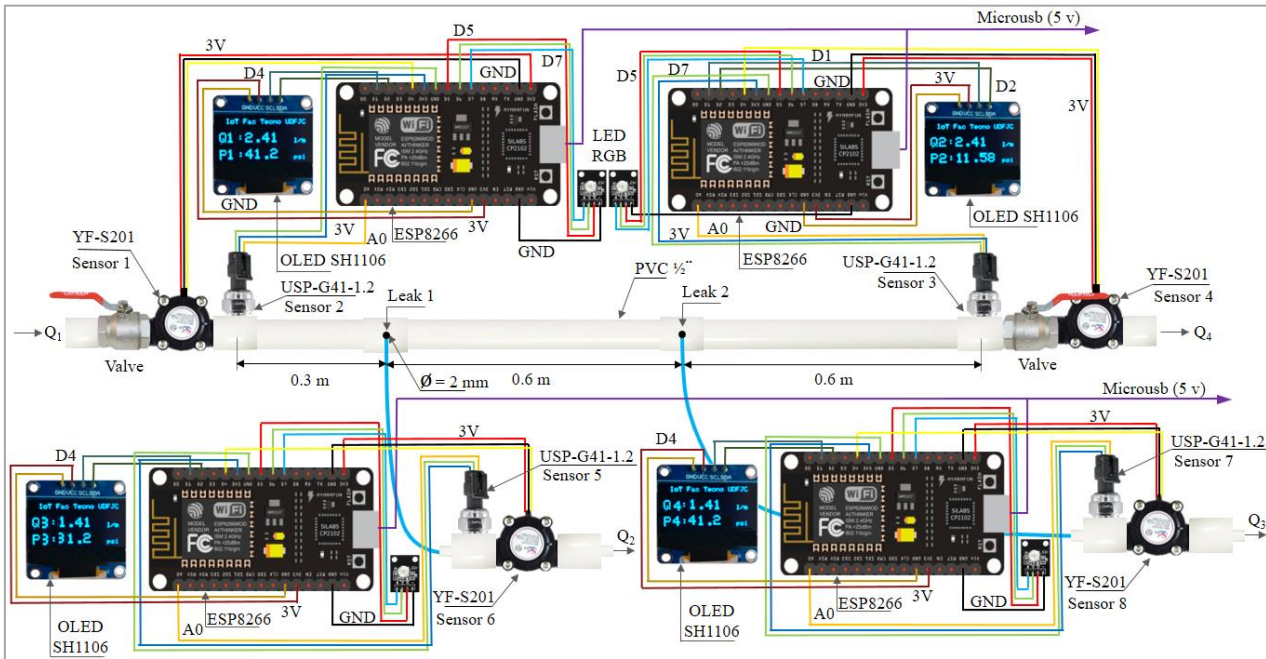


Figure 3. Electronic Prototype

During the analysis of the data from the USP-G41-1.2 and YF-S201 sensors, FFT was applied to the signal to identify patterns, trends, or anomalies in the observed data. When performing this transformation, it was found that the frequency spectrum of the flow sensor (YF-S201) showed the presence of subpeaks at frequencies of 75, 250, and 35 Hz, along with a dominant frequency component. In contrast, the signal from the USP-G41-1.2 sensor, which measures the pressure in the pipeline, exhibited dominant sub-peaks at a frequency of 200 Hz, as well as some minor peaks at 260 and 340 Hz. These findings suggest the existence of specific patterns in the signals measured using both sensors. Figure 4 shows the methodological approach used in this study to develop a conservative Hamiltonian dynamic system for the early detection of pipeline leaks. The development was divided into six phases, ranging from the application of the mass and energy conservation equations to the coupling and solution of the Hamiltonian equations.

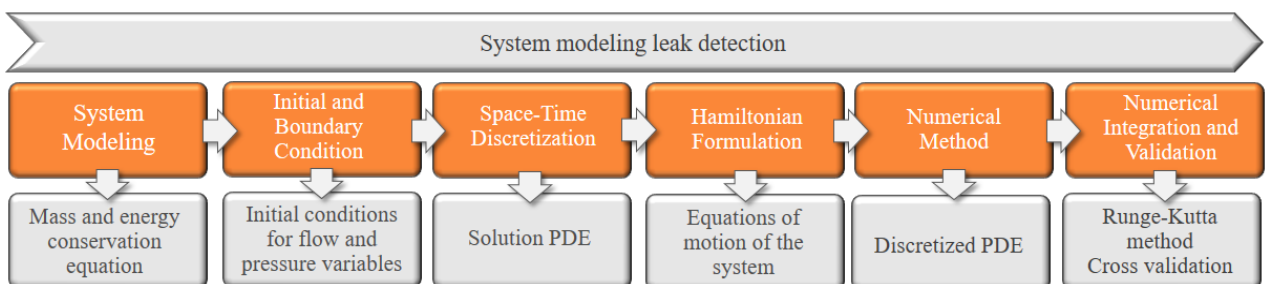


Figure 4. Leak detection modeling

2.4. Filters

The application of filters in a time series implies a reduction in the noise present in the signal, both from the sensor and that generated by environmental conditions. The challenge lies in selecting an appropriate filter that eliminates noise without significantly affecting the key signal information, particularly the detection of peaks and subpeaks that indicate the presence of leaks in piping systems. For example, Kulmány et al. (2023) [23] maintained that calibration could be performed using capacitive sensors. For this reason, the calibration of the sensors was carried out using as a reference a standard average obtained from a pressure manometer of the SCJN series, with a precision of $\pm 0.5\%$ FS.

In addition, a YF-S201 sensor was used to measure the amount of fluid passing through the system. For this calibration process, a LUXQ series intelligent vortex flow meter with a two-wire 4–20-mA output and high precision was used. The time series of the pressure and flow were affected by the implementation of three filters: low-pass, high-pass, and moving average filters. The statistical behaviors of these filtered signals are shown in Tables 4 and 5.

Table 4. Implemented filter statistics (Pressure)

Filter	Average	Typical error	Median	Standard deviation	Kurtosis	Skewness
Low-pass	45.963	9.013	9.032	52.582	0.053	23.303
High-pass	-0.001	-0.0086	-0.005	-1.27e-06	0.155	0.024
Moving average	50.500	9.002	9.0125	50.500	0.0673	28.961

Table 5. Implemented filter statistics (Flow)

Filter	Average	Typical error	Median	Standard deviation	Kurtosis	Skewness
Low-pass	45.964	5.942	5.965	52.582	0.0407	23.303
High-pass	-0.005	0.002	-0.0008	-1.27e-06	0.144	0.024
Moving average	50.500	5.934	5.9619	50.500	0.049	28.961

In Figure 5, the proposed filters for the pressure and flow signal are shown. It can be observed that, in the case of flow, the high-pass filter eliminates peaks whose amplitudes are in the range -0.3 to 0.3 , which affects the detection of peaks and subpeaks generated by the sudden appearance of leaks in the flow hydraulic system. In statistical terms, it was decided to use the moving average filter for the USP-G41-1.2 and YF-S201 sensors. This filter was programmed in Arduino, which allowed for obtaining a clean signal at the output of the ESP8266 microcontroller, clearly indicating the peaks generated by the two leaks in the system.

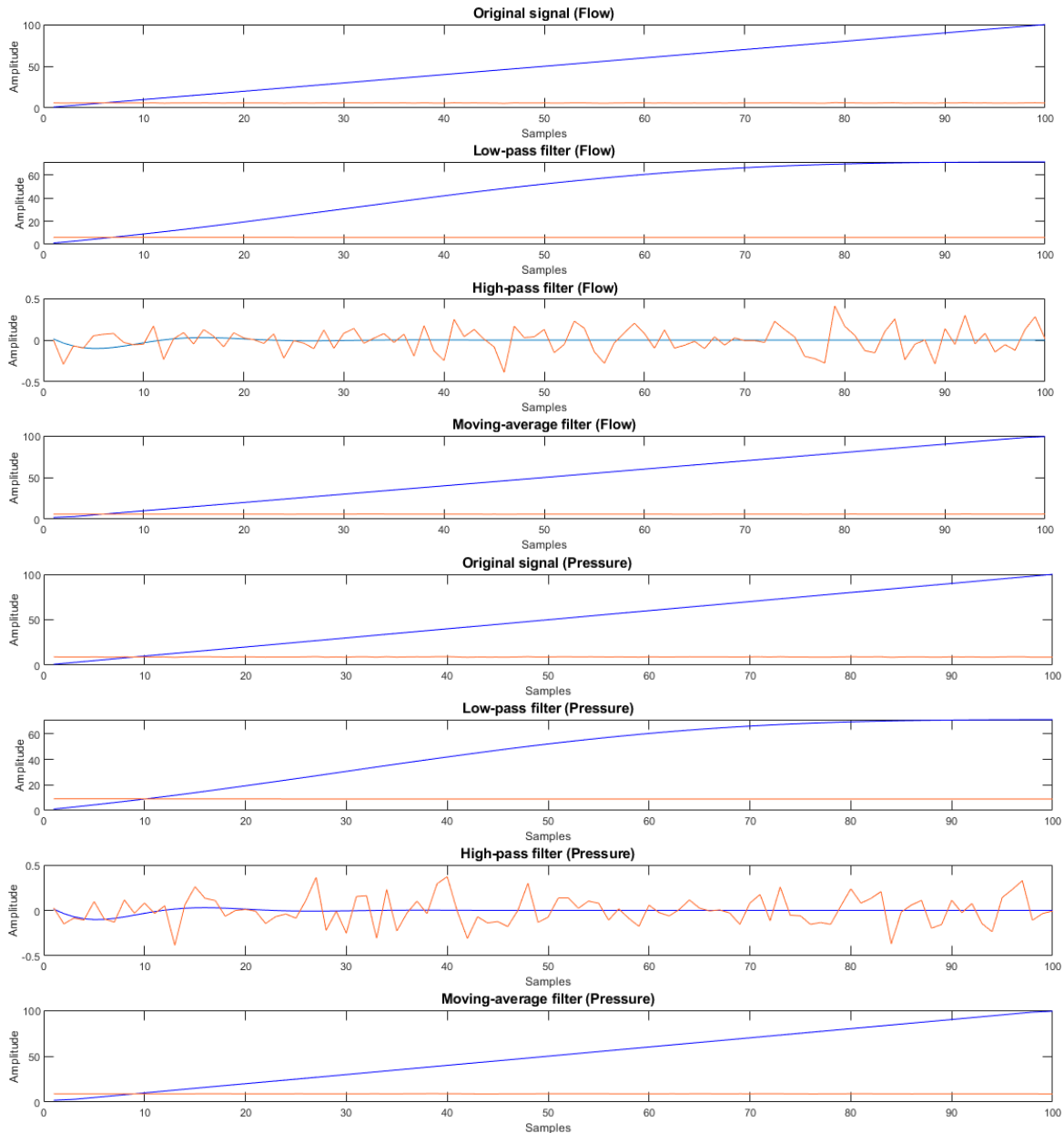


Figure 5. Filters USP-G41-1.2 y YF-S201

During the analysis of the spectral frequency of the flow, significant subpeaks were observed at two specific frequencies: 250 and 35 Hz. (Figure 6). These sub-peaks indicate the existence of prominent frequency components in the flow signal. Regarding the pressure signal, notable sub-peaks were also identified in the frequency spectrum. Specifically, one sub-peak was observed at a frequency of 260 Hz and the other at 340 Hz. These sub-peaks indicate the presence of specific frequency components in the pressure signal. Thus, the analysis of the spectral frequency of both signals provides important information regarding the characteristics and behavior of the studied hydraulic system. This information can be used to identify possible problems or anomalies in the system caused by a leak.

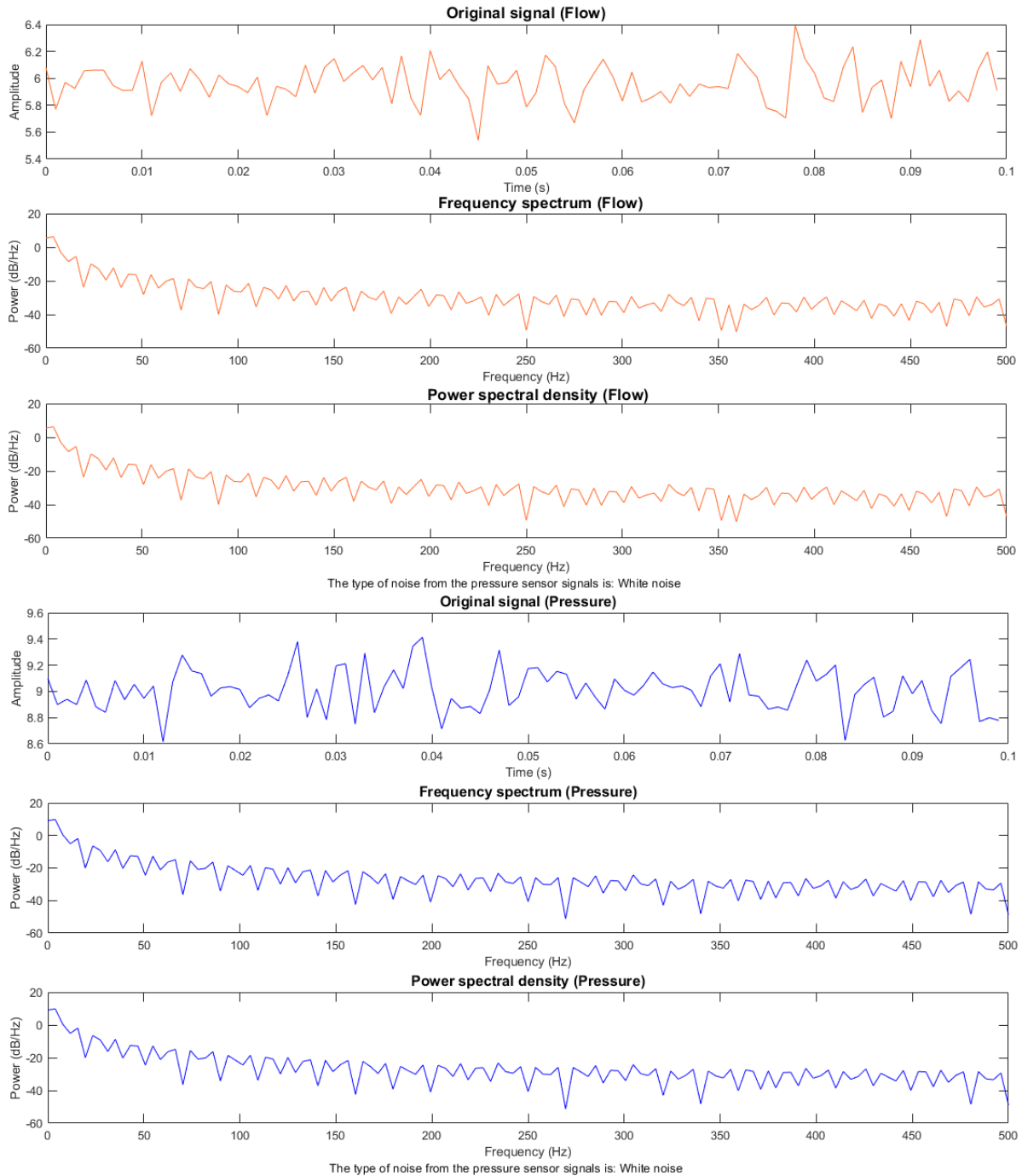


Figure 6. Event detection

The analysis of the spectrogram of the YF-S201 flow sensor allowed for the visualization of the energy distribution as a function of time and frequency. This provides detailed information regarding the variations in flow over time and the frequencies at which they occur.

For example, when observing the spectrogram, recurring patterns were identified for frequencies of 100–200 Hz, evidencing rapid high-energy fluctuations at higher frequencies, whereas at other times, the energy was concentrated at lower frequencies, indicating a more rapid flow stability (Figure 7).

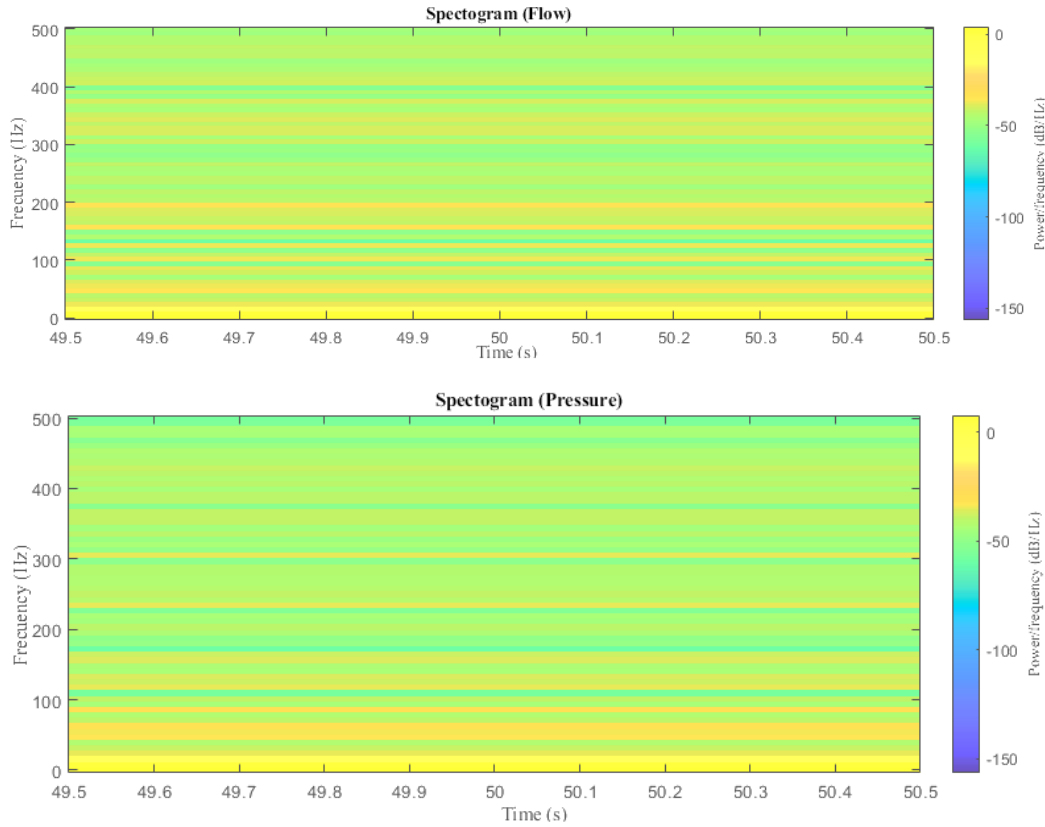


Figure 7. Spectrogram (Flow and pressure)

2.5. Flow Rate and Pressure Functions

To achieve successful coupling of the conservative Hamiltonian method, it is essential to accurately model the pressure and flow behaviors at each leak. This involves carrying out an observation and quantification of the pressure and flow in each leak, to generate a regression that optimally fits the data obtained. These modeled equations are added to the existing Hamiltonian model, thus creating a system of two differential equations that allows for energy contributions to the hydraulic system to be monitored and evaluated. This comprehensive approach provides a more complete and precise understanding of the interactions and energy flows in a system in the event of disturbances (leaks). Figure 8 shows the models for the flow rate and pressure for leak₁.

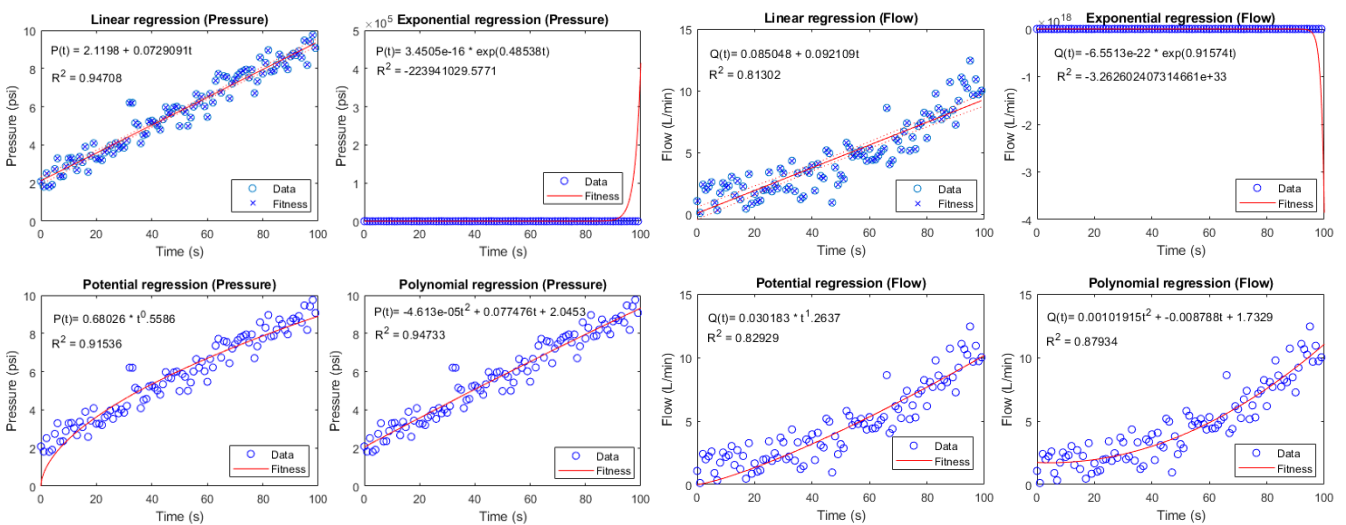


Figure 8. Flow rate and pressure models for initial leak

For leak₂, located 0.9 m from the upstream flow sensor, a linear regression function is established for pressure with a coefficient of determination equal to 0.948. Likewise, for the behavior of the flow rate of leak₂, a polynomial was obtained with a coefficient of determination equal to 0.849 (Figure 9).

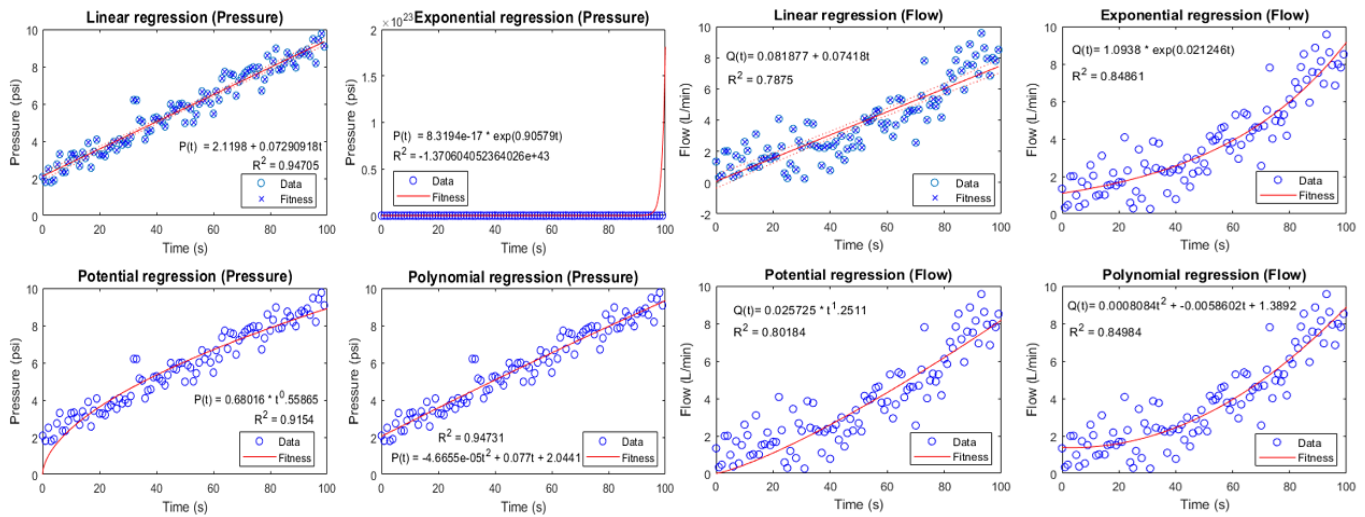


Figure 9. Flow rate and pressure models for the final leak

Table 6 presents a list of functions relating to the flow rate and pressure in the context of leaks.

Table 6. Flow rate and pressure models

Leak	Location (m)	Flow function	Pressure function
Leak ₁	0.3	$Q_1(t) = 0.00101915t^2 - 0.008788t + 1.7329$	$P_1(t) = 2.1198 + 0.0729091t$
Leak ₂	0.9	$Q_2(t) = 0.00080849t^2 - 0.0058602t + 1.3892$	$P_2(t) = 2.1195 + 0.072918t$

2.6. Hamiltonian System for Leak Detection

According to Bedford (2021) [24] the application of Hamilton's principle in classical fluid mechanics involves the use of this principle to describe and analyze the behavior of moving fluids in energetic terms. The implementation of the Hamiltonian model in the study of leaks requires mathematical models that describe the disturbances and flow rates of each leak. In this study, the real-time monitoring of pressure and flow at four strategic points along a pipeline was proposed. Four YF-S201 sensors were used to measure the flow, which provided information regarding the flow of water in the system along the pipe and at predefined leak points. These sensors were placed at the beginning of the system, at the end of the pipe, and each of the induced leaks. The mass change rate owing to leakage was modeled as a function of the flow rate concerning time. In addition, four USP-G41-1.2 sensors were installed to capture pressure records at the points mentioned above.

This allowed disturbances associated with the pressure in the system to be detected. Thus, it is essential to consider the temporality of events when analyzing dynamic systems. At the onset of a leak, a transient event occurs in which the flow is unstable and fluctuating. As time progressed, the flow tended to stabilize and approached a steady state where it remained constant. Therefore, when modeling a leak, it is necessary to consider its temporal evolution. This involves considering how the flow rate changes over time and approaches a steady state. By considering this temporal evolution in a hydraulic system in the presence of two simultaneous leaks, the incidence of leaks can be evaluated in terms of flow and pressure. First, the positions of the leaks in the pipe are identified by establishing the corresponding abscissa. Subsequently, the physical characteristics of the leak, such as the size, shape, and duration, were established. The size of the hole significantly affects the behavior of the leak over time; in this study, the hole size for each leak was equal to 2 mm. Once this was completed, the flow rate was modeled for the flow rate and disturbances in terms of pressure, determining four functions that represented the temporal evolution of the two leaks induced in the system. Subsequently, these functions were added to the mass-conservation and Bernoulli equations to configure the Hamiltonian dynamic models. Figure 10 shows the methodology proposed in this study.

Subsequently, a simulation of the model with different leakage scenarios was performed to evaluate the detection and quantification capacities of the mass generated by the two leaks. These simulations made it possible to adjust the model parameters and optimize their performance. Various tests were conducted to validate the Hamiltonian model based on the experimental model. Controlled leaks were induced in the hydraulic system and compared with the measurements obtained from model predictions. The advantage of using a Hamiltonian dynamic system is that it allows the behavior of state variables, such as the flow and pressure in the pipe, to be precisely modeled and analyzed based on the conservative properties of the system.

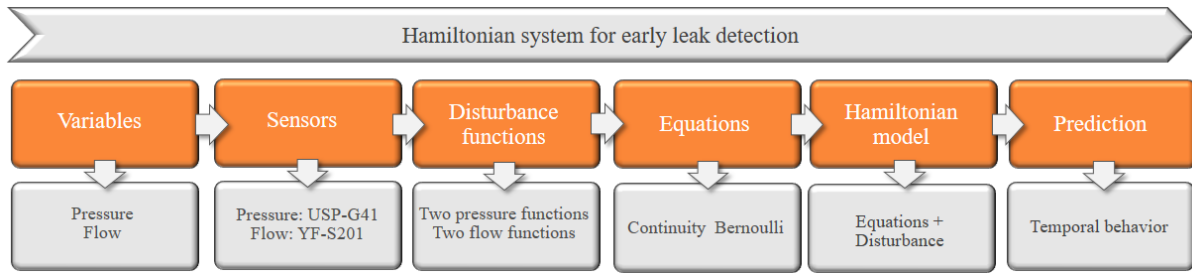


Figure 10. Hamiltonian method for leak detection

3. Results and Discussion

If we consider a pipe with two leaks and the functions for the flow and pressure in each leak, it is possible to propose a system of Hamiltonian equations that considers both the conservation of mass and energy in the pipe, as well as

$$\frac{\partial Q}{\partial t} = -\frac{\partial H}{\partial P} = -\frac{\partial(P^2/2A)}{\partial x} + Leak(Q_1(t)) + Leak(Q_2(t)) \tag{9}$$

where $Q(t)$ is the flow, $P(t)$ is the pressure, A is the cross-sectional area of the pipe, $Leak_1(Q_1(t))$ is leak rate₁ and $Leak_2(Q_2(t))$ leak rate₂. For the pressure in the system, we have

$$\frac{\partial P}{\partial t} = -\frac{\partial H}{\partial Q} = -\frac{\partial(Q^2/2A)}{\partial x} + Perturbation_1(P_1(t)) + Perturbation_2(P_2(t)) \tag{10}$$

where $Perturbation_1(P_1(t))$ is Pressure₁ in leak₁ and $Perturbation_2(P_2(t))$ is Pressure₂ in Leak₂. In this study, it was found that the first leak ($Leak_1$) was located at a distance of 0.3 m from the initial valve, while the second leak ($Leak_2$) was located at a distance of 0.9 m from the initial valve. Using the data collected by YF-S201 for flow and USP-G41-1.2 for pressure, four mathematical models were developed to describe the observed variables concerning time. Therefore, the system of Hamiltonian equations is represented by

$$\frac{\partial Q}{\partial t} = -\frac{\partial H}{\partial P} = -\frac{\partial(P^2/2A)}{\partial x} + 0.00101915t^2 - 0.008788t + 1.7329 + 0.00080849t^2 - 0.0058602t + 1.3892 \tag{11}$$

$$\frac{\partial Q}{\partial t} = -\frac{\partial(P^2/2A)}{\partial x} + 0.00182764t^2 - 0.0146482t + 3.1221 \tag{12}$$

For pressure, we have

$$\frac{\partial P}{\partial t} = -\frac{\partial(Q^2/2A)}{\partial x} + 2.1198 + 0.0729091t + 2.1195 + 0.072918t \tag{13}$$

$$\frac{\partial P}{\partial t} = -\frac{\partial(Q^2/2A)}{\partial x} + 4.2393 + 0.1458271t \tag{14}$$

The Hamiltonian system proposed in Equations 12 and 14 was solved using the Runge–Kutta method. Considering the length of the pipe, $L = 1.5 \text{ m}$, it was divided into 15 intervals of length (N), where $\Delta x = L/N = 1.5/15 = 0.1$, and time will move forward with one step $\Delta t = 0.1$. The spatial step (Δx) is equal to 15. Subsequently, the variables and initial conditions are initialized, for which vectors Q and P of size $N + 1$ represent the values of Q and P on each abscissa of the pipe. The initial conditions $Q(x, 0) = 0$ and $P(x, 0) = 1$ were established for all x . Then, it iterated in time for each time step $t = 0, \Delta t, 2\Delta t, \dots, T$ (where T is the desired final time) and for each point in the pipeline $i = 1, 2, \dots, N - 1$. Given the above, the spatial derivatives were calculated using centered finite differences (Figure 11).

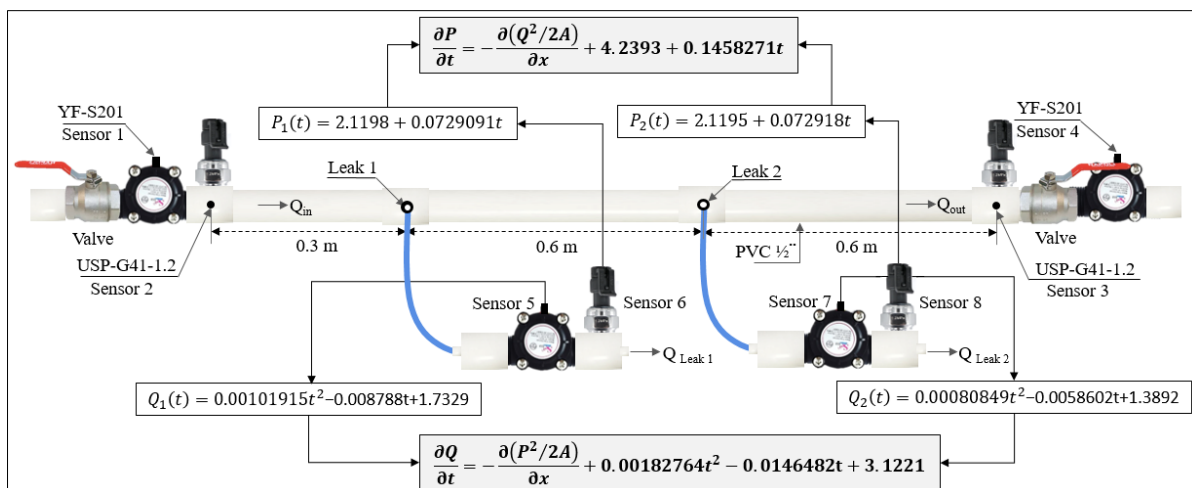


Figure 11. Assembly system of differential equations

Applying the fourth-order Runge–Kutta method to solve the Hamiltonian ensemble, we obtain

$$k_1 = h \cdot f(t_n, P_n) \tag{15}$$

$$k_2 = h \cdot f\left(t_n + \frac{h}{2}, P_n + \frac{k_1}{2}\right) \tag{16}$$

$$k_3 = h \cdot f\left(t_n + \frac{h}{2}, P_n + \frac{k_2}{2}\right) \tag{17}$$

$$k_4 = h \cdot f(t_n + h, P_n + k_3) \tag{18}$$

where h is the time step, t_n is the time at step n , P_n is the value of P at step n , and $f(t, P)$ is the function on the right side of the difference equation; thus, the update is given by

$$P_{n+1} = P_n + \frac{1}{6}(k_1 + 2k_2 + 2k_3 + k_4) \tag{19}$$

In terms of pressure, we have;

$$\frac{\partial(P^2/2A)}{\partial x} \tag{20}$$

For the flow, we have

$$\frac{\partial(Q^2/2A)}{\partial x} \tag{21}$$

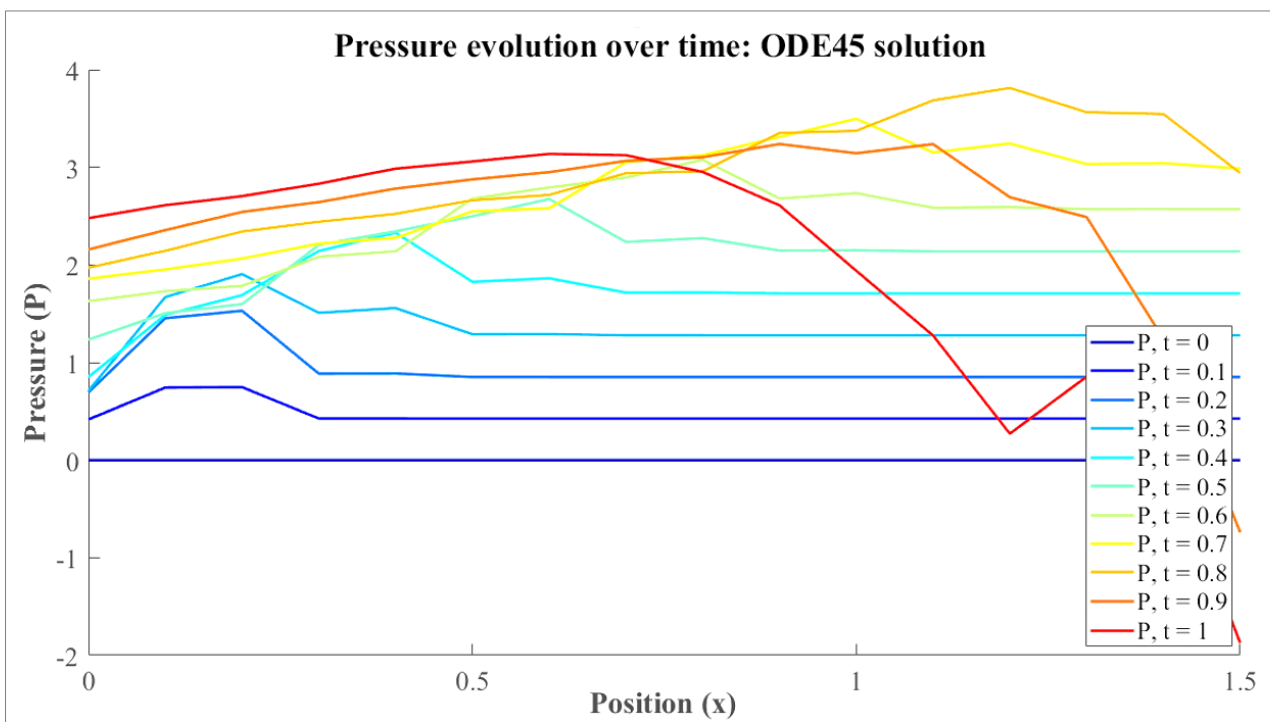
Then, the time derivatives are calculated as $\frac{\partial Q}{\partial t}$ and $\frac{\partial P}{\partial t}$ using the equations of the Hamiltonian system. Next, the fourth-order Runge-Kutta method was applied to update the values of Q and P . From the calculated derivatives, we obtained $k_1Q, k_1P, k_2Q, k_2P, k_3Q, k_3P, k_4Q, k_4P$, where the values of Q and P were updated.

$$Q[i] = Q[i] + (\Delta t/6)(k_1Q + 2k_2Q + 2k_3Q + k_4Q) \tag{22}$$

For the pressure, we have

$$P[i] = P[i] + (\Delta t/6)(k_1P + 2k_2P + 2k_3P + k_4P) \tag{23}$$

Finally, boundary conditions were applied as $P(0, t) = P(L, t) = 1$, to update the values of $P[0]$ and $P[N]$. Figure 12 presents the solution system of differential equations using the fourth-order Runge–Kutta method (ODE45), where the evolution of the state variables is graphed as Q and P at that time. After the ODE45 algorithm was used to solve the system of differential equations that modeled the pressure in a pipe, it was found that there was a minimum pressure equal to 0.3 psi for one second at a distance of 1 m from the pipe. This result indicates that at a specific point in the pipe, there was a significant reduction in the pressure of the fluid caused by the appearance of leaks 1 and 2. The solution obtained using the ODE45 method allowed us to analyze the evolution of the pressure over time and position in the pipeline.



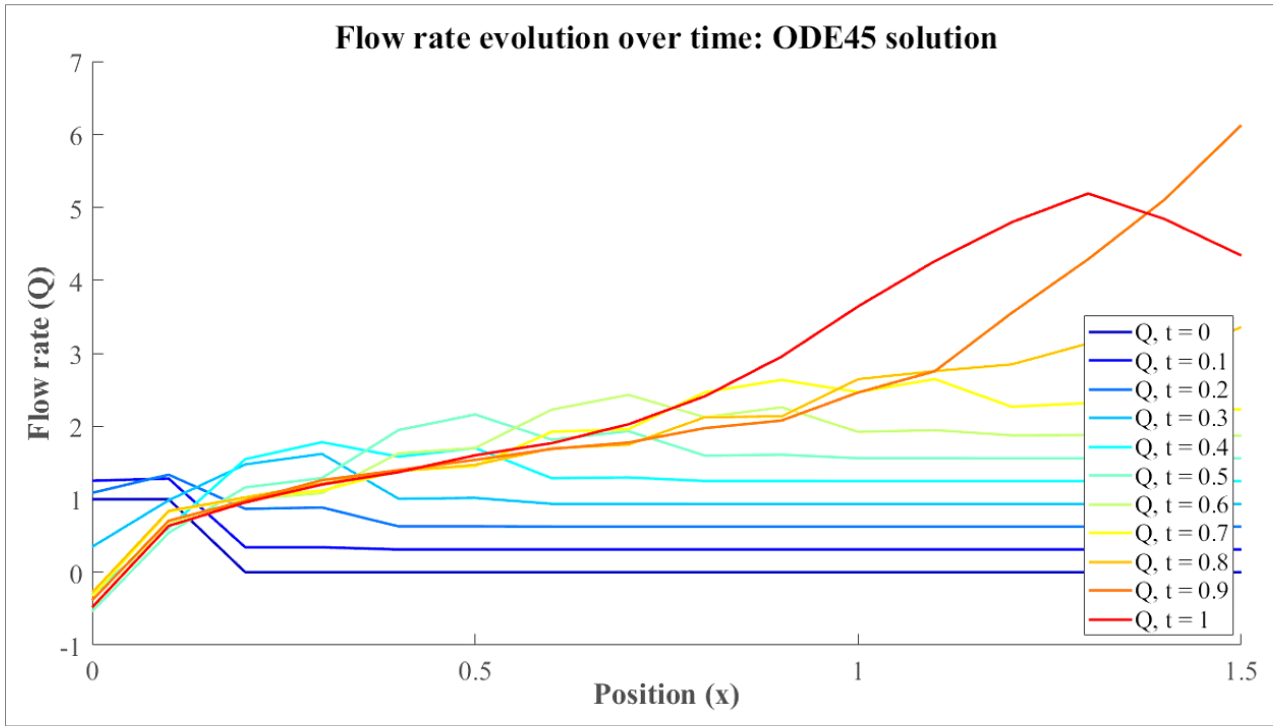
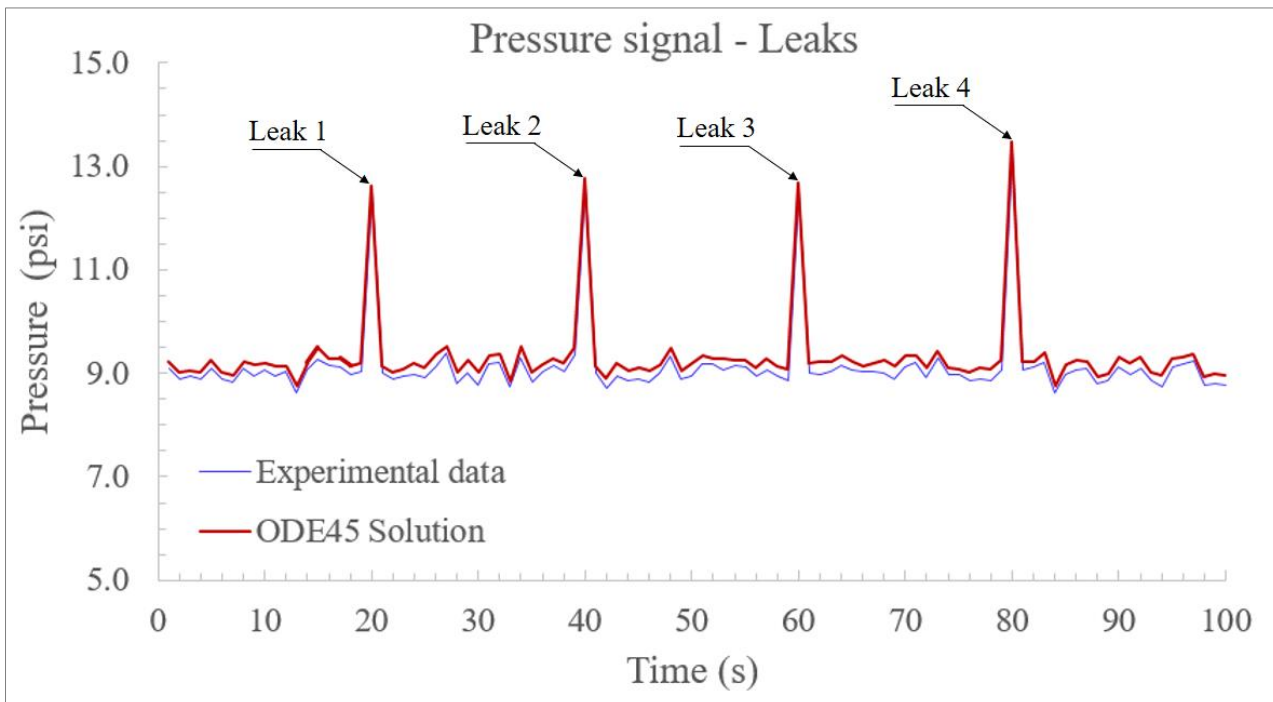


Figure 12. ODE45 Solution (Pipe Length)

Figure 13 shows a comparison of the results obtained using the Hamiltonian model and the data observed in the experimental model. The precision of the pressure and flow quantification for each leak was evaluated, and an accuracy level of 95% was obtained. This demonstrates the ability of the numerical model to accurately estimate the mass and position of each leak.



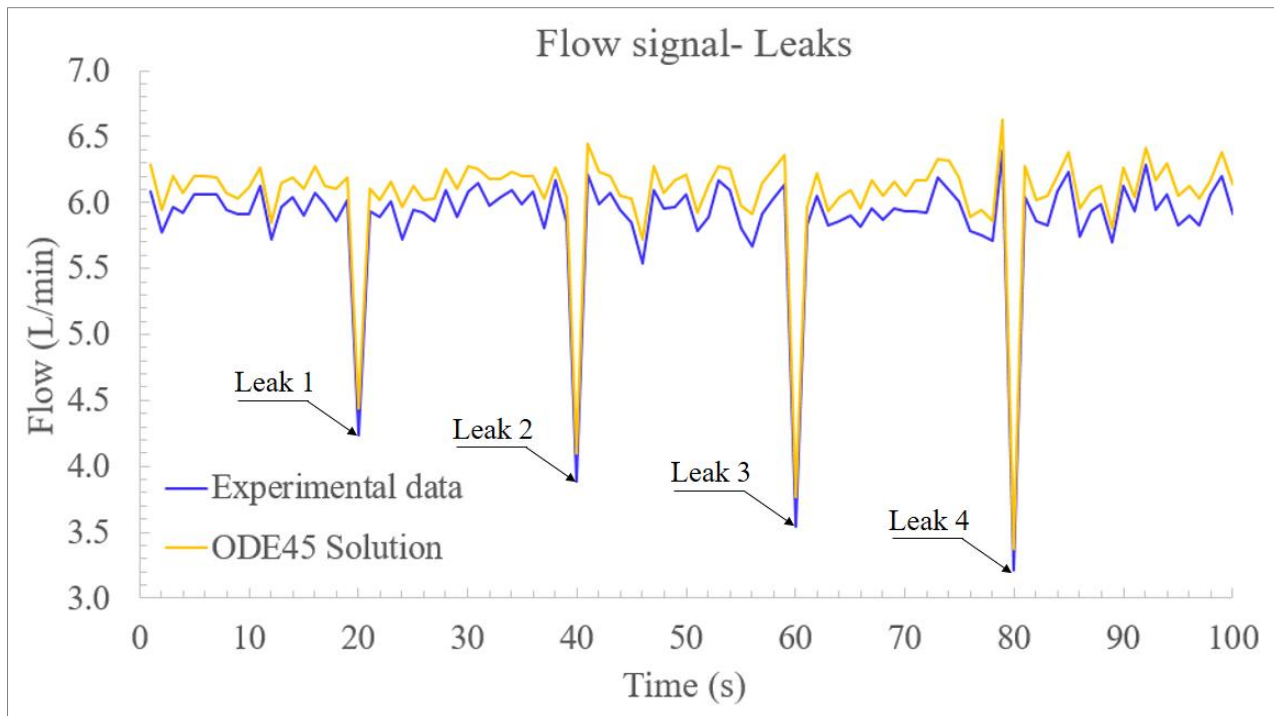


Figure 13. ODE45 Solution (Time)

4. Conclusion

The development of a conservative Hamiltonian dynamic system for the early detection of leaks in pressure pipelines represents a significant innovation in applied research and contributes significantly to the field of applied mathematical modeling. This study demonstrates how this approach can be used to understand and predict the behavior of dynamic systems, such as hydraulic networks. The fusion of conservative Hamiltonian equations with IoT technologies and the implementation of a hybrid model proved to be highly effective, achieving an accuracy of 95% for leak detection. This level of precision validated the ability of the proposed model to identify anomalies in real-time, thus contributing to improvements in the management of drinking water distribution systems.

The fusion of mathematical models and IoT technologies offers a comprehensive methodology for addressing the challenge of detecting and quantifying leaks in hydraulic systems in real-time. The application of filters to sensor signals, identification of patterns in the spectral frequency, and successful coupling of the flow rate and pressure functions demonstrate the effectiveness of integrating mathematical models and advanced technologies in leak detection and monitoring. The application of the conservative Hamiltonian model in the early detection of leaks can contribute to the efficient management of water resources because of the model's ability to maintain the total energy of the system constant, monitor it in real-time, and generate synchronous responses for decision-making when an event occurs. Finally, the ability to model and understand the interactions between variables in a multi-perturbed system demonstrates the applicability of the conservative Hamiltonian approach to real-world situations. This contribution is relevant to researchers interested in the analysis and modeling of complex systems in various disciplines.

5. Declarations

5.1. Author Contributions

Conceptualization, C.A.G.U. and E.Z.H.; methodology, C.A.G.U., E.Z.H., and E.O.L.M.; software, E.O.L.M.; validation, E.O.L.M.; formal analysis, C.A.G.U., E.Z.H., and E.O.L.M.; investigation, E.O.L.M.; data curation, C.A.G.U. and E.Z.H.; writing—original draft preparation, C.A.G.U., E.Z.H., and E.O.L.M.; writing—review and editing, C.A.G.U., E.Z.H., and E.O.L.M.; visualization, E.O.L.M.; supervision, E.O.L.M. All authors have read and agreed to the published version of the manuscript.

5.2. Data Availability Statement

Data supporting the findings of this study are available upon request from the corresponding authors.

5.3. Funding

The authors received no financial support for the research, authorship, and/or publication of this article.

5.4. Acknowledgements

The authors express their gratitude to the Technological Faculty of Francisco José de Caldas District University (Bogotá, Colombia) for their support in this study and for providing access to the Hydraulics Laboratory equipment.

5.5. Conflicts of Interest

The authors declare no conflict of interest.

6. References

- [1] Xie, J., Huang, B., & Dubljevic, S. (2024). Moving Horizon Estimation for Pipeline Leak Detection, Localization, and Constrained Size Estimation. doi:10.2139/ssrn.4730270.
- [2] Speziali, S., Bianchi, F., Marini, A., Menculini, L., Proietti, M., Termete, L. F., Garinei, A., Marconi, M., & Delogu, A. (2021). Solving Sensor Placement Problems in Real Water Distribution Networks Using Adiabatic Quantum Computation. IEEE International Conference on Quantum Computing and Engineering (QCE), Broomfield, Colorado, United States. doi:10.1109/qce52317.2021.00079.
- [3] Verde, C., & Torres, L. (2017). Modeling and monitoring of pipelines and networks. Springer, Cham, Switzerland. doi:10.1007/978-3-319-55944-5.
- [4] Rodríguez Calderón, W., & Pallares Muñoz, M. R. (2007). A numerical water-hammer model using Scilab. *Ingeniería e Investigación*, 27(3), 98–105. doi:10.15446/ing.investig.v27n3.14850. (In Spanish).
- [5] Firouzi, A., Yang, W., Shi, W., & Li, C.-Q. (2021). Failure of corrosion affected buried cast iron pipes subject to water hammer. *Engineering Failure Analysis*, 120, 104993. doi:10.1016/j.engfailanal.2020.104993.
- [6] Sánchez-Jiménez, A. D., Torres, L., & López-Estrada, F. R. (2020). Euler-Lagrange approach for modeling water pipelines with leaks. *Memorias del Congreso Nacional de Control Automático*, 1-7.
- [7] Macias, G., & Lee, K. (2022). Optimal Gas Leak Localization and Detection using an Autonomous Mobile Robot. Proceedings of the 9th International Conference of Control, Dynamic Systems, and Robotics (CDSR'22), Niagara Falls, Canada. doi:10.11159/cdsr22.122.
- [8] Schneider, J., Tél, T., & Neufeld, Z. (2002). Dynamics of “leaking” Hamiltonian systems. *Physical Review E - Statistical Physics, Plasmas, Fluids, and Related Interdisciplinary Topics*, 66(6), 6. doi:10.1103/PhysRevE.66.066218.
- [9] Torres, L., & Besancon, G. (2019). Port-Hamiltonian Models for Flow of Incompressible Fluids in Rigid Pipelines with Faults. 2019 IEEE 58th Conference on Decision and Control (CDC), Nice, France. doi:10.1109/cdc40024.2019.9029170.
- [10] Perryman, R., Taylor, J. A., & Karney, B. (2022). Port-Hamiltonian based control of water distribution networks. *Systems & Control Letters*, 170. doi:10.1016/j.sysconle.2022.105402.
- [11] Lopezlena, R. (2014). Computer implementation of a boundary feedback leak detector and estimator for pipelines II: Leak estimation. *Memorias del XVI Congreso Latinoamericano*, 14-17 October, 2014, Cancún, Mexico.
- [12] Rashad, R., Califano, F., Schuller, F. P., & Stramigioli, S. (2021). Port-Hamiltonian modeling of ideal fluid flow: Part II. Compressible and incompressible flow. *Journal of Geometry and Physics*, 164. doi:10.1016/j.geomphys.2021.104199.
- [13] Beattie, C., Mehrmann, V., Xu, H., & Zwart, H. (2018). Linear port-Hamiltonian descriptor systems. *Mathematics of Control, Signals, and Systems*, 30(4). doi:10.1007/s00498-018-0223-3.
- [14] Zi Li, L., Rosli, M. I., & Panuh, D. (2019). Velocity Modelling for Pipeline Inspection Gauge. *Jurnal Kejuruteraan*, 31(2), 275–280. doi:10.17576/jkukm-2019-31(2)-11.
- [15] Bendimerad-Hohl, A., Matignon, D., Haine, G., & Lefèvre, L. (2024). On implicit and explicit representations for 1D distributed port-Hamiltonian systems. *arXiv Preprint*, arXiv:2402.07628. doi:10.48550/arXiv.2402.07628.
- [16] Zhang, J., Zhu, Q., & Lin, W. (2024). Learning Hamiltonian neural Koopman operator and simultaneously sustaining and discovering conservation laws. *Physical Review Research*, 6(1), 12031. doi:10.1103/PhysRevResearch.6.L012031.
- [17] Eidnes, S., Stasik, A. J., Sterud, C., Bøhn, E., & Riemer-Sørensen, S. (2023). Pseudo-Hamiltonian neural networks with state-dependent external forces. *Physica D: Nonlinear Phenomena*, 446, 446. doi:10.1016/j.physd.2023.133673.
- [18] Sultana, S., & Rahman, Z. (2013). Hamiltonian Formulation for Water Wave Equation. *Open Journal of Fluid Dynamics*, 3(2), 75–81. doi:10.4236/ojfd.2013.32010.
- [19] Przystupa, K., Ambrozkiewicz, B., & Litak, G. (2020). Diagnostics of Transient States in Hydraulic Pump System with Short Time Fourier Transform. *Advances in Science and Technology Research Journal*, 14(1), 178–183. doi:10.12913/22998624/116971.

- [20] Ji'e, M., Yan, D., Sun, S., Zhang, F., Duan, S., & Wang, L. (2022). A Simple Method for Constructing a Family of Hamiltonian Conservative Chaotic Systems. *IEEE Transactions on Circuits and Systems I: Regular Papers*, 69(8), 3328–3338. doi:10.1109/TCSI.2022.3172313.
- [21] Phipps Electronics. (2024). YF-S201 Hall Effect Water Flow Meter / Sensor. Phipps Electronics, North Revesby, Australia. Available online: <https://www.phippselectronics.com/product/yf-s201-hall-effect-water-flow-meter-sensor/> (accessed on March 2024).
- [22] Urbanowicz, K., Duan, H. F., & Bergant, A. (2020). Transient liquid flow in plastic pipes. *Strojniski Vestnik/Journal of Mechanical Engineering*, 66(2), 77–90. doi:10.5545/sv-jme.2019.6324.
- [23] Kulmány, I. M., Bede-Fazekas, Á., Beslin, A., Giczi, Z., Milics, G., Kovács, B., Kovács, M., Ambrus, B., Bede, L., & Vona, V. (2022). Calibration of an Arduino-based low-cost capacitive soil moisture sensor for smart agriculture. *Journal of Hydrology and Hydromechanics*, 70(3), 330–340. doi:10.2478/johh-2022-0014.
- [24] Bedford, A. (2021). *Hamilton's Principle in Continuum Mechanics*. Springer, Cham, Switzerland. doi:10.1007/978-3-030-90306-0.

Appendix I: Matlab Encoding ®: ODE45

Faculty of Technology | Civil Engineering
 Edgar O. Ladino M. | eoladinom@udistrital.edu.co
 Microcontroller: Esp8266
 www.edgarladino.com

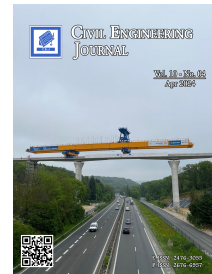
-----//

-----Development of a conservative Hamiltonian dynamic system for the early detection of leaks
 in pressure pipes-----//

```
function main()
    L = 1.5; % Pipe length
    N = 15; % Number of intervals
    dx = L/N; % space step
    SD = 0.1; % Time step
    T = 1; % Final time
% Define initial conditions
    x = 0:dx:L;
    Q0 = zeros(size(x));
    P0 = zeros(size(x));
    Q0(1) = 1; % Initial condition for Q at x = 0
    P0(1) = 1; % Initial condition for P at x = 0
% Solve the system of partial differential equations
    [t, y] = ode45(@rhs, 0:dt:T, [Q0; P0]);
% Plott Q
    figure;
    hold on;
    colors = parula(length(t));
    for i = 1:length(t)
        plot(x, y(i, 1:N+1), 'Color', colors(i,:), 'DisplayName', ['Q, t = ', num2str(t(i))]);
    End
    xlabel('x');
    ylabel('Q');
    legend('show');
    hold off;
% P Chart
    figure;
    hold on;
    for i = 1:length(t)
        plot(x, y(i, N+2:end), 'Color', colors(i,:), 'DisplayName', ['P, t = ', num2str(t(i))]);
    End
    xlabel('x');
    ylabel('P');
    legend('show');
    hold off;
function dydt = rhs(t, y)
    A = 1; % Pipe Area
    Q = y(1:N+1);
    P = y(N+2:end);

    dQdt = -gradient(P.^2/(2*A), dx) + 0.00182764*t^2 - 0.00146482*t + 3.1221;
    dPdt = -gradient(Q.^2/(2*A), dx) + 4.2393 + 0.1458271*t;

    dydt = [dQdt; dPdt];
End
End
```



Corrosion Resistance of Reinforcing Steel in Concrete Using Natural Fibers Treated with Used Engine Oil

Alejandro Flores Nicolás ^{1*}, Elsa. C. Menchaca Campos ¹, Mario Flores Nicolás ², Omar A. Gonzalez Noriega ¹, Cesar A. García Pérez ¹, Jorge Uruchurtu Chavarín ¹

¹ Centro de Investigación en Ingeniería y Ciencias Aplicadas, Universidad Autónoma del Estado de Morelos, Cuernavaca, 62209, México.

² Instituto de Ingeniería, Universidad Nacional Autónoma de México, Cdmx, 04510, México.

Received 16 January 2024; Revised 12 March 2024; Accepted 21 March 2024; Published 01 April 2024

Abstract

The addition of natural fibers in the elaboration of concrete pastes has increased as an innovative alternative for the development of more ecological and environmentally friendly constructions. The objective of this research is to incorporate natural fiber residues from palm leaves and mango stone impregnated with used engine oil (UEO) in the cement matrix to improve the mechanical and electrochemical properties of reinforced concrete. Samples with fiber percentages of 0.2% and 0.4% with respect to the weight of the sand with a length of 10 mm were fabricated. Their properties, such as workability, air content, porosity, and compressive and flexural strength, were analyzed. To understand the corrosion rate of the steel bars, electrochemical techniques of corrosion potential, electrochemical noise, linear polarization resistance, and electrochemical impedance spectroscopy were applied to cubic samples exposed in a 3% sodium chloride saline environment for 365 days. The experimental results showed a positive effect on the corrosion phenomenon with the UEO and mango fiber treatment, decreasing the corrosion rate due to the formation of a protective film at the steel/concrete interface.

Keywords: Concrete; Natural Fibers; Corrosion; Used Engine Oil; Surface Treatment; Electrochemical.

1. Introduction

Concrete is a material used in construction due to its excellent mechanical properties in compression, and combined with reinforcing steel, the material acquires high tensile strengths. The cement paste passivates the steel, protecting it from corrosion agents due to its high alkalinity, which promotes a protective oxide layer that separates it from highly aggressive environments. However, corrosion of steel reinforcement and other embedded metals is the main cause of poor performance and durability problems in reinforced concrete (RC) structures [1]. The passive layer protecting the rebar is easily destroyed by carbonation and/or the presence of chlorides. Corrosion products occupy a larger volume than the original; internal steel corrosion products promoting tensile stresses will accumulate in the concrete [2]. After the passive layer is destroyed, a visible sign of corrosion appears on the surface of the structure, e.g., cracks, rust stains, concrete spalling, etc. [3]. To reduce the effects of corrosion, the need to obtain synthetic, natural, or waste materials as alternatives to conventional reinforced concrete has been sought [4].

The advantage of using natural waste as an alternative is its positive impact on the environment, which can be obtained at a low cost using traditional knowledge and practices [5–7]. How these natural materials are included in the concrete is through fibers such as jute [8], bamboo [9], coconut [10], palm [11], sugarcane bagasse [12], and others,

* Corresponding author: alejandro.floresnic@uaem.edu.mx

 <http://dx.doi.org/10.28991/CEJ-2024-010-04-02>



© 2024 by the authors. Licensee C.E.J, Tehran, Iran. This article is an open access article distributed under the terms and conditions of the Creative Commons Attribution (CC-BY) license (<http://creativecommons.org/licenses/by/4.0/>).

which have several advantages, including low density, high flexural strength, flexibility, and high elastic modulus [13]. These fibers consist of cellulose micro-fibrils suspended in a matrix of amorphous lignin/hemicellulose composition, which gives the natural fibers their chemical composition [14]. The introduction of new types of vegetable fibers to concrete has been investigated as it has a great perspective and potential in the construction sector. Vegetable fibers from palm leaves and mango stones are innovative agricultural residues that can be used in adequate quantities as concrete reinforcement, although they present durability problems. Water absorption is one of the main problems of natural fiber composites, which reduces their mechanical properties and dimensional stability, limiting their use in various applications [15–17].

Zhan et al. [18] explored the effect of natural jute fibers on compressive strength, and the results are critical because natural fibers swell by absorbing water (during casting and their lifetime), creating spaces between the fibers and the matrix. Shah et al. [19] observed that increasing the concentration of natural fiber decreased the settlement values in all specimens. These reported decreases in workability are the result of moisture absorption by hydrophilic natural fibers [20]. Numerous researchers have incorporated chemical or physical treatments into natural fibers to protect them from water absorption and avoid disadvantages such as fiber/cement biocompatibility [21, 22]. Used engine oil (UEO), generated by industrial activity and transportation around the world, generates great pollution because it is discharged specifically into groundwater and soil, generating high levels of carbon dioxide [23, 24]. This material can be added as a natural fiber treatment because it is a hydrophobic material, does not require a manufacturing process, and is an attractive option for the elimination of OEU. Juarez Alvarado et al. [6] used hydrophobic substances: linseed oil, linseed oil + natural resin, kerosene, kerosene + natural resin, wood sealant, and creosote as surface treatments for the lechuguilla fibers to reduce the absorption of water, concluding that the protective treatment with kerosene reduced the absorption capacity of the natural fiber.

Yousif et al. [25] studied the treatment of kenaf fibers immersed in 4 solutions: water, salt water, diesel, and engine oil, and obtained the conclusion that oil and diesel had a lower absorption rate of 20–30% compared to the untreated fiber of 90%, although it reduced the tensile strength. Wong et al. [26] evaluated the effects of fiber treatment on absorption in motor oils and petroleum, and their results showed that vegetable fibers have increased oil absorption, which reduces water absorption. Ramli et al. [27] evaluated coconut fibers incorporated in concrete with a percentage of silica fume as a binder and reported that, for more severe climates such as seawater chlorides, two factors influence the chloride penetration of concrete: the severity of exposure to the chloride source and the permeability of the specimens. However, the impact of the use of natural fibers treated with UEO on the corrosion of cementitious elements is still not clearly known.

The mechanical properties of concrete with natural fibers are variable; however, the scenarios and aggressive environments are still not clearly known. This work will take an innovative approach and provide further insight into the current literature on steel corrosion phenomena, so this research study describes the use of two natural fibers (mango stone and palm leaf) treated superficially with used engine oil (UEO) and used as reinforcements in concrete to improve mechanical and electrochemical properties such as compressive strength, flexural strength, and corrosion rate resistance.

2. Materials and Methods

2.1. Materials

Portland cement CPC 30 R was used for concrete sample preparation; according to the international ASTM C150 standard [28], river sand was used as fine aggregate with a 4.75 mm maximum particle size, crushed gravel (19 mm nominal size) as coarse aggregate, tap water, and natural fibers. The general methodology of the work is shown in the flowchart in Figure 1.

2.2. Fibers

Two types of fibers were used in the concrete: mango fibers (CMF) and palm fibers (CPF). Mango stone residues are considered as wastes, and solitary hermaphrodite Mexican Sabal palm are considered important component sources [29], distributed across the USA, Mexico, and Central America down to Venezuela and Colombia [30]. Both materials were cleaned, eliminating polluting residues, and afterward were dehydrated at room temperature for three days. The hollow tubular structure of the fibers also reduces their volume and density and makes them lighter [31], having different values as shown in Table 1.

Table 1. Fiber density

Fiber	Density (g/cm ³)	Fiber Type	Reference
Mango	0.91-1.08	Woody	[32]
Palm leaf	0.5-0.8	Leaf	[11]

Short fibers were cut manually with dimensions of 10 mm in length and 3-4 mm in width, and 0.1 mm in thickness and presented in Figure 2.

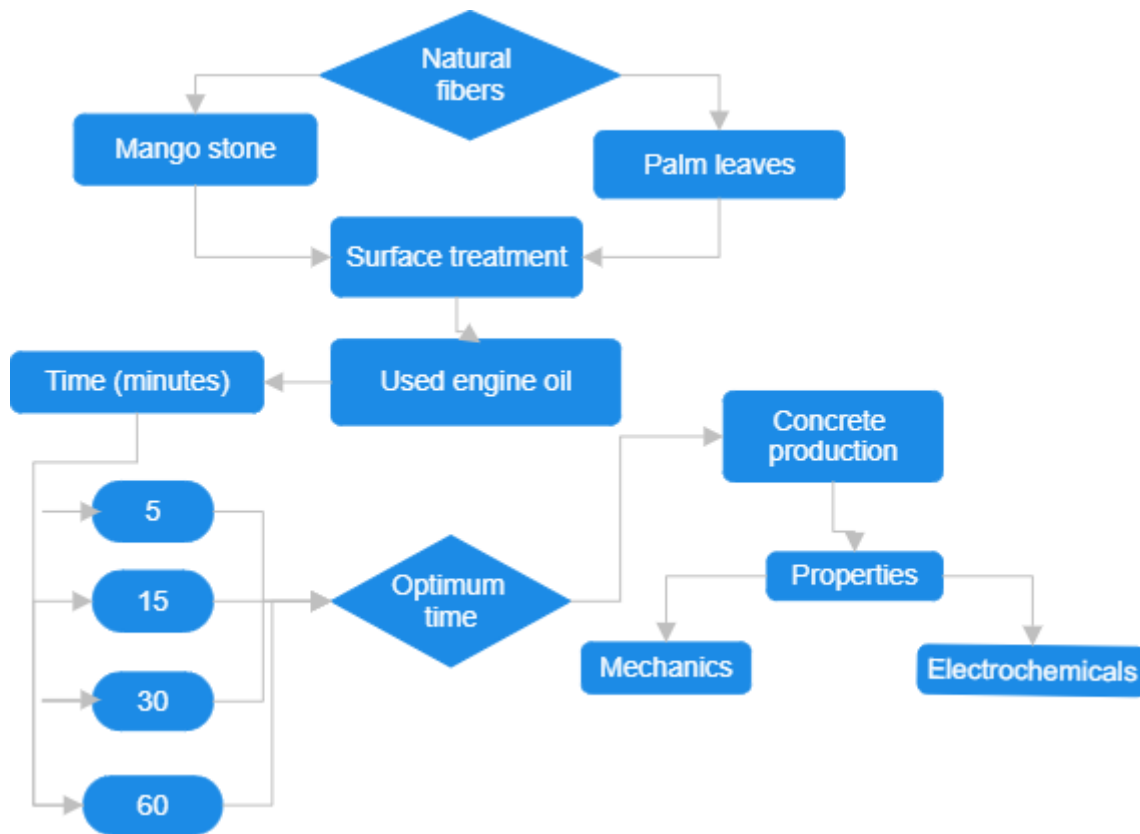


Figure 1. Flowchart of the experimental methodology

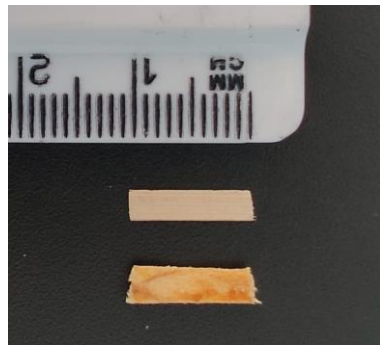


Figure 2. Measurements of natural fibers

2.3. Fibers Treatment

Fiber chemical treatment alters superficial energy and structural characteristics through the shallow cellular walls surfaces modification, without deteriorating its chemical composition [33]. The hydrophobic characteristic substance was used, being easy to obtain, recycled, and economical, with the purpose of reducing high water absorption, giving protection at high alkaline concrete. The UEO chemical properties are shown in Table 2.

Table 2. Used motor oil chemical properties

Chemical composition	Used engine oil (%)	Reference
Sulfur (SO ₃)	31- 37	[34, 35]
Chloride (Cl ⁻)	14.9-15.9	[34, 35]
Lead content (mg/kg)	3.6	[34]
Zinc (ZnO)	17.7-19.2	[34, 35]
Nitrite (Ni)	5.5	[34]
P ₂ O ₅	8.95	[35]
Others	4.12	[35]

Natural fibers surface treatment (TNF) using capillary impregnation using 30 CMF fiber or 50 CPF fiber strips. Afterwards, they were immersed in UEO at 70 °C temperature for 5, 15, 30, and 60 minutes as shown in Figure 3. These times are considered to obtain the best conditions to penetrate fibers completely and less natural fibers water absorption.

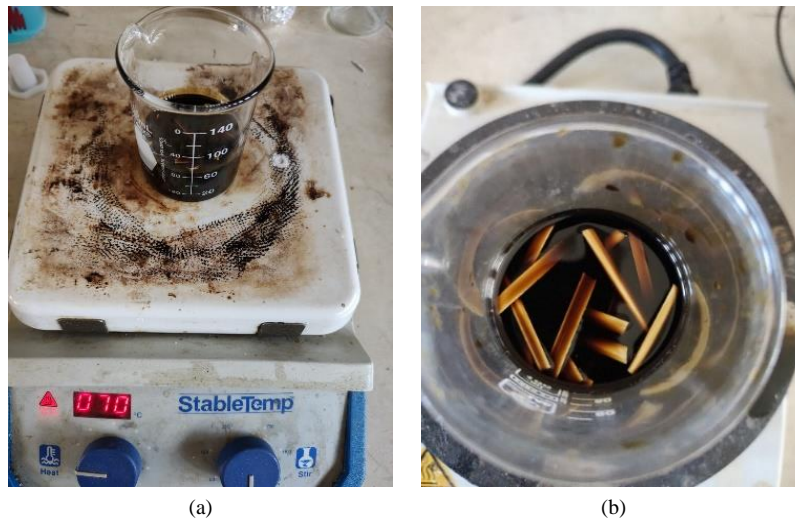


Figure 3. a) Surface impregnation of the fibers b) Fiber saturation

Afterward, humidity absorption was determined, by saturating fibers in distilled water for 24 hours, removing them, and cleansed with an absorbent cloth to retire UEO excess until obtaining dry superficial fibers, as seen in Figure 4. Then fibers were weighed on a 0.0001 g precision Denver Instrument electronic scale. The samples were dried again at 70 °C for one hour and weighed again.



Figure 4. Surface drying of treated fibers

For the calculation of water absorption percent (Wa %) Equation 1 was used, where W is the saturated water humidity weight and Wo dried weight at 70 °C [36-38]:

$$Wa\% = \frac{W - W_0}{W_0} \times 100 \tag{1}$$

Table 3 presents the natural fiber superficial treatment average absorption percent in 5, 15, 30, and 60 minutes immersed in UEO. In general, it can be appreciated the different percentages of mango and palm natural fibers, noticing fibers without treatment absorb a greater water quantity due to the presence of waxes and threads in the external layer from untreated fibers absorbing more from the solutions [25]. The water absorption diminished in treated fibers at 15 minutes immersed in the hydrophobic medium; that is, the treatment time presents a better response to the absorption resistance material as compared with untreated fiber absorption, therefore this immersion time was selected for concrete preparation.

Table 3. Absorption average percent for natural fibers

Fiber	Absorption in %				
	Untreated	Treatment (minutes)			
		5	15	30	60
CMF	39.24	34.69	31.24	29.84	29.92
CPF	56.91	37.71	37.64	45.64	50.33

2.4. Concrete Preparation

Table 4 presents the dosage for 80 liters of concrete using the absolute volumes method. A 300 kg/cm² (29.44 MPa) theoretical mix adding up fiber percents of 0.2 or 0.4 with respect to the sand weight, with 0.54 water/cement relation, without any additive.

Table 4. Concrete proportions for 80 liters

Material	C	0.2% fiber	0.4% fiber
Cement (Kg)	29.286	29.286	29.286
Water (l)	15.811	15.811	15.811
a/c	0.54	0.54	0.54
Sand (Kg)	52.049	51.947	51.842
Gravel (Kg)	83.811	83.811	83.811
Fiber (Kg)	0	0.104	0.208

Five mix designs were prepared, two mixtures of concrete with mango fibers (CMF,) in two percentages mentioned, and two mixtures of palm fiber (CPF) and control concrete (C). The nomenclature of the samples is specified in Table 5.

Table 5. Identification for samples

Material	Type of fiber	Percentage (%)	Nomenclature
	--	--	C
Cement	Mango	0.2	CMF-02
		0.4	CMF-04
	Palm	0.2	CPF-02
		0.4	CPF-04

The mixture was prepared as follows: first gravel, after a small quantity of water was poured. Then sand was added, then the cement, and finally the rest of the water incorporating the TNF. Physical tests such as air contained in the mixture, according to the standards [39, 40], as seen in Figure 5. Cylindrical specimens were prepared with standard dimensions of 15 cm diameter and 30 cm height [41] for 7 and 28 days of compression testing.

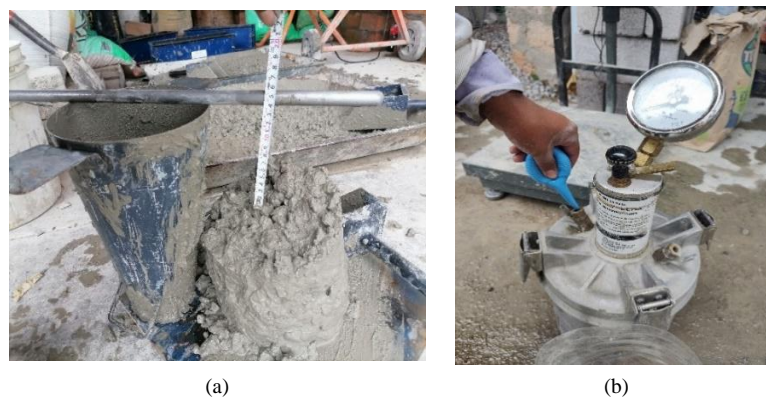


Figure 5. a) Slump test b) Air content

Samples were transported and kept in adequate conditions of humidity, and curing for 28 days. For flexural tests, concrete blocks 50 cm long, 15 cm wide, and 15 cm high were manufactured [41] for 28 days resistance test. A universal press with 120 tons maximum capacity was used for mechanical concrete tests. The standard procedure was used [42, 43] (load at third points) and flexural resistance was calculated using Equation 2:

$$f'f = \frac{PL}{bd^2} \quad (2)$$

where $f'f$ is the flexural resistance, P is the applied load, L is the distance between supporting points, b is the width, and d is the average slope of the sample as shown in Figure 6.



Figure 6. Concrete flexural strength test

Cubic samples were made for the electrochemical tests, with dimensions of 12 cm length, 8 cm width, and 12 cm height as shown in Figure 7, and three low carbon steel rods were embedded. The steel rods were named working electrodes W_1 and W_2 , and a third rod was used as an auxiliary electrode according to the electrochemical cell proposed for the different measurement techniques. The coating of the paste with the steel bar was 3.5 cm, simulating a structural element, and Teflon tape was placed at the steel/paste interface in order to avoid contamination or any alteration in the measurements. The contact area of the rebar embedded in the concrete is 22.30 cm². The specimens were transported to a place with adequate humidity conditions, curing for 28 days.

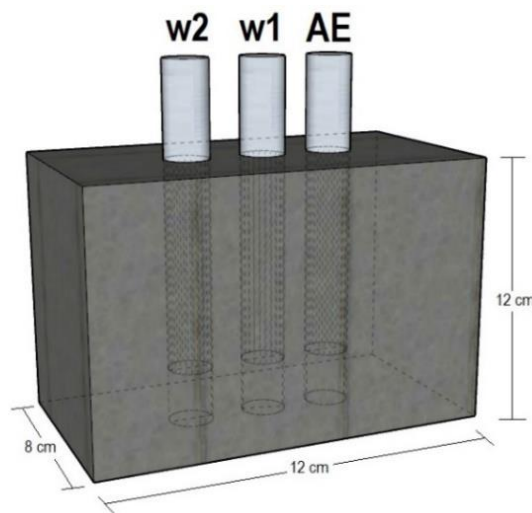


Figure 7. Sample dimension for electrochemical tests

3. Electrochemical Techniques

3.1. Hall-Cell Open Circuit Potential

The E_{corr} corrosion potential, also known as half-cell potential (HCP), is the open circuit potential (OCP) of the rebar [44]. ASTM C876-09 [45] relates HCP to the probability of corrosion of reinforcing bars in concrete. With the values obtained, it is feasible to elaborate a diagnosis of the degree of corrosion risk of the concrete reinforcement [46]. The electrochemical cell for HCP monitoring was made with a saturated silver/silver chloride reference electrode (Ag/AgCl) and a working electrode W, both electrodes were connected to a multimeter. The measurement started 24 hours after the immersion of the specimens in the saline solution, the interpretation of the data is the average of the measurements of the 3 steel rods. Table 6 shows the parameters for interpreting the corrosion potential in reinforced concrete.

Table 6. Corrosion potential parameters E_{corr}

Reference electrode Ag/AgCl (mV)	Corrosion risk (%)
less than -150	10% Corrosion probability
-150 to -300	Uncertain zone
more than -300	90% Corrosion probability

3.2. Electrochemical Noise

The method involves the measurement of small fluctuations in the current signals created between two nominally identical electrodes, and the voltage signals that are generated between the reference electrode and the working electrodes [47]. The electrochemical cell connection for the other electrochemical techniques is described in Figure 8, two working electrodes W_1 and W_2 were used as corrosive working elements, a reference electrode (RE) Ag/AgCl was used, and closing the circuit a third rod was used as auxiliary electrode (AE). A Gill AC-ACM Instruments device was used, and measurements of 1024 readings were taken at a standard rate of 1 reading/second.

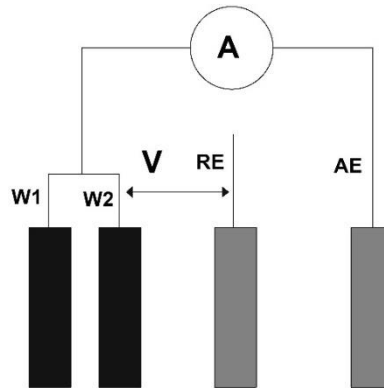


Figure 8. Electrochemical cell configuration

The electrochemical noise resistance (R_n) was calculated with the quotient of the standard deviations of potential (σ_v) over current (σ_i).

$$R_n = \frac{\sigma_v}{\sigma_i} \quad (3)$$

Another statistical data that can be obtained with R_n measurements is the localization index, which is related to the type of corrosion that occurs: generalized (value close to 0) or localized (value close to 1) [48]. Table 7 shows the range of values for the different types of corrosion that occur in the steel bar.

Table 7. Range of current values for the type of corrosion

Location index values	type of corrosion on the steel surface
0.001 - 0.01	Generalized
0.01 - 0.1	Mixed
0.1 - 1	Localized
> 1	Start of pitting

The corrosion rate, V_{corr} represents the volumetric loss of metal per unit area and unit time, and is obtained from the corrosion current, through Faraday's law, and the density of the metal, for steel, $1 \mu\text{A}/\text{cm}^2$ is equivalent to a corrosion rate of 0.0116 mm/year [49]:

$$V_{corr} \left(\frac{\text{mm}}{\text{year}} \right) = 0.116 * I_{corr} \left(\frac{\mu\text{A}}{\text{cm}^2} \right) \quad (3)$$

3.3. Linear Polarization Resistance

A Gill AC-ACM instruments potentiostat was used to measure the LPR technique, the layout of the electrochemical cell is described in the preceding section, a small amplitude of potential values of -50 mV and +50 mV were applied close to E_{corr} , by ASTM G-59 standard [50], and a sweep rate of 60 mV/min.

The polarization resistance R_p was calculated according to Equation 5, which defines the tangent of the polarization curve in the anodic and cathodic regions in the narrowest possible polarization range around the corrosion potential [51, 52]. To obtain I_{corr} , the polarization resistance (R_p) is related to Stern-Geary, then the constant B depends on the anodic and cathodic Tafel slope constants, According to Equation 6, the guidelines for measuring I_{corr} adopt the values of B as 26 and 52 mV for active and passive steels, respectively [53, 54]:

$$R_p = \frac{dE}{di} \quad (4)$$

$$I_{corr} = \frac{bac}{2.303(ba+bc)} = \frac{B}{R_p} \quad (5)$$

According to Andrade & Alonso [49], a current density ratio I_{corr} can be obtained to estimate the degree of corrosion and durability of reinforced concrete structures, parameters as shown in Table 8.

Table 8. Electrochemical parameters of I_{corr} on the service life of reinforced concrete

I_{corr} ($\mu\text{A}/\text{cm}^2$)	Degree of corrosion in the metal
< 0.1	Negligible
0.1 – 0.5	Moderate
0.5 – 1	High
> 1	Very High

3.4. Electrochemical Impedance Spectroscopy

Electrochemical impedance spectroscopy (EIS) is a non-destructive testing method that uses low amplitude and variable frequency sweep alternating currents to study the properties of materials [55]. It can be considered an informative method because does not only measures the polarization resistance but also evaluates the physical processes within the concrete and at the steel/concrete interface [56]. The EIS measurement technique sweep was performed in a frequency range of 0.01 Hz (low) to 10000 Hz (high), and a sinusoidal perturbation of ± 20 mV was applied, with the support of potentiostat equipment attached to a computer and appropriate software.

4. Results and Discussion

4.1. Physical Properties of Fiber-Reinforced Concrete

The slump test is used to evaluate the consistency or workability of the concrete mix. The workability is an indicator of quality control of materials such as fine and coarse aggregates with the cementitious matrix [4]. Workability concrete results are shown in Figure 9 where the concrete control presents a 14 cm slump effect, and when adding treated natural fibers (TNF) an annealing increase due to the reduction in water quantity was obtained, and a consequence of UEO acting as a water reducer during the curing process, and the increase in a slump from high contents of SO_3 in UEO [35, 57]. It was shown that the UEO particles act as a super-plasticizer in the concrete mix and these results are in agreement with other authors [58, 59]. The results for air content are shown in Figure 10, where it can be observed that the specimens with treated fibers increased the amount of voids in the cementitious matrix, which could indicate that the use of WEU caused a bad interaction between the paste and the fiber, i.e., the adhesion decreased drastically for samples CPF-02 and CPF-04 with air content values of 133% and 123% with respect to the control sample, showing that the increase of UEO absorption increases the air content.

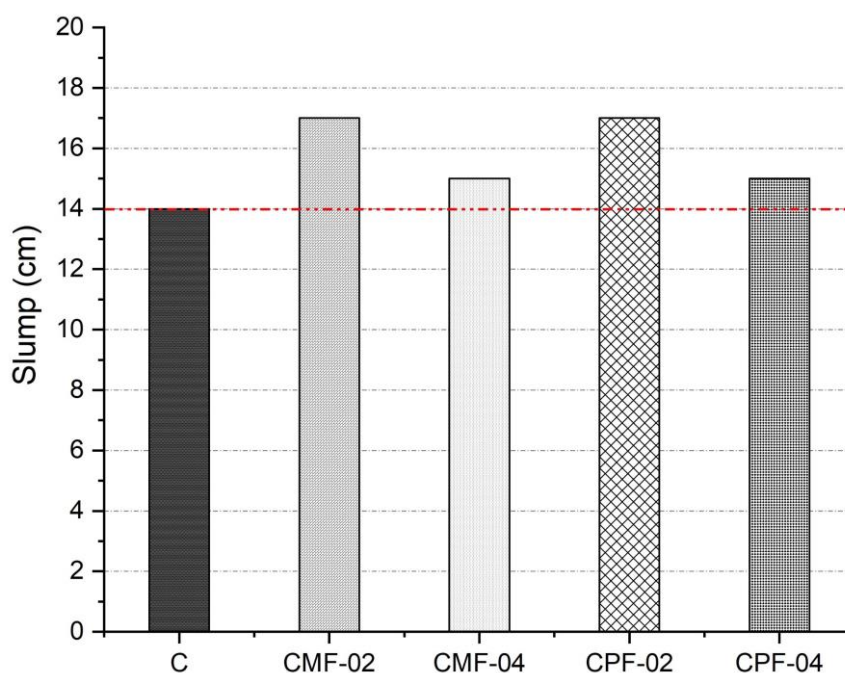


Figure 9. Slump variation in concrete with TNF

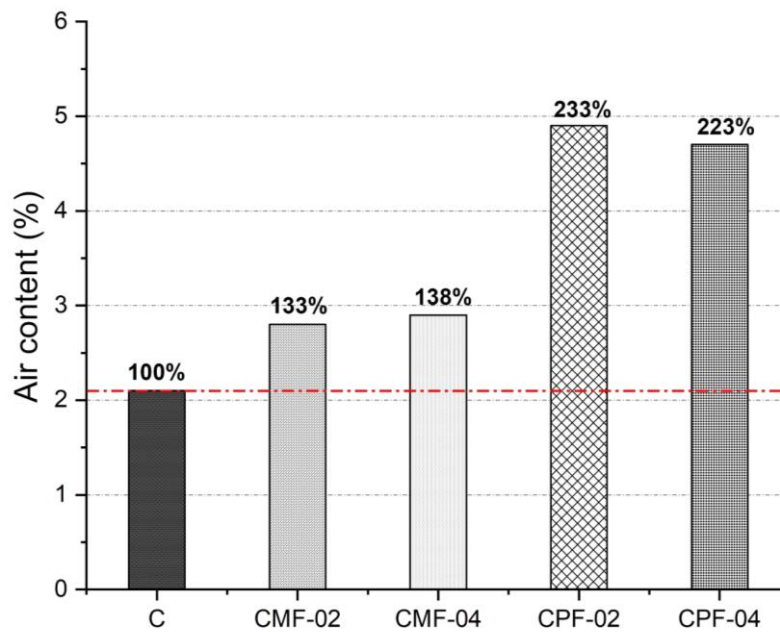


Figure 10. Air content in concrete with UEO-treated fibers

In the complex concrete microstructure, pores may be present in nanometers up to the macro scale [60], and porosity was obtained from air content results [61]. Figure 11 presents the concrete porosity results, where sample C shows 19% porosity, with an a/c relation of 0.54, being this result similar as reported by other authors [46, 62, 63]. All samples with TNF present more void content when compared to the control sample provoking an increase in permeability, directly affecting its compression resistance [64]. It can be appreciated that CPF-02 and CPF-04 samples present a higher percent porosity of 34% and 32%, possibly due to UEO directly affecting the interfacial zone between the aggregates and fibers matrices.

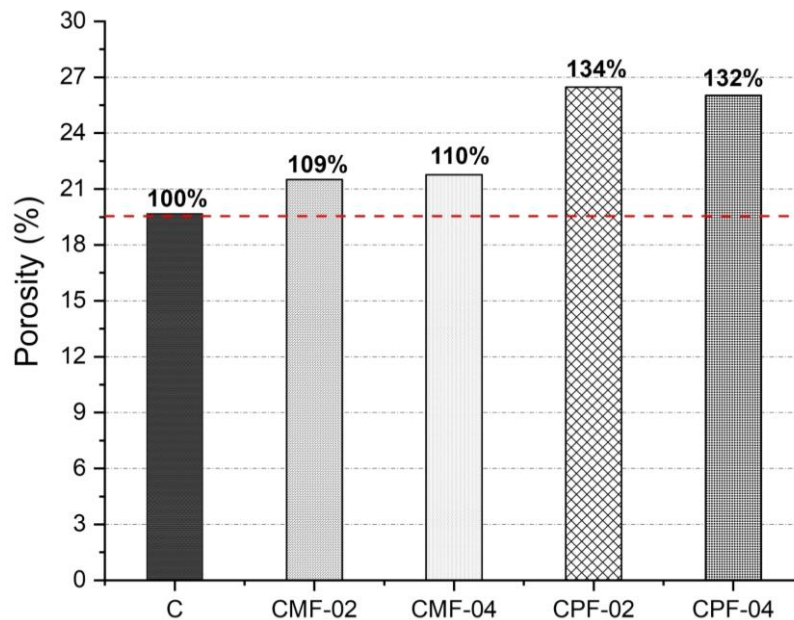


Figure 11. Percentage porosity of concrete with TNF

4.2. Compressive Behavior of Concrete Specimens

Average compression resistance results obtained at 7 and 28 curing days are presented in Table 9. The control sample presents a higher compression resistance (F'_c) as compared to the other samples, due to the presence of UEO from natural fibers; this is due to the increase in the interfacial transition zone (ITZ) surrounding the aggregates with the fiber. A greater ITZ presents a weaker structure as compared with the greater part of the paste being more fragile to mechanical loads [65]. In addition, a reduced level of chemical reactions is demonstrated in the presence of oil along with the weakening of cohesive forces [31].

Table 9. Mechanical compression properties of concrete in its different dosages

Material	F'c 28 days (MPa)						F'c 7 days (MPa)	F'c 28 days (MPa)
	7 days			14 days				
Age	N° 1	N°2	N°3	N° 1	N°2	N°3		
C	26.5	25.79	25.72	33.042	32.23	32.08	26.0	32.5
CMF-02	19.8	20.01	18.93	28.243	27.91	27.74	19.6	28.0
CMF-04	18.351	195.4	17.78	29.342	28.76	28.44	18.4	28.9
CPF-02	19.078	193.3	18.42	26.114	25.65	25.66	18.8	25.8
CPF-04	25.525	252.7	24.57	28.754	28.56	29.04	25.0	28.8

This decrease in the F'c is similar to the ones reported by different authors adding up a small percentage of UEO in the concrete paste [66-70]. The percentage decrease of F'c with oil impregnation in the natural fibers ranges from 11.1% to 20% with respect to sample C, as can be seen in Figure 12. At the early curing time of 7 days, it can be observed that samples CMF-04 and CPF-02 have a lower development in their mechanical properties as a consequence of the hydrophobic characteristic of the UEO. This causes a delayed reaction of Ca(OH)₂, which has not yet been completely consumed for the production of calcium silicate hydrate (CSH); therefore, the bonding between the fiber and the matrix is poor [71].

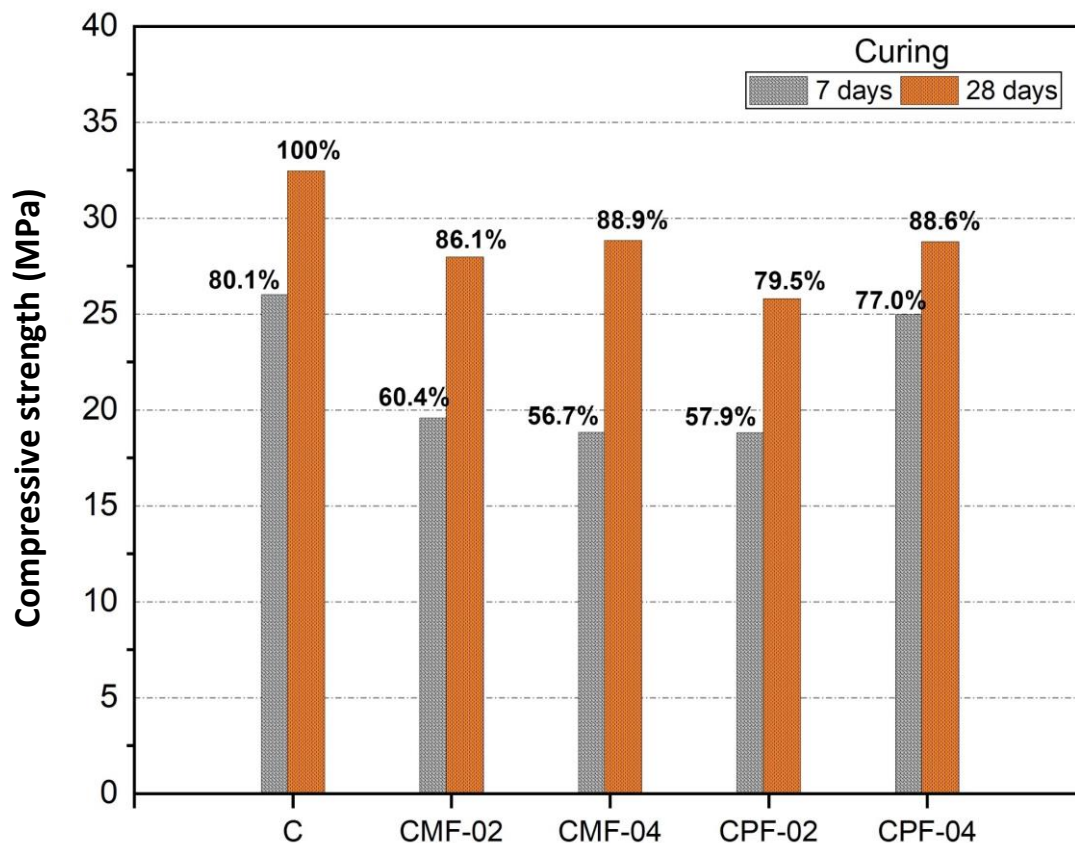


Figure 12. Variations of compressive strength during the curing process

4.3. Flexural Behavior of Concrete Specimens

Average concrete flexural resistance (F'f) at 28 curing days is shown in Figure 13. The effects of the UEO on the flexural strength are negative, decreasing by 25% with respect to the control sample, and the incorporation of the fiber in the concrete paste does not prevent the propagation of cracks when the material is subjected to stresses. The Flexural strength of concrete decreases due to the weakened bond interface, the failure mode of the fibers is predominantly because of heavy metals present in the used oil engine, namely ZnO and P₂O₅ [20, 58]. With the use of UEO and fibers, a decrease in the mechanical properties of concrete has been reported elsewhere [72-74].

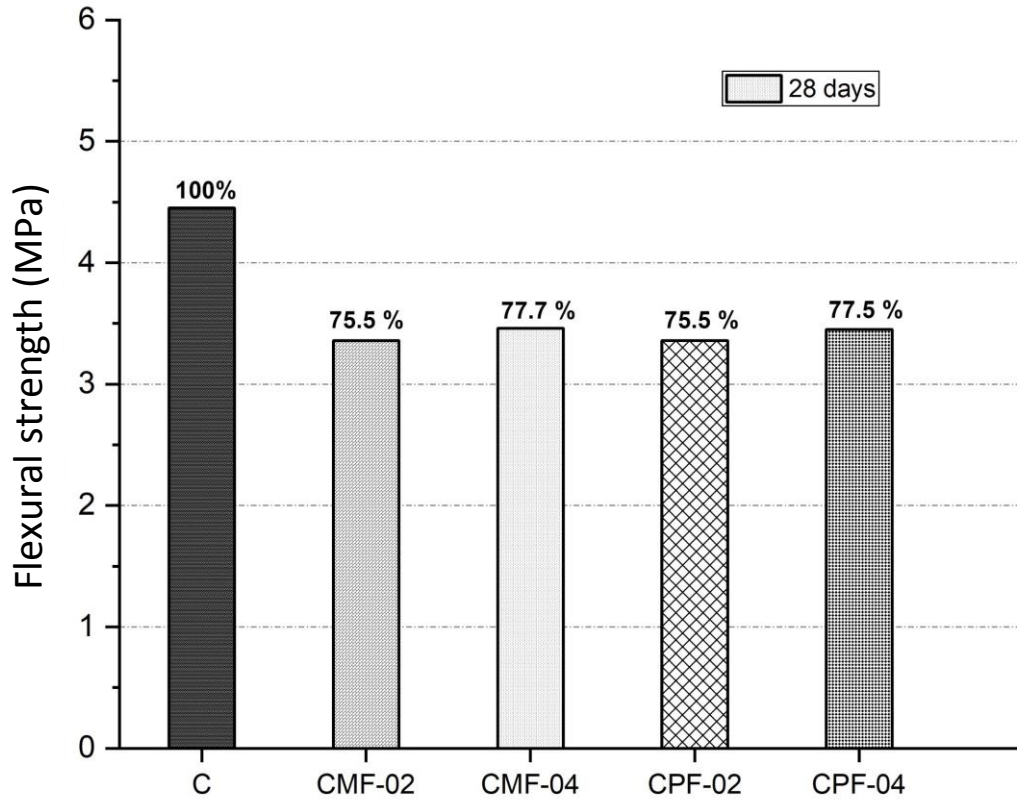


Figure 13. Variation of flexural strength of concrete with TNF, cured at 28 days

The results of the cracks in the flexural test are shown in Figure 14-a), as it can be generally noted that all specimens show a single crack passing through the center in the third of the beam. Specimen control shows a vertical crack characteristic of reinforced concrete; likewise, the specimens with natural fibers CPF-02 and CMF-02, show a brittle shear failure of diagonal type, as previously described the tensile strengths are low, the main cause is the null adhesion of the UEO treated fiber with the cement matrix as can be observed in Figure 14-b).

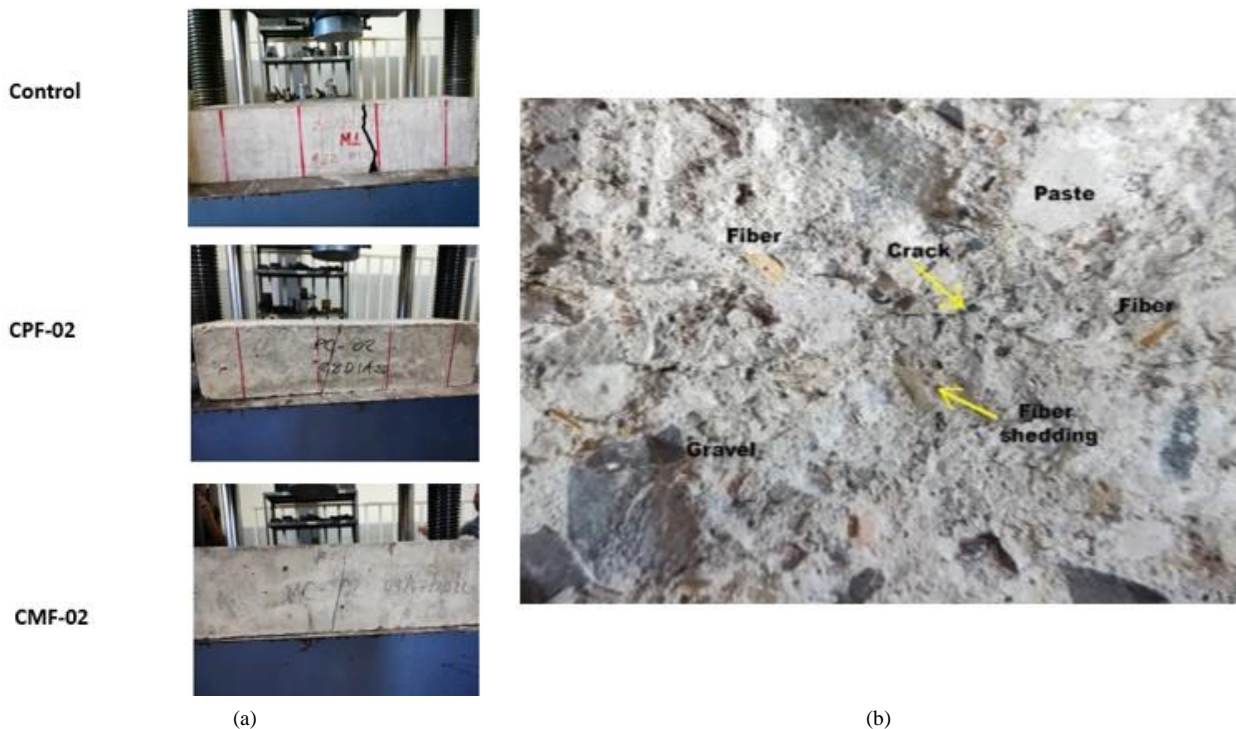


Figure 14. a) Fracture of specimens in flexural tests; b) Macro structure

4.4. Interpretation of Corrosion Potential E_{corr}

During the corrosion process, an electric current flow between the cathodic and anodic sites through the concrete and this flow can be detected by measuring the potential drop across the concrete [75]. Therefore, E_{corr} corrosion potential measurement is a non-destructive method that detects these changes on the metal surface.

The corrosion potentials for the concrete samples with oil-treated fibers are shown in Figure 15. At the beginning of the monitoring, it is observed that the sample CMF-04, presents more positive E_{corr} values of -100 mV compared to the other samples, placing it in a zone of 10% probability of corrosion. This phenomenon indicates a good distribution of the fibers that delay the transport of fluids and chloride ions [34].

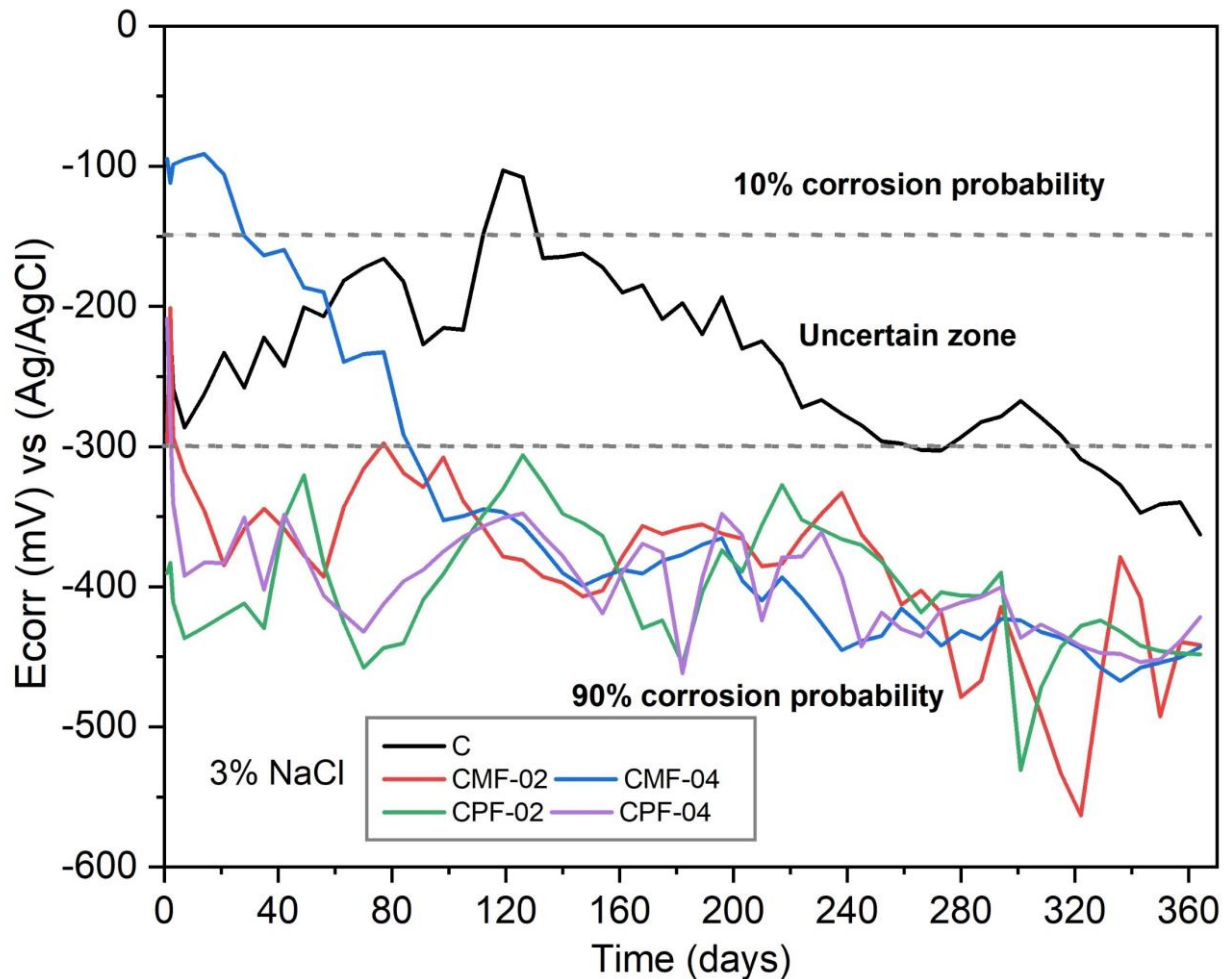


Figure 15. Corrosion potential values for structural steel

After 80 days the sample has a drop in E_{corr} potentials entering a zone of uncertainty, as time progresses and on day 365 of exposure this sample acquires more negative values from -400 mV to -550 mV entering a zone of 90% probability of corrosion, this fact could mean the increase of chloride ion content solution on the surface of the steel/concrete interface [76]. Samples CMF-02, CPF-02 and CPF-04 are in an active zone with 90% probability of corrosion from the beginning to the end of the measurement days, due to the high porosity of the samples, which causes higher voids in the cement paste and higher concentrations of oxygen, water and chloride ions [77, 78]. Chloride and oxygen ions compete to reach the surface of the reinforcing steel through a diffusion phenomenon [79]

4.5. Interpretation of Electrochemical Noise Technique

The maintenance and repair of structural steel reinforced concrete for its safety needs effective monitoring and Inspection methods to evaluate the corrosion of steel reinforcement [80]. The aqueous chloride solution can quickly reach the embedded steel, so the onset of corrosion occurs in the metal [81]. Figures 16 and 17 show the results of Rn and the corrosion rate of concrete with treated fibers.

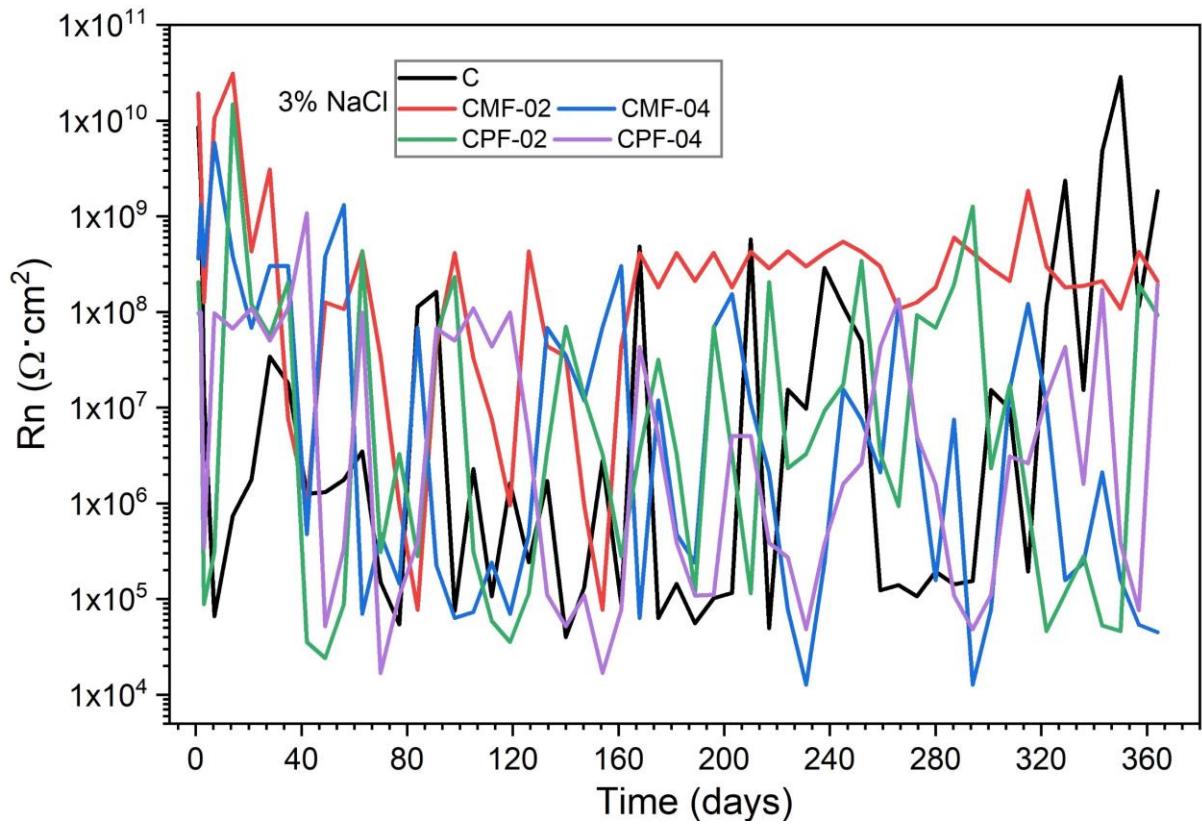


Figure 16. Rn values in the reinforced concrete

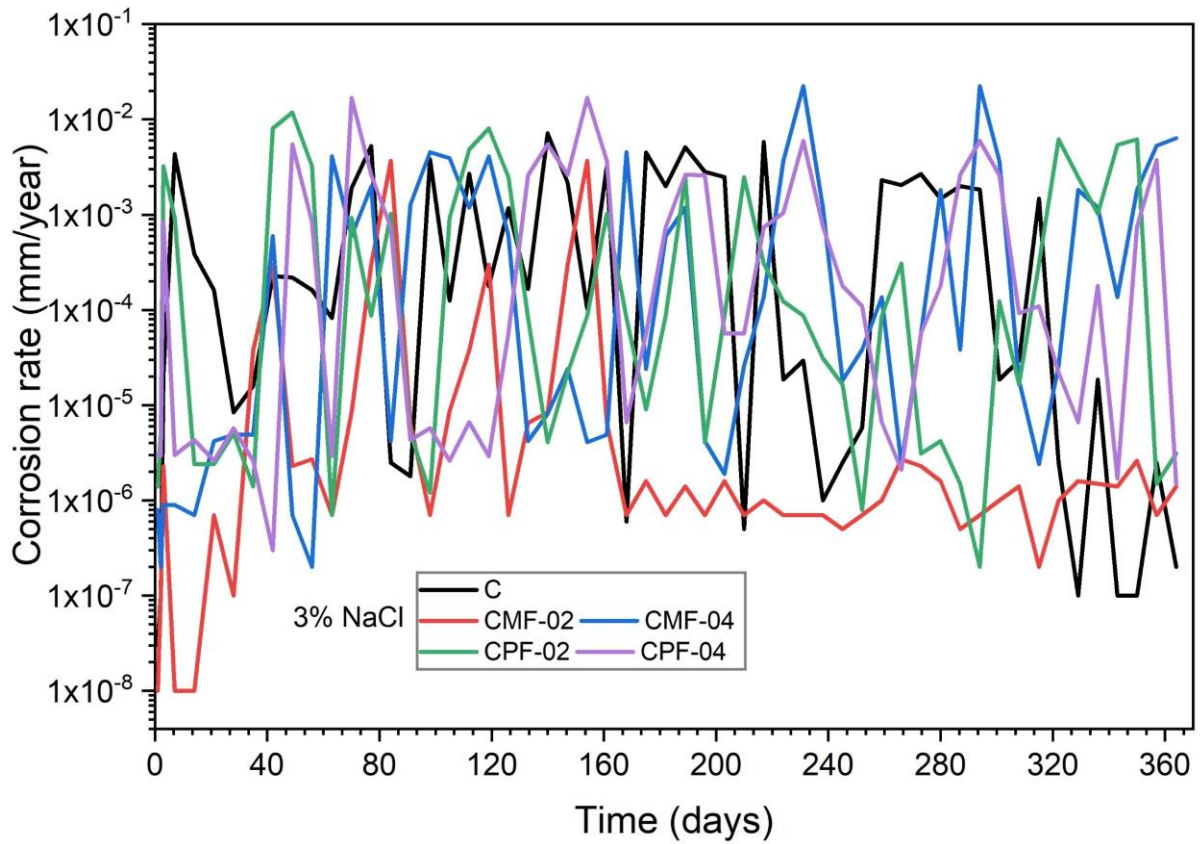


Figure 17. Corrosion rate for steel rod

On day 40 of monitoring, high and low transients of Rn with values between $1 \times 10^{10} \Omega \cdot \text{cm}^2$ and $1 \times 10^5 \Omega \cdot \text{cm}^2$ are observed for all samples, low values of Rn could indicate that the concentration of chloride ion increases on the surface of the steel bar, consequently, the corrosion rate is severe [82], i.e., the corrosion rate is inversely proportional to the values of Rn.

The values of UEO-treated samples are higher than the control sample, as the exposure time progresses the R_n values for natural fibers maintain the increase, high values of noise resistance, corrosion rate decreases, the entry of Cl^- in the concrete increases the rate by the reduction of the alkaline hydrated products of the cement that passivates the embedded steel [83], i.e., the steel bars are passivated and depassivated by the interaction of the aggressive agents that were transported through the pore network of the concrete.

At the end of exposure, all samples show high and low R_n values, these fluctuations possibly due to passivation depassivation events transient behavior. It is not clear if the trend would continue as low or if it would follow the same trend as the control. However, sample CMF-02 shows high and constant R_n values of $1 \times 10^9 \Omega \cdot \text{cm}^2$ from day 160 to 365 days of exposure to the saline medium, this phenomenon may indicate that the treated fiber and the oil behave as a physical barrier, which may cause a slower diffusion of aggressive agents, also high R_n values indicate passivation in the metal and a negligible corrosion rate [46].

Quantitative information on the corrosion rate of steel is of utmost importance for the evaluation of repair methods, for service life prediction and for the structural evaluation of corroded elements [84].

An electrochemical parameter that can be obtained with the EN test is the type of corrosion that is present in the steel bars through the localization index results as shown in Figure 18. It has been argued in the literature that L.I., can be used to determine the nature of the type of corrosion with values approaching 1 being characteristic of localized corrosion [85].

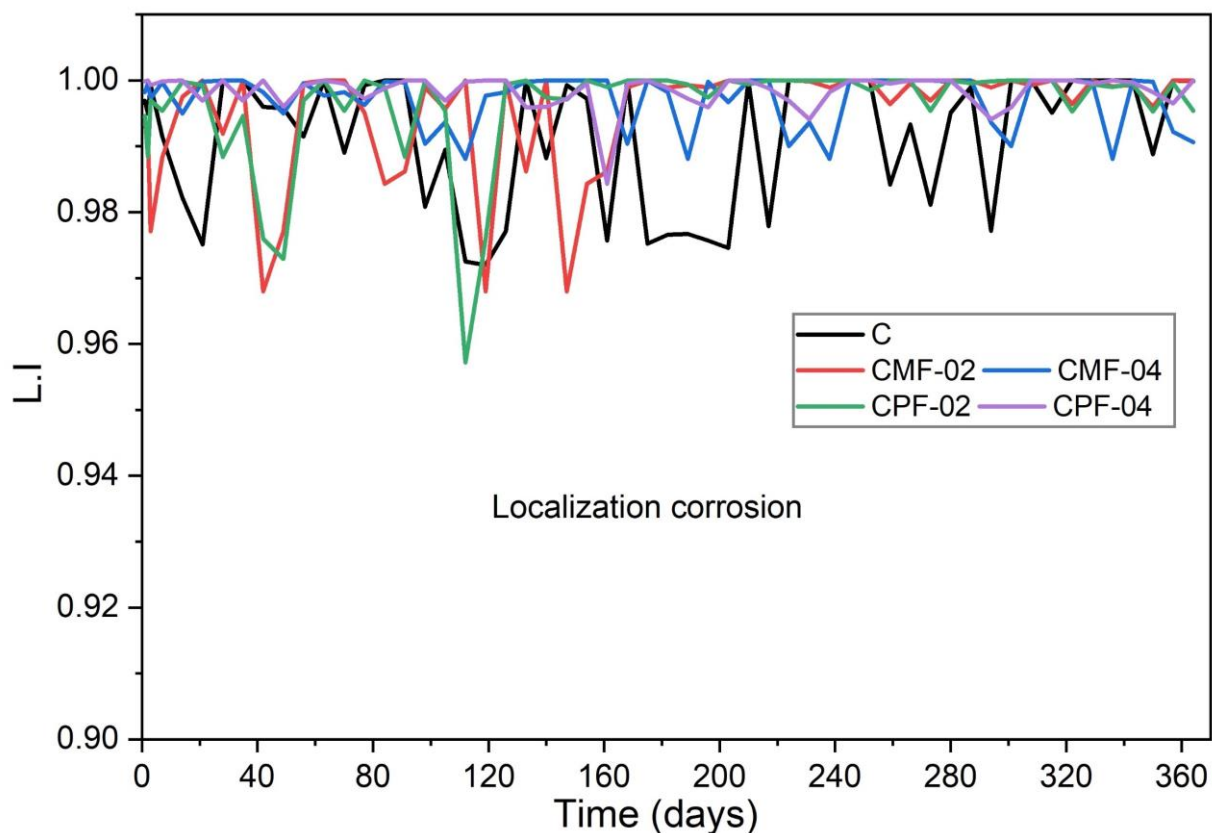


Figure 18. Type of corrosion in the steel/concrete system

It can be observed in a general way that all the samples with treated fibers have localized corrosion, that is, there are small areas of the rod surface, producing an important local reduction of the reinforcement section [64]. This type of corrosion is more likely to occur in reinforced concrete structures exposed to saline environments [86].

4.6. Interpretation of Linear Polarization Resistance

The values of the treated fiber concrete samples can be observed in Figure 19. At the beginning, all samples acquired R_p values of around $1 \times 10^5 \Omega \cdot \text{cm}^2$, indicating that the steel is under low corrosion attack. As the immersion time progresses on days 210 and 365 of monitoring, sample CMF-02 presents a rise in R_p behaviors as observed with high values of between $1 \times 10^5 \Omega \cdot \text{cm}^2$ and $1 \times 10^7 \Omega \cdot \text{cm}^2$, indicating a passivation in the metal surface and obtaining negligible corrosion damage as seen in Figure 20. Generally, steel corrosion is considered to be in the passive state if the current density is less than 0.1 mA/cm^2 and in the active state for values greater than 1 mA/cm^2 [44, 49]. The UEO has a positive effect on the corrosion rate by acting as a film or barrier around the metal; these results are comparable to those of other authors [87].

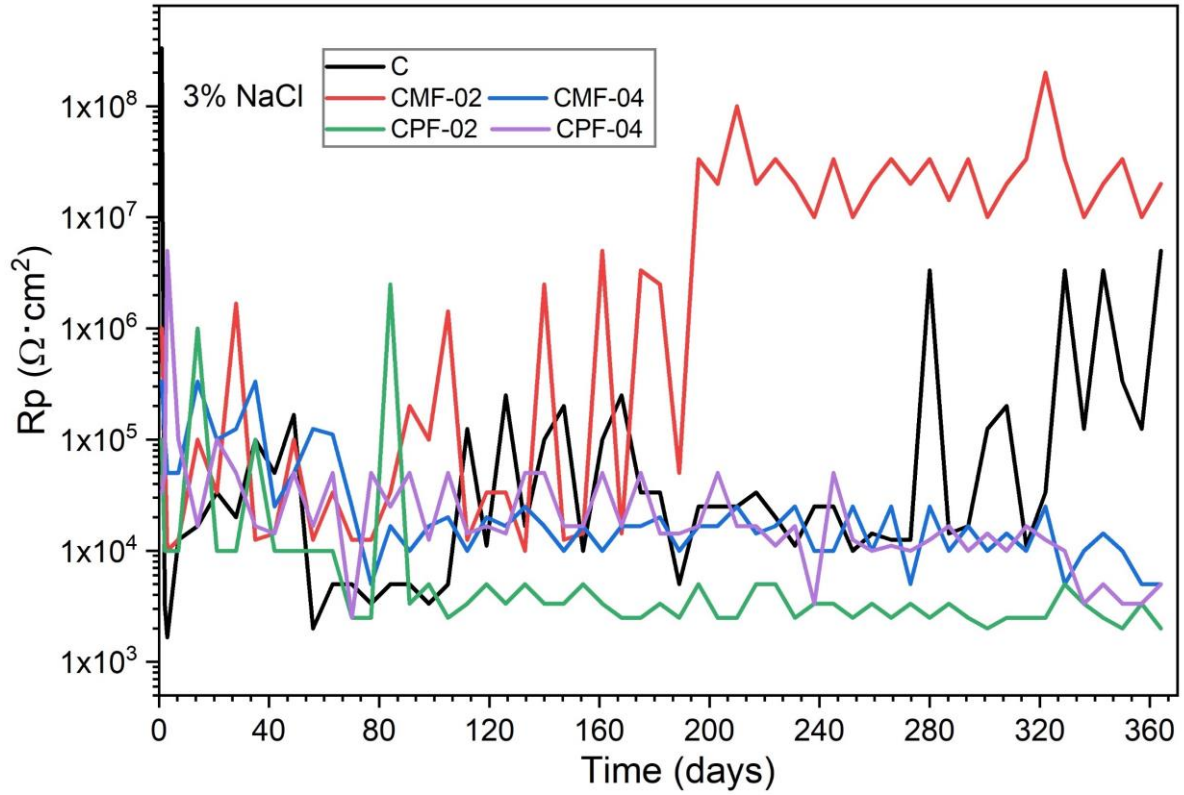


Figure 19. Average values of Rp

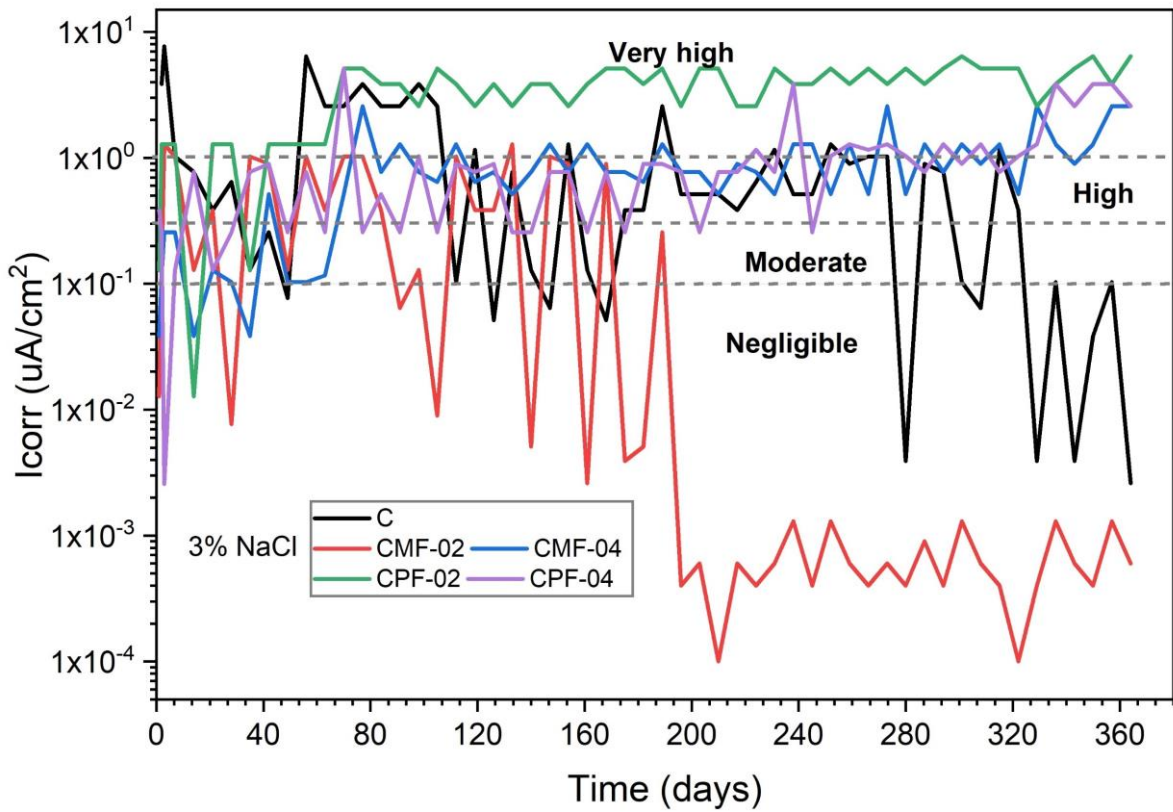


Figure 20. Current density values on the risk of steel corrosion

In the CPF-02 sample, low Rp values can be observed as the days of exposure progress, with values between $1 \times 10^3 \Omega \cdot \text{cm}^2$ and $1 \times 10^4 \Omega \cdot \text{cm}^2$ indicating high corrosion rate in the metal, due to poor adhesion of the fibers with the paste; likewise, the high porosity of the concrete paste by consequence has greater presence of oxygen diffusion and chloride

ions at the steel/paste interface, [88]. The values for the treated fibers have diverse from negligible to very high service life values compared to sample C. The samples CMF-04, CPF-02, and CPF-04 present very high I_{corr} values, increases in I_{corr} over time may not necessarily represent an increase in corrosion rate throughout the rebar, but rather the depassivation and initiation of active corrosion of greater amounts of rebar surface area [89]. Chloride penetration occurs mainly through capillary pores as free Cl^- chlorides by adsorption, diffusion, and capillary permeation [90]. The amount of fibers has a direct influence on the degree of corrosion of reinforcing bars in concrete [77].

4.7. Electrochemical Impedance Interpretations

The graph of real Z' on the abscissa and imaginary Z'' on the ordinate were measured from high to low frequencies which are called Nyquist diagrams [80], these graphs present loops related to time constants originating from the structure and reactions at the electrode [91]. For the interpretation of the diagrams, the loops generated in the test are analyzed. Generally, for reinforced concrete corrosion, graphs present two or three loops (capacitive arcs with or without inductive loop), whose centers are below the real axis (Z_{real}) and which are more or less separated [80, 91]. The high-frequency EIS spectra in the Nyquist diagram are usually a capacitive loop, which is generally attributed to the bulk concrete resistance representing R_e the ohmic resistance of the solution in the pores based on the electrode reaction time, and at middle to low frequencies it is possible to attribute the low-frequency loop to a charge transfer process in combination with a mass transport process (R_p), while the straight line indicates a mechanism of ion diffusion through the pores [91-95].

The EIS results are shown in Figure 21, at the beginning of measurement at 24 hours, it can be widely observed that the control sample presents a better solution resistance R_e and a higher impedance R_p , with values of 1×10^6 and $1 \times 10^7 \Omega \cdot cm^2$ this phenomenon can be explained by the low porosity.

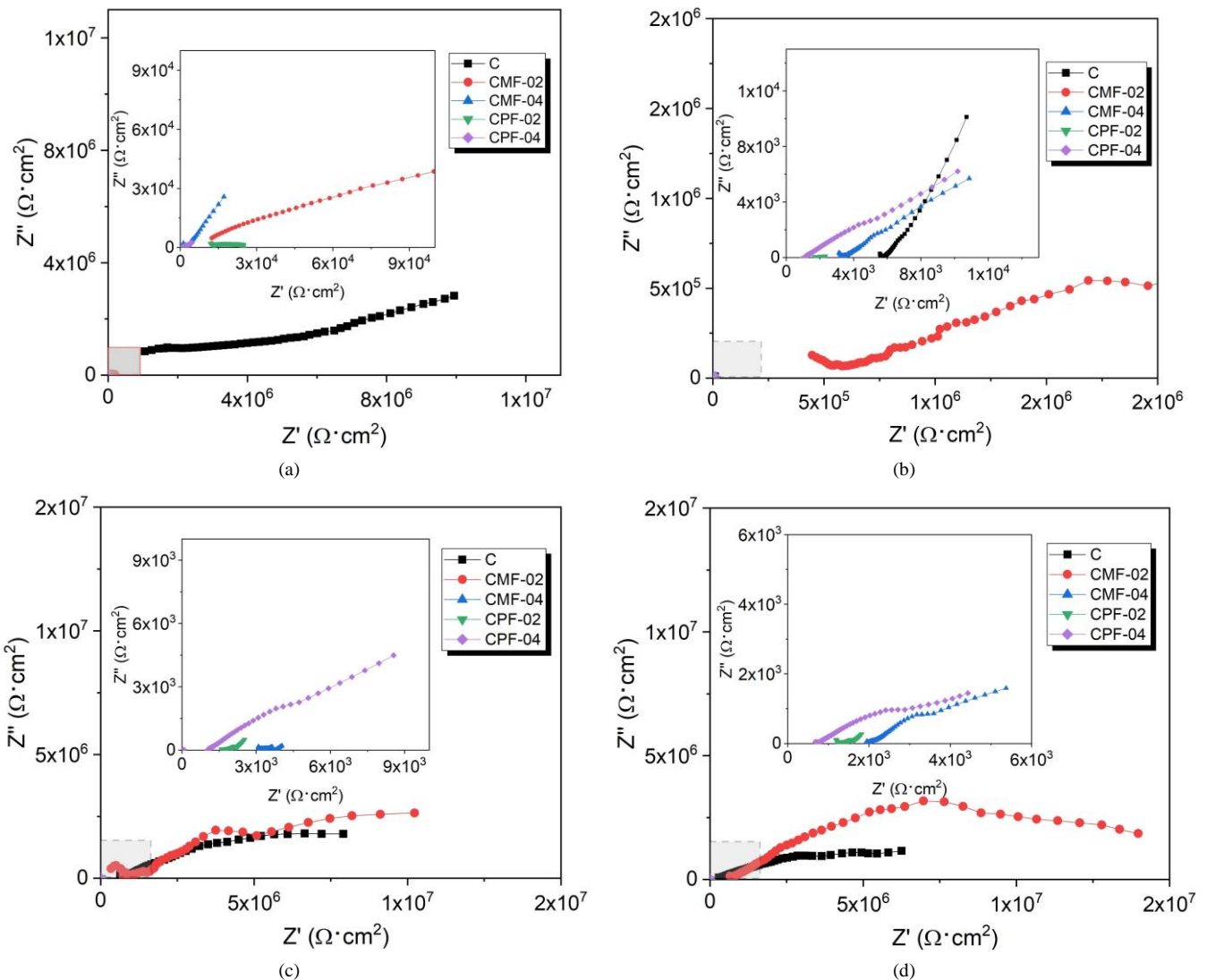


Figure 21. Nyquist diagrams for the days of a) 1, b) 168, c) 280, and d) 365

Small and depressed semicircles can be noticed for samples with treated fibers, indicating low R_e and impedance values due to the presence of larger pores in the concrete, causing not only increased diffusion of chloride Cl^- ions but also diffusion of O_2 and H_2O [54].

For day 168, a remarkable improvement can be noticed for the fibers treated with used oil; the sample CMF-02 presents a better R_e as well as high impedance values of $1 \times 10^6 \Omega \cdot cm^2$ with respect to the control sample. This fact could indicate the formation of a protective film of UEO on the metal surface by the high impedance values indicate a lower corrosion rate in the steel bar [96]. In addition, it was demonstrated that the physical properties of concrete, such as air content and porosity, have a direct relationship with corrosion damage to the metal due to the transport of species at the steel-concrete interface.

During the 240-day measurement, it was observed that the control sample had high values of R_e and R_p of $1 \times 10^7 \Omega \cdot cm^2$, which could indicate passivation in the metal. At the end of the 365 days of monitoring, it is appreciated that the sample CMF-02 has had a positive response to the corrosion process of the steel for 168 days, maintaining a constant impedance until the end of the exposure. High values in this low-frequency region may be associated with the presence of the passive film [97, 98].

5. Conclusions

The following conclusions can be drawn:

- High levels of workability were obtained in all samples incorporating treated fibers from impregnated UEO acting as water reduction and lubricant in cement particles, and aggregates.
- The CPF-02 and CPF-04 samples present 133% and 123% air content greater values, when compared with the control sample, ascribed to UEO high absorption in palm fibers, weakening the adhesion in fibers and cement matrix. As a consequence, the increase in voids in the cement paste porosity increased by 34% and 33%, respectively.
- The UEO impregnated effect in fibers modified the low-level properties of mechanical compression in concrete. The CMF-04 specimen exhibited higher resistance when compared with the other treated samples but was lower than the control sample.
- The $f'f$ of all samples treated showed a decrease between 22% and 25% compared to the sample without added fibers. The UEO modified the fiber surface, losing the rough texture and promoting concrete specimens to present a fragile cracking failure.
- The low performance in mechanical properties may be due to poor adherence and cohesion in fiber paste materials to support external forces and stresses.
- All samples presented a 90% probability of corrosion, with more negative values of corrosion potential ranging from -400 mV to -550 mV.
- The sample CMF-02 presented a better positive performance in the corrosion rate on the steel with high values of R_n and R_p of $1 \times 10^8 \Omega \cdot cm^2$, indicating the formation of a protective film of UEO on the steel surface, decreasing the diffusion of Cl^- , H_2O , and oxygen, and appreciating negligible corrosion damage on the road.
- In all samples, diffusion processes were observed on the steel/concrete interface, according to the EIS data.

6. Declarations

6.1. Author Contributions

Conceptualization, A.F.N.; methodology, A.F.N., J.U.C., and M.F.N.; investigation, A.F.N., E.C.M.C., M.F.N., and J.U.C.; data curation, A.F.N., O.A.G.N., C.A.G.P., and M.F.N.; writing—original draft, A.F.N.; writing—review and editing, A.F.N. and J.U.C.; supervision, J.U.C. and E.C.M.C. All authors have read and agreed to the published version of the manuscript.

6.2. Data Availability Statement

The data presented in this study are available on request from the corresponding author.

6.3. Funding

The authors received no financial support for the research, authorship, and/or publication of this article.

6.4. Acknowledgements

The authors are grateful to the Consejo Nacional de Humanidades Ciencias y Tecnología de México (CONAHCYT).

6.5. Conflicts of Interest

The authors declare no conflict of interest.

7. References

- [1] Feng, W., Tarakbay, A., Ali Memon, S., Tang, W., & Cui, H. (2021). Methods of accelerating chloride-induced corrosion in steel-reinforced concrete: A comparative review. *Construction and Building Materials*, 289, 123165. doi:10.1016/j.conbuildmat.2021.123165.
- [2] Van Steen, C., Nasser, H., Verstrynghe, E., & Wevers, M. (2022). Acoustic emission source characterisation of chloride-induced corrosion damage in reinforced concrete. *Structural Health Monitoring*, 21(3), 1266–1286. doi:10.1177/14759217211013324.
- [3] Tesic, K., Baricevic, A., Serdar, M., & Gucunski, N. (2023). Quantifying the impact of parameters of chloride-induced reinforcement corrosion on the GPR signal. *Construction and Building Materials*, 399, 132594. doi:10.1016/j.conbuildmat.2023.132594.
- [4] Flores Nicolás, A., Menchaca Campos, E. C., Flores Nicolás, M., Martínez González, J. J., González Noriega, O. A., & Uruchurtu Chavarín, J. (2024). Influence of Recycled High-Density Polyethylene Fibers on the Mechanical and Electrochemical Properties of Reinforced Concrete. *Fibers*, 12(3), 24. doi:10.3390/fib12030024.
- [5] Mohammed, M., Rahman, R., Mohammed, A. M., Adam, T., Betar, B. O., Osman, A. F., & Dahham, O. S. (2022). Surface treatment to improve water repellence and compatibility of natural fiber with polymer matrix: Recent advancement. *Polymer Testing*, 115. doi:10.1016/j.polymertesting.2022.107707.
- [6] Juárez Alvarado, C. A., Rodríguez López, P., Rivera Villarreal, R., & Rechy de Von Roth, M. D. L. Á. (2004). Use of natural lechuguilla fibers as reinforcement in concrete. *Ingenierías*, 7(22), 7-19. (In Spanish).
- [7] Juradin, S., Boko, I., Netinger Grubeša, I., Jozić, D., & Mrakovčić, S. (2021). Influence of different treatment and amount of Spanish broom and hemp fibres on the mechanical properties of reinforced cement mortars. *Construction and Building Materials*, 273, 121702. doi:10.1016/j.conbuildmat.2020.121702.
- [8] Ferreira, S. R., Silva, F. de A., Lima, P. R. L., & Toledo Filho, R. D. (2017). Effect of hornification on the structure, tensile behavior and fiber matrix bond of sisal, jute and curauá fiber cement based composite systems. *Construction and Building Materials*, 139, 551–561. doi:10.1016/j.conbuildmat.2016.10.004.
- [9] Xie, X., Zhou, Z., & Yan, Y. (2019). Flexural properties and impact behaviour analysis of bamboo cellulosic fibers filled cement-based composites. *Construction and Building Materials*, 220, 403–414. doi:10.1016/j.conbuildmat.2019.06.029.
- [10] Lumingkewas, R. H., Husen, A., & Andrianus, R. (2017). Effect of Fibers Length and Fibers Content on the Splitting Tensile Strength of Coconut Fibers Reinforced Concrete Composites. *Key Engineering Materials*, 748, 311–315. doi:10.4028/www.scientific.net/kem.748.311.
- [11] Machaka, M., Basha, H., Abou Chakra, H., & Elkordi, A. (2014). Alkali treatment of fan palm natural fibers for use in fiber reinforced concrete. *European Scientific Journal*, 10(12), 186-195.
- [12] Madhwani, H., Sathyan, D., & Mini, K. M. (2019). Study on durability and hardened state properties of sugarcane bagasse fiber reinforced foam concrete. *Materials Today: Proceedings*, 46, 4782–4787. doi:10.1016/j.matpr.2020.10.313.
- [13] Ighalo, J. O., Adeyanju, C. A., Ogunniyi, S., Adeniyi, A. G., & Abdulkareem, S. A. (2021). An empirical review of the recent advances in treatment of natural fibers for reinforced plastic composites. *Composite Interfaces*, 28(9), 925–960. doi:10.1080/09276440.2020.1826274.
- [14] Ahmad, J., & Zhou, Z. (2022). Mechanical Properties of Natural as well as Synthetic Fiber Reinforced Concrete: A Review. *Construction and Building Materials*, 333, 127353. doi:10.1016/j.conbuildmat.2022.127353.
- [15] Ramamoorthy, S. K., Di, Q., Adekunle, K., & Skrifvars, M. (2012). Effect of water absorption on mechanical properties of soybean oil thermosets reinforced with natural fibers. *Journal of Reinforced Plastics and Composites*, 31(18), 1191–1200. doi:10.1177/0731684412455257.
- [16] Kim, H., & Seo, D. (2007). Influence of water saturation on fracture toughness in woven natural fiber reinforced composites. *Advanced Composite Materials*, 16(2), 83–94. doi:10.1163/156855107780918955.
- [17] Symington, M. C., Banks, W. M., West, O. D., & Pethrick, R. A. (2009). Tensile testing of cellulose based natural fibers for structural composite applications. *Journal of Composite Materials*, 43(9), 1083–1108. doi:10.1177/0021998308097740.
- [18] Zhang, D., Tan, K. H., Dasari, A., & Weng, Y. (2020). Effect of natural fibers on thermal spalling resistance of ultra-high-performance concrete. *Cement and Concrete Composites*, 109, 103512. doi:10.1016/j.cemconcomp.2020.103512.
- [19] Shah, I., Li, J., Yang, S., Zhang, Y., & Anwar, A. (2022). Experimental Investigation on the Mechanical Properties of Natural Fiber Reinforced Concrete. *Journal of Renewable Materials*, 10(5), 1307–1320. doi:10.32604/jrm.2022.017513.

- [20] Onuaguluchi, O., & Banthia, N. (2016). Plant-based natural fibre reinforced cement composites: A review. *Cement and Concrete Composites*, 68, 96–108. doi:10.1016/j.cemconcomp.2016.02.014.
- [21] Paricaguán, B., Albano, C., Palacios, J., Torres, R., Camacho, N., Infante, J., & Alvarado, M. (2013). Thermal degradation of coconut fibers with chemical treatment from concrete mixtures (Kinetic Study). *Revista Ingeniería UC*, 20(2), 60-67.
- [22] Li, M., Pu, Y., Thomas, V. M., Yoo, C. G., Ozcan, S., Deng, Y., Nelson, K., & Ragauskas, A. J. (2020). Recent advancements of plant-based natural fiber-reinforced composites and their applications. *Composites Part B: Engineering*, 200, 108254. doi:10.1016/j.compositesb.2020.108254.
- [23] Zhang, K., Cao, Q., Jin, L., Li, P., & Zhang, X. (2017). A novel route to utilize waste engine oil by blending it with water and coal. *Journal of Hazardous Materials*, 332, 51–58. doi:10.1016/j.jhazmat.2017.02.052.
- [24] Chen, H., Qin, R., & Lau, D. (2021). Recycling used engine oil in concrete design mix: An ecofriendly and feasible solution. *Journal of Cleaner Production*, 329, 129555. doi:10.1016/j.jclepro.2021.129555.
- [25] Yousif, B. F., Orupabo, C., & Azwa, Z. N. (2013). Characteristics of Kenaf Fiber Immersed in Different Solutions. *Journal of Natural Fibers*, 9(4), 207–218. doi:10.1080/15440478.2012.733149.
- [26] Wong, C., McGowan, T., Bajwa, S. G., & Bajwa, D. S. (2016). Impact of fiber treatment on the oil absorption characteristics of plant fibers. *BioResources*, 11(3), 6452–6463. doi:10.15376/biores.11.3.6452-6463.
- [27] Ramli, M., Kwan, W. H., & Abas, N. F. (2013). Strength and durability of coconut-fiber-reinforced concrete in aggressive environments. *Construction and Building Materials*, 38, 554–566. doi:10.1016/j.conbuildmat.2012.09.002.
- [28] ASTM C150/C150. (2021). Standard Specification for Portland Cement. ASTM International, Pennsylvania, United States. doi:10.1520/C0150_C0150M-20.
- [29] Martinez, S., Teresa, M., Sánchez Herrera, L. M., Torres García, G., & Garcia Paredes, J. D. (2012). Value network of mango and its waste based on nutritional and functional properties. *Revista Mexicana de Agronegocios*, 1-30.
- [30] Escalante, M. A. M. (2018). Cultural appropriation: The case of traditional crafts. *Anales del Museo Nacional de Antropología. Dirección General de Bellas Artes y de Conservación y Restauración de Bienes Culturales*. Available online: <https://dialnet.unirioja.es/servlet/revista?codigo=81> (accessed on March 2024).
- [31] Djafari Petroudy, S. R. (2017). Physical and mechanical properties of natural fibers. In *Advanced High Strength Natural Fibre Composites in Construction: Woodhead Publishing*, 59–83. doi:10.1016/B978-0-08-100411-1.00003-0.
- [32] Mújica-Paz, H., Valdez-Fragoso, A., López-Malo, A., Palou, E., & Welti-Chanes, J. (2003). Impregnation properties of some fruits at vacuum pressure. *Journal of Food Engineering*, 56(4), 307–314. doi:10.1016/S0260-8774(02)00155-3.
- [33] Ferreira, D. P., Cruz, J., & Fanguero, R. (2018). Surface modification of natural fibers in polymer composites. In *Green Composites for Automotive Applications: Woodhead Publishing* 3–41. doi:10.1016/B978-0-08-102177-4.00001-X.
- [34] Assaad, J. J. (2013). Disposing used engine oils in concrete - Optimum dosage and compatibility with water reducers. *Construction and Building Materials*, 44, 734–742. doi:10.1016/j.conbuildmat.2013.03.078.
- [35] Shafiq, N., Choo, C. S., & Isa, M. H. (2018). Effects of used engine oil on slump, compressive strength and oxygen permeability of normal and blended cement concrete. *Construction and Building Materials*, 187, 178–184. doi:10.1016/j.conbuildmat.2018.07.195.
- [36] Sekar, S., Suresh Kumar, S., Vigneshwaran, S., & Velmurugan, G. (2020). Evaluation of Mechanical and Water Absorption Behavior of Natural Fiber-Reinforced Hybrid Biocomposites. *Journal of Natural Fibers*, 19(5), 1–11. doi:10.1080/15440478.2020.1788487.
- [37] Sumesh, K. R., Kavimani, V., Rajeshkumar, G., Indran, S., & Khan, A. (2022). Mechanical, water absorption and wear characteristics of novel polymeric composites: Impact of hybrid natural fibers and oil cake filler addition. *Journal of Industrial Textiles*, 51(4), 5910S-5937S. doi:10.1177/1528083720971344.
- [38] Nine, M. J., Kabiri, S., Sumona, A. K., Tung, T. T., Moussa, M. M., & Losic, D. (2020). Superhydrophobic/superoleophilic natural fibres for continuous oil-water separation and interfacial dye-adsorption. *Separation and Purification Technology*, 233, 116062. doi:10.1016/j.seppur.2019.116062.
- [39] ASTM C143/C143M-20. (2020). Standard Test Method for Slump of Hydraulic-Cement Concrete. ASTM International, Pennsylvania, United States. doi:10.1520/C0143_C0143M-20.
- [40] ASTM C231/C231M-22. (2024). Standard Test Method for Air Content of Freshly Mixed Concrete by the Pressure Method. ASTM International, Pennsylvania, United States. doi:10.1520/C0231_C0231M-22.
- [41] ASTM C31/C31M-23. (2024). Standard Practice for Making and Curing Concrete Test Specimens in the Field. ASTM International, Pennsylvania, United States. doi:10.1520/C0031_C0031M-23.

- [42] ASTM C78/C78M-22. (2022). Standard Test Method for Flexural Strength of Concrete (Using Simple Beam with Center-Point Loading). ASTM International, Pennsylvania, United States. doi:10.1520/C0078_C0078M-22.
- [43] Yaowarat, T., Suddepong, A., Hoy, M., Horpibulsuk, S., Takaikaew, T., Vichitcholchai, N., Arulrajah, A., & Chinkulkijniwat, A. (2021). Improvement of flexural strength of concrete pavements using natural rubber latex. *Construction and Building Materials*, 282, 122704. doi:10.1016/j.conbuildmat.2021.122704.
- [44] Rodrigues, R., Gaboreau, S., Gance, J., Ignatiadis, I., & Betelu, S. (2021). Reinforced concrete structures: A review of corrosion mechanisms and advances in electrical methods for corrosion monitoring. *Construction and Building Materials*, 269, 121240. doi:10.1016/j.conbuildmat.2020.121240.
- [45] ASTM C876-09. (2016). Standard Test Method for Corrosion Potentials of Uncoated Reinforcing Steel in Concrete. ASTM International, Pennsylvania, United States. doi:10.1520/C0876-09.
- [46] Flores-Nicolás, A., Flores-Nicolás, M., & Uruchurtu-Chavarín, J. (2021). Corrosion effect on reinforced concrete with the addition of graphite powder and its evaluation on physical-electrochemical properties. *Revista ALCONPAT*, 11(1), 18–33. doi:10.21041/ra.v11i1.501.
- [47] Mills, D., Lambert, P., & Yang, S. (2021). Electrochemical noise measurement to assess corrosion of steel reinforcement in concrete. *Materials*, 14(18), 5392. doi:10.3390/ma14185392.
- [48] Calabrese, L., Galeano, M., & Proverbio, E. (2023). Data Mining Applied to the Electrochemical Noise Technique in the Time/Frequency Domain for Stress Corrosion Cracking Recognition. *Corrosion and Materials Degradation*, 4(4), 659–679. doi:10.3390/cmd4040034.
- [49] Andrade, C., & Alonso, C. (2004). Test methods for on-site corrosion rate measurement of steel reinforcement in concrete by means of the polarization resistance method. *Materials and Structures*, 37(9), 623–643. doi:10.1007/bf02483292.
- [50] ASTM G59-97. (2020). Standard Test Method for Conducting Potentiodynamic Polarization Resistance Measurements. ASTM International, Pennsylvania, United States. doi:10.1520/G0059-97R20.
- [51] Lukács, Z., & Kristóf, T. (2023). Linear transformations of the Butler–Volmer equation. *Electrochemistry Communications*, 154, 107556. doi:10.1016/j.elecom.2023.107556.
- [52] Román, A. S., Barrientos, M. S., Harms, F., Mendez, C. M., & Ares, A. E. (2016, March). Corrosion resistance of AISI 304L stainless steel in soy biodiesel. *Anales (Asociación Física Argentina)*, 27(1). (In Spanish).
- [53] Sohail, M. G., Laurens, S., Deby, F., Balayssac, J. P., & Al Nuaimi, N. (2021). Electrochemical corrosion parameters for active and passive reinforcing steel in carbonated and sound concrete. *Materials and Corrosion*, 72(12), 1854–1871. doi:10.1002/maco.202112569.
- [54] Da, B., Yu, H., Ma, H., & Wu, Z. (2018). Reinforcement corrosion research based on the linear polarization resistance method for coral aggregate seawater concrete in a marine environment. *Anti-Corrosion Methods and Materials*, 65(5), 458–470. doi:10.1108/acmm-03-2018-1911.
- [55] Niu, S., Luo, J., Chen, M. T., Chen, Z., Wang, X., Bai, X., & Li, J. (2023). Experimental study of cement-based materials under sulfate attack environment using Electrochemical Impedance Spectroscopy. *International Journal of Electrochemical Science*, 18(5), 100133. doi:10.1016/j.ijoes.2023.100133.
- [56] Sobhani, J., & Najimi, M. (2013). Electrochemical impedance behavior and transport properties of silica fume contained concrete. *Construction and Building Materials*, 47, 910–918. doi:10.1016/j.conbuildmat.2013.05.010.
- [57] Björnström, J., & Chandra, S. (2003). Effect of superplasticizers on the rheological properties of cements. *Materials and Structures*, 36(10), 685–692. doi:10.1007/bf02479503.
- [58] Varghese, R., & Eapen Sakaria, P. (2017). Experimental Investigation on the Properties of Fresh and Hardened Concrete with Used Engine Oil as Super Plasticizer. *International Research Journal of Engineering and Technology*, 04(05), 2230–2236. doi:10.13140/RG.2.2.26601.34400.
- [59] Hasan, B., & Ali, M. (2023). Potential of used-petrol-engine-oil as an admixture in cement composites: A detailed review. *AIP Conference Proceedings*. doi:10.1063/5.0129983.
- [60] Lian, C., Zhuge, Y., & Beecham, S. (2011). The relationship between porosity and strength for porous concrete. *Construction and Building Materials*, 25(11), 4294–4298. doi:10.1016/j.conbuildmat.2011.05.005.
- [61] Solís-Carcaño, R. Ó. M. E. L., & Moreno, E. I. (2006). Analysis of the porosity of concrete with limestone aggregate. *Revista de la Facultad de Ingeniería de la UCV*, 21(3), 57–68. (In Spanish).
- [62] Solís Carcaño, R. G., & Alcocer Fraga, M. Á. (2019). Durabilidad del concreto con agregados de alta absorción. *Ingeniería Investigación y Tecnología*, 20(4), 1–13. doi:10.22201/fi.25940732e.2019.20n4.039. (In Spanish).

- [63] Wang, L., Jin, M., Guo, F., Wang, Y. A. N., & Tang, S. (2021). Pore structural and fractal analysis of the influence of fly ash and silica fume on the mechanical property and abrasion resistance of concrete. *Fractals*, 29(2), 2140003. doi:10.1142/S0218348X2140003X.
- [64] Nicolás, A. F. (2021). Evaluation of the corrosion and protection of reinforcing steel embedded in concrete in the presence of graphite and its effect on the mechanical-electrochemical properties. Master Thesis, Universidad Autónoma del Estado de Morelos, Cuernavaca, Mexico. (In Spanish).
- [65] Yaphary, Y. L., Lam, R. H. W., & Lau, D. (2020). Reduction in cement content of normal strength concrete with used engine oil (UEO) as chemical admixture. *Construction and Building Materials*, 261, 119967. doi:10.1016/j.conbuildmat.2020.119967.
- [66] Shafiq, N., Nuruddin, M. F., & Beddu, S. (2011). Properties of concrete containing used engine oil. *International Journal of Sustainable Construction Engineering and Technology*, 2(1), 72-82.
- [67] Abdelaziz, G. E. (2011). Utilization of used-engine oil in concrete as a chemical admixture. *Benha University, Egypt*, 14-17.
- [68] Burbano-Garcia, C., Hurtado, A., Silva, Y. F., Delvasto, S., & Araya-Letelier, G. (2021). Utilization of waste engine oil for expanded clay aggregate production and assessment of its influence on lightweight concrete properties. *Construction and Building Materials*, 273, 121677. doi:10.1016/j.conbuildmat.2020.121677.
- [69] Alsadey, S. (2018). Effects of used engine oil as chemical admixture in concrete. *International Journal of Energy and Sustainable Development*, 3(2), 38-43.
- [70] Attom, M., Hawileh, R., & Naser, M. (2013). Investigation on concrete compressive strength mixed with sand contaminated by crude oil products. *Construction and Building Materials*, 47, 99-103. doi:10.1016/j.conbuildmat.2013.04.042.
- [71] Zhou, X., Saini, H., & Kastiukas, G. (2017). Engineering properties of treated natural hemp fiber-reinforced concrete. *Frontiers in Built Environment*, 3, 33. doi:10.3389/fbuil.2017.00033.
- [72] Hussen, S. S. (2016). Using of Industrial Waste as a Green Chemical Admixture in Concrete. *Kufa Journal of Engineering*, 7(1), 104-114. doi:10.30572/2018/kje/711216.
- [73] Al-Attar, T. S. (2013). A quantitative evaluation of bond strength between coarse aggregate and cement mortar in concrete. *European scientific journal*, 9(6).
- [74] Nadeem, H., Habib, N. Z., Aun, N. C., Zoorob, S. E., Mustaffa, Z., Mesney, R., & Suubitaa, S. (2017). Used engine oil as alternate binder for buildings - A comparative study. *Proceedings of Institution of Civil Engineers: Waste and Resource Management*, 170(2), 57-65. doi:10.1680/jwarm.17.00005.
- [75] Song, H. W., & Saraswathy, V. (2007). Corrosion monitoring of reinforced concrete structures - A review. *International Journal of Electrochemical Science*, 2(1), 1-28. doi:10.1016/s1452-3981(23)17049-0.
- [76] Yodsudjai, W., & Pattarakittam, T. (2017). Factors influencing half-cell potential measurement and its relationship with corrosion level. *Measurement: Journal of the International Measurement Confederation*, 104, 159-168. doi:10.1016/j.measurement.2017.03.027.
- [77] Kakooei, S., Akil, H. M., Dolati, A., & Rouhi, J. (2012). The corrosion investigation of rebar embedded in the fibers reinforced concrete. *Construction and Building Materials*, 35, 564-570. doi:10.1016/j.conbuildmat.2012.04.051.
- [78] Sappakittipakorn, M., & Banthia, N. (2012). Corrosion of rebar and role of fiber reinforced concrete. *Journal of Testing and Evaluation*, 40(1). doi:10.1520/jte103873.
- [79] Andrade, C., & Alonso, C. (1996). Corrosion rate monitoring in the laboratory and on-site. *Construction and Building Materials*, 10(5), 315-328. doi:10.1016/0950-0618(95)00044-5.
- [80] Daniyal, M., & Akhtar, S. (2020). Corrosion assessment and control techniques for reinforced concrete structures: a review. *Journal of Building Pathology and Rehabilitation*, 5(1), 1-20. doi:10.1007/s41024-019-0067-3.
- [81] Paul, S., van Zijl, G., & Šavija, B. (2020). Effect of Fibers on Durability of Concrete: A Practical Review. *Materials*, 13(20), 4562. doi:10.3390/ma13204562.
- [82] Zhao, B., Li, J. H., Hu, R. G., Du, R. G., & Lin, C. J. (2007). Study on the corrosion behavior of reinforcing steel in cement mortar by electrochemical noise measurements. *Electrochimica Acta*, 52(12), 3976-3984. doi:10.1016/j.electacta.2006.11.015.
- [83] Almashakbeh, Y., Saleh, E., & Al-Akhras, N. M. (2022). Evaluation of Half-Cell Potential Measurements for Reinforced Concrete Corrosion. *Coatings*, 12(7), 975. doi:10.3390/coatings12070975.
- [84] Alexandre Reginato, L., Somensi Lorenzi, L., & Carlos Pinto da Silva Filho, L. (2023). Corrosion in reinforced concrete: Diagnostics through Potential Corrosion Technique. doi:10.21203/rs.3.rs-3156721/v3.
- [85] Mansfeld, F., Sun, Z., & Hsu, C. H. (2001). Electrochemical noise analysis (ENA) for active and passive systems in chloride media. *Electrochimica Acta*, 46(24-25), 3651-3664. doi:10.1016/s0013-4686(01)00643-0.

- [86] Darmawan, M. S. (2010). Pitting corrosion model for reinforced concrete structures in a chloride environment. *Magazine of Concrete Research*, 62(2), 91–101. doi:10.1680/mac.2008.62.2.91.
- [87] Dharma, S., Silitonga, A. S., Shamsuddin, A. H., Sebayang, A. H., Milano, J., Sebayang, R., Sarjianto, Ibrahim, H., Bahri, N., Ginting, B., & Damanik, N. (2023). Properties and corrosion behaviors of mild steel in biodiesel-diesel blends. *Energy Sources, Part A: Recovery, Utilization and Environmental Effects*, 45(2), 3887–3899. doi:10.1080/15567036.2019.1668883.
- [88] Andrade, C. (2019). Propagation of reinforcement corrosion: principles, testing and modelling. *Materials and Structures/Materiaux et Constructions*, 52(1), 2. doi:10.1617/s11527-018-1301-1.
- [89] Blunt, J., Jen, G., & Ostertag, C. P. (2015). Enhancing corrosion resistance of reinforced concrete structures with hybrid fiber reinforced concrete. *Corrosion Science*, 92, 182–191. doi:10.1016/j.corsci.2014.12.003.
- [90] Bertolini, L., Elsener, B., Pedferri, P., Redaelli, E., & Polder, R. B. (2013). *Corrosion of steel in concrete: prevention, diagnosis, repair*. John Wiley & Sons, Hoboken, United States.
- [91] Hoshi, Y., Koike, T., Tokieda, H., Shitanda, I., Itagaki, M., & Kato, Y. (2019). Non-Contact Measurement to Detect Steel Rebar Corrosion in Reinforced Concrete by Electrochemical Impedance Spectroscopy. *Journal of The Electrochemical Society*, 166(11), C3316–C3319. doi:10.1149/2.0371911jes.
- [92] Dhoubi, L., Triki, E., & Raharinaivo, A. (2002). The application of electrochemical impedance spectroscopy to determine the long-term effectiveness of corrosion inhibitors for steel in concrete. *Cement and Concrete Composites*, 24(1), 35–43. doi:10.1016/S0958-9465(01)00062-2.
- [93] Ribeiro, D. V., & Abrantes, J. C. C. (2016). Application of electrochemical impedance spectroscopy (EIS) to monitor the corrosion of reinforced concrete: A new approach. *Construction and Building Materials*, 111, 98–104. doi:10.1016/j.conbuildmat.2016.02.047.
- [94] Song, G. (2000). Equivalent circuit model for AC electrochemical impedance spectroscopy of concrete. *Cement and Concrete Research*, 30(11), 1723–1730. doi:10.1016/S0008-8846(00)00400-2.
- [95] Park, J., & Jung, M. (2021). Evaluation of the corrosion behavior of reinforced concrete with an inhibitor by electrochemical impedance spectroscopy. *Materials*, 14(19), 5508. doi:10.3390/ma14195508.
- [96] Dorothy, R., Sasilatha, T., & Rajendran, S. (2021). Corrosion resistance of mild steel (Hull plate) in sea water in the presence of a coating of an oil extract of plant materials. *International Journal of Corrosion and Scale Inhibition*, 10(2), 676–699. doi:10.17675/2305-6894-2021-10-2-13.
- [97] Fattah-alhosseini, A., Taheri Shoja, S., Heydari Zebardast, B., & Mohamadian Samim, P. (2011). An Electrochemical Impedance Spectroscopic Study of the Passive State on AISI 304 Stainless Steel. *International Journal of Electrochemistry*, 2011, 1–8. doi:10.4061/2011/152143.
- [98] Cellat, K., Tezcan, F., Beyhan, B., Kardaş, G., & Paksoy, H. (2017). A comparative study on corrosion behavior of rebar in concrete with fatty acid additive as phase change material. *Construction and Building Materials*, 143, 490–500. doi:10.1016/j.conbuildmat.2017.03.165.



Strength Assessment of Stiffened-Panel Structures against Buckling Loads: FE Benchmarking and Analysis

M. Sholikhah¹, R. Ridwan^{2*}, A. R. Prabowo^{1*}, T. Ghanbari-Ghazijahani³,
I. Yaningsih¹, N. Muhayat¹, D. D. D. P. Tjahjana¹, R. Adiputra⁴, J. M. Sohn⁵

¹ Department of Mechanical Engineering, Universitas Sebelas Maret, Surakarta, Indonesia.

² Department of Mechanical Engineering, Universitas Merdeka Madiun, Madiun, Indonesia.

³ Faculty of Science and Engineering, School of Engineering, Macquarie University, New South Wales, Australia.

⁴ Research Center for Hydrodynamics Technology, National Research and Innovation Agency (BRIN), Surabaya, Indonesia.

⁵ Department of Naval Architecture and Marine Systems Engineering, Pukyong National University, Busan, South Korea.

Received 16 October 2023; Revised 10 March 2024; Accepted 16 March 2024; Published 01 April 2024

Abstract

This research endeavors to examine the effect of stiffener shapes on the structural capacity of stiffened-plate structures, specifically focusing on Tee (T), Angle (L), and Flat (I) stiffened plates. The primary objectives are threefold: firstly, to quantify the critical load values during the buckling phenomenon for T, L, and I stiffened plates; secondly, to assess model deformation upon failure; and thirdly, to investigate whether the buckling behavior of T, L, and I stiffened plates correlates with distinct failure patterns. Employing numerical simulation through the finite element method, this study sheds light on previously unexplored aspects of structural behavior. The findings indicate that angle stiffeners exhibit superior load-bearing performance compared to flat bars. Notably, the research reveals a substantial increase in maximum compressive load by at least 15.90% with Tee bar and 8.25% with angle bar stiffeners when the stiffened panels undergo a 5 mm displacement, presenting a potential avenue for structural enhancement. Additionally, the study demonstrates that T bars outperform in terms of resisting buckling. Noteworthy is the novel approach of examining the combined effect of transverse frame, longitudinal frame, and hull girder under buckling scenarios, a facet not explored in previous research. Furthermore, the utilization of steel S355JR-EN10210 as a material introduces a unique dimension not previously considered in these scenarios.

Keywords: Ultimate Strength; Stiffened Panel; Buckling Load; Ship Structure; Nonlinear Finite Element Method (NLFEM).

1. Introduction

Ships play a crucial role on a global scale and are an essential element of international commerce. By 2020, nearly 10.7 billion tons of international maritime trade were carried out. Nevertheless, this figure is marginally reduced compared to 2019 as a result of the sequential disruptions caused by the COVID-19 pandemic in supply chains, demand, and logistics. The COVID-19 pandemic has proven to be disrupting maritime transport, although the results are less damaging than previously feared. In the year 2019, the global maritime trade amounted to 11.2 billion tons. Contrary to predictions, the decline in volume during 2020 was less severe than anticipated. By year-end, there was a recovery, setting the stage for a significant shift in worldwide supply chains and the emergence of novel patterns in maritime trade.

* Corresponding author: ridwan@unmer-madiun.ac.id; aditya@ft.uns.ac.id

 <http://dx.doi.org/10.28991/CEJ-2024-010-04-03>



© 2024 by the authors. Licensee C.E.J, Tehran, Iran. This article is an open access article distributed under the terms and conditions of the Creative Commons Attribution (CC-BY) license (<http://creativecommons.org/licenses/by/4.0/>).

The disruptions in the initial half of 2020 led to a contraction of 3.8 percent in maritime trade for the year [1]. Not only that, safety and shipping studies show that there will be 49 missing ships by the end of 2020 worldwide. All in all, in 2019, it was reported that there were 48 missing ships that occurred worldwide [2]. Various factors contribute to this catastrophe, including but not limited to fire or explosion, collisions, grounding, hull impairment, and engine malfunction or failure.

Numerous authors have delved into the investigation of buckling and post-buckling phenomena in thin-walled structures exposed to buckling loads. Among them, Paik & Seo [3] and Omidali & Khedmati [4] focused their research on the thin-walled structures' stability. Paik & Seo [3] contributed valuable insights by applying nonlinear finite element methods (NLFEM) to assess the Ultimate Limit State (ULS) of steel stiffened-plate structures. Their exploration involved utilizing lateral pressure actions and biaxial compression to evaluate the ultimate strength of the panels. Doan et al. [5] conducted a strength assessment of panels made of stiffened aluminium and steel, featuring openings on longitudinal girders under compressive loads. Employing finite element analyses, they provided a detailed description of the models' deformation. Pedram & Khedmati [6] utilized finite element analyses to investigate how welding affects the strength of aluminium-stiffened plates under the influence of both uniaxial compression and lateral pressure. The study incorporated common marine aluminium alloys with mechanical and geometrical imperfections in the stiffened panel. In a case study without finite element analyses, Guedes Soares and Gordo [7] introduced approaches for designing stiffened plates subjected primarily to uniaxial compression. Their approach utilized the method outlined by the American Bureau of Shipping (ABS) to determine buckling strength.

In recent years, researchers have shown a keen interest in the subject of dynamic buckling. An illustrative example is the study conducted by Feng et al. [8]. The study concentrated on conducting a compression test on hull plates to evaluate the influence of interconnected damage on their ultimate strength. Using AH36 steel material, the research investigated the ultimate strength of hull plates affected by both pitting corrosion and cracks simultaneously. Cui & Wang [9] undertook both numerical and experimental examinations of the capacity of corrugated and plane bulkheads subjected to lateral pressure. Their study, employing corrugated stiffener types, revealed that when a corrugated bulkhead deforms under lateral pressure, the flange on the bulge side primarily experiences tensile stress, while the flange on the opposite side bears compressive stress. Lee & Kang [10] explored the elastic local buckling factors of I-shaped beams with a focus on flange-web interaction. Their study aimed to comprehend the local buckling characteristics and strength of I-shaped structural sections using three-dimensional finite element analysis, with a specific emphasis on the interactions between flanges and webs. Another study conducted by Boissonnade et al. [11] employed both experimental and numerical approaches to investigate buckling, utilizing cellular steel beams as structures. Moreover, Ghadami et al. [12] investigated the buckling and post-buckling characteristics of I-beams with coped top flanges and slender web panels. Their study investigated the influence of plate slenderness, cope specifications (depth, length), and initial geometric imperfections on the elastic, inelastic, and post-buckling responses of such beams. Stiffened panel structures featuring flat, angle, and Tee bar stiffeners play a pivotal role in marine engineering, thin-walled structures, particularly within the domain of ship construction. These distinct stiffener types are strategically employed to enhance the structural integrity and strength of ship components, ensuring optimal performance under varying maritime conditions. Observing that the majority of investigations into the buckling phenomenon concentrate primarily on the hull plate structure, it is evident that these studies overlook the interactions among the plate, various stiffener types (L, T, I), transverse frame, longitudinal girder, and the specific marine steel grade material used.

The major aim of this investigation was to look into the behavior of stiffened plates subjected to buckling loads, with a comprehensive consideration of various stiffener types, namely angle, flat, and Tee bar, in conjunction with the influential factors of transverse frames and longitudinal girders. Notably, the study employed S355JR-EN10210 steel as the material of choice, introducing a critical element to the analysis that had not been previously explored in this context. Additionally, a numerical modeling approach employing the FE method was implemented. The reliability and precision of this numerical model were established through a benchmarking study, aligning the simulated outcomes with experimental results. Moreover, this study placed an emphasis on scrutinizing the failure mechanisms inherent in stiffened plates under the influence of buckling loads, as simulated through the finite element method.

2. Research Methodology

2.1. Benchmarking

The inclusion of a benchmarking study in the research methodology serves as a critical measure to guarantee the reliability and robustness of the obtained results by validating the numerical simulations against established reference values or experimental data. Tests of stiffened panels that have been performed by Quinn et al. [13] will become benchmarking studies in this study. Figure 1a shows the specimen geometry and the dimensions of the stiffened panel. The specimen has an arrangement with twelve sub-stiffeners and three stringers, each 590 mm long. The stringers possess a height and thickness of 28 mm and 2.8 mm, respectively, parallel at 167 mm apart.

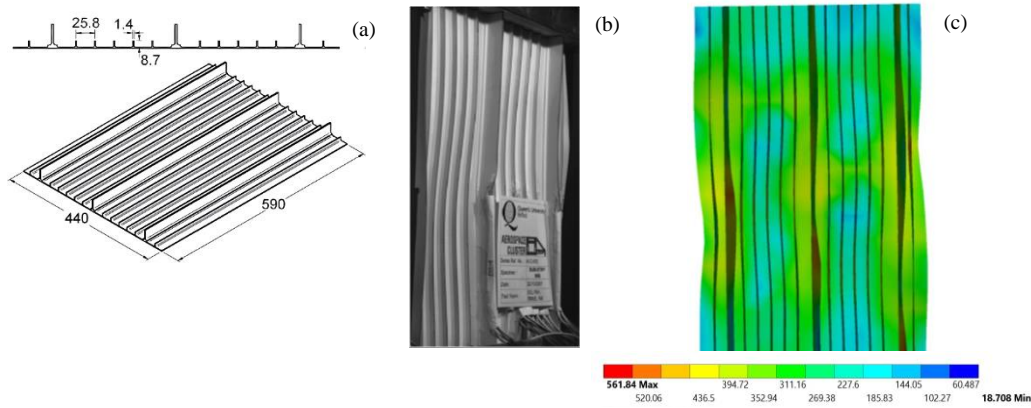


Figure 1. (a) The dimension of the stiffened plate [13]; (b) deformation mode in the experiment [8]; and (c) deformation mode in the numerical finite element.

The sub-stiffeners, measuring 8.7 mm in height and 1.4 mm in thickness, are positioned between the longitudinal stringers. The plating exhibits a thickness of 2.2 mm. Utilizing Aluminium Alloy 2024-T351, specimens were fabricated for experimental testing. A hydraulic testing machine with a 500 kN capacity conducted the tests.

In this study, the material properties of aluminium alloy (2024-T3) were assumed and used since the ones of 2024-T351 were not mentioned in the study conducted by Quinn et al. [13]. The 2024-T3 has materials features as follows: density ρ of 2780 kg/m³, Young's modulus E of 73.4 GPa, Poisson's ratio ν of 0.33, Yield stress σ_y of 315 MPa, Tensile strength σ_u of 550 MPa, and failure strain ϵ_f 0.18 [14, 15]. The ones for 2024-T3 are presented in Table 1. A comparison of the total mass stiffened panel to the original (as calculated by Quinn et al. [13]) and the proposed stiffened panel is presented in Table 2. It is observed that they correlated well and had no significant deference compared to the experimental data. The current stiffened panel has a total mass of 1.993 kg in comparison to the test data of 1.968 kg. Hence, the mass percentage difference is lower than 1.27% if compared to the tests.

Table 1. Material features of 2024-T3

Property	Symbol	Value
Density	ρ	2780 kg/m ³
Yield stress	σ_y	315 MPa
Young's modulus	E	73.4 GPa
Tensile strength	σ_u	550 MPa
Poisson's ratio	ν	0.33
Exponent	n	0.406
Failure strain	ϵ_f	0.18

Table 2. Mass comparative study of the stiffened plate

Data Source	Mass	Mass Difference	Mass Difference (%)
Quinn et al. [13]	1.968 kg	-	-
Current study	1.993 kg	+0.025 kg	+1.27 %

The calculations are executed utilizing the ANSYS commercial software for finite element analysis [16]. The deformation mode obtained from the numerical finite element seems in accordance with the experimental data in Figures 1b and 1c. The load versus displacement is shown in Figure 2. The examination of mesh convergence has been carried out on stiffened panels of varying dimensions, ranging from 40 to 60 mm in the finite element analysis. As shown in Figure 2, the load versus displacement curves for all element sizes are extremely similar to experimental results. Quinn et al. [13] found that the capacity of the experimental buckling of the stiffened panel showed at 255 kN. Here, the 40, 45, 50, 55, and 60 mm of element sizes produce the ultimate strength of 258.43, 250.74, 253.86, 252.18, and 238.81 kN, respectively. It is observed that the error produced by these element sizes does not exceed 6.6%. The choice of a 60-mm mesh size is based on a careful consideration of both computational time and accuracy, as illustrated in Figure 2. This mesh size is sufficiently small to accurately capture the deformation of the model.

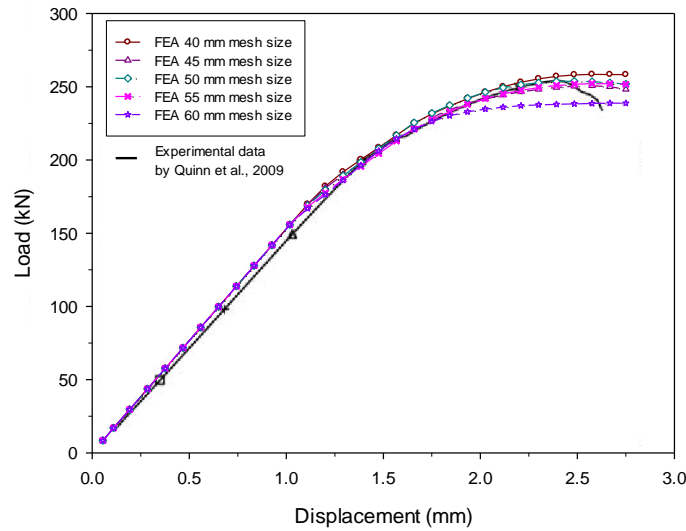


Figure 2. Mesh sensitivity study of the stiffened plate obtained through finite element analysis

2.2. Model and Boundary Conditions

An ANSYS software is utilized to construct a finite element model with non-linear characteristics [16] for simulating the buckling scenarios of stiffened panels. A 4200×24000 mm stiffened panel similar to the one used in the work of Doan et al. [5] is used for the buckling scenario. Figure 3 presents the details of the dimension. The stiffened panel consists of the plate, stiffener, transverse frame and longitudinal girder. Dimension of the plate is observed at width and length of 2400 mm and 4200 mm, respectively. The longitudinal girder is made with the Tee bar type with a stiffener size in height $h_w = 150$ mm, web thickness of stiffener $t_w = 8$ mm, flange breadth of stiffener $b_f = 100$ mm, and flange thickness of stiffener $t_f = 10$ mm. Twelve stiffeners attached to the plate have the dimensions of $h_w = 60$ mm and thickness $t_w = 6$ mm. In this study, the transverse frame is modelled with different stiffeners i.e., angle, flat, and Tee bar and the resulting stiffened panel strength will be assessed for the three types of stiffeners. Typical three types of stiffeners that are commonly used in marine structures are shown in Figure 4.

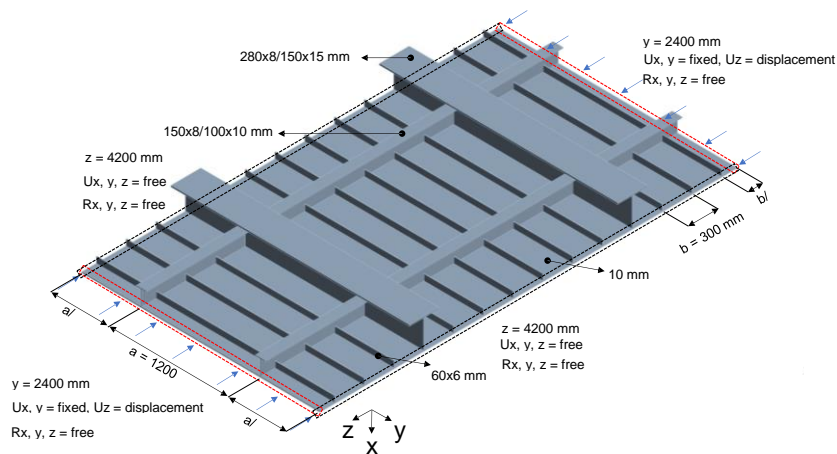


Figure 3. The dimension of a stiffened-plate structure [5]

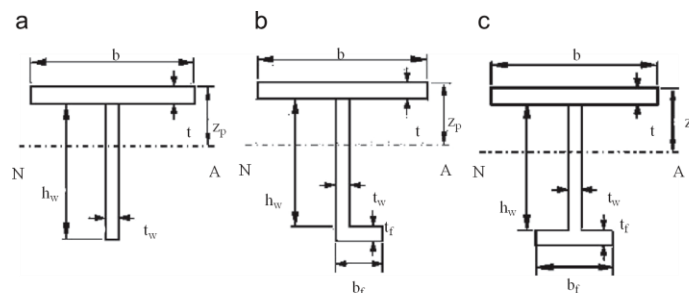


Figure 4. (a) Flat; (b) angle; and (c) Tee bar stiffeners [3]

Table 3 summarizes the geometrical properties of the stiffened panels. For both plating, longitudinal girder, and stiffeners, the S355JR-EN10210 steel becomes the manufacture-grade material. S355JR-EN10210 steel has Young’s modulus $E = 210$ GPa, the density $\rho = 7800$ kg/m³, Poisson’s ratio $\nu = 0.3$, and failure strain $\epsilon_f = 0.28$. The yield stress σ_y and ultimate stress σ_u are 390 MPa and 495 MPa, respectively. The strain hardening exponent (n) and strength coefficient (K) are 0.18 and 830 MPa, respectively. Common steel materials including the mechanical properties used in the finite element analysis can be found in the study conducted by Ridwan et al. [17].

Table 3. Stiffened panels and their geometric dimensions

Panel	a (mm)	y (mm)	z (mm)	b (mm)	t (mm)	h_w (mm)	t_w (mm)	b_f (mm)	t_f (mm)
Flat bar	1200	2400	4200	300	10	150	8	-	-
Angle bar	1200	2400	4200	300	10	150	8	50	10
Tee bar	1200	2400	4200	300	10	150	8	100	10

The boundary condition is an essential part of finite element analysis [18, 19]. Therefore, in this study, applied boundary conditions to the stiffened panel are such as translation constraint, displacement, and rotation constraint. The translation constraints are set at U_x , and U_y at each end of the specimen at coordinates $z = 0$ mm and $z = 4200$ mm. Displacement in the U_z direction is made free at both ends of the specimen to apply the buckling phenomenon. On both sides of the stiffened panel, the translation and rotation constraint are made in $U_x, U_y, U_z = \text{free}$ and $R_x, R_y, R_z = \text{free}$. The simulation time is performed at 1 s. The boundary condition applied on buckling of the stiffened panel is shown in Figure 3. The three different types of stiffener models applied to the transverse frame are assessed in this study to measure their effect on buckling on stiffened panels. The stiffeners are modelled with the flat, angle, and Tee bar, Figure 4. For flat bar, the thickness t_w is set to be 8 mm in height h_w 150 mm. As for the angle and Tee bars, the size is stiffener flange breadth $b_f = 50$ mm and 100 mm dan and stiffener flange thickness t_f made in 10 mm, respectively. The geometric characteristics of the reinforced panels examined in the current investigation are summarized in Table 3.

The buckling scenario was simulated through the utilization of the nonlinear finite element method (NLFEM) in this analysis. The first step of the research is to create the specimen in ANSYS Workbench, which allows the geometric representation and the structural components to be defined in the software. Next, the material properties are assigned, using S355JR-EN10210 steel as the material model for the specimen. Then, the mesh size is carefully determined, which is essential for obtaining accurate and reliable numerical simulations. After that, the boundary conditions are specified, including the constraints and loading conditions that simulate the buckling load. The fifth step is to define the solution parameters, which include the analysis of stress, strain, and deformation patterns in the specimen. This stage enables a comprehensive understanding of the structural response under different conditions. This sequential approach ensures a systematic and methodical execution of the research, which helps to study the behaviour of stiffened plates under buckling loads. Figure 5 shows the flowchart in this research.

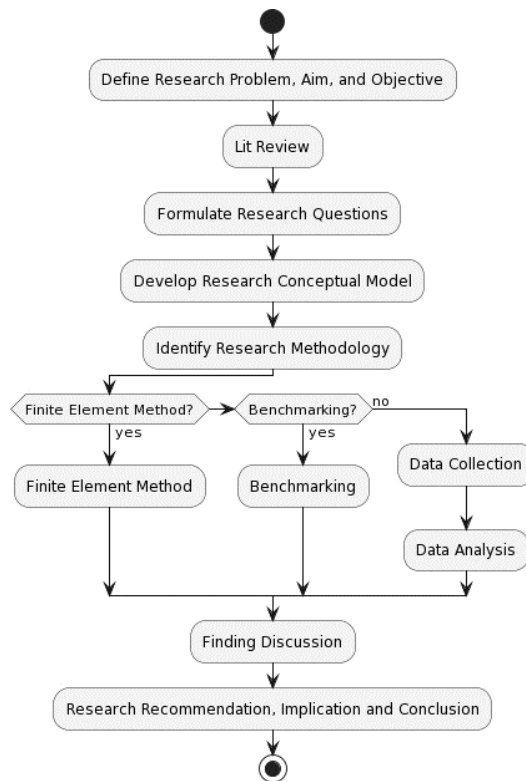


Figure 5. Flowchart presenting the research steps

3. Results and Discussion

3.1. The Stiffeners and Their Effects

Figure 6 shows the comparison of the ultimate compressive strength of stiffened panels subjected to 5 mm displacement with flat, angle, and Tee bar. As shown in Figure 6, the stiffener with the Tee bar type appears to have a maximum load that is greater than the angle and Flat bar. However, at 0 to 1.8 mm displacement seems to have a fairly equal load that can be endured for all three types of stiffener. Upon surpassing a displacement threshold of 1.8 mm, a discernible contrast in load resistance becomes apparent, wherein flat bars exhibit the least capacity when juxtaposed with Tee bars and Angle bars. The maximal compressive strength generated by these three stiffeners manifests as 6191.3 kN for flat bars, 6702.2 kN for angle bars, and 7176 kN for Tee bars, underscoring the substantial disparities in their load-bearing capabilities beyond the specified displacement threshold.

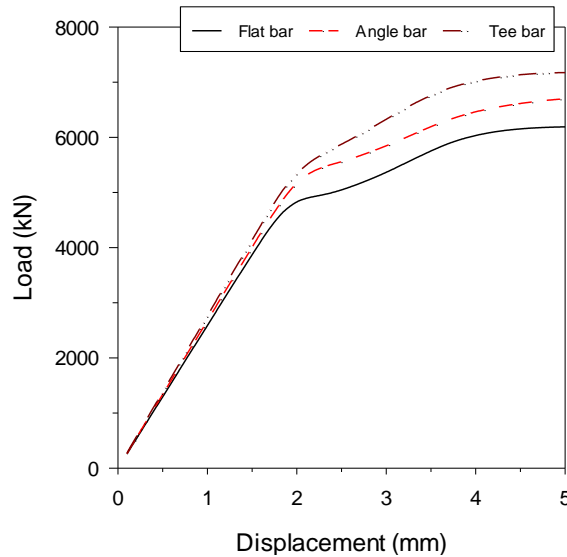


Figure 6. Capacity of stiffened panels with 5 mm displacement.

As it is observed, the maximum compressive strength increases by 15.90 % and 8.25 % for the Tee and angle bar type compared to the flat bar, respectively. The ultimate strength of stiffened panels with 10 mm displacement is presented in Figure 7. It seems that the load versus displacement obtained from 10 mm of displacement is not quite different from the 5 mm of displacement. There are some increases in terms of maximum compressive strength obtained from flat, angle, and Tee bars. Upon observation, it is noted that the maximum compressive strength generated on the ribs of this stiffener manifests as 6297.5 kN, 6832.8 kN, and 7292 N, respectively. Significantly, a discernible enhancement is evident, with the maximum compressive strength increasing by 8.50% and 15.79% for the Tee bar and angle bar types in comparison to the flat bar, respectively. It is noteworthy that this percentage increase remains consistent when subjected to a 5 mm displacement, indicating a sustained and consistent improvement in compressive strength across the different stiffener types, thereby emphasizing the stability and reliability of the observed trends.

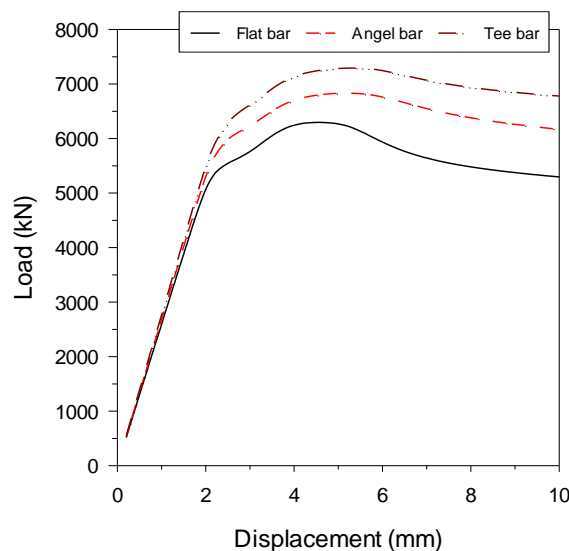


Figure 7. Ultimate strength of stiffened panels subjected to 10 mm displacement

Different things happened to the average stress generated from the three different stiffeners (Figures 8 and 9). Deformation shapes and von-Mises stress of panels subjected to 5 mm and 10 mm of displacement are presented in Figures 10 and 11, respectively. At 5mm displacement, the average stress produces a fairly similar stress result for the three stiffeners. The resulting values are 250.81 MPa, 254.08 MPa, and 249.8 MPa produced from stiffener-type flat, angle, and Tee bar, respectively. This shows that no more than a 1.30 % difference occurs. Significant variations become apparent when a 10mm displacement is applied, as depicted in Figure 9. These disparities manifest when the displacement exceeds 5mm. Among the stiffeners examined, the Tee bar exhibited the highest maximum average stress, measuring approximately 255.94 MPa, followed closely by the angle bar at 249.71 MPa and the flat bar at 240.66 MPa. This translates to percentage increments of about 3.76% and 6.35% for the angle and Tee bars in comparison to the flat type. Moreover, as depicted in Figure 12, the visual representation showcases the equivalent strain distribution within a stiffened panel upon the culmination of the simulation, taking into account both 5 mm and 10mm displacements. Notably, the discernible observation emerges that irrespective of the stiffener type—be it the flat bar, angle bar, or Tee bar—the obtained results exhibit a striking uniformity in terms of maximum strain. This uniformity is distinctly evident, with the maximum strain values converging within the narrow range of 0.0028 to 0.003 for the 5 mm displacement scenario and 0.0034 to 0.0037 for the 10 mm displacement scenario.

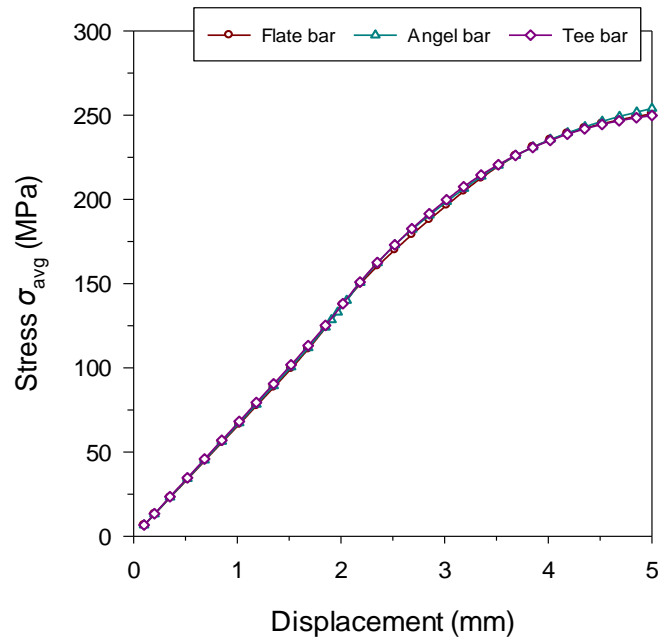


Figure 8. Stress average of stiffened panels subjected to 5 mm displacement

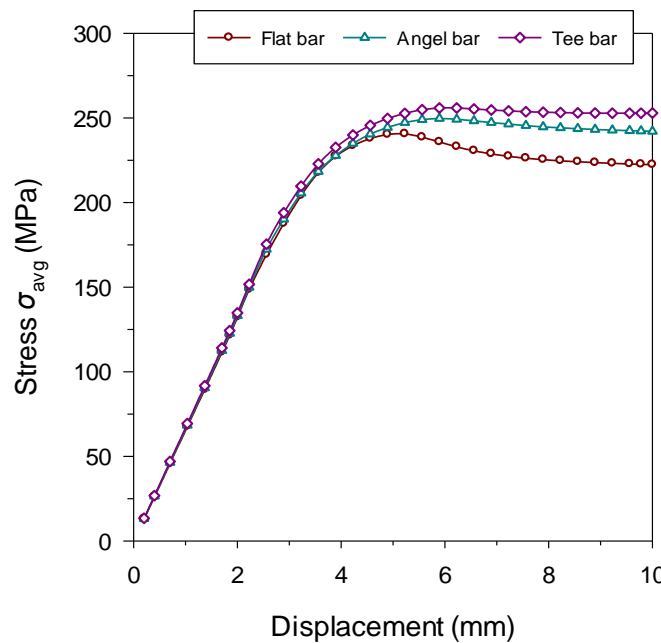


Figure 9. Stress average of stiffened panels subjected to 10 mm displacement

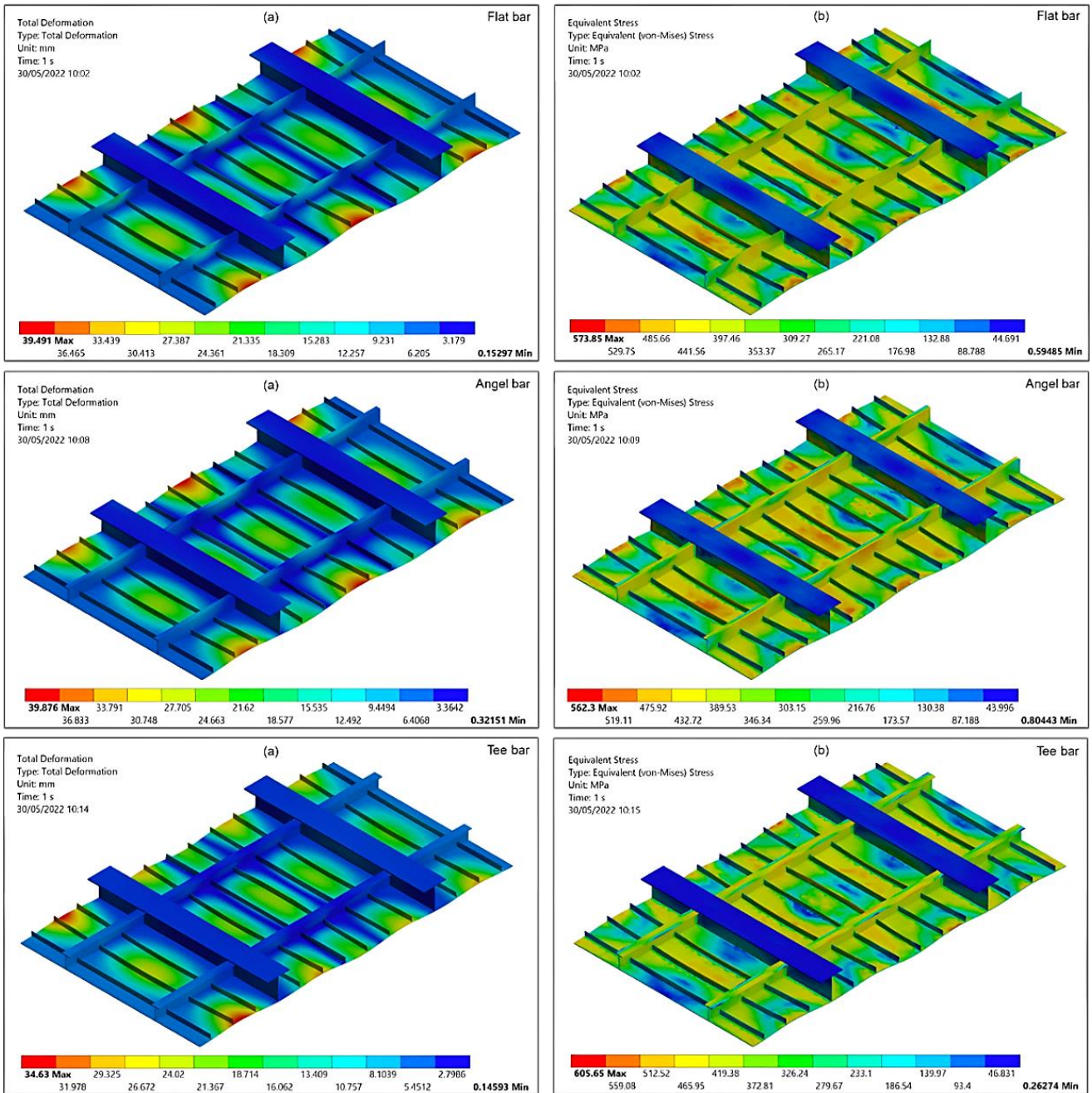
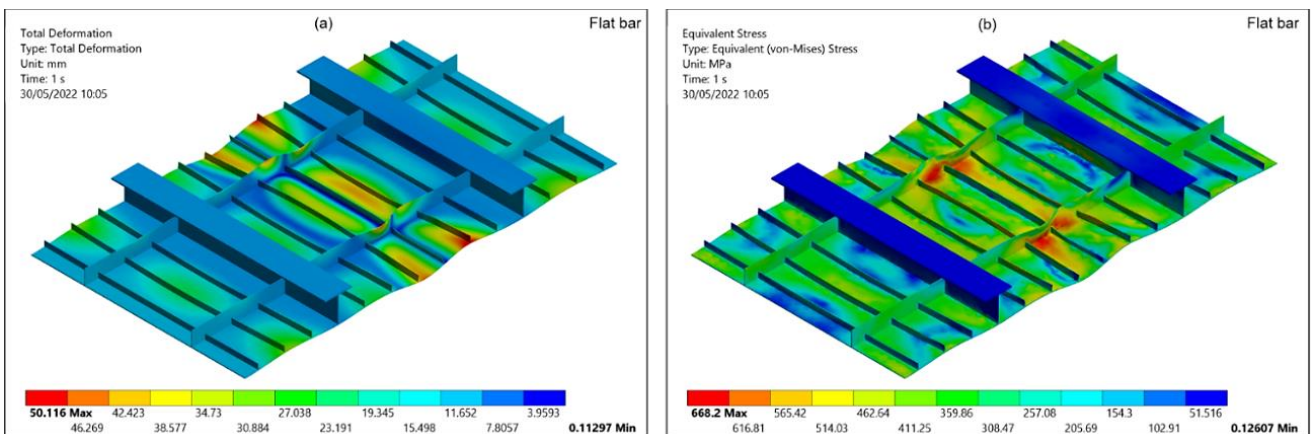


Figure 10. Deformation shapes and von-Mises stress distributions of stiffened panel subjected to 5 mm displacement: (a) Total deformation; and (b) Von-Mises stress contour



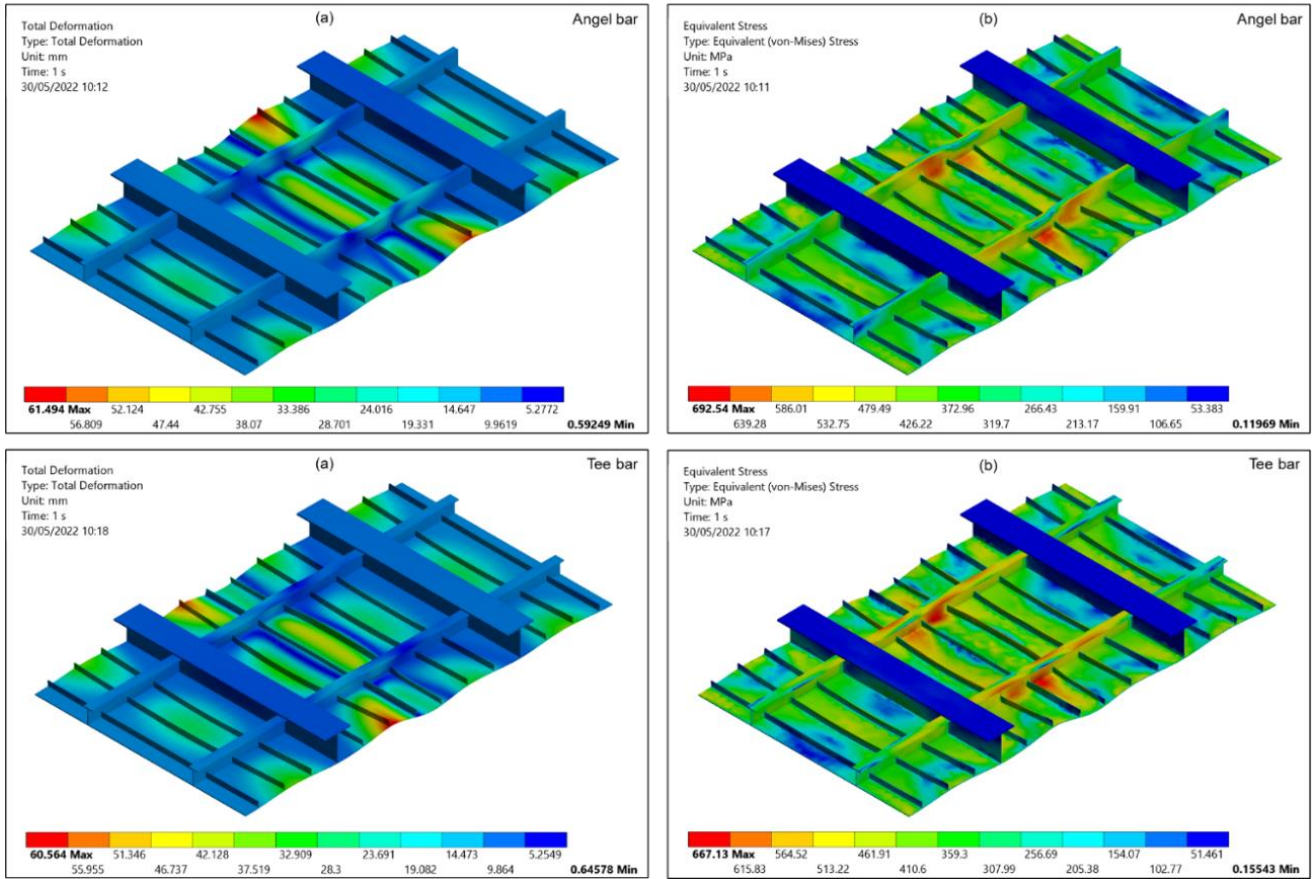
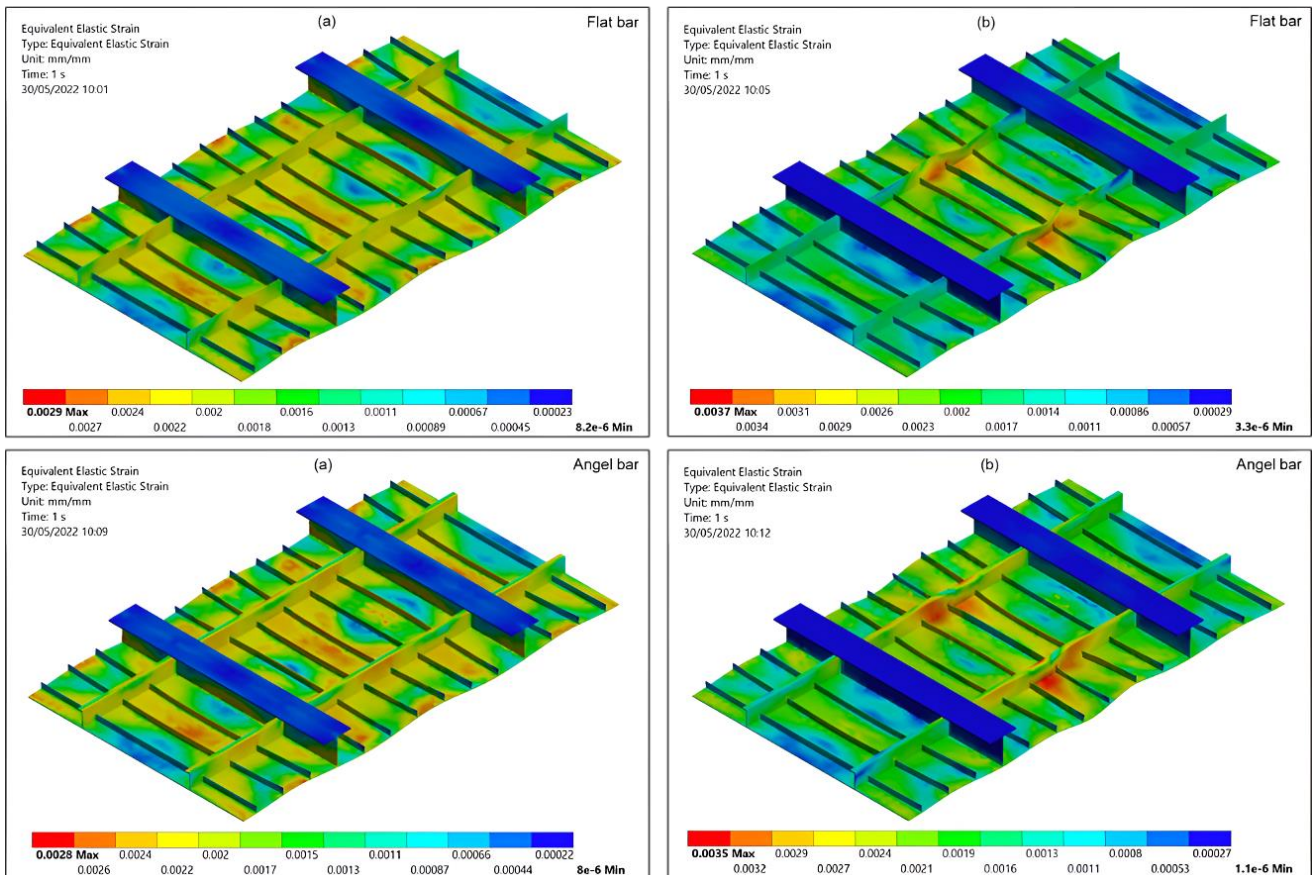


Figure 11. Deformation and stress (von-Mises) of panel subjected to 10 mm displacement: (a) Total deformation; and (b) Von-Mises stress contour



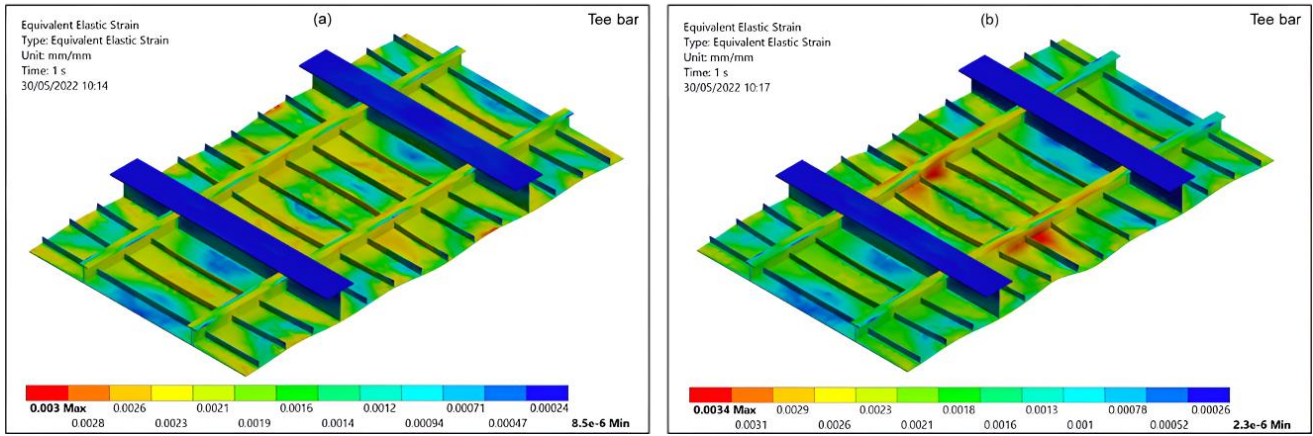


Figure 12. Equivalent strain contour of stiffened panel at the end of simulation: (a) 5 mm displacement; and (b) 10 mm displacement

3.2. Displacement and its Effect

Figure 13 displays the results of load versus displacement subjected to 5 mm and 10 mm of displacement for flat, angle, and Tee bar. The increase in displacement does not remarkably affect the load-bearing strength until the maximum compressive strength occurs (Figure 13). It seems that the load versus displacement obtained from 10 mm of displacement is quite different from the 5 mm of displacement. There are some increases in terms of maximum compressive strength obtained from flat bar, angle bar, and Tee bar stiffener types. However, these increments appear to have not been insignificant. Upon observation, it becomes evident that a 10 mm displacement yields the maximum compressive strength for stiffened panels, considering various types of stiffeners, namely flat, angle, and Tee bar. The numerical values associated with this phenomenon showcase the distinctive responses of each stiffener type, emphasizing the importance of displacement in influencing structural behavior. At the 10 mm displacement mark, the maximum compressive strengths were recorded at 6297.5 kN, 6832.8 kN, and 7292 kN for the flat, angle, and Tee bar stiffeners, respectively. In contrast, at a 5 mm displacement, the compressive strength does not reach its peak for any of the aforementioned stiffener types. The corresponding compressive strengths at 5 mm were measured at 6191.3 kN, 6702.2 kN, and 7176 kN for flat, angle, and Tee bars, respectively. This intriguing phenomenon highlights a substantial difference of approximately 106.2 kN, 130.6 kN, and 116 kN, manifesting as larger compressive strengths at the 10 mm displacement compared to the 5 mm displacement for flat, angle, and Tee bar type stiffeners, respectively. This nuanced comparison underscores the sensitivity of the stiffened plates to varying displacements and offers valuable insights into the nuanced mechanical responses dictated by different stiffener configurations under distinct loading conditions.

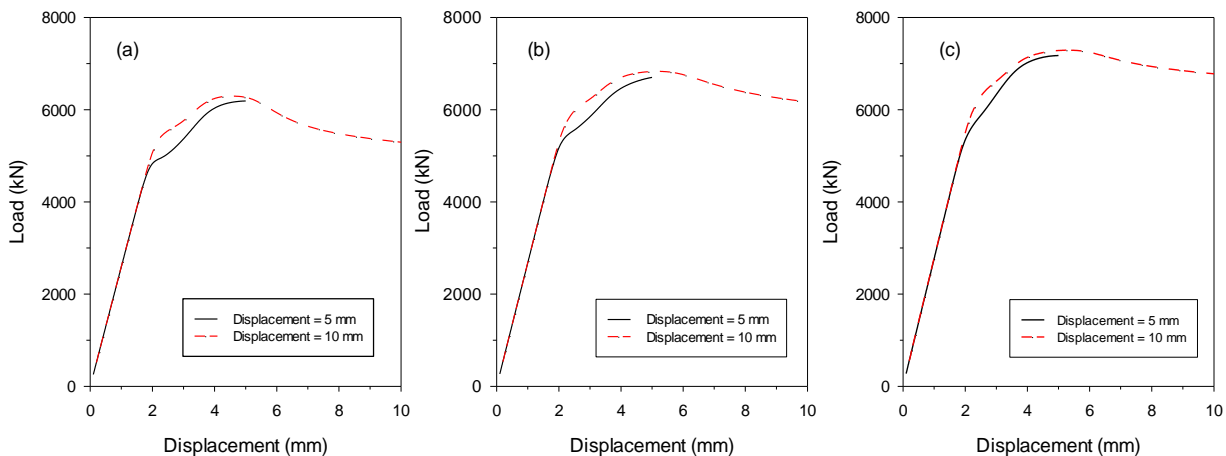


Figure 13. The ultimate strength characteristics of a reinforced panel subjected to biaxial compression involve evaluating three configurations: (a) Flat; (b) Angle; and (c) Tee bar

The comparative analysis of stress average behavior for stiffened panels subjected to 5 mm and 10 mm displacements, considering flat, angle, and Tee bar configurations, is intricately depicted in Figure 14. The stress average behavior manifests itself around 250.81 MPa, 254.08 MPa, and 249.8 MPa for stiffened panels featuring flat, angle, and Tee bars, respectively, when subjected to a 5 mm displacement. In contrast, under a 10 mm displacement, the maximum stress averages approximately 240.66 MPa, 249.71 MPa, and 255.94 MPa, sequentially, for the corresponding stiffened

panel configurations. Intriguingly, these findings suggest a nuanced observation, indicating that the maximum stress average does not exhibit a substantial variance between the results obtained from stiffened panels subjected to 5 mm and 10 mm displacements. This subtle distinction prompts a closer examination of the structural response, implying that the impact of displacement magnitude on stress average may not be as pronounced as anticipated. The convergence of stress averages across the two displacement scenarios raises intriguing questions about the inherent structural characteristics and response patterns of stiffened panels, warranting a more in-depth investigation into the underlying factors influencing their behavior under varying displacement conditions.

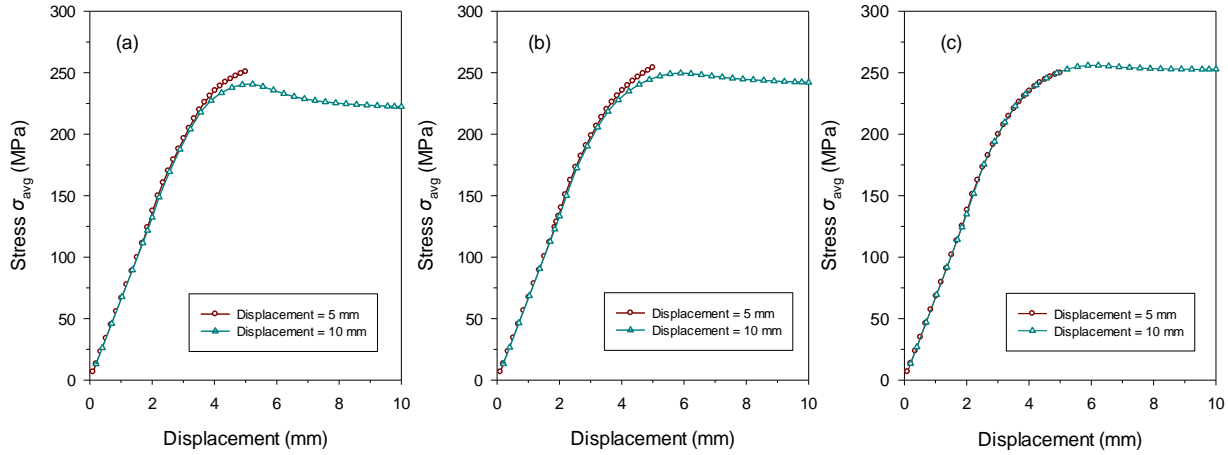


Figure 14. The stress average behavior for the stiffened panel under biaxial compression: (a) Flat; (b) Angle; and (c) Tee bar

3.3. Effect of the Element Size

The finite element method is extremely concerned about proposing the mesh size. The actual structure will be discretized into small elements when using the finite element method. As can be seen in Figures 15 and 16, the mesh size affects the maximum compressive load output on stiffened panels with stiffener type flat, angle, and Tee bar. In this study, it can be seen that the larger the mesh size, the greater the maximum compressive load value. The greater maximum compressive strength value occurs in 5 mm and 10 mm displacement scenarios. For stiffened panels with the Tee bar type itself, the value is 6191.3 kN when a mesh size of 60 mm is obtained from 5 mm displacement. While the results obtained at the 80mm mesh size are at 6544.9 kN. This shows that there is an increase in the maximum compressive strength value of 5.55%. The same phenomenon occurs in the stiffened panel with the other stiffener type which is the angle bar and flat bar. In the analysis encompassing mesh sizes ranging from 60 mm to 80 mm for both types of stiffeners, a discernible increase in maximum compressive strength is observed. Specifically, within this mesh size range, the flat bar stiffener exhibits an approximate increment of 4.56%, reaching a maximum compressive strength value of 6297.5 kN, while the corresponding increase for the angle bar stiffener is approximately 4.13%, resulting in a maximum compressive strength value of 6715.3 kN.

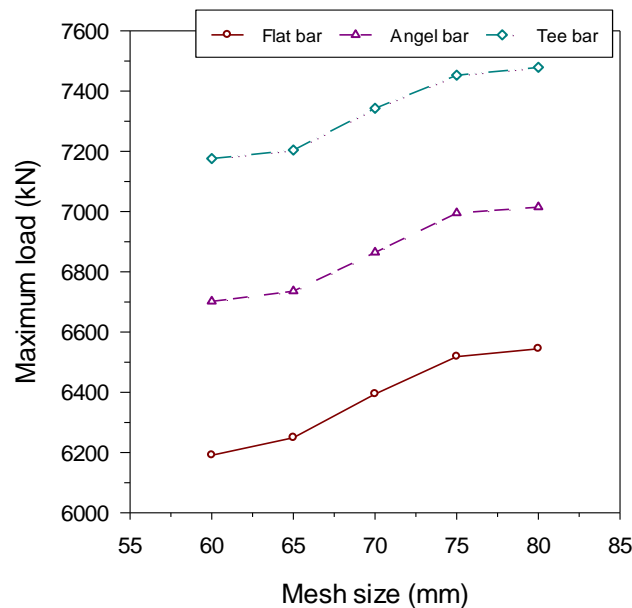


Figure 15. Comparison of the maximum peak strength of stiffened panels obtained from different mesh sizes in 5 mm displacement

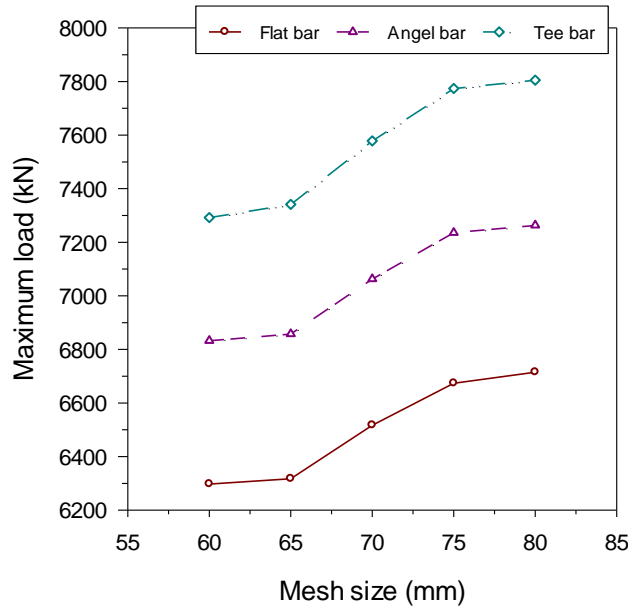


Figure 16. Comparison of the maximum ultimate strength of stiffened panels obtained from different mesh sizes in 10 mm displacement

Furthermore, when subjecting the stiffened panel to a 10 mm displacement, a distinctive divergence in maximum compressive strength values is elucidated for the flat bar stiffener across the specified mesh size range. Notably, the difference in maximum compressive strength values between the 60 mm and 80 mm mesh sizes amounts to 6.42%, signifying a noteworthy variation of 417.8 kN. Specifically, the maximum compressive strength values are recorded at 6297.5 kN and 6715.3 kN for the 60 mm and 80 mm mesh sizes, respectively. This nuanced exploration of the variations in maximum compressive strength under different mesh sizes and displacement conditions provides a comprehensive understanding of the structural performance nuances between the two stiffener types, offering valuable insights for optimizing the design and structural integrity of stiffened plates subjected to buckling loads.

In Figures 17 and 18, a detailed comparison is presented, depicting the average maximum stress levels within stiffened panels that underwent analysis utilizing various mesh sizes and were subjected to displacements of both 5 mm and 10 mm. This investigation reveals a discernible pattern mirroring the trends observed under maximum compressive loads: a direct correlation between the mesh size and the average maximum stress levels. Notably, the findings highlight that as the mesh size increases, there is a corresponding escalation in the average maximum stress. An interesting observation arises when considering a stiffened panel with a Tee bar-type stiffener subjected to a 5 mm displacement, wherein the utilization of a 60 mm mesh size results in an elevated maximum stress level, reaching 249.8 MPa. This nuanced insight underscores the critical role of mesh size in influencing stress distribution and provides valuable information for optimizing numerical simulations for accurate stress predictions in stiffened panels.

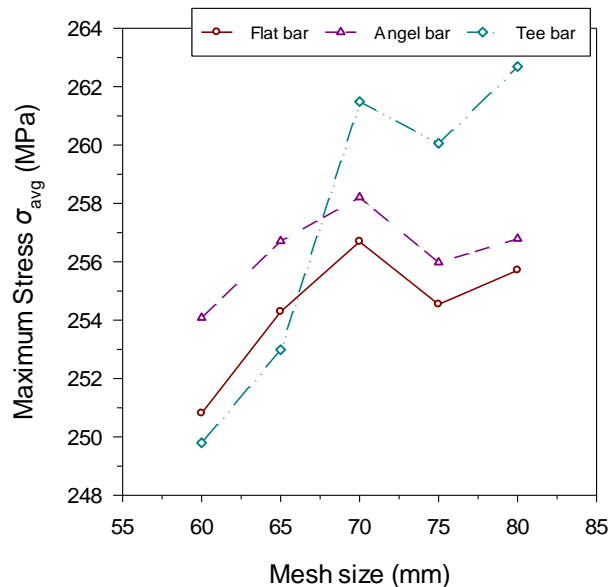


Figure 17. Comparison of the maximum stress average of stiffened panel obtained from different mesh sizes in 5 mm displacement

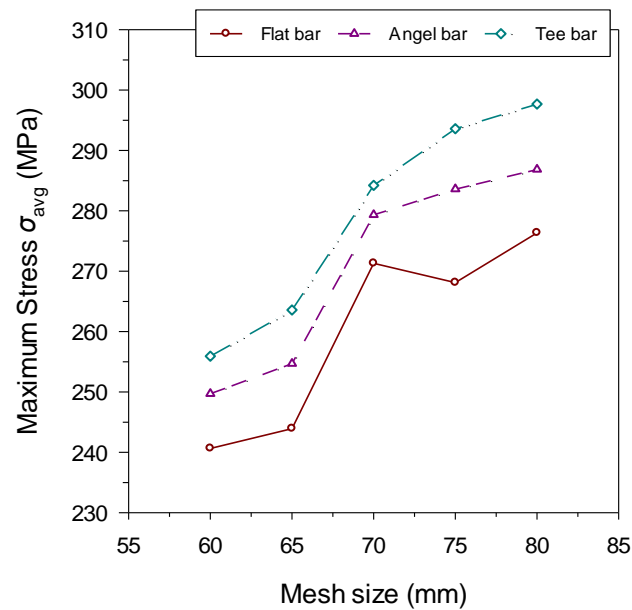


Figure 18. Comparison of the maximum stress average of stiffened panel obtained from different mesh size in 10 mm displacement

Continuing the discussion, it is imperative to emphasize the broader implications derived from the comprehensive analysis of stress patterns within stiffened panels. The exploration of various mesh sizes underlines the intricate relationship between meshing parameters and stress distribution, elucidating crucial nuances that impact the structural response. Figures 17 and 18 not only serve as visual aids but also serve as indispensable tools for researchers and practitioners seeking to enhance the accuracy of finite element simulations in similar structural analyses. Moreover, the specific instance of a Tee bar-type stiffener in a stiffened panel experiencing a 5 mm displacement, yielding a peak stress of 249.8 MPa with a 60 mm mesh size, reinforces the importance of meticulous meshing considerations in capturing localized stress concentrations accurately. This information is invaluable for engineers and designers striving to optimize their simulation models and enhance the predictive capabilities of numerical analyses, ultimately contributing to advancements in the understanding and design of stiffened plate structures under buckling loads.

Meanwhile, the results obtained at the 80 mm mesh size are 262.69 MPa. This shows that there has been an increase in the average maximum stress of 5.03%. The same phenomenon occurs in the other stiffener types, which are the angle bar and flat bar, where the larger the mesh size, the greater the maximum stress average value. Overall, the increase occurred in the range of 1.03% to 1.61% and 1.38%, up to 2.32% of 60-80mm, respectively. Displacement of 10 mm also produces the same phenomenon but has a slightly larger percentage, with a range of maximum increase in average stress reaching 13.81%, 13.85%, and 15.08% for stiffener types flat, angle, and Tee bar, respectively. The selection of the mesh size can indeed produce simulation results with different finite elements. This can be seen in the simulation of stiffened panels with all types of stiffeners subjected to 5 mm displacement at a 75 mm mesh size. In this case, there is a decreasing trend where the maximum stress average value is slightly lower than the 70 mm mesh size. The resulting reductions for the type of stiffener flat, angle, and Tee bar at 70 mm to 75 mm are 256.69 MPa to 254.54 MPa, 258.21 MPa to 255.98 MPa, and 261.49 MPa to 260.06, respectively. It appears that the size of the mesh is crucial in the FE method because the result can be varied along with the size of the mesh.

3.4. Discussion of the Results

A finite element study of the stiffened panel along with the three types of stiffeners subjected to buckling load has been carried out in this study. Stiffened panels are widely used in ship structures. The graph depicting the relationship between load and displacement, as well as the average stress (σ_{avg}), illustrates the ability of the reinforced panel to endure applied loads. The FE results suggest that the stiffener type appears to affect the strength stiffened panel when subjected to buckling load. The findings of this study show that the Tee bar type of stiffener leads to good results for the maximum compressive load on the stiffened panel compared to the flat and angle bar when subjected to the buckling phenomenon. A higher value of maximum compressive load means that the structure of the stiffened panel can withstand the load more greatly.

A typical load versus displacement curve is given in Figures 6 and 7. As seen in these curves, the load for some displacement will reach an initial maximum so the stiffened panel is undergoing maximum capacity. This phenomenon of the relationship between load-bearing strength associated with the maximum compressive strength curve of the stiffened panels under biaxial compression is seen in the studies conducted by Omidali & Khedmati [4] and Paik and Seo [3]. The current study is in accordance with both references which show that maximum compressive load can determine the strength of the stiffened panel when subjected to buckling load. As evidenced by the data presented in

Figures 6 and 7, there is a discernible augmentation in the maximum compressive strength by 15.90% and 8.25% for the Tee bar and angle bar stiffener types, respectively, when subjected to a 5 mm displacement, as compared to the flat bar. The corresponding numerical values for this increase in compressive strength are noteworthy: the flat bar registers at 6191.3 kN, the angle bar at 6702.2 kN, and the Tee bar at an impressive 7176 kN. Furthermore, it is noteworthy that the load versus displacement relationship obtained from a 10 mm displacement exhibits similarity to the trends observed at the 5 mm displacement, with only marginal differences discernible between the two displacement magnitudes.

In the application of the finite element method in simulation, a comprehensive model of a large structure undergoes segmentation into smaller components referred to as finite elements. These elements establish connections among all the key points situated within their boundaries, known as nodes. The criticality of selecting an appropriate mesh size in the finite element method cannot be overstated, as it plays a vital role in the accuracy and reliability of structural simulations; moreover, the partitioning of this mesh necessitates careful consideration to ensure that the chosen size adequately represents the intricacies of the structure [20-23]. Extensive scholarly discourse in the realm of structural analysis emphasizes the profound impact of mesh size on simulation outcomes [24, 25]. Previous research endeavors have demonstrated that variations in mesh size can yield disparate results, thereby underscoring the need for meticulous attention to this parameter.

Studies by Ridwan et al. [26] and Prabowo et al. [27] have elucidated the multifaceted implications of mesh size, revealing its influence not only on the structural response but also on the formation of fractures within a given structure. The consequential effect on energy absorption further accentuates the intricate interplay between mesh size and structural behavior, emphasizing that the nuanced selection of mesh parameters is paramount for a comprehensive understanding of the simulated phenomena. This intricate relationship between mesh size, structural response, and fracture formation underscores the necessity for a judicious approach in choosing mesh parameters, acknowledging that such choices profoundly shape the fidelity and depth of insights derived from finite element simulations in the study of structures subjected to complex loading conditions. This research also demonstrates that different mesh size produces different peak compressive loads and maximum stress averages in the scenario of stiffened panel subjected to buckling load. In this study, the larger the mesh size, the greater the maximum compressive load and maximum stress average. The greater maximum compressive strength value occurs in the 5 mm and 10 mm displacement scenarios. In the examination of stiffened panels featuring flat, angle, and Tee bar types, it was observed that the maximum compressive strength values, obtained under a 60 mm mesh size and a 5 mm displacement, were 6191.3 kN, 6702.2 kN, and 7176 kN, respectively. Subsequent analysis with an 80 mm mesh size yielded results of 6544.9 kN, 7015.3 kN, and 7479 kN for the same stiffener types. Notably, these results indicate a discernible increase in maximum compressive strength by 5.55%, 4.56%, and 4.13% when compared to the outcomes derived from the 60 mm mesh size. This underlines the sensitivity of buckling loads to mesh size and its impact on the structural response. These results regarding the sensitivity of the mesh size to the maximum compressive strength were in accordance with the study conducted by Pratama et al. [28]. The study further emphasizes the critical role of structure stiffness in determining buckling behavior, elucidating that the T bar stiffener type imparts greater stiffness compared to the angle bar and flat bar stiffeners.

Additionally, the assessment of buckling analysis is acknowledged to be contingent upon factors such as column slenderness ratio and plate slenderness ratio, as elucidated in previous studies [29]. Remarkably, this study does not delve into these ratios, presenting a noteworthy avenue for future research endeavors. While the current investigation provides valuable insights into the comparative performance of stiffeners under varying mesh sizes, future studies could incorporate a more comprehensive analysis by including plate and column slenderness ratios. Furthermore, in the pursuit of advancing maritime safety, it is suggested that interested readers refer to a comprehensive source on the subject found in [30-36]. This not only underscores the interconnectedness of diverse research domains but also implies the potential for integrating findings from this study into broader frameworks for maritime safety enhancement.

4. Conclusion

This study delves into a comprehensive analysis and comparison of the buckling load exhibited by steel stiffened panels, exploring various factors such as stiffener types (flat, angle, and Tee bar), displacement conditions, and mesh size, utilizing the finite element method. The investigation yielded insightful conclusions, highlighting the distinct performance of different stiffener types. Notably, the stiffened panel featuring Tee bar stiffeners demonstrated a remarkable increase in maximum compressive load compared to counterparts with flat and angle stiffener types. Additionally, the angle stiffener type exhibited notably superior performance in terms of load-bearing strength when contrasted with the flat bar. The findings revealed a substantial enhancement in maximum compressive load, with at least a 15.90% and 8.25% increase observed in stiffened panels subjected to a 5 mm displacement for Tee and angle bar stiffener types, respectively, in comparison to the flat bar. Intriguingly, the comparison of load versus displacement between 5 mm and 10 mm displacement scenarios indicated minimal variation, suggesting that a 10 mm displacement does not significantly affect the maximum compressive load in the given stiffened panel boundary conditions. It is noteworthy that this study did not quantify and discuss the impact of welding, a critical element in ship structures where stiffened panels are commonly employed. The absence of an examination of the welding effect underscores the need for future research to comprehensively explore and quantify how welding between stiffeners and plates influences the behavior of these stiffened panels.

In the context of the material utilized in this research, the stiffened panels were constructed using S355JR-EN10210 steel, a high-strength structural steel renowned for its significant mechanical features. S355JR-EN10210 steel is significant in providing confidence about the structural performance and integrity of the stiffened panels under the imposed buckling loads. This steel grade is characterized by its robustness, making it well-suited for applications demanding resilience and strength, such as ship structures. However, while the current study has provided valuable insights into the performance of stiffened panels based on geometric and load considerations, the specific influence of the material's properties, including its response to welding, remains unexplored. Future research endeavors should thus focus on a detailed examination of the use of S355JR-EN10210 steel, considering its welding characteristics and its impact on the overall behavior of stiffened panels. Such an investigation would contribute to a more thorough comprehension of the structural dynamics and performance of stiffened panels, especially in practical applications where welding plays a crucial role in the assembly and integrity of these structural elements. In conclusion, while this study has shed light on critical aspects of stiffened panel behavior, further exploration, particularly regarding the material and welding effects, is essential for advancing the knowledge and application of stiffened panels in engineering and structural design.

5. Declarations

5.1. Author Contributions

Conceptualization, M.S., R.R., A.R.P., and I.Y.; methodology, R.R., A.R.P., and R.A.; software, A.R.P., R.A., and J.M.S.; validation, M.S., R.R., and J.M.S.; formal analysis, M.S., R.R., A.R.P., and I.Y.; investigation, M.S., R.R., A.R.P., and R.A.; resources, A.R.P., T.G.G., and D.D.D.P.T.; data curation, R.R., A.R.P., and R.A.; writing—original draft preparation, M.S., R.R., A.R.P., and I.Y.; writing—review and editing, R.R., A.R.P., and T.G.G.; visualization, T.G.G., N.M., and D.D.D.P.T.; supervision, A.R.P., I.Y., and R.A.; project administration, A.R.P., J.M.S., T.G.G., and N.M.; funding acquisition, A.R.P., N.M., D.D.D.P.T., and J.M.S. All authors have read and agreed to the published version of the manuscript.

5.2. Data Availability Statement

The data presented in this study are available in the article.

5.3. Funding

This work was supported by the RKAT PTNBH Universitas Sebelas Maret Year 2024, under the Research Scheme of “Penelitian Kolaborasi Internasional” (KI-UNS), with research grant/contract no. 194.2/UN27.22/PT.01.03/2024. The support is highly acknowledged by the authors.

5.4. Conflicts of Interest

The authors declare no conflict of interest.

6. References




- [1] UNCTAD. (2021). Review of Maritime Transport 2021. United Nations Conference on Trade and Development, United Nations Publication, Geneva, Switzerland.
- [2] Allianz. (2021). Safety and shipping review 2021. Allianz Global Corporate & Specialty, Munich, Germany.
- [3] Paik, J. K., & Seo, J. K. (2009). Nonlinear finite element method models for ultimate strength analysis of steel stiffened-plate structures under combined biaxial compression and lateral pressure actions-Part II: Stiffened panels. *Thin-Walled Structures*, 47(8–9), 998–1007. doi:10.1016/j.tws.2008.08.006.
- [4] Omidali, M., & Khedmati, M. R. (2018). Reliability-based design of stiffened plates in ship structures subject to wheel patch loading. *Thin-Walled Structures*, 127, 416–424. doi:10.1016/j.tws.2018.02.022.
- [5] Doan, V. T., Liu, B., Garbatov, Y., Wu, W., & Guedes Soares, C. (2020). Strength assessment of aluminium and steel stiffened panels with openings on longitudinal girders. *Ocean Engineering*, 200(107047). doi:10.1016/j.oceaneng.2020.107047.
- [6] Pedram, M., & Khedmati, M. R. (2014). The effect of welding on the strength of aluminium stiffened plates subject to combined uniaxial compression and lateral pressure. *International Journal of Naval Architecture and Ocean Engineering*, 6(1), 39–59. doi:10.2478/IJNAOE-2013-0162.
- [7] Guedes Soares, C., & Gordo, J. M. (1997). Design Methods for Stiffened Plates under Predominantly Uniaxial Compression. *Marine Structures*, 10(6), 465–497. doi:10.1016/s0951-8339(97)00002-6.
- [8] Feng, L., Yu, J., Zheng, J., He, W., & Liu, C. (2024). Experimental and numerical study of residual ultimate strength of hull plate subjected to coupled damage of pitting corrosion and crack. *Ocean Engineering*, 294. doi:10.1016/j.oceaneng.2024.116710.

- [9] Cui, J., & Wang, D. (2020). An experimental and numerical investigation on ultimate strength of stiffened plates with opening and perforation corrosion. *Ocean Engineering*, 205. doi:10.1016/j.oceaneng.2020.107282.
- [10] Lee, J., & Kang, Y. J. (2024). Elastic local buckling coefficients of I-shaped beams considering flange–web interaction. *Thin-Walled Structures*, 195. doi:10.1016/j.tws.2023.111325.
- [11] Boissonnade, N., Nseir, J., & Somja, H. (2024). Experimental and numerical investigations towards the lateral torsional buckling of cellular steel beams. *Thin-Walled Structures*, 195. doi:10.1016/j.tws.2023.111388.
- [12] Ghadami, A., Jawdhari, A., & PourMoosavi, G. (2024). Buckling and post-buckling behavior of top flange coped I-beams with slender web panels. *Thin-Walled Structures*, 198(111640). doi:10.1016/j.tws.2024.111640.
- [13] Quinn, D., Murphy, A., McEwan, W., & Lemaitre, F. (2009). Stiffened panel stability behaviour and performance gains with plate prismatic sub-stiffening. *Thin-Walled Structures*, 47(12), 1457–1468. doi:10.1016/j.tws.2009.07.004.
- [14] Esmaili-Goldarag, F., Babaei, A., & Jafarzadeh, H. (2018). An experimental and numerical investigation of clamping force variation in simple bolted and hybrid (bolted-bonded) double lap joints due to applied longitudinal loads. *Engineering Failure Analysis*, 91, 327–340. doi:10.1016/j.engfailanal.2018.04.047.
- [15] Goldarag, F. E., Barzegar, S., & Babaei, A. (2015). An experimental method for measuring the clamping force in double lap simple bolted and hybrid (bolted-bonded) joints. *Transactions of Famena*, 39(3), 87–94.
- [16] ANSYS. (2020). ANSYS LS-DYNA User's Guide. ANSYS Inc., Pennsylvania, United States.
- [17] Ridwan, Putranto, T., Laksono, F. B., & Prabowo, A. R. (2020). Fracture and damage to the material accounting for transportation crash and accident. *Procedia Structural Integrity*, 27, 38–45. doi:10.1016/j.prostr.2020.07.006.
- [18] Prabowo, A. R., Tuswan, T., Prabowoputra, D. M., & Ridwan, R. (2021). Deformation of designed steel plates: An optimisation of the side hull structure using the finite element approach. *Open Engineering*, 11(1), 1034–1047. doi:10.1515/eng-2021-0104.
- [19] Dzulfiqar, M. F., Prabowo, A. R., Ridwan, R., & Nubli, H. (2021). Assessment on the designed structural frame of the automatic thickness checking machine - Numerical validation in FE method. *Procedia Structural Integrity*, 33, 59–66. doi:10.1016/j.prostr.2021.10.009.
- [20] Prabowo, A. R., Ridwan, R., Tuswan, T., Sohn, J. M., Surojo, E., & Imaduddin, F. (2022). Effect of the selected parameters in idealizing material failures under tensile loads: Benchmarks for damage analysis on thin-walled structures. *Curved and Layered Structures*, 9(1), 258–285. doi:10.1515/cls-2022-0021.
- [21] Ridwan, R., Nuriana, W., & Prabowo, A. R. (2022). Energy absorption behaviors of designed metallic square tubes under axial loading: Experiment-based benchmarking and finite element calculation. *Journal of the Mechanical Behavior of Materials*, 31(1), 443–461. doi:10.1515/jmbm-2022-0052.
- [22] Alwan, F. H. A., Prabowo, A. R., Muttaqie, T., Muhayat, N., Ridwan, R., & Laksono, F. B. (2022). Assessment of ballistic impact damage on aluminum and magnesium alloys against high velocity bullets by dynamic FE simulations. *Journal of the Mechanical Behavior of Materials*, 31(1), 595–616. doi:10.1515/jmbm-2022-0064.
- [23] Prabowo, A. R., Ridwan, R., & Muttaqie, T. (2022). On The Resistance to Buckling Loads of Idealized Hull Structures: FE Analysis on Designed-Stiffened Plates. *Designs*, 6(3), 46. doi:10.3390/designs6030046.
- [24] Saleh, S. M., Majeed, F. H., Al-Salih, O., & Hussain, H. K. (2023). Torsional Behavior of Steel-Concrete-Steel Sandwich Beams with Welded Stirrups as Shear Connectors. *Civil Engineering Journal*, 9(1), 208-219. doi:10.28991/CEJ-2023-09-01-016.
- [25] Prabowo, A. R., Do, Q. T., Cao, B., & Bae, D. M. (2020). Land and marine-based structures subjected to explosion loading: A review on critical transportation and infrastructure. *Procedia Structural Integrity*, 27, 77–84. doi:10.1016/j.prostr.2020.07.011.
- [26] Ridwan, R., Prabowo, A. R., Muhayat, N., Putranto, T., & Sohn, J. M. (2020). Tensile analysis and assessment of carbon and alloy steels using Fe approach as an idealization of material fractures under collision and grounding. *Curved and Layered Structures*, 7(1), 188-198. doi:10.1515/cls-2020-0016.
- [27] Prabowo, A. R., & Bae, D. M. (2019). Environmental risk of maritime territory subjected to accidental phenomena: Correlation of oil spill and ship grounding in the Exxon Valdez's case. *Results in Engineering*, 4(100035). doi:10.1016/j.rineng.2019.100035.
- [28] Pratama, A. A., Prabowo, A. R., Muttaqie, T., Muhayat, N., Ridwan, R., Cao, B., & Laksono, F. B. (2023). Hollow tube structures subjected to compressive loading: implementation of the pitting corrosion effect in nonlinear FE analysis. *Journal of the Brazilian Society of Mechanical Sciences and Engineering*, 45, 143. doi:10.1007/s40430-023-04067-3.
- [29] Branquinho, M. Á., & Malite, M. (2021). Effective slenderness ratio approach for thin-walled angle columns connected by the leg. *Journal of Constructional Steel Research*, 176, 106434. doi:10.1016/j.jcsr.2020.106434.
- [30] Demirci, S. M. E., & Elçiçek, H. (2023). Scientific awareness of marine accidents in Europe: A bibliometric and correspondence analysis. *Accident Analysis and Prevention*, 190, 107166. doi:10.1016/j.aap.2023.107166.

- [31] Chen, J., Di, Z., Shi, J., Shu, Y., Wan, Z., Song, L., & Zhang, W. (2020). Marine oil spill pollution causes and governance: A case study of Sanchi tanker collision and explosion. *Journal of Cleaner Production*, 273, 122978. doi:10.1016/j.jclepro.2020.122978.
- [32] Guimarães, L. S. F., de Carvalho-Junior, L., Façanha, G. L., Resende, N. da S., Neves, L. M., & Cardoso, S. J. (2023). Meta-analysis of the thermal pollution caused by coastal nuclear power plants and its effects on marine biodiversity. *Marine Pollution Bulletin*, 195, 115452. doi:10.1016/j.marpolbul.2023.115452.
- [33] Prabowo, A. R., Cahyono, S. I., & Sohn, J. M. (2019). Crashworthiness assessment of thin-walled double bottom tanker: A variety of ship grounding incidents. *Theoretical and Applied Mechanics Letters*, 9(5), 320–327. doi:10.1016/j.taml.2019.05.002.
- [34] Yildiz, S., Uğurlu, Ö., Wang, J., & Loughney, S. (2021). Application of the HFACS-PV approach for identification of human and organizational factors (HOFs) influencing marine accidents. *Reliability Engineering and System Safety*, 208, 107395. doi:10.1016/j.res.2020.107395.
- [35] Bolat, P., & Yongxing, J. (2013). Risk assessment of potential catastrophic accidents for transportation of special nuclear materials through Turkish Straits. *Energy Policy*, 56, 126–135. doi:10.1016/j.enpol.2012.12.010.
- [36] Cao, B., Bae, D.-M., Sohn, J.-M., Prabowo, A. R., Chen, T. H., & Li, H. (2016). Numerical Analysis for Damage Characteristics Caused by Ice Collision on Side Structure. Volume 8: Polar and Arctic Sciences and Technology; Petroleum Technology, OMAE2016-54727, 1-7. doi:10.1115/omae2016-54727.



Stress Concentration Factors in KT-Joints Subjected to Complex Bending Loads Using Artificial Neural Networks

Mohsin Iqbal ^{1*}, Saravanan Karuppanan ¹, Veeradasan Perumal ¹, Mark Ovinis ²,
Afzal Khan ³, Muhammad Faizan ⁴

¹ Department of Mechanical Engineering, Universiti Teknologi PETRONAS, Seri Iskandar 32610, Malaysia.

² School of Engineering and the Built Environment, Birmingham City University, Birmingham, United Kingdom.

³ Department of Mechanical Engineering, University of Engineering and Technology, Peshawar 25120, Pakistan.

⁴ Department of Mechanical Engineering, International Islamic University Islamabad, Islamabad, 44000, Pakistan.

Received 20 October 2023; Revised 19 March 2024; Accepted 26 March 2024; Published 01 April 2024

Abstract

Fatigue analysis of tubular joints based on peak stress concentration factor (SCF) is critical for offshore structures as it determines the fatigue life of the joint and possibly the overall structure. It is known that peak SCF occurs at the crown position for in-plane bending (IPB) and at the saddle position for out-of-plane bending (OPB). Tubular joints of offshore structures are under multiplanar bending, comprising IPB and OPB. When a joint is subjected to IPB and OPB loads simultaneously, the peak SCF occurs somewhere between the crown and the saddle. However, existing equations estimate SCF at the crown and saddle only when a joint is subjected to IPB or OPB. It was found that the position and magnitude of peak SCF under simultaneous IPB and OPB depend on the relative magnitudes of these uniplanar load components. The crown and saddle position SCF can be substantially lower than the cumulative peak SCF. Empirical models are proposed for computing peak SCF for KT-joints subjected to multiplanar bending. These models were developed through regression analysis using artificial neural networks (ANN). The ANN training data was generated through 3716 ANSYS finite element simulations. The empirical model was validated using models available in the literature and can determine peak SCF with an error of less than 1.5%.

Keywords: Fatigue Analysis; Stress Concentration Factor; Empirical Modeling; ANN; Multiplanar Bending Load; Tubular KT-Joint.

1. Introduction

Circular hollow section Steel tubular members are preferred for offshore structures due to their high stiffness-to-weight ratio, low drag, and direction-independent structural response. Fatigue due to environmental and operational loads is the primary cause of failure in offshore structures, and it is critical to design for fatigue loading. The weld line at the interface tubular members is typically the most vulnerable to fatigue failure due to stress amplification caused by geometric variation [1, 2], as illustrated in Figure 1. The failure of a joint causes additional load on the neighboring structural elements and can lead to the collapse of the entire structure [3]. Therefore, careful fatigue life estimation is essential for the reliable design of offshore structures [4].

Fatigue life can be estimated experimentally or numerically. Experimental fatigue analysis is usually difficult, costly, and time-consuming. Among various numerical methods, the structural hot-spot stress-based fatigue life estimation is

* Corresponding author: mohsin_22005143@utp.edu.my

 <http://dx.doi.org/10.28991/CEJ-2024-010-04-04>



© 2024 by the authors. Licensee C.E.J, Tehran, Iran. This article is an open access article distributed under the terms and conditions of the Creative Commons Attribution (CC-BY) license (<http://creativecommons.org/licenses/by/4.0/>).

straightforward and widely used when designing offshore structures [4]. This approach is based on fatigue life determination using peak hot-spot stress (HSS) in conjunction with an S-N curve. The HSS in a joint is usually calculated using the stress concentration factor (SCF) and nominal stress, as shown in Equation 1. The nominal stress (σ_n) is the bending stress calculated using beam theory, given by Equation 2 [5].

$$\sigma_{HSS} = SCF * \sigma_n \quad (1)$$

$$\sigma_n = \frac{32 d M}{\pi[d^4 - (d-2t)^4]} \quad (2)$$

where σ_{HSS} is hot-spot stress (HSS), SCF is stress concentration factor, σ_n is nominal stress in the brace, d is diameter of the brace, M is moment on the brace, t is brace wall thickness.

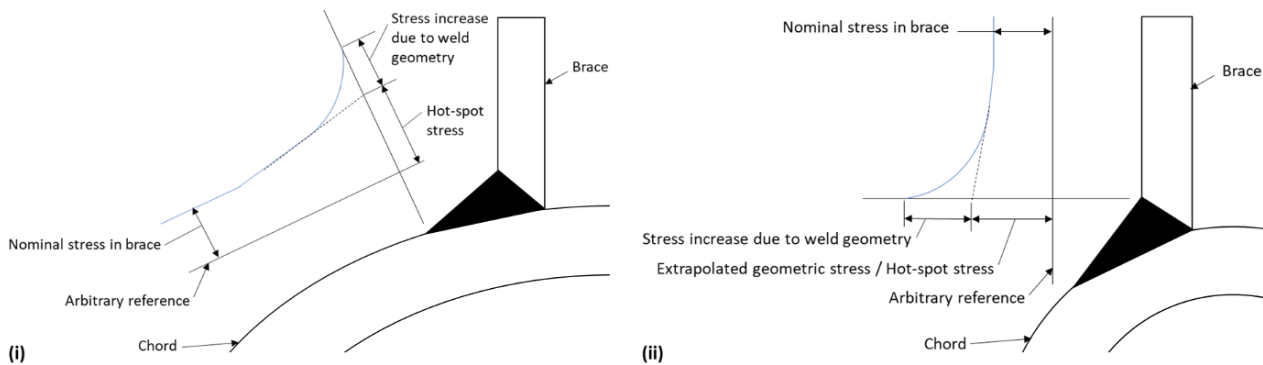


Figure 1. Stress amplification at tubular joints: (i) chord-side of the interface, (ii) brace-side of the interface

The SCF measures stress amplification at a tubular joint and depends on the geometry and load on the joint. Significant efforts have been devoted to investigating and developing empirical models for SCF in various tubular joints. These studies can be traced back to Kuang et al. [6], Wordsworth [7], Wordsworth and Smedley [8], Efthymiou [9], Hellier et al. [10], Lloyd [11], Smedley and Fisher [12], and Morgan et al. [13, 14]. Efthymiou's equations [9] are widely used for estimating the fatigue life of KT-joint and are included in various standards such as DNV-GL-RP203 [15], NORSOK [16], and CIDECT [17]. The geometric configurations and load conditions of KT-joints are varied, and numerous aspects have been actively explored in recent years. Many researchers have investigated SCF concerning different design aspects of KT joints subjected to bending and proposed numerical models to determine SCF rapidly.

Ahmadi & Zavvar [18] investigated KT-joints with internal ring stiffeners under four different configurations of OPB and proposed empirical models for determining SCF at the saddle positions. They conducted a study [19] in which four different IPB load conditions were investigated using 118 finite element (FE) models, and empirical models were developed for the crown position of the central brace and the toe of inclined braces. Simulations of these two studies [18, 19] could be used to determine the combined SCF effect of IPB and OPB using the superposition of stress. However, while the peak SCF of simultaneous loads occurs somewhere between crown and saddle, the empirical models were only for SCF at the saddle for OPB and the crown for IPB. Utilizing these models will underestimate the peak SCF. Therefore, empirical models that can estimate SCF around the brace axis are required. Additionally, they investigated the probability distribution functions for SCFs in internal ring-stiffened KT-joints under IPB [20]. Four IPB load configurations were explored using 108 simulations. Various probability density functions (PDFs) were fitted to the maximum SCFs, and the goodness of fit was evaluated using Kolmogorov-Smirnov and chi-squared tests. These investigations were limited to SCF to locations of maximum SCF when the KT-joint is subjected to either IPB or OPB. They simulated 432 FE models of KT-joint under various OPB loads and investigated the probability distribution of SCF at saddle position [21] under various configurations of IPB loads. Ten parametric equations were proposed for determining SCFs at braces' crown, toe, and heel positions by regression analysis of data obtained through 46 simulations [22]. They also investigated the effect of multilinearity by stimulating 81 finite models [23]. It was found that the SCF in multiplanar joints can be substantially higher than in uniplanar KT-joints. However, SCF equations were only available for uniplanar KT-joints under IPB and OPB, and using these parametric models for multiplanar joints would underestimate the SCF.

New empirical models were proposed for multiplanar KT-joints under bending. However, both the old and new models were only for determining SCF at saddle and crown positions. These models are valid when a joint is subjected to either IPB or OPB, but not both. Zavvar et al. [24] investigated the SCF of uniplanar and multiplanar KT-joints subjected to IPB. Four IPB load configurations were investigated through 81 FE simulations. Empirical models were

proposed for determining SCF at the crown position. They also investigated SCF in FRP-reinforced KT-joints under IPB and OPB [25]. Simulation of 2920 FE models was carried out, and 38 parametric equations were proposed for determining SCF at the crown and saddle of the central brace while at the heel and toe of inclined braces. All existing models are limited to determining SCF at specific locations, as outlined in Table 1. None of these models can determine SCF around the brace axis for a joint subjected to simultaneous in-plane bending (IPB) and out-of-plane bending (OPB).

Table 1. Literature on empirical modeling of SCF in KT-joint under bending loads

S. No.	Article	Ref. No.	Joint	Load	Empirical model
1.	Development of SCF formulae and generalized influence functions for use in fatigue analysis (1988).	[9]	KT-joint (base model)	IPB, OPB (not simultaneous)	Equations were proposed for determining the SCF at the joint crown for IPB and the saddle for OPB.
2.	Stress concentration factors induced by out-of-plane bending loads in ring-stiffened tubular KT-joints of jacket structures (2015).	[18]	KT-joint with internal ring stiffeners	OPB	Empirical models were developed for the SCF at joint saddle under four OPB configurations.
3.	Stress concentration due to in-plane bending (IPB) loads in ring-stiffened tubular KT-joints of offshore structures: parametric study and design formulation (2015).	[19]	KT-joint with internal ring stiffeners	IPB	Empirical models were developed for the SCF at the joint crown under four OPB configurations.
4.	Probabilistic analysis of stress concentration factors in tubular KT-joints reinforced with internal ring stiffeners under in-plane bending loads (2015).	[20]	KT-joint with internal ring stiffeners	IPB	The best-fit probability distribution function was identified for the SCF at the joint crown joint under IPB.
5.	A probability distribution model for SCFs in internally ring-stiffened tubular KT-joints of offshore structures subjected to out-of-plane bending loads (2016).	[21]	KT-joint with internal ring stiffeners	OPB	The best-fit probability distribution function was identified for the SCF at the joint crown.
6.	Stress concentration factors in uniplanar tubular KT-joints of jacket structures subjected to in-plane bending loads (2016).	[22]	KT-joint (base model)	IPB	Ten parametric equations were proposed to determine the SCFs at crown of the central brace, and toe and heel of the outer braces.
7.	The effect of multi-planarity on the SCFs in offshore tubular KT-joints subjected to in-plane and out-of-plane bending loads (2016).	[23]	Uniplanar, and multiplanar KT-joint	IPB, OPB (not simultaneous)	Empirical models were proposed for the SCF at the joint crown for IPB and joint saddle for OPB.
8.	Stress concentration factors of multiplanar tubular KT-joints subjected to in-plane bending moments (2021).	[24]	Uniplanar, and multiplanar KT-joint	IPB	Empirical models were proposed for the SCF at crown of uniplanar and multiplanar KT-joint subjected to IPB.
9.	Stress concentration factors in steel tubular KT-connections with FRP-Wrapping under bending moments (2021).	[25]	FRP reinforced KT-joint	IPB, OPB (not simultaneous)	Parametric equations were proposed for the SCF at the central brace crown and saddle at the heel and toe of inclined braces.
10.	Empirical modeling of stress concentration factors using finite element analysis and artificial neural networks for the fatigue design of tubular KT-joints under combined loading (2023).	[26]	KT-joint (base model)	Axial, IPB, OPB (individual and simultaneous load on central brace only)	Empirical models were presented for the SCF around the axis of the central brace. (including the crown and saddle positions)

Fatigue life estimation is based on the peak SCF and S-N curves. The peak SCF occurs at the crown position when a joint is subjected to IPB, while at the saddle position when it is subjected to OPB. Therefore, while the empirical models are available for IPB and OPB, no models are available when a joint is subjected to multiplanar bending loads, e.g., simultaneous IPB and OPB, as the location of peak SCF varies between the crown and saddle [27]. The peak HSS for joints subjected to combined loads depends on the magnitudes and directions of the load components [28]. In such cases, HSS can be determined by the superposition of stress due to uniplanar load components by determining SCF around the brace axis, superimposing it to find the peak HSS, and calculating fatigue life. However, none of the available empirical models can determine SCF around the brace axis. Recently, Iqbal et al. [26] proposed empirical models capable of determining SCF around the brace axis of a KT-joint; however, only the central brace was subjected to bending loads. In this work, the SCF around the brace axis for the KT-joint is investigated, with all braces subjected to bending. 3716 numerical simulations were carried out, and the results generated were used to develop empirical models. These models were validated with finite element simulations and existing equations.

2. Simulation of KT-joint under Bending Loads

This study investigates KT-joints subjected to bending. FE models of KT-joints were simulated using the static structural module of ANSYS. Artificial neural network (ANN) models were trained using finite element analysis (FEA), and empirical models were developed. The methodology is summarized in Figure 2.

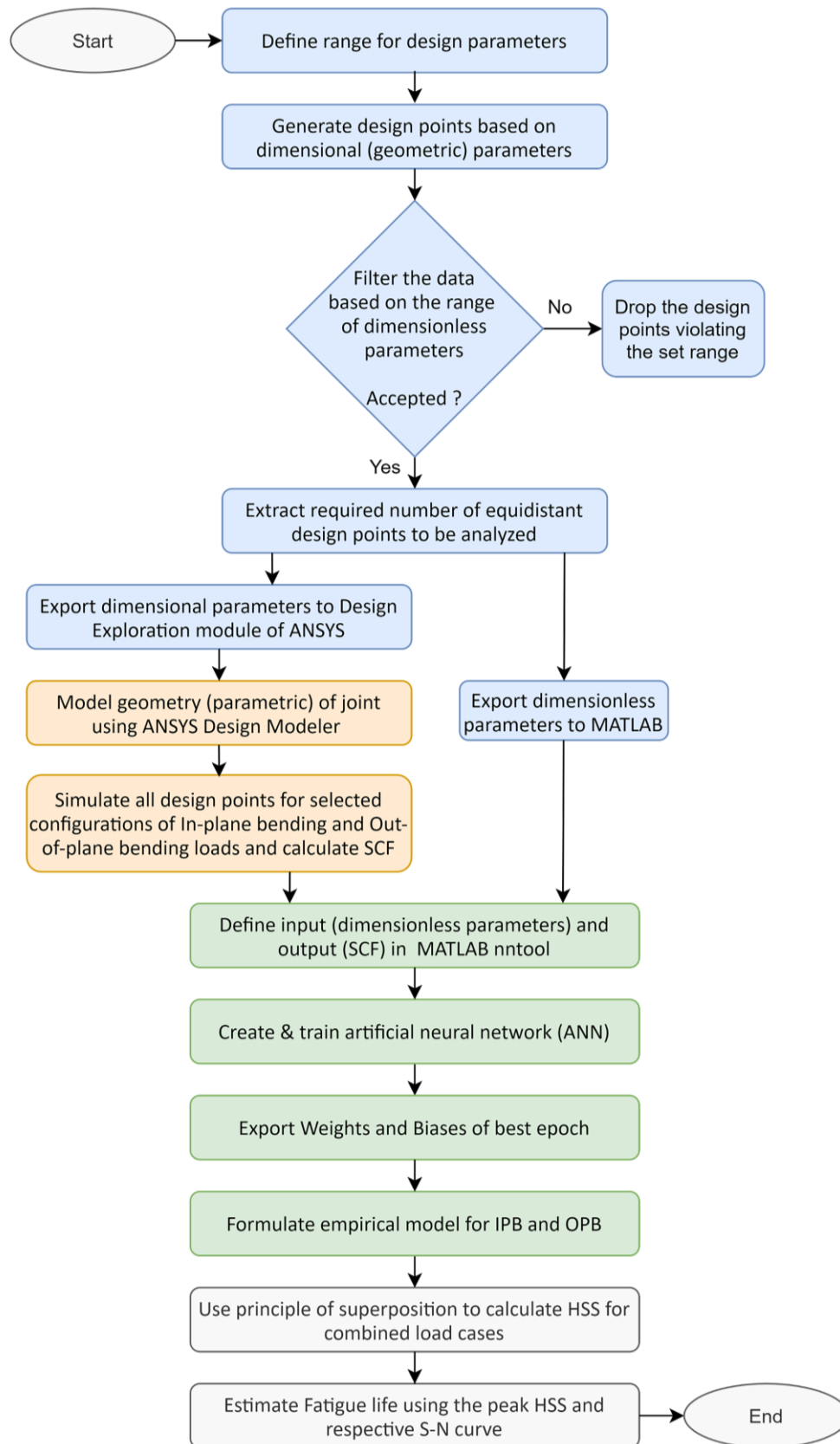


Figure 2. Methodology for determining the SCF in KT-joint under bending

The KT-joint was defined as a function of dimensionless parameters $\beta, \gamma, \tau, \theta, \alpha,$ and ζ , given in Equations 3-7. The range for these parameters is listed in Table 2. The design data set was generated based on the equidistance distribution of variables $D, d, T, t, \theta,$ and g . This initial set of design points was generated using the permutation dimensionless parameters. Some of these data points were violating the range defined. Design points outside the range of dimensionless parameters were excluded. Due to the continuous nature of all dimensionless parameters, the design data set could

contain infinite design points, which need to be limited for simulation in due time. Pre-set data points were selected from this data, ensuring this selection was equally distributed around the initial data set and simulated using ANSYS, following the steps shown in Figure 2.

$$\tau = t/T \tag{3}$$

$$\gamma = D/2T \tag{4}$$

$$\alpha = 2L/D \tag{5}$$

$$\zeta = g/D \tag{6}$$

$$\beta = d/D \tag{7}$$

where D is diameter of chord, d is diameter of brace (all), T is chord wall thickness, t is brace wall thickness (all), L is chord length, g is gap b/w central and inclined braces at the chord surface.

Table 2. Range for the parameters used [26]

Type	Parameters	Range	Reference
Derived Parameters (dimensionless)	τ	0.3–0.7	ARSEM Guide [29]
	γ	12–20	ARSEM Guide [29]
	α	5–40	Lloyd's Register [12], ISO Guide [30]
	ζ	0.25–0.5	Ahmadi et al. [18, 31], Ahmadi [32]
	β	0.4–0.8	ARSEM Guide [29]
Geometric Parameters	θ	30–75°	ARSEM Guide [29]
	g	100 (mm)	Ahmadi [32]
	L	1800–3000 (mm)	α_{max} , D_{max} , α_{min} , and D_{min}
	t	3–10 (mm)	Manufacturing limit (assumption)
	T	3–10 (mm)	Manufacturing limit (assumption)
	d	80–320 (mm)	β_{max} , D_{min} , and D_{max}
	D	200–400 (mm)	$D \geq 150$ (Lloyd's Register [12]), γ_{max} and T_{max}

The 3D model of the KT-joint was generated using ANSYS Design Modeler. Geometric inputs were assigned as parametric variables. The joint geometry was meshed using high-order nonlinear elements, as shown in Figure 3-a. A mesh with 223630 elements was used following a sensitivity study. This model was validated with results by Ahmadi et al. [20], as presented in Figure 3-b, with a difference of less than 3% for the numerical model. However, the difference with the experimental results was 15%, possibly due to approximations in the sizing of joints used. The numerical results are usually based on the nominal wall thickness, and a difference in nominal wall thickness and measured wall thickness would cause a mismatch between the numerical and experimental results [33]. This validated model was used for further investigations.

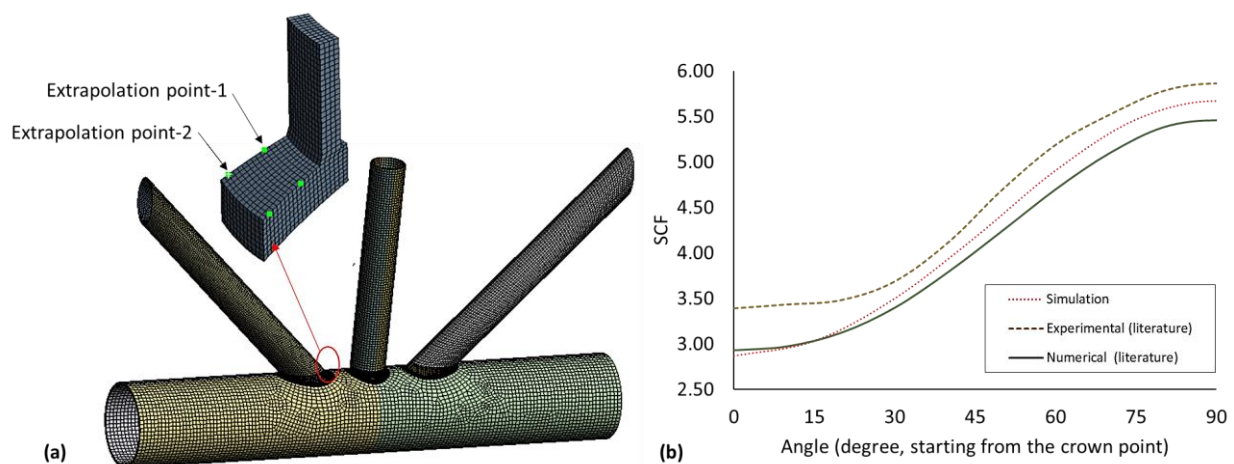


Figure 3. FE model of KT-joint: (a) finite element model, (b) validation of finite element model with the literature [24]

Simulation of 929 geometric design configurations of KT-joints was carried out using ANSYS for each of the four bending configurations, as shown in Figure 4. The first two loadings are IPB, and the latter two are OPB. Bending on a typical KT-joint can be either of these cases or a combination of an IPB and OPB. The chord ends were constrained in all degrees of freedom (three displacements and three rotations), and static structural analysis was performed. Linear elastic simulations are reasonable for determining SCF in tubular joints [34, 35].

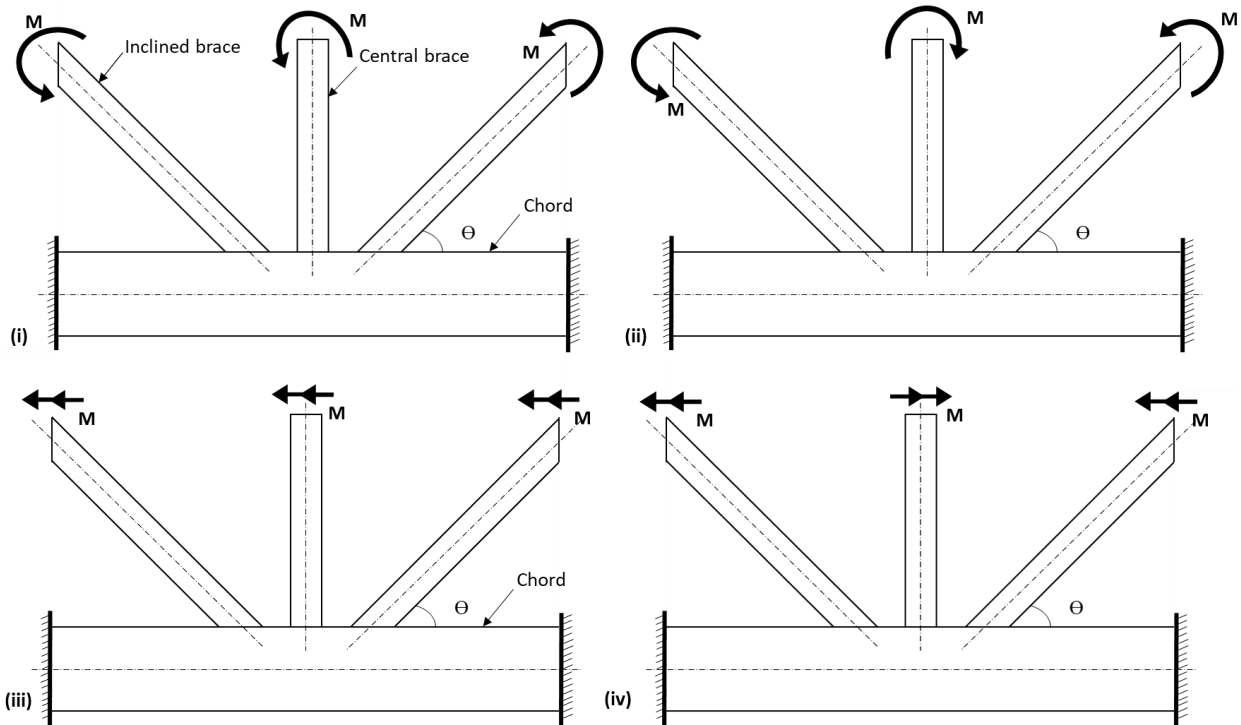


Figure 4. KT-joint subjected to brace bending loads: (i) in-plane bending condition-1, (ii) in-plane bending condition-2, (iii) out-of-plane bending condition-1, (iv) out-of-plane bending condition-2

A Python code was integrated into the ANSYS to automate the determination and extrapolation of stress. This code extracts the stress and position coordinates of the reference points and computes the stress at the weld toe using linear extrapolation. Twenty-four positions were selected to determine stress around the brace axis, as shown in Figure 5-a. For gapped CHS, the variation in stress near the weld toe is almost linear [33]; hence, linear extrapolation was used, as illustrated in Figure 5-b. This extrapolated stress at the weld toe is referred to as HSS. This stress is expressed as a dimensionless parameter (SCF) using Equation 1. Various finite element models were simulated, and SCF was recorded for each simulation. This data was used for regression analysis to develop empirical models for the SCF.

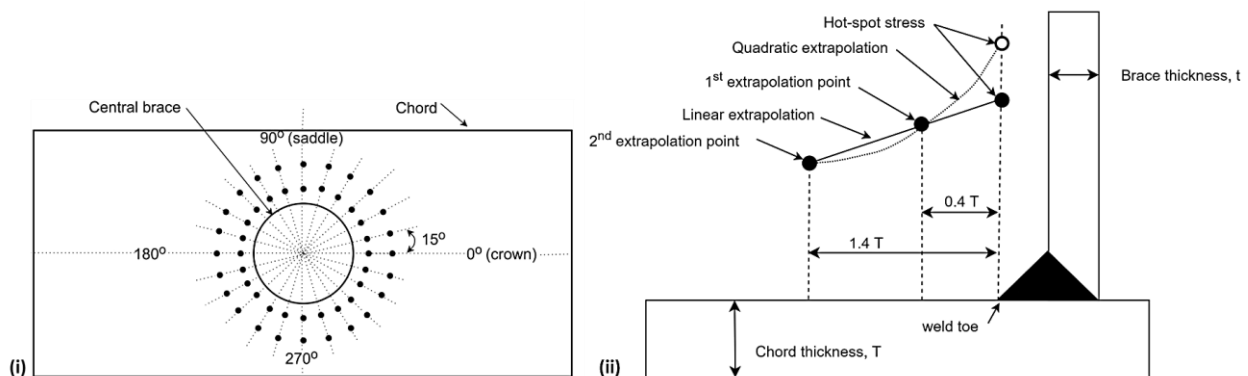


Figure 5. Stress extrapolation: (i) Stress extraction points, (ii) linear extrapolation of principal stress

3. Development and Training of Artificial Neural Networks

An ANN was constructed using MATLAB's tool, as illustrated in Figure 6. The dimensionless parameters served as the inputs, and the SCF along the weld toe of the central brace were the outputs for ANN. Various combinations of hidden layers and neurons were compared, and finally, a configuration with one hidden layer with ten neurons was used

to model the ANN. The Levenberg–Marquardt backpropagation algorithm was applied [36], and the ANN model was trained using the data generated from the FEA with a coefficient of determination $R^2 > 0.999$ and the mean squared error < 0.01 . The regression and performance plots of the training process are shown in Figures 7 and 8. The inputs to empirical expression are normalized to avoid the dominance of a variable with larger magnitudes. The output will be denormalized after calculation. The equations for normalization and denormalization are given as Equations 8 and 9.

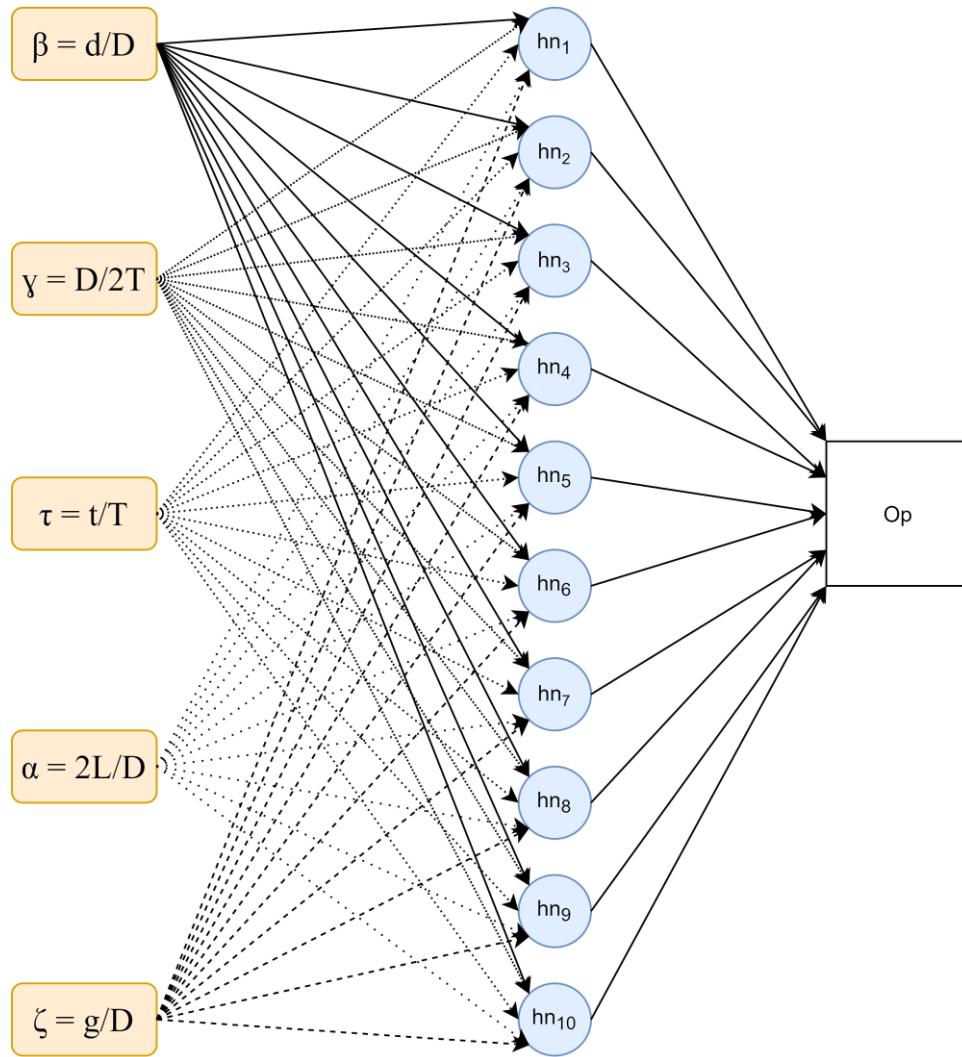
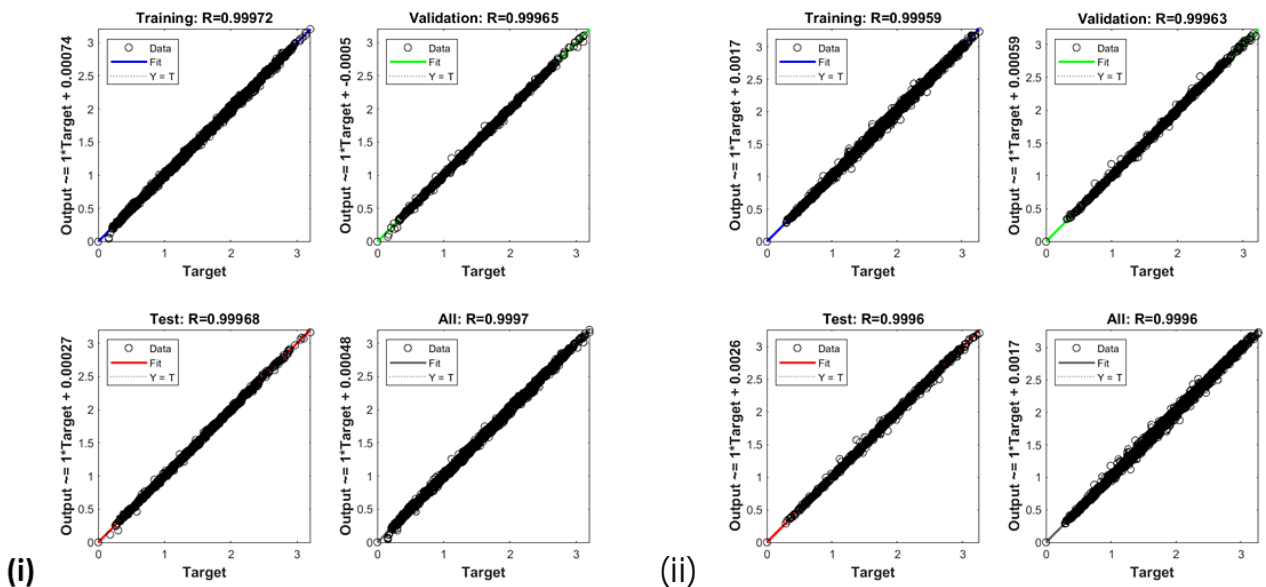


Figure 6. The artificial neural network model



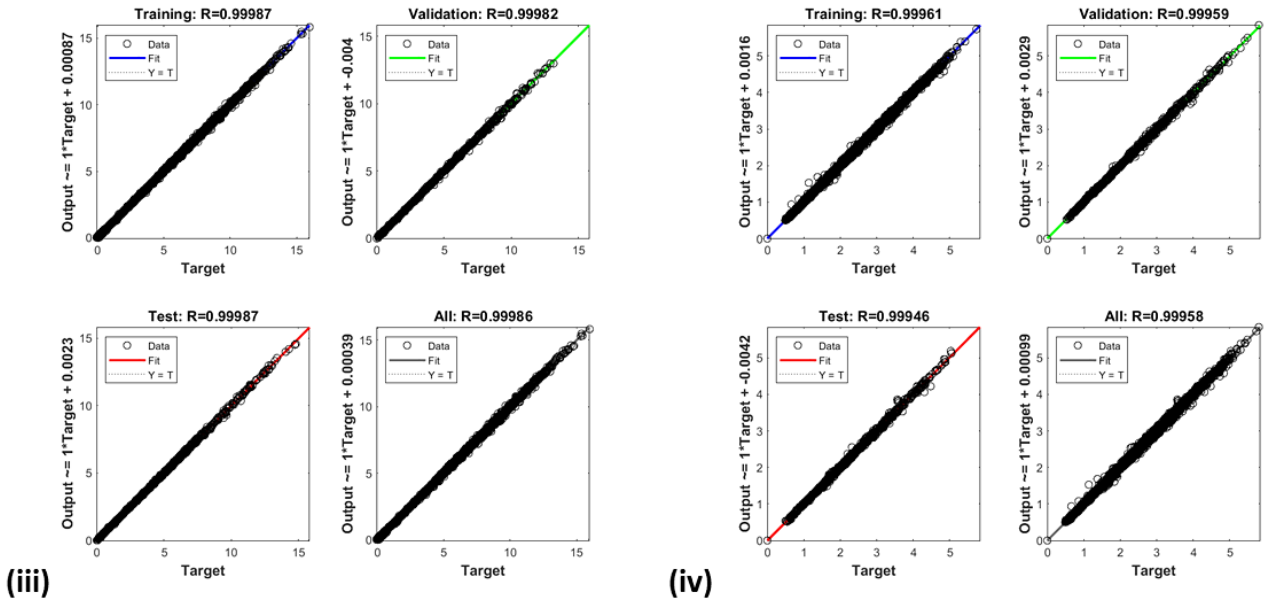


Figure 7. Regression plots: (i) in-plane bending condition-1, (ii) in-plane bending condition-2, (iii) out-of-plane bending condition-1, (iv) out-of-plane bending condition-2

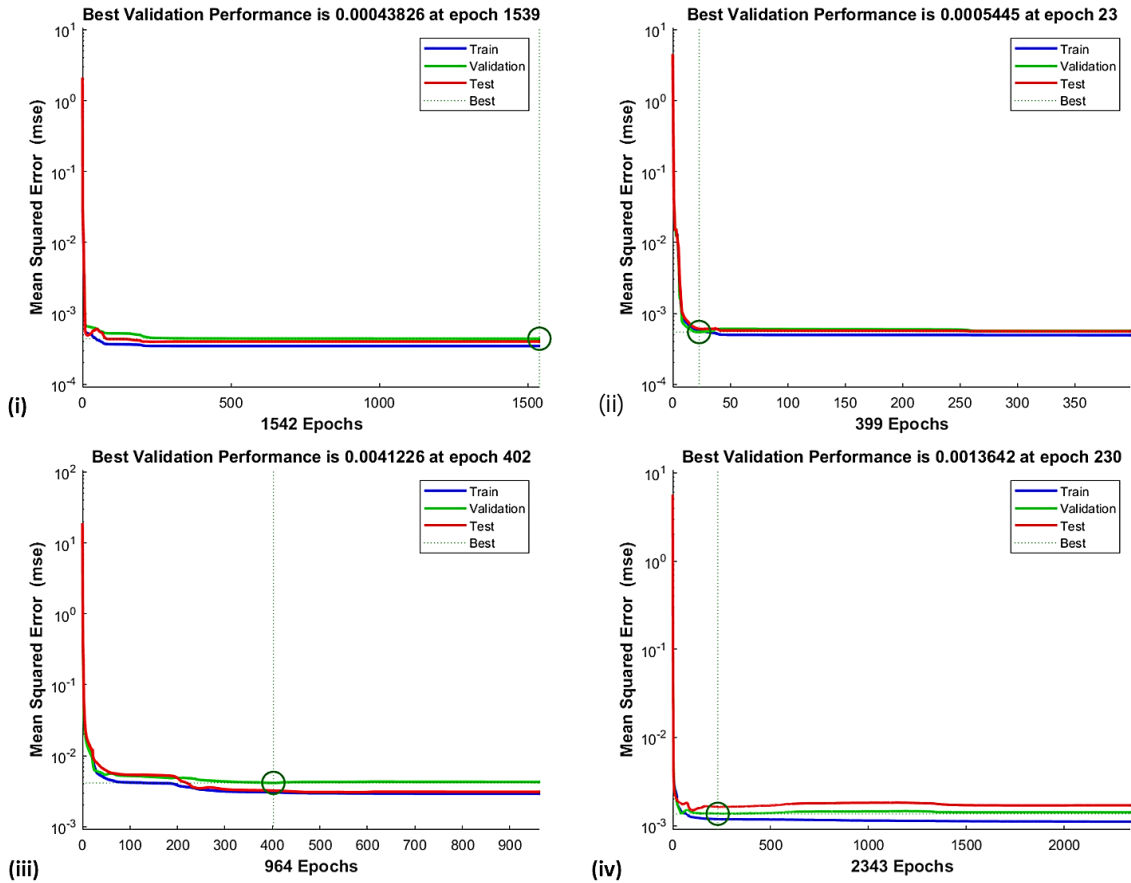


Figure 8. Performance plots: (i) in-plane bending condition-1, (ii) in-plane bending condition-2, (iii) out-of-plane bending condition-1, (iv) out-of-plane bending condition-2

$$i_{normalized} = \frac{(i_{n,max} - i_{n,min})(i - i_{min})}{(i_{max} - i_{min})} + i_{n,min} \tag{8}$$

$$o_{denormalized} = \frac{(o_n - o_{n,min})(o_{max} - o_{min})}{(o_{n,max} - o_{n,min})} + o_{min} \tag{9}$$

where $i_{n,max}$ is 1, i_{max} is max value in input data, $i_{n,min}$ is -1, i_{min} is min value in input data, $o_{n,max}$ is 1, o_{max} is max value of SCF is simulation results, $o_{n,min}$ is -1, o_{min} is min value of SCF in simulation results.

IPB and OPB cases were individually simulated, and ANN was trained for each case. The weights and biases of the trained model were employed for the mathematical modeling of SCF. Stress can be superimposed on IPB and OPB when the joint material remains in the linear elastic range [5, 13, 37]. The combined HSS was computed using Equation 10. The results determined are discussed in the next section.

$$Peak\ HSS = SCF_{ipb}\sigma_{nominal\ ipb} + SCF_{opb}\sigma_{nominal\ opb} \tag{10}$$

4. Empirical Modeling of Stress Concentration Factors

The equations for the SCF in KT-joint subjected to simultaneous brace bending were developed for four configurations applied individually. Two of these represent IPB, and the other two represent OPB. A typical complex bending load can be resolved into IPB and OPB components. For individual load cases, the other component will have null magnitude. Empirical models were developed for each case, and their effect was linearly superimposed using Equation 10. These models were validated with detailed FEA for individual and combined load cases. Empirical equations were developed for quarter geometry (1/4th), with the other quarter having an inverted SCF and the remaining half being symmetric. Equations 15-22 have been developed for SCF along the weld toe of the central brace. The SCF determined through these ANN-based equations was validated through finite element analysis of different KT-joint designs. The SCFs for nine randomly selected designs are shown in Figures 9 to 15. The maximum error in the SCF was 4.7, 4.0, 3.3, and 4.9% for IPB_C1, IPB_C2, OPB_C1 and OPB_C2, respectively. These nine designs were other than those used for training the ANN model, as presented in Table 3.

$$SCF_{chord_crown} = 1.45 \beta \tau^{0.85} \gamma^{(1-0.68\beta)} \sin \theta \tag{11}$$

$$SCF_{chord_saddle} = T_B [1 - 0.8(\beta_A \gamma)^{0.5} \exp(-0.8x_{AB})]^{(\beta_A/\beta_B)^2} \cdot [1 - 0.8(\beta_C \gamma)^{0.5} \exp(-0.8x_{BC})]^{(\beta_C/\beta_B)^2} + T_A [1 - 0.8(\beta_B \gamma)^{0.5} \exp(-0.8x_{AB})] \cdot [2.05(\beta_{max})^{0.5} \exp(-1.3x_{AB})] + T_C [1 - 0.8(\beta_B \gamma)^{0.5} \exp(-0.8x_{BC})] \cdot [2.05(\beta_{max})^{0.5} \exp(-1.3x_{BC})]$$

$$T_i = \gamma \tau_i \beta_A (1.7 - 1.05\beta_i^3) \sin^{1.8} \theta_i \tag{12}$$

where $i = A, B, C$ (inclined brace 1, central brace and inclined brace 2)

$$X_{AB} = 1 + \frac{\zeta_{AB} \sin \theta_B}{\beta_B}$$

$$X_{BC} = 1 + \frac{\zeta_{BC} \sin \theta_B}{\beta_B}$$

$$SCF_{crown} = 0.566 \tau^{0.883} \gamma^{0.715} \beta^{-0.003} \theta^{0.061} \tag{13}$$

$$SCF_{crown} = 0.671 \tau^{0.848} \gamma^{0.683} \beta^{0.115} \theta^{0.023} \tag{14}$$

$$\begin{bmatrix} h_1 \\ h_2 \\ h_3 \\ h_4 \\ h_5 \\ h_6 \\ h_7 \\ h_8 \end{bmatrix} = \begin{bmatrix} 0.04 & 0.04 & 0.29 & 0.26 & 0.06 & -0.46 \\ 0.14 & 0.28 & -0.04 & -0.04 & 0.00 & -0.15 \\ -0.80 & 0.13 & -0.14 & -0.01 & 0.01 & -0.05 \\ 0.14 & 0.27 & -0.04 & -0.04 & 0.00 & -0.15 \\ 0.78 & 0.04 & -0.26 & -0.07 & -1.58 & -0.13 \\ -2.51 & -0.71 & 0.83 & 2.17 & 3.27 & -0.14 \\ -0.31 & 0.14 & 0.35 & -0.01 & -0.04 & 0.25 \\ -0.76 & -0.03 & 0.26 & 0.05 & 1.56 & 0.15 \\ 0.82 & 0.10 & 0.36 & 0.05 & 0.00 & -0.15 \\ 0.82 & 0.10 & 0.36 & 0.05 & 0.00 & -0.15 \end{bmatrix} \begin{bmatrix} \beta_n \\ \gamma_n \\ \tau_n \\ \theta_n \\ \alpha_n \\ \zeta_n \end{bmatrix} + \begin{bmatrix} -1.80 \\ -0.80 \\ 1.39 \\ -0.80 \\ -4.12 \\ 2.64 \\ -0.10 \\ 4.62 \\ 0.15 \\ 0.16 \end{bmatrix} \tag{15}$$

$$\begin{bmatrix} SCF_0 \\ SCF_{15} \\ SCF_{30} \\ SCF_{45} \\ SCF_{60} \\ SCF_{75} \\ SCF_{90} \end{bmatrix} = \begin{bmatrix} 1.63 & -64.27 & 0.08 & 66.61 & 124.42 & 0.04 & 0.60 & 335.10 & -22.04 & 22.52 \\ 1.06 & -74.73 & 0.09 & 77.43 & 47.62 & 0.01 & 0.63 & 127.79 & -24.15 & 24.64 \\ -0.01 & -85.26 & 0.25 & 88.26 & -86.94 & -0.04 & 0.54 & -234.45 & -23.93 & 24.40 \\ -0.55 & -82.97 & 0.41 & 85.92 & -147.43 & -0.06 & 0.44 & -396.42 & -17.20 & 17.59 \\ -0.64 & -87.33 & 0.60 & 90.56 & -164.13 & -0.06 & 0.41 & -440.50 & -10.99 & 11.33 \\ -0.53 & -96.41 & 1.21 & 100.15 & -147.90 & -0.05 & 0.51 & -398.90 & 3.11 & -2.82 \\ 0.49 & -78.73 & -1.89 & 82.40 & 200.67 & 0.11 & 1.31 & 542.80 & 175.02 & -175.93 \end{bmatrix} \begin{bmatrix} h_1 \\ h_2 \\ h_3 \\ h_4 \\ h_5 \\ h_6 \\ h_7 \\ h_8 \end{bmatrix} + \begin{bmatrix} -207.78 \\ -77.46 \\ 149.43 \\ 250.35 \\ 277.68 \\ 252.14 \\ -337.24 \end{bmatrix} \tag{16}$$

$$\begin{bmatrix} h_1 \\ h_2 \\ h_3 \\ h_4 \\ h_5 \\ h_6 \\ h_7 \\ h_8 \\ h_9 \\ h_{10} \end{bmatrix} = \begin{bmatrix} -0.29 & -1.29 & -0.14 & 0.71 & 0.48 & 0.14 \\ -0.11 & -0.40 & 0.55 & -0.02 & 0.01 & 0.04 \\ 1.36 & 0.36 & -0.37 & -0.80 & -2.26 & -0.14 \\ -1.36 & 0.14 & -0.22 & 0.01 & 0.00 & -0.03 \\ 0.20 & 0.27 & 0.30 & 0.01 & 0.00 & -0.07 \\ -0.81 & -0.58 & -0.21 & -0.31 & -0.36 & 0.56 \\ -0.69 & -0.16 & -0.37 & 0.04 & 0.07 & 0.25 \\ 0.64 & -0.02 & -0.18 & -0.08 & -0.10 & -0.14 \\ -0.77 & -0.28 & 0.05 & 0.05 & 0.12 & 0.17 \\ 0.13 & 0.31 & 0.50 & 0.01 & -0.02 & -0.24 \end{bmatrix} \begin{bmatrix} \beta_n \\ \gamma_n \\ \tau_n \\ \theta_n \\ \alpha_n \\ \zeta_n \end{bmatrix} + \begin{bmatrix} -2.02 \\ 0.65 \\ -4.02 \\ 1.53 \\ 0.23 \\ 0.50 \\ -0.64 \\ 0.02 \\ -0.46 \\ -1.05 \end{bmatrix} \tag{17}$$

$$\begin{bmatrix} SCF_0 \\ SCF_{15} \\ SCF_{30} \\ SCF_{45} \\ SCF_{60} \\ SCF_{75} \\ SCF_{90} \end{bmatrix} = \begin{bmatrix} -0.01 & 0.39 & -0.44 & 0.07 & 1.14 & 0.10 & -0.10 & -0.02 & 0.17 & 0.71 \\ -0.02 & 0.44 & -0.23 & 0.08 & 1.08 & 0.09 & -0.15 & -0.25 & 0.07 & 0.74 \\ -0.03 & 0.47 & 0.34 & 0.09 & 0.64 & 0.05 & -0.29 & -0.81 & -0.33 & 0.65 \\ -0.03 & 0.54 & 0.61 & 0.18 & 0.59 & -0.02 & -0.13 & -0.89 & -0.56 & 0.63 \\ -0.03 & 0.53 & 0.58 & 0.28 & 0.66 & -0.06 & 0.07 & -0.73 & -0.60 & 0.75 \\ -0.01 & 0.60 & 0.40 & 0.69 & 0.89 & -0.11 & 0.33 & -0.27 & -0.51 & 0.71 \end{bmatrix} \begin{bmatrix} h_1 \\ h_2 \\ h_3 \\ h_4 \\ h_5 \\ h_6 \\ h_7 \\ h_8 \\ h_9 \\ h_{10} \end{bmatrix} + \begin{bmatrix} -0.47 \\ -0.41 \\ -0.09 \\ 0.05 \\ 0.08 \\ -0.42 \end{bmatrix} \tag{18}$$

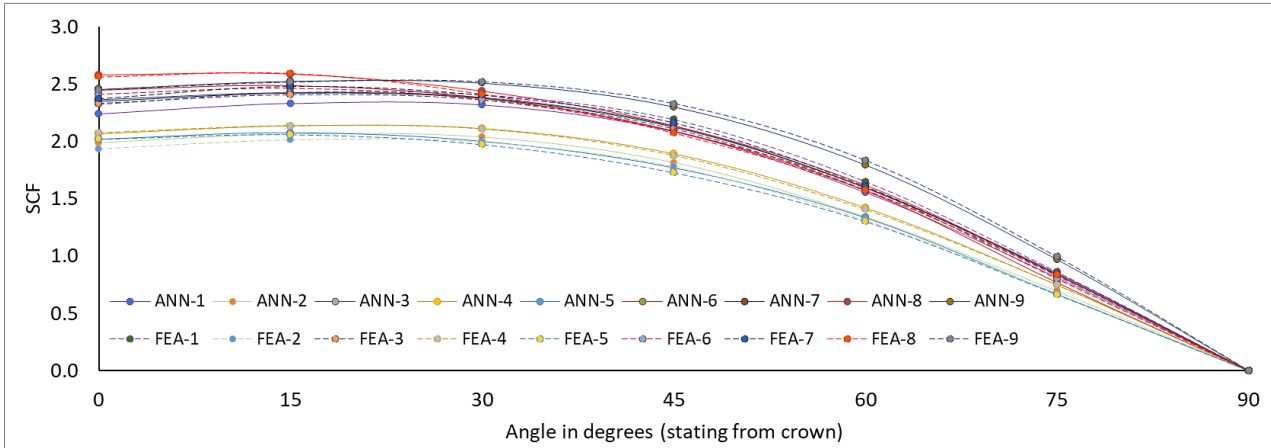


Figure 9. Comparison of stress concentration factor for in-plane bending condition-1 determined using empirical model and finite element analysis

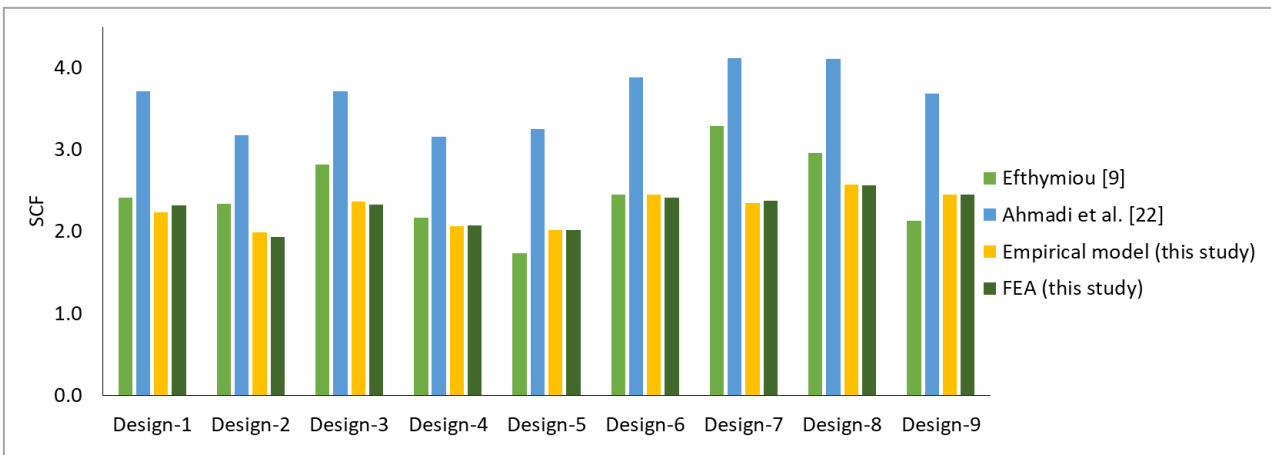


Figure 10. Comparison of stress concentration factor determined using Equations 15 and 16 to existing models

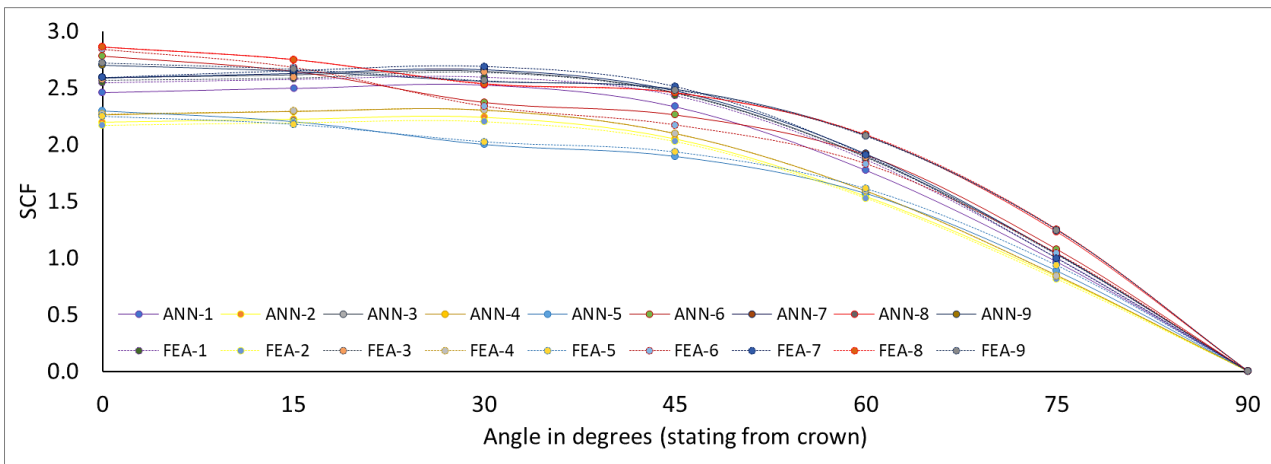


Figure 11. Comparison of stress concentration factor for in-plane bending condition-2 determined using empirical model and finite element analysis

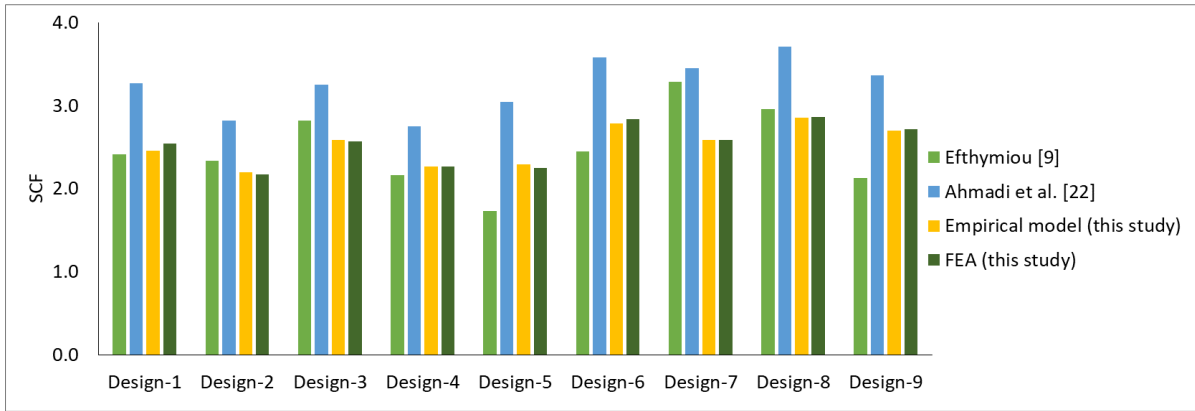


Figure 12. Comparison of stress concentration factor determined using Equations 17 and 18 to existing models

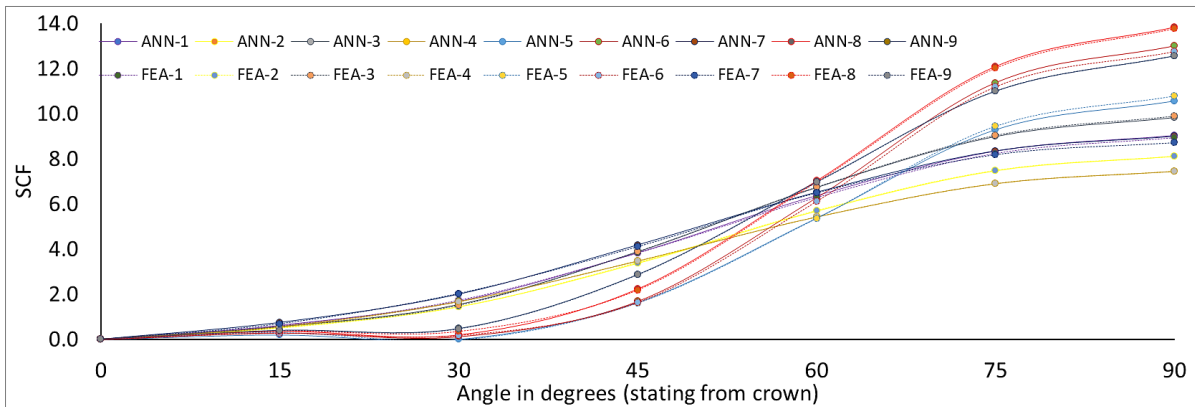


Figure 13. Comparison of stress concentration factor for out-of-plane bending condition-1 determined using empirical model and finite element analysis

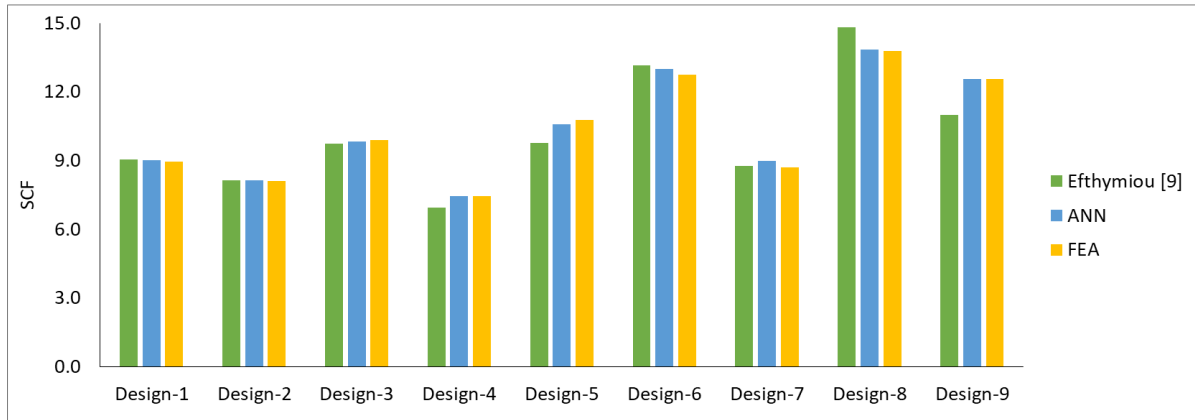


Figure 14. Comparison of stress concentration factor determined using Equations 19 and 20 to existing models

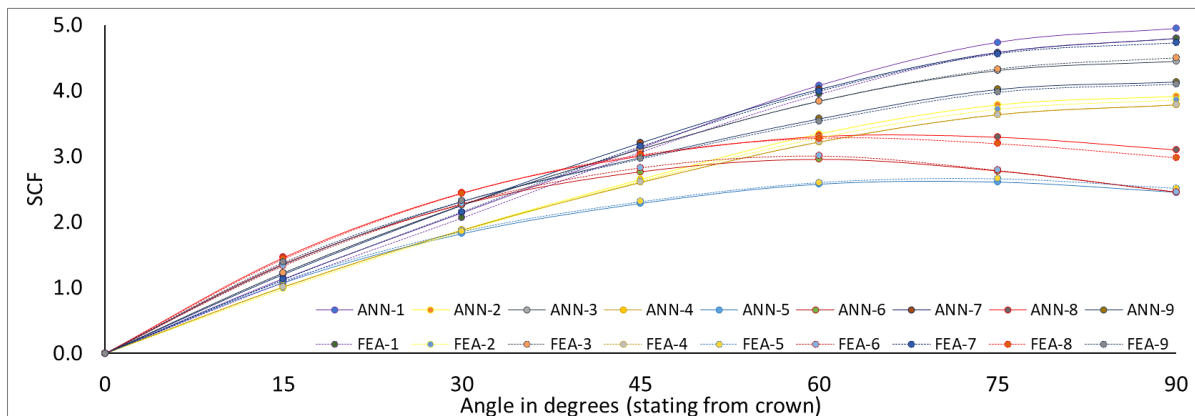


Figure 15. Comparison of stress concentration factor for out-of-plane bending condition-2 determined using empirical model and finite element analysis

Table 3. Details of KT-joints used for validation of empirical models

Design #	Geometric parameters						Dimensionless parameters					
	D	T	L/2	d	t	L	β	γ	τ	Θ	α	ζ
1	200	6	1000	100	4	2000	0.50	16.67	0.67	40.00	20.00	0.50
2	225	7.5	1200	120	4.5	2400	0.53	15.00	0.60	50.00	21.33	0.44
3	250	8	1150	130	5.5	2300	0.52	15.63	0.69	55.00	18.40	0.40
4	300	10	1300	133	6	2600	0.44	15.00	0.60	45.00	17.33	0.33
5	320	8	1350	250	4	2700	0.78	20.00	0.50	35.00	16.88	0.31
6	350	9	1400	280	5.5	2800	0.80	19.44	0.61	50.00	16.00	0.29
7	220	6	1100	90	4	2200	0.41	18.33	0.67	70.00	20.00	0.45
8	320	8	1200	240	5	2400	0.75	20.00	0.63	65.00	15.00	0.31
9	380	10	1300	250	6	2600	0.66	19.00	0.60	35.00	13.68	0.26
Min	200.00	6.00	900.00	90.00	4.00	1800.00	0.41	15.00	0.45	30.00	10.00	0.26
Max	380.00	10.00	1400.00	280.00	6.00	2800.00	0.80	20.00	0.69	70.00	21.33	0.50

The developed empirical models were validated with the literature as well. Efthymiou [9] proposed Equation 11 for determining SCF at the crown in the joint under IPB_C1 and IPB_C2. Similarly, Efthymiou [9] presented Equation 12 for determining SCF at the saddle in the joint under OPB_C1, while OPB_C2 was not covered. Ahmadi & Ali [22] have proposed Equations 13 and 14 for determining SCF at the crown joint under IPB_C1 and IPB_C2, respectively.

4.1. IPB_C1

When the randomly selected KT-joints were subjected to IPB condition-1, according to Figure 1, the peak SCF occurred at the crown position. The SCF determined using the developed empirical models, given as Equations 15 and 16 for IPB_C1, was in good agreement with the FE results, as shown in Figure 9. The difference was less than 5 percent. These equations were extracted from the best epoch of the trained ANN model and validated with equations available in the literature [9, 22] as well, as shown in Figure 10. A good agreement was observed with Efthymiou [9] (less than 6% difference). However, the difference was slightly higher (35–43%) when the SCF determined through the empirical models of this study was compared to the one calculated using the equations proposed by Ahmadi & Ali [22]. The large difference could be due to the limited number of simulations used to extract numerous equations, i.e., only 46 simulations were used to develop ten parametric equations for different IPB load configurations [22].

4.2. IPB_C2

Similar to IPB_C1, the KT-joint under IPB_C2 has a peak SCF at the crown region. Equations 17 and 18 approximate the SCF behavior and are compared with FE model results, as shown in Figure 11. The difference was less than 5%. The position of peak SCF has minor deviations from the crown position, depending on the geometry of the joint. These empirical models were validated with existing equations [9, 22], as shown in Figure 12. The difference was less than 25 percent, which is a bit large but can be considered acceptable, as various critical details regarding the definition of joint geometry are missing in the literature. This comparison imparts confidence in the developed empirical models, which represent a trend similar to that in the literature. Future experimental validation will be beneficial to resolve such discrepancies.

4.3. OPB_C1

The design data set of 929 FE models was simulated under OPB-condition-1, and empirical models were developed and given as Equations 19 and 20. These models were validated by comparing the SCF generated through these models to those generated through detailed FE simulations. A good agreement was observed with a less than 4% difference, as shown in Figure 13. These empirical models were validated with existing equations [9], with less than 15% difference, as shown in Figure 14.

$$\begin{bmatrix} h_1 \\ h_2 \\ h_3 \\ h_4 \\ h_5 \\ h_6 \\ h_7 \\ h_8 \end{bmatrix} = \begin{bmatrix} -0.62 & -0.14 & -0.22 & -0.04 & -0.03 & 0.06 \\ -0.41 & -0.16 & -0.28 & -0.01 & -0.01 & 0.09 \\ -0.75 & -0.35 & -0.36 & -0.04 & 0.14 & 0.29 \\ -0.13 & -0.18 & 0.43 & -0.01 & 0.05 & 0.05 \\ -0.52 & -0.19 & -0.10 & -0.02 & 0.06 & 0.27 \\ -0.07 & -0.20 & -0.39 & 0.66 & 0.14 & -0.02 \\ 0.94 & 0.08 & -0.34 & -0.03 & -0.09 & -0.17 \\ 0.14 & 0.03 & -0.25 & 0.00 & -0.03 & -0.05 \\ 1.03 & 0.18 & -0.40 & -0.01 & -0.10 & -0.20 \\ 0.51 & 0.46 & 0.52 & 0.19 & -2.85 & -0.11 \end{bmatrix} \begin{bmatrix} \beta_n \\ \gamma_n \\ \tau_n \\ \Theta_n \\ \alpha_n \\ \zeta_n \end{bmatrix} + \begin{bmatrix} 1.49 \\ 0.85 \\ 2.21 \\ -0.78 \\ -0.22 \\ 2.45 \\ 1.49 \\ 0.66 \\ 1.64 \\ -3.71 \end{bmatrix} \tag{19}$$

$$\begin{bmatrix} SCF_0 \\ SCF_{15} \\ SCF_{30} \\ SCF_{45} \\ SCF_{60} \\ SCF_{75} \end{bmatrix} = \begin{bmatrix} 4.21 & -0.73 & -3.12 & -0.55 & 0.20 & 0.15 & -1.96 & -2.39 & 1.48 & 0.37 \\ -2.61 & 5.44 & -3.18 & 0.18 & -0.88 & -1.07 & -4.17 & -3.37 & 4.15 & 0.15 \\ 1.99 & 0.96 & -0.81 & -1.67 & -0.91 & 0.22 & -1.62 & -6.63 & 2.27 & 0.01 \\ 3.28 & -1.72 & -0.73 & -2.81 & -0.62 & 1.03 & 1.61 & -7.45 & -0.58 & -0.14 \\ 3.55 & -2.50 & -1.11 & -2.77 & -0.38 & 1.17 & 2.62 & -6.34 & -1.70 & -0.21 \\ 4.23 & -2.89 & -1.30 & -2.71 & -0.30 & 1.31 & 2.90 & -5.95 & -2.03 & -0.23 \end{bmatrix} \begin{bmatrix} h_1 \\ h_2 \\ h_3 \\ h_4 \\ h_5 \\ h_6 \\ h_7 \\ h_8 \end{bmatrix} + \begin{bmatrix} 1.30 \\ 4.68 \\ -0.02 \\ -0.79 \\ -0.87 \\ -1.34 \end{bmatrix} \quad (20)$$

4.4. OPB_C2

Various KT-joints were simulated, and empirical models were developed for OPB_C2. These empirical models are given as Equations 21 and 22. These models were validated through random KT-joints in Table 3. The difference was less than 4% for SCF determined empirically compared to the FEA simulation results, as shown in Figure 15. Equations were unavailable in the literature for validation.

$$\begin{bmatrix} h_1 \\ h_2 \\ h_3 \\ h_4 \\ h_5 \\ h_6 \end{bmatrix} = \begin{bmatrix} -0.58 & -0.10 & -0.27 & 0.00 & 0.15 & 0.02 \\ -0.27 & -0.12 & -0.22 & 0.09 & 0.33 & 0.01 \\ 0.02 & -0.09 & -0.22 & 0.00 & 0.04 & 0.04 \\ 1.10 & 0.07 & -0.52 & -0.55 & -1.45 & -0.27 \\ 0.13 & 0.05 & -0.01 & 0.26 & -0.16 & 0.01 \\ -0.21 & 0.13 & 0.02 & 0.01 & -0.06 & 0.02 \\ -0.46 & 0.13 & 0.03 & -0.02 & -0.06 & 0.18 \\ 0.04 & 0.03 & -0.03 & 0.34 & -0.06 & 0.02 \\ -0.41 & -0.10 & -0.09 & -0.09 & 0.24 & 0.13 \\ -0.37 & -0.17 & 0.45 & -0.01 & -0.01 & -0.01 \end{bmatrix} \begin{bmatrix} \beta_n \\ \gamma_n \\ \tau_n \\ \theta_n \\ \alpha_n \\ \zeta_n \end{bmatrix} + \begin{bmatrix} 1.90 \\ 1.67 \\ 0.57 \\ -1.33 \\ 0.29 \\ -0.61 \\ -0.38 \\ 0.13 \\ -0.71 \\ -1.30 \end{bmatrix} \quad (21)$$

$$\begin{bmatrix} SCF_{15} \\ SCF_{30} \\ SCF_{45} \\ SCF_{60} \\ SCF_{75} \\ SCF_{90} \end{bmatrix} = \begin{bmatrix} 1.84 & 2.89 & -6.38 & -0.11 & 4.14 & -0.88 & -0.87 & -2.61 & 2.32 & -1.53 \\ 1.72 & 3.21 & -6.52 & -0.06 & 2.66 & -1.86 & -0.15 & -1.67 & 1.42 & -1.46 \\ 2.05 & 1.23 & -6.29 & 0.03 & -1.04 & -3.69 & 1.31 & 0.77 & -0.31 & -1.63 \\ 3.01 & -2.44 & -4.60 & 0.10 & -5.17 & -4.71 & 2.45 & 3.48 & -2.21 & -1.59 \\ 4.71 & -5.42 & -3.61 & 0.15 & -7.29 & -4.81 & 2.78 & 4.94 & -2.96 & -1.58 \\ 5.85 & -6.48 & -3.31 & 0.16 & -7.61 & -4.61 & 2.71 & 5.20 & -2.98 & -1.53 \end{bmatrix} \begin{bmatrix} h_1 \\ h_2 \\ h_3 \\ h_4 \\ h_5 \\ h_6 \end{bmatrix} + \begin{bmatrix} -3.06 \\ -3.50 \\ -2.90 \\ -1.60 \\ -0.88 \\ -0.96 \end{bmatrix} \quad (22)$$

5. Computation of Hot-Spot Stress Using Empirical Equations

Fatigue life estimation using S-N curves requires the peak HSS of a tubular joint based on the load condition. The empirical models were used to compute HSS around the chord-central brace interface of KT-joint subjected to different bending load configurations, using the approach by Ahmadi & Ali [22]. A MATLAB code yielding HSS for 0°-360° of the chord-brace interface was developed, with dimensionless parameters (β, γ, τ, θ, α, ζ) and magnitude for IPB and OPB loads as input. This plot identifies the peak HSS along the weld toe for fatigue life estimation using the S-N curve. This method can be used to determine peak HSS along the weld toe of the brace/chord interface, including the crown and saddle.

5.1. Individual Bending Load

The codes can be used for KT-joint under any bending loads. If the joint is subjected to IPB or OPB, the other load will be zero. Figure 16 compares the HSS calculated with the empirical equations for individual bending loads. The error in the computed peak HSS is less than 0.8%. Table 4 lists the error in peak HSS for various bending combinations.

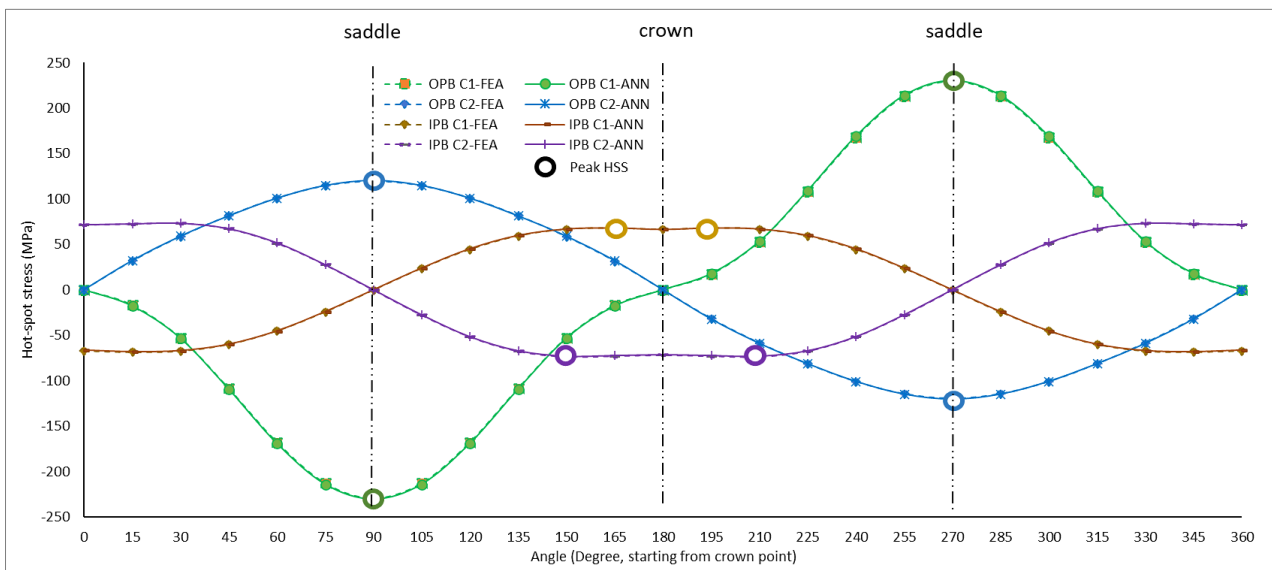


Figure 16. Hot-spot stress due to individual bending loads (30 MPa) on all braces of KT-joint

Table 4. Peak HSS position and error for various bending loads

Load Type	Load case	Position of peak HSS	% Error in peak HSS
Individual bending load (uniplanar)	IPB_C1	15° from crown	0.2
	IPB_C2	30° from crown	0.2
	OPB_C1	saddle (90° from crown)	0.4
	OPB_C2	saddle (90° from crown)	0.8
Simultaneous bending loads (multiplanar)	IPB_C1 + OPB_C1 4:1	60° from crown	1.4
	IPB_C1 + OPB_C1 2:1	75° from crown	0.7
	IPB_C1 + OPB_C1 1:1	75° from crown	0.6
	IPB_C1 + OPB_C1 1:2	saddle (90° from crown)	0.4
	IPB_C1 + OPB_C1 1:4	saddle (90° from crown)	0.4
	IPB_C1 + OPB_C2 4:1	30° from crown	0.3
	IPB_C1 + OPB_C2 2:1	45° from crown	0.3
	IPB_C1 + OPB_C2 1:1	60° from crown	0.1
	IPB_C1 + OPB_C2 1:2	75° from crown	0.3
	IPB_C1 + OPB_C2 1:4	75° from crown	0.3
	IPB_C2 + OPB_C2 4:1	30° from crown	0
	IPB_C2 + OPB_C2 2:1	45° from crown	0.1
	IPB_C2 + OPB_C2 1:1	60° from crown	0.3
	IPB_C2 + OPB_C2 1:2	75° from crown	0.3
IPB_C2 + OPB_C2 1:4	75° from crown	0.3	

5.2. Combined Bending Load

When bending at an angle to the orthogonal axis of the joint, the peak HSS occurs between the crown and saddle points [26]. A KT-joint was simulated for different combinations of combined bending to show this shift and as a proof of concept of the empirical models to determine peak HSS in such scenarios. Table 4 summarizes these loads and the positions of peak HSS. The three possible bending configurations are presented in the following sections:

5.2.1. IPB_C1 + OPB_C1

KT-joints under different combinations of IPB and OPB were simulated. The simultaneous application of IPB_C1 and OPB_C1 causes variation in the position of peak HSS, as shown in Figure 17.

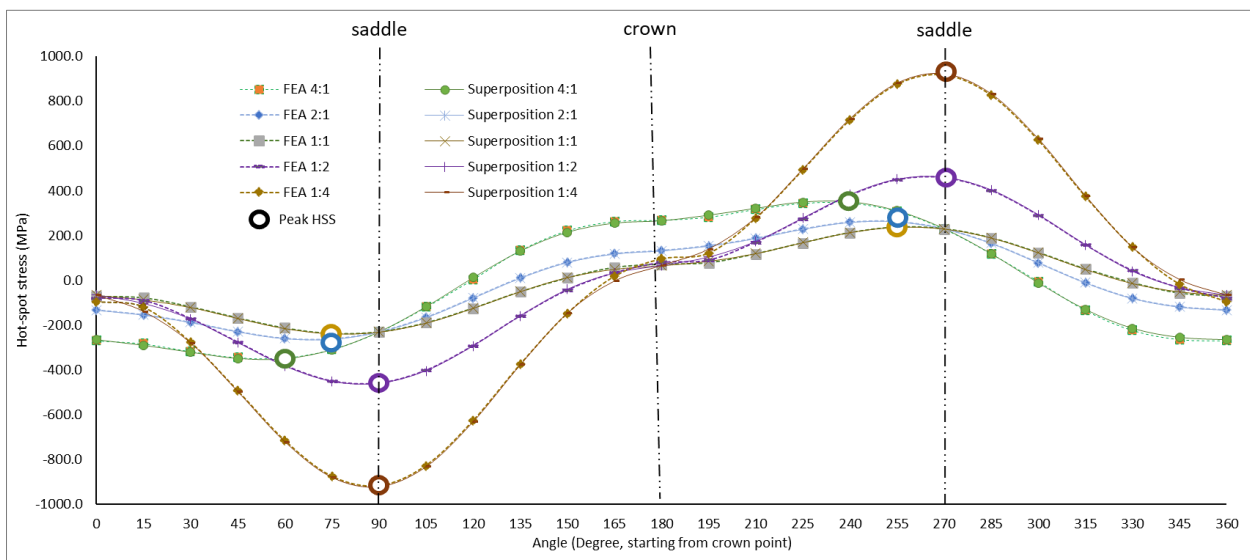


Figure 17. Comparison of hot-spot stress for simultaneous in-plane bending condition-1 and out-of-plane bending condition-1 determined using empirical models and finite element analysis

IPB and OPB ratios of 4:1, 2:1, 1:1, 1:2, and 1:4 were used, with "1" representing a 30 MPa bending stress. Equations 20–23 were used for SCF calculation, and combined HSS was calculated using Equation 10. When an IPB_C1 load of 30 MPa was applied with an OPB_C1 load of 30, 60, and 120 MPa, the peak HSS was at 75° from the crown (15° from the saddle) and remained at the saddle for the following two load combinations. When OPB_C1 magnitude was fixed

and IPB_C1 was varied, the peak HSS was at 75°, 75°, and 60° from the crown. The variation in peak HSS position emphasizes the need for empirical models capable of determining SCF around the axis. If hot-spot stress lower than peak HSS is selected, as would be the case if the equations from the literature were used, it will result in an unrealistic high fatigue life estimation through the respective S-N curve. These findings were validated with detailed FEA and a maximum of 1.4% error at the peak HSS points, as listed in Table 4.

5.2.2. IPB_C1 + OPB_C2

The second load configuration was IPB_C1 and OPB_C2. The same five load cases were simulated, i.e., 4:1, 2:1, 1:1, 1:2, and 1:4 (1 being 30 MPa). For equal magnitudes of IPB_C1 and OPB_C2, the peak HSS was 60° from the crown point. When the magnitude of IPB_C1 was doubled, the peak HSS was at the 45° position. When the IPB_C1 was further increased, the peak was 30° from the crown. Similarly, with IPB_C1 fixed, three magnitudes of OPB_C2 were applied to determine the variation in the position of peak HSS. The peak HSS was 60° from the crown for the same load and 15° from the crown for the following two load cases. The maximum difference was 0.3% compared to the FEA simulation results, as shown in Figure 18.

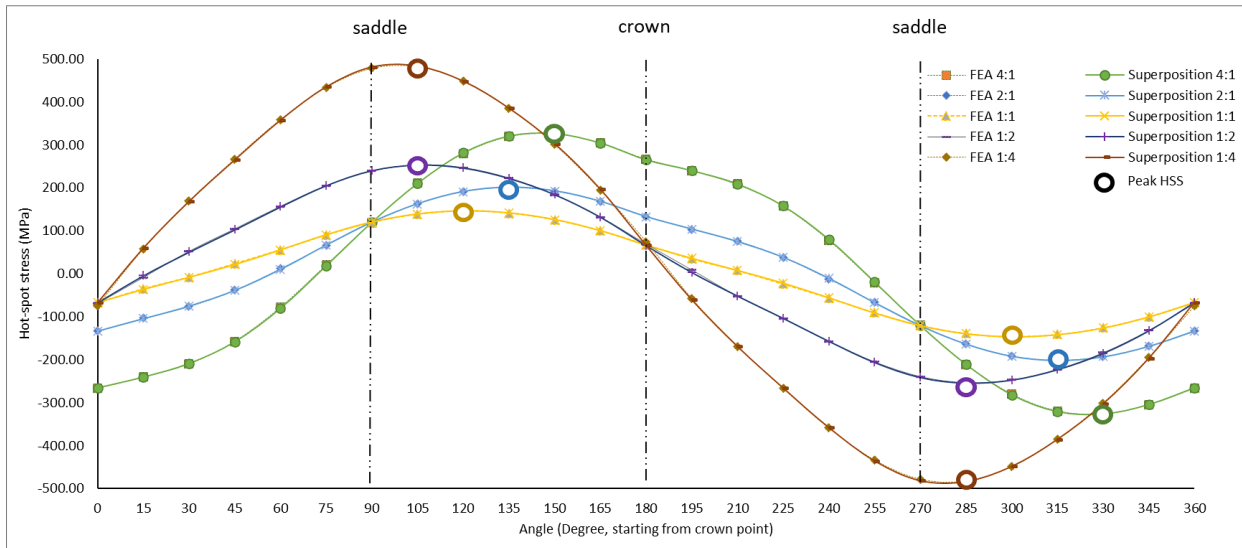


Figure 18. Comparison of hot-spot stress for simultaneous in-plane bending condition-1 and out-of-plane bending condition-2 determined using empirical models and finite element analysis

5.2.3. IPB_C2 + OPB_C2

The last combination was IPB_C2 and OPB_C2. The peak HSS occurred at 60°, 45°, and 30° from the crown when IPB_C2 of 30 MPa was applied with OPB_C2 of 30, 60, and 120 MPa bending stress. The peak HSS occurred at 60°, 75°, and 75° from the crown when 30 MPa OPB_C2 was applied with IPB_C2 of 30, 60, and 120 MPa stress. A similar trend was found for peak HSS based on the equations, with a maximum error of 0.3%, as shown in Figure 19.

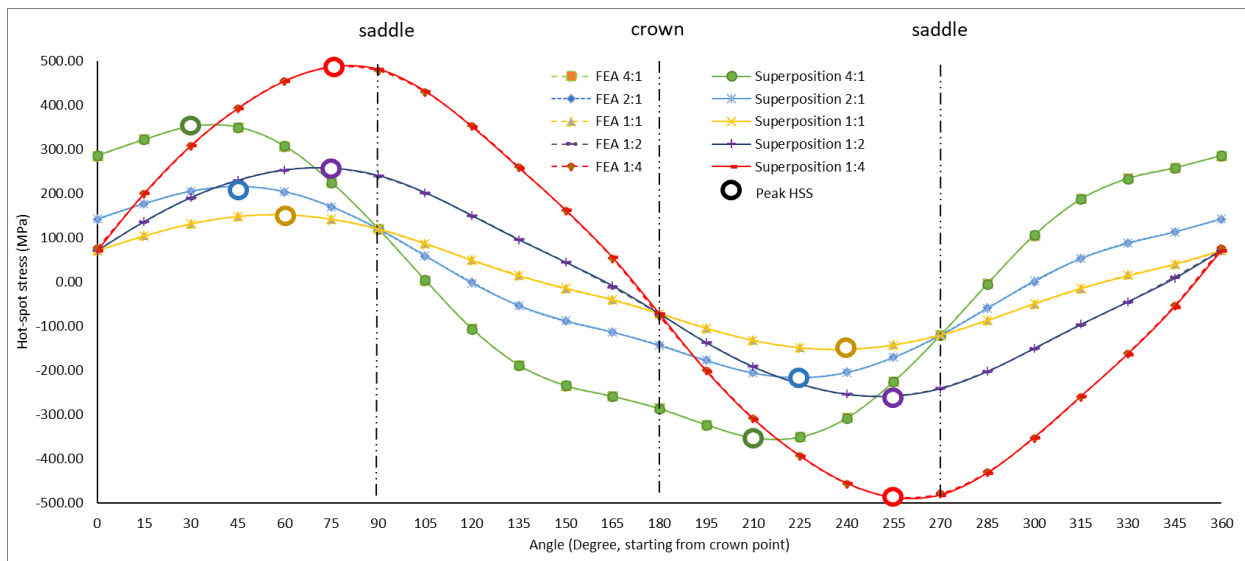


Figure 19. Comparison of hot-spot stress for simultaneous in-plane bending condition-2 and out-of-plane bending condition-2 determined using empirical models and finite element analysis

6. Conclusion

Existing models estimate peak hot-spot stress (HSS) at the crown or saddle. However, for a KT-joint under multiplanar loads, the peak HSS could occur anywhere along the weld toe of the brace-chord interface, which can be significantly higher than the HSS observed at the crown or saddle. As such, fatigue life can be overestimated if the HSS at the crown or saddle is used for fatigue analysis of the KT-joint under multiplanar bending. This study investigated the stress concentration factor (SCF) and HSS in KT-joints under multiplanar bending, addressing the limitations of existing models by proposing new empirical models to predict SCF and HSS with exceptional accuracy. Various KT-joint designs were generated, and 3716 simulations were performed. The HSS at the weld toe at 24 equidistant positions around the brace axis was determined based on the linear extrapolation of maximum principle stress. The HSS was expressed as a SCF at the weld toe. Artificial neural networks were trained using the simulation data, employing dimensionless joint parameters as input and SCF as output. Subsequently, empirical equations were developed to predict peak HSS for any combination of bending loads with less than 1.5% error. It was highlighted that the difference in HSS at the crown or saddle and the peak HSS depends on the relative magnitudes of in-plane and out-of-plane bending loads. These models may be validated experimentally in the future to enhance their reliability. Additionally, similar models could be developed for different joint types and load conditions using similar methodologies.

7. Abbreviations and Symbols

API	American Petroleum Institute	β	d/D
ANN	Artificial neural networks	γ	$D/2T$
DoE	Design of Experiment	τ	t/T
FE	Finite element	α	$2L/D$
FEA	Finite element analysis	ζ	g/D
FEM	Finite element method	ip_x	Input to ANN
HSS	Hot spot stress, the maximum principal stress extrapolated at the weld toe	hn_x	Output of a hidden layer
IPB	In-plane bending moment	W_x	Weight of a neuron
SCF	Stress concentration factor	B_x	Bias of a layer
OPB	Out-of-plane bending moment	$i_{n,max}$	The upper range of normalized input data
Peak HSS	Maximum value of hot-spot stress (HSS) around the brace axis	$i_{n,min}$	The lower range of normalized input data
θ	Angle of the inclined brace with chord axis	i_{max}	Maximum of dimensionless input data
D	Diameter of the chord	i_{min}	Minimum of dimensionless input data
d	Diameter of the brace (all braces kept same)	$o_{n,max}$	The upper range of normalized output data
T	Thickness of the chord	$o_{n,min}$	The lower range of normalized output data
t	The thickness of the brace (all braces kept the same)	o_{max}	Maximum SCF input used for ANN training
g	The gap between the central and inclined brace	o_{min}	Minimum SCF input used for ANN training
σ_n	Nominal stress		

8. Declarations

8.1. Author Contributions

Conceptualization, S.K. and M.I.; methodology, M.I. and A.K.; software, M.I. and M.F.; validation, M.I.; formal analysis, M.I.; investigation, M.I.; resources, S.K.; data curation, S.K. and M.O.; writing—original draft preparation, M.I.; writing—review and editing, M.I. and M.O.; visualization, M.I.; supervision, S.K., V.P., and M.O.; project administration, S.K. and V.P.; funding acquisition, S.K. All authors have read and agreed to the published version of the manuscript.

8.2. Data Availability Statement

The data presented in this study are available on request from the corresponding author.

8.3. Funding

This research received funding from Yayasan Universiti Teknologi PETRONAS under Grant No 015LC0-443.

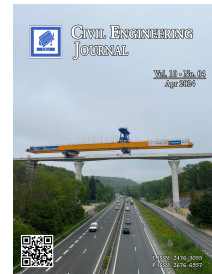
8.4. Conflicts of Interest

The authors declare no conflict of interest.

9. References

- [1] Vieira Ávila, B., Correia, J., Carvalho, H., Fantuzzi, N., De Jesus, A., & Berto, F. (2022). Numerical analysis and discussion on the hot-spot stress concept applied to welded tubular KT joints. *Engineering Failure Analysis*, 135. doi:10.1016/j.engfailanal.2022.106092.
- [2] Zhou, K., Zuo, J., Wang, W., & Bao, S. (2020). Stress Concentration Factors for Multi-planar Tubular Joints Subjected to Axial Loading. *E3S Web of Conferences*, 213. doi:10.1051/e3sconf/202021303014.
- [3] Iqbal, M., Karuppanan, S., Perumal, V., Ovinis, M., & Rasul, A. (2023). Rehabilitation Techniques for Offshore Tubular Joints. *Journal of Marine Science and Engineering*, 11(2), 461. doi:10.3390/jmse11020461.
- [4] Maheswaran, J., & Siriwardane, S. C. (2016). Fatigue life estimation of tubular joints - A comparative study. *Fatigue & Fracture of Engineering Materials & Structures*, 39(1), 30–46. doi:10.1111/ffe.12314.
- [5] Hoon, K. H., Wong, L. K., & Soh, A. K. (2001). Experimental investigation of a doubler-plate reinforced tubular T-joint subjected to combined loadings. *Journal of Constructional Steel Research*, 57(9), 1015–1039. doi:10.1016/S0143-974X(01)00023-2.
- [6] Kuang, J. G., Potvin, A. B., & Leick, R. D. (1975). Stress concentration in tubular joints. *Proceedings of the Annual Offshore Technology Conference*, doi:10.4043/2205-MS.
- [7] Wordsworth, A.C. (1981). *Stress Concentration Factors at K and KT tubular joints. Fatigue in Offshore Structural Steels*, Thomas Telford Publishing, London, United Kingdom.
- [8] Wordsworth, A. C., & Smedley, G. P. (1978). Stress concentrations at unstiffened tubular joints. *European Offshore Steels Research Seminar*, 27-29 November, 1978, Abington Hall, United Kingdom.
- [9] Efthymiou, M. (1988). Development of SCF formulae and generalized influence functions for use in fatigue analysis. OTJ 88. *Recent Developments in Tubular Joints Technology*, Surrey, United Kingdom.
- [10] Hellier, A. K., Connolly, M. P., & Dover, W. D. (1990). Stress concentration factors for tubular Y- and T-joints. *International Journal of Fatigue*, 12(1), 13–23. doi:10.1016/0142-1123(90)90338-F.
- [11] Lloyd's Register. (1992). *Stress Concentration Factors for Tubular Complex Joints*, Lloyd's Register of Shipping for health and Safety Executive, Offshore Technology Report, (OTH 91 353), 1-106.
- [12] Smedley, P., & Fisher, P. (1991). Stress concentration factors for simple tubular joints. *International Ocean and Polar Engineering Conference (ISOPE)*, 11-16 August, 1991, Edinburgh, United Kingdom.
- [13] Morgan, M. R., & Lee, M. M. K. (1997). New parametric equations for stress concentration factors in tubular K-joints under balanced axial loading. *International Journal of Fatigue*, 19(4), 309–317. doi:10.1016/S0142-1123(96)00081-3.
- [14] Morgan, M. R., & Lee, M. M. K. (1998). Parametric equations for distributions of stress concentration factors in tubular K-joints under out-of-plane moment loading. *International Journal of Fatigue*, 20(6), 449–461. doi:10.1016/S0142-1123(98)00011-5.
- [15] DNV. (2016). *DNVGL-RP-C203. Fatigue design of offshore structures*. DNV, Bærum, Norway.
- [16] Norsok: N-004. (2004). *design of steel structures*. Standards Norway, Oslo, Norway.
- [17] Zhao, X.-L., Herion, S., Packer, JA., Puthli, RS., Sedlacek, G., Wardenier, J., Weynand, K., van Wingerde, AM., & Yeomans, NF. (2000). Design guide for circular and rectangular hollow section welded joints under fatigue loading. In *Design guide for circular and rectangular hollow section welded joints under fatigue loading*, 1-121. TUV-Verlag, Koln, Germany.
- [18] Ahmadi, H., & Zavvar, E. (2015). Stress concentration factors induced by out-of-plane bending loads in ring-stiffened tubular KT-joints of jacket structures. *Thin-Walled Structures*, 91, 82–95. doi:10.1016/j.tws.2015.02.011.
- [19] Ahmadi, H., & Lotfollahi-Yaghin, M. A. (2015). Stress concentration due to in-plane bending (IPB) loads in ring-stiffened tubular KT-joints of offshore structures: Parametric study and design formulation. *Applied Ocean Research*, 51, 54–66. doi:10.1016/j.apor.2015.02.009.
- [20] Ahmadi, H., Yeganeh, A., Mohammadi, A. H., & Zavvar, E. (2016). Probabilistic analysis of stress concentration factors in tubular KT-joints reinforced with internal ring stiffeners under in-plane bending loads. *Thin-Walled Structures*, 99, 58–75. doi:10.1016/j.tws.2015.11.010.
- [21] Ahmadi, H. (2016). A probability distribution model for SCFs in internally ring-stiffened tubular KT-joints of offshore structures subjected to out-of-plane bending loads. *Ocean Engineering*, 116, 184–199. doi:10.1016/j.oceaneng.2016.02.037.
- [22] Ahmadi, H., Ali, Z.N. (2016). Stress Concentration Factors in Uniplanar Tubular KT-Joints of Jacket Structures Subjected to In-Plane Bending Loads, *International Journal of Maritime Technology*, 5, 27-39.
- [23] Ahmadi, H., & Zavvar, E. (2016). The effect of multi-planarity on the SCFs in offshore tubular KT-joints subjected to in-plane and out-of-plane bending loads. *Thin-Walled Structures*, 106, 148–165. doi:10.1016/j.tws.2016.04.020.

- [24] Zavvar, E., Hectors, K., & De Waele, W. (2021). Stress concentration factors of multi-planar tubular KT-joints subjected to in-plane bending moments. *Marine Structures*, 78(March), 103000. doi:10.1016/j.marstruc.2021.103000.
- [25] Zavvar, E., Sadat Hosseini, A., & Lotfollahi-Yaghin, M. A. (2021). Stress concentration factors in steel tubular KT-connections with FRP-Wrapping under bending moments. *Structures*, 33, 4743–4765. doi:10.1016/j.istruc.2021.06.100.
- [26] Iqbal, M., Karuppanan, S., Perumal, V., Ovinis, M., & Nouman, H. (2023). Empirical modeling of stress concentration factors using finite element analysis and artificial neural networks for the fatigue design of tubular KT-joints under combined loading. *Fatigue and Fracture of Engineering Materials and Structures*, 46(11), 4333–4349. doi:10.1111/ffe.14122.
- [27] Yeoh, S. K., Soh, A. K., & Soh, C. K. (1995). Behaviour of tubular T-joints subjected to combined loadings. *Journal of Constructional Steel Research*, 32(3), 259–280. doi:10.1016/0143-974X(95)93898-E.
- [28] Gulati, K. C., Wang, W. J., & Kan, D. K. Y. (1982). An analytical study of stress concentration effects in multibrace joints under combined loading. *Proceedings of the Annual Offshore Technology Conference, OTC-4407-MS*, Texas, United States. doi:10.4043/4407-ms.
- [29] ARSEM. (1987). *Design guides for offshore structures - welded tubular joints*, Vol. 1, Technip, Association de recherche sur les structures métalliques marines (ARSEM), Paris, France.
- [30] American Petroleum Institute (API). (2014). *API Recommended Practice 2A-WSD. Planning, Designing, and Constructing Fixed Offshore Platforms—Working Stress Design*. American Petroleum Institute (API), Washington, United States.
- [31] Ahmadi, H., Lotfollahi-yaghin, M. A., & Yong-bo, S. (2013). Experimental and Numerical Investigation of Geometric SCFs in Internally Ring-Stiffened Tubular KT-Joints of Offshore Structures. *Journal of the Persian Gulf*, 43(1), 7–8.
- [32] Ahmadi, H. (2019). Probabilistic analysis of the DoB in axially-loaded tubular KT-joints of offshore structures. *Applied Ocean Research*, 87, 64–80. doi:10.1016/j.apor.2019.03.018.
- [33] van Wingerde, A. M., Packer, J. A., & Wardenier, J. (1995). Criteria for the fatigue assessment of hollow structural section connections. *Journal of Constructional Steel Research*, 35(1), 71–115. doi:10.1016/0143-974X(94)00030-I.
- [34] N'Diaye, A., Hariri, S., Pluvinage, G., & Azari, Z. (2007). Stress concentration factor analysis for notched welded tubular T-joints. *International Journal of Fatigue*, 29(8), 1554–1570. doi:10.1016/j.ijfatigue.2006.10.030.
- [35] Iqbal, M., Karuppanan, S., Perumal, V., Ovinis, M., & Hina, A. (2023). An Artificial Neural Network Model for the Stress Concentration Factors in KT-Joints Subjected to Axial Compressive Load. *Materials Science Forum*, 1103, 163–175. doi:10.4028/p-ypo50i.
- [36] Vijaya Kumar, S. D., Lo, M., Karuppanan, S., & Ovinis, M. (2022). Empirical Failure Pressure Prediction Equations for Pipelines with Longitudinal Interacting Corrosion Defects Based on Artificial Neural Network. *Journal of Marine Science and Engineering*, 10(6). doi:10.3390/jmse10060764.
- [37] Soh, A. K., & Soh, C. K. (1995). Stress analysis of axially loaded T tubular joints reinforced with doubler plates. *Computers and Structures*, 55(1), 141–149. doi:10.1016/0045-7949(94)00412-V.
- [38] Ahmadi, H., & Zavvar, E. (2020). Degree of bending (DoB) in offshore tubular KT-joints under the axial, in-plane bending (IPB), and out-of-plane bending (OPB) loads. *Applied Ocean Research*, 95(2020), 102015. doi:10.1016/j.apor.2019.102015.



Optimizing Alkali-Concentration on Fresh and Durability Properties of Defected Sanitary Ware Porcelain based Geopolymer Concrete

Woratid Wongpattanawut¹, Borvorn Israngkura Na Ayudhya^{1*} 

¹ Department of Civil Engineering, Rajamangala University of Technology Thanyaburi, Pathum Thani, 12110, Thailand.

Received 05 December 2023; Revised 01 March 2024; Accepted 09 March 2024; Published 01 April 2024

Abstract

Introducing defective sanitaryware porcelain as a low-calcium binder for geopolymer mix concrete was regarded as green concrete. Four alkali concentrations (8M, 10M, 12M, and 14M) mixes involving four initial curing temperatures (60°C, 75°C, 90°C, and 105°C) were investigated for porosity, rapid chloride penetration, compressive and abrasive resistance. Tests on geopolymer paste for consistency and initial and final setting times were also assessed. For all the mixes, consistency and setting time decreased with increased alkali concentration levels. An increment in curing temperature increased the setting time rate. Microstructural studies such as X-ray fluorescence analysis (XRF), X-ray diffraction (XRD), and scanning electron microscopy (SEM) were carried out, and the results were presented. The compressive and abrasive resistance of the specimen performance increased with an increase in the initial curing temperature and alkali concentration level. Majorly, the mechanical strength of porcelain-based geopolymer specimens increased by increasing the alkali concentration level. Applying 105°C for the initial curing temperature to the specimen, compressive strength, abrasive resistance, and resistibility to chloride ingress of the specimen enhanced. At the 28-days curing period, the ultimate compressive strength was 68.03 N/mm², the lowest weight loss from abrasive motion was 0.09%, and the lowest passing charge was 1,440.91 coulombs were recorded respectively. As a result, porcelain-based geopolymers required a high initial curing temperature and a high alkali concentration level. It was found that 14M porcelain-based specimens heated at 105°C curing temperature for 24 hours led to an eco-friendly concrete mix with prominent positive results for engineering properties.

Keywords: Geopolymers; Rapid Chloride Penetration; Porosity; Porcelain; Abrasive Resistance.

1. Introduction

The world's prosperity is related to its economic growth. In 2022, the construction industry will contribute 3.1% to the world's total GDP. It accounts for exceeding US\$ 28.26 trillion [1]. Cement is an essential binder material for producing concrete structures. However, burning calcium carbonate and fossil fuels from cement manufacture causes greenhouse gases. The cement industry is responsible for 8% of planet-warming carbon dioxide emissions [2]. Every ton of cement emits 900 kg of CO₂, accounting for 88% of the emissions associated with a concrete mix [3]. The growing interest in reducing carbon emissions related to concrete has sharply increased. One of the mitigation approaches to reducing carbon dioxide emission problems is activated alkali-geopolymer materials. Geopolymers are inorganic aluminosilicate polymers that are produced by the geopolymerization process via calcium-content materials and alkali-activated solutions. Geopolymer offers significantly 80 percent lower CO₂ emissions than ordinary Portland Cement (OPC) concrete [4]. It provides a better thermal insulation property [5, 6], higher temperature/fire resistance [7, 8], and compressive strength [9, 10].

* Corresponding author: borvorn_i@rmutt.ac.th

 <http://dx.doi.org/10.28991/CEJ-2024-010-04-05>



© 2024 by the authors. Licensee C.E.J, Tehran, Iran. This article is an open access article distributed under the terms and conditions of the Creative Commons Attribution (CC-BY) license (<http://creativecommons.org/licenses/by/4.0/>).

The sanitaryware porcelain industry is an important economic segment of global sanitaryware production. However, enormous amounts of waste generated from the production process are often discarded and landfilled [11]. Porcelain is a low-calcium-content binder that can ideally be used as alkali-activated materials (AAMs) [12]. Characteristics of porcelain sanitary ware are very low porosity [13], high mechanical [14, 15], abrasiveness, and stain resistance [16]. Thus, it provides numerous applications in several areas. Recycling defective porcelain sanitary ware waste as a raw material in binder geopolymer material becomes an attractive opportunity to increase the value of discarding waste material and deescalate the environmental impact of their disposal. However, low-calcium binder-based geopolymers require both heat and high alkali concentrations to enhance the geopolymerization process [13] and improve mechanical properties [14, 15], respectively. These two main factors affect the durability of low-calcium materials based on geopolymer specimens [16, 17]. The mechanical strength of low-calcium fly ash-based geopolymers was found to improve after being oven-dried (40°C–85°C) [18, 19]. Similarly, the geopolymerization process for slag binder requires a 60°C–90°C thermal temperature [20, 21]. Several researchers have tried to improve the structural strength by adding calcium oxide to design mixes. As expected, the use of high-volume, low-calcium material helps to increase reactivity. Consequently, increasing calcium content above a certain quantity causes degradation in strength [22, 23].

A low-calcium-based geopolymer was found to have low permeability, a long setting time, less shrinkage and carbonation, and higher chloride resistance. Among common low-calcium precursors, the usage of porcelain and ceramic powder as precursors in the production of AAMs has already been reported in the literature [24–29]. Low-calcium binder materials form and harden slightly when they cure at normal temperatures. Initial strength gain begins at an early age when a high temperature is applied. Due to this situation, the initial curing temperature has impacted the geopolymerization process and caused difficulties in production. Geopolymerization of fly ash (Type F) binder accelerates when initial curing temperatures in the range of 60–80 °C are applied. Whereas porcelain requires a higher initial curing temperature. Wongpattanawut & Ayuhdya [12] found that the geopolymerization process of porcelain-based mortar accelerated when the initial curing temperatures were above 75°C. In addition, they mentioned that applying 105°C to the initial curing temperature gave the highest ultimate compressive strength. Providing a high initial curing temperature to specimens, its obstacles an implementation of on-site concrete application, excluding autoclaved aerated concrete or precast concrete. The evaluation of sanitary ware porcelain as raw material in the production of geopolymer has not yet been fully elucidated. Mainly fly ash (Type F) and ceramics are chosen as low-calcium binder materials, which are studied for their characteristics and performances. Defected sanitary ware porcelain has still few studied in terms of fresh and hardened porcelain-based geopolymer specimens [30–33].

One of the reasons is the hardness of porcelain, which makes it difficult to reduce the particle size when compared with ceramics. Several processes of reduction in particle size engage time and energy consumption. The effect of activator, curing temperatures, and curing conditions on physical-mechanical properties and durability is also needed to further establish the accuracy and validity of porcelain-based geopolymer concrete. Optimization in curing temperature and alkali concentration for improving mechanical and durability has created a great interest for further research. The authors provide experiment results from sanitaryware production waste through the geopolymerization process with low environmental impact and low energy consumption. This paper presents the mechanical properties of defected porcelain-based geopolymer concrete, including surface resistivity and ion chloride penetration tests. Different curing temperatures and alkali concentration solutions are the variations used to make binders of geopolymer porcelain-based concrete.

2. Materials and Methods

2.1. Materials

2.1.1. Porcelain

The defective sanitary ware porcelain products were used as a source of aluminosilicate. The as-received defective porcelain products had an average moisture content of 34% by mass. In this study, the porcelain was originally fragmented by a hammer. The porcelain material was then oven-dried at 60°C for 24 hours until it reached a constant weight. This helped to remove any excess moisture from the intact material. The porcelain material largely consisted of kaolin, clay, feldspar, flint, calcium carbonate, dolomite, and sodium silicate. To achieve successful particle size reduction and distribution, it was necessary to generate forces directly for each particle. At the low-calcium binder preparation stage, the defective porcelain product was first crushed to 10–12 mm in size by a jaw crusher machine. Secondly, it was further ground by a grinding machine until the particle size was less than 75 μm (Figure 1). The prepared porcelain powder was kept in a sealed container until the mixing date. Table 1 presents the X-ray fluorescence (XRF) of porcelain powder and OPC, which was performed by using a Bruker model S8 Tiger in a vacuum atmosphere. It found that the characterization of porcelain powder was rich in silica (SiO₂) and alumina (Al₂O₃) content. It was referred to as a geopolymer, which provided silicon and aluminum (Si+Al) as the reactive binding agents. However, the contents of SiO₂ and Al₂O₃ were different from Geraldo et al. 2021 [34], Zuda et al. 2008 [35], and Ramos et al. 2020 [36], which were 72.0% and 13.80%, 67.7% and 21.0%, 48.6% and 45.4%, respectively. The variation in oxide content was due to the type of porcelain produced and the condition of the firing products, which affected the silica and alumina content [37].



Figure 1. Raw material before and after ground porcelain material

Table 1. Composition of defected sanitary porcelain, low calcium fly ash and OPC material

Oxides (%)	CaO	SiO ₂	Al ₂ O ₃	SO ₃	Fe ₂ O ₃	MgO	K ₂ O	TiO ₂	Na ₂ O	Others	LOI	Ref
Porcelain	2.87	54.88	17.62	0.02	1.68	0.57	3.01	0.32	1.11	8.62	9.3	-
OPC	63.42	17.76	3.88	2.94	2.76	1.82	0.47	0.32	0.27	3.96	2.4	-
Porcelain	-	72.0	13.80	-	2.2	0.20	5.60	0.60	-	2.60	3.0	Geraldo et al. (2021) [34]
Fly ash Type F	5.20	48.50	26.10	1.10	12.50	2.80	1.70	0.90	0.50	-	0.70	Ekaputri et al. (2019) [37]

Figure 2 illustrates the scanning electron microscopy (SEM) images of porcelain powder used as constituents of geopolymer concrete to improve durability and strength. A scanning electron microscopy (JSM-IT500HR model) was used to analyze the morphology of porcelain. A high magnification level was applied to the surfaces of porcelain powder and OPC. The microstructure of porcelain powder is characterized by irregular and angular particles. The observed uneven and flattened particles with shaped edges were porcelain. The average porcelain particle was larger than OPC. In addition, OPC manifested even round-shaped particles when compared with porcelain particles. Therefore, a superplasticizer was needed to reduce friction among mixed materials.

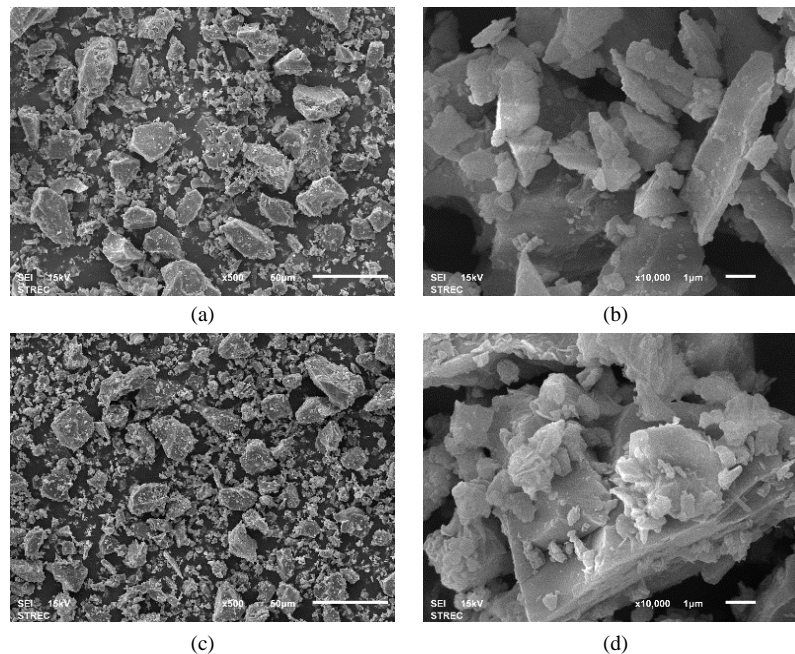


Figure 2. SEM particle images of (a) Porcelain at 500X (b) Porcelain at 10,000X (c) OPC at 500X (d) OPC at 10,000X

The laser particle size distribution analyzer (the Malvern Mastersizer 3000) was used to analyze the particle distribution of porcelain powder. Figure 3 presents the particle size distribution (PSD) of porcelain powder and OPC. The average particle size of porcelain (D_{50}) was 17 μm , while the OPC (D_{50}) was 12.4 μm . The particle size of porcelain was not significantly large when compared with OPC and low calcium fly ash, with a particle size distribution ranging from 0.3 to 100 μm with a major fraction in the range of 40–90 μm [38]. However, the variation in particle size of porcelain was larger than that of OPC. It should be noted that the fineness of particles has a great impact on the hardening process of geopolymer binders. As the size of the particle decreased, the initial setting for hardening significantly decreased [39, 40]. In addition, the particle size of the binder also affects the workability of the fresh geopolymer mix. The finer-grained binders had a larger surface area per unit mass compared to the coarser-grained binders. Therefore, the finer-grained binder reduced the fluidity of geopolymer mixes.

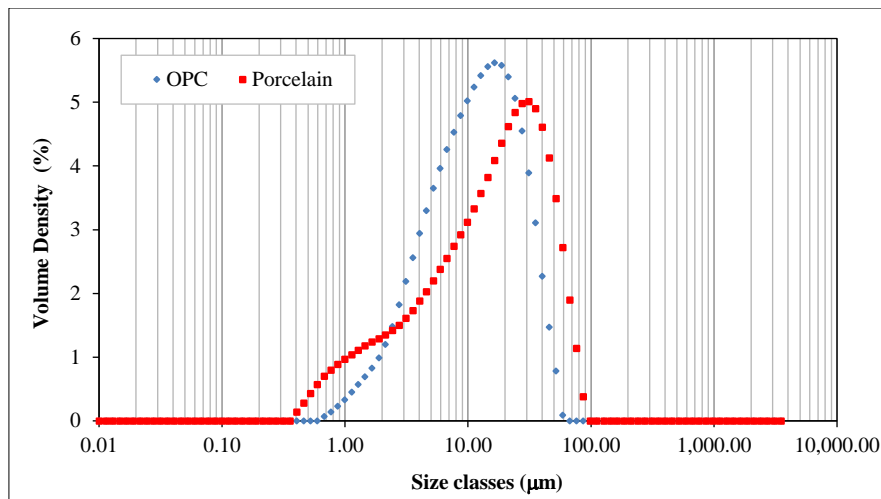


Figure 3. Particle size distribution of OPC and Porcelain

Figure 4 shows the result of the X-ray diffraction technique (XRD), which was implemented to provide the crystallographic structure and chemical composition. The mineral composition of porcelain was characterized by the Bruker D8 Discover model. The primary beam condition was Cu-K α radiation (1.54060 Å), with a voltage of 40 kV, current 40 mA, and a 2 θ range of 5-80°. The crystalline phases were identified by the inorganic crystal structure database (ICSD). It found that the main crystalline phases of porcelain were quartz (SiO₂) and mullite (Al₂SiO₅). Quartz and mullite were common phases of porcelain [41]. Mullite was formed at elevated temperatures in the sintering process of porcelain production as the final product of a series of reactions in clay minerals [42, 43]. The mineralogical composition of porcelain showed a potential for partial reaction as a secondary aluminosilicate source in alkali activation. Moreover, Table 1 exhibits the chemical composition of porcelain, which was measured by X-ray fluorescence (XRF). Porcelain contained 54.88% SiO₂ and 17.62% Al₂O₃. These two major oxides affected the strengths of the specimen [44, 45]. The higher the value of major oxides in the binder material used, the greater the compressive strength of the specimens.

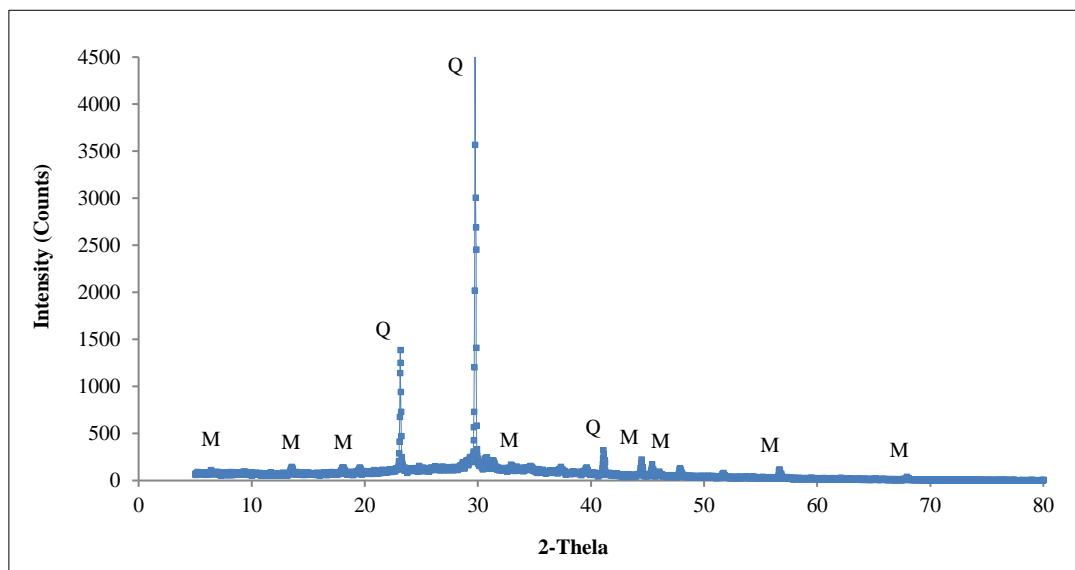


Figure 4. X-Ray diffraction analysis of porcelain

2.1.2. Activators

In this study, sodium hydroxide (NaOH) and sodium silicate (Na₂SiO₃) were used as activators. Sodium hydroxide was in the form of solid flakes. The purity was 99.9%. The concentration of sodium hydroxide was varied by 8M, 10M, 12M, and 14M. Sodium silicate (Na₂SiO₃) contained 11.67% of Na₂O, 28.66% of SiO₂, and 59.67% of H₂O. The mass ratio of sodium silicate to sodium hydroxide was fixed at 2.5.

2.1.3. Superplasticizer (SP)

Polycarboxylates are used in the mixture. It was used in the mixture to ensure the workability of fresh porcelain-based geopolymer. The dosage of SP was 1 by porcelain weight.

2.1.4. Aggregates

The specific gravity in SSD condition and water absorption of the coarse and fine aggregate were 2.69 and 0.99% and 2.6 and 0.25%, respectively. The coarse aggregate was crushed limestone. The fine aggregate was inland sand. Both coarse and fine aggregates were washed and oven-dried at 65°C for 24 hours. Aggregate was kept in the container after it was cooled down. The silt and impurity contents were removed in accordance with ASTM C117 [46]. Figure 5 presents the particle size-dependent cumulative passing percentage of coarse and fine aggregate.

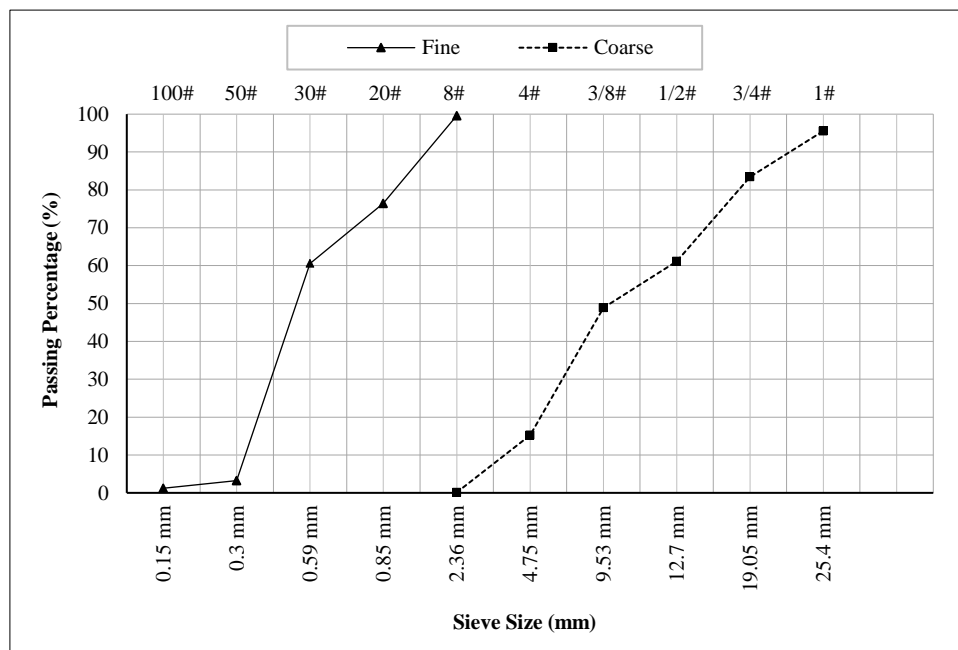


Figure 5. Sieving analysis of aggregate

2.1.1. Mix Design

There were two mixed designs: the first design mix for paste and the trial-and-error design mix for finding the normal consistency of porcelain-based geopolymer paste. Based on the normal consistency of the paste, 400g of dry porcelain powder mixed with different concentrations of alkali-activated solution (AAS) were examined. The trials were conducted with a 0.5% increment of AAS. The weight of the amount of AAS used to achieve the standard consistency was then recorded. The second is the mix design for concrete, which is shown in Table 2. Each binder varied depending on the alkali concentration. The studied porcelain-based geopolymer concrete was prepared by assembling porcelain powder, coarse aggregate (CA), and fine aggregate (FA) homogeneously in a concrete mixing pan for 3 minutes before the prepared alkali solution was added. The alkali solution used was prepared before 24 hours and left to cool before being added to the geopolymer mix, including binder, fine aggregate, and coarse aggregate, respectively. The mixing process was continued for another 3 minutes before homogenous geopolymer concrete was poured into molds.

Table 2. Specimens compositions

Code	NaOH (M)	Solid content (%)	AAS Ratio	Materials (kg/m ³)						Curing temperature (°C)
				NaOH	Na ₂ SiO ₃	Porcelain	Coarse aggregate	Fine aggregate	SP	
GPC8	8	40.5	2.5	110	275	550	962	384.78	5.5	60, 75, 90, 105
GPC10	10	44.5	2.5	110	275	550	962	384.78	5.5	60, 75, 90, 105
GPC12	12	48.5	2.5	110	275	550	962	384.78	5.5	60, 75, 90, 105
GPC14	14	52.5	2.5	110	275	550	962	384.78	5.5	60, 75, 90, 105

In this study, there were two types of molds that were used. The 50×50×50 mm cubic mold was used for the porosity test, and the 100×200 mm cylindrical mold was used for abrasive resistivity, the rapid chloride permeability test (RCPT), and the compressive strength test. All specimens were compacted by a vibration table for 25 seconds. After that, the placing process was completed. The specimens were wrapped in polyethylene film and kept at ambient temperature for 24 hours. The ambient temperature (32°C±2°C) and humidity condition (relatively 75%) were monitored and recorded. The effects of different molarity alkaline solutions (M) and curing temperatures on the properties of a total of four porcelain-based geopolymer concretes were determined. The achieved porcelain-based geopolymer concrete mixes were

initially cured at different temperatures of 60, 75, 90, and 105 °C. Before, it was subjected to air-cure for 1, 3, 7, 14, and 28 days. The result of the tests was compared to studying the effect of alkali concentration and curing temperatures on low-calcium material-based geopolymer concrete.

2.2. Experimental Methods

2.2.1. Fresh Paste and Concrete

Figure 6 shows the experimental process flow chart diagram. The experiment methods for studying the fresh properties of porcelain-based geopolymer specimens were divided into two parts. The first part was to study the normal consistency and setting time of porcelain powder-based geopolymer paste. Normal consistency of porcelain-based geopolymer paste was done by a 10 mm-diameter plunger [47]. Immediately after mixing the porcelain geopolymer paste, it was placed in a conical cone-shaped mold. Experimenting to identify the right amount of alkaline-activated solution used with the porcelain powder started. At every 10-minute interval, the plunger was repeatedly released. The paste was kept at an ambient temperature of $32.5^{\circ}\text{C} \pm 2^{\circ}\text{C}$ and 85% relative humidity. Trials to find the normal consistency of each alkaline-activated concentration paste ceased when the depth of the plunger was 33–35 mm from the surface. The standard consistency of each alkali-activated concentration paste was then recorded. A Vicat test apparatus was also conducted to investigate the effect of alkali concentration on setting time and initial curing temperature on early fresh paste. The testing was done on all four-alkali concentration geopolymer pastes (8M, 10M, 12M, and 14M). The initial curing temperature ranged from 60, 75, 90, and 105°C. The specimens were kept in a curing oven at all times during the process of the experiment. Specimens were only removed from the oven when they were tested. The initial setting time of the paste should not be less than 45 minutes. The final setting time happened when a 1 mm-diameter needle was not able to penetrate the paste specimen after three consecutive trials. The second part was to study the workability of fresh porcelain-based geopolymer concrete.

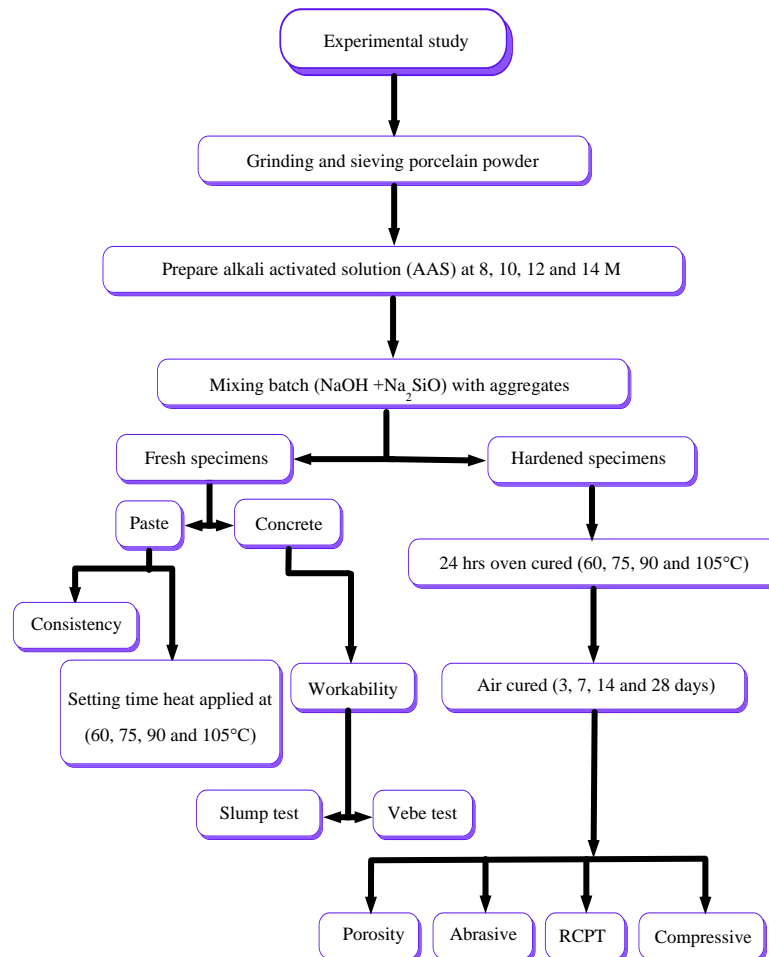


Figure 6. Schematic of process methodology

The slump test and the Vebe test were used to measure the viscosity of fresh specimens. The workability of fresh porcelain-based geopolymer concrete mixes was measured by the slump cone test as ASTM C143/C143M-12 [48] and the Vebe test as BS 1881: Part 104:1983 [49]. The tests were conducted on four alkali-activated concentration parameters. The dynamic viscosity of porcelain-based geopolymer paste was studied to measure the workability degradation affected by alkali concentration levels. The data from the tests is shown in Table 3.

2.2.2. Hardened Concrete

Hardened concrete specimens were subjected to porosity, abrasive resistance, rapid chloride permeability, and compressive strength tests. The hardened concrete specimens were subjected to various initial curing temperatures for 24 hours before being wrapped with polyethylene film and placed at ambient temperature for 3, 7, 14, and 28 days.

(1) Porosity test:

Three 5×5×5 cm. cube specimens were de-aired in a vacuum desiccator by a negative pressure decompressor for three hours before all specimens were fully submerged in ionized water. The decompression process was continued for three hours. The equation used for finding porosity is shown in Equation 1. This method provided an estimate of total porosity, which was ideally based on the absolute weight of the specimen. The pores of the specimen were filled with water and hence the total effective porosity can be calculated from the weight change:

$$\text{Porosity (\%)} = \left(\frac{m_{a(\text{sat})} - m_{a(\text{dry})}}{m_{a(\text{sat})} - m_{w(\text{sat})}} \right) \times 100 \quad (1)$$

where $m_{a(\text{sat})}$ is mass of saturated specimens in air (g), $m_{w(\text{sat})}$ is mass of saturated specimen in water (g), and $m_{a(\text{dry})}$ is Mass of oven-dried specimens in air (g).

(2) Abrasive resistance:

To determine the abrasion resistance of porcelain-based geopolymer concrete, 100×200 mm cylinder specimens were sliced into 100×50 mm cylinder thick. This method was specifically tested on the surface of the specimen by a rolling cutter [50]. The normal constant load of 98 ± 1 N was applied to the cutter through the spindle. The rate of rotation of the abrading cutter was 200 rev/min. The mass of the specimens was weighed before and after the test, which represented the amount of abrasion damage. The equation used to find the resistance ability of a surface specimen in percentage was shown in Equation 2.

$$\text{Mass Loss (\%)} = \left(\frac{m_o - m_a}{m_o} \right) \times 100 \quad (2)$$

where m_o is mass of test specimen before test (mg), and m_a is mass of test specimen after test (mg).

(3) Rapid chloride permeability:

In this study, specimens were also subjected to a chloride ion penetration test in accordance with ASTM C 1202-19 [51]. The setup of RCPT is shown in Figure 7. The specimens were in a water-saturated condition before they were subjected to testing. This was achieved by using the vacuum saturation apparatus. Specimens were also smeared with silicon sealant on a curved surface beneath a latex groove cut into a circumsphere shape. The specimens were then left air-dried for 20 min before being placed in two halves of the cell. To prevent leakage during the experiment, silicon sealant was applied around the specimen and the half cell. The two halves of the cell with the specimen in between were tightened by bolts, a washer, and wing nuts. Three 100 × 50 mm cylinder specimens were subjected to a 60 DC voltage for 6 hours using an apparatus. The test setup consisted of two reservoirs; one of the reservoirs contained a 3.0 NaCl solution, which was connected to the negative half. Another reservoir contained a 0.3M NaOH solution, which was connected to the positive half. The cells were then connected to the interface unit. The total charge passed through was governed at 6 hours. The passing charge rate through the specimen was according to the criteria given in ASTM C 1202. The chloride permeability charge passed (Coulombs) criteria was categorized into five levels. Negative (<100), very low (100–1,000), low (1,000–2,000), moderate (2,000–4,000), and high (>4,000).



Figure 7. Rapid chloride permeability test apparatus

(4) Compressive strength:

Cylindrical specimens were unwrapped from polyethylene film, which was left air-dried for two hours before specimen heads were capped (Figure 8). The sulfur capping method helped to ensure that test cylinder specimens have smooth, parallel, uniform bearing surfaces that are directly perpendicular to the applied axial load during compressive strength testing. Before capping, the specimens were air-dried for two hours. To ensure that the surface of the specimens to be capped was in dry condition. The thickness of the sulfur capping was less than 5 mm. The surface of the specimen was cleaned, and all loose particles were removed. A compressive testing machine (Technotest with a capacity of 3000 kN) was used to deliver the compressive strength results. Similar to the porosity test, all cylindrical specimens (8 M, 10M, 12M, and 14M) subjected to the compressive test were oven-dried for 24 hours and air-cured for 3, 7, 14, and 28 days. The curing temperatures were 60°C, 75°C, 90°C, and 105°C.

3. Results and Discussions

3.1. Chemical Analysis

3.1.1. X-Ray Fluorescence Spectroscopy

The chemical composition of porcelain-based geopolymer concrete was determined by using X-ray fluorescence analysis. To study the alteration of chemical composition under different levels of alkaline and initial curing temperature, 14M specimens of 28 days air-cured were chosen. Two initial curing temperatures were selected (60°C and 105°C). Table 3 shows the chemical composition analysis of porcelain-based geopolymer concrete. It found that the concentration of alkaline levels had a minor influence on the alteration of chemical compositions. It appeared that 14M specimens obtained a higher percentage of oxide content when compared with 8M specimens. However, the difference in oxide content between 8M and 14M was not significant. SiO₂ and Al₂O₃ were the main oxides detected. This was due to the high amount of sodium silicate in the alkaline solution, from which SiO₂ was formed. In addition, the use of a sodium hydroxide solution enhanced the dissolution rates of porcelain material. This allowed for better formation of polymerization products due to its exothermic characteristics. While it was found that an increment in curing temperature had an impact on altering the amount of oxide. The heat helped to enhance the geopolymerization process. The level of SiO₂ and Al₂O₃ content increased as the curing temperature increased. However, as expected, the mineralogical phases of all activated specimens were different from those in the porcelain powder after the geopolymerization process had been completed.

Table 3. Oxides content of porcelain based geopolymer concrete at various curing temperatures

Specimens	Oxides (%)								
	Curing temperature at 60 °C								
	SiO ₂	Al ₂ O ₃	Fe ₂ O ₃	Na ₂ O ₃	K ₂ O	MgO	CaO	TiO ₂	Others
8M	25.13	4.48	0.67	3.21	0.84	2.17	24.55	0.07	38.88
14M	25.30	5.12	0.73	3.57	1.01	2.38	25.23	0.09	36.56
	Curing temperature at 105 °C								
8M	34.11	6.95	0.84	5.97	1.01	1.89	18.70	0.10	30.43
14M	35.30	7.38	0.91	6.28	1.12	2.19	19.70	0.13	26.99

3.1.2. X-Ray Diffraction (XRD)

The XRD patterns for porcelain-based geopolymer concrete at various initial curing temperatures are shown in Figures 8 and 9, where a relative of the kaoline-based geopolymer concrete has fewer crystalline peaks when the curing temperature is low. The X-ray diffractometer pattern of geopolymer-based porcelain was carried out on the Bruker AXS D8 Discover model and recorded using Cu-K (1.5418Å) radiation in the 2-hour range of 5-80°. Several crystalline hydrated phases, including mullite amorphous phases and quartz alpha (Q), were mainly discovered. Figure 8 demonstrated the presence of the crystalline phase, which indicated sharp peaks of CaCO₃, SiO₂, mullite (alumina silicate), and quartz. However, it found that the influence of increasing the activated alkali solution on the crystalline phases of the specimen was minimal. Increasing the initial curing temperature from 60 °C to 105°C, a sodium aluminum silicon oxide hydrate (Na₂O-Al₂O₃-SiO₂-H₂O) was further found. This aluminum-silicon oxide hydrate was found in the range of 14–42°. The characteristic high-intensities at 2q values of 14M geopolymer-based porcelain with a curing temperature of 60°C were in the range of 26–27°, while the presence of high vitreous amorphous at 2q values of 14M geopolymer-based porcelain concrete with a curing temperature of 105°C showed two peaks. The first peak was in the range of 26–29°, and the second peak was in the range of 67–68°, respectively (Figure 9). Both two peaks were mainly composed of CaCO₃ and quartz. However, the intensity of porcelain decreased after calcination and geopolymerization. This might be due to the amorphous phase, which was the main component after geopolymerization [44, 45].

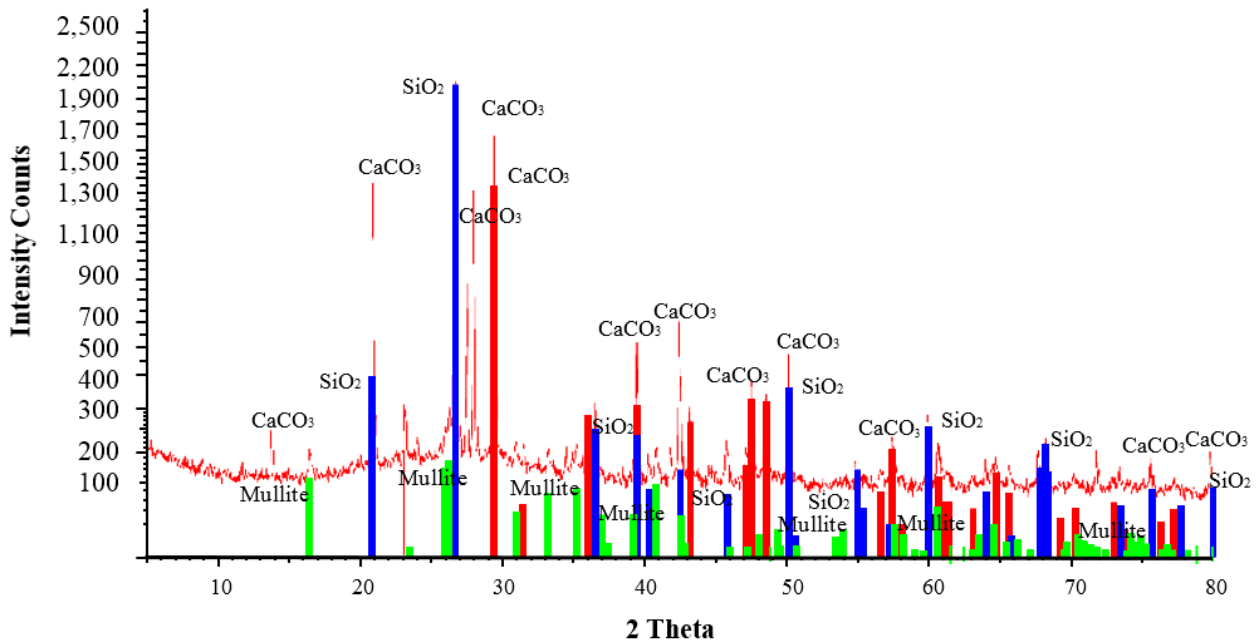


Figure 8. X-Ray diffraction analysis of 14M geopolymer based porcelain concrete heat at 60 °C

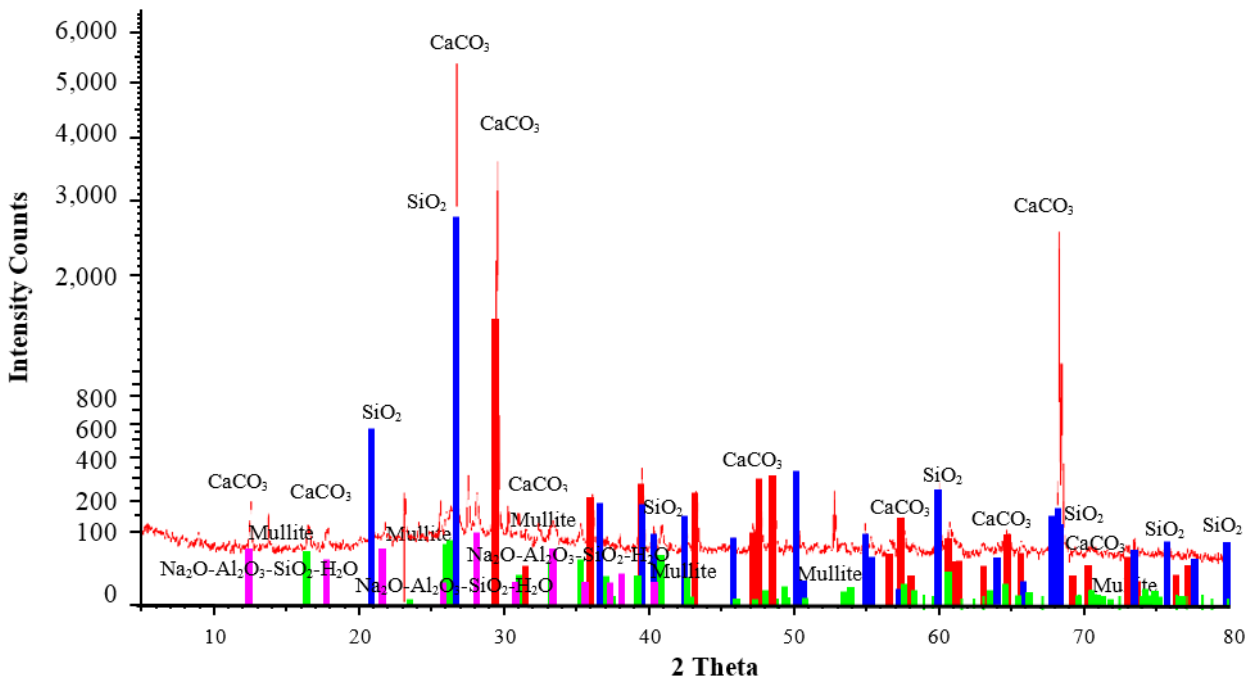


Figure 9. X-Ray diffraction analysis of 14M geopolymer based porcelain concrete heat at 105 °C

3.2. Normal Consistency and Setting Time

3.2.1. Normal Consistency and Workability

The consistency of the defective porcelain-based geopolymer paste was determined by the procedure followed as per ASTM C 187-16 [52]. The specimen was modified by replacing the cement paste with a porcelain-based geopolymer paste. Finding the standard consistency of each different alkaline concentration paste was done by increasing the amount of alkaline solution until the 10 mm plunger was at a depth of 10 ± 1 mm from the surface. The variation in the depth of penetration was presented in Table 4, as was the standard consistency of porcelain-based geopolymer pastes with different molar concentrations. The standard consistency of the porcelain-based geopolymer paste was obtained at 43%. The consistency of the paste increased as the alkali concentration increased. However, the consistency for 8, 10, and 12 M paste was obtained at 42%, 43%, and 43%, respectively. It was observed that the concentration level of the alkali-activated solution affected the consistency of the specimen paste. The fluidity of the alkali solution depended on the alkali concentration level. A highly viscous solution made the geopolymer paste more plastic, which caused the

penetration of the plunger to go deeper. Therefore, the consistency value increased. The fluidity of the NaOH solution depended on its concentration. However, a higher molar concentration required additional water to attain fluidity. This was due to the process of making porcelain powder, which was made by crushing and grinding. The characteristic of porcelain particle shape was angular with shape edges and high residue friction when compared with fly ash particles. This caused difficult movement of the Vicat plunger at a lower alkaline concentration level in the specimen. Similar results were found in fly ash [53] and fly ash slag [54]. The particle shape strongly influenced the paste consistency.

Table 4. Penetration depth and workability of porcelain based geopolimer concrete

Molar (M)	Paste						Concrete	
	Consistency (%)						Slump (mm)	Vebe (sec)
	38	39	40	41	42	43		
	Penetration depth (mm)							
8	4	5	6	7	10	11	27.2	1.85
10	3	5	6	7	9	10	27.0	2.13
12	3	4	5	7	9	10	26.3	2.34
14	2	3	4	6	9	10	25.7	2.81

Workability in terms of slump and Vebe test values could be affected by the moisture content of aggregates, degree of condensation reaction between porcelain and alkaline solution, ambient temperature, and duration of mixing. In addition, the handling time of mixing and placing materials also reduced workability. To maintain workability, the water content needed to increase when the alkali concentration level changed. Otherwise, a superplasticizer was needed to maintain the standard consistency of each molar concentration specimen. Using superplasticizer helped minimize the loss of moisture during testing. In this study, 0.5% of superplasticizer was added to all mixes. The average slump values of different alkali concentration mixes are shown in Table 3. The slump of porcelain-based geopolimer concrete decreased as alkali concentrations increased. Similar, Vebe result tests showed that an increasing molar concentration in specimens affected Vebe time. The Vebe time was in the range of 1.85-2.81 seconds when the alkali concentration of the specimens increased from 8 M to 14 M. The result of workability tests showed that an increment of water contributed to a lower viscosity of the paste, which led to the specimens having a less viscous consistency and contributed to the additional dissolution of the activator solution.

The workability of mixes did not significantly change when compared with other high-calcium-content materials such as red fireclay brick [55] and ground granulated blast furnace slag-recycled fireclay brick powder-fly ash (GGBS-RFBP-FA) ternary composite [56]. A high density of low calcium content material (porcelain) produced a low porosity of porcelain-based geopolimer concrete, which had less water absorption. Therefore, an improvement in the consistency of porcelain-based geopolimer paste with a small increment of alkali concentration (gram) could not be significantly noticed. In addition, porcelain had both a low calcium content and its water-binder ratio mix, which had less effect on the geopolimerization process and slump values [57]. Overall, the increment in alkali concentration level had an effect on the slump of porcelain-based geopolymers. However, maintaining porcelain-based geopolimer concrete with a slump value above 200 mm was advisable. The flow ability of the high viscosity of the alkali solution used in geopolimer concrete was required for casting cylindrical and beam formwork.

3.2.2. Setting Time

The variations in the initial and final setting times were presented in Figure 10. During testing, ambient temperature and relative humidity were $33^{\circ}\text{C}\pm 2$ and $74\% \pm 1$, respectively. The results showed that the initial setting time decreased as the molar concentration level increased. Similar results were also found in the final setting time. The rate of decrease in 1 mm needle depth was observed, and it was found that as curing temperature increased, the setting time of all specimens decreased. The rate of decrease in setting time rapidly occurred when a specimen was initially stipulated to heat (75°C). At the lower curing temperature (60°C), the level of alkali concentration had a lesser effect on the setting time of the specimen paste. The level of alkali concentration had a great effect on the setting time when porcelain-based geopolimer paste was heated to 75°C or above. However, the 8M specimens did not respond well to an increment in curing temperature (from 60°C to 75°C) when compared with the 10M, 12M, and 14M specimens. This was due to the low alkali concentration, which had a small amount of SiO_2 content, which could restrict the formation of gel in both C-S-H and C-A-S-H. This led to prolonging the setting time. This characteristic of elongation in setting time was diminished when the initial curing temperature increased. The effect of heat on setting time reduction was presented in Table 5.

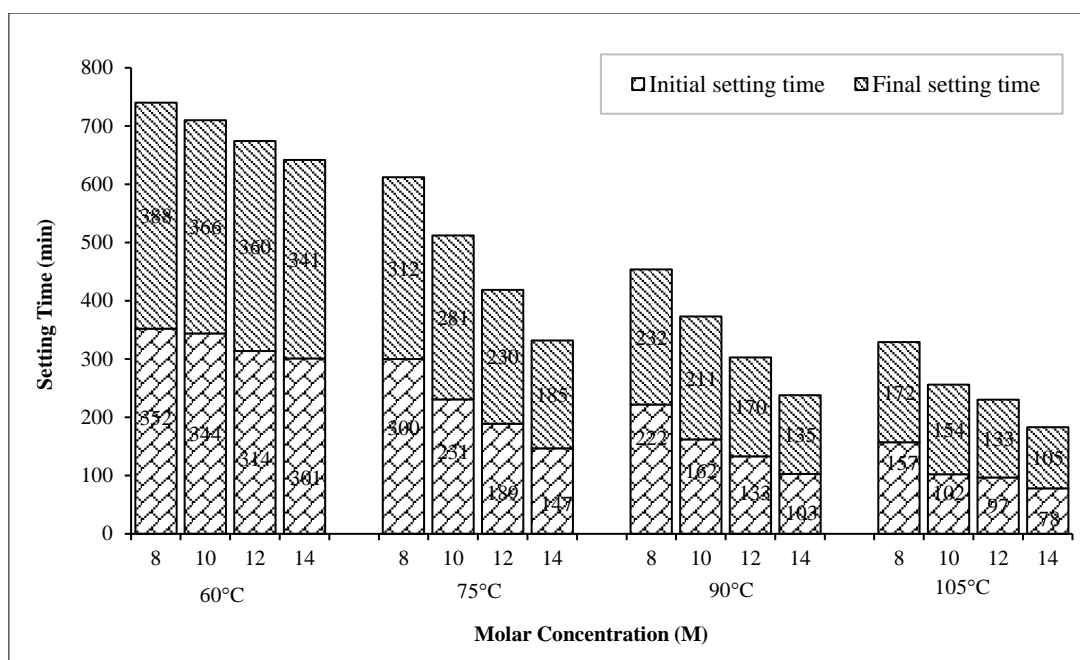


Figure 10. Correlation between molar concentration and setting time

Table 5. The effect of curing temperature in reduction in setting time

Molar concentration (M)	Reduction in setting time (min)					
	60°C ⇒ 75°C		75°C ⇒ 90°C		90°C ⇒ 105°C	
	Initial	Final	Initial	Final	Initial	Final
8	52	76	78	80	65	60
10	113	85	69	70	60	57
12	125	130	56	60	36	37
14	154	156	44	50	25	30

An increase in curing temperature from 75°C upward was found to be a great reduction in both initial and final setting times. The occurrence of a rapid rate in setting time was due to the characteristic dissolution of aluminosilicate precursors, which were sensitive to heat [58]. The effect of the molar concentration on the rate of setting time showed the influence of the alkaline chemical composition (sodium hydroxide and sodium silicate). The tendency for a reduction in setting time clearly indicated that porcelain slowly reacted with NaOH solution at ambient temperature. The release of Ca²⁺ ions occurred beside the release of Si⁴⁺ and Al³⁺ ions to form porcelain particles in an alkali solution of NaOH. The rate of geopolymerization was enhanced by the presence of soluble silica. The presence of an alkaline activator also improved the process of condensation of geopolymer precursors, which stipulated the polymerization process. The rate of decrease in setting time was exponentially with molar concentration and initial curing temperature. Similar results were also found in high-calcium fly ash [59] and blast furnace slag [60]. The reduction in setting time decreased as the alkaline concentration level increased. Therefore, the effect of stipulating with heat and the level of alkali concentration in the geopolymerization process could be noticed when low calcium material (porcelain) was used as binder material in geopolymer paste.

3.3. Porosity and Chloride Permeability

3.3.1. Porosity

Figure 11 displays the average porosity of hardened porcelain-based geopolymer concrete with different initial curing temperatures and air-dry ages. It was observed that there was a decrease in average porosity values toward the curing age. Similarly, the porosity values decreased as the alkaline concentration level increased. The rate of decrease in porosity values increased when specimens were initially heated at 75°C upward for 24 hours. At 7 days, the 8M specimens with a curing temperature of 60°C achieved about a 16.5% reduction in porosity, compared to the corresponding specimens that were initially cured at 105°C for 3 days. While, at 3-days, 14M NaOH specimens with a curing temperature of 105°C reduced porosity by about 10.3%. The decrease in porosity values was due to the geopolymerization process, in which pores were filled by gel products. In addition, heat also stipulated the physicochemical reaction of geopolymerization, in which specimens consisted of dissolving aluminosilicate particles (porcelain powder).

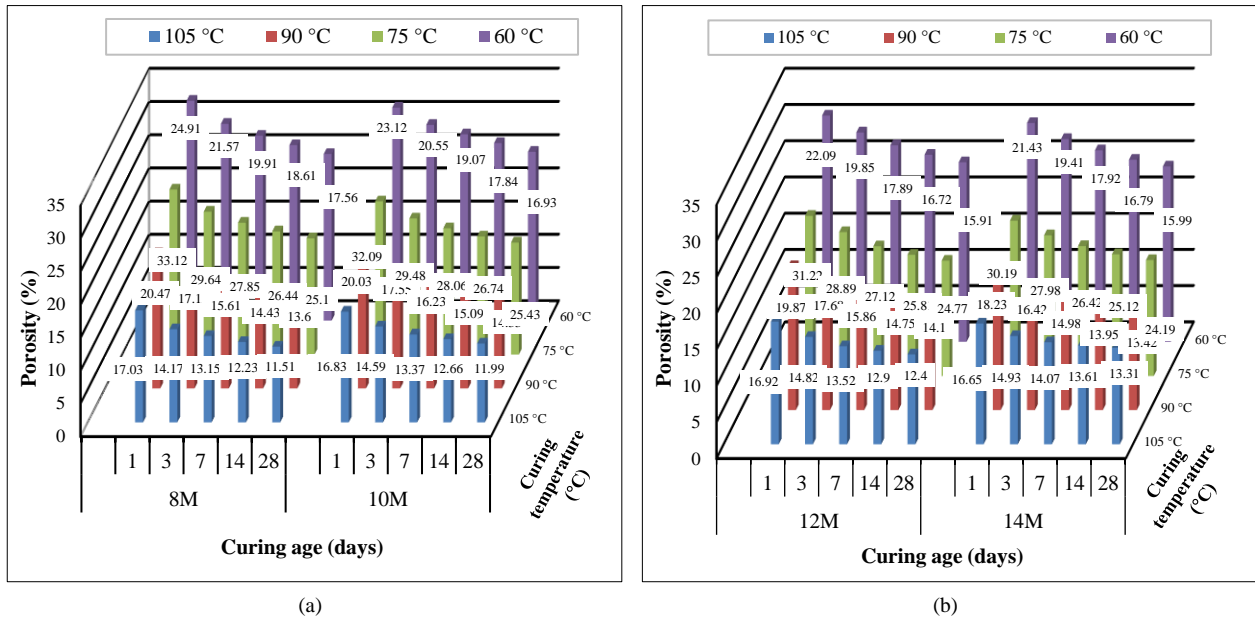


Figure 11. Porosity of specimens at various temperature (a) 8M and 10M (b) 10M and 12M

Moreover, the continued geopolymerization of porcelain-based geopolymers led to the formation of calcium silicate hydrate gel and a consequent reduction in the permeability of specimens over time. The variation in the rate of decreasing porosity values was noticed. This might be due to the particle size of aluminosilicate particles dissolving during mixing [61], the alkaline concentration level [62], and the initial heat applied [63]. In addition, the remaining undissolved porcelain particles gradually became gel, which filled the geopolymer pores. Therefore, the number of closed pores increased and the size of pores in specimens decreased. Therefore, the total porosity values decreased. The 12M NaOH specimens showed the lowest porosity values when compared with 8M, 10M, and 12M specimens at all curing ages and initial curing temperatures. The results showed that the 28-day air-cured with an initial curing temperature of 105 °C had the lowest porosity value (13.31%). While 8M NaOH specimens with a 1-day air-cured and initial curing temperature of 60 °C had the highest porosity value (33.12%).

Figure 12 presents the reduction in porosity values (%). It found that the reduction in porosity was high in the early age of the air-curing specimen. It was clearly observed that curing at high temperatures helped to reduce the porosity of early-age porcelain-based geopolymer specimens.

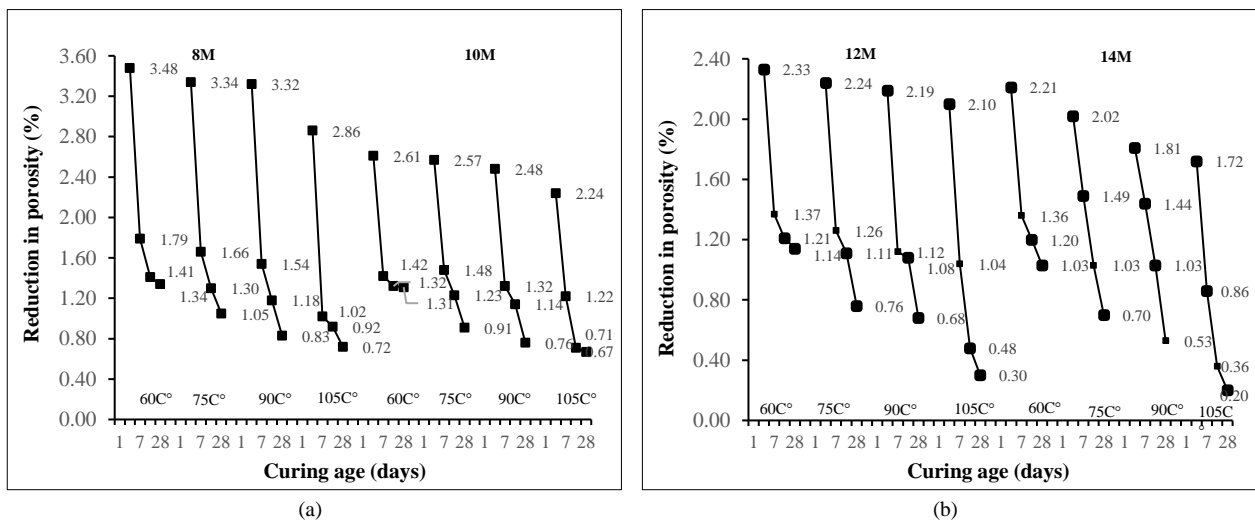


Figure 12. Reduction in porosity of specimens at various temperature (a) 8M and 10M (b) 10M and 12M

The effect of the initial curing temperature on the reduction in porosity was noticed. Significant in the development of decreasing porosity values up to 28 days after initial curing was applied. The rate of reduction in porosity decreased as the curing time of the specimens increased. Similar results were also found in setting time. An increase in the initial curing temperature improved the rate of reduction in porosity. In addition, alkali concentration level and curing period also influenced the rate of reduction in porosity. A high concentration of NaOH allowed further dissolution of Si and Al

from porcelain, enhanced polycondensation, and resulted in a decrease in geopolymer concrete porosity. At lower alkali concentrations, the presence of higher-soluble silicate was needed to decrease the pores. Soluble silica helped reduce interconnection between pores in the concrete matrix. However, porcelain powder was low in calcium, and the rate of decrease in porosity was slower than that of high-calcium materials, which required less to change from plastic to a static state [64]. The amount of geopolymeric gel produced depended on the amount of silica dissolution, the initial curing temperature, and the alkali concentration. In particular, a low curing temperature was applied to specimens [65, 66]. In contrast, with high calcium materials, the strength of the paste gained at an early age with a low curing temperature. Puertas et al. [9] used fly ash mixed with slag for binder material. The results showed that pastes gained early age strength by applying a temperature of 65°C.

3.3.2. Rapid Chloride Permeability (RCP)

This test relied on the relationship between the electrical conductance and the resistance to chloride ion penetration. The test measures the charge (Q) in the measurement result of the RCP test. Permeability performance was vital to the durability of specimens. Figure 13 shows the correlation between porosity and chloride ingress in porcelain-based geopolymer concrete. The porosity test measured permeability, while the RCP test measured the resistivity of concrete specimens. A high voltage applied to the specimen caused the internal temperature of the specimen to increase, which directly affected both the physical and chemical properties of the specimen. It was clear that as the alkali concentration of the specimen increased, the permeability of chloride ingress decreased. The 14M specimens showed better performance when compared with the 8M specimens. This was due to the fact that the 14M NaOH solution specimens required a lesser amount of water for dissolution particles. Therefore, the amount of water loss due to heat was low. Thus, there were fewer pores, which made the geopolymer concrete more impermeable against chloride ingress.

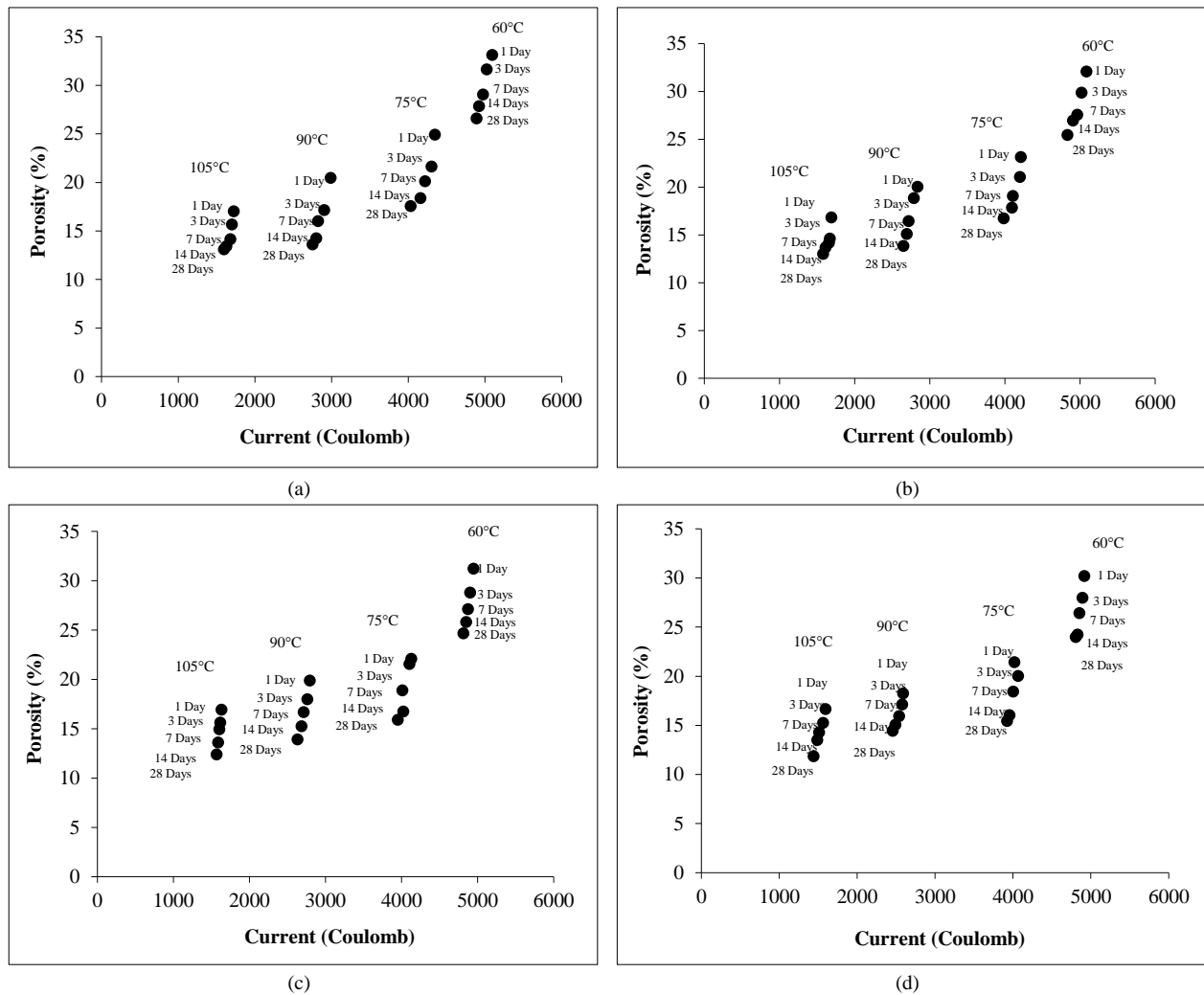


Figure 13. Correlation between porosity and rapid chloride permeability (a) 8M (b) 10M (c) 12M (d) 14M

In addition, the chloride ion penetration resistivity was potentially related to the pore distribution or concrete ingress. It was found that the amount of current passing through the specimen increased when the porosity of the specimen increased. The pore size of the specimen decreased. Selecting a high alkali concentration mix resulted in a smaller pore

volume in the microstructure of the specimen through the formation of calcium silicate hydrate and calcium aluminosilicate hydrate bonds. This increased the resistance of the specimen to chloride penetration. It was observed that specimens with a 14-day curing period or above increased the resistance to chloride ingress. The performance of the specimen in resisting chloride ingress was further enhanced when an initial curing temperature of 75°C or above was applied. Thus, applying 105°C for 24 hours helped specimens resist chloride ingress. While curing at temperatures of 90 °C, 75 °C, and 60 °C, the performance of resistance in chloride ingress was categorized as high, medium to high, and low, respectively. The results showed that the chloride migration rating was higher for low alkali concentrations than for higher alkali concentrations of the same age. These results indicated that the effect of the alkali concentration and initial curing temperatures affected chloride ion penetration in porcelain-based geopolymer concrete [67]. At an early age, specimens required a proper initial curing temperature.

Applying a high initial curing temperature was able to offset the effect of the low geopolymerization rate for low calcium binder materials, which caused high permeability. Thus, specimens could be more resistant to the penetration of chloride ions. In attained low current passing through the specimen, the porosity value of the specimen should be kept under 12%, where the specimen was categorized as low ion chloride permeability group. Table 6 shows the reduction in the percentage of current when the curing temperature was changed. It found that the reduction in current gained when the initial curing temperature increased. The reduction percentage current increased rapidly when specimens were heated with high curing temperatures. The lowest current detected was after a 28-day curing period with 14M and 105°C curing temperature specimens; the current detected was 1440.91 coulomb. While the highest current detected was 5093.38 coulomb, which was collected from 1-day curing period with 8M and 60°C curing temperature specimens. For chloride ingress, the performance of porcelain-based geopolymer concrete was more sensitive to initial curing temperature than alkali concentration level. To maximize the performance of resistivity in chloride ingress, both initial curing temperature and alkali concentration should be applied. Either initial curing temperature or alkali concentration, the resistibility of the specimen was not significantly improved.

Table 6. RCP test results

Age (days)	Current charged (coulomb)				Reduction in coulomb (%)		
	60 °C	75 °C	90 °C	105 °C	60°C⇒75°C	75°C⇒90°C	90°C⇒105°C
8M							
1	5093.58	4346.86	2987.13	1723.45	17.18	45.52	73.32
3	5023.46	4301.21	2903.27	1702.41	16.79	48.15	70.54
7	4975.18	4219.55	2824.04	1682.90	17.91	49.42	67.81
14	4923.62	4157.93	2798.69	1629.15	18.42	48.57	71.79
28	4892.37	4029.89	2753.24	1597.30	21.40	46.37	72.37
10M							
1	5086.89	4214.89	2837.1	1692.34	20.69	48.56	67.64
3	5019.56	4202.44	2790.32	1670.14	19.44	50.61	67.07
7	4963.14	4108.24	2721.09	1659.82	20.81	50.98	63.94
14	4907.46	4092.8	2695.68	1614.93	19.90	51.83	66.92
28	4832.67	3984.05	2648.37	1582.08	21.30	50.43	67.40
12M							
1	4946.16	4126.33	2792.06	1631.75	19.87	47.79	71.11
3	4902.46	4102.6	2760.04	1615.27	19.50	48.64	70.87
7	4872.83	4012.3	2713.6	1603.45	21.45	47.86	69.24
14	4851.39	4023.53	2684.07	1587.89	20.58	49.90	69.03
28	4811.75	3951.66	2633.52	1568.14	21.77	50.05	67.94
14M							
1	4915.3	4017.42	2591.34	1595.66	22.35	55.03	62.40
3	4893.25	4064.21	2576.48	1562.54	20.40	57.74	64.89
7	4851.74	4003.51	2538.26	1510.08	21.19	57.73	68.09
14	4829.01	3954.13	2491.17	1487.89	22.13	58.73	67.43
28	4805.49	3922.33	2457.52	1440.91	22.52	59.61	70.55

3.4. Development of Strength

3.4.1. Compressive Strength

Figure 14 shows the variation in compressive strength of 28 days of cured porcelain concrete specimens with the difference in NaOH solution. It was observed that the concentration of alkali solution affected the development of strength. With an increment of the concentration from 8M to 10M, the compressive strength significantly improved. The concentration of NaOH solution continued to play a key role in strength gain as the concentration of NaOH solution increased. The development of strength depended on the quantity of leaching aluminosilicates from porcelain material. The hydroxide ion (OH⁻) from the alkaline solution acted as a catalyst in the geopolymerization process and stipulated the dissolution of the Si⁴⁺ and Al³⁺ ions from the porcelain powder. In addition, the sodium cation helped to balance the charge deficit of the concrete matrix [68]. The release of chemical ions by leaching caused a reduction in the strength of geopolymer concrete. In the case of low alkali concentrations, the rate of leaching chemical ions released was low, resulting in a weak internal structure of the geopolymer matrix. While specimens were mixed with a high alkali concentration solution, the rate of leaching was high.

The loss of silica ions by leaching was high. It caused a delay in the geopolymerization process by congealing particle surfaces [69]. To maintain the strength development, the addition of Na⁺ ions was needed to form a solid geopolymeric matrix at a low alkali concentration (8M). Although an increment of sodium hydroxide ions enhanced the rate of dissolution, an excessive increment of alkali concentration also caused polycondensation process by precipitating aluminosilicate gel [70]. This caused both compressive strength and a decrease in the rate of development in strength. The rate of strength gained in 8M specimens was slower than in 10M, 12M, and 14M specimens. This was due to the slow leaching of porcelain specimens at a low initial curing temperature (60°C). Porcelain powder took a relative of time to promote its early strength. The compressive strength values increased with increasing curing temperature and time. A longer initial curing period allowed for a greater reaction product, which enhanced the compressive strength. Considering the initial curing temperatures, the 3-day compressive strength of the specimens increased more than 1.94 times when the initial curing temperature increased from 60 °C to 75 °C. While the 7-day compressive strength, the compressive value increased more than 1.93 times. The stipulation with heat to specimens at an early age increased ultimate strength and the rate of gaining in compressive strength. Samantasinghar & Singh [70] mentioned the importance of curing temperature for obtaining high strength for low-calcium fly ash-based geopolymer specimens. The curing temperature increase contributed to the development of both early and final compressive strength. The authors found that early development in the strength of porcelain-based geopolymer specimens was sensitized by the initial curing temperature. However, the final development in strength was less sensitive to the initial curing temperature. The 28-day compressive strength increased 1.89 times. The significance of the initial curing temperature stipulated that the rate of increase in strength decreased as the duration of curing increased (90°C to 105°C).

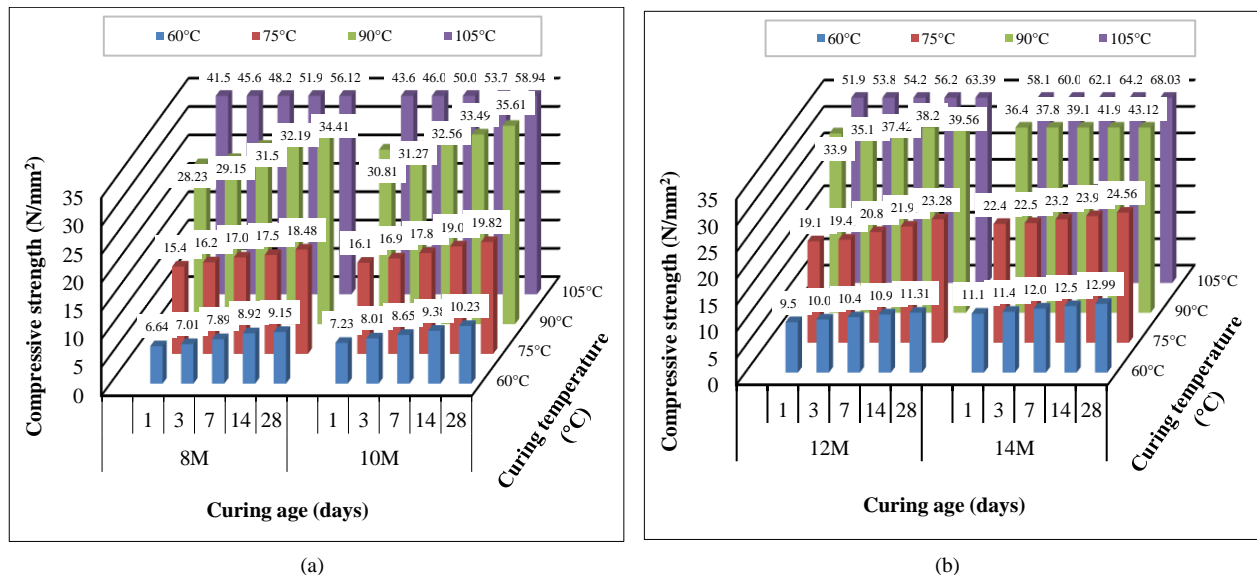


Figure 14. Compressive strength of specimens at various temperature (a) 8M and 10M (b) 10M and 12M

For the 24-hour oven-curing period, the rate of gaining strength was an exponential performance pattern. It was also found that the lowest compressive strength was 8M with a curing temperature of 60°C. The rate of gaining in strength was slow at the initial curing temperature of 60°C when compared with the rate of gaining in strength at the initial curing temperatures of 75°C, 90°C, and 105°C, respectively. However, the highest increase in strength occurred when the curing temperature increased from 90°C to 105°C. The porcelain binder material lost sensitivity to the initial curing

temperature earlier than fly ash (type F) when the rate of gaining in strength was concerned. Table 7 shows the compressive strength values of low calcium material binders. Hardjito et al. [71] found that as the water-geopolymer solids ratio increased, the value of compressive strength also increased. Fernandez-Jimenez et al. [72] produced low-calcium fly ash-based geopolymer concrete with a liquid-to-solid ratio of 0.55. The compressive strength was 45 N/mm² and it was cured at 85°C for 20 hours. Yilmza et al. [38] found that 28-day compressive strength was at 43.4 N/mm² and 54.5 N/mm² for specimens cured at 80°C for 24 hours and 72 hours, respectively. They stated that long-term curing at high temperatures had a positive impact on the freeze-thaw resistance of low-calcium fly ash specimens. Wongpattanawut & Ayudhya [12] mentioned in their study that increasing the initial curing temperature of porcelain-based geopolymer mortar specimens also had a positive impact on compressive strength. Ramos et al. [31] experimented with porcelain mixed with metakaolin geopolymer paste and found that replacing 15% metakaolin with porcelain increased the compressive strength of the geopolymer from 62 to 66 N/mm² at 7 days, while the strengths at 28 days were in the range of 71–72 N/mm². For the effect of duration in oven heating on the compressive strength of porcelain-based geopolymer concrete, in this study, a 24-hour period of initial oven curing was studied. At 60°C and 90°C, the rate of gaining strength rapidly increased. However, above 90°C, the rate of strength gain started to decline for all curing temperatures.

Table 7. The typical compressive strength of low calcium binder concrete mixes

	Binders	Curing temperature and duration	Molar concentration	Composites	Compressive (N/mm ²)
Hardjito et al. (2004) [71]	Fly ash (type F)	60-80°C for 24 hr.	10-16	Concrete	30-80
Fernandez-Jimenez (2006) et al. [72]	Fly ash (type F)	85°C for 20 hr.	8,12	Concrete	29-43.5
Yilmaz et al. (2023) [38]	Fly ash (type F)	40-80°C for 24, 48, 72 hours	12	Mortar	54.5
Wongpattanawut & Ayudhya [12]	Porcelain	60, 75, 90, 105°C for 24 hours	8,10,12,14	Mortar	64.45
Ramos et al. [36]	Porcelain, metakaolin	7-28 days at 23°C	9.2-10.8	Paste, Mortar	66-72

As far as the effect of the air curing period was concerned, the compressive strength of porcelain activated with an 8M NaOH solution for different curing periods was studied. At a curing temperature of 105 °C, it was observed that the porcelain-based geopolymer concrete specimens attained 81.37% and 85.90% of their 28-day strength at curing periods of 3 and 7 days, respectively. While at a curing temperature of 60°C, specimens achieved 76.61% and 86.22% of 28-day strength. The rate of strength gain started to increase rapidly after 7 days of air curing. For the 28-day compressive strength of porcelain geopolymer concrete made with 14M concentration specimens, specimens with a curing temperature of 105°C yielded greater compressive strength than specimens with a curing temperature of 60°C. A similar result was found by Hamidi et al. [73]. According to their study, the optimum concentration for compressive strength was 14M NaOH. This was due to the balanced charges of aluminosilicates at the time of gel formation. In addition, voids in the specimen matrix were filled with fine, unreacted porcelain powder. Once porcelain powder was activated by an alkali solution at a high curing temperature, the leaching of alumino-silicates was released, and the process of polycondensation began. The reaction products then filled voids. There were several voids in the specimen matrix that were filled with unreacted particles that would bind with polycondensation products, and thus a dense structure was formed. Bonding between aggregates in the matrix and reaction products also enhanced the compressive strength.

A visual examination technique was used for studying cracks and spalling on specimens subjected to compressive test. Figure 15-a shows the physical visualization of 14M geopolymer specimens at different elevated temperatures. It found that the formation of cracks on four different initial curing temperature specimens was much damage to the surfaces in touch with the upper and lower areas of the specimens. However, deep crack lines were obviously noticed when specimens were oven-cured at 90°C upward. The cracks were distributed in the quasi-brittle pattern of the failure. In specimens with an initial curing temperature of 60°C, the crack lines were mainly in a zigzag pattern, which represented a non-explosive failure type. The crack lines did not travel through the longitudinal axis, whereas porcelain specimens with high curing temperatures displayed cleavage cracking with a semi-explosive failure pattern. The propagation of the cracks was randomly separated in different directions, with deeper cracks in the middle of the specimen along the longitudinal axis. The patterns of specimen failure were according to BS EN 12390-3:2009.

Figure 15-b exhibits the visual appearance of specimens subjected to 105°C with various alkaline concentration levels. It found that there were visible crack lines and spalling on the surface of the porcelain-based geopolymer specimens subjected to a compressive test. A smaller number of crack lines, a wider spalling width, and discoloration were discovered on the surface of geopolymer specimens with a higher alkaline concentration level. The depth of crack lines increased; spalling depth enlarged when the level of alkaline concentration increased. With high alkaline concentrations, the specimens retain their original shape. Large longitudinal cracks caused spalling of the specimen surface. Specimens underloading failed by compression cracking, followed by peeling off of the specimen surface layer. Cracks were widely distributed along the specimen length with significant compressible performance. For specimens with lower alkaline concentrations, the failure occurred by compression under crushing. The average first crack load of

specimens was considerably reduced when the average peak load value was also reduced. However, the failure patterns of the geopolymer for different NaOH concentrations were not different. The obvious fracture patterns were diagonal fractures for all the molar concentrations. For the lower molar concentrations, the main patterns occurred in the direction perpendicular to the diagonal fractures, starting from the center of the plates and propagating into the middle of the geopolymer specimen. Small aggregates were extruded from the edge of the geopolymer and along the diagonal cracks. A similar result was found by Zhang et al. (2023) [74]. The change in volume of specimens might have occurred during heating at high temperatures, which caused shrinkage and micro cracks. The colors of the specimen surface were also observed. It was noticed that specimens with a curing temperature of 60°C had a dark gray color with the presence of moisture when compared with other curing temperatures. The colors of the specimen went from dark to pale gray as the curing temperature increased. It appeared that a curing temperature of 60°C for 24 hours was not long enough to fully dry out the specimen, which might affect compressive strength. Above 75°C curing temperature, specimens were dry. The specimens were sufficient enough to deliver compressive strength. However, consideration of reducing the alkali concentration in the specimen was recommended if a low curing temperature was implemented. However, applying a curing temperature above 120°C for 24 hours might cause damage to the specimen [75].

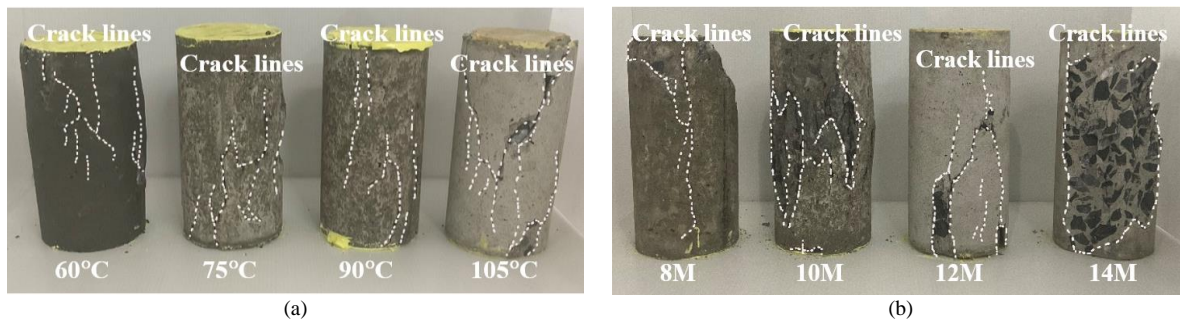


Figure 15. Formation of cracks for 28 days curing age specimens under compressive strength test (a) 14M concentration (b) Curing temperature at 105°C with various alkaline concentration

3.4.2. Abrasion Resistance

The influence of alkali concentration on the abrasion resistance of specimens is shown in Figure 16. The abrasion resistance of porcelain-based geopolymer concrete was determined at ages 1, 3, 7, 14, and 28 days. It was observed that weight loss decreased when alkali concentration and duration of air curing increased. This was due to the transition zone of the porcelain-based geopolymer, which was very strong. The interface between aggregate and reaction products was adhesive and dense, with great rigidity.

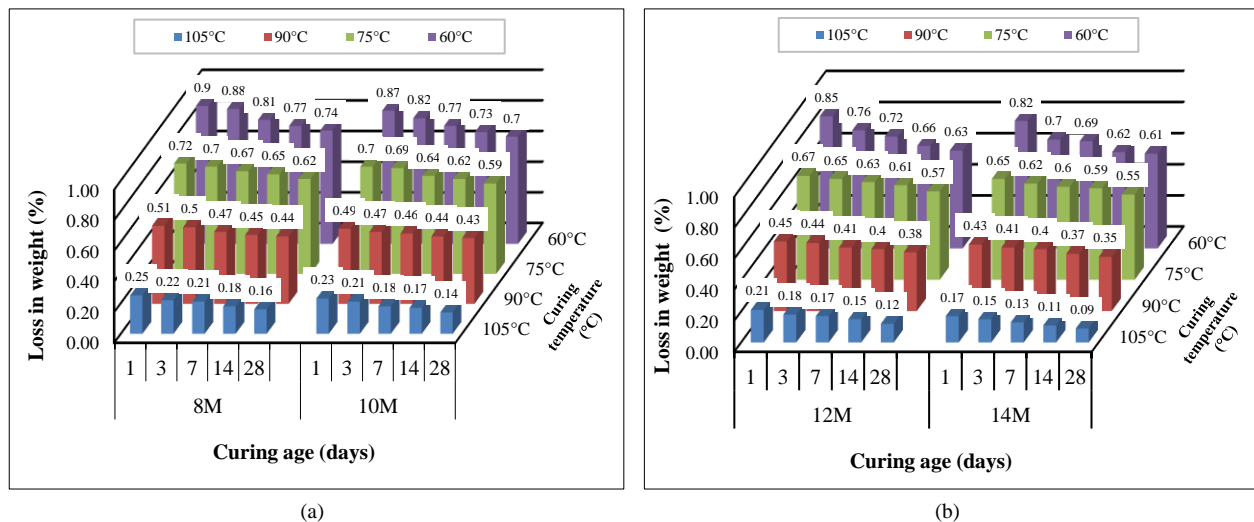


Figure 16. Abrasive resistance of specimens at various temperature (a) 8M and 10M (b) 10M and 12M

In addition, voids on the surface of the aggregate were filled with unreacted porcelain powder, which created further bonding strength between matrix surfaces. It found that the specimens with a curing temperature of 105°C had a lesser loss in weight wear than specimens with a curing temperature of 60°C. The 28-days curing specimens with an initial curing temperature of 60°C had the highest mass loss (0.9%). This was due to a lower degree of reaction in porcelain. The polymerization of geopolymers was not fully complete. Possibly due to impurities present in the porcelain powder. While the specimens with an initial curing temperature of 105°C had the lowest mass loss (0.09%). The ability to resist abrasion was further enhanced when the level of alkali concentration increased. The results indicated that the possibility

of introducing a low initial curing temperature to porcelain-based geopolymer concrete was not applicable. A similar outcome was also shown in the results of compressive strength. It appeared that the curing age enhanced the binding interface between the geopolymer matrix. Thus, the mass loss of specimens decreased as the curing age increased. In addition, increment of curing temperature also showed that the abrasive resistance of specimens significantly improved when curing temperature attained above 75°C for 24 hours period. It showed that the appropriate initial curing temperature and duration of the curing period helped densification of the geopolymer matrix. The amount of silica in porcelain powder enhanced the densification of the specimen, which affected the performance of abrasive resistance. The 28-day curing age of 14M geopolymer specimens had greater surface resistance when compared with 8M, 10M, and 12M specimens. This was due to the concentration of the activator, which controlled the formation of gel and microstructure development [76]. The hydroxide (OH⁻) ion of sodium hydroxide acted as the catalyst for the polymerization reaction in which silicate and aluminate monomers were formed [77]. Thus, specimens mixed with a 14M alkali concentration produced more formation of silicate and aluminate monomers than specimens mixed with a lower alkali concentration. The ability of abrasion resistance of specimens was similar to the relation in compressive strengths. This was due to the fact that abrasion resistance was determined by the density of the structure.

Figure 17 shows the correlation between compressive and abrasive resistance of specimens. It was found that compressive strength increased as the weight loss of the specimen decreased. This was attributed to the bonding strength between the interface of reaction product gels and the matrix of geopolymer developed. The compressive strength and abrasive resistance of porcelain-based geopolymer concrete rapidly increased when specimens were subjected to higher initial curing temperatures. The trend line between weight loss and compressive strength was observed and compared. Comparisons of durability results will help ensure an acceptable goodness-of-fit between compressive and abrasive resistance of porcelain-based geopolymer concrete specimens. This approach will provide effective alternatives and predictions to assess loss in weight under abrasive motion. The gradient of the curve declined as the alkali concentration level increased. Further observations were made in Figures 17-a to 17-d. Based on curing temperature, the resistance against abrasive motion of the specimens could be categorized into three main groups: low, middle, and high. At low curing temperatures, an increment of 15°C from 60°C to 75°C showed that an increase in initial curing temperature did not significantly affect the performance of the specimen, even when the alkali concentration level increased. The weight loss ranged from 0.5% to 0.9%. At the middle curing temperature (90°C), the performance of the specimens against abrasion and compression was observed. The weight loss from abrasive motion ranged between 0.3% and 0.4%. An increment of 15°C from 90°C to 105°C showed that applying a higher initial curing temperature had a greater effect on the durability and resistibility of the specimens. At high curing temperatures (105°C), the weight loss from abrasive motion was in the range of 0.5% to 0.1%. The results further indicated that the performance of porcelain-based geopolymer concrete was affected by the initial curing temperature. At low alkali concentrations, the performance of 8M with 60°C curing temperature specimens decreased sharply as compressive strength increased. The weight reduction decreased with curing time. However, it appeared that an increment of curing period had a lesser influence on stipulating the performance of specimens than increasing alkali concentration. A great loss in weight occurred when specimens were at an early age of air curing, ranging from 0.6% to 0.9%. This trend line gradually decreased as the initial curing temperature increased. However, the rate of response to curing temperature varied. Additionally, the rate of increase in strength with curing temperature was found to be higher than the rate of gain in abrasive resistance. The rate of resistibility to the abrasive motion was clearly on a steady incline with curing temperature.

Table 8 presents the development rate of compressive strength and abrasive resistance. At an early age (3 days curing period), the rate of increase in compressive strength for 8M, 10M, 12M, and 14M at 60°C curing temperature was 0.12, 0.26, 0.17, and 0.12 N/mm² per day respectively. Meanwhile, the rate of development in abrasive resistance was 0.9, 0.87, 0.85, and 0.82% per day respectively. Changing the curing temperature from 60 to 105°C, the rate of development in compressive strength rapidly increased by 651.49%, 574.65%, 537.02%, and 523.43% respectively. In abrasive resistance, the rate of abrasive resistance improvement was 400.00%, 390.47%, 422.22%, and 466.67% respectively. At 28-days curing period for low curing temperature (60°C), the overall rate of increase in compressive strength for 8M, 10M, 12M, and 14M specimens was 0.09 N/mm² per day, 0.11 N/mm² per day, 0.06 N/mm² per day, and 0.07 N/mm² per day respectively. Whereas, the development rate of abrasive resistance for 8M, 10M, 12M, and 14M specimens increased by 5.71×10^{-3} % per day, 6.03×10^{-3} % per day, 7.85×10^{-3} % per day, and 7.5×10^{-3} % per day respectively. The rate of increase in compressive strength declined with time. This was due to the reaction product gel generated from existing porcelain powder used in the geopolymerization process. The increment in compressive strength rate also increased with alkali concentration level. Similar results were found in abrasive resistance, where the weight loss of the specimens at an early age was high when subjected to a low initial curing temperature. The rate of increase in abrasive resistance also increased with increasing alkali concentration. At low curing temperatures (<90°C), the main reaction product was aluminosilicate amorphous-semi-crystalline gel. The gel composition depended on curing condition, type and concentration of activator, and binder material, which affected the bonding strength of the gel [78]. When specimens were exposed to higher temperatures, well-crystalline structure products were formed. The temperature of crystallization of the aluminosilicate depended on the initial composition of porcelain and alkali content. Thus, the performance of specimens in compressive strength and abrasive resistance was affected by the chemical composition of porcelain, alkali concentration, alkali content, and curing condition.

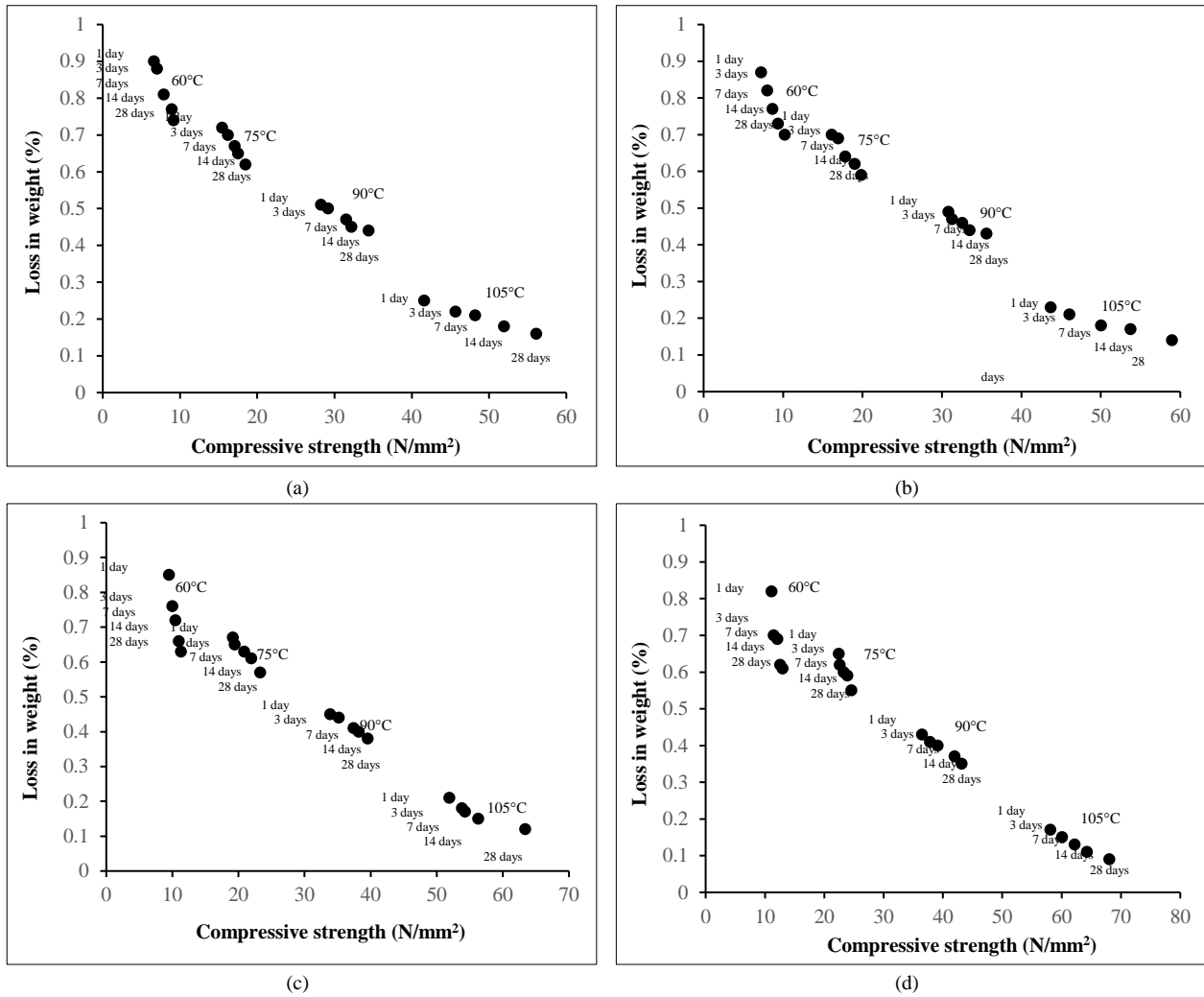


Figure 17. Correlation between compressive and abrasive resistance (a) 8M (b) 10M (c) 12M (d) 14M

Table 8. Development rate of compressive strength and abrasive resistance

Curing temperature (°C)	Alkali concentration (M)	Rate of increasing in compressive strength (N/mm ² per day)				Rate of weight lost (% per day)			
		1⇒3 days	3⇒7 days	7⇒14 days	14⇒28 days	1⇒3 days	3⇒7 days	7⇒14 days	14⇒28 days
60	8	0.12	0.22	1.24	0.02	0.007	0.018	0.006	0.002
	10	0.26	0.16	1.32	0.06	0.017	0.013	0.006	0.002
	12	0.17	0.11	0.08	0.02	0.030	0.010	0.009	0.002
	14	0.12	0.15	0.07	0.03	0.040	0.003	0.010	0.001
75	8	0.25	0.22	2.47	0.07	0.007	0.008	0.003	0.002
	10	0.26	0.23	2.69	0.06	0.003	0.013	0.003	0.002
	12	0.10	0.36	0.15	0.10	0.007	0.005	0.003	0.003
	14	0.05	0.18	0.09	0.05	0.010	0.005	0.001	0.003
90	8	0.31	0.59	4.51	0.16	0.003	0.008	0.003	0.001
	10	0.15	0.32	4.74	0.15	0.007	0.003	0.003	0.001
	12	0.43	0.56	0.11	0.10	0.003	0.008	0.001	0.001
	14	0.44	0.32	0.41	0.08	0.007	0.003	0.004	0.001
105	8	1.36	0.64	7.33	0.30	0.010	0.003	0.004	0.001
	10	0.79	1.00	7.54	0.37	0.007	0.008	0.001	0.002
	12	0.63	0.11	0.29	0.51	0.010	0.003	0.003	0.002
	14	0.66	0.52	0.30	0.27	0.007	0.005	0.003	0.001

4. Conclusion

In this study, it was observed that increasing the molarity of calcium hydroxide led to a decrease in both consistency and setting times. Moreover, increasing the concentration of sodium hydroxide resulted in faster hardening of porcelain-based geopolymer concrete. For all mixes, an increase in the initial curing temperature affected the final setting time more than the initial setting time. The workability of fresh specimens decreased as the alkali concentration level increased. Additionally, the fluidity of geopolymer specimen paste decreased with an increase in the initial curing temperature and time. The results also indicated that porcelain-based geopolymer concrete with a higher alkali concentration mix exhibited lower porosity values for all the specimens. At the 28-day curing period, the lowest porosity value was observed in the 14M mix heated at an initial curing temperature of 105°C (13.31%), while the highest porosity value was found in the 8M mix heated at an initial curing temperature of 60°C (25.1%).

The results of the Rapid Chloride Penetration (RCP) test showed a significant decline in the amount of current (coulombs) passed through specimens as the alkali concentration and initial curing temperature increased. The performance of porcelain-based geopolymer specimens was found to be more sensitive to the initial curing temperature than the alkali concentration level. In the abrasive test, specimens exhibited an average weight loss between 0.1% and 0.5% when cured at 105°C. Compared to specimens cured at 75°C, the weight loss against abrasive motion was in the range of 0.5% to 0.9%. Additionally, an increase in alkali concentration levels led to a lower rate of weight loss. Similar to compressive strength, the improvement in compressive strength was directly influenced by the initial curing temperature and the level of alkali concentration. The ultimate compressive strength was 68.03 N/mm². Specimens mixed with 8M and heated at 60°C curing temperature showed neither a significant reduction in porosity nor chloride ingress. Similar results were found in compressive and abrasion resistance.

5. Declarations

5.1. Author Contributions

Conceptualization, B.I.N.A. and W.W.; methodology, B.I.N.A.; validation, B.I.N.A.; formal analysis, B.I.N.A.; investigation, W.W.; resources, B.I.N.A.; data curation, B.I.N.A.; writing—original draft preparation, B.I.N.A.; writing—review and editing, B.I.N.A. and W.W.; visualization, B.I.N.A.; supervision, B.I.N.A.; project administration, B.I.N.A.; funding acquisition, B.I.N.A. All authors have read and agreed to the published version of the manuscript.

5.2. Data Availability Statement

The data presented in this study are available on request from the corresponding author.

5.3. Funding

Rajamangala University of Technology Thanyaburi (FRB67E0728), Grant Recipient: Borvorn Israngkura Na Ayudhya.

5.4. Acknowledgements

This work was supported by the research fund of the Rajamangala University of Technology Thanyaburi, authors would like to express our sincere gratitude to the scientific research fund for financial support to the project (Project number: FRB67E0728).

5.5. Conflicts of Interest

The authors declare no conflict of interest.

6. References

- [1] The World Bank. (2022). Industry (including construction), value added (% of GDP). The World Bank, Washington, United States. Available online: <https://data.worldbank.org/indicator/NV.IND.TOTL.ZS> (accessed on March 2024).
- [2] Sanjuán, M. Á., Andrade, C., Mora, P., & Zaragoza, A. (2020). Carbon dioxide uptake by cement-based materials: A Spanish case study. *Applied Sciences (Switzerland)*, 10(1), 339. doi:10.3390/app10010339.
- [3] Nisbet, M., Van Geem, M. G., Gajda, J., & Marceau, M. L. (1997). Environmental life cycle inventory of Portland cement and concrete. *World Cement*, 28(4), 3.
- [4] Singh, N. B., & Middendorf, B. (2020). Geopolymers as an alternative to Portland cement: An overview. *Construction and Building Materials*, 237, 117455. doi:10.1016/j.conbuildmat.2019.117455.
- [5] Łach, M., Korniejenko, K., & Mikuła, J. (2016). Thermal Insulation and Thermally Resistant Materials Made of Geopolymer Foams. *Procedia Engineering*, 151, 410–416. doi:10.1016/j.proeng.2016.07.350.

- [6] Duan, P., Yan, C., Zhou, W., & Luo, W. (2015). Thermal Behavior of Portland Cement and Fly Ash–Metakaolin-Based Geopolymer Cement Pastes. *Arabian Journal for Science and Engineering*, 40(8), 2261–2269. doi:10.1007/s13369-015-1748-0.
- [7] Davidovits, J. (1994). Properties of geopolymer cements. First international conference on alkaline cements and concretes, 11-14 October, 1994, Kiev, Ukraine.
- [8] Saillio, M., Baroghel-Bouny, V., Pradelle, S., Bertin, M., Vincent, J., & d'Espinose de Lacaillerie, J. B. (2021). Effect of supplementary cementitious materials on carbonation of cement pastes. *Cement and Concrete Research*, 142, 106358–106375. doi:10.1016/j.cemconres.2021.106358.
- [9] Puertas, F., Martínez-Ramírez, S., Alonso, S., & Vázquez, T. (2000). Alkali-activated fly ash/slag cements. Strength behaviour and hydration products. *Cement and Concrete Research*, 30(10), 1625–1632. doi:10.1016/S0008-8846(00)00298-2.
- [10] Pradhan, P., Dwibedy, S., Pradhan, M., Panda, S., & Panigrahi, S. K. (2022). Durability characteristics of geopolymer concrete - Progress and perspectives. *Journal of Building Engineering*, 59, 105100. doi:10.1016/j.jobbe.2022.105100.
- [11] Ke, S., Wang, Y., Pan, Z., Ning, C., & Zheng, S. (2016). Recycling of polished tile waste as a main raw material in porcelain tiles. *Journal of Cleaner Production*, 115, 238–244. doi:10.1016/j.jclepro.2015.12.064.
- [12] Wongpattanawut, W., & Ayudhya, B. I. N. (2023). Effect of Curing Temperature on Mechanical Properties of Sanitary Ware Porcelain based Geopolymer Mortar. *Civil Engineering Journal*, 9(8), 1808–1827. doi:10.28991/cej-2023-09-08-01.
- [13] Kubba, Z., Fahim Huseien, G., Sam, A. R. M., Shah, K. W., Asaad, M. A., Ismail, M., Tahir, M. M., & Mirza, J. (2018). Impact of curing temperatures and alkaline activators on compressive strength and porosity of ternary blended geopolymer mortars. *Case Studies in Construction Materials*, 9, 205. doi:10.1016/j.cscm.2018.e00205.
- [14] Mangat, P., & Lambert, P. (2016). Sustainability of alkali-activated cementitious materials and geopolymers. *Sustainability of Construction Materials*, 459–476. doi:10.1016/b978-0-08-100370-1.00018-4.
- [15] Matakah, F., Xu, L., Wu, W., & Soroushian, P. (2017). Mechanochemical synthesis of one-part alkali aluminosilicate hydraulic cement. *Materials and Structures/Materiaux et Constructions*, 50(1), 1-12. doi:10.1617/s11527-016-0968-4.
- [16] Ekaputri, J. J., Lie, H. A., Fujiyama, C., Shovitri, M., Alami, N. H., & Setiamarga, D. H. E. (2019). The effect of alkali concentration on chloride penetration in geopolymer concrete. *IOP Conference Series: Materials Science and Engineering*, 615(1), 012114. doi:10.1088/1757-899x/615/1/012114.
- [17] Nodehi, M., & Taghvaei, V. M. (2022). Alkali-Activated Materials and Geopolymer: a Review of Common Precursors and Activators Addressing Circular Economy. *Circular Economy and Sustainability*, 2(1), 165–196. doi:10.1007/s43615-021-00029-w.
- [18] Palomo, A., Fernández-Jiménez, A., Kovalchuk, G., Ordoñez, L. M., & Naranjo, M. C. (2007). Opc-fly ash cementitious systems: Study of gel binders produced during alkaline hydration. *Journal of Materials Science*, 42(9), 2958–2966. doi:10.1007/s10853-006-0585-7.
- [19] Fernandez-Jimenez, A., García-Lodeiro, I., & Palomo, A. (2007). Durability of alkali-activated fly ash cementitious materials. *Journal of Materials Science*, 42(9), 3055–3065. doi:10.1007/s10853-006-0584-8.
- [20] Aydin, S., & Baradan, B. (2012). Mechanical and microstructural properties of heat cured alkali-activated slag mortars. *Materials and Design*, 35, 374–383. doi:10.1016/j.matdes.2011.10.005.
- [21] Provis, J. L., & Van Deventer, J. S. J. (2009). *Geopolymers: Structures, processing, properties and industrial applications*. Woodhead Publishing, Sawston, United Kingdom. doi:10.1533/9781845696382.
- [22] Aydin, S., & Baradan, B. (2014). Effect of activator type and content on properties of alkali-activated slag mortars. *Composites Part B: Engineering*, 57, 166–172. doi:10.1016/j.compositesb.2013.10.001.
- [23] Amaludin, A. E., Asrah, H., Mohamad, H. M., bin Amaludin, H. Z., & bin Amaludin, N. A. (2023). Physicochemical and microstructural characterization of Klias Peat, Lumadan POFA, and GGBFS for geopolymer based soil stabilization. *HighTech and Innovation Journal*, 4(2), 327-348. doi:10.28991/HIJ-2023-04-02-07.
- [24] Mohd Mortar, N. A., Abdullah, M. M. A. B., Abdul Razak, R., Abd Rahim, S. Z., Aziz, I. H., Nabilek, M., Jaya, R. P., Semenescu, A., Mohamed, R., & Ghazali, M. F. (2022). Geopolymer Ceramic Application: A Review on Mix Design, Properties and Reinforcement Enhancement. *Materials*, 15(21), 7567. doi:10.3390/ma15217567.
- [25] Meena, R. V., Jain, J. K., Chouhan, H. S., & Beniwal, A. S. (2022). Use of waste ceramics to produce sustainable concrete: A review. *Cleaner Materials*, 4, 100085. doi:10.1016/j.clema.2022.100085.
- [26] Menger, M. H., Ruviano, A. S., Silvestro, L., Corrêa, T. G., de Matos, P. R., & Pelisser, F. (2023). Utilizing porcelain tile polishing residue in eco-efficient high-strength geopolymers with steel microfibers. *Structures*, 58, 105630. doi:10.1016/j.istruc.2023.105630.
- [27] Yanti, E. D., Mubarak, L., Subari, Erlangga, B. D., Widyaningsih, E., Jakah, Pratiwi, I., Rinovian, A., Nugroho, T., & Herbudiman, B. (2024). Utilization of various ceramic waste as fine aggregate replacement into fly ash-based geopolymer. *Materials Letters*, 357, 135651. doi:10.1016/j.matlet.2023.135651.

- [28] Ricciotti, L., Occhicone, A., Ferone, C., Cioffi, R., & Roviello, G. (2024). Eco-design of geopolymer-based materials recycling porcelain stoneware wastes: a life cycle assessment study. *Environment, Development and Sustainability*, 26(2), 4055–4074. doi:10.1007/s10668-022-02870-x.
- [29] Pitarch, A. M., Reig, L., Tomás, A. E., Forcada, G., Soriano, L., Borrachero, M. V., ... & Monzó, J. M. (2021). Pozzolanic activity of tiles, bricks and ceramic sanitary-ware in eco-friendly Portland blended cements. *Journal of Cleaner Production*, 279, 123713. doi:10.1016/j.jclepro.2020.123713.
- [30] Fortuna, A., Fortuna, D. M., & Martini, E. (2017). An industrial approach to ceramics: sanitaryware. *Plinius*, 43, 138-145.
- [31] Tahwia, A. M., Ellatief, M. A., Bassioni, G., Heniegal, A. M., & Elrahman, M. A. (2023). Influence of high temperature exposure on compressive strength and microstructure of ultra-high performance geopolymer concrete with waste glass and ceramic. *Journal of Materials Research and Technology*, 23, 5681–5697. doi:10.1016/j.jmrt.2023.02.177.
- [32] AL-Oqla, F. M., Faris, H., Habib, M., & Castillo, P. A. (2023). Evolving Genetic Programming Tree Models for Predicting the Mechanical Properties of Green Fibers. *Emerging Science Journal*, 7(6), 1863-1874. doi:10.28991/ESJ-2023-07-06-02.
- [33] Mantovani, V. A., Franco, C. S., Mancini, S. D., Hasegawa, H. L., Gianelli, B. F., Batista, V. X., & Rodrigues, L. L. (2013). Comparison of polymers and ceramics in new and discarded electrical insulators: Reuse and recycling possibilities. *Revista Materia*, 18(4), 1549–1562. doi:10.1590/S1517-70762013000400015.
- [34] Geraldo, R. H., Fernandes, L. F. R., & Camarini, G. (2021). Mechanical properties of porcelain waste alkali-activated mortar. *Open Ceramics*, 8. doi:10.1016/j.oceram.2021.100184.
- [35] Zuda, L., Bayer, P., Rovnaník, P., & Černý, R. (2008). Mechanical and hydric properties of alkali-activated aluminosilicate composite with electrical porcelain aggregates. *Cement and Concrete Composites*, 30(4), 266–273. doi:10.1016/j.cemconcomp.2007.11.003.
- [36] Ramos, G. A., de Matos, P. R., Pelisser, F., & Gleize, P. J. P. (2020). Effect of porcelain tile polishing residue on eco-efficient geopolymer: Rheological performance of pastes and mortars. *Journal of Building Engineering*, 32, 101699. doi:10.1016/j.jobe.2020.101699.
- [37] Chindaprasirt, P., & Chalee, W. (2014). Effect of sodium hydroxide concentration on chloride penetration and steel corrosion of fly ash-based geopolymer concrete under marine site. *Construction and building materials*, 63, 303-310. doi:10.1016/j.conbuildmat.2014.04.010.
- [38] Yılmaz, A., Degirmenci, F. N., & Aygörmec, Y. (2023). Effect of initial curing conditions on the durability performance of low-calcium fly ash-based geopolymer mortars. *Boletín de La Sociedad Española de Cerámica y Vidrio*, 398. doi:10.1016/j.bsecv.2023.10.006.
- [39] Amigó, J. M., Serrano, F. J., Kojdecki, M. A., Bastida, J., Esteve, V., Reventós, M. M., & Martí, F. (2005). X-ray diffraction microstructure analysis of mullite, quartz and corundum in porcelain insulators. *Journal of the European Ceramic Society*, 25(9), 1479–1486. doi:10.1016/j.jeurceramsoc.2004.05.019.
- [40] Kohout, J., Koutník, P., Hájková, P., Kohoutová, E., Soukup, A., & Vakili, M. (2023). Effect of Aluminosilicates' Particle Size Distribution on the Microstructural and Mechanical Properties of Metakaolinite-Based Geopolymers. *Materials*, 16(14), 5008. doi:10.3390/ma16145008.
- [41] Kohout, J., Koutník, P., Bezucha, P., & Kwoczyński, Z. (2019). Leachability of the metakaolinite-rich materials in different alkaline solutions. *Materials Today Communications*, 21, 100669. doi:10.1016/j.mtcomm.2019.100669.
- [42] Kovářík, T., Rieger, D., Kadlec, J., Křenek, T., Kullová, L., Pola, M., Bělský, P., Franče, P., & Říha, J. (2017). Thermomechanical properties of particle-reinforced geopolymer composite with various aggregate gradation of fine ceramic filler. *Construction and Building Materials*, 143, 599–606. doi:10.1016/j.conbuildmat.2017.03.134.
- [43] Davis, R. F. (1991). Mullite. *Concise Encyclopedia of Advanced Ceramic Materials*, 315–317, Pergamon, Oxford, United Kingdom. doi:10.1016/b978-0-08-034720-2.50087-3.
- [44] Xu, N., Li, S., Li, Y., Xue, Z., Yuan, L., Zhang, J., & Wang, L. (2015). Preparation and properties of porous ceramic aggregates using electrical insulators waste. *Ceramics International*, 41(4), 5807–5811. doi:10.1016/j.ceramint.2015.01.009.
- [45] Rahman, M. M., Law, D. W., & Patnaikuni, I. (2017). Effect of curing temperature on the properties of 100% clay-based geopolymer concrete. *Proceedings of International Structural Engineering and Construction*, 4(1), 1–11. doi:10.14455/ISEC.res.2017.98.
- [46] STM C117-17. (2023). Standard test method for materials finer than 75 µm (No. 200) Sieve in Mineral Aggregates by Washing. ASTM International, Pennsylvania, United States. doi:10.1520/C0117-17.
- [47] ASTM C191-21. (2021). Standard Test Method for Time of Setting of Hydraulic Cement by Vicat Needle. ASTM International, Pennsylvania, United States. doi:10.1520/C0191-21.

- [48] ASTM C143/C143M-12. (2015). Standard Test Method for Slump of Hydraulic-Cement Concrete. ASTM International, Pennsylvania, United States. doi:10.1520/C0143_C0143M-12.
- [49] BS 1881: part 104: 1983. (1983). Testing concrete Part 104. Method for determination of Vebe time. British Standard, London, United Kingdom.
- [50] ASTM C944M. (2017). Standard Test Method for Abrasion Resistance of Concrete or Mortar Surfaces by the Rotating-Cutter Method. ASTM International, Pennsylvania, United States. doi:10.1520/C0944-99.
- [51] ASTM C1202-19. (2022). Standard Test Method for Electrical Indication of Concrete's Ability to Resist Chloride Ion Penetration. ASTM International, Pennsylvania, United States. doi:10.1520/C1202-19.
- [52] ASTM C187-16. (2023). Standard Test Method for Amount of Water Required for Normal Consistency of Hydraulic Cement Paste. ASTM International, Pennsylvania, United States. doi:10.1520/C187-16.
- [53] Sun, Q., Tian, S., Sun, Q., Li, B., Cai, C., Xia, Y., ... & Mu, Q. (2019). Preparation and microstructure of fly ash geopolymers paste backfill material. *Journal of Cleaner Production*, 225, 376-390. doi:10.1016/j.jclepro.2019.03.310.
- [54] Dineshkumar, M., & Umarani, C. (2020). Effect of Alkali Activator on the Standard Consistency and Setting Times of Fly Ash and GGBS-Based Sustainable Geopolymer Pastes. *Advances in Civil Engineering*, 2020, 10. doi:10.1155/2020/2593207.
- [55] Li, Y., Huang, L., Gao, C., Mao, Z., & Qin, M. (2023). Workability and mechanical properties of GGBS-RFBP-FA ternary composite geopolymer concrete with recycled aggregates containing recycled fireclay brick aggregates. *Construction and Building Materials*, 392, 131450. doi:10.1016/j.conbuildmat.2023.131450.
- [56] Rafeet, A., Vinai, R., Soutsos, M., & Sha, W. (2017). Guidelines for mix proportioning of fly ash/GGBS based alkali activated concretes. *Construction and Building Materials*, 147, 130–142. doi:10.1016/j.conbuildmat.2017.04.036.
- [57] Nath, P., & Sarker, P. K. (2014). Effect of GGBFS on setting, workability and early strength properties of fly ash geopolymer concrete cured in ambient condition. *Construction and Building Materials*, 66, 163–171. doi:10.1016/j.conbuildmat.2014.05.080.
- [58] Ranjbar, N., Kashefi, A., & Maheri, M. R. (2018). Hot-pressed geopolymer: Dual effects of heat and curing time. *Cement and Concrete Composites*, 86, 1–8. doi:10.1016/j.cemconcomp.2017.11.004.
- [59] Criado, M., Fernández-Jiménez, A., & Palomo, A. (2007). Alkali activation of fly ash: Effect of the SiO₂/Na₂O ratio. Part I: FTIR study. *Microporous and Mesoporous Materials*, 106(1–3), 180–191. doi:10.1016/j.micromeso.2007.02.055.
- [60] Ukritnukun, S., Koshy, P., Rawal, A., Castel, A., & Sorrell, C. C. (2020). Predictive model of setting times and compressive strengths for low-alkali, ambient-cured, fly ash/slag-based geopolymers. *Minerals*, 10(10), 920. doi:10.3390/min10100920.
- [61] Kohout, J., Koutník, P., Bezucha, P., & Kwoczyński, Z. (2019). Leachability of the metakaolinite-rich materials in different alkaline solutions. *Materials Today Communications*, 21. doi:10.1016/j.mtcomm.2019.100669.
- [62] Ramli, M. I. I., Salleh, M. A. A. M., Abdullah, M. M. A. B., Aziz, I. H., Ying, T. C., Shahedan, N. F., Kockelmann, W., Fedrigo, A., Sandu, A. V., Vizureanu, P., Chaiprapa, J., & Nergis, D. D. B. (2022). The Influence of Sintering Temperature on the Pore Structure of an Alkali-Activated Kaolin-Based Geopolymer Ceramic. *Materials*, 15(7), 2667. doi:10.3390/ma15072667.
- [63] Rovnaník, P. (2010). Effect of curing temperature on the development of hard structure of metakaolin-based geopolymer. *Construction and Building Materials*, 24(7), 1176–1183. doi:10.1016/j.conbuildmat.2009.12.023.
- [64] El-Hassan, H., & Elkholy, S. (2021). Enhancing the performance of Alkali-Activated Slag-Fly ash blended concrete through hybrid steel fiber reinforcement. *Construction and Building Materials*, 311, 125313. doi:10.1016/j.conbuildmat.2021.125313
- [65] Nath, S. K., Maitra, S., Mukherjee, S., & Kumar, S. (2016). Microstructural and morphological evolution of fly ash based geopolymers. *Construction and Building Materials*, 111, 758–765. doi:10.1016/j.conbuildmat.2016.02.106.
- [66] Zhao, F. Q., Ni, W., Wang, H. J., & Liu, H. J. (2007). Activated fly ash/slag blended cement. *Resources, Conservation and Recycling*, 52(2), 303-313. doi:10.1016/j.resconrec.2007.04.002.
- [67] Kewalramani, M., & Khartabil, A. (2021). Porosity evaluation of concrete containing supplementary cementitious materials for durability assessment through volume of permeable voids and water immersion conditions. *Buildings*, 11(9), 378. doi:10.3390/buildings11090378.
- [68] Marjanović, N., Komljenović, M., Baščarević, Z., Nikolić, V., & Petrović, R. (2015). Physical-mechanical and microstructural properties of alkali-activated fly ash-blast furnace slag blends. *Ceramics International*, 41(1), 1421–1435. doi:10.1016/j.ceramint.2014.09.075.
- [69] Kotwal, A. R., Kim, Y. J., Hu, J., & Sriraman, V. (2015). Characterization and Early Age Physical Properties of Ambient Cured Geopolymer Mortar Based on Class C Fly Ash. *International Journal of Concrete Structures and Materials*, 9(1), 35–43. doi:10.1007/s40069-014-0085-0.
- [70] Samantasinghar, S., & Singh, S. P. (2019). Fresh and Hardened Properties of Fly Ash–Slag Blended Geopolymer Paste and Mortar. *International Journal of Concrete Structures and Materials*, 13(1), 1–12. doi:10.1186/s40069-019-0360-1.

- [71] Hardjito, D., Wallah, S. E., Sumajouw, D. M. J., & Rangan, B. V. (2004). On the development of fly ash-based geopolymer concrete. *ACI Materials Journal*, 101(6), 467–472. doi:10.14359/13485.
- [72] Fernández-Jiménez, A. M., Palomo, A., & López-Hombrados, C. (2006). Engineering properties of alkali-activated fly ash concrete. *ACI Materials Journal*, 103(2), 106–112. doi:10.14359/15261.
- [73] Hamidi, R. M., Man, Z., & Azizli, K. A. (2016). Concentration of NaOH and the Effect on the Properties of Fly Ash Based Geopolymer. *Procedia Engineering*, 148, 189–193. doi:10.1016/j.proeng.2016.06.568.
- [74] Zhang, N., Hedayat, A., Figueroa, L., Steirer, K. X., Li, L., & Bolaños Sosa, H. G. (2023). Physical, mechanical, cracking, and damage properties of mine tailings-based geopolymer: Experimental and numerical investigations. *Journal of Building Engineering*, 75, 107075. doi:10.1016/j.job.2023.107075.
- [75] Rattanasak, U., & Chindapasirt, P. (2009). Influence of NaOH solution on the synthesis of fly ash geopolymer. *Minerals Engineering*, 22(12), 1073–1078. doi:10.1016/j.mineng.2009.03.022.
- [76] Singh, B., Rahman, M. R., Paswan, R., & Bhattacharyya, S. K. (2016). Effect of activator concentration on the strength, ITZ and drying shrinkage of fly ash/slag geopolymer concrete. *Construction and Building Materials*, 118, 171–179. doi:10.1016/j.conbuildmat.2016.05.008.
- [77] Duxson, P., Fernández-Jiménez, A., Provis, J. L., Lukey, G. C., Palomo, A., & Van Deventer, J. S. J. (2007). Geopolymer technology: The current state of the art. *Journal of Materials Science*, 42(9), 2917–2933. doi:10.1007/s10853-006-0637-z.
- [78] Krivenko, P. V., & Kovalchuk, G. Y. (2007). Directed synthesis of alkaline aluminosilicate minerals in a geocement matrix. *Journal of Materials Science*, 42(9), 2944–2952. doi:10.1007/s10853-006-0528-3.



Innovative Method for Reinforcing Beams with Different Types of Concrete Using Cross-Rod Steel Bracing Under Pure Torsion

Adnan I. Abdullah ^{1*}, Assim M. Lateef ¹

¹ Department of Civil Engineering, College of Engineering, Tikrit University, Tikrit, Iraq.

Received 24 November 2023; Revised 07 March 2024; Accepted 12 March 2024; Published 01 April 2024

Abstract

This study aimed to investigate the effectiveness of an innovative way to reinforce the concrete beams using cross-rod steel bracing under pure torsion. The experimental program consists of casting and testing eighteen concrete beams made of three types of concrete in the form of three groups, with the same dimensions for all beams (200×200×2000) mm. The parameters of the study included concrete types (normal strength, high strength, and steel fiber), as well as the number of internally cross rods (4, 8, 12, 16, 20). The experimental results showed that the number of internally cross-rod reinforcements and concrete type had an effect on ultimate torque, crack width, toughness, and stiffness. The torsional capacity of all concrete beams increased with the increase in internally cross-rod reinforcement. The ultimate torque of normal-strength concrete beams, high-strength concrete beams, and steel fiber concrete beams reinforced with twenty internally cross rods increased (88.34%, 53.20%, and 40.60%), respectively, compared to beams without cross rods in each type of concrete beam. Increasing the internally cross rod in all concrete beams effectively inhibited the development of crack width and improved torsional stiffness, especially in fibrous concrete beams that contained steel fiber. The torsional toughness of all concrete beams increased with the increase of internally cross-rod reinforcement, and it was higher in steel fiber concrete beams. The steel fiber concrete beams reinforced with internally cross-rod steel bracing have better torsional properties compared to ordinary concrete beams and high-strength concrete beams.

Keywords: Cross-Rod Steel Reinforcement; Normal Strength Concrete Beams; High Strength Concrete Beams; Steel Fiber Concrete Beams; Ultimate Torsional Capacity; Torsional Stiffness; Torsional Toughness.

1. Introduction

In recent years, there has been a notable increase in the complexity and irregularity of building and bridge structures. This is particularly evident in the presence of beams that are exposed to significant torque, particularly canopies, frontier beams, and curvature structures. Under these particular scenarios, it is imperative for the beams to possess a significant level of torsional capacity and ductility, particularly in regions that are susceptible to typhoons or earthquakes. This circumstance adds new complexities to the torsional behavior of the beam [1–3]. Numerous researchers and specialists in the field have conducted extensive studies on the flexural and shear behavior of concrete members [4–7]. However, comparatively less emphasis has been placed on investigating the torsional performance of such members. Historically, the augmentation of stirrups and the longitudinal reinforcement ratio have served to counteract the torsional forces exerted on structural elements. The building components are currently undergoing advancements in terms of their properties, specifically in the areas of weight reduction, enhanced strength, and ease of assembly, due to the progress and utilization of novel materials. The architectural design of buildings has evolved to incorporate increased height, complexity, and flexibility. The issue of torsion in the components must not be disregarded.

* Corresponding author: adnan.i.abdullah43807@st.tu.edu.iq

 <http://dx.doi.org/10.28991/CEJ-2024-010-04-06>



© 2024 by the authors. Licensee C.E.J, Tehran, Iran. This article is an open access article distributed under the terms and conditions of the Creative Commons Attribution (CC-BY) license (<http://creativecommons.org/licenses/by/4.0/>).

For torsion in concrete beams, Rahal et al. [8] presented a straightforward model to determine the torque capacity of concrete elements subjected to torsion. This model incorporates the effects of longitudinal reinforcement, stirrups, concrete compressive strength, and cross-sectional area. Nevertheless, the limited tensile strength and brittleness of conventional concrete and high-strength concrete impose restrictions on their use in torsion members. The incorporation of steel fibers into concrete results in the formation of fiber concrete, which effectively enhances the strength of the tensile force and reduces the fragility of the material. Rao et al. [9] observed that the incorporation of fibers made of steel led to enhancements in both torsional strength and ductility. This conclusion was drawn based on the results obtained from conducting torsional tests on concrete beams. Okay et al. [10] conducted an analysis on the impact of longitudinal reinforcement content, fiber length and width ratio, and steel fiber under torsion behavior for concrete members. A study finding indicates that the presence of steel fiber has a notable impact on the energy absorption capacity. The inclusion of steel fiber in concrete induces distinct mechanical properties when subjected to torsional forces. Yang et al. [11] observed that the torsion capacity of concrete beams showed a rise as the amount of steel fiber, stirrup proportion, as well as longitudinal ratios of reinforcement were increased. Fehling [12] experimentally demonstrated that a steel content of fibers over 0.9% is necessary for establishing an efficient bearing load mechanism following the occurrence of cracking, together with the presence of longitudinal reinforcements.

Improving the ability of reinforced concrete (RC) beams to resist twisting while keeping the cross-sections cost-effective and efficient is a practical difficulty in their design. Developing and testing cost-effective methods to improve the torsional strength of beams is an important focus. The continuous spiral reinforcement system is a technology that has demonstrated promising results in improving concrete sections' torsional performance. Moreover, in recent years, there has been a growing recognition of the benefits associated with the utilization of continuous spiral reinforcing (SP) as opposed to conventional stirrups. These advantages primarily pertain to the enhancement of both the load-carrying capacity and the ability to undergo deformation without fracturing structural elements. The utilization of structural strengthening techniques, specifically the implementation of spiral reinforcement (SP), has been found to greatly enhance the shear behavior of beams as well as improve the capacity for deformation and dissipation of energy in column-beam connections. Furthermore, the application of SP reinforcement has been shown to enhance the seismic strength and bearing load capability of walls that shear [13–17]. As a result, studies on the use of SP in twisting beams have been carried out gradually.

Ibrahim et al. [18] studied how rectangular spiral stirrups improve the torsion performance of solid and hollow concrete beams as transverse reinforcement. Results indicated that utilizing an inclined spiral rectangular stirrup in reinforcing solid and hollow concrete beams significantly increased the torsional capacity by approximately 16% and 18%, respectively, in comparison to conventional closed stirrups. Shatarat et al. [19] developed the concrete beams by using three forms of spiral reinforcements, then investigated the effect of spiral reinforcement shape on beam torsion ability. The continuous circular spiral stirrup demonstrated the greatest increase in ultimate torque, followed by the continuous SP, the advanced rectangular spiral reinforcement, and the conventional stirrups. However, circular spiral stirrups were rarely used in beams, while researchers devoted more attention to rectangular spiral reinforcement. Hadhood et al. [20] studied the influence of spiral stirrup distances on concrete beam torsion effectiveness. It was shown that when the stirrup spacing increased, the beams' ultimate torque and stiffness decreased. Simultaneously, the spiral stirrup has a restriction that prevents it from efficiently increasing the cracking torque of the beams [19, 21]. The presence of torsional cracks has been observed to decrease both torsional performance and durability [22–24]. Yang et al. [11] and Zhou et al. [25] have shown that the use of steel fibers in ultra-high-performance concrete beams leads to an increase in both cracking torque and ultimate torque. Kwahk et al. [26] performed torsion tests exclusively on hollow concrete beams. Their findings showed the effects of steel fibers on cracking torque exceeded the impact of the stirrups. Muhammed et al. [27] utilized internally framed steel stiffness ribs (FSSRs) to enhance the torsional strength of reinforced concrete hollow beams. The study evaluated the influence of FSSRs and their number on torsion performance. The study found that the torsional ability capacity increased by 32.7%, 59.2%, and 93.9% when using one, three, and five FSSRs to strengthen beams, compared to the reference beam without strengthening.

In fact, according to the studies that preceded us in this field above, beams are often internally reinforced against torsion, either through rectangular stirrups or longitudinal steel or by adding additives such as steel fibers, spiral stirrups, internal steel ribs, or diagonal stirrups. Due to the geometry of the beam or the complexity of the system, performing external reinforcement on concrete beams is challenging despite the use of internal reinforcement. The study gap is to find a method of reinforcement for beams that is more practical than the previous reinforcements and can be implemented in practical applications of structural engineering because some of the previous anti-torsion reinforcements for beams are considered complex and difficult to implement. The study aims to use an innovative method to resist the torsional forces of concrete beams using internal cross-rod steel bracing. Internal reinforcement of beams with internally cross-rod steel bracing is innovative to the best of our knowledge and research in this study. Constructing this reinforcement with ordinary steel is straightforward and not complex, unlike the challenging implementation of spiral stirrups or other types in practical applications. The study will investigate the torsional behavior of concrete beams to determine the effectiveness of this reinforcement with the different variables adopted in this study, including the number of internal cross rod steel braces and the type of concrete used: normal strength concrete (NSC), high strength concrete (HSC), and steel fiber concrete (SFC).

2. Research Methodology

2.1. Materials

- **Cement:** this study used normal cement in accordance with Iraqi standard (I.O.S. No. 5/1984) [28].
- **Fine aggregate:** natural sand from Tikrit region was used in the concrete mixture. It conforms with Iraq's NO. 45/1984 specification.[29] . It has modulus of fineness 2.68.
- **Coarse aggregate:** The concrete mixture used Tikrit-sourced crushed river gravel. Conforms to Iraqi specifications No. 45/1984 [29] with maximum size aggregate 12.5mm. Crushed gravel plays a major role in obtaining high compressive strength concrete that is used in this study.
- **Water (W):** clean tap water was used for both, mixing and curing.
- **Superplasticizer (SP):** a superplasticizer used throughout this study was (Sika® Visco Crete®-180 GS, and manufactured by sika Construction Chemicals, Iraq), with nominal dosage 1 liter per 100 kg of cement).
- **Steel Fiber:** hooked-end steel fibers (Bekaert-Dra mix® ZP305) of length 50 mm and diameter 0.5 mm. It has an aspect ratio of 100 and a density of 7860 kg/m³. It is used in this study to make fibrous concrete with a constant content of the volume fraction of steel fibers ($V_f = 1.0\%$), as shown in Figure 1. A ratio of 1% steel fiber provides sufficient workability without segregation, while a ratio of more than 1% steel fiber causes issues during implementation [30].
- **Steel Reinforcement:**
 - Steel bars: steel reinforcement bars with deformed surfaces were used in all specimens, with diameters of (10 mm) for main reinforcement and (6 mm) for closed stirrup reinforcement. Table 1 shows the tensile results for all reinforcement rebars that tested in accordance with American Standard (ASTM A615-09) [31]. The steel reinforcement is shown in Figure 2.
 - Cross-rod steel bracing: stirrups in the form of internal cross rod of steel with a diameter of 8 mm. This steel reinforcement is used as an innovative way to reinforce concrete beams against torsional forces in this study. Table 1 shows the tensile results for steel bracing rods tested according to American Standard (ASTM A615/A615M-09)[31]. The internal cross rod (CR) of steel bracing is shown in Figure 2.



Figure 1. Granulation diagram for the materials used to cast concrete beams

Table 1. Properties of reinforcing bars

Bars diameter (mm)	Function	Yield strength (f_y) MPa	Ultimate strength (f_u) MPa	Elongation %
6	Stirrup	520	544	7.08
8	Cross-rod	442	589	11.2
10	Longitudinal rebar	583	672	12.32

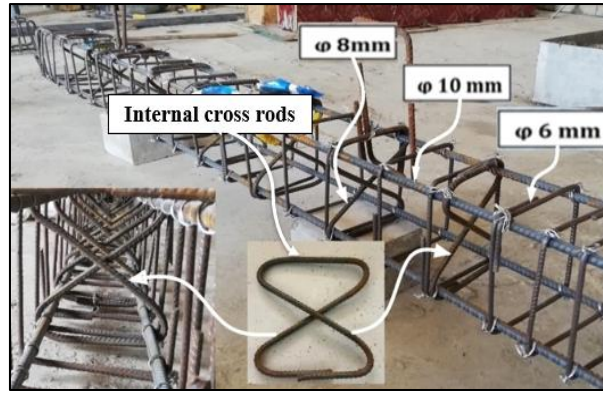


Figure 2. Internal cross rod of steel bracing and steel bars reinforcement

2.2. Mixtures

Three kinds of concrete mixtures have been utilized in this study for casting concrete beams: ordinary concrete, high-strength concrete, and fibrous concrete using steel fibers. The quantities of materials used to produce the three concrete mixtures are shown in Table 2. For each concrete, its compressive strength was tested by casting cylinders (150×300) mm according to ASTM C39 specifications. The splitting tensile strength was also tested according to ASTM C496 by casting cylinders (150×300) mm. The modulus of rupture was also tested by casting prisms (100×100×500) mm according to ASTM C293. All tests were performed 28 days after casting the samples. The properties of ordinary concrete, high-strength concrete, and steel fiber concrete are shown in Table 3. Figure 3 shows the flowchart of work.

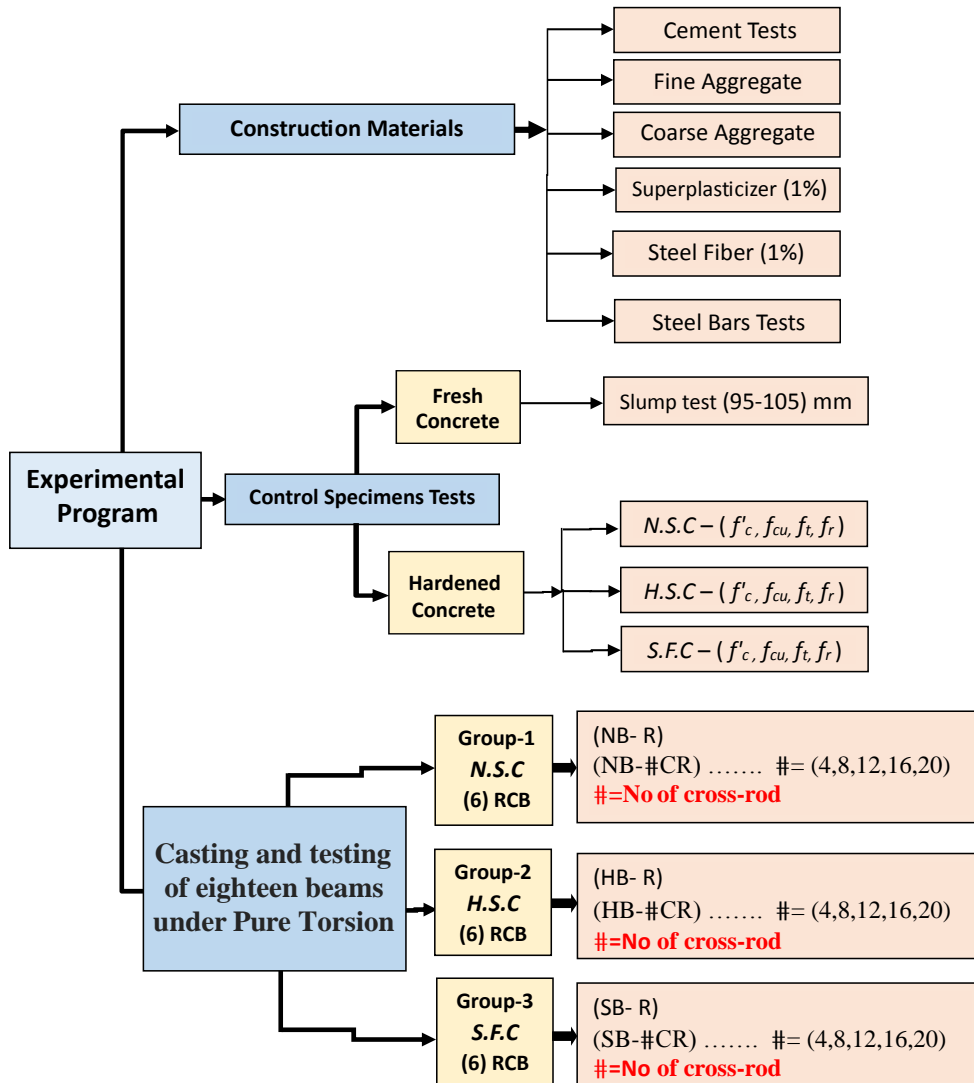


Figure 3. Flowchart of the work

Table 2. Quantities of materials used in the concrete mixes

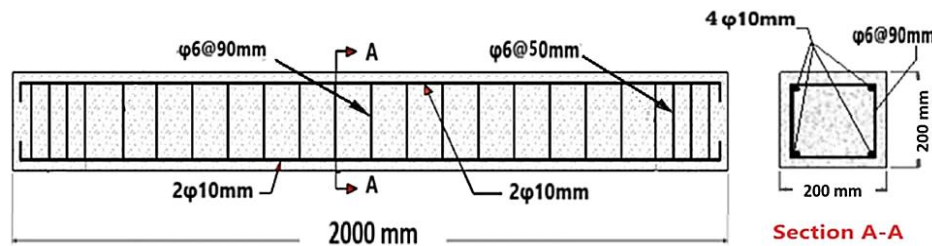
Mixture type	W/C	Cement (kg/m ³)	Fine Aggregate (kg/m ³)	Coarse Aggregate (kg/m ³)	Water (kg/m ³)	SP (kg/m ³)	Steel fiber (kg/m ³)	Density (kg/m ³)
Normal strength concrete (NSC)	0.46	427	797	910	197	-	-	2311
High strength concrete (HSC)	0.3	480	740	986	140	4.8	-	2346
Steel fiber concrete (SFC)	0.3	480	740	986	140	7.2	79	2425

Table 3. Concrete characteristics

Mixture type	Compressive strength (MPa)	Splitting strength (MPa)	Flexural strength (MPa)
Normal strength concrete (NSC)	34.21	3.1	5.12
High strength concrete (HSC)	62.13	4.9	6.97
Steel fiber concrete (SFC)	65.52	7.55	9.75

2.3. Details of the Specimens

Eighteen reinforced beams were cast for testing under pure torsion. These beams were divided into three groups. Group-1 includes six beams made of normal strength concrete. Group-2 includes six beams made of high-strength concrete. Group-3 includes six concrete beams made of steel fiber. The dimensions of all beams were (200×200×2000) mm in (width × height × length), as shown in Figure 4. All of these beams were reinforced longitudinally with 2Φ10 mm bars at the top and bottom in cross section of beam. Each of the beam was transversely reinforced by stirrups Φ6mm@90mm. Design of both transverse and longitudinal reinforcement of beams according to ACI 318 torsion code requirements [32]. As for the steel bracing for the internally crossing rod using Φ8 mm, they were placed at different spaces (0, 75, 95, 125, 175, 320) mm, represented by the six beams for each of the three groups. Table 4 shows the reinforcement details for all concrete beams. Figure 5 shows the mechanism of reinforcement and distribution of internal cross rod for concrete beams, which was applied to each concrete group of the three groups.

**Figure 4. Specimen dimensions****Table 4. Reinforcements of concrete beams**

Group No.	Beam designation	Cross-rod	No. of Cross-rod	Top reinforcing	Bottom reinforcing	Stirrups	Mixing type
Group-1	NB-R*	0	2Φ10	2Φ10	Φ6@90mm	Normal strength concrete
	NB-4CR	Φ8@320mm	4				
	NB-8CR	Φ8@175mm	8				
	NB-12CR	Φ8@125mm	12				
	NB-16CR	Φ8@95mm	16				
	NB-20CR	Φ8@75mm	20				
Group-2	HB-R*	0	2Φ10	2Φ10	Φ6@90mm	High strength concrete
	HB-4CR	Φ8@320mm	4				
	HB-8CR	Φ8@175mm	8				
	HB-12CR	Φ8@125mm	12				
	HB-16CR	Φ8@95mm	16				
	HB-20CR	Φ8@75mm	20				
Group-3	SB-R*	0	2Φ10	2Φ10	Φ6@90mm	Steel fiber concrete
	SB-4CR	Φ8@320mm	4				
	SB-8CR	Φ8@175mm	8				
	SB-12CR	Φ8@125mm	12				
	SB-16CR	Φ8@95mm	16				
	SB-20CR	Φ8@75mm	20				

* Where: R is reference beam, NB is normal strength concrete beam, HB is high strength concrete beam, SB is steel fiber concrete beam, CR is cross -Rods steel bracing.

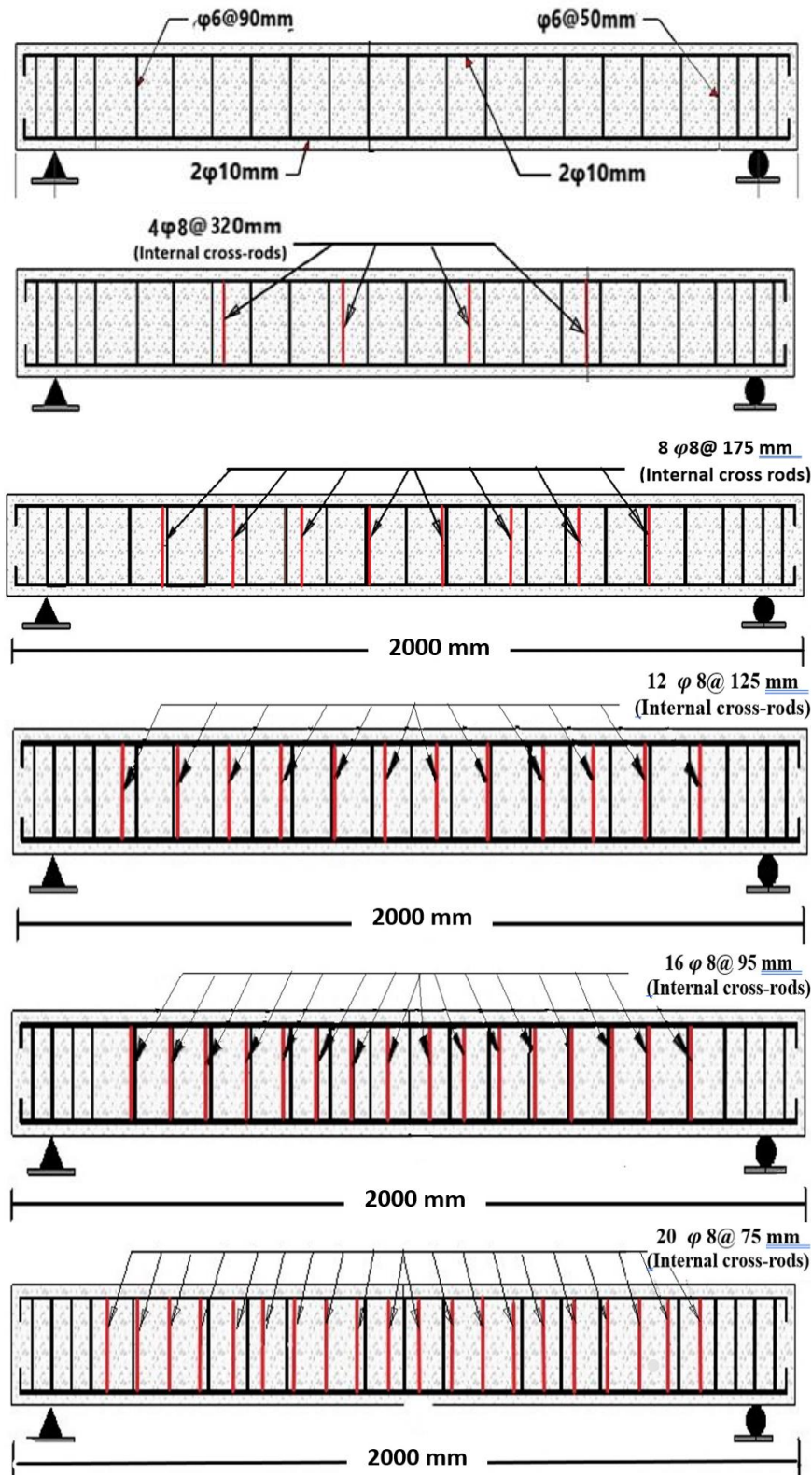


Figure 5. Reinforcement and distribution of internally cross-rod for concrete beams in each of the three concrete groups

2.4. Casting and Curing of Specimens

To cast concrete beams, a rotary mixer with a capacity of (0.07 m³) was used. Molds were used according to the required sizes and dimensions (200 × 200 × 2000) mm to cast concrete beams. During the process of casting the beams, the mold was filled with three layers of the mixture, and each layer was compacted using an electric vibrator to shake the mixture and compact it in the mold. The surface of the specimens is levelled with a trowel, and all beams are left in their molds until they are dismantled after 24 hours. The specimens were treated with burlap bags that were continuously moistened with water for 28 days before the examination was performed. Figure 6 shows the casting and curing processes.



Figure 6. Casting and curing processes of concrete beams

2.5. Beams Test

All eighteen beams were tested under pure torque using a hydraulic testing machine with a load capacity of 3000 kN. The work of this machine is to stabilize the sample on one side and rotate the sample on the other side using the hydraulic arm. The hydraulic arm to rotate the sample is 200 mm (0.20 m). The main parts of the machine can be illustrated in Figure 7. In this study, reinforced concrete beams from the three groups were subjected to torsional loads until failure. Load readings are taken during the test using the load cell located below the hydraulic jack. These readings are recorded by the data logger on the computer and appear in Excel, as shown in Figure 8. To calculate the torsion angle of the beams, the vertical deflection recorded from the LVDT reading is divided by the horizontal distance from the center of the beam to the location of the gauge reading LVDT. Also, before testing the beams, the beams were painted with white dye so that it was easy to notice the crack patterns using a digital camera prepared for this purpose. The crack pattern was also observed at each loading stage. The locations and development of cracks were determined on all faces of the beam.

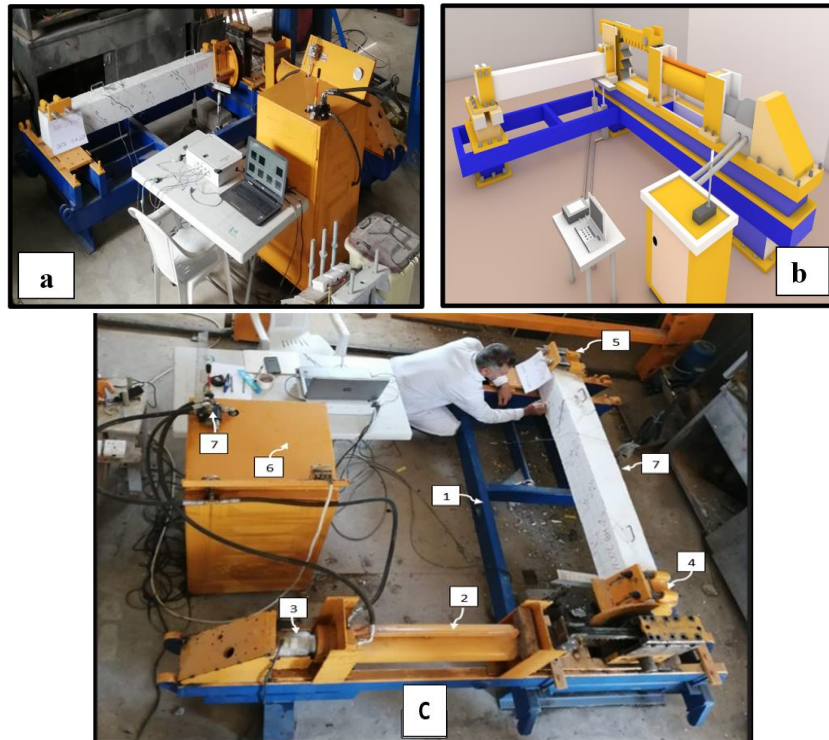
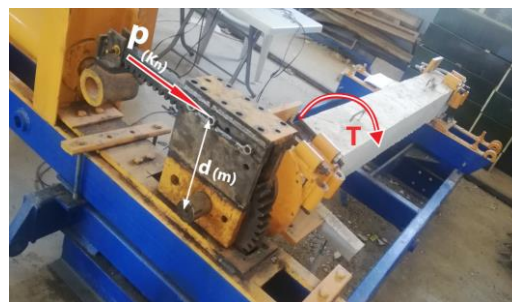


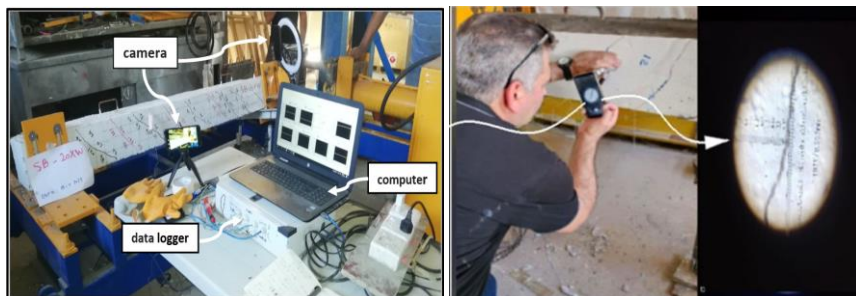
Figure 7. Diagram of beams test. (a) Loading Frame, (b) 3D Model of Machine, (c) Test Machine (1- Steel loading base 2- Hydraulic jack 3- Load cell 4- Rotating support 5- Fixed support 6- Control box 7- Hand shifter 8- Tested beam)



(a) Beam test



(b) LVDT, Angle of twist measurements



(c) Computer, data logger and micro crack width (camera system)

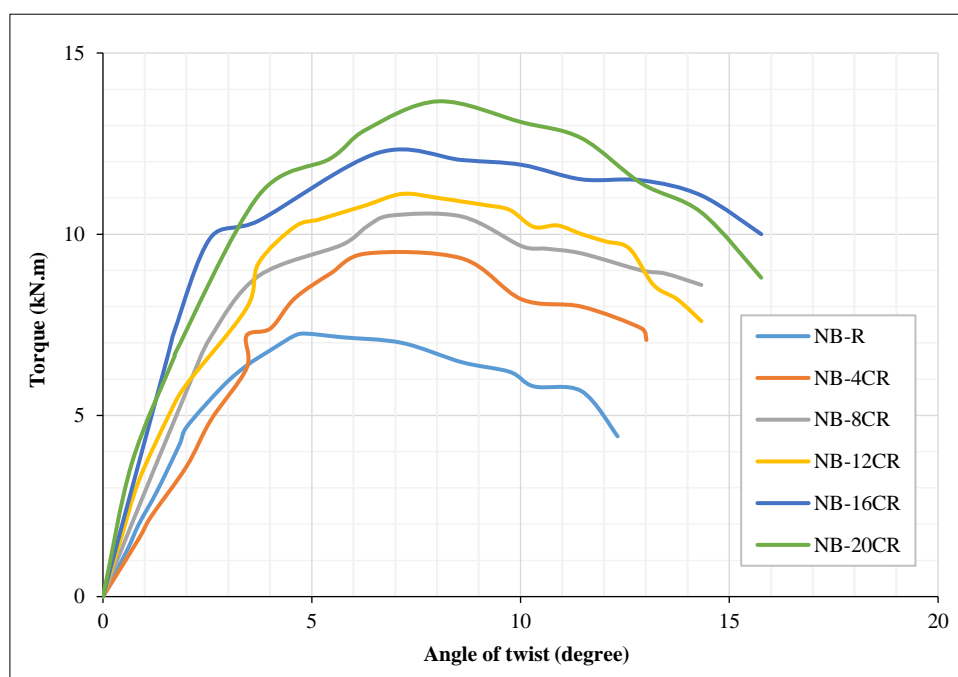
Figure 8. Testing of beams models

3. Results

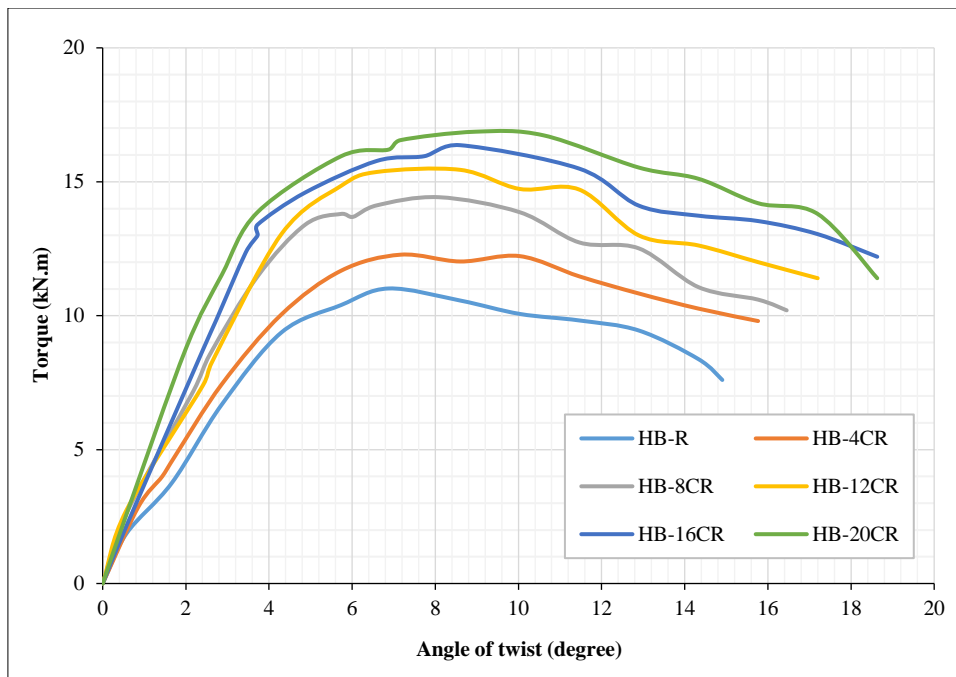
The characteristics examined involved torque of the initial crack, ultimate torque, twist angle at the crack's initial torque, twist angle at the ultimate torque, torsional stiffness, torsional toughness, crack pattern, and failure mechanism. In addition, torque-twist curves were drawn for the examined beams. The torque at which the first visible crack appeared was defined as the cracking torque. Figure 9 depicts the torque - twist of the tested specimens. Table 5 illustrates the results of all the concrete beams with different types of concrete reinforced with internal cross-rod steel bracing.

Table 5. Results of all the specimens reinforced using internally cross-rod bracing

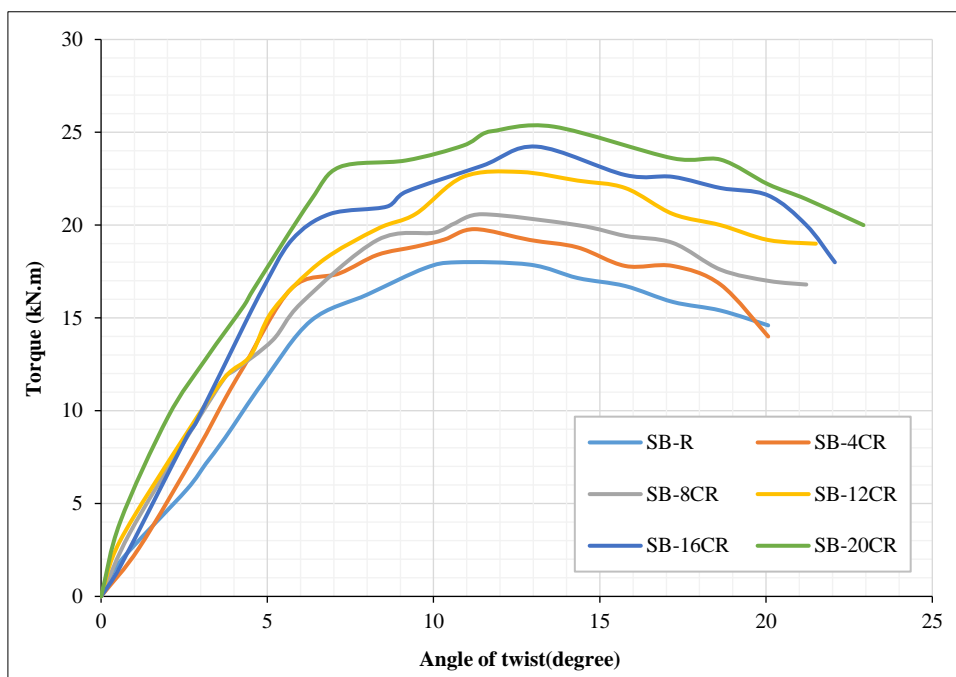
Group No.	Beam designation	Cracking Load P_{cr} (kN)	Cracking torque T_{cr} (kN.m)	Cracking twist θ_{cr} (deg.)	Ultimate Load P_u (kN)	Ultimate torque T_u (kN.m)	Ultimate twist θ_u (deg.)	Torsional stiffness K (kN.m/deg.)	Torsional toughness (kN.m.deg.)
Group-1	NB-R	14.49	2.898	1.43	36.28	7.256	4.872	1.489	23.952
	NB-4CR	23.32	4.664	2.01	47.33	9.466	6.37	1.503	27.768
	NB-8CR	24.44	4.888	2.13	52.56	10.512	6.88	1.528	38.067
	NB-12CR	26.11	5.222	2.21	55.56	11.112	7.16	1.552	50.260
	NB-16CR	31.78	6.356	2.32	61.23	12.246	7.33	1.671	60.438
	NB-20CR	33.43	6.686	2.89	68.33	13.666	8.13	1.703	69.484
Group-2	HB-R	18.77	3.754	1.66	55.08	11.016	6.87	1.603	41.974
	HB-4CR	24.53	4.906	1.89	61.39	12.278	7.13	1.729	45.706
	HB-8CR	32.88	6.576	2.29	72.12	14.424	8.08	1.785	60.132
	HB-12CR	36.94	7.388	2.47	77.23	15.446	8.53	1.817	79.867
	HB-16CR	44.04	8.808	3.41	81.83	16.366	8.89	1.841	91.679
	HB-20CR	52.63	10.526	3.72	88.35	16.877	8.97	1.881	102.455
Group-3	SB-R	33.77	6.754	3.43	89.99	17.998	10.71	1.680	111.034
	SB-4CR	46.53	9.306	3.75	98.92	19.784	11.23	1.762	136.762
	SB-8CR	57.88	11.576	4.98	102.94	20.588	11.42	1.806	143.623
	SB-12CR	62.94	12.588	5.07	115.32	23.064	12.61	1.829	183.239
	SB-16CR	69.04	13.808	5.21	121.15	24.23	13.09	1.851	190.876
	SB-20CR	71.63	14.326	6.01	126.53	25.306	13.61	1.909	236.227



(a) Normal strength concrete beams



(b) High strength concrete beams



(c) Steel fiber concrete beams

Figure 9. Torque-twist relationships of different groups of test beams

3.1. Torque–Twist Relationships

Figures 9-a to 9-c shows the torque-twist relations of all the beams. All of the figures illustrate the relationship among normal-strength concrete (NSC) beams, high-strength concrete (HSC) beams, and steel fiber concrete (SFC) beams, all reinforced with internally cross rods of different spacing. Table 5 shows the results for all these beams. For normally strength concrete beams, as shown in Figure 9 (a) and Table 5, the ultimate torque increases with the number of cross rod. The ultimate torque of normal strength concrete beams (NB-4CR, NB-8CR, NB-12CR, NB-16CR and NB-20CR) increased by (30.45%, 44.87%, 53.14%, 68.77% and 88.34%) respectively, compared to beams (NB-R) without cross rods. Also, the angle of twist for these beams increases with the number of cross rod. The angle of twist of normal strength concrete beams (NB-4CR, NB-8CR, NB-12CR, NB-16CR and NB-20CR) increased by (30.74%, 41.21%, 46.96%, 50.45% and 66.87%) respectively, compared to beams (NB-R) without cross rod.

Figure 9-b shows the torque-twist relationships of highly strength concrete beams. The ultimate torque increases with the number of cross rod. The ultimate torque of high strength concrete beams (HB-4CR, HB-8CR, HB-12CR, HB-16CR and HB-20CR) increased by (11.45%, 30.93%, 40.21%, 48.56% and 53.20%) respectively, compared to beams (HB-R) without cross rods. Also, the angle of twist for these beams increases with the number of cross rod. The angle of twist of high strength concrete beams (HB-4CR, HB-8CR, HB-12CR, HB-16CR and HB-20CR) increased by (3.78%, 17.61%, 24.16%, 29.40% and 30.56%) respectively, compared to beams (HB-R) without cross rod. When compared, these beams with (NSC) beams show that the ultimate torque and twist angle of (HSC) beams higher than (NSC) beams with the same reinforcement. This increase in torque was due to the high compressive strength of the concrete in these beams compared to beams with normal concrete strength with the same reinforcement.

For steel fiber concrete (SFC) beams, as shown in Figure 9-c, the ultimate torque increases with the number of cross rod. The ultimate torque of steel fiber concrete beams (SB-4CR, SB-8CR, SB-12CR, SB-16CR and SB-20CR) increased by (9.92%, 14.39%, 28.14%, 34.62% and 40.60%) respectively, compared to beams (SB-R) without cross rod. Also, the angle of twist for these beams increases with the number of cross rod, as shown in Table 5. The angle of twist of steel fiber concrete beams (SB-4CR, SB-8CR, SB-12CR, SB-16CR and SB-20CR) increased by (4.85%, 6.62%, 17.74%, 22.22% and 27.07%) respectively, compared to beams (SB-R) without cross rod.

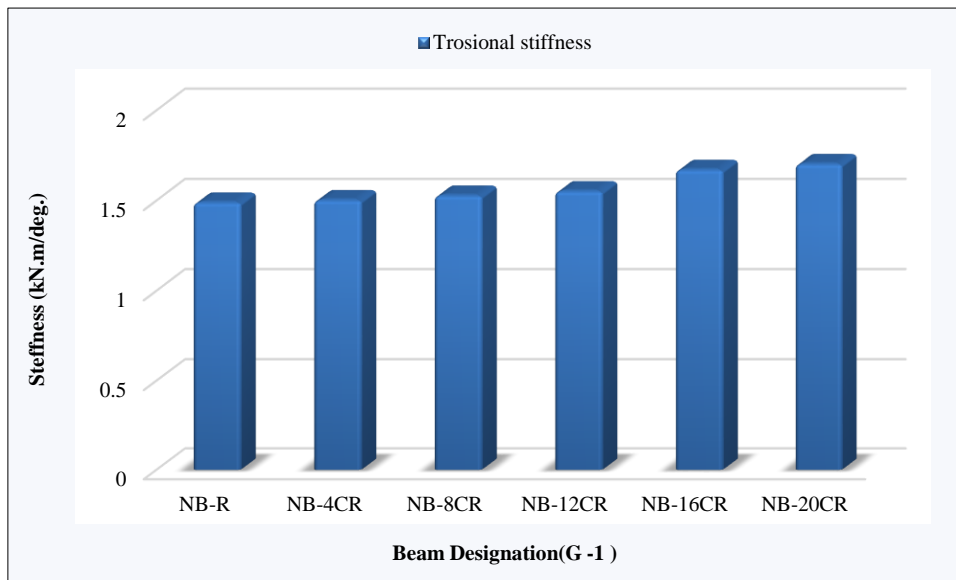
Comparisons between concrete beams show that the ultimate torque and twist angle of steel fiber concrete (SFC) beams higher than those of high strength concrete (HSC) beams and the normal strength (NSC) beams with the same reinforcement. The ultimate torque of steel fiber concrete (SFC) beams (SB-4CR, SB-8CR, SB-12CR, SB-16CR and SB-20CR) higher than that of the high strength concrete (HSC) beams (HB-4CR, HB-8CR, HB-12CR, HB-16CR and HB-20CR) by (63.38%, 61.13%, 42.73%, 49.32%, 48.05% and 49.94%) respectively, with the same reinforcement. The ultimate twist angle of steel fiber concrete (SFC) beams (SB-4CR, SB-8CR, SB-12CR, SB-16CR and SB-20CR) higher than that of the high strength concrete (HSC) beams (HB-4CR, HB-8CR, HB-12CR, HB-16CR and HB-20CR) by (55.89%, 57.50%, 41.33%, 47.83%, 47.24% and 51.72%) respectively, with the same reinforcement. The ultimate torque of steel fiber concrete (SFC) beams (SN-R, SB-4CR, SB-8CR, SB-12CR, SB-16CR and SB-20CR) higher than that of the normal strength concrete (NSC) beams (NB-R, NB-4CR, NB-8CR, NB-12CR, NB-16CR and NB-20CR) by (148.04%, 109%, 95.85%, 107.55%, 97.86% and 85.17%) respectively, with same reinforcement. The ultimate twist angle of steel fiber concrete (SFC) beams (SN-R, SB-4CR, SB-8CR, SB-12CR, SB-16CR and SB-20CR) higher than the normal strength concrete (NSC) beams (NB-R, NB-4CR, NB-8CR, NB-12CR, NB-16CR and NB-20CR) by (119.82%, 76.29%, 65.98%, 76.11%, 78.58% and 67.40%) respectively, with the same reinforcement. The steel fibers had a greater influence on the ultimate torque of the beams. Steel fibers' influence on torque in the presence of cross rods, stirrups and longitudinal reinforcement is very clear in increasing the capacity of these beams. The reasoning is that the steel fibers in the concrete matrix improve its bridging effect. This indicates that when the steel fiber content in the concrete was high, agglomerations that collectively created clusters of steel fibers inside the concrete were the cause of the stress concentration inside the concrete [33]. The test beam's torque was enhanced as a result of the concrete's greater tensile strength. Since raising the reinforcement ratio could significantly increase the ultimate load capacity, the tensile strength of the reinforcement was greater than the tensile strength of the concrete. Furthermore, compared to the longitudinal reinforcement ratio, the impact of internally cross rods and stirrups on maximum torque was larger, similar to a result by Yang et al. [11]. This indicates that the ultimate load capacity of steel fiber concrete beams is effectively improved with steel fiber and internal cross rods, stirrups and longitudinal bars with reasonable strength. Using steel fibers improved the concrete's tensile strength in addition to the stirrups' tension strength. It's obvious which ultimate torque increases using steel fibers, and this agrees with Gao et al. [34, 35].

By studying Table 5, the cracking torque and crack twist angle of all concrete beams increase with the internally cross rods reinforcement. Table 5 summarises the cracking torques for all beams. Compared with normal strength concrete (NSC) beams, high strength concrete (HSC) beams and steel fiber concrete (SFC) beams, a cracking torque as well as twist angle of high strength concrete (HSC) beams were higher than those of normal strength concrete (NSC) beams. The cracking and crack twist angle of steel fiber concrete (SFC) beams were higher than normal strength concrete (NSC) beams and high strength concrete (HSC) beams. The cracking torque of steel fiber concrete (SFC) beams was strongly affected by steel fibres, in agreement with the conclusion of Kwahk et al. [26]. It was found that the fibers of steel prevented the formation of cracks and applied tension to the beams through the bonding force. Additionally, the steel fibers in the beams distribute tension, preventing stress concentration.

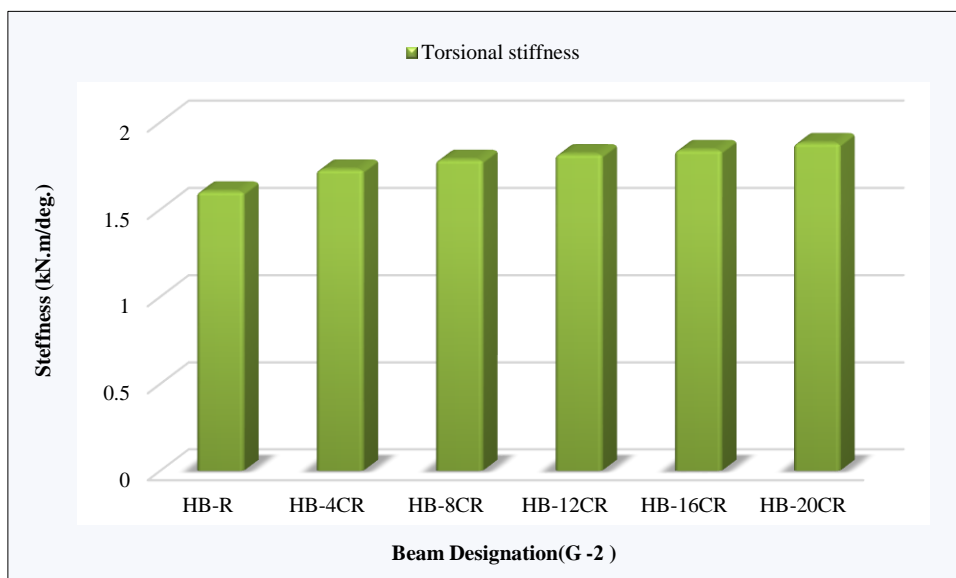
3.2. Torsional Stiffness

The ability of members of the structure to withstand deformations as a result of any applied load is defined as rotational stiffness. It is an indicator of rigidity (a material property). The ultimate torque divided by the ultimate twist angle determines the ultimate torsional stiffness of beams [20, 34–36]. Table 5 shows the torsional stiffness of all beams. The maximum torsional stiffness refers to the rigidity of the specimen until it fails. For normally strength concrete beams, the stiffness increases with the number of cross rod. The stiffness of normal strength concrete beams (NB-4CR, NB-8CR, NB-12CR, NB-16CR and NB-20CR) increased by (0.90%, 2.61%, 4.22%, 12.20% and 14.36%) respectively, compared to beams (NB-R) without cross rod, as shown in Figure 10-a.

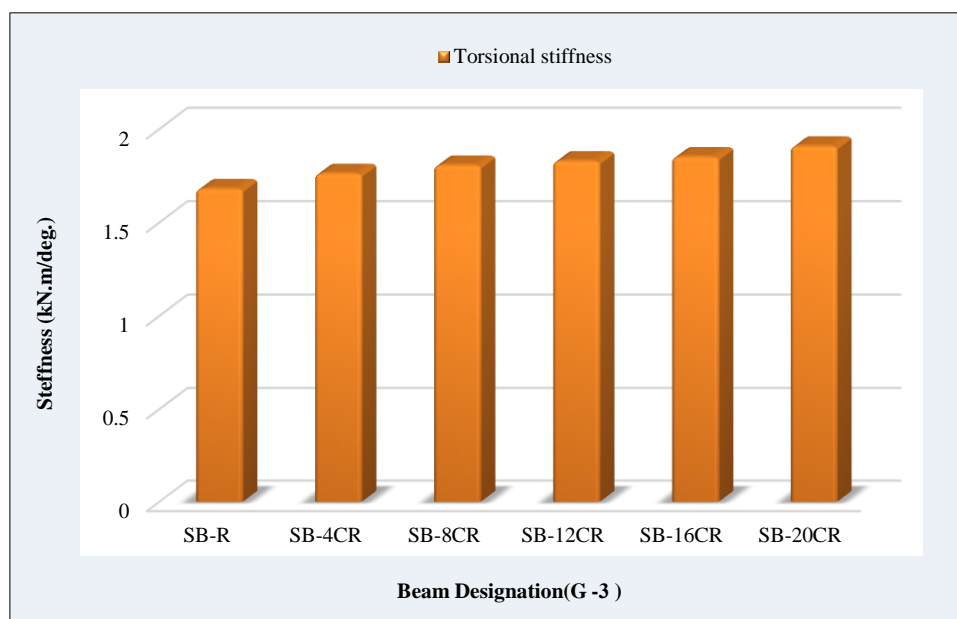
Figure 10-b shows the stiffness of highly strength concrete beams. The stiffness increases with the number of cross rods. The stiffness of high strength concrete beams (HB-4CR, HB-8CR, HB-12CR, HB-16CR and HB-20CR) increased by (7.87%, 11.36%, 13.36%, 14.84% and 17.32%) respectively, compared to beams (HB-R) without cross rod. When compared, these beams with (NSC) beams show that the stiffness of (HSC) beams was higher than that of (NSC) beams with the same reinforcement. This increase in stiffness was due to the high compressive strength of the concrete in these beams compared to beams with normal concrete strength with the same reinforcement. For steel fiber concrete (SFC) beams, the stiffness increases with the number of cross rod. The stiffness of steel fiber concrete beams (SB-4CR, SB-8CR, SB-12CR, SB-16CR and SB-20CR) increased by (4.86%, 7.49%, 8.87%, 10.18% and 13.60%) respectively, compared to beams (SB-R) without cross rod as shown in Figure 10-c. The stiffness of steel fiber concrete (SFC) beams was higher than that of high strength concrete (HSC) beams and the normal strength (NSC) beams with the same reinforcement. The stiffness of steel fiber concrete (SFC) beams (SB-R, SB-4CR, SB-8CR, SB-12CR, SB-16CR and SB-20CR) higher than that of the high strength concrete (HSC) beams (HB-R, HB-4CR, HB-8CR, HB-12CR, HB-16CR and HB-20CR) by (4.80%, 1.87%, 1.16%, 0.65%, 0.54% and 1.48%) respectively, with the same reinforcement. The stiffness of steel fiber concrete (SFC) beams (SN-R, SB-4CR, SB-8CR, SB-12CR, SB-16CR and SB-20CR) higher than that of the normal strength concrete (NSC) beams (NB-R, NB-4CR, NB-8CR, NB-12CR, NB-16CR and NB-20CR) by (12.83%, 17.24%, 18.19%, 17.85%, 10.79% and 12.08%) respectively, with the same reinforcement. Steel fibers increase the stiffness of concrete beams, as mentioned by many researchers, such as Rao et al. [37], Hassan et al. [38] and Gao et al. [34, 35]. The cause is because the fibers of steel weren't fully pulled out of the concrete's matrix during this level, as well as the fibrous concrete linked through internal cross rods, stirrups, longitudinal rebar, and steel fibers, which appeared to exhibit a pseudo-hardening phenomenon [39, 40].



(a) Normal strength concrete beams



(b) High strength concrete beams



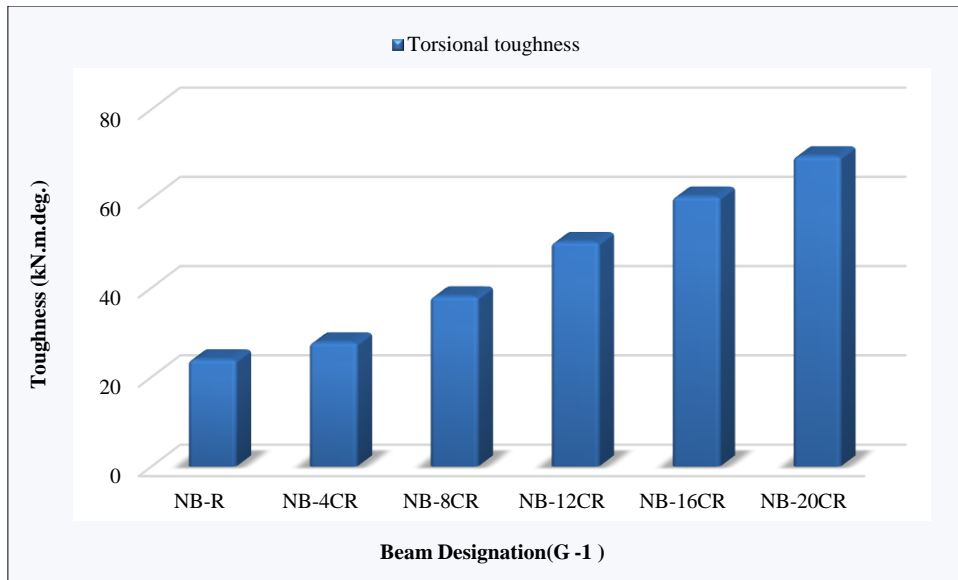
(c) Steel fiber concrete beams

Figure 10. Torsional stiffness of all the concrete beams

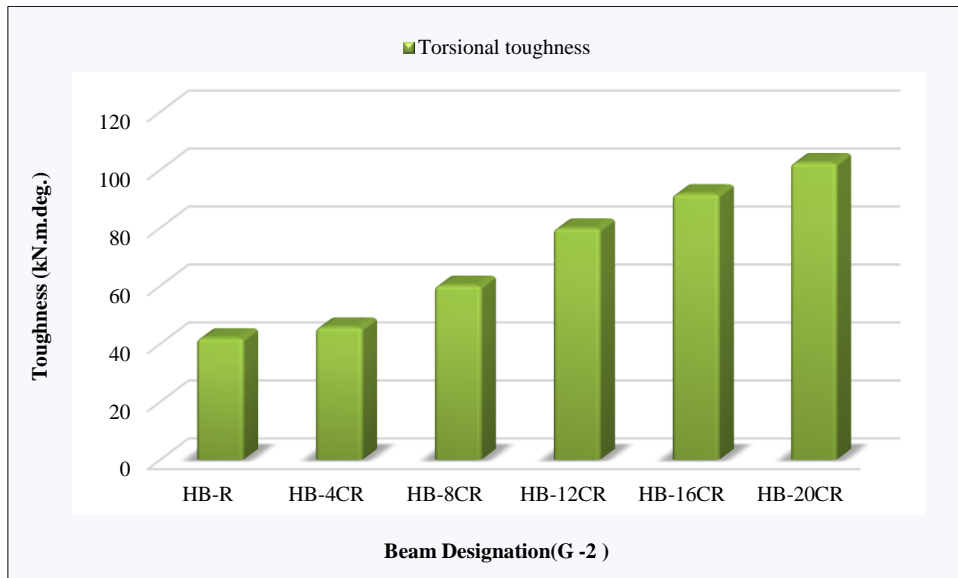
3.3. Torsional Toughness

Toughness can be expressed as the amount of energy needed to break the specimen. Toughness may be determined from the torque-twist curve to the ultimate torque since it is the area under the curve [37, 38, 41]. Table 5 reveals the torsional toughness of specimens. The ultimate torsional toughness denotes the toughness of the test beam until it fails. For normally strength concrete beams, the toughness increases with the number of cross rod. The toughness of normal strength concrete beams (NB-4CR, NB-8CR, NB-12CR, NB-16CR and NB-20CR) increased by (15.92%, 58.92%, 109.83%, 152.32% and 190.09%) respectively, compared to beams (NB-R) without cross rod, as shown in Figure 11-a. Figure 11-b shows the toughness of highly strength concrete beams. The toughness increases with the number of cross rod. The toughness of high strength concrete beams (HB-4CR, HB-8CR, HB-12CR, HB-16CR and HB-20CR) increased by (8.89%, 43.26%, 90.27%, 118.41% and 144.09%) respectively, compared to beams (HB-R) without cross rod. When compared, these beams with (NSC) beams show that the toughness of (HSC) beams was higher than that of (NSC) beams with the same reinforcement. This increase in toughness was due to the high compressive strength in these beams compared to beams with normal concrete strength with the same reinforcement. For steel fiber concrete (SFC) beams, the toughness increases with the number of cross rod. The toughness of steel fiber concrete beams (SB-4CR, SB-8CR, SB-12CR, SB-16CR and SB-20CR) increased by (23.17%, 29.35%, 65.02%, 71.90% and 112.75%) respectively, compared to beams (SB-R) without cross rod, as shown in Figure 11-c.

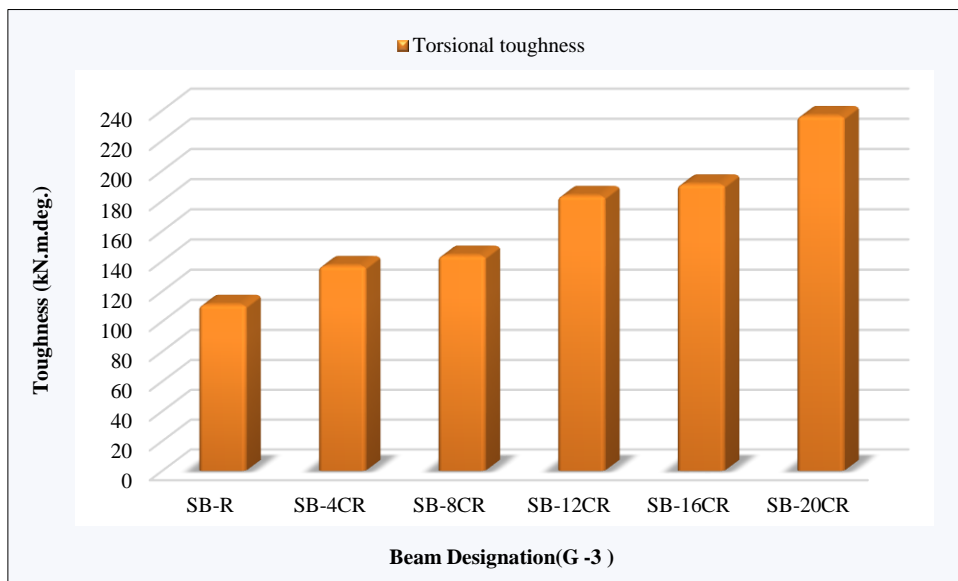
The toughness of steel fiber concrete (SFC) beams was higher than that of high strength concrete (HSC) beams and the normal strength (NSC) beams with the same reinforcement. The toughness of steel fiber concrete (SFC) beams (SB-R, SB-4CR, SB-8CR, SB-12CR, SB-16CR and SB-20CR) higher than that of the high strength concrete (HSC) beams (HB-R, HB-4CR, HB-8CR, HB-12CR, HB-16CR and HB-20CR) by (164.52%, 199.22%, 138.84%, 129.42%, 108.20% and 130.56%) respectively, with the same reinforcement. The toughness of steel fiber concrete (SFC) beams (SN-R, SB-4CR, SB-8CR, SB-12CR, SB-16CR and SB-20CR) higher than that of the normal strength concrete (NSC) beams (NB-R, NB-4CR, NB-8CR, NB-12CR, NB-16CR and NB-20CR) by (363.56%, 392.52%, 277.29%, 264.58%, 215.82% and 239.97%) respectively, with the same reinforcement. Steel fibers increase the stiffness of concrete beams, as mentioned by many researchers, such as Hassan et al. [38] and Gao et al. [34,35]. The highest torsional toughness was (236.227 kN.m.deg.) for the steel fiber concrete beam (SB-20CR) reinforced with twenty internally cross rod steel bracing. While for the same beam, but high-strength concrete beam (HB-20CR) and normal-strength concrete beam (NB-20CR), the energy was (102.455 kN.m.deg.) and (69.484 kN.m.deg.), as shown in Table 5. This could be because steel fiber concrete beams have a high tensile strength which increases the torque to twist curve area of these specimens.



(a) Normal strength concrete beams



(b) High strength concrete beams



(c) Steel fiber concrete beams

Figure 11. Torsional toughness of all the concrete beams

3.4. Crack Pattern and Failure Mechanism of Beams

Figure 12 depicts the torque-crack width relationship for each group of concrete beams. Figure 13 depicts the crack pattern as well as the mechanisms of failure of concrete specimens. For each group of concrete beams, the development of cracks was characterised by the addition of new cracks to the surface and the simultaneous development of multiple cracks. The cracks width grew gradually, as well as every crack width was comparable. The primary crack hadn't been determined. The crack widened significantly following every load, ultimately developing into its primary crack. The maximal crack had been roughly proportional to the torque. After the appearance of the main crack, the cracks rapidly entered the unstable phase. At the cracks in the fibrous concrete beams, a steel fibre was fully pulled out. When beams of concrete were damaged by an increase in torque, the crack width expanded significantly [9, 42].

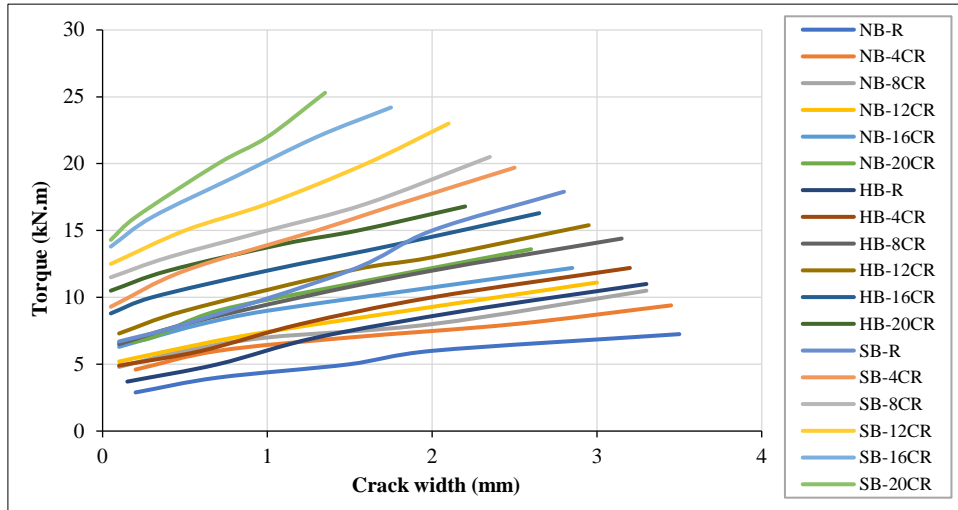


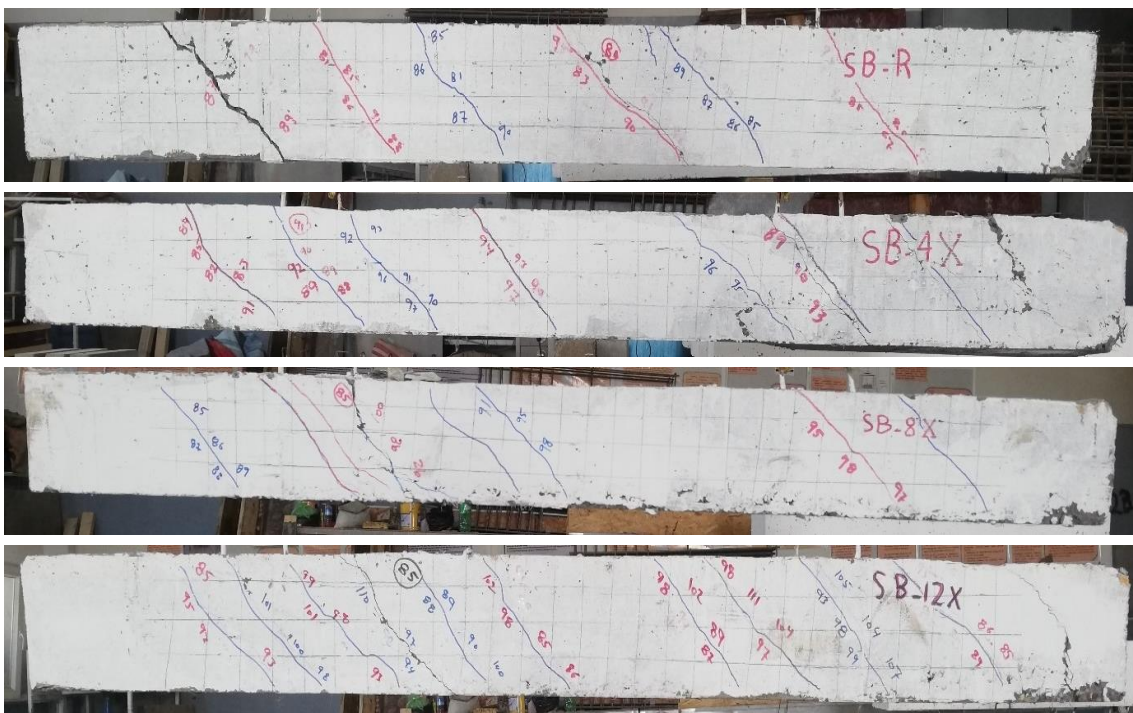
Figure 12. Torque-crack width relationship for different of test beams

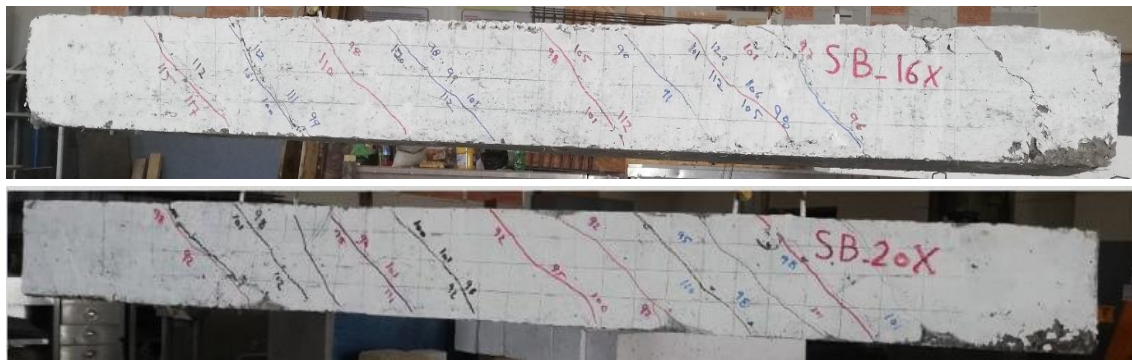


(a) Group-1 (Normal strength concrete beams)



(b) Group-2 (High strength concrete beams)





(c) Steel fiber concrete beams

Figure 13. Cracking patterns in beams reinforced by internally cross rods

Figure 12 shows the torque to crack width relationship of normal strength concrete beams reinforced with internally cross rod. With the same torque, increasing the internal cross rod reduced the crack width. Due to diagonal cracks on the surface, they intersected the internally cross rod and stirrups. The crack width for these beams (NB-CR, NB-4CR, NB-8CR, NB-12CR, NB-16CR and NB-20CR) was (3.5 mm, 3.45 mm, 3.3 mm, 3 mm, 2.85 mm and 2.6 mm) respectively at ultimate torque. The more densely the internal cross-rods and stirrups, the stronger the inhibition affects the crack formation following the crack. The primary diagonal crack angle is also shown in Figure 13. The diagonal cracks angles in these beams ranged from 43° to 47° . The presence of internally cross rods increases the ductility and deformations of these beams. Moreover, there was no big concrete falling off when the beams were damaged in the failure process of these beams.

Figure 12 shows the torque-crack width curves for high strength concrete beams. The influence of internally cross-rod reinforcement in these beams on crack width was different from that of normal strength concrete beams. The type of concrete had an influence on the maximum crack width. With increasing internally cross rods the crack width decreased more than normal strength concrete beams. The crack width for these beams (HB-CR, HB-4CR, HB-8CR, HB-12CR, HB-16CR and HB-20CR) was (3.3 mm, 3.2 mm, 3.15 mm, 2.95 mm, 2.65 mm and 2.2 mm) respectively at ultimate torque. The cracks began to appear in the portion somewhere in the middle and continued all the way to the edges of the beam. The primary diagonal crack angle is also shown in Figure 13. The average of diagonal cracks angle in these beams was 45° . The internally cross rods, stirrups and longitudinal bars increased the ductility and torsional deformation of these high strength concrete beams. Moreover, during the failure, there was no spalling on the surface of the high strength concrete beams.

Figure 12 shows torque-crack width curve of steel fiber concrete beams. As the width of the crack increased, the fiber in the cracks was progressively drawn out. After the first crack appeared, the crack became wider and soon caused damage to the beam. In fibrous concrete beams with steel fibers and stirrups, the influence of various in-situ cross-rod reinforcement states on the cracking process was slight. These beams' cracking behavior was documented, as seen in Figure 13. The initial audible diagonal crack appeared on the beam's side when the cracking torque was achieved. With each increment in torque, a continuous appearance of new diagonal cracks was observed, with their inclination remaining essentially unaltered. Along the surface of the beam, numerous diagonal cracks had developed spiral cracks as they extended to the top and bottom. Further diagonal cracks were not observed, and as the beam underwent increasing angles of twisting, the extent of the pre-existing diagonal cracks progressively expanded until its sustained damage.

The quantity of cracks in these beams developed in correlation with an increase in cross rods and steel fiber contents. This indicates that by increasing the internal cross-rod and steel fiber, the stress redistribution could be effectively enhanced, preventing the expansion of the crack width while fostering the tendency towards numerous cracks. The effects of the internal cross rod and the steel fiber were comparable, but the two components' mechanisms of action were distinct. By enhancing the internal cross-rod, the tension of the concrete was increased, resulting in an increase in the torque transferred to the concrete of the test beam. However, the fibers of steel effectively removed the concentration of stress in the concrete matrix and prevented the growth of crack width, promoting numerous cracks. Thus, failures of steel fiber concrete beams were classified as ductile failures. The utilization of the tensile properties of the longitudinal bars, stirrups, and internally cross rods prior to the crushing of the concrete is what caused this type of failure. In addition, there wasn't any concrete crashing off due to the existence of steel fibers when the specimen failed. Compared with ordinary concrete beams and high-strength concrete, this phenomenon appeared very different [43,44].

The crack width decreased with the number of cross rod steel bracing increased in these steel fiber concrete beams. The crack width for these beams (SB-R, SB-4CR, SB-8CR, SB-12CR, SB-16CR and SB-20CR) was (2.8 mm, 2.5 mm, 2.35 mm, 2.1 mm, 1.75 mm and 1.35 mm) respectively at ultimate torque. This is in agreement with Gao et al. [34,35] and Abdullah et al. [45], those who showed that the number of cracks is increased and their width the decreases with the increase in the stirrups and steel fibers in concrete beams. The primary diagonal crack angle of these beams is also

shown in Figure 13. The test parameters had an effect on the primary crack inclination angle. This is because the crack's angle is determined by the direction of the major tensile stress, which is related with the stress condition of steel fiber as well as stirrups. The average of diagonal cracks angle in these steel fiber concrete beams was 45° . By comparing the beams of the three concrete groups, we conclude that concrete beam containing steel fibers and twenty internally cross rod (SB-20CR) are better at controlling the width and development of numerous cracks. The crack width was reduced by 38.6% for this beam compared to high-strength concrete beams with twenty internally cross rods (HB-20CR) and 48% compared to normal-strength concrete beam with twenty internally cross rod (NB-20CR).

4. Conclusions and Recommendations

The following conclusions can be drawn:

- The torsional capacity of all concrete beams increased with the increase in internally cross-rod reinforcement. The ultimate torque of normal-strength concrete beams, high-strength concrete beams, and steel fiber concrete beams reinforced with twenty internally cross rods increased (88.34%, 53.20%, and 40.60%), respectively, compared to beams without cross rods in each type of concrete beam.
- The ultimate torque and twist angle of steel fiber concrete beams are higher than those of high-strength concrete beams and normal-strength concrete beams with the same reinforcement.
- The stiffness of steel fiber concrete beams was higher than that of high-strength concrete beams and normal-strength beams with the same reinforcement.
- The torsional toughness of concrete beams improved as the internally cross rod reinforcing increased, as well as being higher in steel fiber concrete beams. The highest torsional toughness was (236.227 kN.m.deg.) for the steel fiber concrete beam reinforced with twenty internally cross-rod steel bracing. While for the same beam, but high-strength concrete beams and normal-strength concrete beams, the torsional toughness was (102.455 kN.m.deg.) and (69.484 kN.m.deg.), respectively. This is due to the high tensile strength of steel fiber concrete beams, which increases the torque-twist curve area of these beams.
- Increasing the internally cross-rod in all concrete beams prevented crack width progression as well as improved stiffness under torsional loads, especially in fibrous concrete beams that contained steel fiber. The crack width was reduced by 38.6% for this beam compared to high-strength concrete beams with twenty internally cross rods and by 48% compared to normal-strength concrete beams with twenty internally cross rods.
- The steel fiber concrete beams reinforced with internally cross-rod steel bracing have better torsional properties compared to ordinary concrete beams and high-strength concrete beams.

5. Declarations

5.1. Author Contributions

Conceptualization, A.I.A. and A.M.L.; methodology, A.I.A.; software, A.I.A.; validation, A.M.L.; investigation, A.M.L.; writing—original draft preparation, A.I.A.; writing—review and editing, A.M.L.; visualization, A.M.L.; supervision, A.M.L. All authors have read and agreed to the published version of the manuscript.

5.2. Data Availability Statement

The data presented in this study are available on request from the corresponding author.

5.3. Funding

The authors received no financial support for the research, authorship, and/or publication of this article.

5.4. Conflicts of Interest

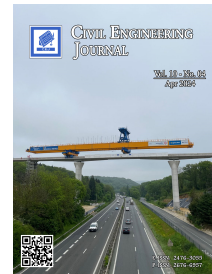
The authors declare no conflict of interest.

6. References

- [1] Lee, H. S., & Hwang, K. R. (2015). Torsion design implications from shake-table responses of an RC low-rise building model having irregularities at the ground story. *Earthquake Engineering and Structural Dynamics*, 44(6), 907–927. doi:10.1002/eqe.2492.
- [2] Mondal, T. G., & Prakash, S. S. (2016). Nonlinear Finite-Element Analysis of RC Bridge Columns under Torsion with and without Axial Compression. *Journal of Bridge Engineering*, 21(2), 04015037. doi:10.1061/(asce)be.1943-5592.0000798.
- [3] Eom, T. S., Kang, S. M., Park, H. G., Choi, T. W., & Jin, J. M. (2014). Cyclic loading test for reinforced concrete columns with continuous rectangular and polygonal hoops. *Engineering Structures*, 67, 39–49. doi:10.1016/j.engstruct.2014.02.023.

- [4] Cao, X., Ren, Y. C., Zhang, L., Jin, L. Z., & Qian, K. (2022). Flexural behavior of ultra-high-performance concrete beams with various types of rebar. *Composite Structures*, 292, 115674. doi:10.1016/j.compstruct.2022.115674.
- [5] Turker, K., & Torun, I. B. (2020). Flexural performance of highly reinforced composite beams with ultra-high performance fiber reinforced concrete layer. *Engineering Structures*, 219, 110722. doi:10.1016/j.engstruct.2020.110722.
- [6] Wang, Q., Song, H. L., Lu, C. L., & Jin, L. Z. (2020). Shear performance of reinforced ultra-high performance concrete rectangular section beams. *Structures*, 27, 1184–1194. doi:10.1016/j.istruc.2020.07.036.
- [7] Cao, X., Ren, Y. C., Qian, K., Fu, F., Deng, X. F., & Zhang, W. J. (2022). Size effect on flexural behavior of ultra-high-performance concrete beams with different reinforcement. *Structures*, 41, 969–981. doi:10.1016/j.istruc.2022.05.062.
- [8] Rahal, K. N. (2013). Torsional strength of normal and high strength reinforced concrete beams. *Engineering Structures*, 56, 2206–2216. doi:10.1016/j.engstruct.2013.09.005.
- [9] Rao, T. D. G., & Seshu, D. R. (2003). Torsion of steel fiber reinforced concrete members. *Cement and Concrete Research*, 33(11), 1783–1788. doi:10.1016/S0008-8846(03)00174-1.
- [10] Okay, F., & Engin, S. (2012). Torsional behavior of steel fiber reinforced concrete beams. *Construction and Building Materials*, 28(1), 269–275. doi:10.1016/j.conbuildmat.2011.08.062.
- [11] Yang, I. H., Joh, C., Lee, J. W., & Kim, B. S. (2013). Torsional behavior of ultra-high performance concrete squared beams. *Engineering Structures*, 56, 372–383. doi:10.1016/j.engstruct.2013.05.027.
- [12] Fehling, E., & Ismail, M. (2012). *Experimental investigations on UHPC structural elements subject to pure torsion. Ultra-high Performance Concrete and Nanotechnology in Construction*, Kassel University Press, Kassel, Germany.
- [13] Karayannis, C. G., & Chalioris, C. E. (2013). Shear tests of reinforced concrete beams with continuous rectangular spiral reinforcement. *Construction and Building Materials*, 46, 86–97. doi:10.1016/j.conbuildmat.2013.04.023.
- [14] De Corte, W., & Boel, V. (2013). Effectiveness of spirally shaped stirrups in reinforced concrete beams. *Engineering Structures*, 52, 667–675. doi:10.1016/j.engstruct.2013.03.032.
- [15] Azimi, M., Campos, U. A., Matthews, J. C., Lu, H., Tehrani, F. M., Sun, S., & Alam, S. (2020). Experimental and Numerical Study of Cyclic Performance of Reinforced Concrete Exterior Connections with Rectangular-Spiral Reinforcement. *Journal of Structural Engineering*, 146(3), 04019219. doi:10.1061/(asce)st.1943-541x.0002506.
- [16] Saha, P., & Meesaraganda, L. V. P. (2019). Experimental investigation of reinforced SCC beam-column joint with rectangular spiral reinforcement under cyclic loading. *Construction and Building Materials*, 201, 171–185. doi:10.1016/j.conbuildmat.2018.12.192.
- [17] Fan, G., Zhao, Z., & Yang, G. (2018). Cyclic Response of Reinforced Concrete Shear Walls with Continuous Rectangular Spiral Stirrups. *KSCSE Journal of Civil Engineering*, 22(5), 1771–1781. doi:10.1007/s12205-017-1134-4.
- [18] Ibrahim, A., Askar, H. S., & El-Zoughiby, M. E. (2022). Torsional behavior of solid and hollow concrete beams reinforced with inclined spirals. *Journal of King Saud University - Engineering Sciences*, 34(5), 309–321. doi:10.1016/j.jksues.2020.10.008.
- [19] Shatarat, N., Hunifat, R., Murad, Y., Katkhuda, H., & Abdel Jaber, M. (2020). Torsional capacity investigation of reinforced concrete beams with different configurations of welded and unwelded transverse reinforcement. *Structural Concrete*, 21(2), 484–500. doi:10.1002/suco.201900054.
- [20] Hadhood, A., Gouda, M. G., Agamy, M. H., Mohamed, H. M., & Sherif, A. (2020). Torsion in concrete beams reinforced with GFRP spirals. *Engineering Structures*, 206, 110174. doi:10.1016/j.engstruct.2020.110174.
- [21] Chalioris, C. E., & Karayannis, C. G. (2013). Experimental investigation of RC beams with rectangular spiral reinforcement in torsion. *Engineering Structures*, 56, 286–297. doi:10.1016/j.engstruct.2013.05.003.
- [22] Yalciner, H., Kumbasaroglu, A., & Turan, A. İ. (2019). Torsional behavior of reinforced concrete beams with corroded reinforcement. *Structures*, 20, 476–488. doi:10.1016/j.istruc.2019.05.013.
- [23] Mohamed, H. M., & Benmokrane, B. (2016). Reinforced Concrete Beams with and without FRP Web Reinforcement under Pure Torsion. *Journal of Bridge Engineering*, 21(3). doi:10.1061/(asce)be.1943-5592.0000839.
- [24] Lopes, S. M. R., & Bernardo, L. F. A. (2014). Cracking and failure mode in HSC hollow beams under torsion. *Construction and Building Materials*, 51, 163–178. doi:10.1016/j.conbuildmat.2013.10.062.
- [25] Zhou, J., Li, C., Feng, Z., & Yoo, D.-Y. (2022). Experimental investigation on torsional behaviors of ultra-high-performance fiber-reinforced concrete hollow beams. *Cement and Concrete Composites*, 129, 104504. doi:10.1016/j.cemconcomp.2022.104504.
- [26] Kwahk, I., Joh, C., & Lee, J. W. (2015). Torsional Behavior Design of UHPC Box Beams Based on Thin-Walled Tube Theory. *Engineering*, 07(03), 101–114. doi:10.4236/eng.2015.73009.

- [27] Muhammed, S. H., & Aziz, A. H. (2020). Using Internal Framed Steel Stiffening Ribs as an Alternative Technique for Torsional Strengthening of RC Box Beams. *IOP Conference Series: Materials Science and Engineering*, 671(1), 12112. doi:10.1088/1757-899X/671/1/012112.
- [28] Iraqi Standard No. 5. (1984). Portland Cement. Central Organization for Standardization and Quality Control, Baghdad, Iraq.
- [29] Iraqi Standard Specification No.45. (1984). Aggregate from Natural Sources for Concrete and Building Construction. Central Organization for Standardization and Quality Control, Baghdad, Iraq.
- [30] Mures, J. K., Chkheiw, A. H., & Ahmed, Mazin. A. (2021). Experimental Study on Torsional Behavior of steel Fiber Reinforced Concrete Members under Pure Torsion. *IOP Conference Series: Materials Science and Engineering*, 1090, 012065. doi:10.1088/1757-899x/1090/1/012065.
- [31] ASTM A615/A615M-09b. (2022). Standard Specification for Deformed and Plain Carbon-Steel Bars for Concrete Reinforcement. ASTM International, Pennsylvania, United States. doi:10.1520/A0615_A0615M-09B.
- [32] ACI 318-08. (2008). Building Code Requirements for Structural Concrete (ACI 318-08) and Commentary. American Concrete (ACI), Michigan, United States.
- [33] Gao, S. L. (2006). Study on pseudo strain-hardening and fracture characteristic of polyvinyl alcohol fiber reinforced cementitious composites. Dalian University of Technology, Liaoning, China.
- [34] Cao, X., Quan, Y., Ren, Y., Fu, F., Jin, Q., He, D., & Zheng, Y. (2023). Experiment study on reactive powder concrete beams using spirals reinforcement under torsion. *Engineering Structures*, 290, 116361. doi:10.1016/j.engstruct.2023.116361.
- [35] Cao, X., Zhang, W. J., Ren, Y. C., Fu, F., Li, Y. hua, He, D. B., & Zheng, Y. (2023). Torsional capacity of ultra-high-performance concrete beams using rectangle stirrup. *Journal of Building Engineering*, 69, 106231. doi:10.1016/j.job.2023.106231.
- [36] Elsheikh, A., Albo-Hassan, A. S., & Al-Zayadi, S. K. (2023). Torsion Improvement of Reinforced Self-Compacting Concrete Beams Using Epoxy Injection and CFRP. *Civil Engineering Journal*, 9(11), 2706-2724. doi:10.28991/CEJ-2023-09-11-05.
- [37] Rao, T. D. G., & Rama Seshu, D. (2005). Analytical model for the torsional response of steel fiber reinforced concrete members under pure torsion. *Cement and Concrete Composites*, 27(4), 493–501. doi:10.1016/j.cemconcomp.2004.03.006.
- [38] Hassan, R. F., Jaber, M. H., Al-Salim, N. H., & Hussein, H. H. (2020). Experimental research on torsional strength of synthetic/steel fiber-reinforced hollow concrete beam. *Engineering Structures*, 220(110948). doi:10.1016/j.engstruct.2020.110948.
- [39] Hassan, A. M. T., Jones, S. W., & Mahmud, G. H. (2012). Experimental test methods to determine the uniaxial tensile and compressive behaviour of Ultra High Performance Fibre Reinforced Concrete (UHPFRC). *Construction and Building Materials*, 37, 874–882. doi:10.1016/j.conbuildmat.2012.04.030.
- [40] Trung Le, T. (2008). Ultra high performance fibre reinforced concrete paving flags. Ph.D. Thesis, University of Liverpool, Liverpool, United Kingdom.
- [41] Behera, G. C., Rao, T. D. G., & Rao, C. B. K. (2016). Torsional behaviour of reinforced concrete beams with ferrocement U-jacketing-Experimental study. *Case Studies in Construction Materials*, 4, 15–31. doi:10.1016/j.cscm.2015.10.003.
- [42] Chalioris, C. E. (2006). Experimental study of the torsion of reinforced concrete members. *Structural Engineering and Mechanics*, 23(6), 713–737. doi:10.12989/sem.2006.23.6.713.
- [43] Deifalla, A., & Ghobarah, A. (2014). Behavior and analysis of inverted T-shaped RC beams under shear and torsion. *Engineering Structures*, 68, 57–70. doi:10.1016/j.engstruct.2014.02.011.
- [44] Zhou, J., Chen, Z., Chen, Y., Song, C., Li, J., & Zhong, M. (2022). Torsional behavior of steel reinforced concrete beam with welded studs: Experimental investigation. *Journal of Building Engineering*, 48(103879). doi:10.1016/j.job.2021.103879.
- [45] Abdullah, A. I., & Lateef, A. M. (2023). Novel Torsional Reinforcement of Concrete Beams Utilizing Cross-Rod Steel Reinforcement. *Tikrit Journal of Engineering Sciences*, 30(3), 49–58. doi:10.25130/tjes.30.3.6.



An Empirical Formula for Assessing the Characteristic Strength of Unreinforced Laterite Stone Masonry

Hassane Seini Moussa ¹, Decroly Djoubissié Denouwé ¹, Abdou Lawane ^{1*},
Anne Pantet ², Mamadou Diop ¹, Koami Wisdom Boko ¹

¹ *Laboratoire Eco-Matériaux et Habitats durables (LEMHaD), Institut international d'Ingénierie de l'Eau et de l'Environnement (2iE), Rue de la Science, 01 BP 594 Ouagadougou, Burkina Faso.*

² *Laboratoire Ondes et Milieux Complexes (LOMC), Université Le Havre Normandie, 25 Rue Philippe Lebon, 76600 Le Havre, France.*

Received 23 October 2023; Revised 12 March 2024; Accepted 18 March 2024; Published 01 April 2024

Abstract

This study aims to determine the needed coefficients for evaluating the uniaxial compressive strength characteristic value for masonry structures made of Laterite Stone (LS) and cement mortar, resulting from experiments conducted in the laboratory evaluating the compressive strengths of the laterite stone and mortar separately in masonry. It proposes calculation coefficients for the completion of Eurocode 6 data that fit the behavior of laterite stone-based masonry. The laterite stone blocks are extracted from three quarries in southern Burkina Faso. The dimensions of the masonry samples tested are 800 mm × 800 mm × 135 mm (±5 mm) with a cement mortar joint of 20 mm (±5 mm) thick. The different failure modes of masonry were also explored. The tests carried out on the masonry showed that the failure is initiated by vertical cracks through the block-mortar interface at a quarter of the width of the walls, generally at 40 to 60% of their maximum strength. The statistical analysis made through a linear regression from the standard model of approximation of the characteristic strength of masonry in Eurocode 6 was used to set out parameters for the empirical relation. The proposed formula considers the intrinsic properties of the block and the mortar, the thickness of the mortar, the dimensions of the masonry block, and the geometry of the masonry itself to evaluate its compression strength. The adequacy between the model and the experimental values is evaluated through the coefficient of determination and the standard error of 0.94 and 0.041 MPa, respectively.

Keywords: Laterite Stone; Masonry; Uniaxial Compression; Empirical Formula.

1. Introduction

Stone masonry is one of the oldest construction methods that has gained renewed interest in its environment-friendly status and the social and environmental challenges of eco-housing. In Burkina Faso, Laterite Stone (LS) has been one of the materials used for masonry purposes for millennia because of its wide availability in many regions [1]. The term “laterite” is described as a reddish ferruginous, vesicular, unstratified, and porous material with yellow ochers [2, 3]. It is a relatively soft material extracted manually or mechanically with pickaxes or saws, depending on the quarry, the availability of the materials or modern technologies, and the hardness of the stone. Variations in characteristics regarding the location of quarries, the geological history, the depth of extraction, the direction of loading about anisotropy plans, and the mineral composition have been studied in the past, and some interesting conclusions have been highlighted. The properties of laterite stone vary significantly within the same quarry depending on the extraction layer and the moisture content [1, 4–6].

* Corresponding author: abdou.lawane@2ie-edu.org

<http://dx.doi.org/10.28991/CEJ-2024-010-04-07>



© 2024 by the authors. Licensee C.E.J, Tehran, Iran. This article is an open access article distributed under the terms and conditions of the Creative Commons Attribution (CC-BY) license (<http://creativecommons.org/licenses/by/4.0/>).

In developing countries such as Burkina Faso, construction with earthen materials should represent a suitable solution for the problem of sustainable housing for the population since it is cheap and so-called sustainable. The socio-economic impact of constructions based on earthen materials in the context of Burkina Faso has been studied by authors such as Zoungrana, and it confirms the eco-friendly status of raw earth construction materials [7–9]. Furthermore, earthen materials such as LS present very good comfort properties for Sahelian cities, villages, and hot environments due to their hygrothermal properties [10–13]. If LS has so many advantages, why is it not one of the most used materials for construction in tropical countries such as Burkina Faso? Indeed, some difficulties slow its expansion as a construction material. Firstly, in most constructions in Burkina Faso, where it is used, it is considered an infill wall material that does not bear main structural loads. Secondly, its structural behavior, as in structural masonry, is not well known, and the existing calculation methods do not fit the behavior observed experimentally for LS masonry. Thirdly, as mentioned previously, LS mechanical properties vary greatly within the same quarry and from one quarry to another. Some studies conducted in the recent past have shown that the available formulas for calculating masonry structures in compression do not accurately report the behavior of laterite stone masonry; furthermore, they overestimate the LS masonry load-bearing capacity [1, 14]. Its use needs to be standardized to upgrade Laterite stone at a status of construction material for confident structures. More information is needed concerning the complex structures that LS and mortar joints form. This study generally aims to contribute to standardizing laterite stone as a construction material. The specific objectives are set to be the characterization of laterite stone and mortar joints for masonry purposes, an experimental study of several low-size walls made of laterite stone and cement mortar joints, statistical analysis of the experimental and literature results, and setting out an empirical formula for assessing the behavior of laterite stone masonry under compressive loads. The scientific literature studies various types of masonry made from natural stones.

Kabore et al. [14], studying LS-based masonry walls from the DANO quarries, set a starting point for understanding the mechanical behavior of LS masonry under uniaxial compressive load. This study focused on the performance and limits of LS masonry by determining the range of compressive strength of this masonry calculated through existing formulas for other masonry materials and then comparing the empirical values to those determined experimentally. Indeed, the compressive strength of masonry is generally assessed by carrying out tests on prisms or walls in the laboratory. However, they are rarely performed due to the complexity of these experiments and their time and resource-consumption. Therefore, since masonry's strength depends on its elementary elements' characteristics (i.e., blocks and mortar), empirical formulas have been developed to establish links between the compressive strength of blocks and mortar and the load-bearing capacity of bulk masonry. Kaboré et al. [14], the authors have shown that the existing calculation codes, such as Eurocode 6 [15] and CNERIB [16], as well as the formulas proposed in the literature [17–19] for evaluating the uniaxial compressive strength characteristic value for masonry, do not accurately report the behavior of LS masonry. Table 1 presents some empirical formulas proposed in the literature to predict the compressive strength of different types of masonry. Most of these formulas are expressed as power functions and use the compressive strength of the block and the mortar as input parameters and their geometric characteristics. Some of these expressions are linear [20, 21] or polynomials [22] and consider only the strength of the block and the mortar. Most of these analytical models can thus be expressed in the following form:

Table 1. Some analytical models for predicting the characteristic strength of masonry

Type of masonry	Formulas
Unperforated Solid Brick [17]	$0.32 \times f_b^{0.53} \times f_m^{0.21}$
Clay Brick [23]	$0.63 \times f_b^{0.49} \times f_m^{0.32}$
Fly Ash Blocks [24]	$1.34 \times f_b^{0.1} \times f_m^{0.33}$
Clay Brick [25]	$0.1 \times f_b^{0.34} \times f_m^{1.93}$
Cambodian Blocks [26]	$0.24 \times f_b^{0.59} \times f_m^{0.32}$
Clay Blocks [24]	$0.69 \times f_b^{0.6} \times f_m^{0.35}$
Any Masonry with A Thick Joint [15]	$k \times f_b^{0.65} \times f_m^{0.25}$
Compressed Earth Brick [28]	$0.2 \times f_b^{1.26} \times f_m^{0.15}$
Unreinforced Solid Masonry [29]	$0.63 \times f_b^{0.49} \times f_m^{0.32}$
Laterite Block [30]	$0.482 \times f_b^{0.729} \times f_m^{0.365}$
Earth Brick Stabilized with Cement [31]	$0.25 \times f_b^{1.03} \times f_m^{0.28}$
Arch Bridge Masonry [20]	$\frac{1}{3} \times f_b + \frac{2}{3} \times f_m$
Clay Brick [21]	$0.53 \times f_b + 0.93 f_m - 10.32$
Clay Brick [22]	$0.327 f_b (1 - 0.003 f_b + 0.015 f_m)$

Many other authors have proposed similar formulas for various materials [32–38].

$$f_k = k \times f_b^\alpha \times f_m^\beta \tag{1}$$

where f_k is the characteristic compressive strength value of the masonry, f_b is the characteristic compressive strength value of the block. f_m is the characteristic compressive strength value of the mortar, α , β are corrective factors related respectively to the block and the mortar. k depends on the geometrical characteristics of the block and the mortar, as mentioned in [15]. The general remark about these previous studies is that the value of α is greater than the value β . The strength of the masonry would, therefore, be more sensitive to a variation in the strength of the block than of the mortar. Only Basha & Kaushik [24] and Llorens et al. [25] found contradictory results. For the formula proposed by Chourasia et al. [30], the data used are based on scattered values from the literature regardless of the original experimental conditions and standard used. However, the experimental conditions and the standard used for evaluating the characteristic mechanical values of the masonry constituents impact the outputs deeply. So, it is important to consider the concomitant properties of the block and mortar used in the constitution of the masonry. Also, the lack of accuracy in this study regarding the calculation of the approximation error of the formula makes its general use biased.

The main objective of this study is to propose an empirical, analytical model to evaluate the characteristic uniaxial compressive strength of LS masonry. This model is based on experimental values of the block and mortars' compressive strength while exploring their failure modes under uniaxial compression.

2. Materials and Methods

2.1. Materials

Three blocks (Figure 1) from three quarries in Burkina Faso were used to build the sample walls. The raw blocks from the quarry are sawed to a size of 135 mm × 135 mm × 290 mm (±5 mm). The coordinates of the quarries are presented in Table 2. Two cement mortars, MO1 and MO2, were mixed from sand of two types: river sand and crushed granite sand from a quarry. The particle size distribution curves of the sands used are shown in Figure 1. The studied sands have relatively similar particle sizes. The proportions for a mixture of mortars are a ratio from 1:5 to 1:6 for cement/sand and 2:3 for the water/cement ratio in mass. The variation in cement content has intentionally been made to ensure that the characteristic values of compression strength will differ at 28 days of age since the compressive strength of the mortar is highly sensitive to the cement-sand ratio. The cement used is a Portland CEM II-42.5 N cement.

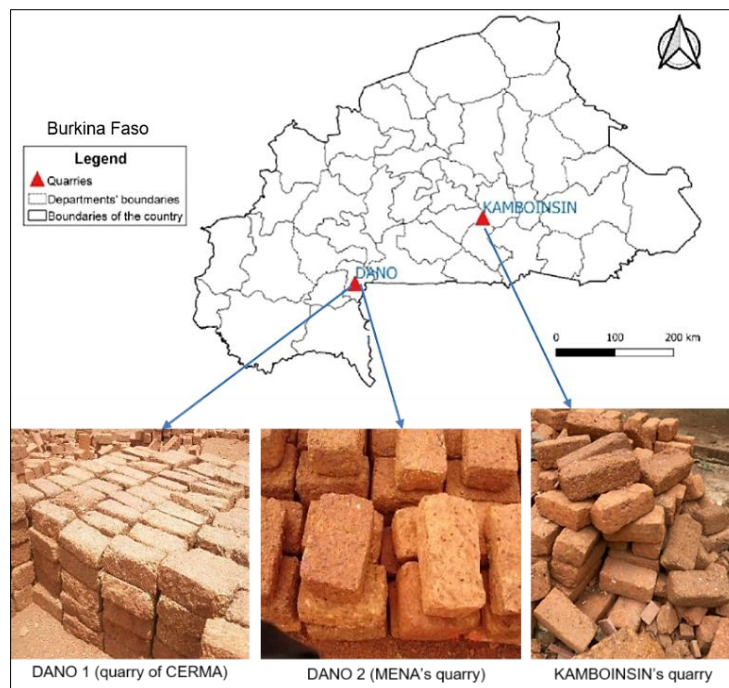


Figure 1. Blocks from the three quarries

Table 2. Location of the LS quarries

Quarry name	Latitude	Longitude	Altitude (m)
DANO 1 (CERMA Quarry)	11° 8'38.20"North	3° 3'59.50"West	322
DANO 2 (MENA Quarry)	11° 10'29.14"North	3° 2'32.78" West	278
KAMBOINSIN	12° 26' 48" North	1° 33' 45" West	301

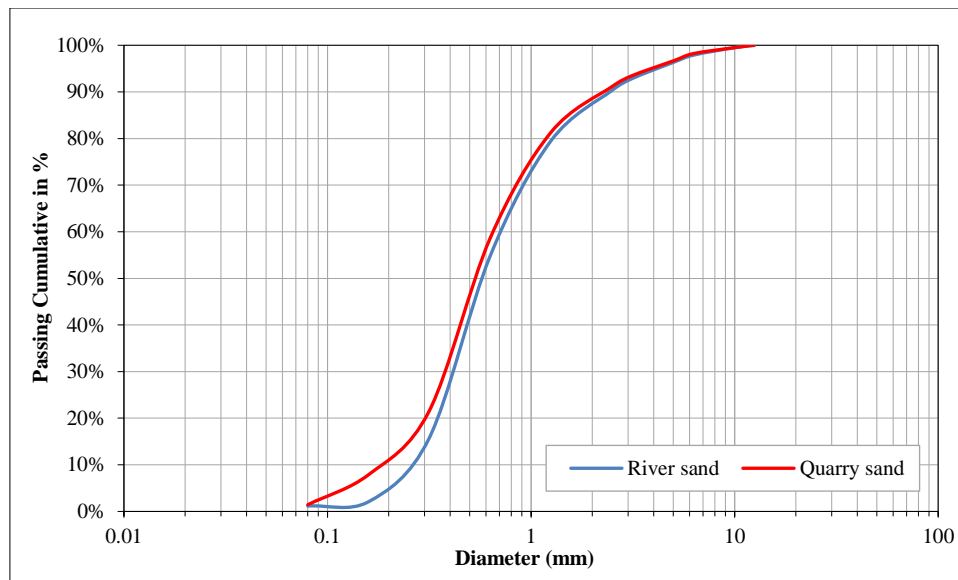


Figure 2. Particle size distribution curves of the sands used for mortar mix

The dimensions of the sample walls tested are 800 mm × 800 mm × 135 mm (± 5 mm) with a joint of 20 mm (± 5 mm) thickness. The blocks' dimensions, the mortar's thickness, and the mix proportions have been chosen according to the construction practices commonly used in LS buildings in Burkina Faso. These values are also determined according to the European standard guidelines [39-42].

2.2. Experimental Methods

The compressive strengths of blocks, mortar, and masonry are determined according to European standards [43-45].

Figure 3(a) and (b) present the samples prepared for the compression test for the mortar and masonry units. For the compression test on masonry blocks, raw blocks from the quarries were cut into smaller parallelepipedal shape blocks of 70 mm x 70 mm x 70 mm (± 5 mm) size (Figure 3b) with a mechanical saw. Then, the samples shaped for compressive strength tests in dry conditions are dried in an oven at 70 ± 2 °C until reaching constant mass. Samples designed for compression strength tests in a saturated state are immersed in water for at least 48 hours until reaching constant mass. When the samples are ready for the tests, they are placed on a 300 kN load capacity hydraulic press cell and loaded at a loading rate of 0.05 mm/s until failure.



(a) Samples 40 × 40 × 160 (mm) for mortar compression test (b) Samples 70 × 70 × 70 (mm) for compression test on the block

Figure 3. Samples for compression tests on blocks and mortar

For the compression test on mortar samples, mortar is taken from the bulk mixture during the masonry sample wall construction and filled in three 40 mm × 40 mm × 160 mm (± 1 mm) triplet mold (Figure 3a) and compacted on a shock table. The masonry mortar mix is carefully prepared to ensure accuracy and consistency in testing by combining the proportions of cement, sand, and water to create a homogeneous mixture. Firstly, the required quantity of cement is measured precisely using a scale. Next, the appropriate quantity of sand is added and thoroughly mixed with the cement until they form a uniform blend. Finally, water is gradually added to the mixture while continuously mixing until the desired consistency is achieved. The mold is filled with three layers of mortar, and each layer is compacted with 25 shocks by the shock table. For this study, regarding the low dispersion of measured strength among the collected samples onto the same quarry, the normalized strengths of the blocks are taken equal to the average value. However, in the general application of the formula, the characteristic values following the confidence interval will be the input data. A total of ten (10) walls were built by a professional mason for the experimentation. Six specimens were used for the

calibration of the formula and four for validating the model, in addition to results from the literature. Onto the same quarry, the mean strength for a load in a direction perpendicular to anisotropy plans of the stone (Figure 4a) or parallel to anisotropy plans (Figure 4b) is quite different. A wall is constructed for each quarry, whether with MO1 or MO2, and blocks are laid following a direction perpendicular or parallel to anisotropy plans. The device for the compression test on the wall is presented in Figure 5. The tests on the mortar and the wall are carried out after 28 days of maturation of the specimens and conserved at room temperature.

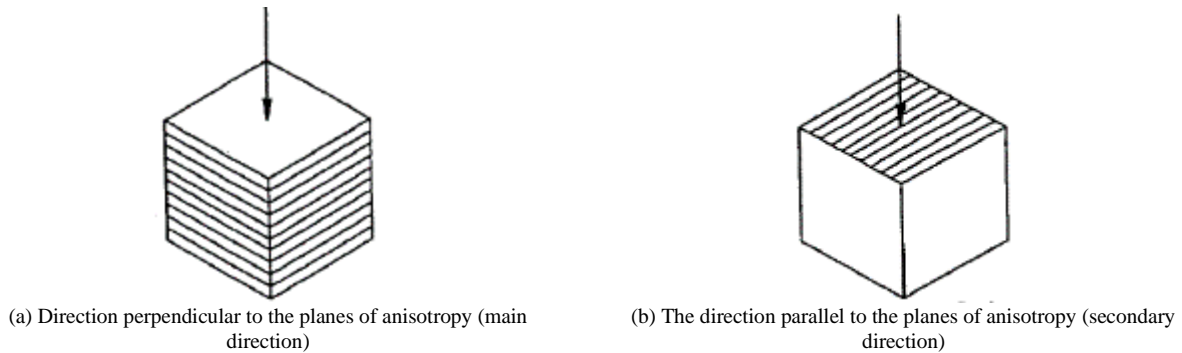


Figure 4. Direction of loading according to the anisotropy plan

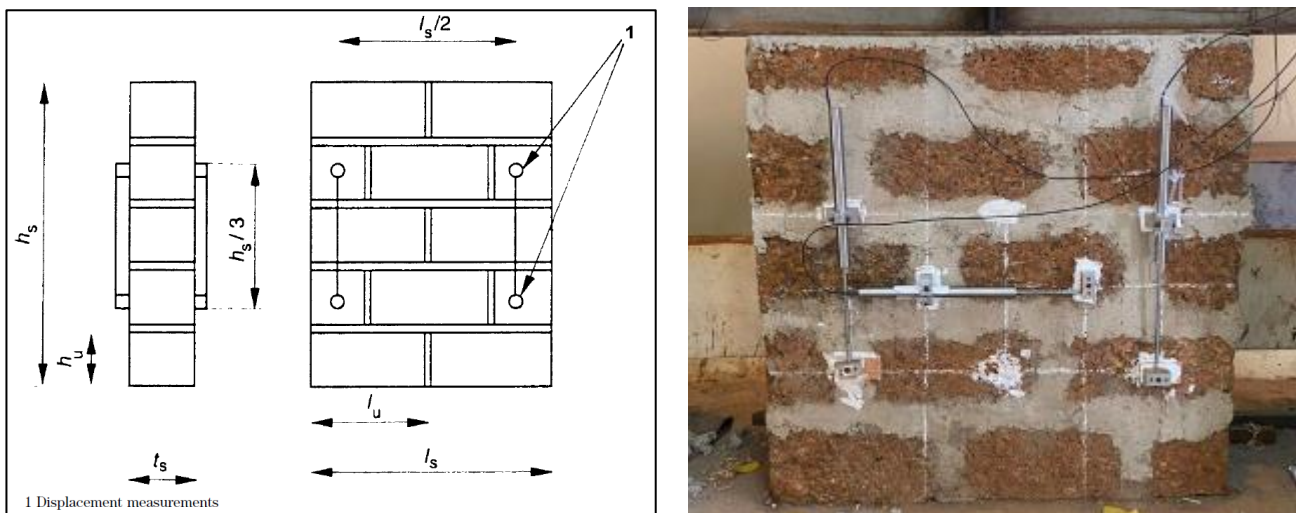


Figure 5. Device for compressive strength tests on walls

The specimens are equipped with four Linear Variable Differential Transformers (LVDT) displacement sensors placed in the vertical direction (2 on the front side and two on the back side) and an LVDT placed horizontally to measure the associated displacements (see Figure 5). The compressive load is applied gradually during the test by laps of 30% of the probable maximum load value from 0 to 30%, 30% to 60%, and then loaded until failure. The load is maintained constant for two minutes after each loading step. The compressive load is kept constant for two minutes to determine the deformations that have appeared and the creep degree. The maximum strength of the sample is obtained by dividing the load at the failure point by the loaded area of the sample. The characteristic strength equals the maximum strength divided by a safety factor 1.2 [45].

2.3. Empirical Formula

The empirical formula was determined based on the model defined in Equation 1. By composing this Equation by the natural logarithm function, it ends up with a linear equation with three variables:

$$\ln(f_k) = \ln(k) + \alpha \ln(f_b) + \beta \ln(f_m) \Rightarrow Z = \alpha X + \beta Y + K \tag{2}$$

where Z is $\ln(f_k)$, f_k is the characteristic compressive strength of the masonry, X is $\ln(f_b)$, f_b is the characteristic compressive strength of the block, Y is $\ln(f_m)$, f_m is the characteristic compressive strength of the mortar, K is $\ln(k)$, α , β and k are the coefficients to be determined.

The least squares method was used to determine the scalars by minimizing the errors between the predicted values of the model and the experimental values.

The least squares method for similar models on n values is given by the expression in Equation 3.

$$S(X, Y, Z) = \sum_{i=1}^n e_i^2 = \sum_{i=1}^n (\alpha X_i + \beta Y_i + K - Z_i)^2 \quad (3)$$

The minimum of the function S is found when its partial derivatives regarding the parameters needed are equal to zero.

The system, therefore, summarizes as solving the following matrix Equation:

$$\begin{bmatrix} \sum_i X_i^2 & \sum_i X_i Y_i & \sum_i X_i \\ \sum_i X_i Y_i & \sum_i Y_i^2 & \sum_i Y_i \\ \sum_i X_i & \sum_i Y_i & n \end{bmatrix} \begin{bmatrix} \alpha \\ \beta \\ K \end{bmatrix} = \begin{bmatrix} \sum_i X_i Z_i \\ \sum_i Y_i Z_i \\ \sum_i Z_i \end{bmatrix} \quad (4)$$

The accuracy of the model was evaluated by using the coefficient of determination (R^2), which is the percentage of variability explained by the model and the standard error of estimation (σ) expressed in MPa and given by the following Equations:

$$R^2 = 1 - \frac{\sqrt{\sum (f_i - f_k)^2}}{\sqrt{\sum (f_i - f_{moy})^2}} \quad (5)$$

$$\sigma = \sqrt{\frac{\sum (f_i - f_k)^2}{n-3}} \quad (6)$$

where f_i is the strength of the masonry predicted by the model, f_k is the strength measured experimentally, f_{moy} the arithmetic mean value of the experimental strengths, and n is the number of data studied. A value of R^2 close to 1 indicates a good fit of the model, and a value close to zero indicates a bad fit. At the same time, it is desirable that σ be as small as possible, implying that the data dispersion for the estimated value is minimal. The divisor $n - 3$ is used in Equation 6 rather than n to get an unbiased estimation; the value “3” is chosen since three parameters are to be determined: K , α , and β .

3. Results and Discussion

3.1. Failure Modes under Uniaxial Compression

Table 3 presents the compressive strength values of the LS blocks, mortar, and walls regarding the combinations. It is noticeable that there is no real impact on the type of sand used in the mix, whether it was the river's sand or quarry sand since there is no significant difference in their particle size distribution and for the same cement/sand ratio content, the compressive strength of the mortar are sensitively the same. Significant differences are noted when the cement/sand or water/cement ratio in mass varies.

Table 3. Result of compression tests

Quarry	Loading direction on the LS	Mortar	Block strength (MPa)	Mortar strength (MPa)	Characteristic strength of the wall (MPa)
DANO 1	Secondary	MO1	6.86	1.37	0.74
	Main	MO2	5.72	3.29	1.48
DANO 2	Secondary	MO2	5.50	1.37	0.62
	Main	MO1	2.18	3.03	0.88
KAMBOINSIN	Secondary	MO1	3.93	2.1	0.99
	Main	MO2	3.55	5.2	1.81

The failure modes observed during experiments are presented in Figure 6. The wall failure is initiated with vertical cracks parallel to the loading direction (Figure 6a). For walls assembled with blocks, they are laid in a direction parallel to the anisotropy planes of the blocks. In addition to longitudinal cracks, lateral cracks are crossing the thickness of the wall (Figure 6b). Most cracks are initiated in the upper quarter of the block's width (at the block-joint interface), between 40 and 60% of the breaking load on either side, and spread with ramifications up to the bottom of the wall. Similar observations have been made by Thamboo & Dhanasekar [28] on clay and compressed earth blocks and by Page [46] on terracotta blocks. Similar conclusions can be inferred from studies on some stone masonry structures [47].

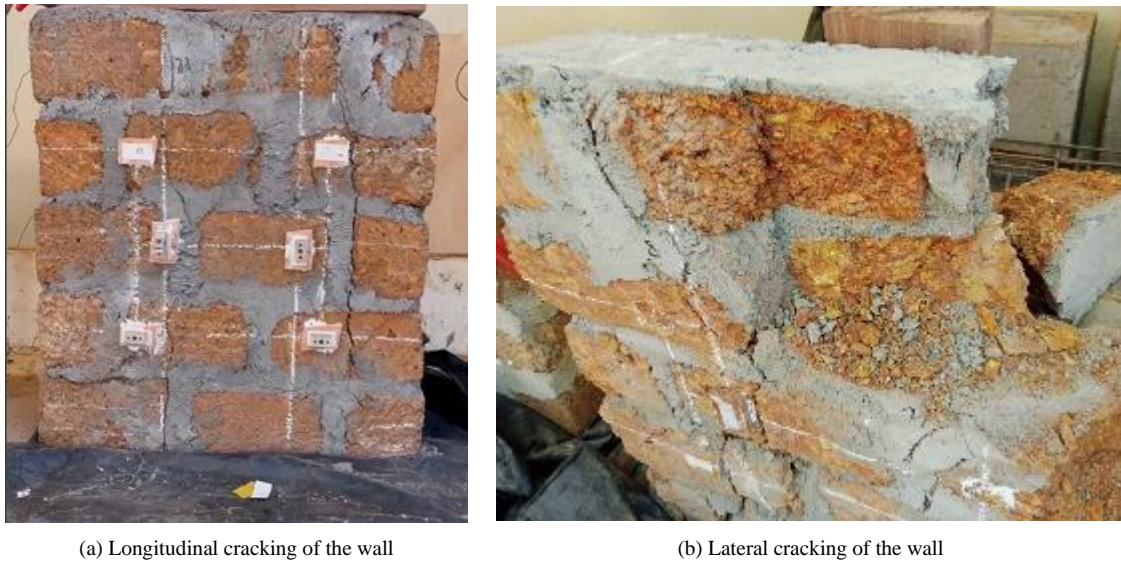


Figure 6. Failure mode of walls

Contrary to the works of Page [46], in most of the studied cases, the block presents a higher strength value than the mortar, which presents a higher strength value than the bulk masonry. Figure 7 presents the stress-strain curve of the tested walls. It should be noticed that the specimens constructed with blocks from DANO 1, which are the most rigid, present less deep axial deformations than those constructed with blocks from DANO 2, which are softer. In addition, the linear phase of the curve extends up to 100% of the failure strength for the walls of DANO 1 (brittle behavior) against 86% for the walls of DANO 2 (DANO 2 parallel direction taken as reference) with a slight ductility plateau after the peak (ductile behavior). These values are beyond the values observed by Kaushik et al. [23] (33%), Domède et al. [48] (40-50%), and Costigan et al. [49].

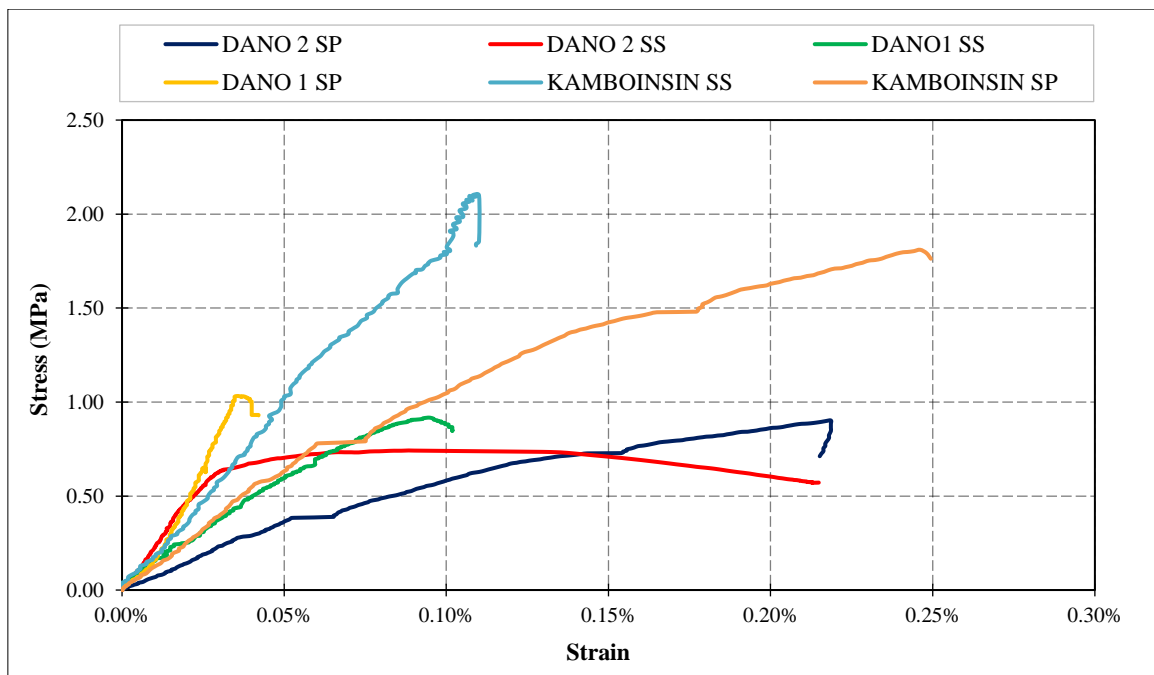


Figure 7. Stress-stain curves of the walls under uniaxial load

The notation "SP" and "SS" stand for "Main direction" and "Secondary direction," respectively, regarding the anisotropy plans presented in Figure 4.

3.2. Empirical Formula

The determined empirical formula (Equation 7) presents a greater sensitivity of the model to the strength of the mortar compared to the strength of the block with a coefficient of determination for the estimate R^2 equal to 0.94 and an approximation error of estimation σ of 4.13×10^{-2} MPa. The values of α and β proposed in the formula, obtained from the experimental campaign, show variations compared to the scientific literature. Contrary to the works of Pasala

Dayaratnam [29], who gives $\alpha = \beta = 0,5$, in this study, α is sensitively half of the value of β ; $\alpha \simeq \frac{\beta}{2}$. Even though the experimental tests conducted are limited, these variations show that the formulas proposed in the previous scientific literature do not correctly fit LS masonry behavior, including the results of Chourasia et al. [30], because of the biased input data used, as explained previously. It should also be noted that most of the studies on this subject are done on prism masonry. According to Thamboo & Dhanasekar [28], prisms overestimate the strength of masonry compared to walls.

$$f_k = 0.21(f_b)^{0.48}(f_m)^{0.94} \quad (7)$$

Furthermore, since primal failure signs appear at the interface between LS and vertical bed joint, the present solution seems more consistent than the formulas from prism masonry. The relationship established here was represented in 3 dimensions, with axis 1 for the compressive strength of the block, axis 2 for the compressive strength of the mortar, and axis 3 for the compressive strength of the masonry (Figure 8).

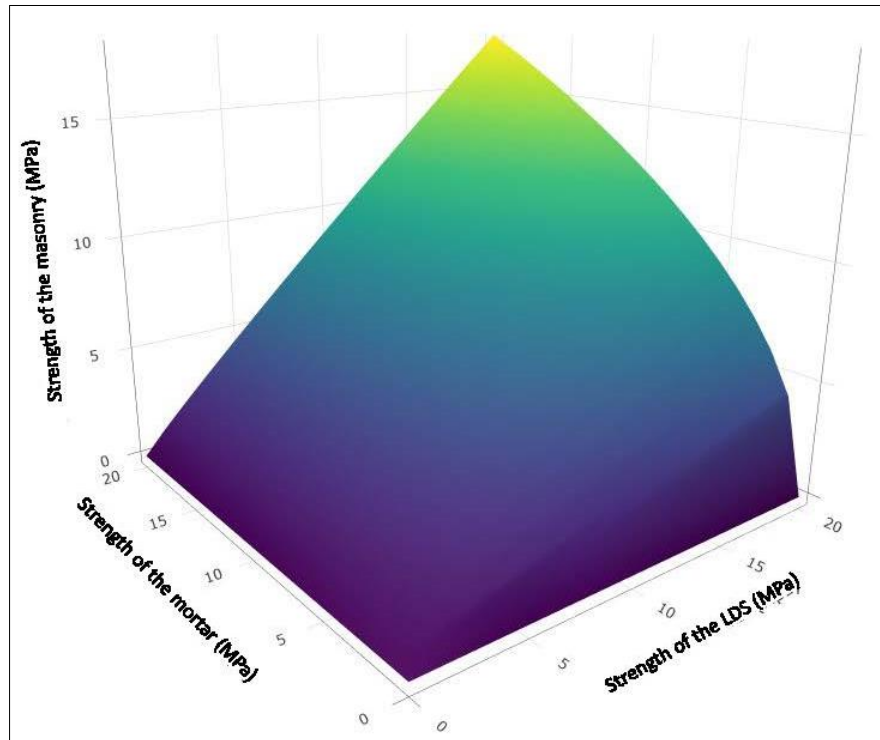


Figure 8. Graph showing the relationship between the strength of LS, mortar, and masonry

On the one hand, this figure shows a trend of logarithmic evolution of the masonry's compressive strength regarding the mortar's compressive strength in the plane formed by axes 2 and 3. On the other hand, Figure 8 shows a trend of linear evolution of the masonry's compressive strength regarding the block's compressive strength in the plane formed by axes 1 and 3. Regarding those profiles and based on the mathematical behaviors known of logarithm and linear functions and the fact that linear functions increase or decrease faster than logarithmic functions, it can be inferred that it is the strength of the laterite stone that primarily limits the resistance of the LS-based masonry since it reached its extremum values faster than the logarithm function of the mortar. Furthermore, the greater the mortar's compressive strength compared to the LS implies a better load-bearing capacity mobilization of the LS blocks and a more efficient structure. Thus, this induces greater resistance for the masonry. It is important to note that the European standard [15] avoids mortars over twice as strong as the masonry block. The opposite trend is observed when the masonry block is far stronger than the bed joint [50, 51].

Generally, the compressive strength of a masonry wall varies depending on different parameters. The compressive strength of the mortar used to bond the blocks plays a significant role in determining the overall compressive strength of the masonry wall. If the mortar is weaker than the blocks, it can become a weak link in the system, limiting the overall strength of the wall. The bond quality between the blocks and the mortar also affects the compressive strength of the masonry wall. Properly bonded blocks with good mortar joints can distribute loads more effectively and enhance the overall strength of the wall. The compressive strength of the individual blocks used in the masonry wall is crucial. Higher quality and stronger blocks will contribute to a stronger masonry wall overall. Weaker blocks may limit the overall strength of the wall, even if the mortar is strong. The construction techniques employed and the workmanship during the masonry wall assembly can impact its compressive strength. Proper installation methods, including correct mortar mixing and application, block placement, and curing practices, are essential for achieving optimal strength. The

design of the masonry wall, including factors such as wall height, thickness, reinforcement, and load-bearing requirements, can influence its compressive strength. A well-designed masonry wall, considering these factors, will typically have higher compressive strength. Overall, the compressive strength of a masonry wall about its constituent blocks and mortar is a complex interplay of various factors, and careful consideration of all these factors is necessary to ensure a structurally sound and strong masonry wall [52-54].

4. Conclusions

The main objective of this study was to propose an empirical, analytical model based on experimentations to calculate the characteristic compressive strength of unreinforced LS masonry having as inputs the compressive strength of blocks and mortar and exploring their different failure modes under uniaxial compression:

The analysis of the results allows the following conclusions to be drawn:

- The characteristic strength of LS-based masonry with thin joints (2 cm) and mortar of which the compressive strength does not exceed twice the strength of laterite stone block is quite accurate by the relation $f_k = 0,21(f_b)^{0,48}(f_m)^{0,94}$ for 135 mm thick walls.
- The strength of the walls varies between 0.6 and 1.8 MPa, with a failure that generally begins at 40 to 60% of the maximum strength by the appearance of vertical cracks at a quarter of their width.
- The walls made with the blocks of DANO 1 have a brittle behavior, with a linear phase of the axial stress-strain curve reaching 100% of the breaking strength of the walls, contrary to the blocks of DANO 2, which are softer and have a ductile behavior. The blocks from KAMBOINSIN are in an interval between brittle and low ductile behavior.

However, to generalize the empirical formula to large-scale walls, it would be relevant to study the model's sensitivity to the variation in the size of the blocks and the mortar thickness. It should also be suitable for further studies to integrate as additional parameters various geometries of the wall that will impact the parameter "k" value.

5. Declarations

5.1. Author Contributions

Conceptualization, A.L. and A.P.; methodology, D.D.D. and M.D.; software, W.K.B.; validation, A.L., A.P., M.P., and D.D.D.; formal analysis, H.S.M.; investigation, H.S.M. and W.K.B.; resources, A.L.; writing—original draft preparation, H.S.M. and W.K.B.; writing—review and editing, A.L. and A.P.; supervision, A.L., D.D.D., and M.D.; project administration, A.L.; funding acquisition, A.L. All authors have read and agreed to the published version of the manuscript.

5.2. Data Availability Statement

The data presented in this study are available on request from the corresponding author.

5.3. Funding

The World Bank Group and Institute 2iE have funded the thesis of which this study is part.

5.4. Acknowledgements

The World Bank supported this work through its project "African Center of Excellence" (CEA-IMPACT) and College of Engineering (CoE).

5.5. Conflicts of Interest

The authors declare no conflict of interest.

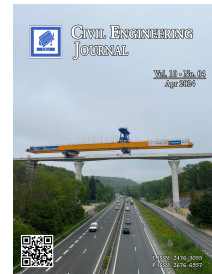
6. References

- [1] Lawane Gana, A. (2014). Characterization of indurated lateritic materials for better use in housing in Africa. PhD Thesis, University of Le Havre, Le Havre, France. (In French).
- [2] Ndzié Mvindi, A. T., Onana, V. L., Ngo'o Ze, A., Ohandja, H. N., & Ekodeck, G. E. (2017). Influence of hydromorphic conditions in the variability of geotechnical parameters of gneiss-derived lateritic gravels in a savannah tropical humid area (Centre Cameroon), for road construction purposes. *Transportation Geotechnics*, 12, 70–84. doi:10.1016/j.trgeo.2017.08.003.
- [3] Oyelami, C. A., & Van Rooy, J. L. (2016). A review of the use of lateritic soils in the construction/development of sustainable housing in Africa: A geological perspective. *Journal of African Earth Sciences*, 119, 226–237. doi:10.1016/j.jafrearsci.2016.03.018.





- [4] Abhilash, H. N., McGregor, F., Millogo, Y., Fabbri, A., Séré, A. D., Aubert, J. E., & Morel, J. C. (2016). Physical, mechanical and hygrothermal properties of lateritic building stones (LBS) from Burkina Faso. *Construction and Building Materials*, 125, 731–741. doi:10.1016/j.conbuildmat.2016.08.082.
- [5] Lawane, A., Pantet, A., Vinai, R., & Thomassin, J. H. (2011). Geological and geomechanical study of Dano laterites (Burkina Faso) for use in housing. (In French).
- [6] Kasthurba, A. K., Santhanam, M., & Mathews, M. S. (2007). Investigation of laterite stones for building purpose from Malabar region, Kerala state, SW India - Part 1: Field studies and profile characterisation. *Construction and Building Materials*, 21(1), 73–82. doi:10.1016/j.conbuildmat.2005.07.006.
- [7] Vasanelli, E., Colangiuli, D., Calia, A., Sbartaï, Z. M., & Breyse, D. (2017). Combining non-invasive techniques for reliable prediction of soft stone strength in historic masonries. *Construction and Building Materials*, 146, 744–754. doi:10.1016/j.conbuildmat.2017.04.146.
- [8] Zoungrana, O., Bologo/Traoré, M., Messan, A., Nshimiyimana, P., & Pirotte, G. (2021). The Paradox around the Social Representations of Compressed Earth Block Building Material in Burkina Faso: The Material for the Poor or the Luxury Material? *Open Journal of Social Sciences*, 9(1), 50–65. doi:10.4236/jss.2021.91004.
- [9] Zoungrana, O., Bologo-Traore, M., Hema, C., Nshimiyimana, P., Pirotte, G., & Messan, A. (2020). Sustainable habitat in Burkina Faso: Social trajectories, logics and motivations for the use of compressed earth blocks for housing construction in ouagadougou. *WIT Transactions on the Built Environment*, 195, 165–172. doi:10.2495/ARC200131.
- [10] Ouedraogo, A. L. S.-N., Hema, C., N'guiro, S. M., Nshimiyimana, P., & Messan, A. (2024). Optimisation of Thermal Comfort of Building in a Hot and Dry Tropical Climate: A Comparative Approach between Compressed Earth/Concrete Block Envelopes. *Journal of Minerals and Materials Characterization and Engineering*, 12(1), 1–16. doi:10.4236/jmmce.2024.121001.
- [11] Nshimiyimana, P., Hema, C., Zoungrana, O., Courard, L., & Messan, A. (2022). Contribution to improving the quality of raw earth habitat in Burkina Faso. *NoMaD 2022*, 16-17 November, 2022, Montpellier, French. (In French).
- [12] Moussa, H. S., Nshimiyimana, P., Hema, C., Zoungrana, O., Messan, A., & Courard, L. (2019). Comparative Study of Thermal Comfort Induced from Masonry Made of Stabilized Compressed Earth Block vs Conventional Cementitious Material. *Journal of Minerals and Materials Characterization and Engineering*, 7(6), 385–403. doi:10.4236/jmmce.2019.76026.
- [13] Hema, C., Ouédraogo, A. L. S. N., Bationo, G. B., Kabore, M., Nshimiyimana, P., & Messan, A. (2024). A field study on thermal acceptability and energy consumption of mixed-mode offices building located in the hot-dry climate of Burkina Faso. *Science and Technology for the Built Environment*, 30(2), 184–193. doi:10.1080/23744731.2023.2291007.
- [14] Kaboré, M., Lawane, A., Sawadogo, C., Lo, M., Messan, A., & Pantet, A. (2019). Études expérimentales du comportement mécanique sous charges verticales des maçonneries en Blocs de Latérite Taillée (BLT). *Afrique SCIENCE*, 15(1), 201–213.
- [15] NF EN 1996-1-1+A1. (2013). Eurocode 6 - Design of masonry structures - Part 1-1: general rules for reinforced and unreinforced masonry structures. AFNOR Editions, Saint-Denis, France. (In French).
- [16] Alili, S. (2013). Technical guide for an operation to rehabilitate the village architectural heritage of Kabylie. Ph.D. Thesis, University of Tizi Ouzou, Tizi Ouzou, Algeria. (In French).
- [17] Hendry, A. W., & Malek, M. H. (1986). Characteristic Compressive Strength of Brickwork Walls from Collected Test Results. *International Masonry Institute*, 7, 15–24.
- [18] Lourenço, P. B., & Pina-Henriques, J. (2006). Validation of analytical and continuum numerical methods for estimating the compressive strength of masonry. *Computers and Structures*, 84(29–30), 1977–1989. doi:10.1016/j.compstruc.2006.08.009.
- [19] Mann, W. (1982). Statistical evaluation of tests on masonry by potential functions. Sixth international brick masonry conference, 16-19 May, 1982, Rome, Italy.
- [20] Engesser, F. (1907). Over long-span arched bridges. *Zeitschrift für Architekturs und Ingenieurwesen*, 53, 403-440. (In German).
- [21] Garzón-Roca, J., Marco, C. O., & Adam, J. M. (2013). Compressive strength of masonry made of clay bricks and cement mortar: Estimation based on Neural Networks and Fuzzy Logic. *Engineering Structures*, 48, 21–27. doi:10.1016/j.engstruct.2012.09.029.
- [22] Dymiotis, C., & Gutleiderer, B. M. (2002). Allowing for uncertainties in the modelling of masonry compressive strength. *Construction and Building Materials*, 16(8), 443–452. doi:10.1016/S0950-0618(02)00108-3.
- [23] Kaushik, H. B., Rai, D. C., & Jain, S. K. (2007). Stress-Strain Characteristics of Clay Brick Masonry under Uniaxial Compression. *Journal of Materials in Civil Engineering*, 19(9), 728–739. doi:10.1061/(asce)0899-1561(2007)19:9(728).
- [24] Basha, S. H., & Kaushik, H. B. (2015). Evaluation of Nonlinear Material Properties of Fly Ash Brick Masonry under Compression and Shear. *Journal of Materials in Civil Engineering*, 27(8), 4014227. doi:10.1061/(asce)mt.1943-5533.0001188.
- [25] Llorens, J., Llorens, M., Chamorro, M. A., & Soler, J. (2020). Experimental Behavior of Brick Masonry under Uniaxial Compression on Parallel-to-Face Brick. Single-Leaf Case Study. *International Journal of Architectural Heritage*, 14(1), 23–37. doi:10.1080/15583058.2018.1503361.

- [26] Kandymov, N., Mohd Hashim, N. F., Ismail, S., & Durdyev, S. (2022). Derivation of Empirical Relationships to Predict Cambodian Masonry Strength. *Materials*, 15(14), 5030. doi:10.3390/ma15145030.
- [27] Kumavat, H. R. (2016). An Experimental Investigation of Mechanical Properties in Clay Brick Masonry by Partial Replacement of Fine Aggregate with Clay Brick Waste. *Journal of The Institution of Engineers (India): Series A*, 97(3), 199–204. doi:10.1007/s40030-016-0178-7.
- [28] Thamboo, J. A., & Dhanasekar, M. (2019). Correlation between the performance of solid masonry prisms and wallettes under compression. *Journal of Building Engineering*, 22, 429–438. doi:10.1016/j.jobe.2019.01.007.
- [29] Dayaratnam, P. (1987). *Brick and reinforced brick structures*. South Asia Books, Delhi, India.
- [30] Chourasia, A., Singhal, S., & Chourasia, A. (2023). Numerical simulation of laterite confined masonry building subjected to quasi-static monotonic lateral loading. *Journal of Structural Integrity and Maintenance*, 8(1), 1–11. doi:10.1080/24705314.2022.2142895.
- [31] Sajanthan, K., Balagasan, B., & Sathiparan, N. (2019). Prediction of compressive strength of stabilized earth block masonry. *Advances in Civil Engineering*, 2019. doi:10.1155/2019/2072430.
- [32] Caldeira, F. E., Nalon, G. H., Oliveira, D. S. de, Pedroti, L. G., Ribeiro, J. C. L., Ferreira, F. A., & Carvalho, J. M. F. de. (2020). Influence of joint thickness and strength of mortars on the compressive behavior of prisms made of normal and high-strength concrete blocks. *Construction and Building Materials*, 234. doi:10.1016/j.conbuildmat.2019.117419.
- [33] Lawrence, S. J., & Page, A. W. (2008). *New Australian standards for masonry in small structures*. Proc. 14 IBMAC, Sydney, Australia.
- [34] Mojsilović, N., & Stewart, M. G. (2015). Probability and structural reliability assessment of mortar joint thickness in load-bearing masonry walls. *Structural Safety*, 52, 209–218. doi:10.1016/j.strusafe.2014.02.005.
- [35] Sarhat, S. R., & Sherwood, E. G. (2014). The prediction of compressive strength of ungrouted hollow concrete block masonry. *Construction and Building Materials*, 58, 111–121. doi:10.1016/j.conbuildmat.2014.01.025.
- [36] Thaickavil, N. N., & Thomas, J. (2018). Behaviour and strength assessment of masonry prisms. *Case Studies in Construction Materials*, 8, 23–38. doi:10.1016/j.cscm.2017.12.007.
- [37] Fortes, E. S., Parsekian, G. A., & Fonseca, F. S. (2015). Relationship between the Compressive Strength of Concrete Masonry and the Compressive Strength of Concrete Masonry Units. *Journal of Materials in Civil Engineering*, 27(9), 4014238. doi:10.1061/(asce)mt.1943-5533.0001204.
- [38] Rizaee, S., Hagel, M. D., Kaheh, P., & Shrive, N. (2016). *Comparison of compressive strength of concrete block masonry prisms and solid concrete prisms*. Brick and Block Masonry, CRC Press, Boca Raton, United States. doi:10.1201/b21889-228.
- [39] NF EN 771-6 + A1. (2015). *Specifications for masonry units - Part 6: natural stone masonry units*. AFNOR Editions, Saint-Denis, France. (In French).
- [40] NF EN 13373. (2020). *Test methods for natural stones - Determination of dimensions and other geometric characteristics*. AFNOR Editions, Saint-Denis, France. (In French).
- [41] NF EN 998-2. (2016). *Definitions and specifications of mortars for masonry - Part 2: mortars for mounting masonry units*. AFNOR Editions, Saint-Denis, France. (In French).
- [42] NF EN 772-16. (2011). *Methods of testing masonry elements - Part 16: determination of dimensions*. AFNOR Editions, Saint-Denis, France. (In French).
- [43] NF EN 772-1 + A1. (2015). *Methods of testing masonry units - Part 1: determination of compressive strength*. AFNOR Editions, Saint-Denis, France. (In French).
- [44] NF EN 1015-11. (2019). *Methods of testing mortars for masonry - Part 11: determination of flexural and compressive strength of hardened mortar*. AFNOR Editions, Saint-Denis, France. (In French).
- [45] NF EN 1052-1. (1999). *Masonry testing methods - Part 1: determination of compressive strength*. AFNOR Editions, Saint-Denis, France. (In French).
- [46] PAGE, A. (1981). The Biaxial Compressive Strength of Brick Masonry. *Proceedings of the Institution of Civil Engineers*, 71(3), 893–906. doi:10.1680/iicep.1981.1825.
- [47] Wang, Z., Li, L., Zhou, J., Chen, R., Leng, J., Zhang, H., & Yang, J. (2024). Experimental investigation and calculation method of the interfacial bonding performance of stone masonry reinforced with UHPC. *Journal of Building Engineering*, 85, 108435. doi:10.1016/j.jobe.2024.108435.
- [48] Domède, N., Pons, G., Sellier, A., & Fritih, Y. (2009). Mechanical behaviour of ancient masonry. *Materials and Structures/Materiaux et Constructions*, 42(1), 123–133. doi:10.1617/s11527-008-9372-z.

- [49] Costigan, A., Pavía, S., & Kinnane, O. (2015). An experimental evaluation of prediction models for the mechanical behavior of unreinforced, lime-mortar masonry under compression. *Journal of Building Engineering*, 4, 283–294. doi:10.1016/j.jobe.2015.10.001.
- [50] Zahra, T., Thamboo, J., & Asad, M. (2021). Compressive strength and deformation characteristics of concrete block masonry made with different mortars, blocks and mortar beddings types. *Journal of Building Engineering*, 38. doi:10.1016/j.jobe.2021.102213.
- [51] Álvarez-Pérez, J., Chávez-Gómez, J. H., Terán-Torres, B. T., Mesa-Lavista, M., & Balandrano-Vázquez, R. (2020). Multifactorial behavior of the elastic modulus and compressive strength in masonry prisms of hollow concrete blocks. *Construction and Building Materials*, 241. doi:10.1016/j.conbuildmat.2020.118002.
- [52] Abu-Bakr, M., Mahmood, H. F., Mohammed, A. A., & Ahmed, S. A. (2024). Evaluation of mechanical properties and shear-bond strength of mortar containing natural extract admixture. *Construction and Building Materials*, 418, 135377. doi:10.1016/j.conbuildmat.2024.135377.
- [53] Zhang, P., Fan, S., Liu, Y., Su, C., Hu, J., & Sheikh, S. A. (2024). Axial compressive performance of masonry columns strengthened with ECC jacket and FRP strips. *Engineering Structures*, 304, 117661. doi:10.1016/j.engstruct.2024.117661.
- [54] Corradi, M., Borri, A., & Vignoli, A. (2003). Experimental study on the determination of strength of masonry walls. *Construction and Building Materials*, 17(5), 325–337. doi:10.1016/S0950-0618(03)00007-2.



Properties and Microstructure of Treated Coal Bottom Ash as Cement Concrete Replacement

Moad Alost ¹, Ahmed Mamdouh ², Hussein Al Mufargi ¹, Farah N. A. Abd Aziz ²,
Ahmed Rashid ², Otman M. M. Elbasir ³, Husam Al Dughaiishi ^{1, 4*}

¹ Department of Civil and Environmental Engineering, College of Engineering, University of Nizwa, Ad-Dakhliyah, Oman.

² Housing Research Centre, Department of Civil Engineering, Faculty of Engineering, Universiti Putra Malaysia, Serdang, Selangor, Malaysia.

³ Department of Civil Engineering, High Institute of Science and Technology, Qasr Bin Ghashir 22131, Libya.

⁴ Department of Civil Engineering, Faculty of Engineering, Universiti Malaya, Kuala Lumpur 50603, Malaysia.

Received 05 December 2023; Revised 14 March 2024; Accepted 19 March 2024; Published 01 April 2024

Abstract

Sustainable construction is a rapidly growing area of research focused on using industrial waste to replace Portland cement in concrete. This approach not only reduces CO₂ emissions from cement production but also serves as an effective way to diminish the environmental impact of concrete production. This study aims to investigate the properties of Coal Bottom Ash (CBA) after undergoing two different treatments: flotation and burning. It also evaluates the impact of CBA as a cement replacement in concrete with different replacement percentages (5%, 10%, 15%, and 20%). Chemical analysis of CBA has revealed that it can be classified as a pozzolanic material due to its high content of silicates, aluminates, and iron oxides. The microstructure of CBA showed a porous, angular, and irregular surface with many voids. The findings of this study revealed that the optimum mix was 10% CBA, resulting in a 2% increase in compressive strength compared to the control mix after 56 days of curing. Additionally, the study evaluated the effects of sulfate and chloride on concrete. It was found that the mix with the burning treatment showed an overall increase in strength, while the flotation treatment did not reach the control mix's strength in any of the curing periods. Furthermore, the results demonstrated that CBA has significant potential as a cement replacement material, and the burning treatment showed improvement in concrete's overall properties compared to the raw material in terms of mechanical and chemical properties while reducing greenhouse gas emissions and enhancing the environment.

Keywords: Industrial Waste; Material Properties; Coal Bottom Ash; Compressive Strength; Microstructure.

1. Introduction

1.1. Research Background

Concrete is one of the most widely used and versatile construction materials in the world, capable of being molded into various shapes and sizes and known for its high strength and durability [1–3]. It is used to build structures, bridges, dams, and other infrastructure, including the Burj Khalifa, the tallest building in the world, which was constructed with 333,000 cubic meters of concrete [4–6]. However, concrete also has a significant environmental impact, as its main ingredient, Portland cement, accounts for about 8% of global CO₂ emissions [7–10]. Furthermore, the production and disposal of concrete generate large amounts of waste and pollution.

* Corresponding author: husam@unizwa.edu.om

 <http://dx.doi.org/10.28991/CEJ-2024-010-04-08>



© 2024 by the authors. Licensee C.E.J, Tehran, Iran. This article is an open access article distributed under the terms and conditions of the Creative Commons Attribution (CC-BY) license (<http://creativecommons.org/licenses/by/4.0/>).

Therefore, there is a need for more sustainable and eco-friendly alternatives to Portland cement in concrete production. One of the potential alternatives is the use of industrial waste materials, such as fly ash, slag, silica fume, and rice husk ash, as cement substitutes in concrete. These materials, known as pozzolans, are substances that react with calcium hydroxide and water to form cementitious compounds. Using pozzolans in concrete can reduce the amount of Portland cement required, thereby lowering CO₂ emissions and the cost of concrete production. Moreover, pozzolans can improve the properties and performance of concrete, such as its strength, durability, workability, and resistance to chemical attacks.

However, not all pozzolans are equally available and suitable for concrete production. Some, such as fly ash and slag, are in high demand and may face supply shortages in the future [11, 12]. Others, like silica fume and rice husk ash, are expensive and difficult to handle and store. Therefore, more research is needed on the feasibility and effectiveness of other pozzolanic materials that are abundant, inexpensive, and easy to use.

One such material is Coal Bottom Ash (CBA), a by-product of coal combustion in thermal power plants. According to the American Coal Ash Association (ACAA), 40.13 percent of the coal ash production rate, or 12 million tons of CBA, was produced in 2015 [13, 14]. CBA has been identified as a substance that endangers human health and safety. However, it also has a high potential to be used as a pozzolan in concrete due to its high content of silicate, aluminate, and iron oxide, which are the main components of pozzolanic reactions. Moreover, CBA's porous, angular, and irregular shape and texture can enhance the interlocking and bonding between aggregates and the cement paste in concrete.

The use of CBA as a cement substitute in concrete has been studied by several researchers, but the results are inconsistent and inconclusive. Some studies have reported that CBA can improve the strength, durability, and workability of concrete [15–22], while others have found that CBA can reduce these properties [23–25]. The discrepancies may be due to the different sources, compositions, and treatments of CBA, as well as the different mix proportions, curing conditions, and testing methods of concrete.

Therefore, there is a research gap in the literature on the properties and effects of CBA as a cement substitute in concrete, especially after undergoing different treatments. These treatments can alter the physical and chemical characteristics of CBA, affecting its performance and compatibility with concrete. They can also reduce the environmental impact of CBA disposal by transforming it into a more valuable and useful material. The aim of this research is to bridge this crucial knowledge gap by thoroughly exploring the effects of two distinct treatments—flotation and burning—on CBA, with a particular emphasis on the use of finer particles (100 microns). Flotation, a method that leverages air bubbles and water, segregates these lighter, finer CBA particles from their heavier, coarser counterparts. Conversely, the burning process incinerates organic matter and carbon content within CBA through the application of high temperatures and oxygen. Furthermore, this study delves into the potential of finely processed CBA to serve as a substitute for traditional cement in concrete, examining a range of replacement ratios (5%, 10%, 15%, and 20%).

1.2. Literature Review

CBA, a by-product of coal combustion in thermal power plants, is influenced by coal type, combustion conditions, and collection methods. In 2015, the ACAA reported that 40.13 percent of the coal ash production, equivalent to 12 million tons of CBA, was generated [11]. CBA exhibits diverse sizes (0.075 to 19 mm) and shapes (spherical, angular, or irregular). The ratio of fly ash to bottom ash, dependent on coal type and combustion temperature, typically ranges from 25% to 90% [16, 26]. Key concrete production parameters like specific gravity, water absorption, and fineness modulus are influenced by CBA's size and shape variations. The specific gravity of CBA ranges from 1.39 to 2.66, which is lower than that of natural aggregates, and water absorption ranges from 3.7% to 20%, with the fineness modulus ranging from 2.2 to 3.0 [1, 13, 23, 27]. CBA's chemical composition, comprising silica (SiO₂), alumina (Al₂O₃), and iron oxide (Fe₂O₃), accounts for 50% to 80% of its mass [25]. These components contribute to pozzolanic reactions in concrete. However, impurities like carbon (1% to 20%), sulfur (0.1% to 2%), and chlorine (0.01% to 0.1%) vary, impacting CBA's reactivity [17, 24, 28]. High carbon content reduces specific gravity and increases water absorption, affecting mix design and workability. Sulfur content may lead to sulfate attack, damaging concrete structures, while chlorine content can cause chloride attack, potentially corroding steel reinforcement in concrete [8, 27, 29]. Careful consideration of CBA's variability is crucial for its effective use in concrete applications.

The impact of CBA on the workability of freshly made concrete is highlighted by its influence on the surface area, shape, water content, and texture of the added materials. The use of CBA as an alternative to Portland Cement (PC) notably affects concrete's fresh properties by enhancing inter-particle friction, which restricts the free flow of concrete. Specifically, concrete with 10% Ground CBA showed a decrease in slump values by about 10%, indicating reduced workability compared to control concrete due to the Ground CBA's additional water absorption and its uneven surface texture [11]. Conversely, other investigations noted an improvement in workability with increased Ground CBA content, though explanations for these findings were not fully discussed [30].

Grinding can also reduce the water absorption and increase the specific gravity of CBA, which can affect the mix design and the workability of concrete. Singh et al. reported that grinding CBA for 60 minutes reduced the particle size

from 4.75 mm to 75 μm and increased the pozzolanic activity index from 55% to 85%. Ground CBA in concrete significantly enhances resistance to chloride attack, reducing chloride migration and diffusion. Concrete with 10% CBA shows 1.7 times lower chloride migration than with Fly Ash (FA), and 25% CBA achieves 3.8 times lower diffusion than with 25% FA. The chloride penetration depth decreases from 76 mm in control concrete to 17 mm with increased CBA content, indicating improved chloride resistance with CBA use [17, 30].

Pulverizing is a process that crushes and grinds the CBA particles into a fine powder using high pressure and impact. Pulverizing can increase the fineness and pozzolanicity of CBA, which can improve the reactivity and strength of concrete. Pulverizing can also reduce the water absorption and increase the specific gravity of CBA, affecting the mix design and workability of concrete. Jamaluddin et al. reported that pulverizing CBA for 30 minutes reduced the particle size from 4.75 mm to 45 μm [13, 27].

The compressive strength of concrete with CBA replacement varies with CBA content and curing time. At low replacement levels (3.7%), compressive strength increased by 6%, while higher levels (up to 43.7%) reduced strength by 8% to 30% after 28–90 days, compared to control concrete. However, extended curing showed strength improvements, attributed to CBA's pozzolanic activity. Certain studies found that 15%–20% CBA replacements could equal or surpass control strength at later curing stages, indicating a complex relationship between CBA's physical properties, replacement percentage, and concrete's compressive strength over time [30].

Flexural strength results from CBA in concrete show variable outcomes. Up to a 15% CBA substitution, improvements are noted, with flexural strength increasing by 23% at a 30% replacement level when mixed with Aluminum powder. However, high-volume substitutions (70%) lead to decreased strength, although adding lime can mitigate this effect, enhancing strength at all curing periods. The impact of CBA on flexural strength is thus dependent on the level of substitution and the addition of other materials [23, 28, 30]. On the other hand, Jamaluddin et al. demonstrated that self-compacting concrete (SCC) incorporating CBA as a partial fine aggregate replacement exhibited decreased flexural strength, particularly as the water to cement ratio increased from 0.35 to 0.45. The reduction in flexural strength was observed with the increase in CBA content up to 30% volumetric replacement of natural sand. This suggests that while CBA can be used in SCC, its inclusion at higher percentages may adversely affect the concrete's structural performance, especially in terms of its flexural capabilities [13].

Khan et al. research highlights the potential of ground CBA as a supplementary cementitious material to improve the durability of concrete against acid and sulfate attacks [31]. The findings suggest that not only does the replacement level of CBA influence the concrete's resistance to such attacks, but also that ground CBA can enhance the long-term performance of concrete by reducing the penetrability of harmful agents. Resistance to sulfate attack in concrete with a 10% replacement of Portland Cement (PC) by Ground CBA was evaluated over curing periods of 28 to 90 days. Results indicated that mixes with Ground CBA demonstrated comparable or improved resistance against sulfate deterioration compared to control mixes without CBA.

1.3. Motivation and Objective

Several researchers have emphasized that CBA is a toxic material posing risks to human health and safety, as noted in the literature review. To enhance the quality of concrete while promoting a greener and more sustainable world, an innovative and environmentally friendly method has been developed for reusing or recycling industrial waste, such as CBA, in concrete mixtures. Key factors considered to improve the mechanical properties of concrete include the amount of cement replacement material, the treatment method applied to the CBA, and the curing times. The microstructure and chemical composition of CBA are also crucial elements for concrete bonding that must be considered. The durability of ordinary Portland cement (OPC) in harsh environmental conditions—such as those encountered in wastewater treatment plants, underground structures, and coastal structures—significantly impacts the performance of concrete structures. Therefore, enhancing concrete's permeability might accelerate damage by facilitating quicker penetration of harmful substances.

This study aims to enhance the mechanical and durability properties of concrete, including its compressive, tensile, and flexural strengths, alongside evaluating slump test results. It will also examine concrete's resilience against environmental challenges like sulfate and chloride attacks to fully utilize CBA as a sustainable cement alternative. Given the inconsistent findings from previous research on CBA's impact—particularly regarding the effects of flotation, burning treatments, and the incorporation of finer particles (100 microns)—this research seeks to address these discrepancies. It focuses on a thorough assessment of CBA's role as a cement substitute, aiming to clarify its application for improved concrete sustainability and durability.

The purpose of this study is to illustrate the importance of evaluating the effects of different CBA replacement percentages on the fresh properties of concrete. It aims to assess the impact of CBA percentages as a replacement for cement on the characteristics of freshly poured and hardened concrete. Furthermore, the study seeks to determine the impact of carbon treatments, such as burning and flotation, on CBA-enhanced concrete, focusing on the mechanical characteristics of both fresh and hardened concrete. Additionally, it involves evaluating the impact of various CBA treatments on the strength and durability development of concrete incorporating CBA.

2. Material and Methods

The quality of Concrete Bottom Ash (CBA) concrete, as illustrated in Figure 1, is analyzed by examining the chemical and mechanical properties of CBA as a substitute for cement, as well as the microstructure of the ash particles. This study typically begins with a literature review, gathering data from various publications and scholarly articles, before proceeding to experimental testing. To enhance the pozzolanic reaction, CBA will undergo two types of treatments in this study: burning therapy and flotation treatment. The mechanical characteristics of CBA and the microstructure of each treatment will be examined using varied CBA proportions of 5%, 10%, 15%, and 20% to identify the most optimal and efficient percentage for CBA concrete proportions as a cement replacement material. The mechanical properties to be evaluated include splitting tensile, compressive strength, and flexural strength tests. On the other hand, X-ray fluorescence (XRF) tests and scanning electron microscopy (SEM) are used to examine the microstructure and chemical composition of CBA. Additionally, after every 28 and 56 days for various mixes, the following tests for chemical properties will be carried out: compression test, water absorption test, sulfate penetration test, and chloride penetration test.

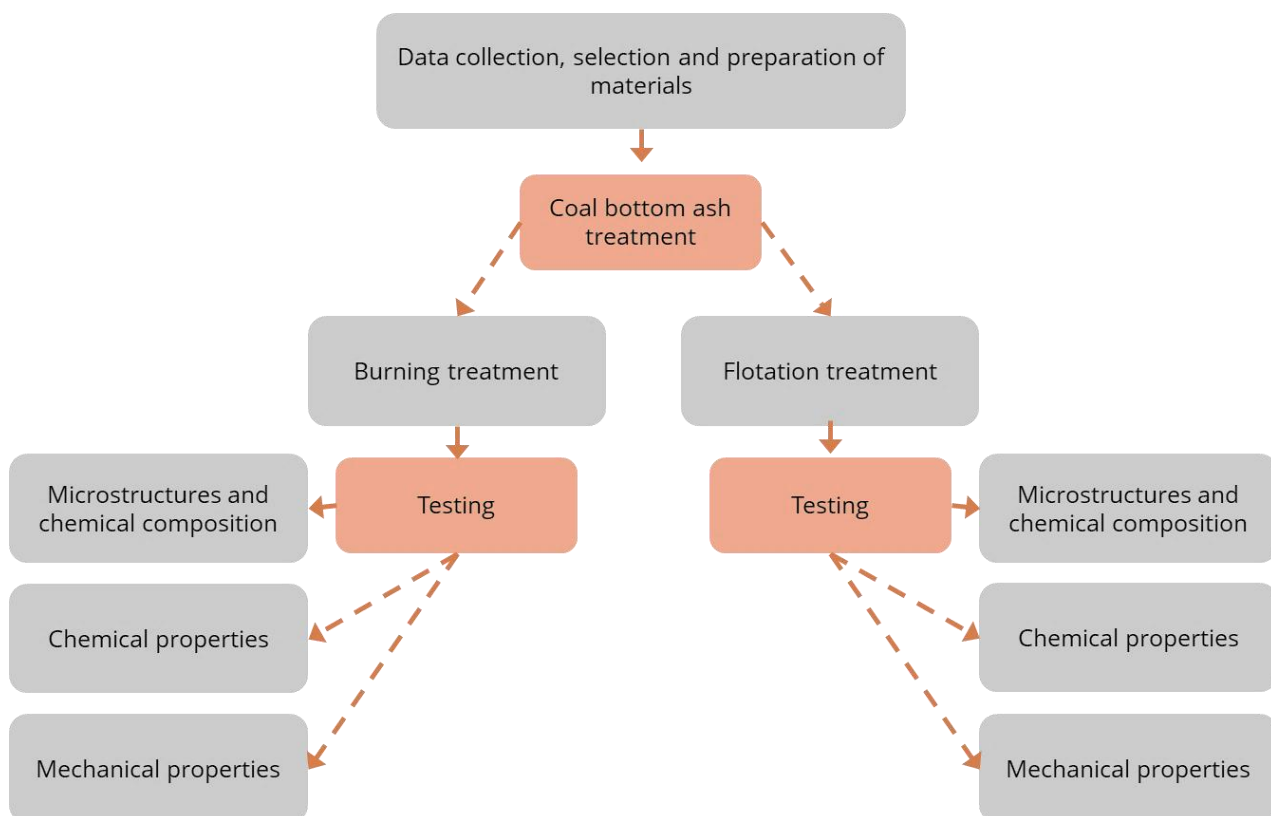


Figure 1. Flowchart of methodology

Throughout this research, nine cubes for each mix of CBA as a cement replacement material—5%, 10%, 15%, and 20%, as well as the control mix, with three cubes for varying curing times of 7, 28, and 56 days—were subjected to compression tests. Additionally, only a 28-day curing period is used for the flexural test on three prism specimens for each combination. Similar to the splitting tensile test, six specimens are prepared for each combination for curing times of 7 and 28 days. Additionally, the samples' chemical properties will be determined by a 5% concentration of chloride and sulfate solution, which other researchers have identified as appropriate. Three samples from each mixture will be evaluated to obtain an average result. The two different treatment techniques used in this investigation, flotation and burning, are depicted in Figure 1.

2.1.1. Burning Treatment

According to Ibrahim et al. [32], this treatment procedure begins with burning the CBA at a temperature of 110 ± 5 for 24 hours before grinding it in a Los Angeles machine for two hours. The particles formed from such a process are then employed in the experiment and have passed a sieve size of 100 microns as shown in Figure 2.

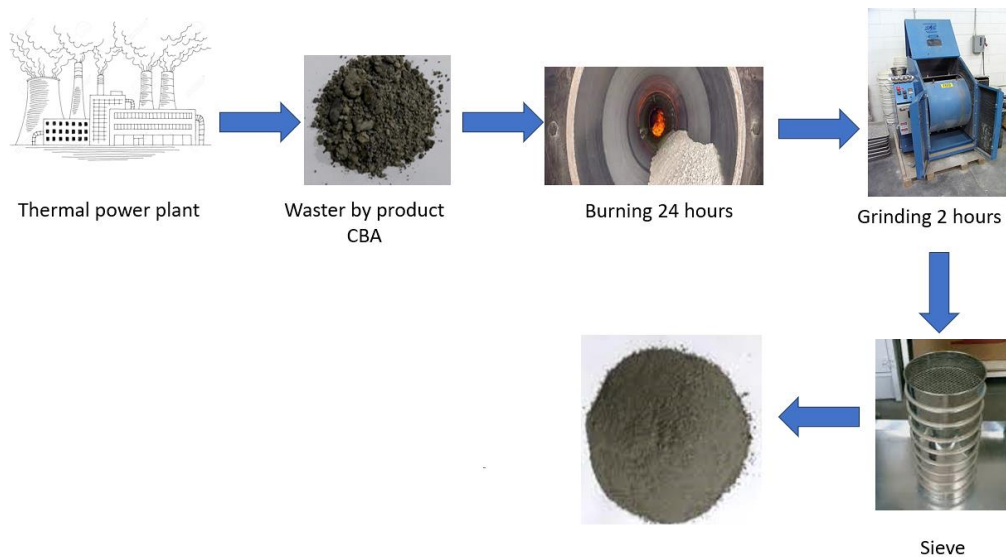


Figure 2. Flotation treatment

2.1.2. Flotation Treatment

According to Um et al. [17], during the column flotation, air was injected at a flow rate of 10 L/min with a pH of 8. Each sample, weighing between 6.5 and 52 g/L, was subjected to the flotation procedure. 500 g/ton of kerosene and 80 g/ton of MIBC (Methyl Isobutyl Carbinol) were employed as reagents. After being ground for two hours in a Los Angeles machine and passing through a 100-micron sieve size, it will be employed in the experiment as shown in Figure 3.

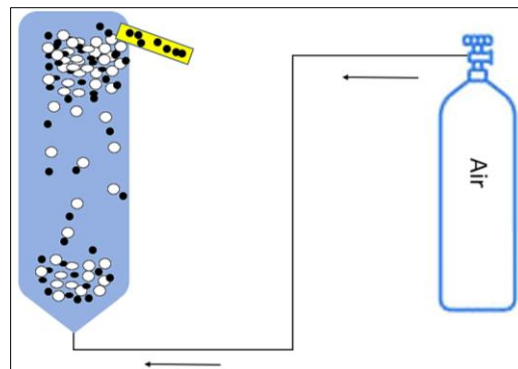


Figure 3. Flotation treatment

2.1.3. Chemical Compositions

The XRF test results, displayed in Table 1, demonstrate that CBA qualifies as a Class F natural pozzolan according to ASTM C 618 [33], containing SiO₂, Al₂O₃, and Fe₂O₃ at levels totalling 70%. With less than 9% lime (CaO) content, raw CBA exhibits very low pozzolanic (lime) properties. To form cementitious mixtures, CBA requires a cementing agent, such as quicklime, hydrated lime, or Portland cement, which reacts with water. In terms of treated CBA, the main differences include a 20% reduction in the percentage of SiO₂ following the burning treatment compared to the flotation treatment. Conversely, Fe₂O₃ increases by 40% in the flotation treatment compared to the burning treatment. However, the higher percentage of silicates (SiO₂) in the burning treatment enhances the hydration reaction in concrete compared to the flotation treatment.

Table 1. Results from the XRF

Element	Burning	Flotation	RAW
SiO ₂	40.72%	32.52%	43.61%
AL ₂ O ₃	13.79%	10.96%	14.47%
Fe ₂ O ₃	9.55 %	15.95 %	10.99%
CaO	8.00 %	16.63 %	8.82%
K ₂ O	0.77 %	0.71 %	0.85%
Na ₂ O	0.64 %	0.63 %	0.83%

2.1.4. Cement

In this study, Ordinary Portland Cement (OPC) type I is used, classified according to ASTM C150 / C150M [34] and supplied by a local manufacturer.

2.1.5. Coarse Aggregates and Fine Aggregate

Following ASTM C33 [35] standard practice, the coarse aggregates used in this study had a maximum size of a pass-through 20mm sieve. According to ASTM C33 [19] standard practice, the fine aggregates used in this study had a maximum size of pass-through 4.75mm sieve.

2.1. Specimen Mix Design

As can be seen in Table 2, the mix design method employed in this study was based on (DOE) to design concrete grade G35. The water content is fixed at 225 kg/m³ and the water-to-cement/binder ratio is 0.55. 5%, 10%, 15%, and 20% of the cement is replaced with CBA.

Table 2. Mixture proportions of the binary blended-based CBA

Description	Notation	Rep by weight %	Cement kg/m ²	CBA kg/m ²	Fine aggregate kg/m ²	Coarse aggregate kg/m ²	Water kg/m ²
Control mix concrete	M1	0	409	0	486	1250	225
Concrete Mix with CBA	M2	5%	388.55	20.45	486	1250	225
Concrete Mix with CBA	M3	10%	368.1	40.9	486	1250	225
Concrete Mix with CBA	M4	15%	347.65	61.35	486	1250	225
Concrete Mix with CBA	M5	20%	327.2	81.8	486	1250	225

2.1.1. Molds Preparation

The summary of the total number, and dimensions of the samples is tabulated where (OPC s referring to control mix) in Tables 3 and 4.

Table 3. Specimen details for every mix

Sample	Name	Specimen	Dimensions (mm)	Test Age
1	Compression	Cube	100x100x100	7 days
2	Compression	Cube	100x100x101	28 days
3	Compression	Cube	100x100x102	56 days
4	Flexural	Prism	100x100x500	28 days
5	Splitting tensile	Cylinders	dia 100x200	7 days
6	Splitting tensile	Cylinders	dia 100x201	28 days

Table 4. Number of samples for every mix

Curing time	Compressive test MPa			Flexural Strength MPa	Splitting tensile MPa		Total
	7 days	28 days	56 days	28 days	7 days	28 days	
100% OPC	3	12	12	3	3	3	
5% CBA 95% OPC	3	12	12	3	3	3	
10% CBA 90% OPC	3	12	12	3	3	3	
15% CBA 85% OPC	3	12	12	3	3	3	
20% CBA 80% OPC	3	12	12	3	3	3	
Total	15	60	60	15	15	15	180

2.2. Tests for Mechanical Properties of Concrete

2.2.1. Compression Test

This concrete is properly poured into molds and tamped to prevent any voids. The molds are removed after 24 hours, and the test specimens are then submerged in water to cure. The top surfaces of these specimens should be level and smooth. After 7, 28, and 56 days of curing, these specimens are tested by a compression testing machine to determine the pozzolanic reaction of CBA. The load should be gradually added until the specimens fail. The compressive strength

of the concrete is calculated by dividing the load at failure by the specimen's area, in accordance with ASTM C109/C109M [36]. Compression tests are performed on cubic specimens with an edge length of 100 mm. Before testing, the cubes should be dried in the sun. Three specimens per mix are tested, and their average strength is computed. When testing cubes, the specimen must be positioned in the machine so that the load is applied to the opposite sides as they were cast. The specimen's axes must align precisely with the plate's center of thrust. The compression test is conducted on a laboratory universal testing machine with a load rate of 6 KN/s and a capacity of 5000 KN.

2.2.2. Flexural Test

The flexural test on concrete can be conducted using either a four-point load test, as used in this experiment according to ASTM C78 [37], or a center point load test according to ASTM C293 [38]. The sample is placed on two supporting pins set a certain distance apart, with two loading pins placed at an equal distance around the center, as shown in Figures. The test should be conducted immediately after removing the specimen from the curing condition to prevent surface drying, which decreases flexural strength. The machine used has a capacity of 5000KN, and the load rate of the experiment is 1.57 KN/s, as shown in Figures 4 and 5.

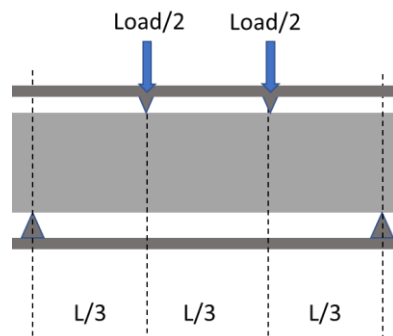


Figure 4. Four-point load test



Figure 5. Four point's flexural test

2.2.3. Splitting Tensile Test

The splitting tensile strength test on a concrete cylinder, adhering to ASTM C496 [39], is used to determine the tensile strength of concrete. The equipment utilized for this test has a capacity of 5000KN, with a load rate set at 1.57 KN/s. After curing, ensure the specimen's surface is completely dry, conforming to ASTM C496. The machine should apply the load steadily until the specimen breaks, as depicted in Figures 6 and 7.

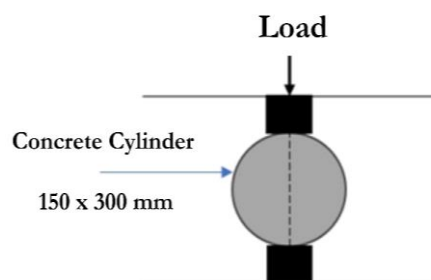


Figure 6. Splitting tensile test



Figure 7. Splitting tensile sample after fail

2.3. Tests for Chemical Properties of Concrete

2.3.1. Water Absorption Test

The concrete cubes required 28 and 56 days to cure after casting. A saturated water absorption (SWA) test was conducted according to ASTM C 642-81 [40], 28 and 56 days after curing. The samples were removed from the curing tank, dried at 105°C for 24 hours in the oven, cooled to room temperature, and then precisely weighed (dry weight) as W_1 . Then, the dried samples were submerged in water. After wiping the surface with a dry cloth at predetermined intervals of 12 hours, specimen weights were recorded. A constant weight, W_2 , was obtained in two consecutive observations after at least 48 hours. The percentage of water absorption was calculated using the formula below:

$$\text{Water absorbed} = (W_1 - W_2 / W_2) \times 100 \quad (1)$$

2.3.2. Sulphate Penetration Test

According to Mangi et al. [27], sodium sulphate (Na_2SO_4) solution was made. Ten grams of sodium sulphate were dissolved in 100 ml of solution to make a 5% Na_2SO_4 solution, which was mixed with water by percentage by weight (w/v). The cubes were then submerged in this solution after curing for 28 days. After being in the solution for 28, 56 days, the cubes were removed and dried on the surface. The cubes' surfaces were scrubbed and cleaned, and the final weights were determined as shown in Figure 8.

The formula for weight percent (w/v) is: $[\text{Mass of solute (g)} / \text{Volume of solution (ml)}] \times 100$ (2)



Figure 8. samples under 5% Na_2SO_4 solution

2.3.3. Chloride Penetration Test

According to Mangi et al. [27], sodium chloride (NaCl) solution was made. Ten grams of sodium chloride were dissolved in 100 ml of water to create a 5% sodium chloride solution. This mixture was done using percentage by weight (w/v). The cubes were then submerged in this solution after curing for 28 days. After 28, 56 days, the cubes were removed from this solution and the surface dried. After cleaning and scrubbing the cubes' surface, the specimen's final surface dry weights were determined.

3. Results and Discussion

3.1. Microstructure

The microstructure of the three samples of the CBA of (raw, burning and flotation) shows that CBA has a porous surface. Many voids were observed due to their angular, rough textured and irregular shaped particles. Also, the raw material has several impurities such as dust on the surface compared to the treated sample as shown in Figure 9.

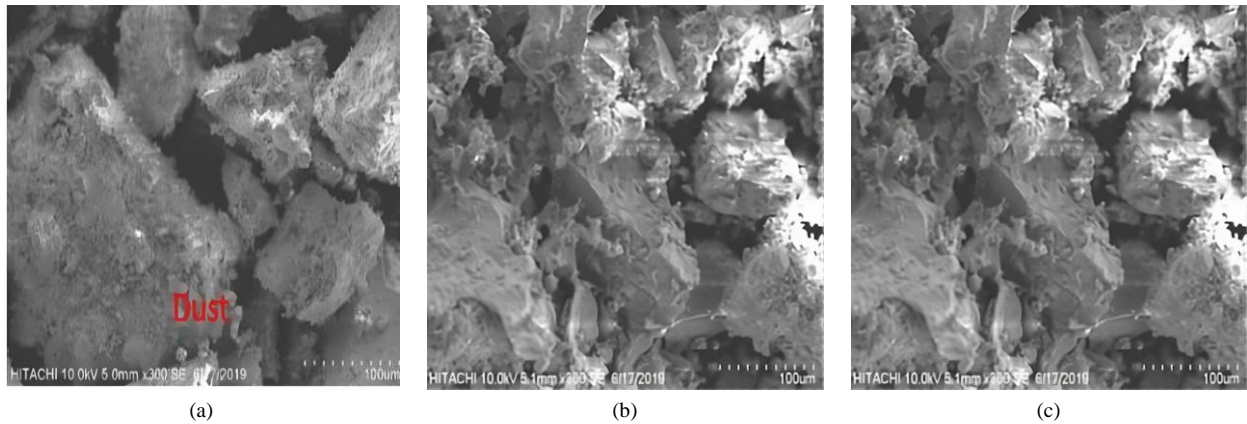


Figure 9. Raw CBA (a) Burning (b) Flotation (c) at 100 μm

3.2. Mechanical Properties

The mechanical properties of normal and CBA concrete are discussed in this section which includes the results of a compression strength, flexural strength and splitting tensile strength of the rubberized concrete.

3.2.1. Slump Test

The data in Figure 10 shows that the slump value of concrete decreases as the CBA percentage increases, for both burning and flotation treatment methods. This trend can be attributed to the high-water absorption ratio of CBA, which results from its porous surface and numerous voids. Additionally, the uneven surface texture of the CBA particles also plays a role in diminishing slump values. Notably, the treatment method applied to the CBA whether burning or flotation does not markedly influence the concrete's workability; the decline in slump values follows a similar trajectory for both treatments. The slope of this decline for each treatment method is roughly equivalent, indicating that the workability of concrete incorporating CBA is not significantly altered by the method of CBA treatment.

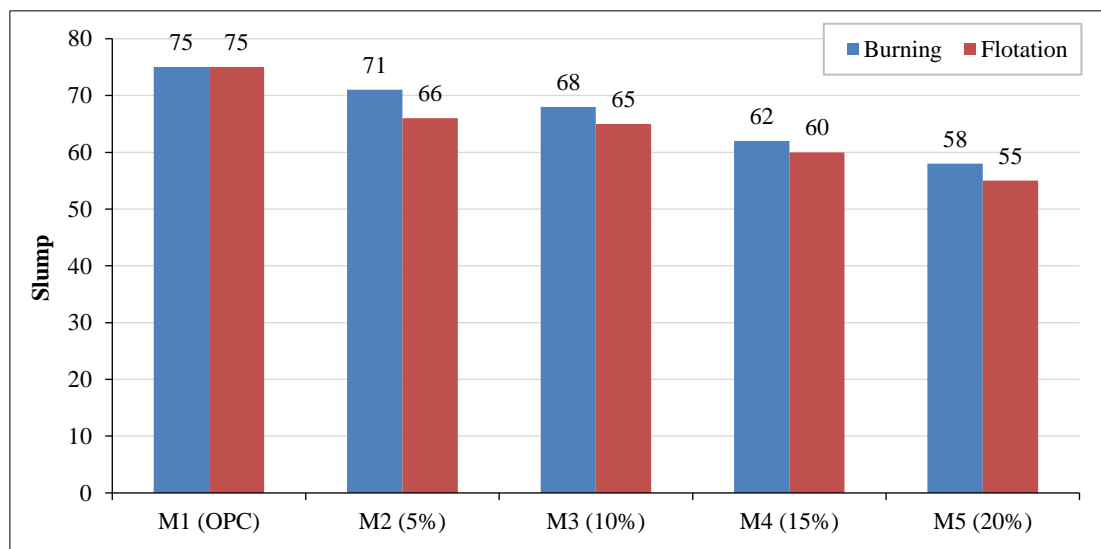


Figure 10. Slump test of CBA mixes after burning and flotation treatment

3.2.2. Compressive Strength

At 7, 28, and 56 days, all mixes underwent compression testing. Except for 10% CBA by burning treatment, all concrete samples produced with CBA replacement are generally lower than the control mix. Additionally, the findings show that burning CBA concrete rather than flotation treatment is preferred because it exhibits exceptional improvement, as shown in Figures 11 and 12.

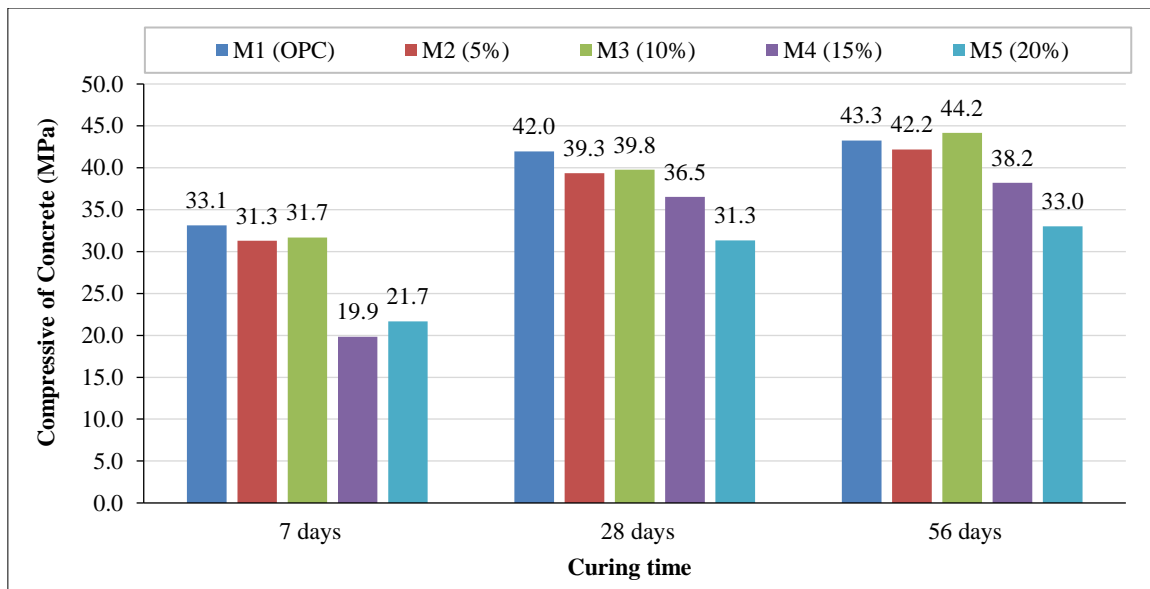


Figure 11. Compressive Strength of CBA mixes after Burning Treatment

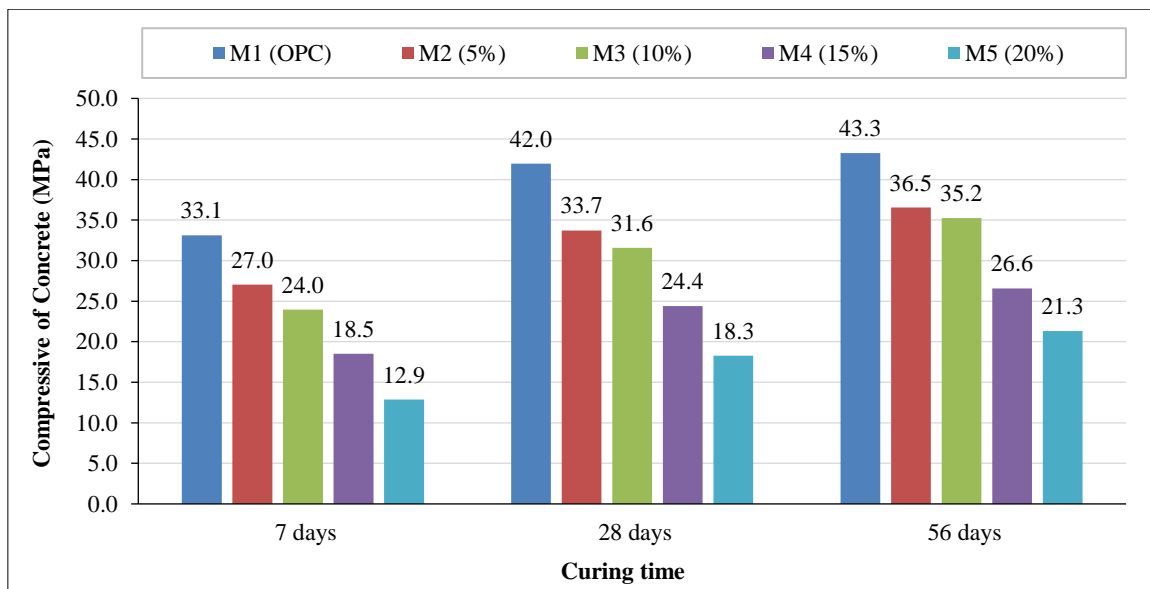


Figure 12. Compressive Strength of CBA mixes after Flotation Treatment

Additionally, the compressive strength of CBA treated by burning improves as CBA percentage rises until 10% before declining. However, the results show that, except for 20% CBA sample, CBA concrete reached the design strength of 35MPa after 28 days of curing. Figure 11 illustrates the strength starting to decline below the control mix at 56 days with a compressive strength of 10% CBA exceeding the control mix by 2%. As shown in Figure 12 the CBA samples that are treated by flotation present a drop in the strength as the CBA percentage increase and it never reach the control mix strength in any of the curing times. Some observations from Flotation Compression test results are that it took CBA concrete of 5% and 10% 56 days of curing to reach the design strength 35 MPa then the strength start to drop for 15% and 20%.

From Figure 11 and Figure 12 the huge difference between the burning and flotation treatment as most of the sample reached the designed strength at 28 days by burning treatment as for the flotation treatment it took it 56 days. However, that difference is indicated in the chemical compositions between the two of treatment methods as percentage of SiO₂ in the burning treatment is more than the flotation treatment by 20%. The difference in the chemical composition made burning treatment improve the concrete compressive strength by improving the hydration process, as SiO₂ is one of its main components. Also, the chemical composition helped to explain the slope of increasing strength at 10% of CBA then decreasing for 15% and 20% that is due the bottom ash requires a cementing agent such as Portland cement to reacts with water, if that percentage exceeded the CBA cannot be active in the hydration process. Beyond a 10% threshold, excess CBA does not contribute actively to the hydration process, thereby limiting further strength improvements.

3.2.3. Splitting Tensile Test

By conducting the test on cylinder specimens at 7 and 28 days after curing, the splitting tensile test is used to determine the tensile strength of the concrete. The split tensile of the CBA increased for the two treatment methods up to 10% CBA before starting to decline for 15% and 20%, according to the results shown in Figures 13 and 14. The control sample also produced strengths of 7.75 MPa after 7 days and 11.72 MPa after 28 days. Where burning treatment CBA concrete of 10% which resulted in 7.88 MPa and 13.02 MPa exceeded the control mix at 7 day and 28 days, respectively shown in Figure 13. As for the Flotation treatment the 10% CBA concrete exceeded the control mix at 7 days split tensile strength but at 28 days it decreases by 8.3% compared to the control mix. Because of the slow hydration process that is caused by less silicate compared to burning CBA sample as shown in Figure 14. The improvement in split tensile strength, particularly with burning treatment, underscores the chemical composition and particle shape of CBA as key factors enhancing concrete's bonding and paste quality. This detailed analysis confirms the nuanced role of CBA in concrete's tensile strength, emphasizing the importance of treatment method and CBA content in achieving optimal concrete performance.

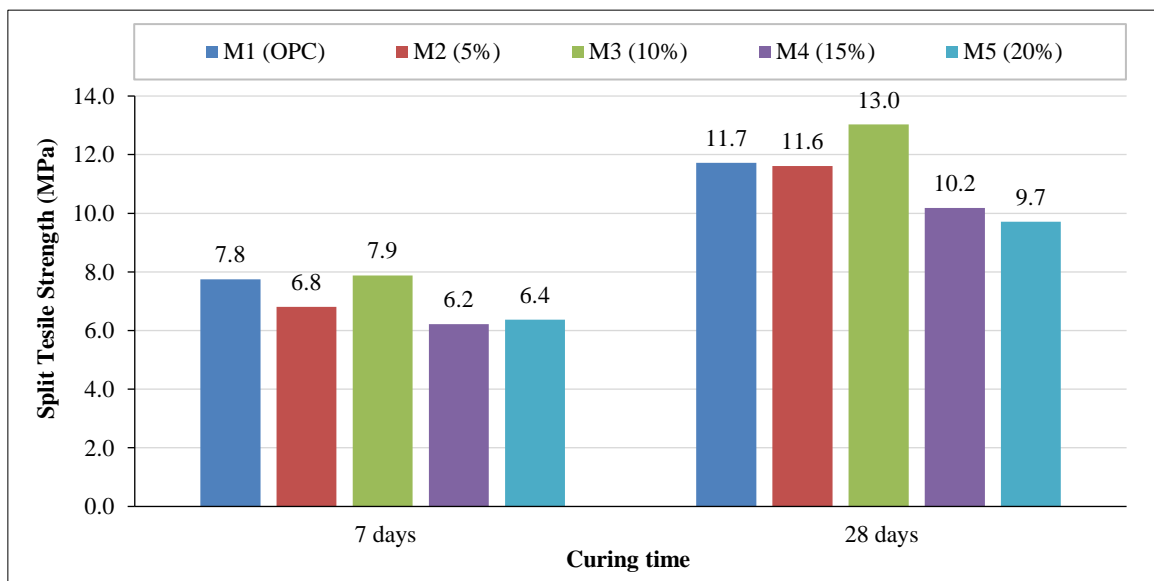


Figure 13. Split Tensile Strength of CBA mixes after Burning Treatment

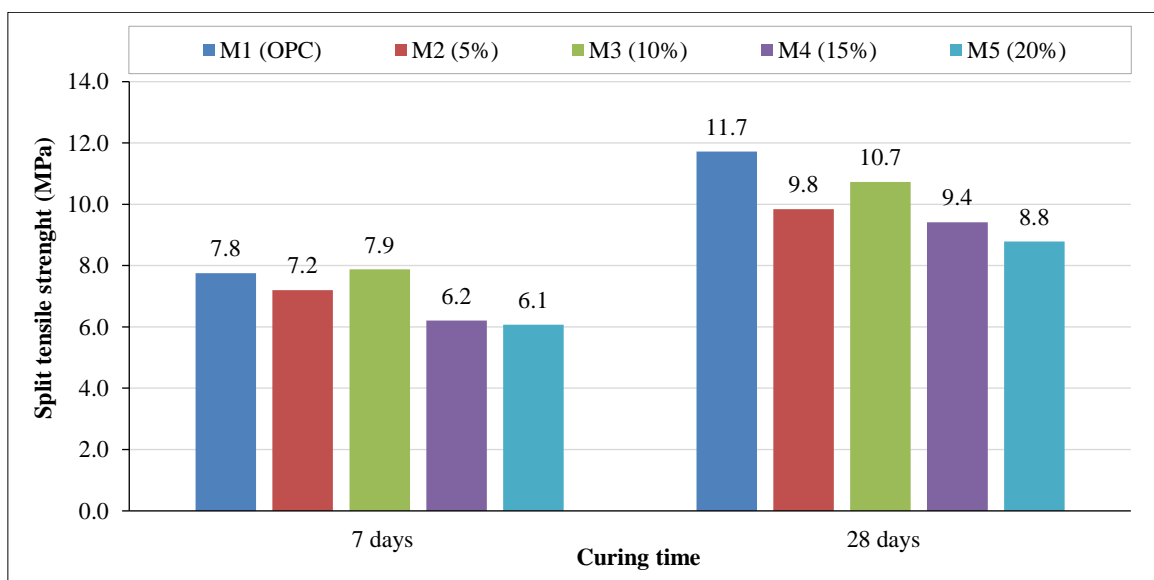


Figure 14. Split Tensile Strength of CBA mixes after Flotation Treatment

3.2.4. Flexural Strength

The specimens used for the four-point bending flexural tests were prepared 28 days after curing. Normal concrete mix is denoted by M1, and CBA concrete is denoted by M2 to M5. Figures 15 and 16 display the results, which demonstrate that the CBA concrete outperformed the control mix in terms of flexural strength.

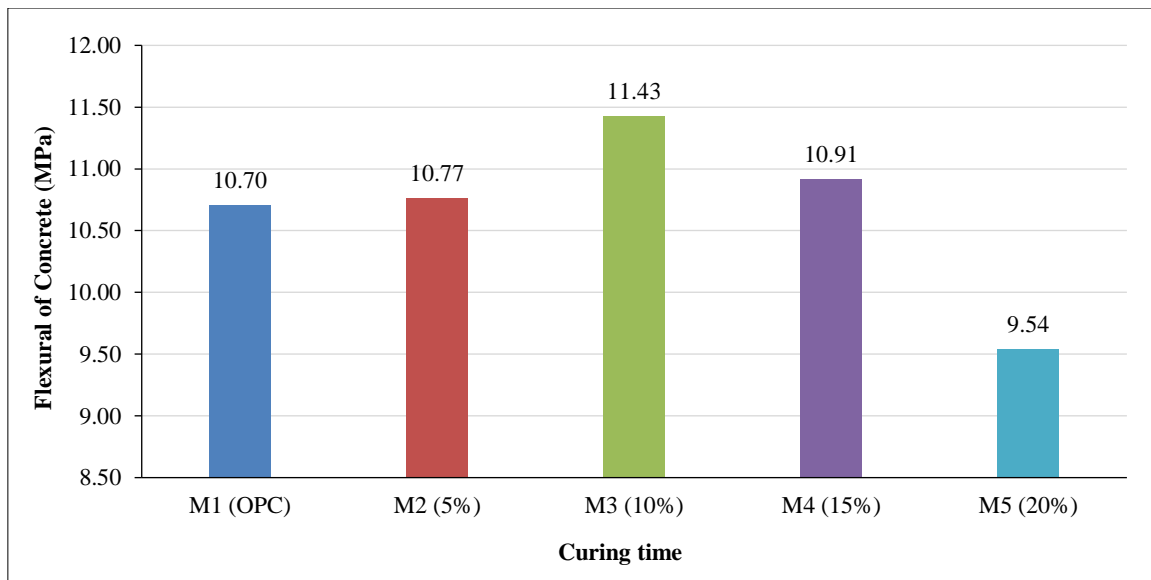


Figure 15. Flexural Strength of CBA mixes after Burning Treatment

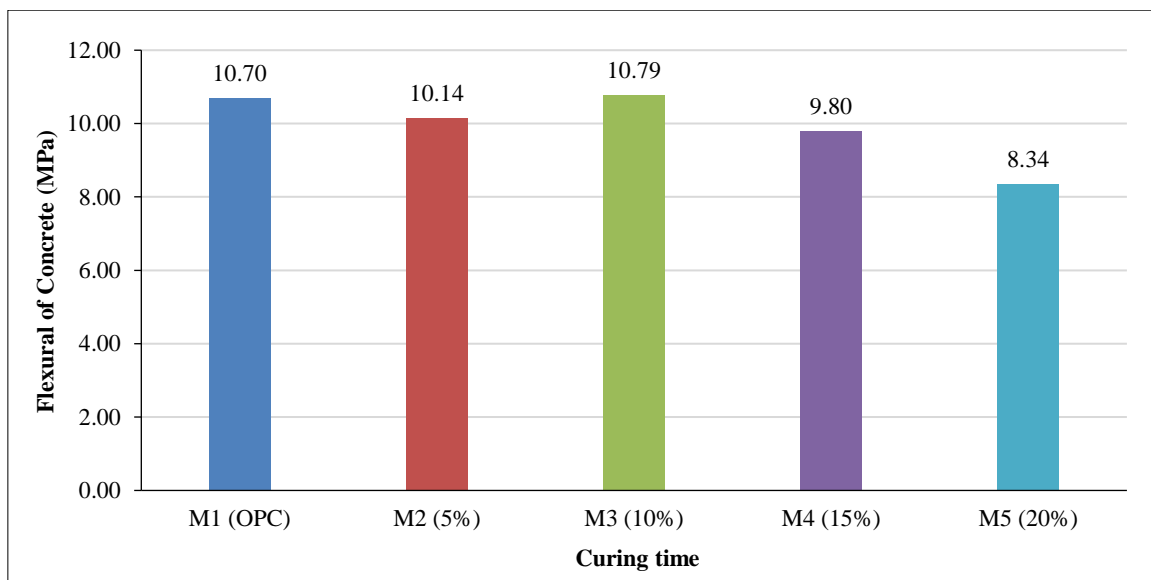


Figure 16. Flexural Strength of CBA mixes after Flotation Treatment

Figure 15 shows CBA concrete by burning treatment rise in the strength until 10% then reduction for 15% and 20%. The CBA concrete produced better results by 7% in flexural strength than normal concrete by producing 11.43 MPa average strength for 10% CBA compared to the control mix average of 10.7 MPa. The specimens were capable of withstanding measurable post failure load. As for the flotation treatment sample shown in Figure 16 the flexural strength has the same behavior as the burning treatment as the strength increases until 10% CBA then it starts to decline. The CBA concrete gave better flexural strength by 0.7% than the control mix by a small margin. That indicated in the CBA 10% by 10.78 MPa compared to control mix of 10.7 MPa. Furthermore, this analysis underscores the CBA's ability to withstand significant post-failure loads and its contribution to the spread of cracks within the tension region of the beam specimens. The CBA particles not only supported additional loads during crack formation but also expanded the failure surface area, attributing to their large deformation capacity and high compressive strength.

The flotation treatment samples mirrored the burning treatment's performance, improving strength up to 10% CBA before declining. However, the flexural strength improvement over the control mix was marginal at 0.7%, indicating a nuanced impact of CBA treatment methods on flexural strength. This enhancement in flexural strength, despite being slight with flotation treatment, suggests that the CBA's chemical composition and particle shape significantly contribute to the concrete mix's bonding and paste quality. The distinction between burning and flotation treatment outcomes emphasizes the critical role of CBA's silicate content in the hydration process, influencing the flexural strength development in concrete.

3.3. Chemical Properties

3.3.1. Saturated Water Absorption

The water absorption of burned CBA at 28 days of all the mixes contain CBA M2, M3, and M4 was found less than the control mix M1 except M5 which was higher than control mix, while the burned CBA at 56 days for the mixes M2 and M3 were found less than M1 and the rest of mixes were found higher than M1. The volume of water absorption in the concrete corresponds with the degree of porosity. Consequently, the result revealed that the concrete contains 5% and 10% of burned CBA will be able to enhance the degree of porosity of concrete more than control mix M1 for 28 and 56 days, as presented in Figure 17.

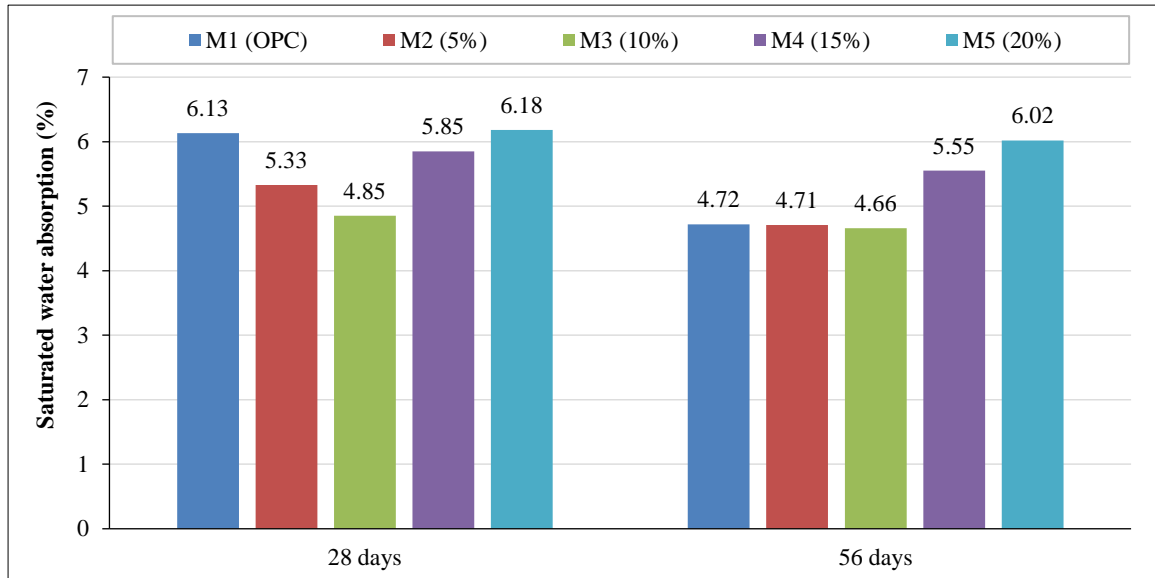


Figure 17. Saturated water absorption of all mixes subjected to burning treatment

On the contrary, the result of the CBA that treated with flotation revealed that at 28 days the water absorption of the mixes M2 and M3 was lesser than M1, while at 56 days all mixes M2, M3, M4, and M5 was higher than control mix M1. Hence, the degree of porosity for control mix superior on all the mixes contain CBA that treated with flotation, because the flotation treatment failed to enhance the degree of porosity for all mixes for short-term period, as presented in Figure 18. The expected drop in capillary absorption coefficients was noticed due to a reduction in overall porosity levels due to optimal particle packing and distribution. This suggests that while flotation treatment may initially improve porosity, its long-term effects do not sustain reduced water absorption, potentially due to the slower hydration process within the concrete matrix.

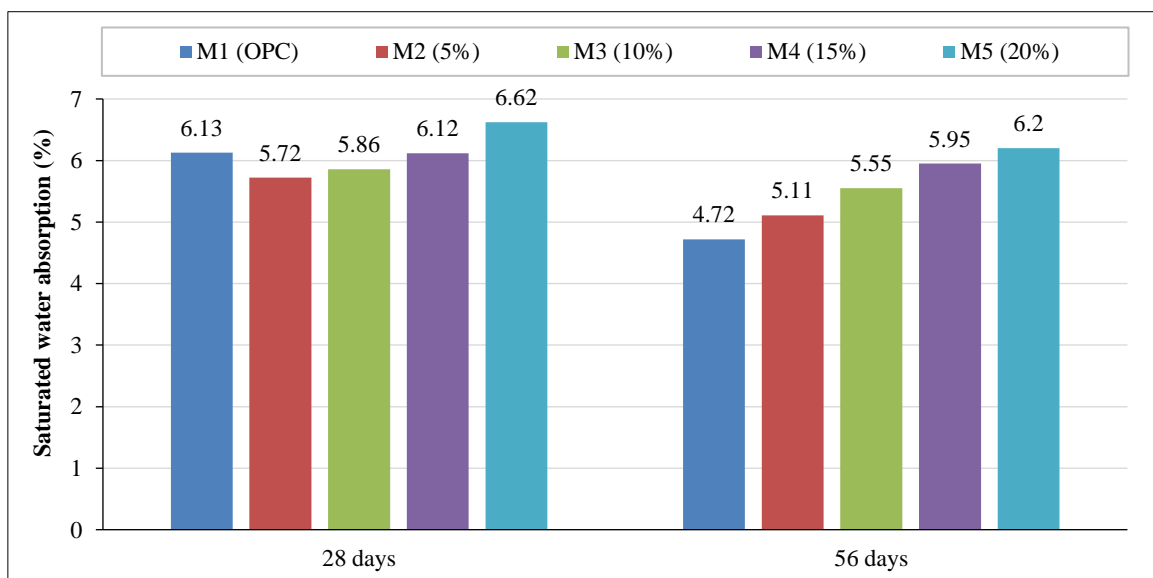


Figure 18. Saturated water absorption of all mixes subjected to flotation treatment

3.3.2. Compressive Strength of Concrete Submerged in 5% NaCl

The study investigated the effectiveness of concrete exposed for 28 and 56 days to a 5% sodium chloride (NaCl) solution under burning and flotation conditions. The findings indicated that the strength development of concrete mixes M2, M3, M4, and M5 was slower under 5% sodium chloride (NaCl) exposure conditions compared to the control mix M1. This slower development is attributed to the chloride solution producing chloro aluminate, which can cause deterioration at later ages. Additionally, the inclusion of CBA, containing amorphous silica, reacts with this chloro aluminate at later stages. The leaching of calcium hydroxide, CaOH₂, created by cement hydration and the formation of C-S-H (calcium silicate hydrate) gel, crucial in concrete, leads to a reduction in calcium hydroxide present due to the reaction between amorphous silica and calcium hydroxide. Thus, the presence of chloride solution impacts pore sizes and disrupts the hydration process, affecting the external appearance of concrete. Moreover, chloride ions influence the pore size distribution, critical for the properties of hardened concrete, resulting in potential harm or alterations, as depicted in Figures 19 and 20.

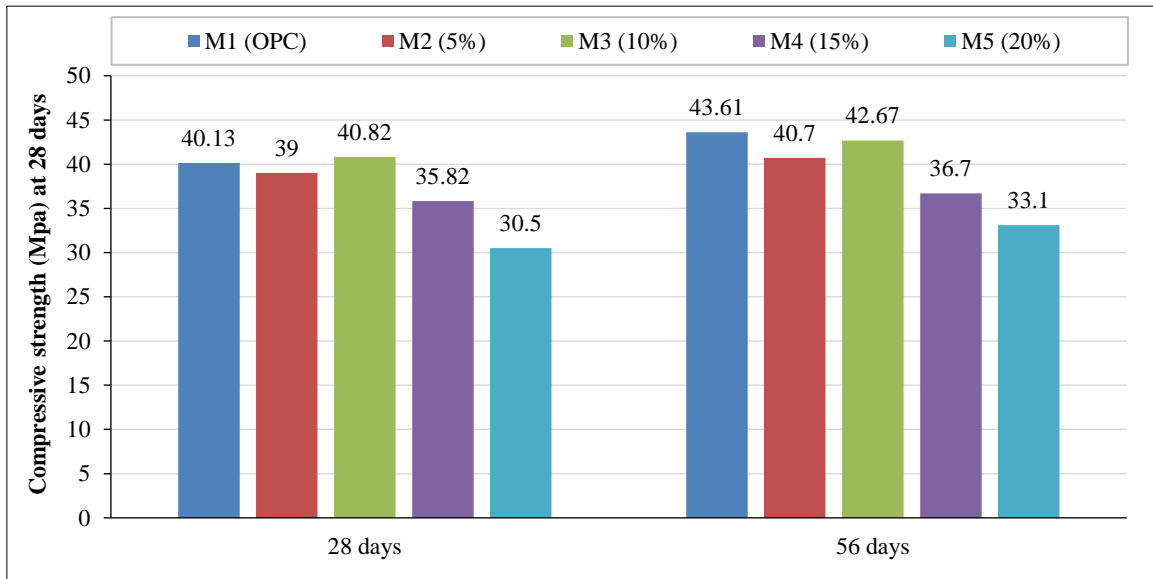


Figure 19. Compressive strength of concrete submerged in 5% NaCl Burning treatment

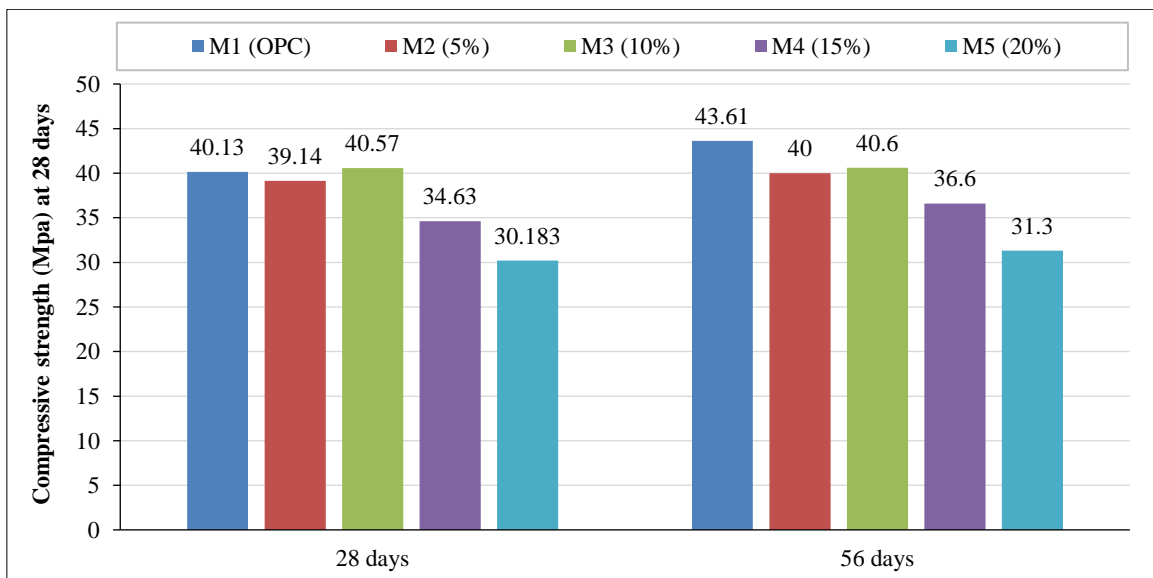


Figure 20. Compressive strength of concrete submerged in 5% NaCl Flotation treatment

3.3.3. Compressive Strength of Concrete Submerged in 5% Na₂SO₄

Figures 21 and 22 depict the performance of concrete containing CBA for burning and flotation treatment while submerged in a 5% Na₂SO₄ exposure condition. Except for mixes M4 and M5, which have lower strengths than the control mix, the results showed that the concrete containing CBA for mixes M2 and M3 was comparable with the control mix M1 for 28 days. Because, under short-term exposure conditions, sodium sulphate solution has no discernible effect on concrete with or without CBA.

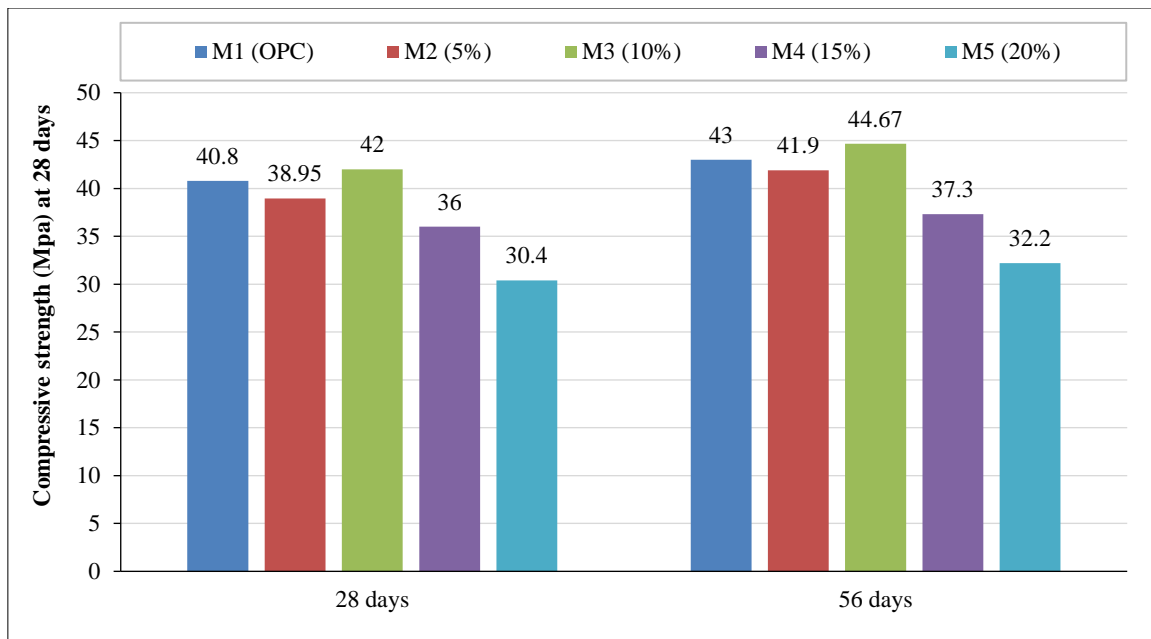


Figure 21. Compressive strength of concrete submerged in 5% Na₂SO₄ Burning treatment

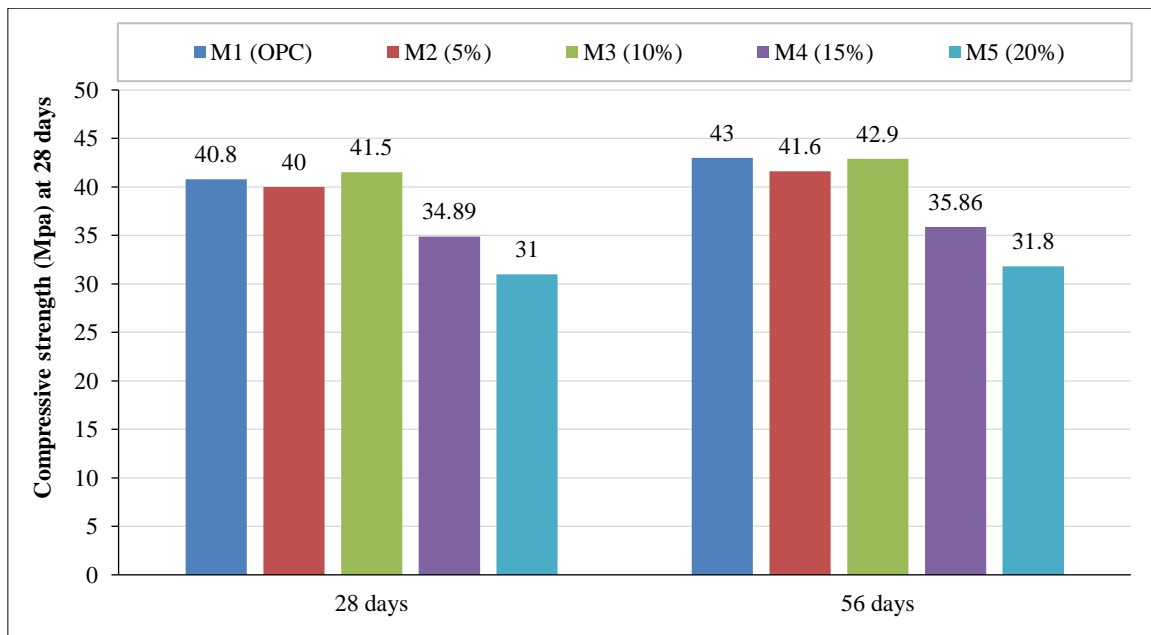


Figure 22. Compressive strength of concrete submerged in 5% Na₂SO₄ Flotation treatment

On the other hand, for mixes M3 and M2, the performance of concrete containing CBA was found to be superior to control mixes M1 and M2, respectively, for 56 days. Because the process of the Na₂SO₄ reaction was previously known as the sulfate ions that were present in the pores of the concrete, a chemical reaction between cement hydration and sulfate ions and sodium sulphate reacting with CaOH₂ to create gypsum and ettringite may occur in the pores of the concrete. Additionally, the pozzolanic reaction consumed calcium hydroxide, making the concrete denser and preventing the development of ettringite through sulfate attack. However, because the CBA contains less calcium oxide, it may be able to lessen the sulphate attack.

3.3.4. Sodium Chloride Penetration

Figures 23 and 24 show the findings for the weight change of concrete immersed in 5% NaCl solution for the burning and flotation treatment specimens at 28 and 56 days. The outcome reveals that M5 experienced the highest weight gain, while M1 experienced the lowest weight gain under the same conditions. Additionally, the M2, M3, and M4 mixes have gained more weight than M1. Because the presence of CBA in concrete for all mixes could not be able to reduce the hydration process and reduce salts penetrability in the concrete, the result shows that the concrete with lower effective

was noticed in all mixes of concrete with CBA than the control mix. As a result, less weight gain was observed in control mix M1. Furthermore, the adverse effects of a NaCl solution on concrete mixes caused a compromised formation of calcium silicate hydrate (C-S-H) gel, which led to affecting pore sizes and disrupts the hydration process.

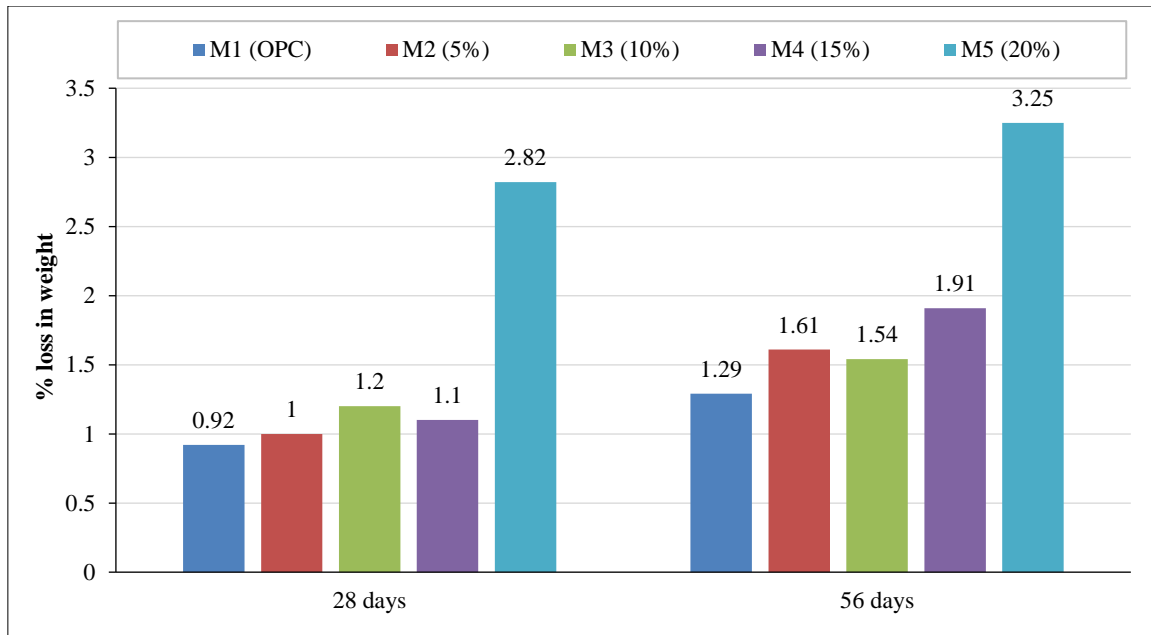


Figure 23. Change in weight for concrete submerged in 5% NaCl Burning treatment

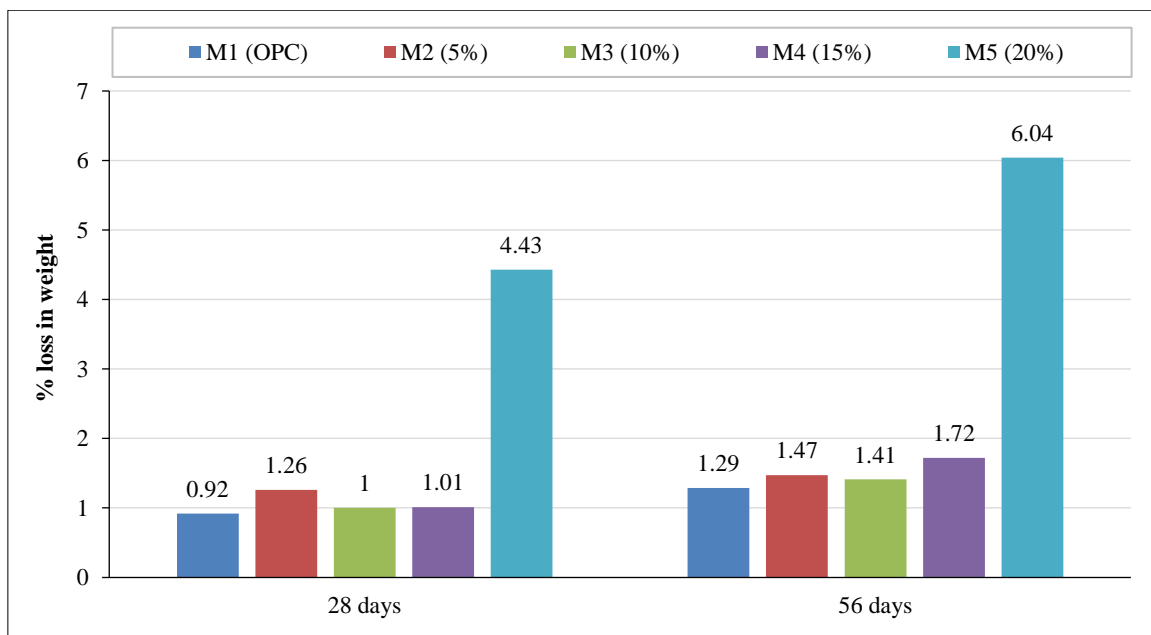


Figure 24. Change in weight for concrete submerged in 5% NaCl Flotation treatment

3.3.5. Sodium Sulphate Penetration

The impact of immersing concrete samples in a 5% Na₂SO₄ solution on weight change was evaluated for specimens subjected to burning and flotation treatments at 28 and 56 days, as depicted in Figures 24 and 25. The data indicate that mix M1 exhibited the highest weight gain, whereas mixes M3 and M2 experienced lower weight gains under identical conditions. Furthermore, while mixes M4 and M5 also gained less weight than M1, they were less effective in reducing weight gain compared to M3 and M2. The observed lower weight gain in mixes M3 and M2, relative to the control mix M1, suggests that the incorporation of CBA in these mixes could effectively reduce the hydration process and decrease the concrete's permeability to salts. This inclusion of CBA appears to have partially clogged the voids within the concrete matrix, thereby potentially enhancing the strength development in the concrete mix.

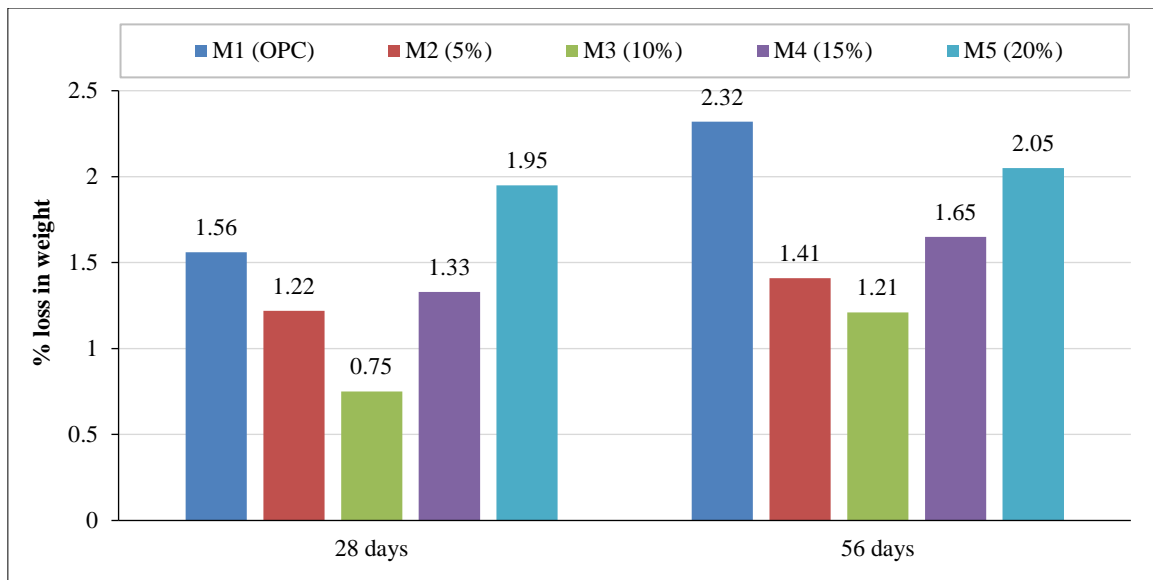


Figure 25. Change in weight for concrete submerged in 5% Na₂SO₄ Burning treatment

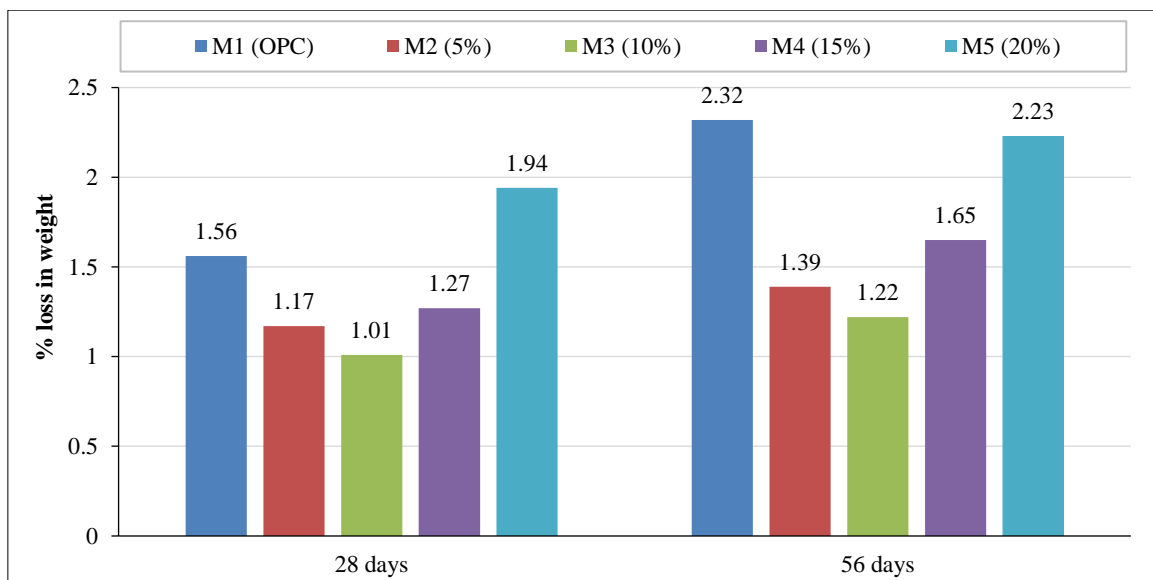


Figure 26. Change in weight for concrete submerged in 5% Na₂SO₄ Flotation treatment

4. Conclusions

The study and experimental results discussed in the previous chapter have led to the following conclusions:

- The slump decreases as the CBA percentage increases because CBA has a high-water absorption capacity.
- The compressive strength of concrete using burnt CBA showed an improvement compared to the control mix and flotation CBA concrete. This improvement is attributed to the high SiO₂ content in its chemical composition.
- Flexural and split tensile test results indicated an increase in strength for burnt CBA concrete compared to normal concrete. This is due to additional pozzolanic reactions within the concrete, which enhance the quality of the cement paste and interfacial transition zones.
- The chemical compositions of the two treatments show that the burning treatment provides more significant improvements in the mechanical properties of concrete compared to the flotation treatment. This improvement is due to the high SiO₂ content observed in the burning treatment, which enhances pozzolanic reactions.
- The durability performance of concrete containing a 10% increment of burnt CBA shows more enhancement and effectiveness than other mixes and is comparable to OPC concrete.
- The inclusion of a 10% increment of CBA in concrete can reduce the hydration process and increase porosity, leading to decreased salt penetrability in concrete compared to OPC concrete.

- Concrete containing CBA provides sufficient compressive strength, higher than the control mix with a 10% increment of CBA, when exposed to a 5% Na₂SO₄ solution. Moreover, it is not adversely affected under Na₂SO₄ solution exposure. However, under a 5% sodium chloride (NaCl) solution, the pozzolanic reaction becomes slower and requires more time to recover.
- The burning treatment proves to be more effective in enhancing the durability and strength of CBA concrete than the flotation treatment.
- The microstructure of treated coal bottom ash reveals particles that are denser and less porous, which could be comparable to OPC particles.

5. Declarations

5.1. Author Contributions

Conceptualization, F.N.A.A.A. and A.M.; methodology, A.M.; software, O.M.M.E.; validation, O.M.M.E., M.A., and H.A.D.; formal analysis, A.M.; investigation, A.M.; data curation, A.M.; writing—original draft preparation, A.I.; writing—review and editing, H.A.M. and M.A.; visualization, O.M.M.E.; supervision, F.N.A.A.A.; project administration, M.A.; funding acquisition, H.A.D. All authors have read and agreed to the published version of the manuscript.

5.2. Data Availability Statement

The data presented in this study are available in the article.

5.3. Funding

The Article Processing Charges (APC) of this project are funded by the TRC research project BFP/RGP/EI/23/073, University of Nizwa, Oman.

5.4. Acknowledgements

Experimental work was carried out at Construction Material Laboratory, Universiti Putra Malaysia, Author is thankful to the academic advisors and mentors for supervising this research, and also, the authors would like to thank the University of Nizwa for its financial support.

5.5. Conflicts of Interest

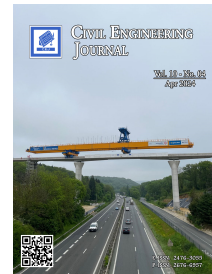
The authors declare no conflict of interest.

6. References



- [1] El-Bitouri, Y. (2023). Rheological Behavior of Cement Paste: A Phenomenological State of the Art. *Eng (Switzerland)*, 4(3), 1891–1904. doi:10.3390/eng4030107.
- [2] Alaneme, G. U., Iro, U. I., Milad, A., Olaiya, B. C., Otu, O. N., Chibuisi, U. P., & Agada, J. (2023). Mechanical Properties Optimization and Simulation of Soil–Saw Dust Ash Blend Using Extreme Vertex Design (EVD) Method. *International Journal of Pavement Research and Technology*, 1–27. doi:10.1007/s42947-023-00272-4.
- [3] Arafa, S., Milad, A., Yusoff, N. I. M., Al-Ansari, N., & Yaseen, Z. M. (2021). Investigation into the permeability and strength of pervious geopolymer concrete containing coated biomass aggregate material. *Journal of Materials Research and Technology*, 15, 2075–2087. doi:10.1016/j.jmrt.2021.09.045.
- [4] Elbasir, O. M. M., Johari, M. A. M., Ahmad, Z. A., Mashaan, N. S., & Milad, A. (2023). The Compressive Strength and Microstructure of Alkali-Activated Mortars Utilizing By-Product-Based Binary-Blended Precursors. *Applied Mechanics*, 4(3), 885–898. doi:10.3390/applmech4030046.
- [5] Dehwah, H. A. F. (2007). Effect of sulfate concentration and associated cation type on concrete deterioration and morphological changes in cement hydrates. *Construction and Building Materials*, 21(1), 29–39. doi:10.1016/j.conbuildmat.2005.07.010.
- [6] Abdul Kadir, A., & Hassan, M. I. H. (2015). Leachability of Self-Compacting Concrete (SCC) Incorporated with Fly Ash and Bottom Ash by Using Synthetic Precipitation Leaching Procedure (SPLP). *Applied Mechanics and Materials*, 773–774, 1375–1379. doi:10.4028/www.scientific.net/amm.773-774.1375.
- [7] Sandhya, B., & Reshma, E. K. (2013). A study on mechanical properties of cement concrete by partial replacement of fine aggregates with bottom ash. *International Journal of students research in Technology & Management*, 1(4), 416–430.
- [8] Qaidi, S., Najm, H. M., Abed, S. M., Ahmed, H. U., Al Dughaisi, H., Al Lawati, J., Sabri, M. M., Alkhatib, F., & Milad, A. (2022). Fly Ash-Based Geopolymer Composites: A Review of the Compressive Strength and Microstructure Analysis. *Materials*, 15(20), 7098. doi:10.3390/ma15207098.

- [9] Kadam, M. P., & Patil, Y. D. (2015). Effect of sieved coal bottom ash as a sand replacement on the properties of cement concrete. *Magazine of Concrete Research*, 67(5), 227–234. doi:10.1680/mac.14.00179.
- [10] Rafieizonooz, M., Salim, M. R., Mirza, J., Hussin, M. W., Salmiati, Khan, R., & Khankhaje, E. (2017). Toxicity characteristics and durability of concrete containing coal ash as substitute for cement and river sand. *Construction and Building Materials*, 143, 234–246. doi:10.1016/j.conbuildmat.2017.03.151.
- [11] An American recycling success story. (2015). Beneficial use of Coal Bottom Combustion Products. American Coal Ash Association (ACAA), Denver, United States.
- [12] Dewi, S. J., Ramadhansyah, P. J., Norhidayah, A. H., Md. Maniruzzaman, A. A., Hainin, M. R., & Che Norazman, C. W. (2014). Performance of RHA Blended Cement Concrete under Sodium Chloride via Wetting and Drying. *Applied Mechanics and Materials*, 554, 106–110. doi:10.4028/www.scientific.net/amm.554.106.
- [13] Jamaluddin, N., Hamzah, A. F., Wan Ibrahim, M. H., Jaya, R. P., Arshad, M. F., Zainal Abidin, N. E., & Dahalan, N. H. (2016). Fresh Properties and Flexural Strength of Self-Compacting Concrete Integrating Coal Bottom Ash. *MATEC Web of Conferences*, 47, 01010. doi:10.1051/mateconf/20164701010.
- [14] Ibe Iro, U., Alaneme, G. U., Milad, A., Olaiya, B. C., Otu, O. N., Isu, E. U., & Amuzie, M. N. (2022). Optimization and Simulation of Saw Dust Ash Concrete Using Extreme Vertex Design Method. *Advances in Materials Science and Engineering*, 5082139. doi:10.1155/2022/5082139.
- [15] Kadir, A. A., Hassan, M. I. H., & Abdullah, M. M. A. B. (2016). Investigation on Leaching Behaviour of Fly Ash and Bottom Ash Replacement in Self-Compacting Concrete. *IOP Conference Series: Materials Science and Engineering*, 133(1), 012036. doi:10.1088/1757-899X/133/1/012036.
- [16] Ewa, D. E., Ukpata, J. O., Otu, O. N., Memon, Z. A., Alaneme, G. U., & Milad, A. (2023). Scheffe's Simplex Optimization of Flexural Strength of Quarry Dust and Sawdust Ash Pervious Concrete for Sustainable Pavement Construction. *Materials*, 16(2), 598. doi:10.3390/ma16020598.
- [17] Um, N.-I., Ahn, J.-W., Han, G.-C., Lee, S.-J., Kim, H.-S., & Cho, H. (2008). Flotation process in coal bottom ash and their effect on the removal of unburned carbon. *Geosystem Engineering*, 11(4), 75–80. doi:10.1080/12269328.2008.10541289.
- [18] Qaidi, S., Najm, H. M., Abed, S. M., Özkılıç, Y. O., Al Dughaihi, H., Alost, M., Sabri, M. M. S., Alkhatib, F., & Milad, A. (2022). Concrete Containing Waste Glass as an Environmentally Friendly Aggregate: A Review on Fresh and Mechanical Characteristics. *Materials*, 15(18), 6222. doi:10.3390/ma15186222.
- [19] ASTM C33/C33M-18. (2023). Standard Specification for Concrete Aggregates. ASTM International, Pennsylvania, United States. doi:10.1520/C0033_C0033M-18.
- [20] Meena, A., Singh, N., & Singh, S. P. (2023). High-volume fly ash Self Consolidating Concrete with coal bottom ash and recycled concrete aggregates: Fresh, mechanical and microstructural properties. *Journal of Building Engineering*, 63, 105447. doi:10.1016/j.job.2022.105447.
- [21] Singh, G., & ShriRam. (2023). Microstructural and other properties of copper slag–coal bottom ash incorporated concrete using fly ash as cement replacement. *Innovative Infrastructure Solutions*, 8(2), 78. doi:10.1007/s41062-023-01051-7.
- [22] Muthusamy, K., Wong, W. H., Mohamad, N., Rajan, J., Budiea, A. M. A., P.P. Abdul Majeed, A., & Kirgiz, M. S. (2023). Properties of concrete containing coal bottom ash as hydraulic binder substitution. In *Advance Upcycling of By-products in Binder and Binder-Based Materials*: Woodhead Publishing, 243–250. Woodhead Publishing. doi:10.1016/B978-0-323-90791-0.00002-0.
- [23] Sorum, M. G., & Kalita, A. (2023). Effect of Bio-Cementation with Rice Husk Ash on Permeability of Silty Sand. *Civil Engineering Journal*, 9(11), 2854–2867. doi:10.28991/CEJ-2023-09-11-016.
- [24] Singh, M., & Siddique, R. (2016). Effect of coal bottom ash as partial replacement of sand on workability and strength properties of concrete. *Journal of Cleaner Production*, 112, 620–630. doi:10.1016/j.jclepro.2015.08.001.
- [25] Rafieizonooz, M., Mirza, J., Salim, M. R., Hussin, M. W., & Khankhaje, E. (2016). Investigation of coal bottom ash and fly ash in concrete as replacement for sand and cement. *Construction and Building Materials*, 116, 15–24. doi:10.1016/j.conbuildmat.2016.04.080.
- [26] Milad, A., Ali, A. S. B., Babalghaith, A. M., Memon, Z. A., Mashaan, N. S., Arafa, S., & Nur, N. I. (2021). Utilisation of waste-based geopolymer in asphalt pavement modification and construction; a review. *Sustainability (Switzerland)*, 13(6), 3330. doi:10.3390/su13063330.
- [27] Mangi, S. A., Wan Ibrahim, M. H., Jamaluddin, N., Arshad, M. F., & Putra Jaya, R. (2019). Short-term effects of sulphate and chloride on the concrete containing coal bottom ash as supplementary cementitious material. *Engineering Science and Technology, an International Journal*, 22(2), 515–522. doi:10.1016/j.jestch.2018.09.001.

- [28] Benson, C. H., & Bradshaw, S. (2011). User guideline for coal bottom ash and boiler slag in green infrastructure construction. University of Wisconsin, Madison, United States.
- [29] Alawi, A., Milad, A., Barbieri, D., Alostta, M., Alaneme, G. U., & Imran Latif, Q. B. alias. (2023). Eco-Friendly Geopolymer Composites Prepared from Agro-Industrial Wastes: A State-of-the-Art Review. *CivilEng (Switzerland)*, 4(2), 433–453. doi:10.3390/civileng4020025.
- [30] Singh, N., Shehnazdeep, & Bhardwaj, A. (2020). Reviewing the role of coal bottom ash as an alternative of cement. *Construction and Building Materials*, 233, 117276. doi:10.1016/j.conbuildmat.2019.117276.
- [31] Khan, R. A., & Ganesh, A. (2016). The effect of coal bottom ash (CBA) on mechanical and durability characteristics of concrete. *Journal of building materials and structures*, 3(1), 31-42. doi:10.34118/jbms.v3i1.22.
- [32] Ibrahim, A. H., Choong, K. K., Megat Johari, M. A., Md Noor, S. I., Zainal, N. L., & Ariffin, K. S. (2015). Effects of Coal Bottom Ash on the Compressive Strength of Portland Cement Mortar. *Applied Mechanics and Materials*, 802, 149–154. doi:10.4028/www.scientific.net/amm.802.149.
- [33] ASTM C618-19. (2022). Standard Specification for Coal Fly Ash and Raw or Calcined Natural Pozzolan for Use in Concrete. ASTM International, Pennsylvania, United States. doi:10.1520/C0618-19.
- [34] ASTM C150 / C150M-19a. (2020). Standard Specification for Portland Cement. ASTM International, Pennsylvania, United States. doi:10.1520/C0150_C0150M-19A.
- [35] ASTM C33-03. (2010). Standard Specification for Concrete Aggregates. ASTM International, Pennsylvania, United States. doi:10.1520/C0033-03.
- [36] ASTM C109 / C109M-16. (2016). Standard Test Method for Compressive Strength of Hydraulic Cement Mortars (Using 2-in. or [50-mm] Cube Specimens). ASTM International, Pennsylvania, United States. doi:10.1520/C0109_C0109M-16.
- [37] ASTM C78 / C78M-18. (2021). Standard Test Method for Flexural Strength of Concrete (Using Simple Beam with Third-Point Loading). ASTM International, Pennsylvania, United States. doi:10.1520/C0078_C0078M-18.
- [38] ASTM C293/C293M-16. (2016). Standard Test Method for Flexural Strength of Concrete (Using Simple Beam with Center-Point Loading). ASTM International, Pennsylvania, United States. doi:10.1520/C0293_C0293M-16.
- [39] ASTM C496 / C496M-17. (2017). Standard Test Method for Splitting Tensile Strength of Cylindrical Concrete Specimens, ASTM International, Pennsylvania, United States. doi:10.1520/C0496_C0496M-17.
- [40] ASTM C642-21. (2022). Standard Test Method for Density, Absorption, and Voids in Hardened Concrete. ASTM International, Pennsylvania, United States. doi:10.1520/C0642-21.



Unveiling Effectiveness of Lean Construction Practices: A Comprehensive Study through Surveys and Case Studies

Mughees Aslam¹ , Edmund Baffoe-Twum^{2*} , Muhammad Ahmed¹, Aman Ulhaq¹

¹ National University of Science and Technology (NUST), Risalpur Campus, Risalpur, Pakistan.

² Department of Engineering Management and Technology, University of Tennessee, Chattanooga, TN 37403, United States.

Received 07 November 2023; Revised 18 March 2024; Accepted 23 March 2024; Published 01 April 2024

Abstract

Construction projects frequently encounter challenges such as stagnant productivity, excessive waste, cost overruns, and delays, contributing to sustainability issues. In response to these issues, Lean Construction (LC) has emerged as a methodology aimed at eradicating inefficiencies and wasteful practices. However, the construction industry has been slow to embrace LC, primarily due to a lack of comprehensive evaluations regarding its real-world effectiveness. This study seeks to thoroughly assess the effectiveness of LC when implemented in construction projects in Pakistan. The research involved conducting a survey among experts in the construction industry, utilizing a comprehensive questionnaire to evaluate the extent of LC adoption and its impact on construction project performance. The collected data underwent rigorous statistical analysis to ascertain the influence of LC practices on project outcomes. To validate the survey results, the study selected five case study projects for in-depth analysis. These case studies assessed how well the projects adhered to LC principles and examined the resulting effects on project delays, cost overruns, quality issues, rework, and health-related concerns. The findings consistently confirmed that a higher level of adherence to LC principles led to significant reductions in project delays, cost overruns, quality issues, and health-related problems. This analysis strongly supports the notion that a more extensive adoption of LC practices results in substantial improvements in project performance. By presenting these compelling results, this study offers valuable insights to the construction industry, providing a clearer path for the effective integration of LC practices.

Keywords: Lean Construction; Waste; Construction Management; Lean Principles; Quality Management.

1. Introduction

The construction industry has grappled with persistent issues of waste, occurring throughout the construction process, material management, and design and planning phases. These wasteful practices significantly contribute to cost overruns and, at times, lead to project delays due to disrupted cash flows [1, 2]. Furthermore, the construction sector has been slow to embrace effective change management approaches, exacerbating the issue [3, 4]. In response to these challenges, some developed and a few developing countries have adopted innovative technologies, sustainable methods, and environmentally friendly materials to curtail waste. Strategies such as Total Quality Management [5], Just-In-Time [6], Lean Construction [7], and value engineering [8] have collectively contributed to reducing wasteful practices. Lean management principles, renowned for fostering sustainable development in industries, have proven effective in enhancing coordination, waste reduction, sustainability, cost and time efficiency, quality, productivity, and resource utilization [9, 10]. The success story of Toyota serves as a testament to the positive effects of lean management principles [11].

* Corresponding author: edmund-baffoe-twum@utc.edu

 <http://dx.doi.org/10.28991/CEJ-2024-010-04-09>



© 2024 by the authors. Licensee C.E.J, Tehran, Iran. This article is an open access article distributed under the terms and conditions of the Creative Commons Attribution (CC-BY) license (<http://creativecommons.org/licenses/by/4.0/>).

Despite numerous reports citing significant benefits from implementing Lean Construction (LC) principles, its adoption rate remains relatively low, with many firms hesitating to implement LC practices [12–14]. Lack of awareness has been identified as one of the top barriers to LC adoption by many researchers [15–19]. Similarly, fear of failure or uncertainty associated with LC has prevented the construction industry from embracing Lean practices [20–22]. The true potential and efficacy of existing LC practices are questioned, as the industry lacks awareness of the tangible benefits LC can offer in real-world projects [23]. Additionally, theoretical concerns have led some researchers to oppose the utilization of LC practices [24, 25]. These challenges are compounded by insufficient support from industry stakeholders, limiting the full realization of LC's potential and rendering it seemingly unnecessary [10]. Confidence in the implementation of Lean Construction (LC) within the construction industry would significantly benefit from a thorough comparison and evaluation of LC's efficacy in actual projects. Currently, there is a scarcity of case studies measuring the practical benefits of LC in contemporary research, with much of the existing literature relying on theoretical comparisons to assess LC efficacy and potential [26]. Moreover, while many case studies focus on time and cost overruns, there is a limited exploration of the impact of LC on quality, safety, and health issues [27]. Evaluating the effectiveness of LC practices can play a pivotal role in educating industry stakeholders about the value of lean practices.

To address this gap, this study primarily aims to assess the efficacy of LC practices through real-world projects. The hypothesis, examining whether LC delivers benefits to the construction industry and to what extent, will be rigorously tested. A literature review will be conducted to identify LC principles, and their percentage conformance within the construction industry of Pakistan will be assessed using a questionnaire survey. Case studies will then be undertaken to investigate the efficacy of LC in projects with higher percentage conformance compared to those with lower adherence to LC principles, thereby evaluating the impact of LC implementation. Through this comprehensive investigation, the team aims to provide insights into the utility of LC and contribute to boosting the confidence of the construction industry in its adoption. The main objectives of this study include:

- To assess the percentage adherence of Lean Construction (LC) practices within the construction industry of Pakistan.
- To compare the performance (in terms of time, cost, safety, health, and quality) of projects where the maximum LC principles are implemented with those where the least LC principles are implemented.

2. Literature Review

2.1. Problems in Construction

Construction projects are widely recognized for their inherent uncertainty and volatility, primarily arising from the diverse and collaborative nature of the environments in which they take place. These projects involve multiple specialized teams working together to achieve common objectives [28]. The resulting uncertainty leads to significant waste generation, both in the final product and throughout various processes, often considered inherent to the nature of construction projects. According to Babalola et al. [29], the construction industry grapples with numerous non-value-adding activities, which have emerged as a primary source of waste. Lauri Koskela, along with Watson et al. [30], identify non-value-adding activities such as waiting, rework, inspection, overproduction, large inventories, and movement as significant contributors to waste generation [30].

Substantial research, including assessments by the Construction Industry Institute, emphasizes the severity of this issue, concluding that non-value-added efforts or waste account for an average of 50% in construction projects [31]. Similarly, Mossman [21] reveals that an astounding 55–65% of construction efforts are wasted, significantly undermining construction productivity. The sheer volume of waste production exerts a profound impact on the performance of the construction industry, accentuating inefficiencies [32, 33].

In the United Kingdom, concerning statistics indicate up to 30% rework, 40–60% labor inefficiency, and a minimum of 10% material wastage, with time wastage reaching a staggering 57% [32]. Furthermore, research conducted by Love et al. [34, 35] in Australia, involving an analysis of 346 construction projects, exposes that rework events account for 34% of total costs, with owners contributing 50%, and contractors 43% of these rework occurrences [35].

The extensive prevalence of waste in both materials and effort underscores a pivotal factor responsible for the lackluster performance and inefficiencies in the construction industry. Urgent measures are imperative to mitigate waste generation, enhance efficiency, and drive meaningful improvements within the construction sector.

2.2. Emergence of Lean Construction

The construction industry drew inspiration from the Toyota Production System (TPS) and began integrating TPS tools and techniques to enhance construction efficiency and address operational challenges. This approach, known as Lean Construction (LC), has been shaped by influential researchers such as James P. Womack, Glenn Ballard, Lauri Koskela, Diekmann, and others [36, 37]. James P. Womack and his co-authors made significant contributions by

introducing lean principles in their seminal work, "The Machine That Changed the World." This book conducted a comparative analysis of lean practices within the automotive industry, specifically focusing on Toyota, General Motors, and Ford. This thorough examination underscored the effectiveness and advantages of lean production principles, leading to the global spread of the concept.

Lauri Koskela is credited with laying the theoretical foundation for LC in 1992. He introduced the Transformation-Flow-Value (TFV) theory in 2000 and played a crucial role in developing lean principles tailored for the construction industry [37]. Koskela identified a fundamental set of LC principles critical for lean production in construction. These principles encompass meeting customer requirements, minimizing non-value-added activities, reducing variability, shortening cycle times, enhancing transparency and flexibility, continuous improvement, process simplification, optimizing flow and conversion, benchmarking, and concentrating on process control [38, 39].

Diekmann further refined this framework by categorizing Lean Construction (LC) principles into five key areas: customer focus, cultural/people factors, workplace standardization, waste elimination, and continuous improvement/built-in quality [31]. Case study outcomes have yielded a comprehensive set of sub-principles supporting each major lean principle, as outlined in Table 1. Institutions such as the LC Institute (LCI) and the International Group for LC (IGLC) have played pivotal roles in promoting and endorsing lean principles and practices within the construction sector.

Table 1. Lean Principles and Sub-Principles (Adapted from Diekmann et al. [31])

	Principles	Subprinciples
Lean Construction	Standardization	Visual management
		Workplace organization
		Defined work process
	Cultural/people	People involvement
		Organizational commitment
		Training
	Eliminate Waste	Reduce Process cycle
		Supply chain management
		Optimize work content
		Optimize production system
Continuous Improvement/ Build in Quality	Error proofing	
	Organizational learning	
	Response to defects	
Customer Focus	Flexible resource	
	Optimize value	

Over three decades, the construction industry has witnessed successful implementations of LC, particularly in developed countries. Recent instances of effective LC applications have resulted in significant improvements in cost and time efficiency, as well as increased productivity [22, 40, 41]. These achievements underscore the potential of LC to enhance construction performance and alleviate inefficiencies.

2.3. Why lean Construction not Taking off

Despite well-established theories and several successful case studies, Lean Construction (LC) has faced challenges in gaining widespread acceptance in the expansive construction industry [42]. According to Ballard et al. [43], significant barriers hindering the adoption of LC include strong resistance to change among various stakeholders and a lack of commitment and leadership. Jorgensen (2006) [44] adds that the construction sector has not been as exposed to the principles of LC as the manufacturing industry, resulting in a limited understanding of its core concepts. To address this issue, it is essential to enhance awareness and knowledge of LC. Ballard et al. [43] suggest that increasing government-sponsored events and programs that promote LC would raise industry awareness.

Sarhan & Fox [15] conducted a questionnaire survey, revealing a lack of sufficient awareness and understanding of lean concepts as the primary barrier to implementing LC. The authors advocate for a more impactful approach to promotion, emphasizing the importance of discussing practical lean implementation stories rather than presenting abstract, metrics-based improvements. Similarly, Simonsen et al. [6] echo this sentiment, suggesting strategies such as showcasing LC success stories through media, organizing meetings and conferences, and allocating funds for LC research. Aslam et al. [45] further emphasize the importance of sharing success stories related to LC implementations to raise industry-wide awareness.

In response to these challenges, this research takes a pragmatic approach by evaluating different projects based on their adherence to LC principles. This study aims to provide concrete insights into the impact of implementing LC principles on project performance. Through this approach, the research aims to contribute to a clearer understanding of how LC can positively influence construction projects and potentially pave the way for its broader adoption in the industry.

3. Research Methodology

Analyzing the effectiveness of implementing Lean Construction (LC) in the construction industry is challenging due to the complex nature of lean principles and variations in these fundamental concepts proposed by different scholars [36]. To address this challenge, this research selected the lean principles and sub-principles introduced by Diekmann as the foundation for developing a questionnaire (see Table 1) [31]. Diekmann's principles and sub-principles are notably comprehensive and cover nearly all the essential principles discussed by other researchers, such as Sacks et al. [46] and Ballard et al. [47].

This study tests four main alternative hypotheses against a single null hypothesis (H_0) that LC practices have no significant reduction in project delays, cost overruns, quality issues/reworks, and health issues. The four alternative hypotheses are as follows:

H₁: LC practices enhance project performance by mitigating delays.

H₂: LC practices enhance project performance by mitigating cost overruns.

H₃: LC practices diminish quality-related issues and prevent reworks.

H₄: LC practices mitigate health-related issues otherwise faced on construction sites.

Our research methodology, depicted in Figure 1, adopts a two-stage approach that encompasses both quantitative analysis and case studies. In the initial stage, the research team conducted a questionnaire survey using a 5-point Likert scale. The decision to employ a 5-point scale was based on its comparable validity to other scales while optimizing efficiency in data collection and analysis [48]. The questionnaire comprised 31 questions, including 27 questions to assess lean conformance based on LC principles/sub-principles and 4 questions related to project outcomes (delays, cost overruns, quality/reworks, and health/safety issues). A total of 220 questionnaires were distributed via email, and 72 complete responses were received, resulting in a response rate of 32.72%. Such response rates are typical and have been observed in previous research [49-51].

To calculate the lean conformance percentage, the following formula was utilized:

$$\text{Lean Conformance (\%)} = \frac{\text{Sum of all the actual answers} \times 100}{\text{Sum of highest answer scores}} \quad (1)$$

For data analysis, the latest version of SPSS was utilized. Additionally, skewness and kurtosis tests were employed to assess data symmetry and distribution tails. The Shapiro-Wilk test was used to determine data normality, following the methodology of [52]. The results of the normality test assist in determining the nature of the data and the suitable analysis tool for that type of data. For a dataset to be considered normally distributed, the p-value of the Shapiro-Wilk normality test should be greater than 0.05 when tested for a 95% confidence level [53].

To rank and prioritize lean principles and sub-principles based on their significance, the Relative Importance Index (RII) was employed as recommended by Naji et al. [54]. The RII is recognized for its utility in ranking factors based on expert perceptions, as highlighted by Baig et al. [55]. RII not only helps in ranking factors but also assists in shortlisting important factors based on the RII score. A threshold of 0.50 is used, below which factors are considered less important and hence discarded [56].

To examine correlations between lean principal categories, Pearson chi-square tests were conducted, following the approach of [57]. The Pearson chi-square value and its p-value help in understanding statistically significant associations among variables being analyzed. A p-value less than 0.05 indicates that observed frequencies in the data are significantly different from what would be expected if there were no associations [58]. Given the non-parametric nature of the data, Kruskal-Wallis tests were employed to assess association-independence among groups, as suggested by Wei et al. [59]. A p-value of less than 0.05 shows that a strong association exists among LC practices and individual project outcomes, hence rejecting the null hypothesis that the factors have no association with each other [59].

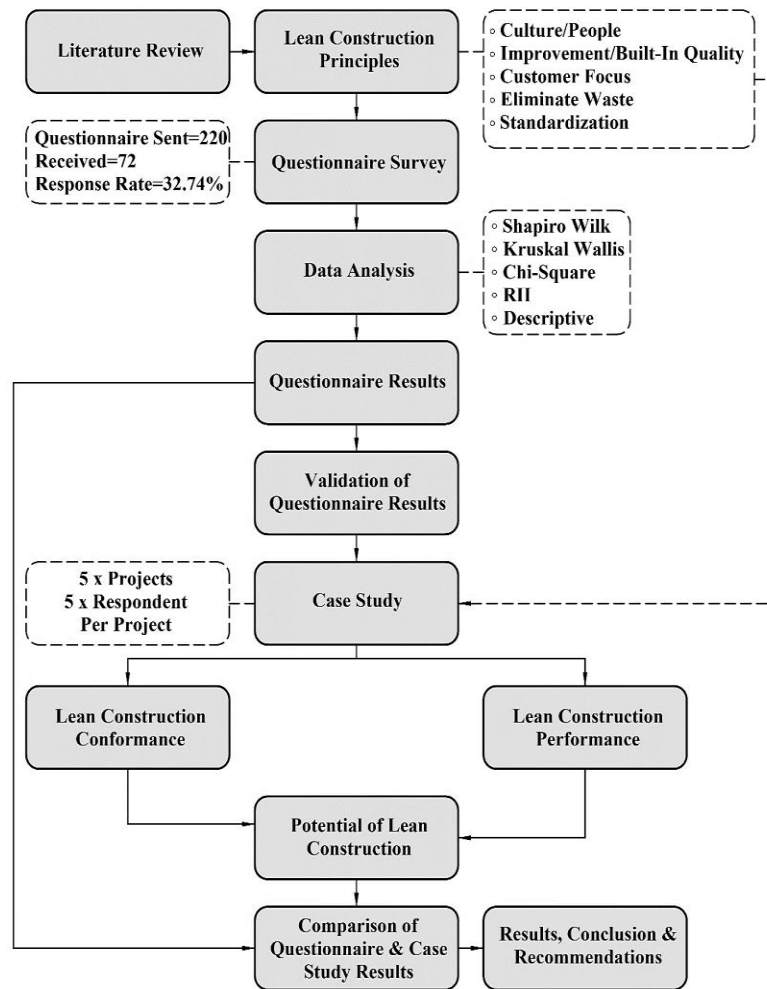


Figure 1. Research Methodology

To validate the survey findings, face-to-face interviews were conducted with 25 experts, drawn from five distinct case study projects. These experts represented a diverse range of project performance levels, including cost overruns, delays, and on-time/on-cost completion. The structured interviews consisted of 16 questions, with 12 focused on Lean Construction (LC) principles and 4 centered on real-time project outputs. Detailed information about the selected case study projects is presented in Table 2. Participants responded to LC principle-based questions using a score scale ranging from -10 to +10. A positive +5 score indicated a 50% adoption of a specific LC principle, while a negative score of -5 implied opposition to the principle up to 50%, following the approach of Rogers [60]. A sample question and the scale are shown in Table 3. Additionally, Table 4 provides sample questions related to real-time output assessment, aimed at comparing project outcomes based on LC principles adoption.

Table 2. Case Study Projects for Lean Practices Assessment

Sr. #	Project Name	Project Type and Detail
01	Infectious Treatment Centre, Hospital (ITCH)	During the COVID-19 pandemic, a prefabricated steel structure hospital was built in just 40 days at a cost of 980 million. The hospital, known as ITCH, encompasses 250 beds and is spread over 40 kanals of land. The project exhibited excellent performance, with no significant delays or budget overruns.
02	Building of Tunnelling Institute (BTI)	This building is a prefabricated steel structure that was completed in six months. The project was executed smoothly, and there were no significant delays or cost overruns.
03	High-Rise Residential Building (HRB)	This is a high-rise apartment building constructed with an RCC frame structure. Originally scheduled for completion in 2 years, the project encountered a delay of 9 months. Additionally, there was a minor cost overrun of 0.03%. The main cause of this delay was a 6-month period of extensive rework required to address quality issues.
04	Approach Roads and Roundabout (ARR)	The project was initiated to improve the traffic flow in Rawalpindi city. It was completed without any significant delays or cost overruns, and the project's performance met expectations in most cases.
05	Road in Hilly Terrain (RHT)	This project involves the rehabilitation and widening of a 164 km hilly road. While the original plan aimed for completion within 3 years, it faced a delay of 13 months and an approximate 10% cost overrun. The primary reasons for these challenges include the harsh environment and rugged terrain in the area.

Table 3. Sample Question of Interview along with used along with used Scale

Was coordination and cooperation among all the departments, like mechanical, electrical, architectural, civil, design, etc., given enough importance to minimize the internal conflicts?																				
Score																				
-10	-9	-8	-7	-6	-5	-4	-3	-2	-1	0	+1	+2	+3	+4	+5	+6	+7	+8	+9	+10

Table 4. Sample Interview Question for Project Output Investigation

Were there any cost overruns?
If yes, then: -
Initially planned cost of the project:
Actual cost of the project:
Percentage of cost overrun:

4. Results

4.1. Questionnaire Survey

The team conducted statistical analysis and RII analysis for all five principles and fifteen sub-principles, in addition to the four output-based questions included in the Likert scale questionnaire. The results are presented in Table 5. The mean scores of all Lean Construction (LC) sub-principles indicate that certain sub-principles, including response to defects, error-proofing, flexible resources, visual management, and defined work processes, are widely adopted within the construction industry. While other LC principles are also followed to some extent, there is no standardized method employed by the construction industry for planning the adoption of LC principles to achieve better results. Results in Table 5 show that the sub-principles with the highest mean score in each category are people involvement (3.875), error proofing (4.083), flexible resources (4.028), reduced process cycle time (3.889), and defined work processes (3.986). Meanwhile, the sub-principles with the least mean score in each category are organizational commitment (3.653), response to defects (3.583), optimize value (3.667), supply chain management (3.625), and workplace organization (3.764), respectively.

Table 5. Results (Mean Score, Normality, RII)

Principle	Sub Principle	Statement	Mean	Shapiro Wilk P Value	RII	Rank
Culture/ People	People involvement	Employees are considered an integral part of the organization, and their viewpoint is given consideration by top management.	3.875	<0.001	0.775	8
	Organizational Commitment	Management at all levels have developed a mechanism to keep themselves updated with new developments.	3.653	<0.001	0.73	24
	Training	Firm focuses on incorporating new skills in employees that are considered necessary to fulfil changing demands.	3.708	<0.001	0.741	18
Continuous Improvement/ Built in Quality	Response to defects	During defects identification process, quality plans are prepared which assign responsibilities to concerned members.	3.667	<0.001	0.733	21
		Defects are identified and remedial actions are recorded for future use.	3.917	<0.001	0.783	5
	Error proofing	Every team is quite responsible in ensuring quality in the product by their own.	3.583	<0.001	0.716	26
		Supervisors always plan their work methodologies through due consultation with team members on a regular basis.	4.083	<0.001	0.816	1
Customer Focus	Organization learning	Information related to techniques and changes are always communicated timely with concerned departments.	3.514	<0.001	0.702	27
	Flexible Resources	Firm is flexible and can cope with changes while utilizing the minimum number of resources.	3.944	<0.001	0.788	4
		Firms do depend on actual resources but change directions with changing customer needs without losing much time or money.	3.681	<0.001	0.736	19
	Optimize Value	All changes are passed immediately via telephone call first, and then through the proper channel.	4.028	<0.001	0.805	2
		The project value is defined with the customer and known to everyone.	3.667	<0.001	0.733	22
		Customer needs are studied throughout the project rather than initially only.	3.75	<0.001	0.75	16

	Supply Chain Management	Materials predominantly reach at site just before their usage and minimum inventory is required.	3.625	<0.001	0.725	25
		Firms select reliable suppliers who meet requirements in time. Changing suppliers is never planned.	3.819	<0.001	0.763	12
Eliminate Waste	Optimize Production System	Employees are multi-skilled and can utilize diverse activities.	3.722	<0.001	0.744	17
		Detailed sequencing, flow charts, and scheduling are carried out regularly and consultation is performed before and after activities execution.	3.847	<0.001	0.769	9
	Reduce Process Cycle Time	Coordination and cooperation among all departments is given enough importance.	3.819	<0.001	0.763	13
		Risk management is carried out and planned. Risk register is also maintained regularly.	3.889	<0.001	0.777	7
Standardization	Workplace Organization	Master schedule, Back-schedule and look-ahead plans are maintained through input of foremen and key workers.	3.83	<0.001	0.766	11
		Standard, prefabricated, preassembled, repetitive construction elements are preferred.	3.681	<0.001	0.736	20
	Defined Work Processes	Non-value-added activities and identified and efforts to eliminate their resource utilization are made.	3.667	<0.001	0.733	23
Standardization	Visual Management	Jobsite uses visual devices showing requirements of schedule, quality, safety, and productivity.	3.903	<0.001	0.78	6
		Firms give due emphasis to organization and structuring of resources, materials, tools.	3.764	<0.001	0.752	15
	Workplace Organization	Firms pay enough attention to housekeeping in administration blocks as well as jobsite.	3.792	<0.001	0.758	14
Defined Work Processes		Processes are identified and continuously monitored.	3.986	<0.001	0.797	3
		Regular meetings are carried out instead of inspections only	3.847	<0.001	0.769	10

When comparing the adoption rate of all LC principles with project outcomes, the team observed an inverse relationship between LC practices and negative outcomes, such as delays, cost overruns, quality issues, and health problems, as depicted in Figure 2. This clearly indicates that an increase in the adoption rate of LC practices reduces the occurrences of cost overruns, delays, quality issues, and health problems. For example, on projects with a 20% lean principles adoption rate, the probability of delays is 73%, cost overrun is 74%, quality issues are 75%, and health issues are 71%. As the LC adoption rate increases to 81%, the chance of delays is reduced to 20%, cost overrun to 26%, quality issues to 15%, and health issues to 24%, respectively. Hence, the trend shows the inverse relation between LC practice adoption rate and negative project outcomes. The most improvement with an increase in LC adoption is visible in quality, followed by delays, health issues, and cost overrun.

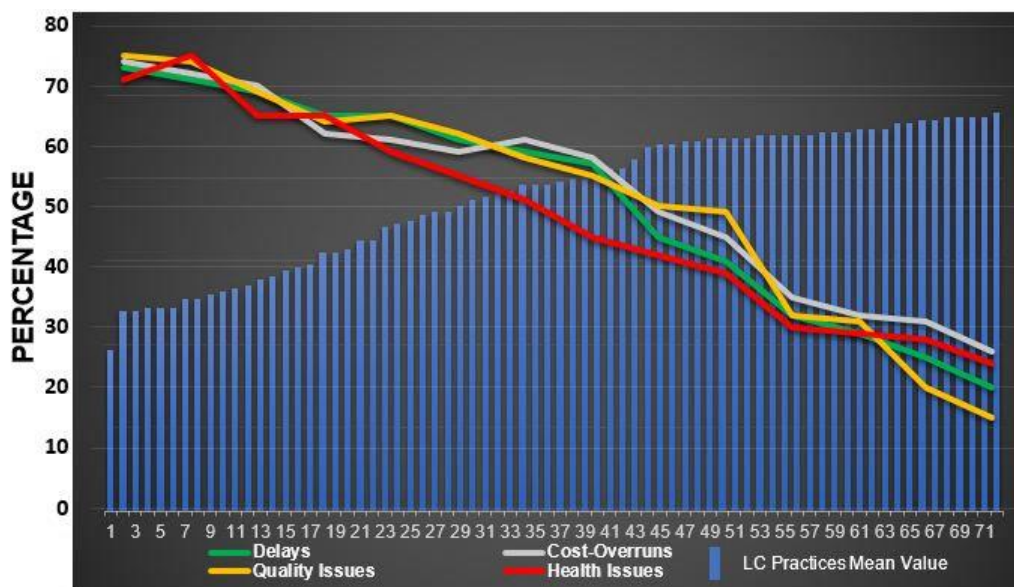


Figure 2. Comparison - LC Practices Followed vs Project Outputs

Furthermore, the mean values for all 27 sub-principles and four project outputs were utilized as inputs in the Chi-square test to individually assess whether LC practices improved performance or not. The input mean scores were rounded to whole numbers to meet the data type requirements of the Chi-square test, following the method suggested by García-Bernal and García-Casarejos [5]. The conversion of mean values to whole numbers was executed using the scale provided by Sozen & Guven [61].

The results of the Chi-square analysis demonstrate that the enhancement in project execution performance offered by LC practices is statistically significant. Based on a p-value of <0.05, all four alternative hypotheses are accepted, proving that LC practices significantly improve project performance by reducing project delays, cost overruns, quality issues and reworks, as well as reducing health-related issues faced on construction sites. An overview of the study's overall results can be found in Table 6.

Table 6. Chi-Square Mean Comparison of LC and Traditional Approaches

No.	Relation Studied	Likelihood Ratio		(Kruskal Wallis Test P value)		Remarks
		Value	P-value	Value	P-value	
01	LP vs Delays	33.80	<0.001	35.085	<0.001	LC practices improve project performance by reducing delays.
02	LP vs Cost Overrun	27.119	<0.001	28.704	<0.001	LC practices improves project performance by reducing cost overruns.
03	LP vs. Quality issues/ Reworks	21.104	<0.001	20.646	<0.001	LC practices ensure a decrease in quality related issues and prevent requirement for reworks.
04	LP vs Health Issues	20.661	<0.001	19.845	<0.001	Results conclude that increase LC practices reduce health related issues otherwise faced on construction sites.

To further explore the association or independence between LC practices and individual project outcomes, a Kruskal-Walli's test was conducted. As the p-value obtained is significantly less than 0.05, it provides strong evidence against the null hypothesis, suggesting there is indeed an association or relationship between LC practices and individual project outcomes. Consequently, the alternative hypothesis is accepted, which asserts that LC practices lead to improved project performance outcomes. Therefore, based on the results of the Kruskal-Walli's test, it can be concluded that the efficacy of LC practices is valid, and further adoption is recommended (see Table 6).

4.2. Case Study

A total of 25 interviews were conducted, with five interviewees selected from each project. These interviews were carried out face-to-face to facilitate the resolution of any communication or understanding gaps before collecting responses. To streamline the analysis and interpretation of interview results, the interviews were mapped to the Lean principles and sub-principles. In the Tunneling Institute (BTI) project, most of the 12 Lean principles were adopted, with the exception of training. The overall adoption rate for these principles was 67%. Regarding the adopted LC principles, the project experienced only a 1.67% delay, with no significant issues related to cost overruns, quality, or health (see Table 7).

Table 7. Mean Percentage Value of Conformance to LC Principles by Case Study Projects

LC Principles	Statement	ITCH Disease Centre (%)	Tunneling Institute (BTI) (%)	Approach road project (ARR) (%)	High-rise Residential (HRB) (%)	Hilly terrain project (HTR) (%)
Error Proofing	Did supervisors always plan their work methodologies through due consultation with team members on regular basis?	52	74	62	15	30
Workplace Organization	Did your firms pay enough attention to housekeeping in administration block as well as jobsite?	64	76	62	10	60
Supply Chain Management	Firms select reliable suppliers who meet requirements in time. Changing suppliers is never planned.	70	72	48	30	50
Waste reduction/ Supply Chain Management	Did companies identify construction waste and was there any effort made to minimize it?	66	68	58	0	0
Optimize Work Content	Did your company use repetitive, pre-assembled or prefabricated standard construction elements?	76	84	56	0	0
People Involvement	Was input of foreman and key workers considered in preparation of plans and schedule?	68	82	64	30	40
Reduce Process Cycle Time/ coordination	Was coordination and cooperation ensured among all departments of the organization given importance to minimize internal conflicts?	52	48	54	18	26
Reduce Process Cycle Time/ risk management	Was risk management performed throughout the project and risk register maintained?	50	60	60	2	10
Training	Did the organization train and utilize employees for multi-skilled activities?	0	0	52	0	0
Optimize Value	Was the company focusing on customer needs throughout the project? And what efforts were made to execute a project based on those needs?	82	84	58	30	70
Response to Defects	Were defects identified and monitored through quality plans and RACI charts so that future occurrences can be minimized?	80	80	56	0	0
Organizational Commitment	Were changes in construction management techniques readily adopted by your top-level management, and were these changes reflected in the training of employees to incorporate new skills in them?	76	76	62	0	0
Lean Construction Conformance		61.33	67.00	57.67	11.25	23.83

Similarly, the Isolation hospital and infectious treatment center project had a 61% adoption rate of LC principles, which effectively prevented cost overruns, quality issues, and health problems, resulting in only a 2.5% project delay. The Approach Road project (ARR) exhibited an adoption rate of 57.66%, and the project faced a 5.1% delay, 6% quality issues, with minimal cost overruns and safety issues (see Table 7).

On the other hand, the High-rise residential building project had a much lower LC adoption rate of only 11.25%, leading to a 37.5% project delay, a 0.03% cost overrun, 6% quality and rework-related issues, and 5% health issues. Similar results were observed in the Hilly terrain road project (HTR), where the LC principles adoption rate was only 23.5%, resulting in a 33% delay, 10% cost overrun, 12% quality issues, and 3% health-related issues. Mean percentage values of LC principles conformance by case study projects can be found in Table 7.

By combining these conformance values with the mean output values, a trend was observed in which increased LC conformance leads to a reduction in delays, cost overruns, quality issues, and health problems. The BTI project recorded the highest conformance to LC principles at 67%, resulting in comparatively fewer health, quality, delay, and cost overrun issues. Conversely, the High-rise residential project (HRB) had the lowest LC principle adoption rate, at only 11.25%. This project experienced the highest project delays (37%) and relatively more quality issues (6%)

In Figure 3, a clear trend emerges, demonstrating that an increase in LC conformance leads to a reduction in project delays, cost overruns, quality issues, and health concerns. Conversely, projects with low LC conformance rates experienced higher rates of project delays, cost overruns, quality issues, and health problems. Therefore, the idea that LC principles conformance significantly enhances overall project and product performance has been substantiated. This conclusion underscores that embracing LC principles in their true sense can substantially mitigate these four adverse outcomes, as noted by Aziz & Hafez [32] (2013).

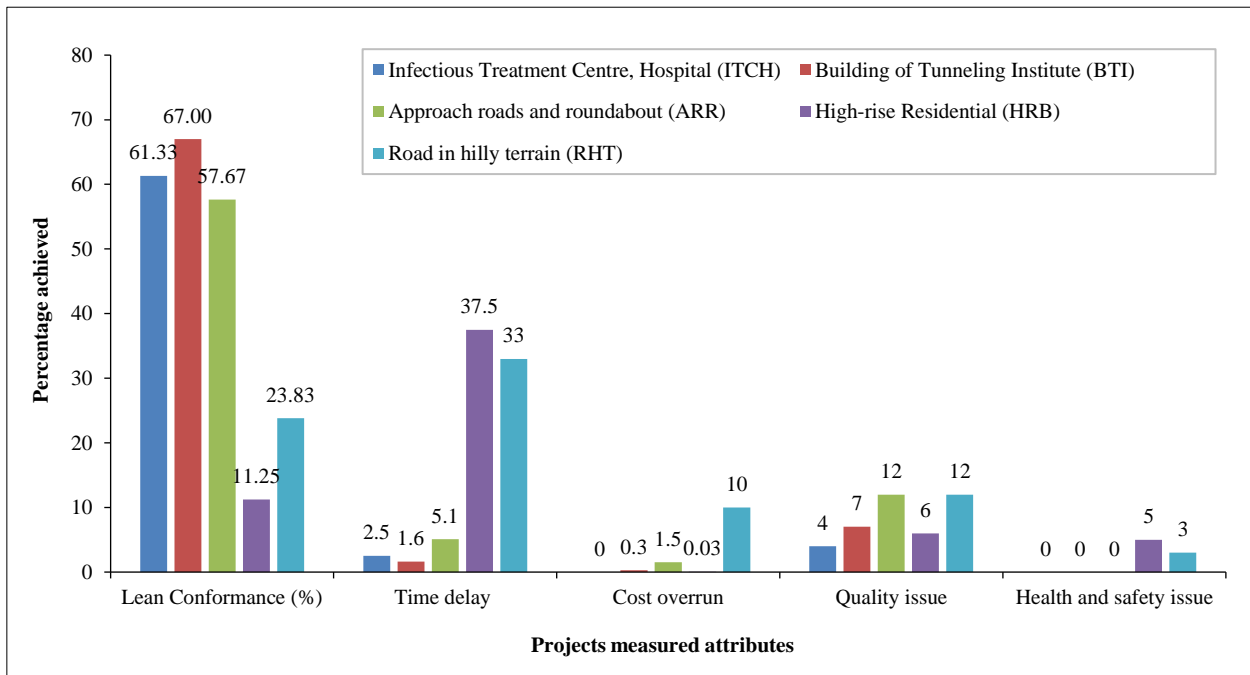


Figure 3. LC Conformance vs. Project Performance

These results also affirm the conclusion that the adoption of lean practices leads to reductions in waste and project delays, as highlighted by Likita et al. [62].

The findings indicate that projects still relying on conventional management tools and methods suffered from cost overruns, delays, quality issues, and safety concerns. In contrast, projects that incorporated some level of LC principles witnessed a decrease in cost overruns, delays, improved quality, and reduced health issues.

5. Discussion

The primary objectives of this study were to evaluate adherence to LC practices and their impact on performance in the construction industry. To achieve this, a questionnaire survey was conducted to assess LC conformance concerning project performance. Results from the questionnaire survey indicate that some LC principles, such as "Error proofing," "Flexibility in resources," "Defined work processes," "Response to defects," "Value management," and "People involvement," are relatively well-adopted in the construction industry. Conversely, certain principles have limited adoption, including "Organizational learning," "Organizational commitment," "Optimized value," and "Optimize

production systems." Addressing these less-adopted principles is essential to establishing a standardized environment for complete LC adherence. Mean scores for all LC principles reveal the highest level of conformity for "Optimizing value," followed by "Supply chain management," "Error proofing," "Response to defect," "Organizational commitment," and "Workplace organization." Conversely, there is lower conformity for other LC principles, highlighting the need for focused efforts to establish a standardized implementation process for comprehensive LC adherence [11].

To further assess significance, Pearson Chi-square and Likelihood ratio tests were conducted to compare mean scores of lean practices with the four major outcomes. The consistent results from these tests demonstrate that lean practices enhance project performance by reducing delays, cost overruns, preventing quality issues, and mitigating health concerns. The Kruskal-Wallis test results reject the null hypothesis and confirm the validity of lean practices within the construction industry, reinforcing the recommendation for further adoption.

To validate the results, five case study projects were selected to examine their adherence to LC principles and how this relates to issues such as delays, cost overruns, quality problems, and health concerns. The analysis of the mean scores indicates the degree of conformity to LC principles for each of the selected projects. The Tunneling Institute (BTI) achieved a 67% conformance rate, while the ITCH disease center scored 61.33%, the Approach Road project (ARR) scored 57.66%, the Hilly terrain road scored 23.83%, and the High-Rise Residential project (HRB) scored 11.25%. The delays experienced on these projects ranged from 1.67% (projects where LC principles are implemented) to 37.5% (projects where LC principles are not implemented), while quality issues varied from 0% to 10%. Similar patterns were observed for cost overruns and health issues. This pattern demonstrates that as adherence to LC principles increases, project performance improves in terms of reduced delays, cost overruns, quality issues, and health concerns. Berawi et al., [2] (2023) also reported that using LC tools and techniques, the industry can experience a 19.14% reduction in project completion time. This finding aligns with expectations from the literature, which suggests that conforming to lean practices leads to time savings, cost savings, improved quality, and sustainable product development [26, 27, 63].

The results challenge the misconception that LC practices result in additional costs. Instead, it is observed that lean practices prevent cost overruns by saving expenses related to defect correction, reworks, and non-value-adding activities [2, 19, 64].

One limitation of this study was the availability of data for the selected projects in case studies. Data related to quality and health/safety issues were not documented, and researchers had to rely on input from the interviewees for these two project performances. Additionally, all these projects are funded by the Federal Government, so minimal cost overrun is observed. However, the contractors working on these projects reported cost overruns, as documented in this research.

6. Conclusion

This study has offered valuable insights into adherence to LC practices and their profound impact on project performance within the construction industry. Through a comprehensive questionnaire survey and thorough analysis of case study projects, both strengths and areas for improvement in the adoption of LC principles are identified within the Pakistani construction industry. While some principles, such as "error proofing" and "flexibility in resources," are relatively well-adopted, others, like "organizational learning" and "optimized value," show limited adoption, underscoring the need for focused efforts to establish a standardized environment for complete LC adherence.

Our findings unequivocally affirm the positive correlation between adherence to LC principles and improved project outcomes. This is evidenced by reduced delays, cost overruns, quality issues, and health concerns. Statistical tests further validate the significance of lean practices in enhancing project performance within the construction industry, reinforcing the recommendation for their further adoption. The analysis of case study projects emphasizes the practical implications of adhering to LC principles. Projects with higher conformity to LC principles demonstrated superior performance metrics, underscoring the importance of systematic implementation. Moreover, our findings align with previous studies, highlighting the benefits of lean practices in terms of time and cost savings, improved quality, and sustainable development. Contrary to common misconceptions, LC practices were found to prevent cost overruns by addressing issues such as defect correction, reworks, and non-value-adding activities.

Despite encountered limitations, such as data availability for case studies, our study contributes significantly to the growing body of literature on LC. It provides empirical evidence of its effectiveness in enhancing project performance, urging stakeholders in the construction industry to prioritize the adoption and implementation of lean practices.

This study serves as a guiding beacon for the construction industry, dispelling lingering doubts about the tangible benefits of LC. Academia stands to gain valuable insights from this study, providing a robust framework to assess the effectiveness of their own research efforts in LC. Industry stakeholders can leverage the results of this study to identify weaknesses in implementing LC practices and gain confidence in adopting them by recognizing the efficacy of LC to enhance project outcomes.

7. Declarations

7.1. Author Contributions

M.As., E.B.T., M.Ah., and A.U. contributed to the design and implementation of the research, to the analysis of the results and to the writing of the manuscript. All authors have read and agreed to the published version of the manuscript.

7.2. Data Availability Statement

The data presented in this study are available on request from the corresponding author.

7.3. Funding

The authors received no financial support for the research, authorship, and/or publication of this article.

7.4. Conflicts of Interest

The authors declare no conflict of interest.

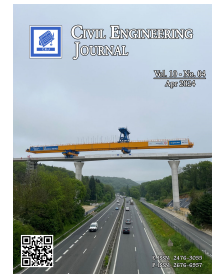
8. References

- [1] Suresh, M., Antony, J., Nair, G., & Garza-Reyes, J. A. (2023). Lean-sustainability assessment framework development: evidence from the construction industry. *Total Quality Management & Business Excellence*, 34(15–16), 2046–2081. doi:10.1080/14783363.2023.2222088.
- [2] Berawi, M. A., Sari, M., Miraj, P., Mardiansyah, Saroji, G., & Susantono, B. (2023). Lean Construction Practice on Toll Road Project Improvement: A Case Study in Developing Country. *Civil Engineering Journal*, 9(12), 3186–3201. doi:10.28991/CEJ-2023-09-12-016.
- [3] Johansen, E., Porter, G., & Greenwood, D. (2004). Implementing lean: UK culture and systems change. The 12th Annual Conference of the International Group for Lean Construction, 3-6 August, 2004, Helsingør, Denmark.
- [4] Santorella, G. (2017). *Lean Culture for the Construction Industry: Building Responsible and Committed Project Teams* (2nd Ed.). Productivity Press, New York, United States. doi:10.1201/9781315186368.
- [5] García-Bernal, J., & García-Casarejos, N. (2014). Economic analysis of TQM adoption in the construction sector. *Total Quality Management and Business Excellence*, 25(3–4), 209–221. doi:10.1080/14783363.2012.728848.
- [6] Bamana, F., Lehoux, N., & Cloutier, C. (2017). Just in Time in Construction: Description and Implementation Insights. Annual Conference of the International Group for Lean Construction. doi:10.24928/2017/0064.
- [7] Gao, S., & Low, S. P. (2014). The Toyota Way model: An alternative framework for lean construction. *Total Quality Management and Business Excellence*, 25(5–6), 664–682. doi:10.1080/14783363.2013.820022.
- [8] Lin, X., Mazlan, A. N., Ismail, S., Hu, L., Kasiman, E. H. B., & Yahya, K. (2023). Status of value management studies in construction projects: A systematic review. *Ain Shams Engineering Journal*, 14(1), 101820. doi:10.1016/j.asej.2022.101820.
- [9] Alsmadi, M., Almani, A., & Jerisat, R. (2012). A comparative analysis of Lean practices and performance in the UK manufacturing and service sector firms. *Total Quality Management & Business Excellence*, 23(3–4), 381–396. doi:10.1080/14783363.2012.669993.
- [10] Hussain, K., He, Z., Ahmad, N., Iqbal, M., & Taskheer mumtaz, S. M. (2019). Green, lean, Six Sigma barriers at a glance: A case from the construction sector of Pakistan. *Building and Environment*, 161, 106225. doi:10.1016/j.buildenv.2019.106225.
- [11] Hines, P., Taylor, D., & Walsh, A. (2020). The Lean journey: have we got it wrong? *Total Quality Management and Business Excellence*, 31(3–4), 389–406. doi:10.1080/14783363.2018.1429258.
- [12] Bernstein, H. M., & Jones, S. A. (2013). *Lean construction: Leveraging collaboration and advanced practices to increase project efficiency*. Intelligence, McGraw Hill Construction, Bedford, United States.
- [13] Wandahl, S. (2014). Lean Construction with or without Lean - Challenges of implementing Lean construction. 22nd Annual Conference of the International Group for Lean Construction, 25-27 June, 2014, Oslo, Norway.
- [14] Bashir, A. M., Suresh, S., Oloke, D. A., Proverbs, D. G., & Gameson, R. (2015). Overcoming the Challenges facing Lean Construction Practice in the UK Contracting Organizations. *International Journal of Architecture, Engineering and Construction*, 4(1), 10–18. doi:10.7492/ijaec.2015.002.
- [15] Sarhan, S., & Fox, A. (2013). Barriers to implementing lean construction in the UK construction industry. *The Built & Human Environment Review*, 6.
- [16] Simonsen, R., Thyssen, M. H., & Sander, D. (2014, June). Is lean construction another fading management concept? 22nd Annual Conference of the International Group for Lean Construction, 25-27 June, 2014, Oslo, Norway.

- [17] Jørgensen, B., & Emmitt, S. (2008). Lost in transition: The transfer of lean manufacturing to construction. *Engineering, Construction and Architectural Management*, 15(4), 383–398. doi:10.1108/09699980810886874.
- [18] Musa, M. M., Mallam Saleh, I., Ibrahim, Y., & Adamu Dandajeh, M. (2023). Assessment of Awareness and Barriers to the Application of Lean Construction Techniques in Kano State, Nigeria. *Journal of Construction Business and Management*, 6(1), 33–42. doi:10.15641/jcbm.6.1.1262.
- [19] Singh, A., Kumar, V., Mittal, A., & Verma, P. (2024). Identifying critical challenges to lean construction adoption. *Construction Innovation*, 24(1), 67–105. doi:10.1108/CI-09-2022-0229.
- [20] Abdullah, S., Abdul-Razak, A., Abubakar, A., & Mohammad, I. S. (2009). Towards producing best practice in the Malaysian construction industry: the barriers in implementing the Lean Construction Approach. Faculty of Engineering and Geoinformation science, Universiti Teknologi, Malaysia.
- [21] Mossman, A. (2009). Why isn't the UK construction industry going lean with gusto? *Lean Construction Journal*, 24-36.
- [22] Warcup, R. (2015). Successful paths to becoming a lean organization in the construction industry. Ph.D. Thesis, Utah State University, Old Main Hill, United States.
- [23] Wiengarten, F., Gimenez, C., Fynes, B., & Ferdows, K. (2015). Exploring the importance of cultural collectivism on the efficacy of lean practices taking an organisational and national perspective. *International Journal of Operations and Production Management*, 35(3), 370–391. doi:10.1108/IJOPM-09-2012-0357.
- [24] Green, S. D., & May, S. C. (2005). Lean construction: Arenas of enactment, models of diffusion and the meaning of “leanness.” *Building Research & Information*, 33(6), 498–511. doi:10.1080/09613210500285106.
- [25] Green, S. D., Harty, C., Elmualim, A. A., Larsen, G. D., & Kao, C. C. (2008). On the discourse of construction competitiveness. *Building Research & Information*, 36(5), 426–435. doi:10.1080/09613210802076666.
- [26] Hei, S., Zhang, H., Luo, S., Zhang, R., Zhou, C., Cong, M., & Ye, H. (2024). Implementing BIM and Lean Construction Methods for the Improved Performance of a Construction Project at the Disassembly and Reuse Stage: A Case Study in Dezhou, China. *Sustainability*, 16(2), 656. doi:10.3390/su16020656.
- [27] Gao, M., Wu, X., Wang, Y., & Yin, Y. (2023). Study on the mechanism of a lean construction safety planning and control system: An empirical analysis in China. *Ain Shams Engineering Journal*, 14(2), 101856. doi:10.1016/j.asej.2022.101856.
- [28] Sinesilassie, E. G., Tabish, S. Z. S., & Jha, K. N. (2018). Critical factors affecting cost performance: a case of Ethiopian public construction projects. *International Journal of Construction Management*, 18(2), 108–119. doi:10.1080/15623599.2016.1277058.
- [29] Babalola, O., Ibem, E. O., & Ezema, I. C. (2019). Implementation of lean practices in the construction industry: A systematic review. *Building and Environment*, 148, 34–43. doi:10.1016/j.buildenv.2018.10.051.
- [30] Watson, G. H., Tucker, R. L., & Walters, J. K. (1993). Automation and robotics in construction. Proceedings of the 10th International Symposium on Automation and Robotics in Construction (ISARC), 24-26 May, 1993 Houston, Texas, United States.
- [31] Diekmann, J. E., Krewedl, M., Balonick, J., Stewart, T., & Won, S. (2004). Application of lean manufacturing principles to construction. Boulder, CO, Construction Industry Institute, 191.
- [32] Aziz, R. F., & Hafez, S. M. (2013). Applying lean thinking in construction and performance improvement. *Alexandria Engineering Journal*, 52(4), 679–695. doi:10.1016/j.aej.2013.04.008.
- [33] Nikakhtar, A., Hosseini, A. A., Wong, K. Y., & Zavichi, A. (2015). Application of lean construction principles to reduce construction process waste using computer simulation: A case study. *International Journal of Services and Operations Management*, 20(4), 461–480. doi:10.1504/IJSOM.2015.068528.
- [34] Love, P. E. D., Smith, J., Ackermann, F., Irani, Z., & Teo, P. (2018). The costs of rework: insights from construction and opportunities for learning. *Production Planning and Control*, 29(13), 1082–1095. doi:10.1080/09537287.2018.1513177.
- [35] Love, P. E. D., Teo, P., & Morrison, J. (2018). Revisiting Quality Failure Costs in Construction. *Journal of Construction Engineering and Management*, 144(2), 5017020. doi:10.1061/(asce)co.1943-7862.0001427.
- [36] Albalkhy, W., & Sweis, R. (2021). Barriers to adopting lean construction in the construction industry: a literature review. *International Journal of Lean Six Sigma*, 12(2), 210–236. doi:10.1108/IJLSS-12-2018-0144.
- [37] Koskela, L. (1992). Application of the New Production Philosophy to Construction. Technical Report No. 72, Stanford University, Stanford, United States.
- [38] Khaskheli, F. A., Ali, T. H., & Memon, A. H. (2020). Lean Construction Practices in Public Projects of Pakistan. *IOSR Journal of Mechanical and Civil Engineering*, 17(1), 57–60. doi:10.9790/1684-1701035760.

- [39] Maqbool, R., Bhuvaneshwaran, M., Rashid, Y., Altuwaim, A., & Ashfaq, S. (2023). A Decision Approach for Analyzing the Role of Modern Methods, Project Management and Integrated Approaches in Environmentally Sustainable Construction Projects. *KSCE Journal of Civil Engineering*, 27(8), 3175–3191. doi:10.1007/s12205-023-0701-0.
- [40] Šuman, N., & Semič El-Masr, M. (2013). The Integrated Approach for Introducing Innovation in construction Industry. *Organization, Technology & Management in Construction: An International Journal*, 5(2), 834–843. doi:10.5592/otmcj.2013.2.2.
- [41] More, V. D., Charhate, S., Sinha, M., & Student, P. G. (2016). Lean Construction Techniques in Indian Construction Industry: Some Analysis. *International Journal of Civil Engineering Research*, 7(1), 59–65.
- [42] Moradi, S., & Sormunen, P. (2023). Implementing Lean Construction: A Literature Study of Barriers, Enablers, and Implications. *Buildings*, 13(2), 556. doi:10.3390/buildings13020556.
- [43] Ballard, G., Kim, Y. W., Jang, J. W., & Liu, M. (2007). Road Map for Lean Implementation at the Project Level. The Construction Industry Institute, University of Texas, Austin, United States.
- [44] Jørgensen, B. (2006). Integrating Lean Design and Lean Construction: Processes and Methods. Ph.D. Thesis, The Technical University of Denmark, Lyngby, Denmark.
- [45] Aslam, M., Gao, Z., & Smith, G. (2020). Optimizing construction design process using the lean based approach. *Lean Construction Journal*, 2020, 176–204.
- [46] Sacks, R., Koskela, L., Dave, B. A., & Owen, R. (2010). Interaction of Lean and Building Information Modeling in Construction. *Journal of Construction Engineering and Management*, 136(9), 968–980. doi:10.1061/(asce)co.1943-7862.0000203.
- [47] Ballard, G., Koskela, L., Howell, G., & Zabelle, T. (2001). Production system design: Work Structuring Revisited. White Paper, 11.
- [48] Preston, C. C., & Colman, A. M. (2000). Optimal number of response categories in rating scales: Reliability, validity, discriminating power, and respondent preferences. *Acta Psychologica*, 104(1), 1–15. doi:10.1016/S0001-6918(99)00050-5.
- [49] Murmura, F., Casolani, N., Liberatore, L., & Vicentini, A. (2018). An empirical analysis of ISO 9001:2008 application in Italian services and manufacturing companies. *Total Quality Management & Business Excellence*, 29(7–8), 786–797. doi:10.1080/14783363.2016.1237286.
- [50] Stewart, D., & Waddell, D. (2008). Knowledge Management: The fundamental component for delivery of quality. *Total Quality Management and Business Excellence*, 19(9), 987–996. doi:10.1080/14783360802227803.
- [51] van der Wiele, T., van Iwaarden, J., Brown, A., Steimle, U., & Zink, K. J. (2009). An international comparison of the perceptions about the revised ISO 9000 quality system standards. *Total Quality Management*, 20(4), 393–408. doi:10.1080/14783360902781840.
- [52] Murali, G., Gayathri, R., Ramkumar, V. R., & Karthikeyan, K. (2018). Two statistical scrutinize of impact strength and strength reliability of steel Fibre-Reinforced Concrete. *KSCE Journal of Civil Engineering*, 22(1), 257–269. doi:10.1007/s12205-017-1554-1.
- [53] Nimon, K. F. (2012). Statistical assumptions of substantive analyses across the general linear model: A mini-review. *Frontiers in Psychology*, 3. doi:10.3389/fpsyg.2012.00322.
- [54] Naji, K. K., Gunduz, M., & Falamarzi, M. H. (2022). Assessment of Construction Project Contractor Selection Success Factors considering Their Interconnections. *KSCE Journal of Civil Engineering*, 26(9), 3677–3690. doi:10.1007/s12205-022-1377-6.
- [55] Baig, U. M. A. I. R., Khan, A. A., Abbas, M. G., Shaikh, Z. A., Mikhaylov, A. L. E. X. E. Y., Laghari, A. A., and Hussain, B. M. (2022). “Crucial causes of delay in completion and performance management of the construction work: Study on the base of relative importance index”. *Journal of Tianjin University Science and Technology*, 55(6), 75–102.
- [56] Wu, G., Yang, R., Li, L., Bi, X., Liu, B., Li, S., & Zhou, S. (2019). Factors influencing the application of prefabricated construction in China: From perspectives of technology promotion and cleaner production. *Journal of Cleaner Production*, 219, 753–762. doi:10.1016/j.jclepro.2019.02.110.
- [57] Singh, J., Sharma, S. K., Srivastava, R., & Das, D. (2018). Evolving constructs & measurements of aviation fuel consumption: An analytical view. *KSCE Journal of Civil Engineering*, 22(7), 2578–2592. doi:10.1007/s12205-017-0813-5.
- [58] Ramachandra, T., & Rotimi, J. O. B. (2015). Causes of Payment Problems in the New Zealand Construction Industry. *Construction Economics and Building*, 15(1), 43–55. doi:10.5130/ajceb.v15i1.4214.
- [59] Wei, Y., Hashim, H., Chong, K. L., Huang, Y. F., Ahmed, A. N., & El-Shafie, A. (2023). Investigation of Meta-heuristics Algorithms in ANN Streamflow Forecasting. *KSCE Journal of Civil Engineering*, 27(5), 2297–2312. doi:10.1007/s12205-023-0821-6.

- [60] Rogers, S. (2009). Survey and Analysis of Electronic Journal Licenses for Long-Term Access Provisions in Tertiary New Zealand Academic Libraries. *Serials Review*, 35(1), 3–15. doi:10.1016/j.serrev.2008.11.002.
- [61] Sözen, E., & Güven, U. (2019). The Effect of Online Assessments on Students' Attitudes Towards Undergraduate-Level Geography Courses. *International Education Studies*, 12(10), 1. doi:10.5539/ies.v12n10p1.
- [62] Likita, A. J., Jelodar, M. B., Vishnupriya, V., & Rotimi, J. O. B. (2024). Lean and BIM integration benefits construction management practices in New Zealand. *Construction Innovation*, 24(1), 106–133. doi:10.1108/CI-06-2022-0136.
- [63] Ahmed, S., Hossain, M. M., & Haq, I. (2021). Implementation of lean construction in the construction industry in Bangladesh: awareness, benefits and challenges. *International Journal of Building Pathology and Adaptation*, 39(2), 368–406. doi:10.1108/IJBPA-04-2019-0037.
- [64] D'Aureliano, F. S., Costa, A. A. F., Júnior, I. F., & Rodrigues, R. A. (2019). Application of lean manufacturing in construction management. *Procedia Manufacturing*, 38, 241–247. doi:10.1016/j.promfg.2020.01.032.



Valuation of Urban Green Open Spaces Using the Life Satisfaction Approach

Retno Setiowati ^{1*}, Raldi H. Koestoer ^{1*}

¹ School of Environmental Science, Universitas Indonesia, Jakarta 10430, Indonesia.

Received 11 November 2023; Revised 09 March 2024; Accepted 15 March 2024; Published 01 April 2024

Abstract

This study conducts the valuation of the urban Green Open Spaces (GOS) in Jakarta (Indonesia) using the life satisfaction approach (LSA). We integrated the important elements of the LSA, such as housing structure and environmental facilities, into a comprehensive valuation model (using hedonic variables). By explicitly acknowledging the limited application of these methodologies in developing nations, this study endeavors to provide a context-specific understanding of the economic value of GOS in Jakarta. The LSA model, a novel non-market valuation tool, employs community life satisfaction as its primary metric. In this study, we analyzed the satisfaction levels of residents of Jakarta based on a 10-point scale; the responses of a total of 1,592 participants were collected through online questionnaires in 2021 (during the pandemic). We considered various independent variables, including socioeconomic factors, housing attributes, environmental facilities, location amenities, and the presence of GOS. The analysis involved LSA and ordinary least squares (OLS) models in the Statistical Package for the Social Sciences (SPSS). The results indicate that several variables, such as longer residence duration, good employment status, high income “over 20 million Indonesian Rupiah (IDR); approximately USD 1281.56”, and access to more shopping centers, positively influenced the life satisfaction of the residents, which is in line with the studies conducted in western countries. Surprisingly, the economic evaluation of urban GOS portrayed a limited impact on the residents’ life satisfaction, while negative aspects, e.g., the presence of cemeteries around residential areas (19.1%), impacted the residents significantly. Urban parks did not portray statistical significance in influencing the residents’ life satisfaction, despite having a positive impact across all radii of urban regions. Urban forests exhibited a positive impact, mainly within the 100–500-m radius, with a significant impact on resident life satisfaction. Our attempt to assess the values of landscape amenities in Jakarta using LSA marks a pioneering effort in the field of environmental science with respect to community preferences. Consequently, this study contributes significantly to the evolving yet limited literature in this domain. The results differ from those of the Global North research, emphasizing the need for context-specific urban planning strategies. Our study offers valuable insights for urban planners and government entities and can guide GOS development to enhance urban sustainability and community satisfaction. The implications extend to urban centers in Indonesia and other developing countries, emphasizing the importance of optimizing limited urban spaces based on community preferences.

Keywords: Economic Valuation; Green Open Space (GOS); Green Spaces; Life Satisfaction; Life Satisfaction Approach (LSA); Jakarta.

1. Introduction

Urban green open spaces (GOS) play a pivotal role in urban ecosystems; they provide ecological, social, and economic benefits. Additionally, GOS contributes significantly to the resilience of cities to the adverse impacts of climate change and natural disasters [1]. These spaces are essential for mitigating the effects of climate change and fostering sustainable urban development. They offer a range of ecosystem services that address several health-related

* Corresponding author: retno.setiowati01@ui.ac.id; ralkoest@gmail.com

 <http://dx.doi.org/10.28991/CEJ-2024-010-04-010>



© 2024 by the authors. Licensee C.E.J, Tehran, Iran. This article is an open access article distributed under the terms and conditions of the Creative Commons Attribution (CC-BY) license (<http://creativecommons.org/licenses/by/4.0/>).

challenges, such as heat waves and air pollution, while enhancing the well-being of residents through physical activities and social interactions [2]. Sustainable urban development focuses on enhancing the overall quality of life for residents. Achieving sustainability and urban regeneration requires a meticulous examination of human-made aspects within urban environments, especially in rapidly urbanizing low- and middle-income countries, thus emphasizing the importance of GOS [3]. This study explores the interplay between the GOS, public perception, and urban sustainability in Jakarta. We aim to understand the public perceptions of GOS with respect to their contribution to the social dimensions of quality of life and as integral components of sustainable development in the region. The study aligns with the United Nations Sustainable Development Goals, ensuring universal access to safe, inclusive, and accessible green spaces by 2030.

Urban planning strategies are critical in achieving environmental aesthetics and fostering socially and economically resilient environments, thereby significantly contributing to sustainable development [4]. In particular, during the COVID-19 pandemic, urban GOS has been vital to the community. These spaces offer diverse environmental and health benefits that become even more critical during such scenarios. Despite the temporary closures of GOS during the pandemic, evidence suggests their ongoing importance for the mental and physical well-being of residents, as they offer recreational activities [5]. However, a noticeable shift toward recreational activities necessitated adjustments to pandemic-related urban policies. Numerous studies have reported the benefits of these spaces [6]. Urban green infrastructure, essentially a landscape element, acts as a conduit that offers various environmental, economic, and social advantages. Understanding the benefits of GOS allows planners to develop evidence-based policies for their effortless integration into urban environments. This maximizes the ecological and socioeconomic advantages of such space while managing costs [7].

In this context, valuation serves as a powerful tool for policymakers and decision-makers, offering significant insights into the crucial role of ecosystems in ecological sustainability and human well-being. This simultaneously guides efforts related to the development and use of the environment. Ambrey & Fleming [8] emphasize the need for policymakers to consider the role of public urban GOS in supporting the well-being of residents and serving their preferences. This has led to the need for economic scrutiny when assessing the community preferences for recreational activities within GOS during urban planning. The application of economic valuation methods serves the specific purpose of bridging the gap between planning, financing, and implementation considerations [9]. It is also perceived as an indispensable element in the decision-making process of the government for urban planning. Policymakers have emphasized calculating the economic value of GOS as a critical component of strategic urban planning for future development [1]. While the multifaceted role of GOS is well established, its valuation is considered a pivotal area of investigation in developed countries.

The lack of studies on the economic valuation of urban GOS in Indonesia can be attributed to the intangible and public nature of these goods, often making them appear insignificant because they cannot be included in market transactions. To address this, monetary valuation methods have been designed to analyze the inherent characteristics of these goods and capture individual preferences [10]. A considerable body of literature focuses on determining the monetary value of GOS, with the most common method being the hedonic price model (HPM), wherein the GOS value is deduced from its discernible impact on the valuation of land or property. Several studies that employed HPM attempted to determine the monetary value of a GOS by assessing its impact on the property value. For example, Tyrväinen [11], Saphores & Li [12], Xu et al. [13], Wu et al. [14], Kolbe & Wüstemann [15], and Setiowati et al. [16] demonstrated the effectiveness of the HPM for the valuation of green spaces, with the GOS value being inferred from its discernible influence on the property value (based on the urban context).

An alternative to traditional methods such as the HPM is the use of non-market environmental valuation methods, e.g., the life satisfaction approach (LSA). Unlike the HPM, which relies on market equilibrium conditions, the LSA eliminates the need for individuals to directly appraise non-market goods. Instead, it measures the value by quantifying the influence of the GOS on the life satisfaction of community/residents [17]. The concept of sustainability extends beyond economic prosperity and serves a broader perspective on human well-being, including aspects such as the quality of life, happiness, equality, justice, and the fulfillment of basic needs. Concurrently, LSA has emerged as an alternative method to gauge the value of GOS by assessing its influence on the life satisfaction of individuals. This study highlights the effectiveness of the LSA model for capturing individual preferences for GOS while considering the subjective well-being and satisfaction of residents. Tsurum & Managi [18] suggested a potential correlation between greenspace quality and the moods of residents, proposing that higher-quality greenspaces may improve the overall well-being of the local residents. This departure from market-based methods is particularly relevant for non-market environmental goods, for which conventional market prices are not applicable.

Environmental quality plays a crucial role in shaping individual well-being and guiding well-informed policy decisions [19]. The LSA model offers a valuation technique for an environment that subjectively calculates individual life satisfaction scores. It operates on the assumption that if a GOS is considered essential, its presence in the city should be maintained while avoiding degradation. Our study assesses the relationship between life satisfaction and the presence of GOS in individual residential areas. A significant lack of studies exists on the valuation of urban public GOS in

Indonesia; our study addresses this gap in the literature. Assigning monetary value to environmental goods and services that are not applicable to conventional market pricing is a broad area of study in environmental economics. This field originated from the need to incorporate the values of environment-centric areas into cost-benefit analyses while considering environmental damage litigation.

In Jakarta (Indonesia), rapid urbanization has led to significant population growth and environmental challenges. The area of particular concern is the noticeable decline in the public GOS in the city. Currently, the GOS area in Jakarta covers only 5.1% of the total area of the city, falling considerably short of the mandated 20% of the 30% GOS coverage outlined in the Central Government Spatial Planning Law. Achieving this ambitious target may be difficult due to the rapidly advancing urbanization trend. The issue of urban GOS is becoming increasingly important because of rapid growth in population and urbanization. According to preliminary studies, the GOS area in Jakarta, which accounted for 5.84% in 2011, declined to 5.31% in 2018. This decline caused the region to rank lowest among the cities with GOS [20]. The decrease in the GOS area in Jakarta, which is categorized under non-market environmental goods or services, reflects a lack of emphasis on the city's development plans. The externalities that arise from environmental factors necessitate the implementation of government policies aimed at preserving and enhancing the environment. Recognizing the unique benefits of these greenspaces in urban life, Indonesia enacted the Ministry of Environment and Forestry Regulation No. 15 of 2012, emphasizing the need for effective planning of these resources. This regulation guides the economic valuation of forest ecosystems by emphasizing careful planning and the adoption of valuation as a tool for implementing strategies that incorporate a precautionary approach. The assessment methods outlined in this ministerial regulation do not explicitly mention LSA. Thus, this study provides valuable insights that can be used by the central government, particularly regarding the incorporation of the LSA approach in determining the economic value of environmental goods and services in Indonesia.

Although the HPM and LSA have been extensively applied for GOS valuation in developed countries, their utilization in developing nations, including Indonesia, is limited. This study addresses this gap by employing a comprehensive valuation model that integrates hedonic price variables and the relevant elements of the LSA. The lack of studies on GOS valuation in Indonesia, combined with its unique socioeconomic and environmental context, highlights the necessity for a nuanced understanding of the economic value of the GOS in Jakarta. This study is a novel attempt to construct an LSA model for evaluating the value of urban public GOS on a provincial-regional scale using an HPM approach. As mentioned previously, this study aims to develop a preference valuation model that is specifically designed for urban GOS in Jakarta. This includes categorizing various GOS types, such as parks, urban forests, and cemeteries, using the LSA method. In line with Law No. 26 of 2007 on spatial planning, cemeteries were officially classified as GOS. To realize this objective, we focused on understanding the local community preferences for GOS.

This study also recognizes the likelihood of conflicting preferences arising from the diverse attitudes and subjective opinions of residents. The importance of integrating environmental amenities into urban planning while considering factors such as proximity to the nearest train station, income level, and population density has been highlighted by Tsurum & Managi [18]. This study explores whether residents, in pursuit of enhanced well-being, prefer to live in areas surrounded by green spaces. The study utilized satisfaction data gathered through online surveys conducted during the pandemic; we surveyed due to the lack of available data. The challenges encountered during the survey process included the potential impacts of the pandemic on Internet access and the unwillingness of the residents to participate in the survey. Notably, public perceptions and attitudes may have been influenced by the pandemic, potentially affecting their responses related to well-being and green spaces. Nonetheless, online surveys offer advantages by enabling real-time data collection and analysis, extending geographical reach, and facilitating diverse respondent participation.

The exploration process included investigating the functional relationships among socioeconomic variables, urban GOS attributes, environmental amenities, residential structures, and the impact of public green spaces on life satisfaction. This comprehensive analysis was crucial for estimating the value of the GOS. Our approach also recognizes the importance of considering community decision-making processes when selecting residential areas. This served as a reference point for identifying the specific environmental amenities that significantly influenced community preferences. Furthermore, this study incorporated community life-satisfaction preferences as the main dependent variable in the LSA model, enabling a comprehensive valuation of GOS in the urban landscape. Gaining absolute knowledge of the dynamics and perceptions associated with these spaces in Jakarta has fundamental significance; it informs the development of effective urban-planning strategies and contributes to enhancing the well-being of the residents.

The structure of this paper is as follows: Section 2 presents a literature review of the studies on greenspaces and the LSA model. Sections 3 and 4 present the study methodology, the results, and the discussion in detail. The research methodology is categorized into survey areas, data and methods, and respondent characteristics. Section 5 presents the conclusions of the study and highlights the political implications of our findings for urban planners. Notably, our study emphasizes the significance of incorporating the perceptions of people into the valuation of urban GOS to ensure the effective utilization of these resources and achieve sustainable development.

2. Literature Review

2.1. Green Open Spaces (GOS) in Jakarta

Frequent visitors to urban green spaces demonstrate elevated levels of well-being [21], e.g., such individuals portrayed improved mental health during the COVID-19 pandemic [5]. Extensive studies highlight the positive effects of urban green spaces on health [22]. Additionally, residents who live in areas with more green spaces consistently reported greater levels of subjective life satisfaction than those who live in areas with fewer green spaces [8, 23]. The positive impact of high biodiversity on the well-being of greenspace visitors highlights the importance of comprehending the determinants of self-reported greenspaces for informed decision-making in green policy initiatives; additionally, it is important to acknowledge the ongoing debate surrounding the disparity between physically measured and self-reported data in environmental assessment [24, 25].

The primary objective of sustainable urban development is to improve the overall quality of life for the residents. To achieve sustainability and urban regeneration, the consideration of human-made elements within urban environments is crucial, while also including the important role of GOS. The United Nations Sustainable Development Goals, specifically Proposed Goal 11 Target 7, state the importance of universal access to safe, inclusive, and accessible green and public spaces by 2030. This target focuses on meeting the needs of various groups, including women, children, older individuals, and those with disabilities. Urban GOS plays a critical role in making cities more livable, enjoyable, and appealing to their inhabitants. Within the community, these spaces serve as platforms for promoting health awareness, specifically in urban settings where GOS are often perceived as recreational areas in a natural and flourishing environment [26]. The enhancement of GOS necessitates the need for child-friendly facilities and activities that support the growth, development, education, and safety of children while encouraging participation and collaboration [27]. Furthermore, the development of sustainable cities extends beyond ecological considerations and the social aspects of urban life, including the satisfaction, experiences, and perceptions of residents with respect to the environmental quality in residential areas. Increasing citizen awareness about the significance of these areas in urban environments is important and can improve the quality of life in cities and the general urban environment [28].

The development in Jakarta and its nearby cities of Bogor, Depok, Tangerang, and Bekasi (collectively known as Jabodetabek) has led to a significant population increase of approximately 14 million residents. This has resulted in rapid urbanization, posing significant challenges related to environmental degradation; this is of particular concern in scenarios of elevated temperatures [29]. As a megapolitan city, Jakarta has experienced substantial development across multiple sectors, including industry, commerce, transportation, and housing, leading to various environmental challenges [28]. One particular urban challenge in the city is the reduction of the GOS area. Between 2011 and 2018, the city witnessed a decrease in the area of these spaces (~342.40 ha), with the most significant reduction occurring in South Jakarta (109.42 ha) [30]. The current area of public GOS in Jakarta accounts for only 5.1% of the total area of the city, which is significantly lower than the mandated threshold of 20% set by the Central Government Spatial Planning Law. The management of a significant portion of these spaces falls under the jurisdiction of the Jakarta City Parks and Forestry Agency [31].

Jakarta has an ambitious objective to increase the area of GOS to 30% by 2030, in line with the requirements of Law No. 26 of 2007 on spatial planning. However, reaching this target poses significant challenges for Indonesian cities that are experiencing rapid urbanization. Despite the government's efforts and policies aimed at enhancing public parks, protecting urban forests, and establishing GOS, these initiatives have struggled to keep pace with rapid population growth. This emphasizes the need for urban planners to prioritize GOS preservation, ensure public access to these spaces, and integrate ecologically driven utilization into inclusive planning. Presidential Regulation No. 60 of 2020 proposes a strategy for the Jabodetabek Metropolitan Area, designating the protected zones with a minimum of 30% of the total region allocated as GOS within this metropolitan area. This provision differs from the policy outlined in Law No. 26 of 2007 and Government Regulation No. 15 of 2021 on spatial planning, which states that 30% of the total area of a city should consist of GOS. The Ministerial Regulation No. 14 of 2022 from the Ministry of Agrarian Affairs and Spatial Planning/National Land Agency also states that urban GOS should constitute a minimum of 30% of the total area.

The ongoing reduction in the GOS area each year can be attributed to the urban planning practices of the Jakarta Provincial Government due to the consistent downsizing of the allocation of these spaces in spatial regulations. Sutapa et al. [32] indicate that, as one of the largest cities in Indonesia, Jakarta tends to experience high-intensity and unsustainable urban development, resulting in landscape degradation. The presence and management of public spaces, particularly the green plan delineated in regional regulations, are closely intertwined with urban spatial planning; this includes the plans enacted by the Jakarta Provincial Government. The history of such plans implemented in the city can be traced to the Jakarta Master Plan 1965–1985, wherein the area designated for GOS was 24,315.04 ha, accounting for 37.2% of the total area of the city. However, in subsequent developments, e.g., in the 1984 General Spatial Plan, this proportion was reduced to 29.92%. Further reductions resulted in the proportion being 13.94%, corresponding to the 1999 amendments to the 2010 Jakarta Spatial Plan. In 2014, the Jakarta Provincial Government enacted Regional Regulation No. 1 of 2014, further reducing the area allocated to GOS and the allocated space to 11.51%, or 7,520.96 ha.

This downward trend continued with a subsequent revision in Governor Regulation No. 31 of 2022 on the Detailed Spatial Plan or the Provincial Planning of Jakarta, further limiting the allocated GOS to 7.56% of the total area of the region [5]. These successive regulatory modifications consistently eroded the allotment of green spaces in Jakarta, posing a substantial challenge to meeting the minimum requirements mandated by national laws. This decline had a significant impact on the quality of life and well-being of the city residents, as these spaces played a critical role in urban sustainability, including the health and happiness of its inhabitants. According to previous studies, community interviews in West Jakarta revealed a substantial demand for cities with environmental parks [33]. This demand highlights the need to facilitate urban activities and enhance the local urban environment to provide better experiences and amenities to communities. The decline in the GOS area can be linked to a consistent reduction in GOS allocation in urban planning regulations. Successive modifications to such regulations resulted in a decrease in greenspace allotment, affecting the quality of life and well-being of city residents. Carrying out an economic valuation of urban GOS through LSA is essential for understanding the monetary value of GOS and its impact on urban sustainability. Aoshima et al. [25] explored the significance of subjective perceptions in the assessment and preservation of urban green spaces. While planners commonly emphasize the importance of the physical attributes of GOS, this study explores the role of public perceptions in GOS allotment [25]. The intersection of urban green spaces and human well-being is a captivating subject, with numerous studies highlighting the multifaceted benefits of such spaces for urban residents.

2.2. Economic Valuation Model Using the Life Satisfaction Approach (LSA)

The exploration of greenspace value has been a central focus of environmental economics. Valuation methodologies, such as contingent valuation, have been extensively used to assess the quality of greenspaces, as highlighted by Tsurum & Managi [18]. However, these methods have limitations, e.g., participants may provide shallow responses, and there may be disparities between the expressed and actual behaviors of the respondents. Additionally, Tsurum & Managi [18] cautioned against biases in the HPM results, especially if environmental changes are not promptly reflected in land value assessments. Notably, the LSA model can address these challenges while offering a distinct perspective on environmental valuation by explicitly capturing individual well-being without relying on market equilibrium. Therefore, several studies employed LSA data for environmental valuation [17, 18, 25, 34–38].

Life satisfaction is influenced by the complex interplay between social and economic factors. These factors included income, marital status, employment, parenthood, health, and educational attainment. In addition to these traditional factors, recent related studies include environmental variables such as air quality, floods, climate conditions, natural landscapes, droughts, and the presence of urban GOS. Public perceptions of equally sized GOS have yielded different outcomes based on specific types [25]. These findings have significant implications for urban planners and experts and highlight the importance of considering both the physical attributes of the GOS and the public perceptions of environmental planning, specifically for areas with limited space. To achieve effective and efficient outcomes, it is crucial to incorporate public preferences quantitatively and qualitatively, particularly when life satisfaction is used as a dependent variable in valuation models. This necessitates the incorporation of socioeconomic factors, residential structures, environmental amenities, and standard GOS variables that are commonly used in HPM construction. Consequently, the economic valuation of these spaces in urban areas extends beyond policy recommendations and requires academic effort.

In public policy decision-making, understanding the value of services provided by GOS is essential, especially when uncertainty is related to the costs associated with their preservation [39]. This comprehension is particularly crucial in urban settings, where policymakers need to make well-informed decisions. This approach can be used to assess whether the economic benefits derived from these open spaces, which are regarded as part of nature, outweigh the costs associated with their development and maintenance [40]. Policymakers often evaluate the monetary valuation of environmental services to address conservation, social, and economic objectives. This approach provides more concrete estimates than qualitative studies, offering a clearer picture of the benefits at stake [11]. However, there is no universally perfect method for valuing urban GOS, with only a limited number of studies being conducted in developing countries [41]. Urban development has societal implications; policymakers must consider how improved facilities affect land prices [42]. These methods and practices can be used to assign monetary value to environmental goods and services when conventional market prices are not applicable [10].

For instance, a study conducted in the United Kingdom (UK) reported that individuals were happier in natural green habitats than in urban settings [43]. Similarly, an investigation in Australia focused on the impact of public GOS on the life satisfaction of residents [8]. A positive correlation was observed between the proportions of these spaces and self-reported life satisfaction. Public GOS, also categorized as environmental goods, often pose challenges in terms of economic measurement/valuation, leading to the undervaluation of such goods and their designation as low-worth assets. The economic value of these spaces plays a significant role in the context of sustainability assessments. This aspect has remained relatively unexplored in Indonesia, contributing to its marginalization in the decision-making process of urban policies. The valuation of such areas forms the basis on which public policies are enacted, offering insights into the extent to which communities value these spaces. Environmental policies and regulations have been implemented to

improve environmental quality for individual well-being [37]. A case study in London revealed that the strength of the association between personality traits and life satisfaction depends on the environmental characteristics of the region [44]. The LSA technique for GOS valuation enables the estimation of different coefficients and individual income, which can then be used to analyze the public perception of and community preferences for GOS.

Valuation determines the precise economic value of goods and services that cannot be traded in traditional markets. Urban GOS plays an important role in enhancing property values, attracting investments, and boosting tourism. As public goods, these spaces should be maximized to generate social benefits for the community. Two analytical approaches are commonly used for assessing urban landscapes. One focuses on the psychological aspects related to human perception [45], while the other involves economic (monetary) evaluation methods. Urban GOS lack price tags; therefore, it is challenging to incorporate them into government policies and decision-making processes that rely on cost-benefit analysis. To address this challenge, scholars have developed valuation models using a preference-based approach that combines the elements of both LSA and HPM. This approach complements the HPM while emphasizing the mutual enhancement of the LSA and HPM theories [36, 46, 47]. Previous studies on the LSA demonstrate numerous personal, demographic, and socioeconomic factors that influence life satisfaction [48, 49]. A study on preference heterogeneity analyzed the impact of GOS on life satisfaction within an Australian urban context [8]. The influence of these spaces depends on different variables, such as the percentage of public areas, population density, and characteristics, with the majority of interactions portraying nonsignificant distinctions, indicating relatively consistent preferences for GOS [8].

For instance, a study conducted on the urban quality of life in the Buenos Aires Metropolitan Area using both HPM and LSA [50] revealed a strong correlation between real estate prices, income levels, environmental characteristics, and subjective life satisfaction. A significant relationship between urban environments and life satisfaction was reported, signifying the importance of considering both methods in the development of urban public policies aimed at enhancing the quality of life of residents. A theoretical and methodological framework for understanding the relationship between HPM and LSA further emphasizes how these approaches complement each other [51]. Van Praag et al. [47] and Brereton et al. [52] identified the similarities between the HPM and LSA methods, proving that both can effectively analyze the effects of location attributes on the quality of life and preferences of individuals. Notably, the majority of studies on LSA have been conducted in developed countries, typically categorized as part of the Global North, with limited application for developing nations. Expanding its use to more diverse regions and contexts could provide a broader understanding of the relationship between urban environments, socioeconomic factors, and resident well-being, thus supporting policymakers in making informed decisions to enhance the quality of life for the local community. The unique capability of LSA is to capture external factors that affect life satisfaction, even when these influences are not consciously acknowledged by individuals [53]. Note that LSA is a versatile method for assessing the positive and negative externalities associated with various public goods [18].

The LSA model uses an econometric function to estimate the environmental value based on individual income [53]. Unlike other approaches, LSA uses surveys similar to those used for HPM construction and provides distinct advantages by uncovering the externalities that influence individual well-being, even when people may not consciously recognize the presence of GOS [53]. Tsurum & Managi [18] used LSA to assess the impact of green spaces on human well-being, community preferences for greenery, and the proximity of GOS to residential areas. The values of GOS around residences were determined using geographic information systems (GIS) at various distance intervals. According to previous studies, residents tend to experience higher levels of satisfaction when residing near GOS [10, 54]. Using self-reported well-being as a proxy for individual utility functions facilitates the direct computation of implicit prices associated with environmental amenities [51]. In microeconomic functions, aspects such as life satisfaction, environmental conditions, and income determine the willingness of individuals to pay for resource preservation [53]. Multiple investigations used the LSA model to assess the economic value of diverse factors, including urban air pollution, air quality [35, 55], airport noise [47], climate [56], scenic amenities [10], and flooding [57].

3. Research Methodology

3.1. Study Area

This study was conducted in Jakarta, the capital city of Indonesia, with respect to Law No. 5 of 1974. The city is known for its high population density and rapid urbanization, which pose significant challenges in terms of environmental sustainability and quality of life. Jakarta is particularly noteworthy for its swift urbanization, elevated levels of air pollution, and limited access to clean water. As one of the megacities of the world, it covers an area of 662.33 km² and an additional sea area of 6,977.5 km². The city has the highest population density in Indonesia, with 20,618 people/km², resulting in a total of 10,679,951; the annual population growth rate of Jakarta is 0.66% [58].

Within the Jakarta Province, central Jakarta has the highest population density (20,618 people/km²). Geographically, the northern boundary of Jakarta comprises a 32-km coastline, serving as an estuary for 13 rivers, two canals, and multiple floodways. Figure 1 portrays a map of the city; Banten Province borders Jakarta in the west, whereas West Java

Province borders its southern and eastern boundaries. Regarding its administrative structure, Jakarta experienced significant territorial reformation in 2001. This transformation involved the transition from five municipalities to one administrative district and five administrative cities. The expansion also extended to administrative subdivisions, increasing the number from 43 subdistricts and 265 villages to 44 subdistricts and 267 villages. In 2022, the city experienced a wide temperature range, with the minimum and maximum recorded temperature being 23.0 °C and 35.4 °C, respectively, humidity levels varying from 34% to 100%, and the total annual precipitation being 2,136.3 mm [46]. However, during this period, 502,040 people lived below the poverty line, with North Jakarta hosting the largest concentration of impoverished individuals (133,730 people). In 2021, the territory of Jakarta included protected forests and nature reserves that covered an area of 270,889.20 ha. By focusing on Jakarta, this study recognizes and addresses the contextual factors unique to developing nations while providing insights into the valuation of GOS in the context of rapid urbanization, population growth, and distinct urban challenges.

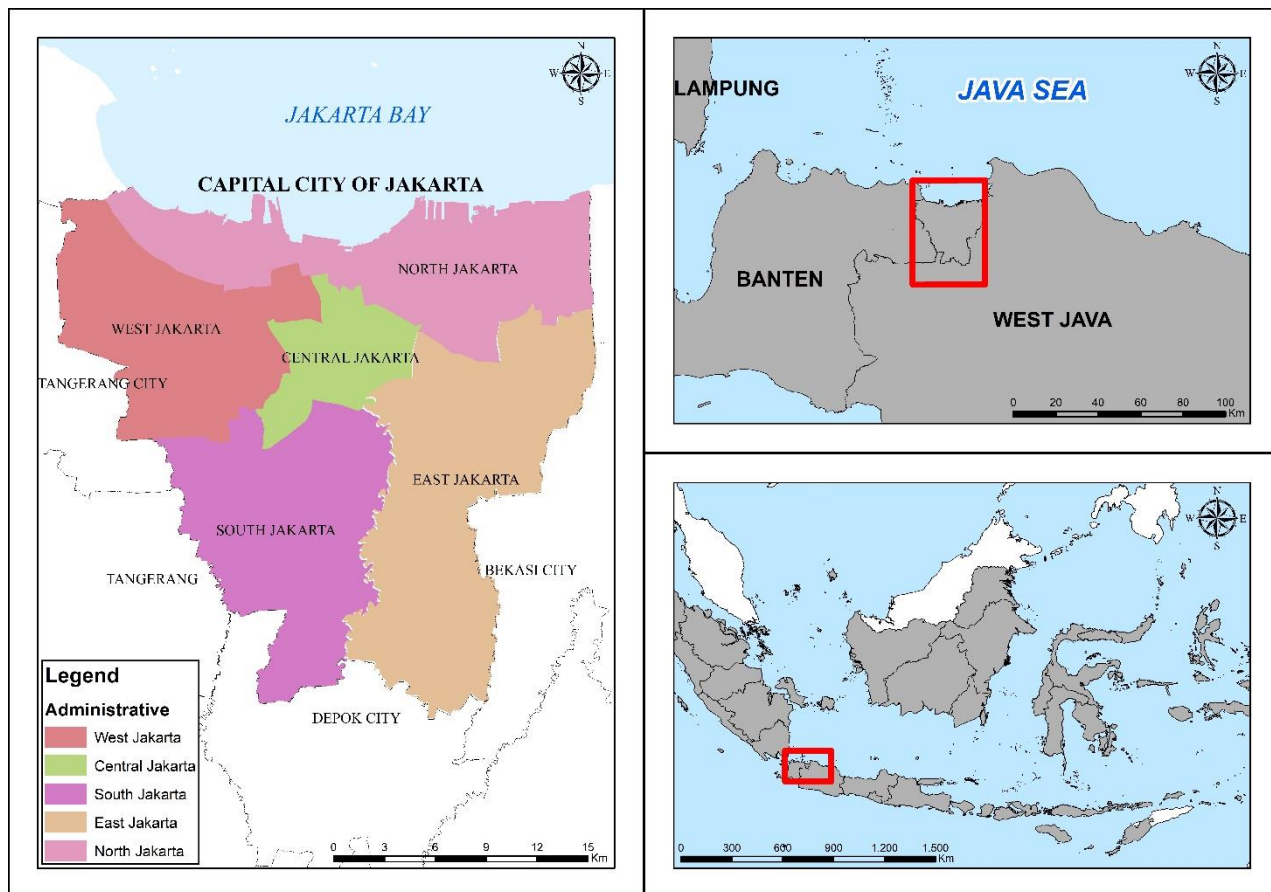


Figure 1. Geographic location of Jakarta, Indonesia

3.2. Data and Method

The data collection process required the distribution of questionnaires to the public through Google Forms. Similar surveys on subjective well-being (in the field of economics) were conducted by Frey & Stutzer [59], Layard [60], Di Tella and MacCulloch [61], and Clark et al. [62]. The online survey, which focused on measuring life satisfaction, was conducted for three months, from March 2021 to May 2021, coinciding with the pandemic. The responses were collected from 1,660 individuals across 244 neighborhoods, representing the residents across all five administrative parts of the city. The distribution of the respondents was as follows: East (26.99%), South (20.48%), West (19.64%), Central (17.23%), and North Jakarta (15.66%). The main survey questions are listed in Table A1. The survey was used to create a comprehensive profile of the respondents and included information on their housing situation, educational background, employment status, income, length of residence, and age. To simplify the data, we conducted a cluster analysis of 1,660 respondents, as shown in Figure 2, by grouping individuals with similar preferences. Figure 2 also illustrates the distribution of GOS in Jakarta, specifically parks, urban forests, and cemeteries, in accordance with the data obtained from the Jakarta City Parks and Urban Forest Agency. Following the cluster analysis, we constructed a valuation model for the GOS in Jakarta using LSA. This process adopted dendrogram hierarchical clustering using the statistical package for the social sciences (SPSS) software while considering various socioeconomic characteristics, such as the age, education level, occupation, and income of the respondents. A dendrogram-hierarchical cluster analysis revealed the formation of two major clusters. Clusters 1 and 2 comprised of 1,592 and 68 respondents, respectively. The GOS valuation model, which was developed based on the preferences of Cluster 1, represented a large subset (of 1,592

respondents). In the subsequent stage, the distances between the residential locations of the respondents and the nearby urban amenities and GOS were computed using GIS. In the final stage, we conducted an ordinary least squares (OLS) analysis using the SPSS software to establish the valuation of GOS through the LSA model. Figure 3 presents the framework used for our analysis.

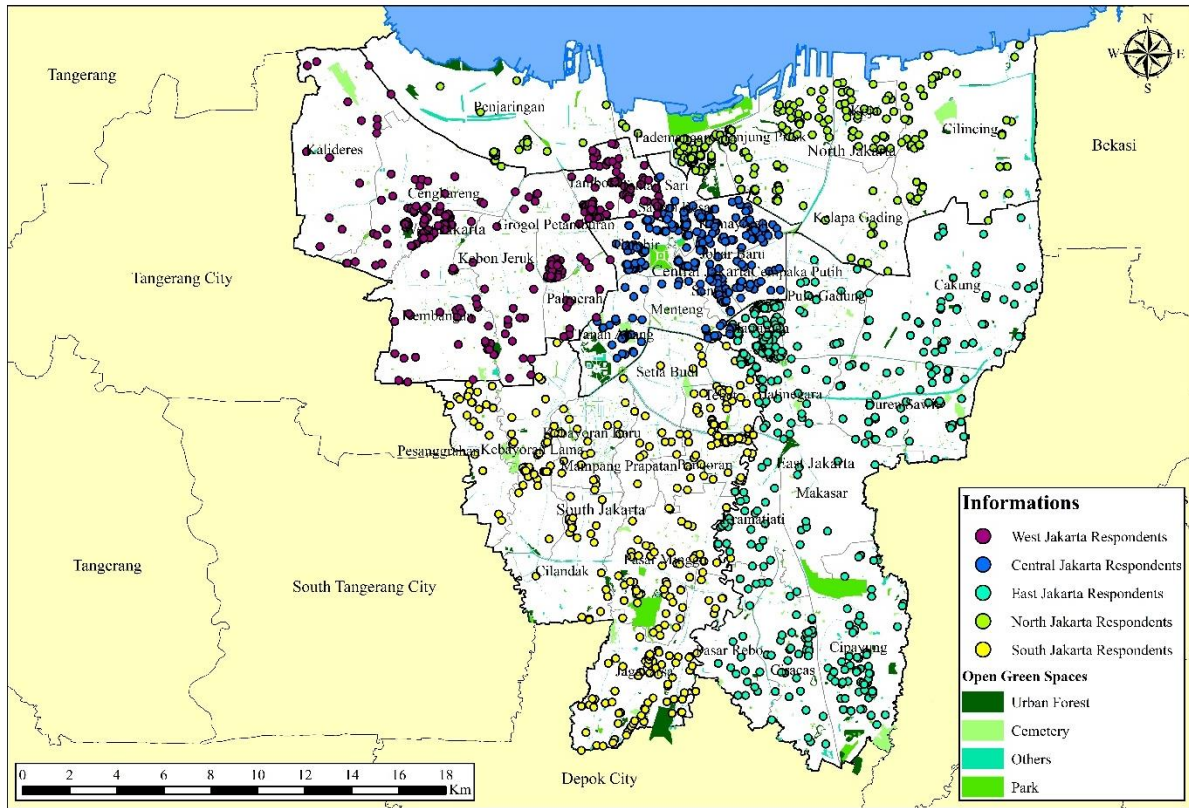


Figure 2. Distribution of respondents and urban green open spaces (GOS) in Jakarta, Indonesia

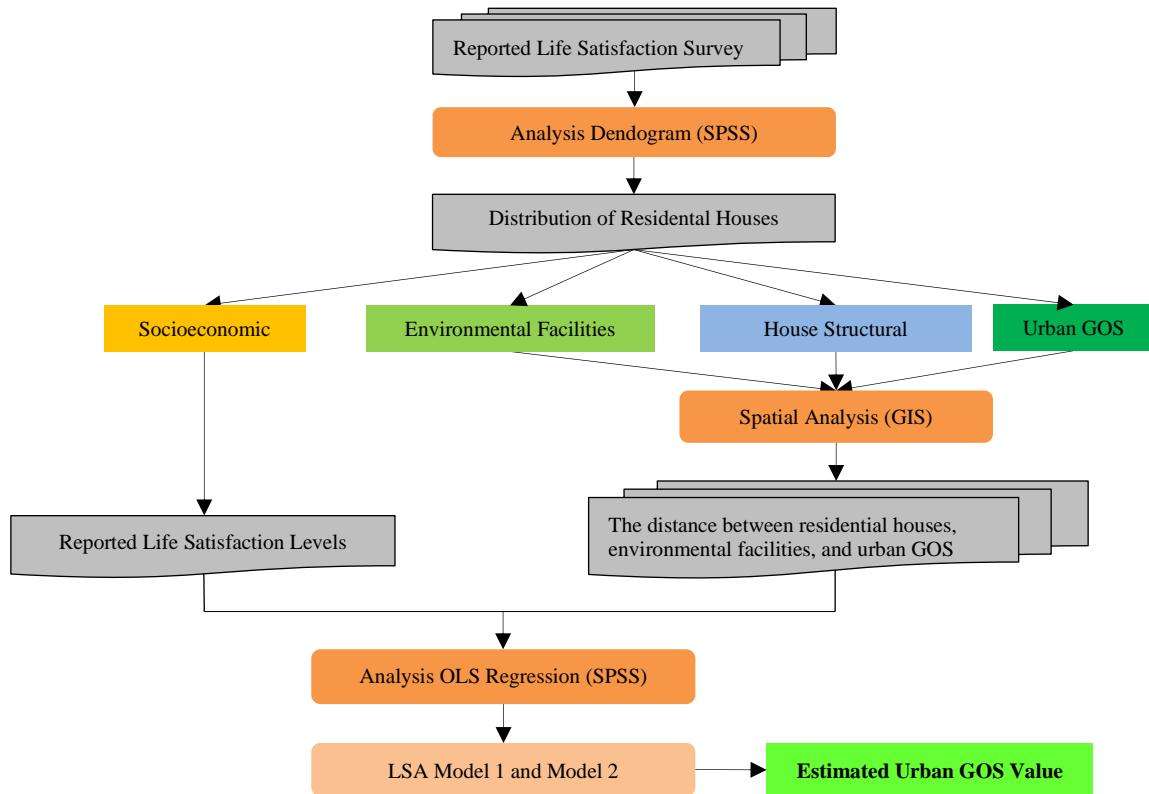


Figure 3. Illustration of the framework used in this study. (SPSS): Statistical Package for the Social Sciences; (OLS): Ordinary Least Squares; (LSA): Life Satisfaction Approach; (GOS): Green Open Space; (GIS): Geographic Information System

3.3. Characteristics of Respondents

A comprehensive description of the demographics of participants, mainly focusing on socioeconomic factors, is presented in Table 1. The data revealed that the majority of the respondents (94.1%) were within the age range of 20–60 years, indicating a predominant proportion of working-age adults. The participants who were under 20 years old and over 60 years old accounted for 2.23% and 3.67% of the total number of participants, respectively. In terms of education, the majority of participants (60.54%) had completed high school, and a significant proportion (38.86%) had college degrees. A small proportion of the study group (0.6%) lacked formal education. Regarding employment, the distribution was diverse, with approximately a quarter (24.82%) being unemployed, 25.42% working in government and private sectors, 9.88% being entrepreneurs, and 5.72% having blue-collar occupations. A substantial proportion (34.16%) was considered in the “Others” category, which comprised various job roles and types, including self-employment.

With respect to income, in 2023, the majority (68.31%) earned below the Jakarta Regional Minimum Wage standard of Indonesian Rupiah (IDR) 4.9 million/month or United States Dollar (USD) 313.98. A smaller group (15.90%) earned IDR 4.5–10 million/month (USD 288.35–640.78) in 2022, while the minority (10.42%) had incomes exceeding IDR 20 million/month (USD 1281.56), which were the higher-income individuals in the study group. Thus, our analysis provides valuable insights into the age distribution, educational background, employment status, and income level of participants, thereby portraying the sociodemographic characteristics of the participants.

Table 1. Characteristics of the participants of this study

Variable	Sub-variable	Frequency	Percentage (%)
<i>Age</i>	<20 years	37	2.23
	20–60 years	1,562	94.1
	>60 years	61	3.67
<i>Education Level</i>	Those without education or formal degrees	10	0.6
	High-school graduates	1,005	60.54
	College graduates	645	38.86
<i>Occupational Status</i>	Unemployed	412	24.82
	Employed in government and private sectors	422	25.42
	Entrepreneurs	164	9.88
	Blue-collar laborers	95	5.72
	Others	567	34.16
<i>Average Monthly Income</i>	< IDR 4.5 million	1,134	68.31
	IDR 4.5–10 million	264	15.9
	IDR 10–20 million	89	5.36
	> IDR 20 million	173	10.42

3.4. Descriptive Statistics

The descriptive statistics for OLS Models I and II are shown in Table 2; the table incorporates the important findings from the questionnaire results. It comprises different variables, including reported life satisfaction levels, socioeconomic factors, housing structure, environmental or location facilities, and GOS characteristics. Notably, the data on reported life-satisfaction levels as gathered through previous surveys, wherein questions like “Overall, how satisfied are you with your life?” were measured using a Likert scale [34]. The descriptive statistics were complemented by the insights gathered from the questionnaire responses, which provided a comprehensive overview of the survey population and their living conditions.

Table 2. Descriptive statistics ordinary least squares (OLS) Models I and II

Variable	Descriptive Statistics					
	Model I			Model II		
	Mean	Standard deviation	N (Number)	Mean	Standard deviation	N (Number)
Reported Life Satisfaction Levels (scale of 1–10)	8.1422	1.60011	640	8.1237	1.58295	1,592
Socioeconomic Variables						
Age (<20 years) (dummy)	0.0016	0.03953	640	0.0013	0.03543	1,592
Age (20–60 years) (dummy)	0.9766	0.15141	640	0.9812	0.13602	1,592
Age (>60 years) (dummy)	-	-	-	-	-	-
Length of residence >10 years (dummy)	0.6422	0.47973	640	0.6476	0.47786	1,592
Not schooled/did not complete elementary school (dummy)	0.0094	0.09645	640	0.0063	0.07903	1,592
College-educated (dummy)	0.4063	0.49152	640	0.4052	0.49108	1,592
Employed (dummy)	0.7500	0.43335	640	0.7601	0.42719	1,592
Income <IDR 4.5 million (dummy)	0.6688	0.47103	640	0.6696	0.47051	1,592
Income IDR 4.5–10 million	-	-	-	-	-	-
Income IDR 10–20 million (dummy)	0.0547	0.22755	640	0.0559	0.22981	1,592
Income >IDR 20 million (dummy)	0.1047	0.30639	640	0.1087	0.31132	1,592
Residential location comfort satisfaction	8.1563	1.74975	640	8.1124	1.73166	1,592
Housing Structure Variables						
Source of clean water (dummy)	0.4469	0.49756	640	0.4912	0.50008	1,592
Environmental / Location Facilities Variables						
Number of shopping centers	17.0156	6.43152	640	16.7714	6.01814	1,592
Population density per neighborhood (people/km ²)	23347.4891	16482.78474	640	25605.8304	18607.54882	1,592
Distance to toll road (1000 m) (dummy)	0.4453	0.49739	640	0.4083	0.49167	1,592
Distance to main road (200 m) (dummy)	0.1859	0.38936	640	0.1859	0.38917	1,592
Distance to train station (500 m) (dummy)	0.1000	0.30023	640	0.1043	0.30571	1,592
Distance to Central Business District (9000 m) (dummy)	0.5047	0.50037	640	0.5396	0.49859	1,592
Distance to the river (200 m) (dummy)	0.2875	0.45295	640	0.2808	0.44952	1,592
Location of Respondent (a categorical variable)	2.6063	1.36968	640	2.8536	1.40102	1,592
Public High School	2.7922	1.67152	640	2.6376	1.65805	1,592
Urban Green Open Spaces Variables						
Distance to Urban Forests						
Less than 500 m	78.4547	145.89117	640			
0–500 m, as a dummy variable				0.1118	0.31523	1,592
500–1000 m, as a dummy variable				0.1916	0.39367	1,592
1000–2000 m, as a dummy variable				0.3386	0.47337	1,592
Distance to Parks						
Less than 500 m	182.6344	177.34022	640			
0–500 m, as a dummy variable				0.2494	0.43279	1,592
500–1000 m, as a dummy variable				0.2739	0.44608	1,592
1000–2000 m, as a dummy variable				0.3097	0.46250	1,592
Distance to Cemeteries						
Less than 500 m	101.3172	159.79211	640			
0–500 m as a dummy variable				0.1420	0.34912	1,592
500–1000 m, as a dummy variable				0.3656	0.48174	1,592
1000–2000 m, as a dummy variable				0.3461	0.47588	1,592

4. Results and Discussion

4.1. Life Satisfaction Level of Resident

The assessment of public satisfaction levels required the use of a satisfaction scale [25]; for this study, the scale ranged from 1 (low) to 10 (high). The community satisfaction survey conducted in our study focused on three significant aspects: evaluating the comfort of residential locations, measuring the satisfaction of the respondents with respect to the availability of GOS facilities in residential areas, and assessing their general life satisfaction in the urban context, the last being the dependent variable in the LSA model. To analyze the responses effectively, we aggregated the data based on the administrative city level; for clarity, the resulting average values were converted into percentages, achieved by multiplying the values by 100%. The satisfaction levels were further categorized using the life satisfaction index (LSI) to facilitate the descriptive analysis. The satisfaction level of the respondents with respect to the comfort of residential locations yielded an average LSI score of 81.30% across the five administrative cities, indicating that the residents in Jakarta were “very satisfied,” as shown in Figure 4. However, certain variations were evident when examining their satisfaction at the city level. The LSI values were high for the residents of East (83%), South (82.3%), and West (80.9%) Jakarta, while those for the residents of Central and North Jakarta were slightly lower (79.3% and 79.4%, respectively).

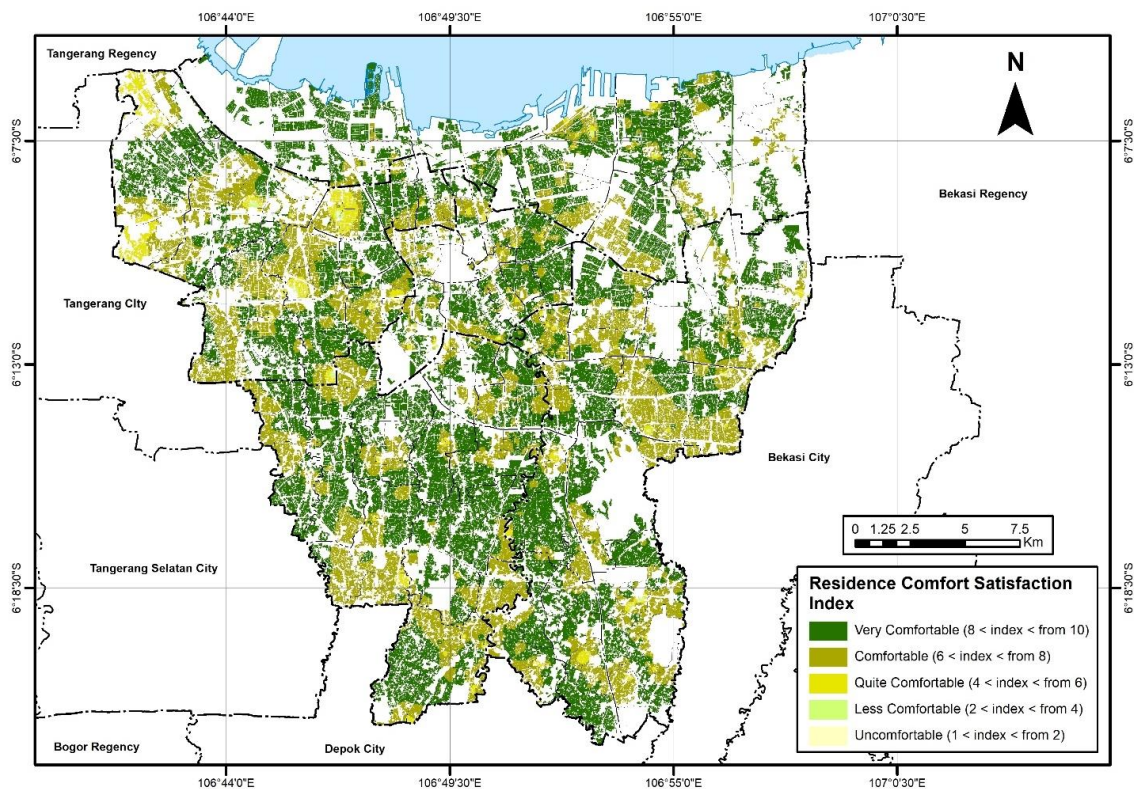


Figure 4. Distribution of self-reported location comfort levels in Jakarta, Indonesia

The satisfaction with the availability of GOS facilities in their residential areas portrayed an average LSI score of 57.60% across the five administrative units of the city (see Figure 5). However, South Jakarta reported a significantly higher LSI result (61.2%) compared to the other administrative units of the city. The LSI percentages for the other areas were as follows: East (59%), West (54%), Central (54.5%), and North (58.2%) Jakarta. The data suggested that even though there was a moderate level of satisfaction with the number of GOS facilities, the residents across all the administrative units of Jakarta generally perceived the availability of these GOS as inadequate. This finding emphasizes the importance of optimizing and increasing the number of GOS facilities across the five administrative units, thus providing valuable feedback and recommendations for the government.

The respondents from the five administrative units reported an impressive average LSI of 81.30%, indicating a high satisfaction rating, as shown in Figure 6. This was in line with the satisfaction typically associated with residential comfort, albeit the variations among individual cities. All five administrative units portrayed high LSI values, with South Jakarta portraying the highest LSI of 82.7%, followed by West (82.1%), North (81.7%), East (80.3%), and Central (80%) Jakarta. Notably, despite the online survey being conducted during the pandemic, the respondents reported remarkably high LSI scores. These scores were used as the LSA dependent variables; the LSA is a valuation technique that considers different factors, such as life satisfaction, environmental conditions, socioeconomic determinants, and income, to determine an individual's willingness to pay for available facilities.

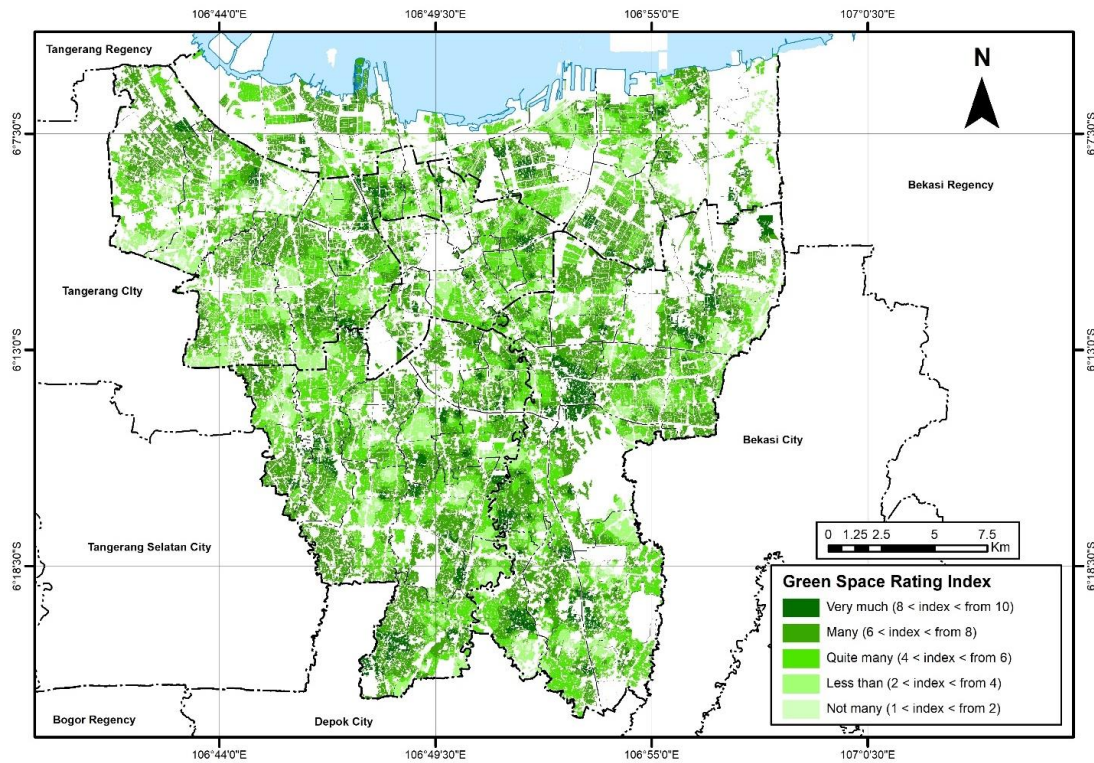


Figure 5. Distribution of self-reported data on green open spaces (GOS) around the residential areas in Jakarta, Indonesia

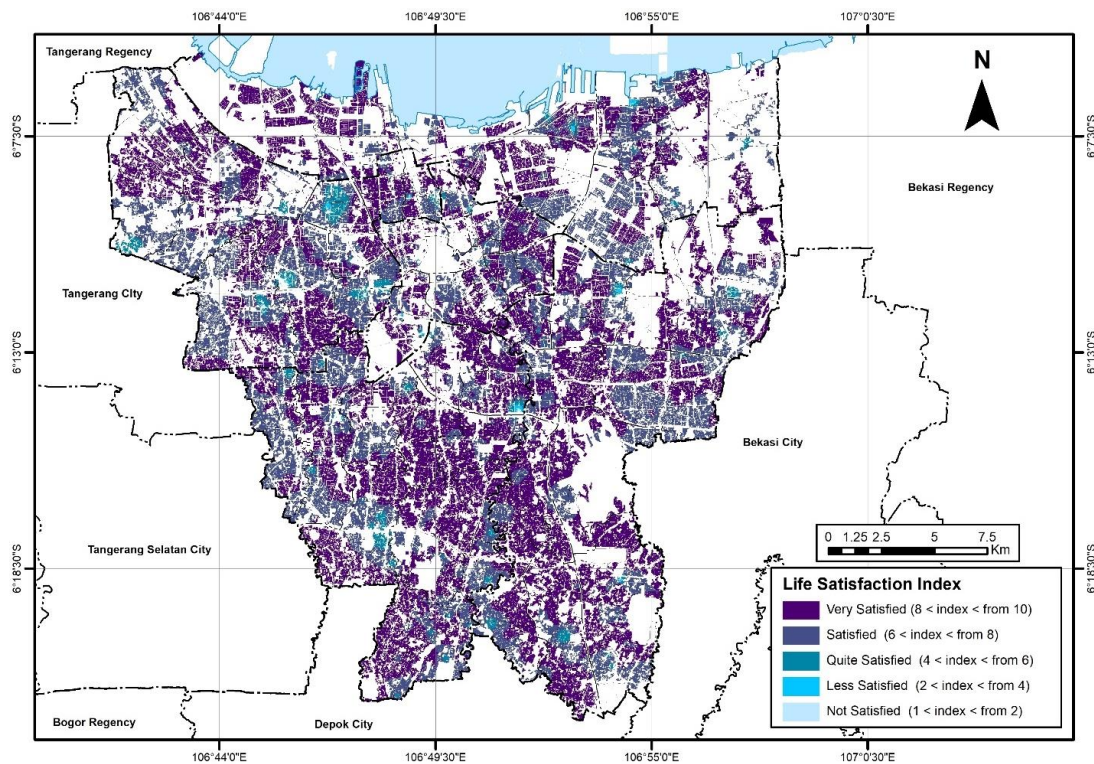


Figure 6. Distribution of self-reported data on the life satisfaction levels of the residents in Jakarta, Indonesia

4.2. Life Satisfaction Approach (LSA) Model Results

In this study, we adopted an innovative approach for the valuation of GOS to explore the correlation between urban GOS and life satisfaction while transcending the traditional approach of considering income as the sole valuation criterion. We attempted to capture the external effects associated with the urban GOS in Jakarta by examining the link between income and life satisfaction. This study aims to comprehensively understand the economic value of the GOS in Jakarta, Indonesia, using a valuation model that integrates LSA and hedonic price variables. Furthermore, we aim to elucidate the socioeconomic and environmental factors that influence the value of GOS in the urban landscape of a developing nation. This exploration is crucial for advancing our understanding of the diverse dimensions that contribute

to the values of GOS; notably, the factors differed significantly from those observed in developed countries. To address this issue, the questionnaire data is used to evaluate the dependent variables (in this case, life satisfaction). The explanatory variables are comprised of a wide range of factors, including household income, sociodemographic characteristics, socioeconomic attributes, social conditions, economic indicators, and institutional determinants [53, 63]. Building on the work of Tsurum & Managi [18], this study investigates the impact of greenspaces on diverse populations based on the distance of such areas from residential areas, specifically for the ranges of 0–500, 500–1000, and 1000–2000 m.

Our investigation incorporates various independent variables, including socioeconomic factors and the HPM variables, e.g., the presence of urban GOS, residential structure, and environmental/location amenities. Additionally, the analytical model used in this study includes various socioeconomic variables to examine their impact on the life satisfaction of residents. These variables focus on specific aspects of the socioeconomic backgrounds of respondents, e.g., their length of residence in the region (for identifying individuals who have lived in the same location for >10 years). The respondents were categorized into two groups: those under 20 years of age and those aged between 20 and 60 years. The aspect of educational attainment was divided into the following two categories: no education, elementary education, and college education. The occupational variable was binary to indicate employment status. The income-related variable was segmented into three categories: >IDR 4.5 million, IDR 10–20 million, and <IDR 20 million. Additionally, the model included an independent variable that reflected the comfort level of respondents with their residence, derived from the questionnaire responses. The analyzed variables comprised socioeconomic attributes and components featured in the HPM, including the structural characteristics of residential properties, environmental amenities, and the presence of urban GOS, which were used to create a comprehensive OLS regression model (Table 3).

Table 3. Coefficients of the ordinary least squares (OLS) regression models with respect to the life satisfaction approach (LSA)

Variable	Coefficients	
	Model I	Model II
<i>(Constant)</i>	2.576	3.584
<i>Socioeconomic Variables</i>		
Age (<20 years) (dummy)	1.334	1.153
Age (20–60 years) (dummy)	0.019	-0.010
Age (>60 years) (dummy)	-	-
Length of residence >10 years (dummy)	-0.114	-0.176**
Not schooled/did not complete elementary school (dummy)	-0.108	-0.454
College-educated (dummy)	0.142	-0.005
Employed (dummy)	0.157	0.156*
Income <IDR 4.5 million (dummy)	0.138	-0.042
Income IDR 4.5–10 million	-	-
Income IDR 10–20 million (dummy)	-0.120	0.020
Income >IDR 20 million (dummy)	0.318	0.243**
Residential location comfort satisfaction	0.562***	0.523***
<i>Housing Structure Variables</i>		
Source of clean water (dummy)	-0.188*	-0.118
<i>Environmental / Location Facilities Variables</i>		
Number of shopping centers	0.026**	0.013*
Population density per neighborhood (people/km ²)	1.089E-07	-5.167E-7
Distance to toll road (1000 m) (dummy)	0.159	0.110
Distance to main road (200 m) (dummy)	-0.142	-0.135
Distance to train station (500 m) (dummy)	-0.042	-0.083
Distance to Central Business District (9000 m) (dummy)	-0.244*	-0.046
Distance to the river (200 m) (dummy)	-0.016	-0.094
Respondent's Location (a categorical variable)	0.147***	0.054
Public High School	0.036	0.027
<i>Urban Green Open Spaces Variables</i>		
Urban Forest		
Less than 500 m	-0.0001	
0–500 m, as a dummy variable		-0.123
500–1000 m, as a dummy variable		0.096
1000–2000 m, as a dummy variable		-0.049

<i>Park</i>		
Less than 500 m	0.00008	
0–500 m as a dummy variable		0.120
500–1000 m, as a dummy variable		0.123
1000–2000 m, as a dummy variable		0.012
<i>Cemetery</i>		
Less than 500 m	-0.0001	
0–500 m, as a dummy variable		0.068
500–1000 m, as a dummy variable		-0.191**
1000–2000 m, as a dummy variable		-0.074
Coefficient of determination (R^2)	0.401	0.338
Adjusted R^2	0.378	0.325
Number (N)	640	1.592
Significance levels: ***0.01; **0.05; *0.1		

In Model I, the R-squared (R^2 value was 0.401, or 40.1 %) indicates a relatively robust relationship within the constructed model. However, in the OLS regression analysis, it was evident that the three urban GOS variables were not significant to our analysis (portraying low coefficients). The only variable that portrayed a significant correlation with life satisfaction was the proximity of the residential areas to cemeteries (within a distance or radius of 500–1000 m). The economic valuation of these greenspaces based on the LSA in the context of Jakarta was only able to estimate their value in cemeteries at a distance or radius of 1000–2000 m, which amounted to 0.191 with a negative impact, as determined using GIS. This finding is inconsistent with the results of Bertram & Larondelle [54], who combined survey data with a GIS database of the greenspaces in Germany and reported that quantity and proximity had significant effects on life satisfaction levels.

The R^2 value of OLS Model I (0.338, or 33.8%) was lower than that of OLS Model II. In both models, not all variables portrayed a significant relationship with the life satisfaction level of residents. Variables such as residential location comfort and the number of shopping centers were significant in both models. The LSA models developed for Jakarta yielded R^2 values of 0.401 and 0.338 for Models I and II, respectively, in line with previous LSA studies that reported R^2 values less than 0.40; Cruces et al. [50], Rehdanz & Maddison [64], and Ambrey and Fleming [10] obtained R^2 values of 0.33, 0.3684, and 0.1518, respectively. These results indicated that the models effectively captured a significant portion of the variations in the life satisfaction level. Thus, the model is a valuable tool for gaining insight into the factors that influence community well-being in Jakarta. Interestingly, it appears that in this city, the concept of positive externalities from the urban GOS does not substantially impact the life satisfaction level.

The results from Model II of the LSA valuation present a unique perspective, indicating that only negative externalities—specifically, the presence of cemeteries—have a statistically significant relationship with life satisfaction levels (the closer the cemeteries to residential areas, the lower the satisfaction level). The cemeteries in Jakarta, managed by the City Parks and Urban Forest Agency, are an integral part of the urban GOS. Therefore, local governments should reconsider the cemetery design to alleviate the perceived dissatisfaction among the residents despite the abundance of tree cover. Transforming the perceptions of cemeteries into positive contributors to residents' overall well-being in Jakarta should be a priority in urban planning, emphasizing the importance of considering both positive and negative external factors when assessing the impact of environmental factors on community well-being. This also raises the possibility that cultural or contextual factors specific to Jakarta may have contributed to these outcomes. Notably, the presence of GOS did not yield the same positive impact on life satisfaction as that reported in previous LSA studies conducted in northern global countries.

Our study results differ from those of the Tsurum & Managi [18] regression results, as the residents in this study did not exhibit statistically significant associations with the greenspaces within the specified distance ranges. This suggests a scenario wherein Jakarta residents may prefer alternative land uses or indicate an incomplete acknowledgment of the significance of the GOS. The negative impact of the distance to cemeteries on life satisfaction level aligns with the findings of Dong et al. [34], who stated a significantly negative relationship between air pollution and life satisfaction level in Beijing, China. Notably, the urban green spaces examined by Aoshima et al. [25] and Tsurum & Managi [18] did not include cemeteries. Our study emphasizes that, excluding cemeteries, urban green spaces have a positive influence on life satisfaction.

The results of this study differ from those of previous investigations conducted in the capital city of Australia [8], wherein the residents were willing to allocate an annual household amount of USD 1168 for a 1-% increase in the public GOS, indicating a strong preference. However, the initial assumptions proposed that the individuals in high-density areas may portray homogeneous preferences, even though certain heterogeneity was discovered during the actual

analysis [8]. Single parents, individuals with less than 12 years of education, and those residing in high-rise apartments benefited more from the increased number of greenspaces, and their preferences remained relatively consistent. From a conceptual viewpoint, the HPM and LSA methods complement each other and offer valuable insights into the relationships among socioeconomic factors, environmental characteristics, and individual well-being. These investigations consistently report the existence of a relationship between GOS, the life satisfaction level of residents, and community well-being. This finding does not agree with the results of Ambrey and Fleming [8, 38] and Bertram & Rehdanz [49], who have consistently reported that urban GOS significantly influences life satisfaction and well-being. Furthermore, these findings contradict those of Krekel et al. [23], who stated that the life-satisfaction level was associated with the number of GOS around the residence of an individual.

This method aligns with the approach used by Luechinger & Raschky [36], wherein the life-satisfaction level, assessed on an ordinal scale, was analyzed using the OLS regression technique. The use of OLS regression in the context of LSA was consistent with previous studies conducted by Ambrey & Fleming [8, 10], Brereton et al. [52], Kristoffersen [65], and Stutzer & Frey [66]. Prior investigations report that the determinants of life satisfaction level portray a high level of consistency when both the ordinal and cardinal variables were modeled using OLS regression [67]. However, Dong et al. [34] reported a statistically significant negative association between air pollution and life satisfaction, with variations across different geographical areas. Maddison & Rehdanz [56] analyzed the impact of climate on the average life satisfaction level across 87 countries using OLS regression. By estimating the coefficients and individual income levels, this approach allowed for the calculation of the implicit value attributed to environmental amenities.

The discrepancies in the findings between the current studies and the Western-centric LSA theory, with respect to the significant differences in the models for the Eastern and Western countries, suggest that the relationship between GOS and life satisfaction level may be influenced by regional or cultural factors. This emphasizes the need for tailored investigations into how environmental factors affect community well-being in specific contexts. It is important to stress that the outcomes of this research should not be interpreted as developing countries being inherently less concerned about environmental issues. Instead, the distinctions may reflect variations in the economic circumstances and priorities within these regions. For example, when examining the monetary valuation of air pollution, it was apparent that the residents of Beijing were willing to allocate approximately 2.6% of their annual income to a unit reduction in the average air pollution level [34]. However, Dong et al. [34] stated that the preference of the public for cleaner air in Beijing might not be as strong as that in developed countries, as the residents were reluctant to sacrifice a larger portion of their income to control air pollution. These findings emphasize the complex interplay among economic factors, environmental concerns, and individual preferences across different regions. They shed light on the intricate relationship between economic development and environmental priorities while emphasizing that the willingness to invest in environmental improvements can vary significantly based on contextual factors. Therefore, it is important to consider these nuances when evaluating and addressing environmental challenges in diverse settings.

The results of our study indicate that higher levels of education do not significantly impact the life satisfaction level, which is in line with the findings of Ambrey & Fleming [10]. Ambrey & Fleming [10] also reported a strong positive relationship between income and life satisfaction, consistent with the findings of our study. The variations in the findings emphasize the contextual nature of such investigations in the fields of life satisfaction and community well-being. The impact of individual preferences on life satisfaction differs significantly between regions, populations, and economic contexts, emphasizing the importance of conducting localized and nuanced investigations when examining the link between socioeconomic factors and community well-being. The application of LSA theory to Jakarta does not appear to be a suitable method for the valuation of the GOS in the city, as it failed to reveal significant relationships with the presence of parks and urban forests. However, previous studies failed to state the negative influence of cemeteries on life satisfaction levels. This finding contradicts the results of Mayer et al. [68], who reported that an increase in the connection of community with nature could enhance attention, positive emotions, and the ability to reflect on life issues. Bowler et al. [69], Nisbet et al. [70], and MacKerron & Mourato [43] reported the positive effects of physical activities in natural environments on life satisfaction and happiness levels. Protected areas, ecosystem diversity, and GOS have a positive relationship with life satisfaction, as reported by Ambrey & Fleming [8, 10]. Although using life satisfaction as the basis for evaluating the GOS in Jakarta mainly captures negative externalities, these findings offer an alternative approach for valuing environmental assets in urban settings. Our study results indicate that the preferences of Jakarta residents generally exhibit a degree of homogeneity, consistent with the investigation conducted by Ambrey & Fleming [8]. These findings have significant implications for urban planning and development, suggesting that government initiatives that aim to establish public GOS should consider the preferences of the population and treat such areas as a form of public infrastructure that is capable of enhancing life satisfaction and the general well-being of the community.

The key parameters in the LSA model for valuing the GOS in Jakarta encompass crucial socioeconomic variables: satisfaction of respondents with residential location, employment status, and income. The variable used for gauging satisfaction with their residential location was a significant metric that provided a subjective measure of the comfort of the respondents concerning their living environment. This parameter is crucial for comprehending the broader aspects of community well-being with respect to the residential context. The number of shopping centers may indicate

convenience and the commercial impact on life satisfaction. Standard socioeconomic variables, such as employment status, offer valuable insights into the demographic dimensions of the study area. Moreover, the income variable is pivotal, given its recognized role in shaping quality of life. This study systematically explored the intricate relationship between income and life satisfaction, especially for those whose income exceeds IDR 20 million, thus recognizing the significance of economic factors in influencing the overall well-being of an individual. These parameters contribute to a nuanced understanding of the complex interplay between socioeconomic variables and life satisfaction while offering valuable insights for improving urban planning and development strategies in Jakarta.

Future studies on urban planning and green space design should consider the integration of the variables associated with security and crime rates into the LSA model. Notably, Fleming et al. [71] explored the correlation between accessibility to green spaces and crime rates in New Zealand. Improved access to these spaces is associated with higher levels of life satisfaction. The investigation further proved that the psychological benefits of access could diminish, assuming that the residents perceive the area as unsafe. This study focused on the crucial role of safety considerations in urban planning and green space design [71]. Furthermore, the findings of this investigation indicated that the distribution and presence of GOS did not significantly enhance the life satisfaction level of the residents of Jakarta. Notably, the presence of GOS does not satisfy the concept of human well-being, particularly in terms of sustainability aspects such as quality of life and happiness level. This raises the possibility that, in Jakarta, citizens tend to prioritize meeting their basic needs.

Our research contributes significantly to the literature on spatial planning by offering insights into the challenges associated with the provision and management of urban GOS in a context characterized by limited land availability and high land prices. The LSA technique is an innovative approach to understanding community preferences for public goods. Unlike traditional methods, this technique does not mandate individuals to directly assess public goods but instead evaluates life satisfaction levels, offering a unique perspective on how environmental facilities impact human well-being and the quality of life.

This study contributes to the field of environmental economics by introducing an alternative method for the valuation of GOS in urban areas. The proposed economic valuation process can be used for evaluating urban sustainability, guiding resource allocation decisions, and shaping GOS design choices. In general, our study provides valuable insights into the complexities and significance of considering individual preferences while focusing on improving community well-being during urban planning and development. It evaluates the role of self-reported life satisfaction as a proxy measure of utility in happiness-related studies while offering valuable insight into how individuals perceive and value urban environments. Notably, life satisfaction did not fully capture the value associated with green spaces. The proximity to cemeteries affected the life satisfaction level of the community. The investigation did not effectively capture the value of interactions, knowledge of GOS functions, quality of GOS, or potential preferences for alternative land uses. We noted a statistically nonsignificant relationship between the life-satisfaction level and public GOS for the area radius range of 0–2000 m. Therefore, simply increasing the availability of public GOS, such as urban parks and forests, will not necessarily improve the level of well-being and life satisfaction of residents.

This study offers valuable insights into urban planning and management, particularly regarding the improvement of the environment through the planning and development of GOS. The valuation models adopted in this study focused on optimizing the efficient use of the limited urban space in Jakarta while considering the diverse preferences and well-being of its residents. These findings serve as relevant tools for local governments and city planners, providing them with a clearer understanding of the locals' preferences concerning both the quantity and quality of GOS. Thus, this information can significantly impact the decision-making processes related to the development and maintenance of public GOS. Our study highlights the importance of GOS in urban areas, particularly in densely populated regions with limited green spaces. The main goal of increasing the number of GOS is to ensure a more equitable distribution of greenspaces throughout the city, ensuring that such areas are accessible to a broader and more diverse population.

Enhancing the quality and equitable distribution of GOS in Jakarta is important for the advancement of environmental sustainability. This is crucial given the global trend of urbanization, particularly in developing nations experiencing rapid rural-to-urban migration. Note that a well-functioning GOS network is critical for the establishment of sustainable ecological landscapes, e.g., the creation of green corridors and the selection of cost-effective plant species. City quality is closely linked to the conception, management, and conservation of spaces. Therefore, there is a critical need for thoughtful GOS management, informed planning, effective design, and seamless policy implementation at both the regional and national levels. In this context, local governments play a significant role in maintaining current GOS databases and carrying out rigorous evaluations, particularly concerning landscape and ecological attributes. This approach is crucial in developing countries that are experiencing an expansion in transportation networks and an increase in urban heat levels.

Green open spaces (GOS) offer diverse ecological benefits, including the preservation of biodiversity in urban regions. Therefore, in developing nations that are influenced by complex economic, political, and cultural factors, an integrated approach toward environmental sustainability is not only recommended but also crucial. A comprehensive perspective on GOS development includes the following factors: investment, effective management, meticulous planning, public policy formulation, and resolving the challenges related to political instability. The active participation

of residents in shaping the urban environment is essential, as a sustainable city should cater to the needs of its inhabitants. In this study, we focused on parameters related to the public GOS, using indices to understand the satisfaction level of the community and their perceptions of the living environment. Notably, GOS facilities serve various social functions and fulfill certain psychological needs, thereby contributing to urban sustainability. When designing and managing GOS, it is important to consider the recreational requirements of all the community segments to promote health and stress reduction. Evaluating the intangible benefits of these spaces can support urban sustainability strategies. Public engagement, community participation, and qualitative assessment empower communities to articulate values and can support city planners in conceptualizing sustainable urban strategies. To enhance GOS valuation, this study advocates the application of LSA with more detailed GOS data, including a refined radius, specific categorization of the tree species grown in GOS, and thematic classification of greenspaces. This study also highlights the potential impact of park greenery on community life satisfaction.

This study has some limitations. For instance, the model relies on online survey satisfaction data and introduces biases or constraints associated with self-reported information. The assumption that respondents represented all the households in Jakarta Province does not fully capture regional diversity, and the presumption that users were exclusively residents limits the applicability of the findings. This study focused on understanding the impact of GOS on the well-being of Jakarta residents. By focusing on the households in Jakarta Province, this study seeks to gain nuanced insights into contextual intricacies. The focus on residential areas aligns with our study objective, which is to provide data for customized urban planning for the local populations. The presumption is that the users, exclusively comprised of residents, can portray the influence of GOS on those deeply entrenched in urban environments, ensuring a concentrated analysis of experiences and perceptions. Owing to their continuous presence, residents are likely to foster a deeper connection with the local green spaces than occasional visitors. This exclusivity ensures a concentrated analysis of the experiences and perceptions of those profoundly entrenched in the community fabric.

This study focuses on publicly owned GOS, such as parks, urban forests, and cemeteries, while excluding the valuation of private GOS (due to data unavailability). Notably, the Jakarta Provincial Government lacks comprehensive information on privately owned GOS, justifying this exclusion. Publicly owned GOS managed by local government entities are generally more accessible to diverse populations, significantly contributing to the overall well-being of the local community. Focusing on these spaces prioritizes the evaluation of areas that directly affect public health, recreation, and community engagement. Publicly owned GOS are often considered under urban planning and municipal management; thus, they can be directly influenced through public policies and urban development initiatives. Assessing privately owned GOS poses greater challenges from both regulatory and planning perspectives. The strategic focus on publicly owned GOS ensures a more feasible and impactful analysis that aligns with the objectives of our study and serves the broader context of urban governance.

5. Conclusion

In conclusion, this study utilized LSA and hedonic price variables to thoroughly assess the values of GOS in Jakarta while considering the ecological, economic, and social dimensions of the quality of life. Our study proposes a novel application of the LSA model to evaluate GOS in the Indonesian context. In the analysis, OLS Model II revealed that factors such as the length of residence, employment status, income, and the number of shopping centers affected the subjective life satisfaction levels of the respondents. These results are consistent with previous studies conducted in Western countries. While the economic valuation of urban GOS had a limited impact on the life satisfaction of residents of Jakarta, negative externalities, notably the presence of cemeteries (19.1%) within a 500–1000 m radius, significantly influenced the life-satisfaction coefficients in Model II. The results deviate from those of previous studies conducted in the Global North, emphasizing the significance of formulating urban planning strategies that are tailored to local contexts.

Furthermore, we noted that the LSA theory does not offer a practical alternative valuation method for urban GOS, primarily because of its inability to fully capture and leverage the positive externalities associated with parks and urban forests. The study also indicates a weak correlation between the presence of GOS and life satisfaction levels. Nevertheless, the LSA model pinpoints the negative externalities associated with the presence of cemeteries. This emphasizes the critical need to understand the multifaceted factors that influence people's perceptions and well-being in urban environments. Our study suggests that the residents of Jakarta tend to have relatively consistent preferences for urban GOS. Thus, urban planners and policymakers must design these spaces with a thorough understanding of their contributions to public well-being.

Our study enhances the current understanding of the complex interplay between urban environments, socioeconomic factors, and residents' overall well-being. Our findings highlight the crucial role of GOS in enhancing the quality of life and urge policymakers to consider both the physical attributes of the region and the locals' perceptions during urban planning. The use of LSA to evaluate the economic value of GOS offers a versatile approach to capturing external factors that affect individual well-being, even when these influences may not be consciously recognized. Ultimately, this study aims to inform policymakers about the economic implications of the GOS in Jakarta and suggest the implementation of sustainable practices for the development of the city. It acknowledges the limited studies that apply these valuation methods to developing nations that are experiencing rapid urbanization and facing unique urban challenges.

The LSA method meticulously analyzes the intricate interplay between social, economic, and environmental variables while offering invaluable insights for policymakers. While GOS valuation studies that use LSA are well-established in developed nations, the application of the approach to developing countries, such as Indonesia, is still in its nascent stages. To bridge this gap, our study employs a comprehensive valuation model that integrates the elements from the LSA and HPM (e.g., housing structures and environmental facilities). The economic valuation of the GOS extends beyond mere policy recommendations; it represents an academic endeavor with substantial relevance to the advancement of urban spaces in Indonesia. Understanding the economic values of GOS is crucial for informed decision-making in public policy. This understanding is pivotal in urban settings, wherein policymakers must assess whether preserving these open spaces outweighs the costs associated with their development and maintenance. The ongoing decrease in the GOS emphasizes the urgency for urban planners to prioritize preservation, guarantee public access, and integrate ecologically driven utilization into planning.

Furthermore, our approach contributes to the field of environmental economics by advancing the understanding of life satisfaction in urban populations and elucidating the complexities of the valuation of GOS in diverse urban contexts. Although our investigation did not identify a substantial positive impact of these spaces on life satisfaction, it provides insights into the critical aspects of urban planning and environmental economics in a rapidly growing city. It also emphasizes the importance of recognizing that the relationship between GOS and human well-being could be context-specific, while highlighting the need for a deeper understanding of how different elements of urban environments interact with the perceptions of the residents.

In the broader context of urban sustainability, this research highlights the significant role that public GOS plays in enhancing the quality of life of city residents. Achieving a balance between urban development and the provision of these spaces is considered crucial, particularly in cities with limited land availability and exorbitant property prices. Although the LSA did not significantly identify the positive externalities, it offered essential insights into urban planning and environmental economics while shedding light on the complex relationships between these spaces and community well-being. The insights derived from these findings can help policymakers and city planners design more livable and sustainable environments, while ensuring that the distribution and quality of greenspaces cater to the well-being of all residents.

Future studies should explore additional factors that influence community preferences for GOS by incorporating a wider array of variables and considering the distinct attributes of public GOS, including their size, purpose, and ecosystem services. This approach can enable urban planners and policymakers to better correlate GOS development to population preferences and human well-being. Future investigations could leverage these findings to enhance the development of these spaces and ensure their alignment with the preferences and well-being of the local population. The insights from this study are significant for policymakers, urban planners, and stakeholders in shaping the urban landscape of Jakarta. Understanding the economic value of the GOS can support policymakers in making informed decisions on the sustainability of city planning and the well-being of residents.

6. Declarations

6.1. Author Contributions

Conceptualization, R.S.; methodology, R.S.; software, R.S.; validation, R.S. and R.H.K.; formal analysis, R.S.; investigation, R.S.; resources, R.S.; data curation, R.S.; writing—original draft preparation, R.S.; writing—review and editing, R.S.; visualization, R.S.; supervision, R.H.K.; project administration, R.S.; funding acquisition, R.H.K. All authors have read and agreed to the published version of the manuscript.

6.2. Data Availability Statement

The data presented in this study are available on request from the corresponding author.

6.3. Funding

This study was funded by The University of Indonesia Research Grant 2023 PUTI Funding, grant number: NKB-555/UN2.RST/HKP.05.00/2023.

6.4. Acknowledgements

We express our gratitude to Rini Astuti, Ph.D., from The Australia National University for her valuable comments and suggestions on the manuscript. Sincere appreciation is also extended to anonymous reviewers for corrections and comments but all mistakes bear on the authors.

6.5. Conflicts of Interest

The authors declare no conflict of interest.

7. References

- [1] Van Oijstaeijen, W., Van Passel, S., & Cools, J. (2020). Urban green infrastructure: A review on valuation toolkits from an urban planning perspective. *Journal of Environmental Management*, 267, 110603. doi:10.1016/j.jenvman.2020.110603.
- [2] Kabisch, N., Kraemer, R., Brenck, M. E., Haase, D., Lausch, A., Luttkus, M. L., Mueller, T., Remmler, P., von Döhren, P., Voigtländer, J., & Bumberger, J. (2021). A methodological framework for the assessment of regulating and recreational ecosystem services in urban parks under heat and drought conditions. *Ecosystems and People*, 17(1), 464–475. doi:10.1080/26395916.2021.1958062.
- [3] Haruna, A. I., Oppong, R. A., & Marful, A. B. (2018). Exploring eco-aesthetics for urban green infrastructure development and building resilient cities: A theoretical overview. *Cogent Social Sciences*, 4(1), 1–18. doi:10.1080/23311886.2018.1478492.
- [4] Shuvo, F. K., Feng, X., Akaraci, S., & Astell-Burt, T. (2020). Urban green space and health in low and middle-income countries: A critical review. *Urban Forestry and Urban Greening*, 52, 126662. doi:10.1016/j.ufug.2020.126662.
- [5] Setiowati, R., Mizuno, K., Hasibuan, H. S., & Koestoer, R. H. (2022). Urban green spaces for support healthiness in Jakarta during the COVID-19 pandemic: A quantitative study. *Environmental Engineering Research*, 28(2), 210598–0. doi:10.4491/eer.2021.598.
- [6] Setiowati, R., Koestoer, R. H., Mizuno, K., & Hasibuan, H. S. (2023). Urban green space during the Coronavirus disease pandemic with regard to the socioeconomic characteristics. *Global Journal of Environmental Science and Management*, 9(3), 589–606.
- [7] Farrugia, S., Hudson, M. D., & McCulloch, L. (2013). An evaluation of flood control and urban cooling ecosystem services delivered by urban green infrastructure. *International Journal of Biodiversity Science, Ecosystem Services & Management*, 9(2), 136–145. doi:10.1080/21513732.2013.782342.
- [8] Ambrey, C. L., & Fleming, C. M. (2012). Valuing Australia's protected areas: A life satisfaction approach. *New Zealand Economic Papers*, 46(3), 191–209. doi:10.1080/00779954.2012.697354.
- [9] Wild, T. C., Henneberry, J., & Gill, L. (2017). Comprehending the multiple 'values' of green infrastructure – Valuing nature-based solutions for urban water management from multiple perspectives. *Environmental Research*, 158, 179–187. doi:10.1016/j.envres.2017.05.043.
- [10] Ambrey, C. L., & Fleming, C. M. (2011). Valuing scenic amenity using life satisfaction data. *Ecological Economics*, 72, 106–115. doi:10.1016/j.ecolecon.2011.09.011.
- [11] Tyrväinen, L. (1997). The amenity value of the urban forest: An application of the hedonic pricing method. *Landscape and Urban Planning*, 37(3–4), 211–222. doi:10.1016/S0169-2046(97)80005-9.
- [12] Saphores, J. D., & Li, W. (2012). Estimating the value of urban green areas: A hedonic pricing analysis of the single-family housing market in Los Angeles, CA. *Landscape and Urban Planning*, 104(3–4), 373–387. doi:10.1016/j.landurbplan.2011.11.012.
- [13] Xu, L., You, H., Li, D., & Yu, K. (2016). Urban green spaces, their spatial pattern, and ecosystem service value: The case of Beijing. *Habitat International*, 56, 84–95. doi:10.1016/j.habitatint.2016.04.005.
- [14] Wu, J., Wang, M., Li, W., Peng, J., & Huang, L. (2015). Impact of Urban Green Space on Residential Housing Prices: Case Study in Shenzhen. *Journal of Urban Planning and Development*, 141(4), 5014023. doi:10.1061/(asce)up.1943-5444.0000241.
- [15] Kolbe, J., & Wüstemann, H. (2014). Estimating the Value of Urban Green Space: A Hedonic Pricing Analysis of the Housing Market in Cologne, Germany. *Technical University of Berlin, Germany*.
- [16] Setiowati, R., Koestoer, R. H., & Andajani, R. D. (2024). Valuation of urban green open space using the Hedonic price model. *Global Journal of Environmental Science and Management*, 10(2), 451–472. doi:10.22035/gjesm.2024.02.03.
- [17] Frey, B. S., Luechinger, S., & Stutzer, A. (2009). The life satisfaction approach to valuing public goods: The case of terrorism. *Public Choice*, 138(3–4), 317–345. doi:10.1007/s11127-008-9361-3.
- [18] Tsurumi, T., & Managi, S. (2015). Environmental value of green spaces in Japan: An application of the life satisfaction approach. *Ecological Economics*, 120, 1–12. doi:10.1016/j.ecolecon.2015.09.023.
- [19] Van Kamp, I., Leidelmeijer, K., Marsman, G., & De Hollander, A. (2003). Urban environmental quality and human well-being towards a conceptual framework and demarcation of concepts; a literature study. *Landscape and Urban Planning*, 65(1–2), 5–18. doi:10.1016/S0169-2046(02)00232-3.
- [20] Setiowati, R., Hasibuan, H. S., & Koestoer, R. H. (2018). Green open space masterplan at Jakarta Capital City, Indonesia for climate change mitigation. *IOP Conference Series: Earth and Environmental Science*, 200(1), 12042. doi:10.1088/1755-1315/200/1/012042.

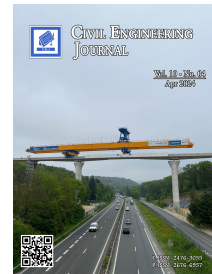
- [21] Kardan, O., Gozdyra, P., Mistic, B., Moola, F., Palmer, L. J., Paus, T., & Berman, M. G. (2015). Neighborhood greenspace and health in a large urban center. *Scientific Reports*, 5(1), 11610. doi:10.1038/srep11610.
- [22] Tyrväinen, L., Ojala, A., Korpela, K., Lanki, T., Tsunetsugu, Y., & Kagawa, T. (2014). The influence of urban green environments on stress relief measures: A field experiment. *Journal of Environmental Psychology*, 38, 1–9. doi:10.1016/j.jenvp.2013.12.005.
- [23] Krekel, C., Kolbe, J., & Wüstemann, H. (2016). The greener, the happier? The effect of urban land use on residential well-being. *Ecological Economics*, 121, 117–127. doi:10.1016/j.ecolecon.2015.11.005.
- [24] Carrus, G., Scopelliti, M., Laforteza, R., Colangelo, G., Ferrini, F., Salbitano, F., Agrimi, M., Portoghesi, L., Semenzato, P., & Sanesi, G. (2015). Go greener, feel better? The positive effects of biodiversity on the well-being of individuals visiting urban and peri-urban green areas. *Landscape and Urban Planning*, 134, 221–228. doi:10.1016/j.landurbplan.2014.10.022.
- [25] Aoshima, I., Uchida, K., Ushimaru, A., & Sato, M. (2018). The influence of subjective perceptions on the valuation of green spaces in Japanese urban areas. *Urban Forestry and Urban Greening*, 34, 166–174. doi:10.1016/j.ufug.2018.06.018.
- [26] Dewi, O. C., Chairunnisa, I., Hidayat, T., Anggraini, M., & Napitupulu, A. (2018). Green Open Space: Awareness for Health or Sustainability? *IOP Conference Series: Earth and Environmental Science*, 120(1), 12014. doi:10.1088/1755-1315/120/1/012014.
- [27] Yuniastuti, E., & Hasibuan, H. S. (2019). Child-friendly green open space to enhance the education process for children. *IOP Conference Series: Earth and Environmental Science*, 243, 012161. doi:10.1088/1755-1315/243/1/012161.
- [28] Salsabila, P., Maarif, S., & Sari, D. A. P. (2023). Strategy for improving Green Open Space (RTH) based on community participation in reduce the risk of flood disaster in Jakarta. *IOP Conference Series: Earth and Environmental Science*, 1173(1), 12061. doi:10.1088/1755-1315/1173/1/012061.
- [29] Zain, A. F. M., Permatasari, P. A., Ainy, C. N., Destriana, N., Mulyati, D. F., & Edi, S. (2015). The Detection of Urban Open Space at Jakarta, Bogor, Depok, and Tangerang – Indonesia by Using Remote Sensing Technique for Urban Ecology Analysis. *Procedia Environmental Sciences*, 24, 87–94. doi:10.1016/j.proenv.2015.03.012.
- [30] Setiowati, R., Hasibuan, H. S., Koestoer, R. H., & Harmain, R. (2019). Planning for Urban Green Area and Its Importance for Sustainability: The Case of Jakarta. *IOP Conference Series: Earth and Environmental Science*, 328(1), 12027. doi:10.1088/1755-1315/328/1/012027.
- [31] Setiowati, R., Mizuno, K., Hasibuan, H. S., & Koestoer, R. H. (2022). Actor-network theory approach for urban green spaces planning: Study in Jakarta Capital City, Indonesia. *Kasetsart Journal of Social Sciences*, 43(4), 1075–1084. doi:10.34044/j.kjss.2022.43.4.33.
- [32] Sutapa, I. D. A., Mbarep, D. P. P., Hasibuan, H. S., & Zalewski, M. (2023). Ecohydrology Approach to Strengthen Public Green Open Space Management towards Comfortable Common Space and Playground in Kalijodo Area – Jakarta Province, Indonesia. *Ecohydrology & Hydrobiology*, 23(4), 518–531. doi:10.1016/j.ecohyd.2023.04.005.
- [33] Aryaguna, P. A., Gaffara, G. R., Sari, D. A. K., & Arianto, A. (2022). Green Open Space Priority Modelling Using GIS Analysis In West Jakarta. *Indonesian Journal of Geography*, 54(2), 263–271. doi:10.22146/ijg.68184.
- [34] Dong, K., Sun, R., & Dong, X. (2018). CO₂ emissions, natural gas and renewables, economic growth: Assessing the evidence from China. *Science of The Total Environment*, 640–641, 293–302. doi:10.1016/j.scitotenv.2018.05.322.
- [35] Ferreira, S., & Moro, M. (2010). On the use of subjective well-being data for environmental valuation. *Environmental and Resource Economics*, 46(3), 249–273. doi:10.1007/s10640-009-9339-8.
- [36] Luechinger, S., & Raschky, P. A. (2009). Valuing flood disasters using the life satisfaction approach. *Journal of Public Economics*, 93(3–4), 620–633. doi:10.1016/j.jpubeco.2008.10.003.
- [37] Frey, B. S., Luechinger, S., & Stutzer, A. (2010). The life satisfaction approach to environmental valuation. *Annual Review of Resource Economics*, 2(1), 139–160. doi:10.1146/annurev.resource.012809.103926.
- [38] Ambrey, C., & Fleming, C. (2014). Public Greenspace and Life Satisfaction in Urban Australia. *Urban Studies*, 51(6), 1290–1321. doi:10.1177/0042098013494417.
- [39] Brander, L. M., & Koetse, M. J. (2011). The value of urban open space: Meta-analyses of contingent valuation and hedonic pricing results. *Journal of Environmental Management*, 92(10), 2763–2773. doi:10.1016/j.jenvman.2011.06.019.
- [40] Bockarjova, M., Botzen, W. J. W., & Koetse, M. J. (2020). Economic valuation of green and blue nature in cities: A meta-analysis. *Ecological Economics*, 169, 106480. doi:10.1016/j.ecolecon.2019.106480.
- [41] Aziz, A., Anwar, M. M., & Dawood, M. (2021). The impact of neighborhood services on land values: an estimation through the hedonic pricing model. *GeoJournal*, 86(4), 1915–1925. doi:10.1007/s10708-019-10127-w.

- [42] Glumac, B., Herrera-Gomez, M., & Licheron, J. (2019). A hedonic urban land price index. *Land Use Policy*, 81, 802–812. doi:10.1016/j.landusepol.2018.11.032.
- [43] MacKerron, G., & Mourato, S. (2013). Happiness is greater in natural environments. *Global Environmental Change*, 23(5), 992–1000. doi:10.1016/j.gloenvcha.2013.03.010.
- [44] Jokela, M., Bleidorn, W., Lamb, M. E., Gosling, S. D., & Rentfrow, P. J. (2015). Geographically varying associations between personality and life satisfaction in the London metropolitan area. *Proceedings of the National Academy of Sciences*, 112(3), 725–730. doi:10.1073/pnas.1415800112.
- [45] Fukahori, K., & Kubota, Y. (2003). The role of design elements on the cost-effectiveness of streetscape improvement. *Landscape and Urban Planning*, 63(2), 75–91. doi:10.1016/S0169-2046(02)00180-9.
- [46] Dolan, P., & Metcalf, R. (2008). Comparing willingness-to-pay and subjective well-being in the context of non-market goods. CEP Discussion Paper No 890, Centre for Economic Performance, London School of Economics and Political Science, London, United Kingdom.
- [47] Van Praag, B. M. S., & Baarsma, B. E. (2005). Using happiness surveys to value intangibles: The case of airport noise. *Economic Journal*, 115(500), 224–246. doi:10.1111/j.1468-0297.2004.00967.x.
- [48] Dolan, P., Peasgood, T., & White, M. (2008). Do we really know what makes us happy? A review of the economic literature on the factors associated with subjective well-being. *Journal of Economic Psychology*, 29(1), 94–122. doi:10.1016/j.joep.2007.09.001.
- [49] Bertram, C., & Rehdanz, K. (2015). The role of urban green space for human well-being. *Ecological Economics*, 120, 139–152. doi:10.1016/j.ecolecon.2015.10.013.
- [50] Cruces, G., Ham, A., & Tetaz, M. (2012). Quality of Life in Buenos Aires Neighborhoods: Hedonic Price Regressions and the Life Satisfaction Approach. *SSRN Electronic Journal*. doi:10.2139/ssrn.1815924.
- [51] Ferreira, S., Moro, M., & Clinch, P. (2006). Valuing the Environment Using the Life-Satisfaction Approach. *SSRN Electronic Journal*. doi:10.2139/ssrn.904355.
- [52] Brereton, F., Clinch, J. P., & Ferreira, S. (2008). Happiness, geography and the environment. *Ecological Economics*, 65(2), 386–396. doi:10.1016/j.ecolecon.2007.07.008.
- [53] Frey, B. S., Luechinger, S., & Stutzer, A. (2004). Valuing Public Goods: The Life Satisfaction Approach. *SSRN Electronic Journal*, CESifo Working Paper No. 1158. doi:10.2139/ssrn.528182.
- [54] Bertram, C., & Larondelle, N. (2017). Going to the Woods Is Going Home: Recreational Benefits of a Larger Urban Forest Site — A Travel Cost Analysis for Berlin, Germany. *Ecological Economics*, 132, 255–263. doi:10.1016/j.ecolecon.2016.10.017.
- [55] Menz, T. (2011). Do people habituate to air pollution? Evidence from international life satisfaction data. *Ecological Economics*, 71(1), 211–219. doi:10.1016/j.ecolecon.2011.09.012.
- [56] Maddison, D., & Rehdanz, K. (2011). The impact of climate on life satisfaction. *Ecological Economics*, 70(12), 2437–2445. doi:10.1016/j.ecolecon.2011.07.027.
- [57] Luechinger, S. (2009). Valuing air quality using the life satisfaction approach. *Economic Journal*, 119(536), 482–515. doi:10.1111/j.1468-0297.2008.02241.x.
- [58] BPS-Statistics (2023). Jakarta in Numbers 2023. DKI Jakarta Provincial Central Statistics Agency, Indonesia. Available online: <https://jakarta.bps.go.id/publication/2023/02/28/fd35fcb5d10a1e03f0d71348/provinsi-dki-jakarta-dalam-angka-2023.html>. (accessed on March 2024).
- [59] Frey, B. S., & Stutzer, A. (2002). What can economists learn from happiness research? *Journal of Economic Literature*, 40(2), 402–435. doi:10.1257/jel.40.2.402.
- [60] Layard, R. (2005). Mental health: Britain's biggest social problem?. Seminar on Mental Health, 20 January, 2005, London, United Kingdom.
- [61] Di Tella, R., & MacCulloch, R. (2006). Some uses of happiness data in economics. *Journal of Economic Perspectives*, 20(1), 25–46. doi:10.1257/089533006776526111.
- [62] Clark, A. E., Diener, E., Georgellis, Y., & Lucas, R. E. (2008). Lags and leads in life satisfaction: A test of the baseline hypothesis. *Economic Journal*, 118(529), 222–243. doi:10.1111/j.1468-0297.2008.02150.x.
- [63] Hidayat, R., Liu, S., & Saad, M. R. M. (2023). The Role of Mastery Goal on Life Satisfaction Using PERMA as A Mediator for College Students. *Emerging Science Journal*, 7, 238-252. doi:10.28991/ESJ-2023-SIED2-018.
- [64] Rehdanz, K., & Maddison, D. (2008). Local environmental quality and life-satisfaction in Germany. *Ecological Economics*, 64(4), 787–797. doi:10.1016/j.ecolecon.2007.04.016.

- [65] Kristoffersen, I. (2015). The Metrics of Subjective Wellbeing Data: An Empirical Evaluation of the Ordinal and Cardinal Comparability of Life Satisfaction Scores. *Social Indicators Research*, 130(2), 845–865. doi:10.1007/s11205-015-1200-6.
- [66] Stutzer, A., & Frey, B. S. (2008). Stress that doesn't pay: The commuting paradox. *Scandinavian Journal of Economics*, 110(2), 339–366. doi:10.1111/j.1467-9442.2008.00542.x.
- [67] Ferrer-i-Carbonell, A., & Frijters, P. (2004). How important is methodology for the estimates of the determinants of happiness? *Economic Journal*, 114(497), 641–659. doi:10.1111/j.1468-0297.2004.00235.x.
- [68] Mayer, J. D., Salovey, P., & Caruso, D. R. (2008). Emotional Intelligence: New Ability or Eclectic Traits? *American Psychologist*, 63(6), 503–517. doi:10.1037/0003-066X.63.6.503.
- [69] Bowler, D. E., Buyung-Ali, L., Knight, T. M., & Pullin, A. S. (2010). Urban greening to cool towns and cities: A systematic review of the empirical evidence. *Landscape and Urban Planning*, 97(3), 147–155. doi:10.1016/j.landurbplan.2010.05.006.
- [70] Nisbet, E. K., Zelenski, J. M., & Murphy, S. A. (2011). Happiness is in our Nature: Exploring Nature Relatedness as a Contributor to Subjective Well-Being. *Journal of Happiness Studies*, 12(2), 303–322. doi:10.1007/s10902-010-9197-7.
- [71] Fleming, C. M., Manning, M., & Ambrey, C. L. (2016). Crime, greenspace and life satisfaction: An evaluation of the New Zealand experience. *Landscape and Urban Planning*, 149, 1–10. doi:10.1016/j.landurbplan.2015.12.014.

Appendix I

Variable	Content of Question / Parameters / Values
Socioeconomic	
1. Name (not mandatory)	-
2. Handphone number (not mandatory)	-
3. Home address	Street Name/Housing Complex/Alley Number of neighborhood Subdistrict District Administrative City
4. Age	Less than 20 years old Aged between 20 and 60 years old Over 60 years old
5. Education level	Those without education or formal degrees High school graduates College graduates
6. Occupational status	Unemployed Employed in government/private sectors Entrepreneurs Blue-collar labourers Others
7. Average monthly income	IDR < 4.5 million IDR 4.5 – 10 million IDR 10 – 20 million IDR > 20 million
Structural Housing	
1. Type of residence	Landed house Apartment
2. Resident status	Ownership Rent/Lease If the house is rented/leased, what is the monthly rental payment amount (in IDR)? If the house is owned, what is the estimated rental/lease amount per month (in IDR) based on market price estimates? (Fill in 0 if the house is rented/leased)
3. Length of residence	< 5 years 5-10 years > 10 years
4. Source of clean water	Piped water Others
5. Bathroom	Inside the house Outside the house
6. Size of the residential building in m ²	< 100 ≥ 100
7. Number of bedrooms	1 2 3 4 ≥ 5
Satisfaction and Comfort Level	
1. To what extent are you satisfied with the level of comfort in the location of your residence?	Very dissatisfied (1) – Very satisfied (10)
2. According to you, how much green open space (park/urban forest/cemetery) is there in the location of your residence?	Very few (1) – Very much (10)
3. Overall, what level of satisfaction do you feel in life?	Very dissatisfied (1) – Very satisfied (10)



Utilization of Sand Cushion for Stabilization of Peat Layer Considering Dynamic Response of Compaction

Ali Basha ^{1*} , Waseim Azzam ² , Mohamed Elsiragy ³

¹ Faculty of Engineering, Kafrelsheikh University, 33511, Egypt.

² Faculty of Engineering, Tanta University, Tanta, Egypt.

³ Faculty of Engineering, 6 October University, Cairo, Egypt.

Received 11 October 2023; Revised 15 March 2024; Accepted 20 March 2024; Published 01 April 2024

Abstract

Soft peat soils are located in many zones and at a given depth all over the world and are characterized by their low shear strength and high settlement. It can also cause progressive failure of roads, embankments, and foundations. Sand cushioning is the most beneficial technique used to relieve the stress transmitted to the peat layer to mitigate any deformation and shear failure. In this research, a field study of a road with a soft peat layer located at a depth 4m below the ground surface is carried out. The plate load test is conducted on three cases over the peat layer using sand cushions with and without reinforcement. The results were compared with plate footing on the surface of the road without stabilization. The field tests of the improved technique were verified and deeply analyzed using the numerical program Plaxis. The finite element analysis mainly sheds light on the simulation of the dynamic response that represents the compaction of the sand cushion over the peat layer. A series of numerical models has been done considering the effect of repeated load compaction on the adopted sand cushions with and without reinforcement. The numerical analysis is directed to show the effect of repeated loads of compaction equipment that were used on decreasing the stress over the peat layer. The results showed that the composite compacted cushion with both a higher number of cycles and stress has a great effect on relieving the stresses transmitted to the face of the peat. As a result, the footing capacity is increased with less deformation.

Keywords: Plate Load Test; Geotextile; Repeated Load; Compaction; Sand Cushion.

1. Introduction

Geotechnical engineering names any soil that contains organic matter (plants or animals) organic soil when the organic matter represents less than 25% of its content, muck when the content range of organic matter is between 25% to 75%, and called a peat when the organic matter represents 75% or more of its content. Due to the high content of organic matter, they are distinguished by a dark brown to black color, a spongy consistency, a high initial void ratio, low bulk density, high natural water content, high initial permeability, low shear strength, and high compressibility [1, 2].

The geotechnical characteristics of peat have been studied by Hobbs (1986) [3], Edil & Dhowian (1981) [4], and Edil (2003) [5]. An extensive investigation has been carried out to study the best technique to improve the geotechnical properties of peat, for example, by using cement or a different binder and deep mixing methods [6–8]. Also, fiber-polyester and shredded rubber-crumbs as reinforcement materials were adopted for treating peat [9–11]. Heneash et al.

* Corresponding author: ealibasha@eng.kfs.edu.eg

 <http://dx.doi.org/10.28991/CEJ-2024-010-04-011>



© 2024 by the authors. Licensee C.E.J, Tehran, Iran. This article is an open access article distributed under the terms and conditions of the Creative Commons Attribution (CC-BY) license (<http://creativecommons.org/licenses/by/4.0/>).

(2023) [12] investigated how the addition of polymer (SBS) improves the qualities of the problematic soil. To attain this goal, experimental programming was planned and conducted on the treated and untreated samples of two types of soils: collapsing silty-sand soil and poor fine-sand soil. Whereas Šiukščius et al. [13] used the geogrid for the application of road subgrade stabilization for pavement evenness. A load load test on stabilized peat subgrade was investigated in the field using geogrid reinforcement within the gravel fills, as stated by Jarrett [14]. It can be seen that the existence of such a reinforced layer significantly reduced the vertical stresses below the reinforced section, and the load was effectively distributed over a wider region.

Mooney et al. [15] stated that the dynamic effect roller relatively decayed when the cyclic responses to soil mass reached 10% of their peak value. Fathi et al. [16] studied numerically in the laboratory and conducted a field measurement to determine the depth of influence of the roller. The obtained results from a wide range of materials indicate that the average depth of influence is 1.80 m, which varies from 1.4 m to 2.2 m.

Adams & Collin [17] studied the behavior of a large-scale model of spread footing load tests on geosynthetic reinforcement to show their beneficial consequences on load transfer technique. This technique of reinforced sections over soft layers can be considered a good method to reduce permanent deformation and stresses that are transmitted to the soft peat layer. Regarding methods of peat stabilization in the literature, which are characterized by a variety of techniques that are applied in the laboratory as small-scale model tests, it can be concluded that there is a lack of knowledge in investigating the large scale in the field to simulate the real behavior of the problem of foundation on the soft peat layer, which is widely tested in the laboratory by different researchers. Basha et al. [18] conducted a series of small-scale model tests to examine the subgrade reaction of the effectiveness of recycled concrete aggregate (RC) in improving the structural performance of sandy soil. Plate bearing experiments were carried out using a footing model (250×250 mm) inside a tank (1500×1500×1000 mm) to determine the stress-strain response, bearing capacity ratio (BCR), ultimate bearing capacity, and modulus of elasticity of the studied mixture. The results demonstrated that the method used to mix the RC with the sand is outstanding and suitable for use in the field.

Therefore, in this research, full-scale field loading tests for two techniques of ground improvement to stabilize a soft peat layer in the site have been carried out in the field to determine the field real load capacity. Afterward, these techniques were verified and further analyzed using finite element analysis using Plaxis 2d. The numerical study helped in better understanding the mechanism of improvement and stress distribution control that transmitted to the soft peat layer in the site. It also shed light on the failure mechanisms and deformation characteristics of reinforced and peat layers. Also, this research presents a novel simulation of sand cushions using dynamic loads to show their beneficial effect on improving the peat layer.

2. Sites and Soil Nature

The investigated site is located in Kafr El-Sheikh Governorate, for the main road in Sidi Salm city, Kafr El-Sheikh governorate, Egypt. A number of five borings are carried out to illustrate the geological nature of soil formation and soil profile, where their depth is extended up to 10 m for the road. Table 1 presents the soil profile related to the ground sampling that was obtained at the site. The subsoil was composed of a layer of fill to level -0.50m below the ground surface, followed by medium-stiff brown clay extended to level -4.00 m. A layer of dark gray peat layer with thickness of 1m (-5.00 m) underneath gray medium silty clay until a level of -10.00 m. A series of laboratory tests were done to obtain the main geotechnical properties of each layer, as shown in Table 1. The ground water table is found to be at -2.00 m below the ground surface.

Table 1. Physical and geotechnical properties of the soil layer in the site

Depth, m	Soil stratification	Sand%	Clay%	Silt%	Wc%	L.L%	PL%	PI%	Cohesion C kN/m ²	Cc	ϕ	Bulk Unit weight kN/m ³
0-0.5	Fill					NA						16
0.5-4	Brown medium stiff clay	0	93	7	29	50	25	25	40	0.17	-	18.1
4-5	Dark gray peat	0	20	80	450	76	47	29	15	0.46	-	9.81
5-10	Brown medium stiff clay	0	93	7	29	50	25	25	40	0.17	-	18.1

where; Wc is the water content, LL is the liquid limit, PL is the plastic limit, PI is plasticity index, Cc is the coefficient of gradation and ϕ is the angle of internal friction.

Special care has been considered during the extraction of the peat samples to be tested in bulk. Duraisamy et al. (2007, 2009) [11, 19] provided and made up a hand auger as a sampler (UPM sampler) to gather undisturbed peat samples as presented in Figure 1. This adopted sampler met the supplies for an undisturbed sampler's requirement or specification.

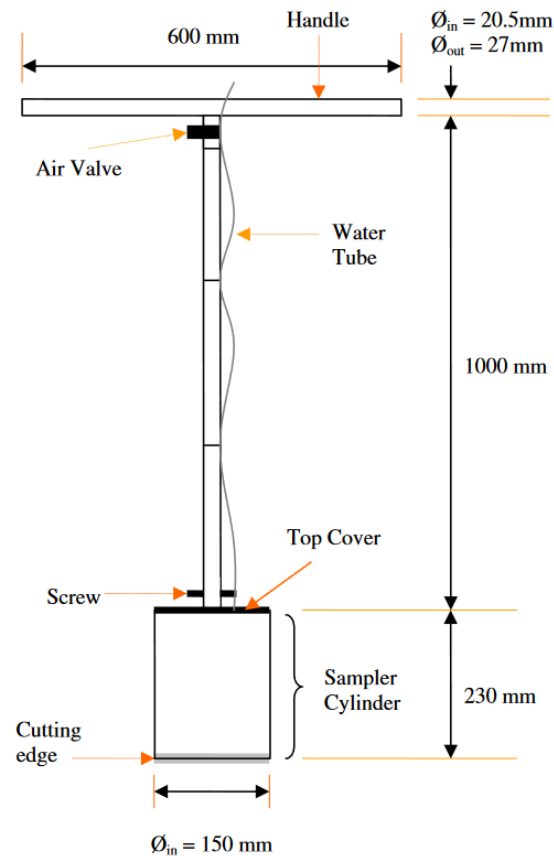


Figure 1. Peat sampler in the site [11]

The physical characteristics of the peat layer, which causes a failure of roads and pavement in the form of excessive settlement and road deformation, are shown in Table 2.

Table 2. Main properties of tested peat tested in this research

Property	
Decomposition degree %	Highly decomposed peat is higher than 40%.
Unit weight/ Bulk density kN/m ³	9.81
Specific gravity (Gs)	1.47
Organic content %	77
Hydraulic conductivity m/day	0.49

3. Strategy of the Field Study

The most important purpose of the existing study was to inspect the static load-deformation behavior of bearing capacity and settlement of surface plate loading tests at different cases of subgrade. In the case of normal ground without improvement, in the case of using a stabilized layer with a given depth (H) using compacted sand fill, and finally in the case of reinforced mattress composites constructed above peat subgrades. In addition, assess the behavior of geo-composites subgrade above the peat by comparing the test results with those obtained for unreinforced sections and compacted sand bases reinforced with a single layer of geotextile.

3.1. Plate Load Test

The ultimate bearing capacity at the site has been obtained according to the ASTM D1195 [20] Standard Test Method for static plate load tests of soils and flexible pavement.

A series of plate loading tests (PLTs) were carried out by a circular steel plate with a diameter of 0.60 m on a 0.50 m compacted subgrade layer with and without reinforcement in the site for the examined road in different cases. The results were compared with a normal plate load test at the surface of plain ground. The static PLT technique was adopted according to ASTM D1194 [21].

The studied strategy in the field and the tested parameters are illustrated in Figure 2. Figure 2-a shows the load test of the normal case when the plate load is placed directly above the fill without stabilization for comparison. Figure 2-b

provides the case of using a compacted fill of a sand layer 0.50 m thick, which is installed in 2 layers (250 mm) as a sand cushion. Each layer was compacted well according to specification (ASTM D 1556-ASTM [22]) to reach the maximum dry density. The granular sand cushion adopted in this investigation was made from dry sand. It was classified according to sieve analysis as well-graded sand. It has a maximum and minimum unit weight of 18.3 and 16 kN/m³, respectively.

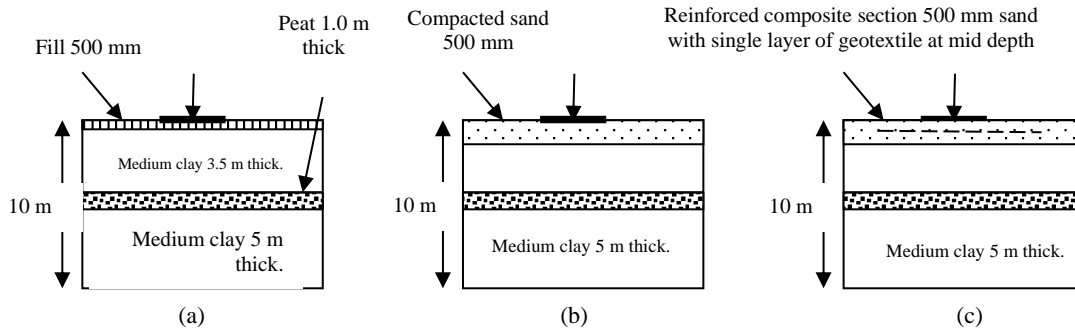


Figure 2. Plate load test for different cases in the field, a: load test on normal ground above the fill, b: load test on stabilized ground above the peat using 500mm compacted fill without reinforcement, c: load test on stabilized ground above the peat using 50.

Figure 3 shows the compaction curve for the tested sand use for stabilization in the site and mention to the optimum moisture content. The specific gravity of the adopted sand is found to be 2.62 and the maximum angle of internal friction is 41°. The compaction efficiency was checked in the site using sand cone test which is found to be 98%. The final case of study is used a single layer of geotextile at mid depth of sand cushion. The reinforced element used in the field was non-woven geotextile (a heat bonded Typar-3857) that made of polypropylene multifilament fibers. According to data of the manufacturer's, it has a thickness of 2 mm and weight per unit area of 290g/m². The elongation at maximum load is 10% that corresponding to tensile strength from the strip test method of 20.1 kN/m. The length of the geotextile was taken the time of plate diameter (3d) [23, 24].

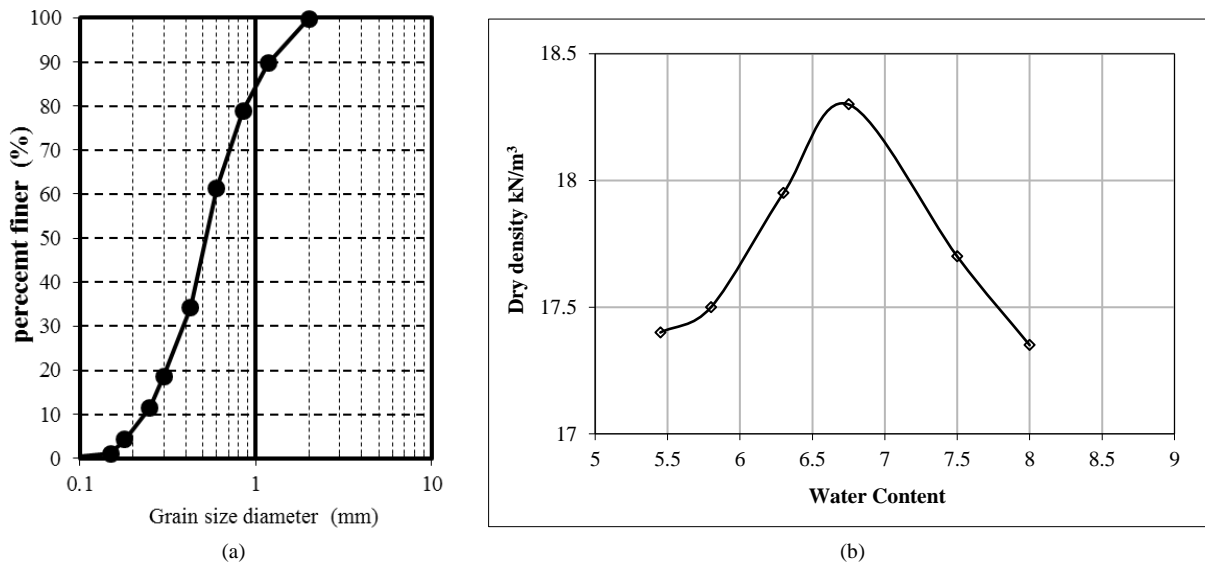


Figure 3. properties of sand cushion a) graduation curve, b) Compaction curve for used sand in the field

4. Field Results and Discussion

4.1. Definition Failure Load and Ultimate Bearing Capacity

In this study, the definition of the ultimate bearing capacity at failure was distinct as the tangent intersection between the initial, straighter segment of the loading-stress-settlement curve and the next steeper, straight part of the curve [17].

4.2. The Stress Settlement Curves

The stress settlement data are provided for the given field tests and presented in Figure 3. It presents the stress settlement curves for plate footing on the surface of fill and pate footing on sand cushions with and without reinforcement. It has been noticed that the stress settlement curves were considerably modified and increased as the

subgrade layer was stabilized with sand cushion. It can be seen that for the footing located directly at the surface without stabilization, the bearing capacity is found to be 35 kN/m² at a settlement ratio of $S/d = 2.17\%$ (d is the plate diameter). While for the stabilized case using a sand cushion with a depth of 50cm without reinforcement, the stress settlement is improved. The existence of such a sand cushion can improve and increase the ultimate bearing capacity compared with plate footing on normal ground. The ultimate stress increases due to both the existence of the replaced sand cushion and the compaction efforts that were adopted to compact the cushion into two layers. The ultimate bearing capacity of footing on stabilized sand cushion without reinforcement is found to be 70 kN/m² at $S/d=1.00\%$. It can be concluded that as the subgrade stiffness increases, the bearing capacity increases. The bearing capacity of footing on stabilized sand cushion over soft clay is 2.0 times that of surface footing without stabilization. Moreover, using a single layer of geotextile has good effects, as illustrated in Figure 4. It can also be observed that the ultimate bearing increases with the existence of a single layer of geotextile within the sand cushion at mid-depth. It is also noticed that the footings on reinforced subgrade have higher ultimate loads than in other cases [23, 25]. The existence of reinforcement over the peat layer within the sand cushion can significantly improve and increase the ultimate bearing capacity with less settlement. The ultimate bearing capacity for reinforced cases is found to be 130 kN/m² at $S/d=0.80\%$. This increase in the ultimate bearing capacity is backed by the combined effect of both the sand cushion and layer of reinforcement. The ultimate bearing capacity of the reinforced case is found to be 3.71, 1.85 times that of footing on normal ground without stabilization and footing on pure sand cushion without reinforcement, respectively.

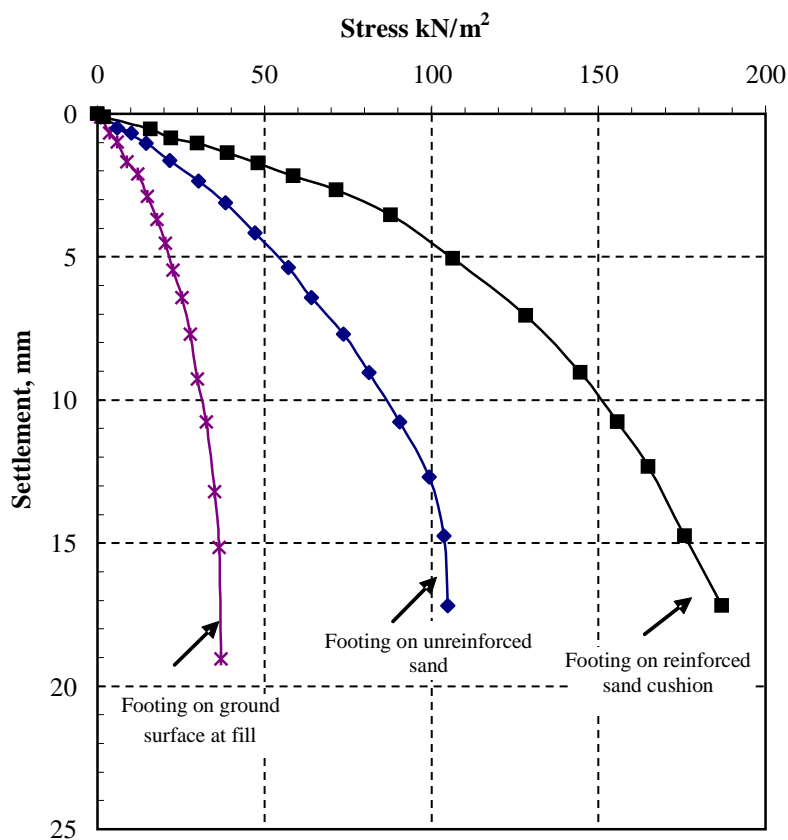


Figure 4. Stress settlement relationship for plate load test at different loading case

The stress carrying by footing over reinforced geotextile layer is higher than the footing without reinforcement; this shows that the geotextile has a substantial effect on increasing the bearing response of the plate load capacity. The footing confirms the better enclosibility of the reinforcement below the plate footing by preventing the sand particles above the geotextile from causing vertical and lateral deformation. Also, the soil between the footing and reinforcement is progressively compacted through the loading stages; as a result, the subgrade soil becomes stiffer and the settlement is reduced. The composite section of sand cushion and reinforcement can also be very significant, particularly when decreasing the transmitted stress to the peat or weak layer.

On the other hand, the use of a geotextile layer as reinforcement can provide an additional improvement where the soil between the plate and the reinforcement is successfully interlocked and acts as a composite rigid section due to the subgrade densification that is achieved. This will decrease the vertical settlement and increase the bearing capacity. It can be seen that a dual effect (the cushion effect and the geotextile effect) was achieved. Thus, the soil over the reinforced layer became stiffer, became one coherent unit, and tended to form a composite stiff section. As a general result, the footing bearing capacity increased and the surface settlement decreased.

The acting stresses above the peat layer for the load condition have been calculated using Boussinesq's method. It is noticed that for normal case footing on ground surface without stabilization, the stress above the peat face is 1 kN/m^2 . While this value is found to be 2 and 3.9 kN/m^2 for footing on pure sand cushion and reinforced case, respectively. These theoretical values that were obtained neglect stabilization and reinforcement effects. Therefore, to analyze the effect of the reinforced section in decreasing the stress over the soft peat layer, a numerical analysis should be submitted to verify the reinforcement technique in relieving the stress and describe the improvement mechanism. In addition, the improvement effect of adopting such a sand cushion that is installed in layers and compacted according to specification can be investigated numerically. The effect of repeated load compaction of the equipment used is distinctly explained, and their effect on decreasing the stress over peat is also submitted.

5. Numerical Modeling

In this part of the study, the validation of the numerical study by the field analysis results is introduced. The results gained from the field plate load tests were verified by carrying out numerical analysis using the finite element scheme. The axisymmetric elasto-plastic finite element analysis for circular plate footing was carried out using the commercial program PLAXIS [26]. This numerical analysis aims to identify the behavior of reinforced systems and transmit stress to the peat layer. It also provides information on and clarifies the failure pattern of the studied system. This scheme can be considered a good method for verifying the variables that cannot be obtained in the field.

The soils (sand cushion, medium clay, and peat) in this analysis are modeled by the Mohr-Coulomb failure theory. The main input data or parameters of the Mohr-Coulomb criteria are those that are effortless, slightly friendly, and agree with field testing results. It needs five parameters that are available and easy to obtain from the basic laboratory tests. The axisymmetric model and 6-node triangle elements were adopted for the current analysis. The modulus of elasticity of the different soils at the tested sites was obtained by performing the triaxial tests. The plate of the test setup was a circular one with a diameter 600 mm. It was simulated by a plate element, which is considered very stiff and rough. For the interface element, the interface strength (R_{inter}) is 0.67, which is appropriate for sand-steel interfaces.

The reinforced element of the adopted reinforcement is modeled as a geotextile element that is mentioned by the axial-horizontal stiffness EA (kN/m) of the geotextile material. In all test series, the length of the reinforced layer is constant, with an adopted length of $4d$. The modeled interface with the geotextile element was specified previous to mesh generation. The virtual thickness for positive and negative interface elements is modeled in the plaxis program. Force control performance is considered in all the calculations mentioned in this paper. Where point forces are placed and acted on a geometry point at the center of the plate / footings. Point loads are really line loads in the out-of-plane. The values of point forces are shown in force per unit of length (kN/m).

The properties of the used sand cushion that were simulated in the program input data are ($\gamma = 18.3 \text{ kN/m}^3$, $\nu = 0.3$, $E = 7500 \text{ kN/m}^2$, angle of internal friction $= 41^\circ$, and angle of dilatancy $= 11^\circ$). The main footing/plate properties are axial stiffness ($EA = 24.30 \text{ kN/m}$) and bending stiffness ($EI = 171200 \text{ kN/m}^2/\text{m}$). Where E is the modulus of elasticity of the plate material of the circular footing, A is the cross-section area, and I is the moment of inertia of the cross-section of the footing model.

5.1. Simulation of Dynamic Roller for Compaction

The most important note in this analysis is to consider the repeated load of the roller on the surface of the used sand cushion. The simulation of the installation method of sand cushion in the Plaxis program is significantly considered the compaction repeated load. This can be done to simulate the real behavior of the compaction process in the sand layer (25 cm). It is also considered to be achieved by transmitting stress from compaction to the underlying layer. Numerical modeling of sand cushion and compactor equipment was investigated in the 1950s [27, 28]. The modeling of vibratory rollers and compaction technique is also stated by Yoo & Selig [29]. Therefore, in this study, a finite element model simulating a static compacting roller for the sand layer installed in the field for stabilizing the peat layer was used using PLAXIS 2D 2002, as simulated by Azzam [30]. The soil layer is subjected to dynamic or repeated loading from compaction equipment at the site. A linear-elastic, perfectly plastic model with a Mohr-Coulomb failure criterion is used. First, the model constructed uses an axisymmetric with four sort of triangular elements of 15 nodes for precision. The axisymmetric model is adopted to simulate the strains induced in the direction of the used roller track. The loading scheme used in this study is a uniformly distributed load. This loading technique is applied to the soil through a rigid, weightless plate. The loading is activated and deactivated in the calculation phases in order to simulate the amount of load cycles or passes by a static roller. The simulation of the roller in the plaxis program to achieve the real compaction effort is adopted according to Roudgari [31]. Based on experience, the average value of 0.50 m for the contact width of the roller is considered over the road area to maintain the distribution of the compaction for all layers. The number of cycles adopted in the analysis is 10 cycle for applied load of 25 kN/m^2 within a time interval of 2 seconds and a frequency of 39 Hz. Which means that in simulation there are a total of 20 phases, 10 of which are activated and the other 10 are deactivated for simulated cycles of load. Table 3 shows applicable specifications for simulated drums based on experience and literature [32].

Table 3. Specifications for simulated roller

Parameter	Value
Radius of the drum	0.60 m
Width of the drum	1.68 m
Mass of the drum	1851 kg
Mass moment of inertia of the drum	412 kgm ²
Static axle load	44130 N
Excitation frequency	39 Hz
Amplitude of the oscillating moment	54947 Nm
Suspension drum/frame - stiffness	4×106 N/m
Suspension drum/frame - damping	3×102 N/m
Roller speed	1.11 m/s

The calculation steps involved the following: the first stage of construction, then removing the fill. The second step is placing the sand cushion in layers, and each layer is compacted with a cycle number of 10 with an applied load of 25kN/m². The third step is placing the footing and applying the static load until it reaches failure. It can be observed that two load techniques are considered: the first is dynamic load due to compaction, and the second is the normal static load applied to the footing plate. The geometry and dimension of the adopted model are given in Figure 5 for both construction cases.

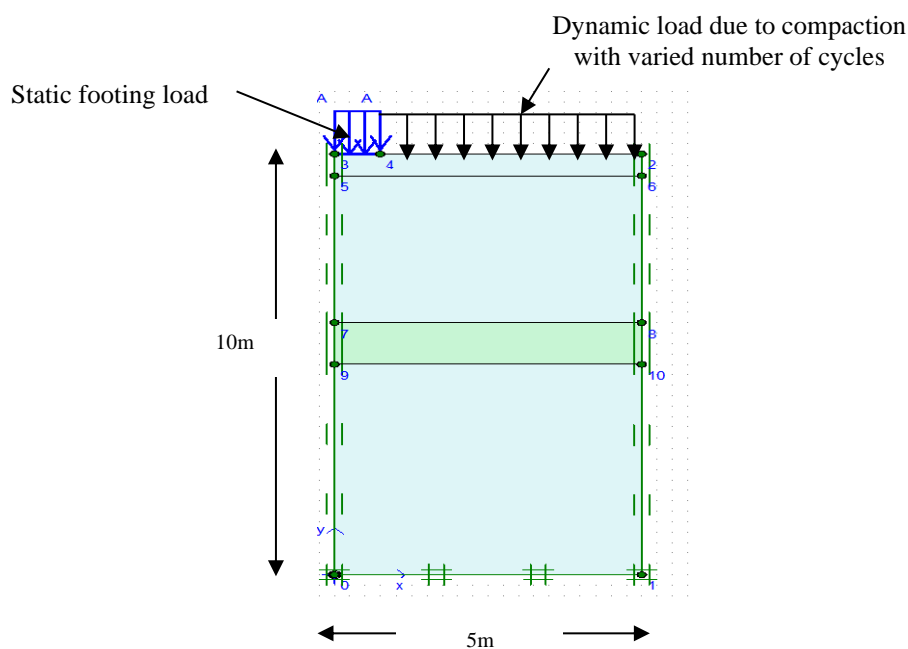


Figure 5. Geometry and dimension of finite element model

5.2. Verification of the Theoretical Analysis Using Field Results

Consider the dynamic response mentioned above; a contrast between the stress settlement responses is obtained using the finite element analysis. The field results that were recorded from the relevant plate load tests for the three cases mentioned in Figure 3 were run with a numerical program. The numerical results of the tested three cases are compared with those obtained in the field and plotted in Figure 6. The finite element results are reasonably accurate for computed values of the ultimate bearing capacity. The numerical results are close to those of field consequences and have the same trends. The results of the numerical study confirm the field value and justify the effectiveness of the dynamic condition applied to the replaced sand cushion. However, a little difference between the results from the numerical analysis and those obtained from the field test is observed. This variation is due to environmental conditions in the field and the accuracy of the input data.

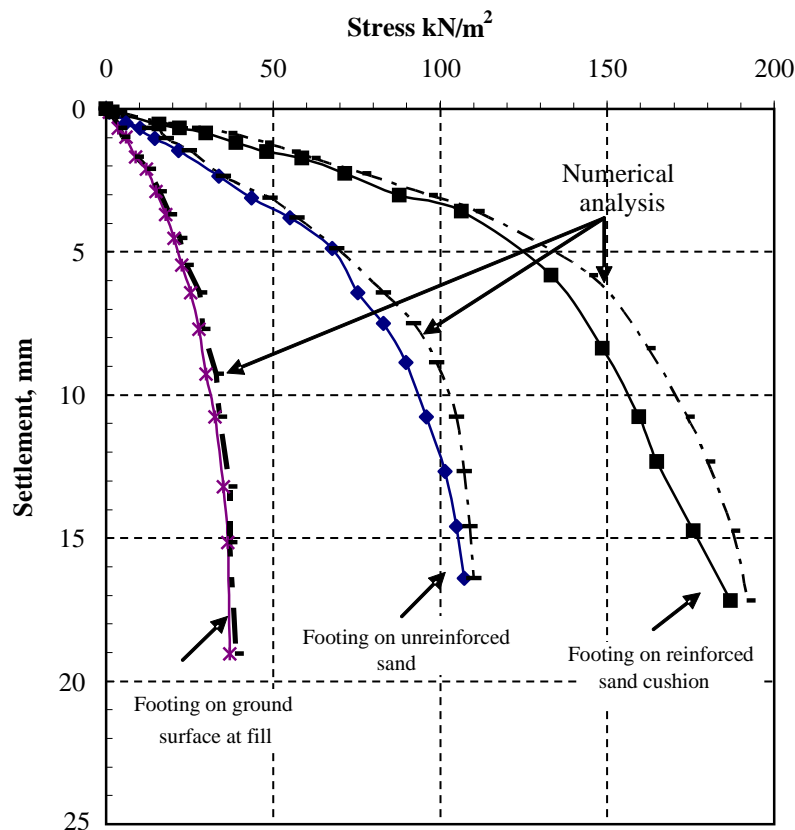


Figure 6. Comparison of stress settlement curves for field test data test and numerical results for different cases

5.3. Numerical Outcomes

The main aims of the finite element study are to verify the field test results and shed light on the parameters that cannot be measured in the field. It also tries to clarify the effectiveness of the adopted dynamic response on the improvement of the underlying soil and relieve the stresses transmitted to the weak peat layer. Therefore, the effect of variation in the number of cycles and applied load is examined to reach an acceptable degree of improvement in controlling the stress and settlement of the peat layer. The studied series using numerical modeling is shown in Table 4, considering the thickness of the sand cushion with or without reinforcement, applied dynamic stress, and number of cycles to repeat the load. These series try to determine and evaluate the effect of dynamic acting repeated stress at the surface of the installed sand cushion on the footing ultimate bearing capacity and transmitted stress to the peat layer. Due to the limited space, some of the studied series for the stress settlement curves for plat/e footing on sand cushions with different thicknesses in the case of sand without/with reinforcement are presented in Figure 7 for the condition of $N = 10$ cycles and a dynamic stress of 25 kPa. This figure confirms that the thickness of the sand cushion has a good effect on modifying stress settlement curves (Figure 7-a) in the case of pure sand cushion without reinforcement. As the sand thickness increased, the ultimate bearing capacity increased with less settlement. The installation of sand cushions with adequate depth can significantly produce stiff subgrade that reduces the transmitted stress to underlying strata with minor settlement. It also modifies the bearing capacity failure from general shear failure to punching shear failure with limited stress. While the existence of reinforced elements within the subgrade sand cushion with a dynamic process can effectively induce a combined effect in improving the load-carrying capacity with obvious values, as confirmed by Figure 7-b. These figures demonstrated that the ultimate bearing capacity improved well with the increase of sand cushion when a reinforced layer was used.

Table 4. Studied series for numerical analysis

Series	Constant parameters	Variable parameters
1	$H/D = 0.5, \phi = 41^\circ, \text{Number of cycle } N = 10$	Sand cushion without reinforcement Applied dynamic stress $\sigma = 25, 30, 40 \text{ kN/m}^2$
	$H/D = 1.0, \phi = 41^\circ, \text{Number of cycle } N = 10$	
	$H/D = 1.5, \phi = 41^\circ, \text{Number of cycle } N = 10$	
2	$H/D = 0.5, \phi = 41^\circ, \text{Number of cycle } N = 10$	Sand cushion with reinforcement, single layer at mid depth Applied dynamic stress $\sigma = 25, 30, 40 \text{ kN/m}^2$
	$H/D = 1.0, \phi = 41^\circ, \text{Number of cycle } N = 10$	
	$H/D = 1.5, \phi = 41^\circ, \text{Number of cycle } N = 10$	
3	$H/D = 0.5, \phi = 41^\circ, \sigma = 25 \text{ kN/m}^2$	Sand cushion without reinforcement Number of cycle $N = 10, 15, 20$
	$H/D = 1.0, \phi = 41^\circ, \sigma = 30 \text{ kN/m}^2$	
4	$H/D = 0.5, \phi = 41^\circ, \sigma = 25 \text{ kN/m}^2$	Sand cushion with reinforcement, single layer at mid depth Number of cycle $N = 10, 15, 20$
	$H/D = 1.0, \phi = 41^\circ, \sigma = 30 \text{ kN/m}^2$	
	$H/D = 1.0, \phi = 41^\circ, \sigma = 30 \text{ kN/m}^2$	

For all studied series, frequency equal 39 Hz is considered. The length of reinforced layer is constant with length of 4d.

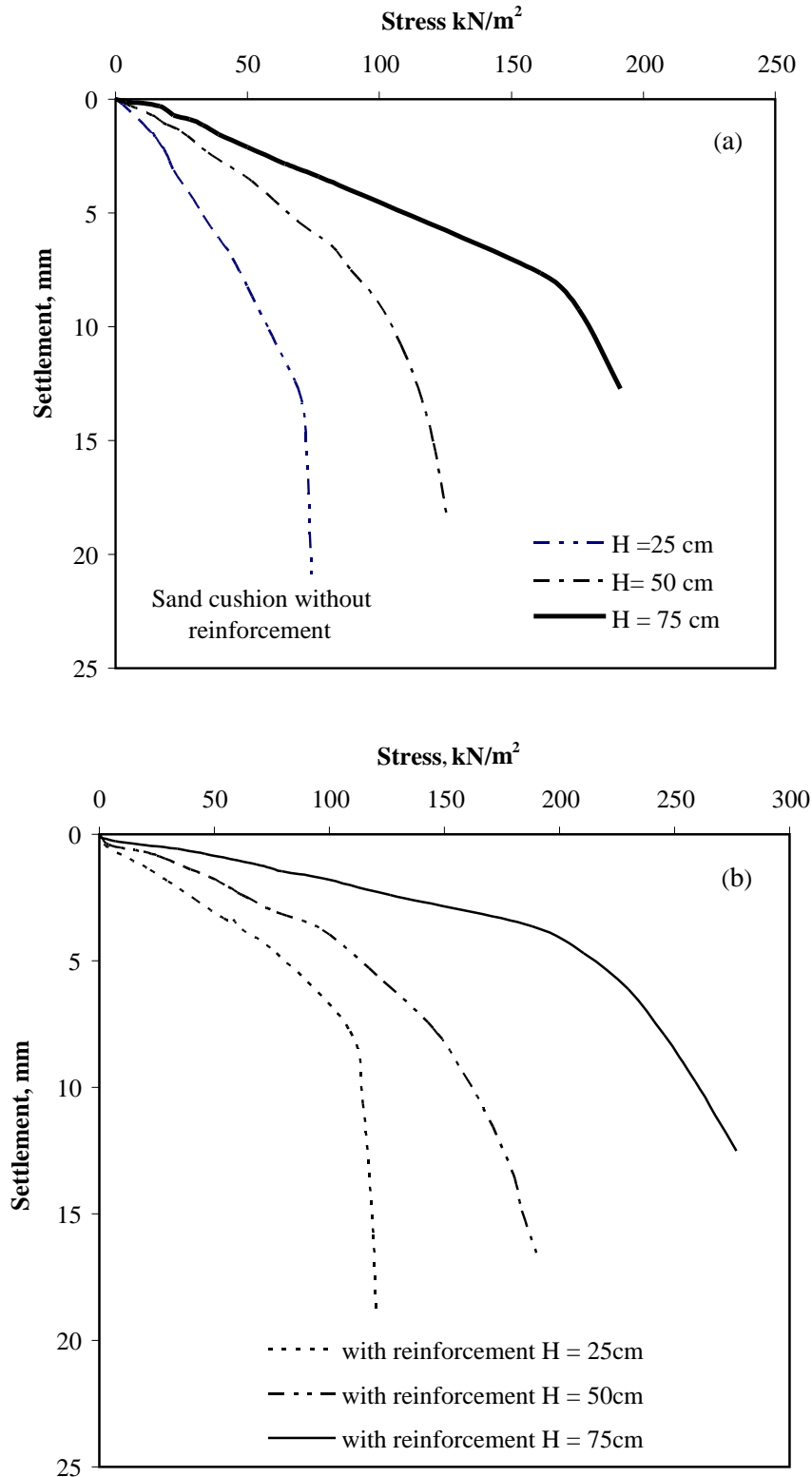


Figure 7. Stress settlement relationship for footing on sand cushion with different thickness (N =10 and $\sigma = 25\text{kPa}$), a: sand cushion without reinforcement, b: Sand cushion with intermediate single layer of reinforcement

The major cause of this occurrence of subgrade improvement is the existence of a reinforced layer within the sand cushions that distinctly produced a stiff composite slab. This slab is more effective in redistributing the stress to the deep layer with minor values. It can be seen that the partial substitute of the soil with the reinforced sand cushion layer results in a redistribution of the stresses to a wider region, consequently eliminating the stress focus and producing an enhanced distribution of the obtained stress. That's why the ultimate bearing capacity can be enhanced while the plate footing settlement is controlled. It is noticed that the stress-settlement curve is curved in shape, tends to be steeper, and takes on

an approximately linear form before attaining failure. A peak stress is not considered, and no definite failure point is recognized (Figure 7-a) [33]. The failure mode can be diverted to punching shear failure due to the reinforced effect.

On the other hand, for a deep analysis of such a phenomenon, Figure 8 shows the relationship between the ultimate bearing capacity of plate footing and sand cushion thickness in the form of a ratio (H/D) for both sand cushions with/without reinforcement at different dynamic stresses. It can be seen that for a normal sand cushion without reinforcement, the increase in thickness H increases the ultimate bearing capacity with upper increase in acting dynamic stress. The bearing capacity is in good relation to H/D [34, 35]. It is noticed that for sand cushion without reinforcement, the variation of ratio H/D from 0.5 to 1.50 (Figure 8-a) has a substantial effect on increasing the ultimate bearing capacity, as it increased from 43 to about 98 kPa (i.e., an increase of about 227%) for an applied dynamic load of 25 ka.

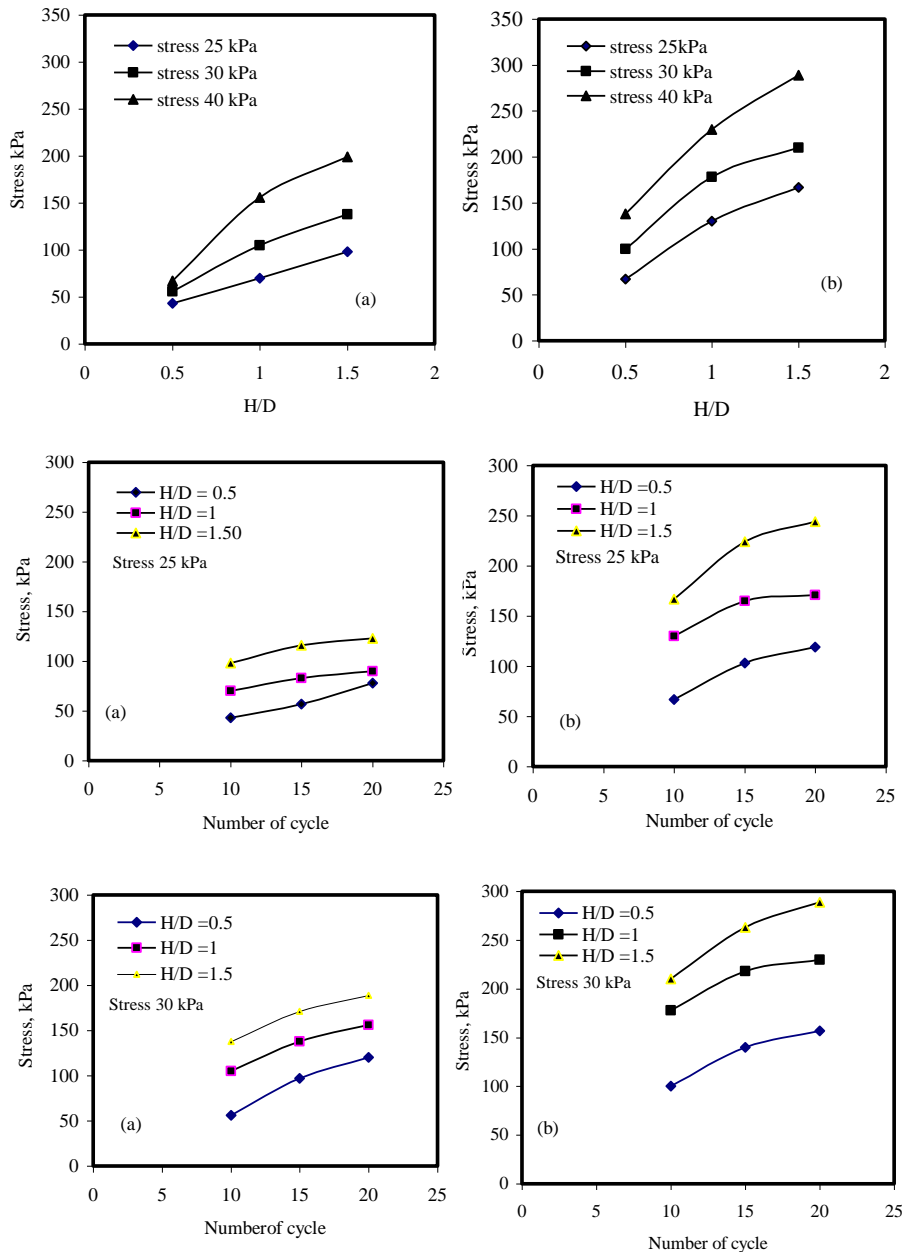


Figure 8. Variation of ultimate bearing capacity- for footing on sand cushion with different thickness at different dynamic stress, a: Sand cushion without reinforcement, b: Sand cushion with intermediate single layer of reinforcement

These values are found to be 246, 297% for applied stress of 30 and 40 kPa, respectively. It is clearly shown that the layer of sand cushion helps to increase the ultimate bearing capacity of the footing because the adopted cushion is stiffer and stronger than the natural clay. Moreover, as the sand cushion depth is increased, this means that the number of layers is also increased, therefore the gradual compaction efforts are increased, and as a result, the under-laying layer is increased. The compacted sand cushion with higher stress values can be considered a stiff subgrade coherent mass that provided a higher bearing capacity.

On the other hand, the effect of using a single layer of reinforcement in the form of geotextile within the sand cushion at mid-depth can also have a great effect with applied compaction efforts (Figure 8-b). It is also found that the combined effect of both the existence of reinforcement and dynamic load is achieved, and the degree of the improvement in the ultimate bearing capacity is attributed. It can be confirmed by the relevant Figure 8-a, which describes the effectiveness of such a reinforced layer compared with cases of normal sand cushion. It has been found that at the same lower value of $H/D = 0.5$, the ultimate bearing capacity of reinforced sand cushion is found to be greater than that of the normal case without reinforcement by as much as 1.55, 1.78, and 2.05 times for applied stress of 25, 30, and 40 kPa, respectively. While at $H/D = 1.50$, these ratios are reached at 1.70, 1.52, and 1.45 times the ultimate bearing capacity of the sand cushion without reinforcement in the same order of applied stress. It can be concluded that using a single layer of reinforcement can effectively increase the ultimate bearing capacity instead of increasing the cushion depth with effective applied stress, as confirmed by Figures 8-a and 8-b.

Moreover, the effect of the number of load cycles on the ultimate bearing capacity of sand cushion without/ with reinforcement is suited at different cushion depths and applied loads of 25 and 30, as shown in Figures 9-a to 9-d. In general, it can be seen that an increase in the number of load cycles can distinctly increase the ultimate bearing until reaching the optimum number of cycles. It is noticed that increasing the load cycle from 10 to 20 can effectively increase the ultimate bearing capacity with an obvious amount for normal and reinforced sand cushions under an applied load of 25 kPa.

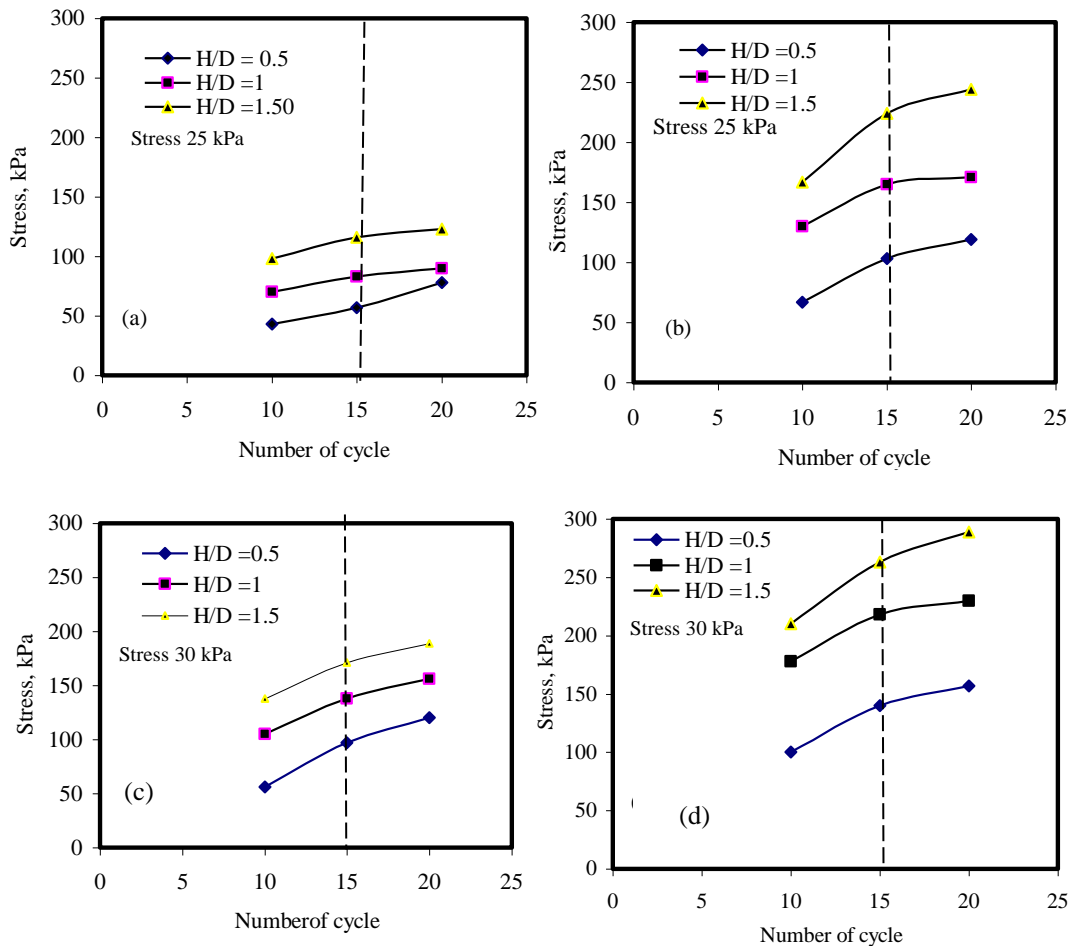


Figure 9. Variation of ultimate bearing capacity for footing on sand cushion with different thickness at different dynamic stress, a: Sand cushion without reinforcement with stress 25kPa, b: Sand cushion with intermediate single layer of reinforcement with stress 25kPa, c: Sand cushion without reinforcement with stress 25kPa, d: Sand cushion with intermediate single layer of reinforcement with stress 25kPa.

The increase in ultimate bearing capacity is found to be 1.46, 1.28, and 1.25 times the initial value at $N = 10$ for non-reinforced sand cushion (Figure 9-a) with a ratio of $H/D = 0.5, 1, \text{ and } 2$, respectively. While for the reinforced case their beneficial effect with increase of load cycle in the same trend (Figure 9-b), these values are extracted to be (1.77, 1.43, and 1.42) times of the initial values of $N = 10$ and correspond to the sand cushion depth ratio of ($H/D = 0.5, 1 \text{ and } 2$), respectively. Whereas, varying the load number of cycles from 10 to 20 for an applied stress of 30 kPa can also increase

the ultimate bearing capacity by as much as 2.14, 1.48, and 1.36 times the initial value of the unreinforced sand cushion in the case of $H/D = 0.5, 1, \text{ and } 2$, respectively. However, for that order, the degree of improvement in the ultimate bearing capacity in the reinforced case is estimated to be 1.57, 1.29, and 1.37 times the system at a load cycle of 10. It can be observed that a lesser variation is achieved when the load cycle is reached at 15. Over this range, the increase in the ultimate load capacity is nearly insignificant for all investigated cases. It may be said that the optimum number of cycles to be adopted is 15. Any additional increase does not have any noteworthy effect on the footing response, but a minor variation is obtained. The most effective parameter is the applied load for compaction effort and the thickness of the sand cushion.

5.4. Prediction Procedure to Assessment the Dynamic Response of Compaction

In general, an extensive cycle of rollers has two major impacts on the surrounding soil. Firstly, reduce the expected settlement by densifying the soil. Secondly, increase the bearing capacity of the bearing soil [30]. Consequently, the major aim of using a sand cushion or geotextile layer is to provide a stiff layer to relieve the increase in vertical stress over the weak layer. So, there is a need to predict the required thickness of sand cushion or use the geotextile layer to achieve the design requirement.

Based on the above-mentioned parametric study and previous studies, the steps for predicting the preliminary thickness of the sand cushion are as follows: (1) predict the vertical and ultimate bearing capacity of using a finite element using the available data from the soil profile; (2) use the available data to simulate the dynamic response of a roller with a number of cycles not less than 10 cycles and a frequency not less than 30 Hz and an applied stress of 25 kPa by calculating the final settlement and ultimate bearing capacity corresponding to different sand cushion thicknesses; (3) estimate the optimum thickness according to the design criteria of the project, such as a road, rail way, building, etc.

6. Conclusions

Based on the field data and numerical simulation for the field test and the parametric study, the following observations were made:

- The results showed that using a geotextile layer as a reinforcement layer reduced the final settlement and distributed the concentrated stress over a large area.
- The results showed that the composite compacted cushion with both a higher number of passes and stress has a great effect on relieving the stresses transmitted to the face of the peat layer with lesser deformation.
- The results showed that the increase in the number of load cycles has a significant effect on the ultimate bearing, where the cycle pass rate value is 10 to 20, with an average value of 15 cycles.

7. Declarations

7.1. Author Contributions

Conceptualization, A.B., W.A., and M.E.; methodology, A.B., W.A., and M.E.; formal analysis, A.B. and W.A.; investigation, X.X.; resources, A.B. and M.E.; writing—original draft preparation, A.B., W.A., and M.E.; writing—review and editing, A.B., W.A., and M.E. All authors have read and agreed to the published version of the manuscript.

7.2. Data Availability Statement

The data presented in this study are available on request from the corresponding author.

7.3. Funding

The authors received no financial support for the research, authorship, and/or publication of this article.

7.4. Conflicts of Interest

The authors declare no conflict of interest.

7.5. Competing Interests

The authors wish to confirm that there are no known conflicts of interest associated with this publication and there has been no significant financial support for this work that could have influenced its outcome.


8. References

- [1] Huat, B. B. K., Gue, S. S., & Haji Ali, F. (2004). *Tropical Residual Soils Engineering*. CRC Press, London, United Kingdom. doi:10.1201/9780203024621.
- [2] El Mouchi, A., Siddiqua, S., Wijewickreme, D., & Polinder, H. (2021). A Review to Develop new Correlations for Geotechnical Properties of Organic Soils. *Geotechnical and Geological Engineering*, 39(5), 3315–3336. doi:10.1007/s10706-021-01723-0.
- [3] Hobbs, N. B. (1986). Mire morphology and the properties and behaviour of some British and foreign peats. *Quarterly Journal of Engineering Geology*, 19(1), 7–80. doi:10.1144/gsl.qjeg.1986.019.01.02.
- [4] Edil, T. B., & Dhowian, A. (1981). At-rest lateral pressure of peat soils. *Journal of the Geotechnical Engineering Division, ASCE*, 107(GT2, Proc. Paper, 16063), 201–217. doi:10.1061/ajgeb6.0001097.
- [5] Edil, T. B. (2003). Recent advances in geotechnical characterization and construction over peats and organic soils. *Proceedings 2nd International Conference on Advances in Soft Soil Engineering and Technology*, 2-4 July, 2003, Putrajaya, Malaysia.
- [6] Hayashi, H., & Nishimoto, S. (2005). Strength characteristic of stabilized peat using different types of binders. *Proceedings of the International Conference of Deep Mixing Best Practices and Recent Advances, Deep Mixing*, 23-25 may, 2005, Stockholm, Sweden.
- [7] Åhnberg, H. (2006). *Strength of stabilised soil-a laboratory study on clays and organic soils stabilised with different types of binder*. PhD Thesis, Lund University, Lund, Sweden.
- [8] Black, J. A., Sivakumar, V., Madhav, M. R., & Hamill, G. A. (2007). Reinforced Stone Columns in Weak Deposits: Laboratory Model Study. *Journal of Geotechnical and Geoenvironmental Engineering*, 133(9), 1154–1161. doi:10.1061/(asce)1090-0241(2007)133:9(1154).
- [9] Chen, H., & Wang, Q. (2006). The behaviour of organic matter in the process of soft soil stabilization using cement. *Bulletin of Engineering Geology and the Environment*, 65(4), 445–448. doi:10.1007/s10064-005-0030-1.
- [10] Islam, S., & Hashim, R. (2008). Stabilization of peat by deep mixing method: a critical review of the state of practices. *Electronic Journal of Geotechnical Engineering*, 13.
- [11] Duraisamy, Y., Huat, B. B. K., & Muniandy, R. (2009). Compressibility behavior of fibrous peat reinforced with cement columns. *Geotechnical and Geological Engineering*, 27(5), 619–629. doi:10.1007/s10706-009-9262-3.
- [12] Heneash, U., Fawzy, H. E. D., Ali, K., & Basha, A. (2023). Utilization of Ionic Organic Polymer to Improve Performance and Properties of Problematic Soils. *Civil Engineering Journal (Iran)*, 9(12), 3019–3037. doi:10.28991/CEJ-2023-09-12-05.
- [13] Šiukščiū, A., Vorobjovas, V., & Vaitkus, A. (2018). Geogrid reinforced road subgrade influence on the pavement evenness. *IOP Conference Series: Materials Science and Engineering*, 356, 012020. doi:10.1088/1757-899x/356/1/012020.
- [14] Jarrett, P. M. (1986). Load tests on geogrid reinforced gravel fills constructed on peat subgrades. *3rd International Conference on Geotextiles*, 7-11 April, 1986, Vienna, Austria.
- [15] Mooney, M. A. (2010). *Intelligent soil compaction*. Transportation Research Board, Washington, United States.
- [16] Fathi, A., Tirado, C., Rocha, S., Mazari, M., & Nazarian, S. (2021). Assessing depth of influence of intelligent compaction rollers by integrating laboratory testing and field measurements. *Transportation Geotechnics*, 28, 100509. doi:10.1016/j.trgeo.2020.100509.
- [17] Adams, M. T., & Collin, J. G. (1997). Large Model Spread Footing Load Tests on Geosynthetic Reinforced Soil Foundations. *Journal of Geotechnical and Geoenvironmental Engineering*, 123(1), 66–72. doi:10.1061/(asce)1090-0241(1997)123:1(66).
- [18] Basha, A., Khalifa, F., & Fayed, S. (2023). Experimental Study on Effect of Recycled Reinforced Concrete Waste on Mechanical Properties and Structural behaviour of the Sandy Soil. *International Journal of Concrete Structures and Materials*, 17(1), 52. doi:10.1186/s40069-023-00612-5.
- [19] Duraisamy, Y. (2008). *Compressibility behavior of tropical peat reinforced with cement column*. PhD Thesis, Universiti Putra Malaysia, Serdang, Malaysia.
- [20] ASTM D1195/D1195M-21. (2021). *Standard Test Method for Repetitive Static Plate Tests of Soils and Flexible Pavement Components for Use in Evaluation and Design of Airport and Highway Pavements*. ASTM International, Pennsylvania, United States. doi:10.1520/D1195_D1195M-21.
- [21] ASTM D1194. (2012). *Test Method for Bearing Capacity of Soil for Static Load and Spread Footing (Withdrawn 2003)*. ASTM International, Pennsylvania, United States.
- [22] *Annual Book of ASTM Standards*. (1989). *Soil and Rock; Building Stones: Geotextiles/Vol 04.08/Pcn01040889-38*. ASTM International, Pennsylvania, United States.

- [23] Chen, Q., & Abu-Farsakh, M. (2011). Numerical Analysis to Study the Scale Effect of Shallow Foundation on Reinforced Soils. *Geo-Frontiers*, 595–604. doi:10.1061/41165(397)62.
- [24] Nasr, A. M. A., & Azzam, W. R. (2017). Behaviour of eccentrically loaded strip footings resting on sand. *International Journal of Physical Modelling in Geotechnics*, 17(3), 177–194. doi:10.1680/jphmg.16.00008.
- [25] Azzam, W. R., & Nasr, A. M. (2015). Bearing capacity of shell strip footing on reinforced sand. *Journal of Advanced Research*, 6(5), 727–737. doi:10.1016/j.jare.2014.04.003.
- [26] Lee, A. (2002). *Finite element analysis in geotechnical engineering. Theory and Application*, Thomas Telford, London, United Kingdom.
- [27] Bathelt, U. (1956). *The working behavior of the vibrating compactor on plastic-elastic ground: With 47 images*. Ph.D. Thesis, Ernst & Sohn, Germany. (In German).
- [28] Moshin, S. H. (1967). *Investigations of the dynamic behavior of ramming systems*. *Baumaschine und Bautechnik*, 14(1), 11-17. (In German).
- [29] Yoo, T.-S., & Selig, E. T. (1979). Dynamics of Vibratory-Roller Compaction. *Journal of the Geotechnical Engineering Division*, 105(10), 1211–1231. doi:10.1061/ajgeb6.0000867.
- [30] Azzam, W. R. (2015). Utilization of the confined cell for improving the machine foundation behavior-numerical study. *Journal of GeoEngineering*, 10(1), 17–23. doi:10.6310/jog.2015.10(1).3.
- [31] Roudgari, R. (2012). *Compaction of Soil by Repeated Loading*. PhD Thesis, Concordia University, Montreal, Canada.
- [32] Paulmichl, I., Furtmüller, T., Adam, C., & Adam, D. (2020). Numerical simulation of the compaction effect and the dynamic response of an oscillation roller based on a hypoplastic soil model. *Soil Dynamics and Earthquake Engineering*, 132, 106057. doi:10.1016/j.soildyn.2020.106057.
- [33] Ochiai, H., Watari, Y., & Tsukamoto, Y. (1996). Soil reinforcement practice for fills over soft ground in Japan. *Geosynthetics International*, 3(1), 31–48. doi:10.1680/gein.3.0052.
- [34] Madhav, M. R., & Vitkar, P. P. (1978). Strip Footing on Weak Clay Stabilized with a Granular Trench or Pile. *Canadian Geotechnical Journal*, 15(4), 605–609. doi:10.1139/t78-066.
- [35] Das, B. M., & Puri, V. K. (1989). Bearing capacity of shallow foundations on granular trench in weak clay. *Numerical Models in Geomechanics. NUMOG III*, 5(5), 289–296. doi:10.1016/0148-9062(91)92547-c.



Applying Harmony Degree Equation and TOPSIS Combined with Entropy Weights in Surface Water Classification

Kieu Diem Le¹, Giao Thanh Nguyen^{2*} 

¹ Department of Environmental Sciences, Faculty of Natural Resources and Environment, Dong Thap University, Dong Thap 81000, Vietnam.

² College of Environment and Natural Resources, Can Tho University, Can Tho 900000, Vietnam.

Received 08 January 2024; Revised 10 March 2024; Accepted 14 March 2024; Published 01 April 2024

Abstract

This study classified surface water quality in Can Tho city using the Eutrophication index, Harmony Degree Equation (HDE), and Technique of Order Preference by Similarity to Ideal Solution (TOPSIS). Water quality data were collected in two seasons at 38 locations with 18 parameters, including temperature, pH, dissolved oxygen (DO), biochemical oxygen demand (BOD), chemical oxygen demand (COD), total suspended solids (TSS), nitrite (N-NO₂⁻), nitrate (N-NO₃⁻), ammonium (N-NH₄⁺), orthophosphate (P-PO₄³⁻), Fe, F, Pb, As, Hg, coliform, chlorine-, and phosphorus-based pesticides. Water quality parameters are compared with national technical regulations on surface water quality (QCVN 08-MT:2015/BTNMT). The HDE method based on entropy weight has been applied to evaluate the comprehensive harmony degree of water quality for various purposes. In addition, the TOPSIS was also used to rank water quality at each location and determine the priority level that required mitigation and treatment solutions. Surface water quality in the study area had low dissolved oxygen content and was contaminated with TSS and coliform in both seasons. Water quality in the rainy season tends to decrease compared to the dry season. Based on HDE results, water quality in the study area in the dry season was assessed as suitable for domestic activities (needs treatment), irrigation, and navigation (HD_{II} = 0.922), while the rainy season was suitable for irrigation and navigation (HD_{III} = 1.00). Moreover, surface water in the study area was in a state of potential eutrophication (EI > 0), in which eutrophication was higher during the dry season. The SW25 and SW28 were the most seriously eutrophic in the dry and rainy seasons, respectively. TOPSIS analysis indicated that SW22 and SW28 need treatment measures in both seasons; furthermore, SW2-SW4 (dry season) and SW23 (rainy season) also need appropriate management and impact mitigation solutions. SW4 was affected by the most significant seasonal impacts, which have high priority in the dry season and are lowest in the rainy season. Therefore, future studies are needed to identify specific sources of variation at these locations to reduce impacts. The study results provide helpful information for the decision-making process and water quality management.

Keywords: Can Tho City; Eutrophication; Harmony Degree Equation; TOPSIS; Water Quality Assessment.

1. Introduction

Rapid socio-economic development seriously affects domestic activities [1, 2] and the ecological environment in many countries worldwide [3]; this can be explained by the combination of impact factors such as land use/land cover changes and waste discharge [4]. According to the previous study by Wehrheim et al. [5], surface water quality in the Mekong Delta is mainly affected by agricultural and aquaculture activities. Therefore, natural ecosystems have been transformed in a more complex manner [4]. For instance, the excessive accumulation of organic matter has changed the nutritional structure, reduced oxygen content, and caused the death of aquatic animals in water bodies [6]. Furthermore, variations in natural processes also affect water quality, typically seasonal changes in rainfall and surface runoff [7].

* Corresponding author: ntgiao@ctu.edu.vn

 <http://dx.doi.org/10.28991/CEJ-2024-010-04-012>



© 2024 by the authors. Licensee C.E.J, Tehran, Iran. This article is an open access article distributed under the terms and conditions of the Creative Commons Attribution (CC-BY) license (<http://creativecommons.org/licenses/by/4.0/>).

Therefore, pollution problems could seriously affect the purpose of various activities and sustainable socio-economic development [8, 9]. Hence, quality monitoring and assessment are critical to forecasting pollution problems accurately, thereby proposing appropriate mitigation and management solutions [4]. However, due to these complex variations in effects, using a single method may not be appropriate and may lead to many discrepancies in results and management [10]. Therefore, multidimensional analysis methods and computing techniques have been focused on development and research [11].

Water quality parameters (i.e., pH, DO, BOD, COD, N-NH_4^+ , N-NO_2^- , N-NO_3^- , and coliform) can be calculated as a Water Quality Index (WQI) [12] or nutrient parameters converted to Eutrophication Index (EI) to describe the level of nutrient pollution [13, 14]. Furthermore, many mathematical methods have been applied to evaluate water quality and propose management solutions, such as the water quality index (entropy-weighted water quality index (EWQI), integrated water quality index (IWQI), modified water quality index (MWQI) [15, 16], Set Pair Analysis (SPA) [17, 18], Technique of Order Preference by Similarity to Ideal Solution (TOPSIS) [19, 20], and other multivariate statistical analysis methods (Principal Component Analysis (PCA), Cluster Analysis (CA), Factor Analysis (FA), Discriminant Analysis (DA) [4, 8, 15, 21-23]. Among them, TOPSIS is commonly used in assessing water quality and identifying alternative solutions [19, 24-27]. In addition, the harmonic degree equation (HDE) is also used in water quality assessment studies [4, 28-30]. The approach based on harmony theory and the TOPSIS model has been applied in many previous studies, such as allocating water resources [31], determining the level of harmony between water quality and people [4, 30, 32], and evaluating and ranking water quality [19, 25, 33, 34]. Therefore, applying diverse assessment methods/techniques can overcome the limitations of a single assessment.

Can Tho is one of the central municipal cities of southern Vietnam. The process of industrialization and urbanization in Can Tho city is developing rapidly and strongly; this has contributed to increasing pressure on the natural environment [35]. Currently, the city is facing serious problems such as climate change (flooding and saltwater intrusion) and water pollution from wastewater and waste from industrial and agricultural production activities [36, 37]. Several previous studies have discovered very high COD, BOD, coliform, TN, and N-NH_4^+ pollutants in water bodies in Can Tho City, which are likely to increase in the future. This has reduced surface water quality and harmed aquatic life in water bodies in Can Tho City [36-38]. In addition, several studies have also applied multivariate statistical techniques to evaluate and identify pollution sources in the study area [22, 37]. Nevertheless, none of these studies has simultaneously applied calculation methods based on Vietnamese standards and the weights of each parameter to propose the use purpose and treatment priority order for each monitoring location. Hence, the study aims to evaluate surface water quality, the status of eutrophication, and the suitability of water bodies for purposeful use by HDE and rank prioritized locations that need treatment solutions using TOPSIS. The results provide crucial scientific information on water quality management in Can Tho City.

2. Material and Methods

2.1. Description of the Study Area

Can Tho city has a total area of 140,894.9 hectares, accounting for 3.5% of the total area of the Mekong Delta region. The city has flat terrain, high in the north and gradually lower in the southwest. The north of Can Tho city borders An Giang province, the south borders Hau Giang province, the west borders Kien Giang province, and the east borders Vinh Long and Dong Thap provinces [39]. Can Tho is located in the tropical monsoon climate zone, with two distinct seasons: the rainy season (from May to November) and the dry season (from December to April of the following year). The hydrological regime is influenced by the Mekong River flowing through the Hau River, the East Sea tidal regime, and intra-regional rainfall. The density of rivers and canals in Can Tho city is quite large, about 1.8 km/km^2 , in which the area along the Hau River in Ninh Kieu, O Mon, Cai Rang, and Thot Not districts is up to more than 2 km/km^2 . A total of 158 large and small rivers and canals are tributaries of two large rivers (i.e., the Hau River and the Can Tho River). The dense system of rivers/canals provides an essential source of fresh water, serves as irrigation in the dry season, and is significant in transportation in Can Tho. Currently, Can Tho city has only one centralized wastewater treatment plant, which collects and treats wastewater for nine wards in Ninh Kieu district. In addition, there is still a situation where the treatment system is overloaded and the treatment efficiency has not reached 100%. Surface water sources are affected by pollutants from domestic, aquaculture, agricultural, and industrial activities and solid waste generated in the city [37, 39]. Hence, surface water environmental monitoring is carried out regularly, and the sampling locations are shown in Figure 1.

2.2. Data Collection

The water quality monitoring data was collected from the Department of Natural Resources and Environment of Can Tho City [40]. Surface water samples were collected at 38 locations on 25 main rivers and canals in districts of Can Tho city and were signed from SW1 to SW38 (Figure 1). The sampling frequency is two times per year in March and September for physicochemical parameters and one time per year in May for two pesticide residue parameters. There were a total of 18 parameters to assess water quality in the study area, namely temperature, pH, dissolved oxygen (DO), biochemical oxygen demand (BOD), chemical oxygen demand (COD), total suspended solids (TSS), nitrite (N-NO_2^-),

nitrate (N-NO₃⁻), ammonium (N-NH₄⁺), orthophosphate (P-PO₄³⁻), Fe, F, Pb, As, Hg, coliform, chlorine-based, and phosphorus-based pesticides. Surface water samples were collected and preserved according to national standards (TCVN 6663-1:2011, TCVN 6663-3:2008, TCVN 5994:1995, TCVN 6663-6:2008). pH, temperature, and DO were measured on-site, while the remaining parameters were analyzed in the laboratory using standard methods [41]. The descriptors of analysis methods and allowable limits in the National Technical Regulation (QCVN 08-MT:2015/BTNMT) [42] are presented in Table 1.

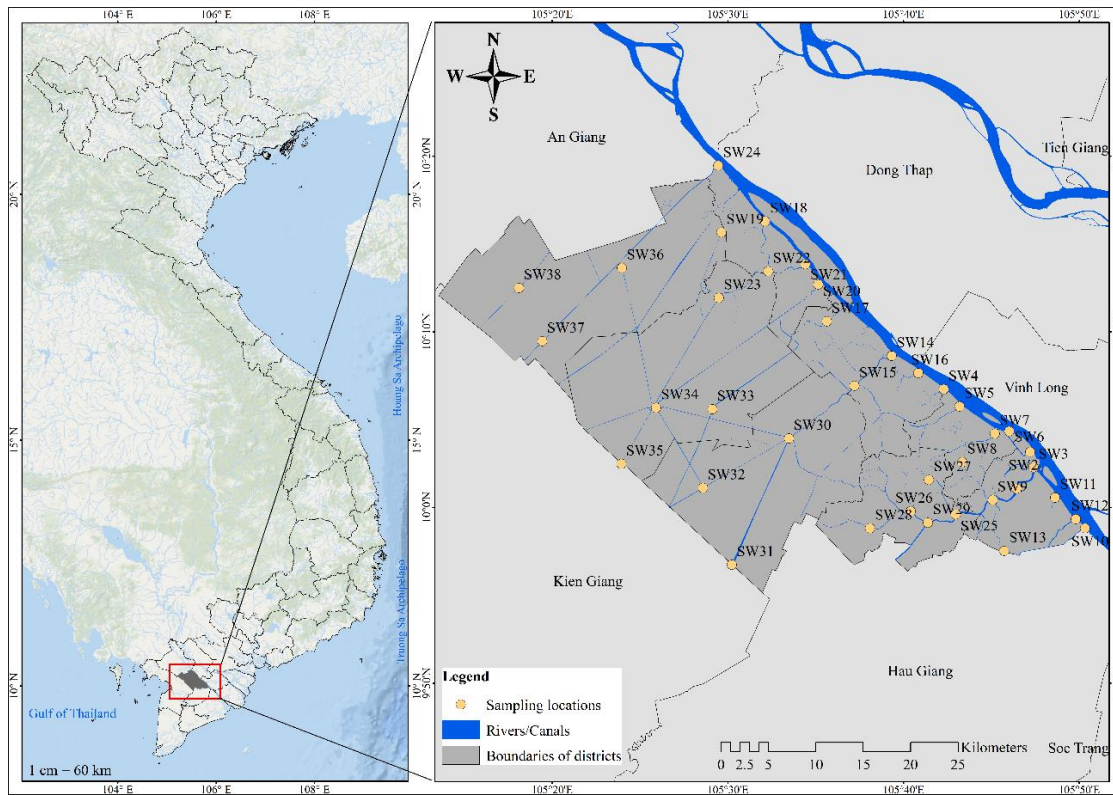


Figure 1. Sampling locations in the study area

Table 1. Surface water quality parameters and analytical methods

Parameters	Unit	Analytical methods	QCVN 08-MT:2015/BTNMT			
			Column A1 (I)	Column A2 (II)	Column B1 (III)	Column B2 (IV)
Temperature	°C	SMEWW 2550B:2012	-	-	-	-
pH	-	TCVN 6492:2011	6-8.5	6-8.5	5.5-9	5.5-9
Dissolved oxygen (DO)	mg/L	TCVN 7325:2004	≥ 6	≥ 5	≥ 4	≥ 2
Biological Oxygen Demand (BOD)	mg/L	TCVN 6001-1:2008	4	6	15	25
Chemical Oxygen Demand (COD)	mg/L	TCVN 6491:1999	10	15	30	50
Total Suspended solids (TSS)	mg/L	TCVN 6625:2000	20	30	50	100
Ammonium (N-NH ₄ ⁺)	mg/L	TCVN 6179:1996	0.3	0.3	0.9	0.9
Nitrite (N-NO ₂ ⁻)	mg/L	SMEWW 4500-NO ₂ ⁻ .B:2012	0.05	0.05	0.05	0.05
Nitrate (N-NO ₃ ⁻)	mg/L	TCVN 6180:1996	2	5	10	15
Phosphate (P-PO ₄ ³⁻)	mg/L	SMEWW 4500-P.E:2012	0.1	0.2	0.3	0.5
Total iron (Fe _t)	mg/L	TCVN 6177:1996	0.5	1	1.5	2
Fluoride (F ⁻)	mg/L	SMEWW 4500-F .B&D:2012	1	1.5	1.5	2
Lead (Pb)	mg/L	SMEWW 3113B:2017	0.02	0.02	0.05	0.05
Arsenic (As)	mg/L	TCVN 6626:2000	0.01	0.02	0.05	0.1
Mercury (Hg)	mg/L	TCVN 7877:2008	0.001	0.001	0.001	0.002
Organochlorine pesticides	µg/L	GC/MS (SCION QC/SCION 456)	-	-	-	-
Organic phosphate pesticides	µg/L	GC/MS (SCION QC/SCION 456)	-	-	-	-
Coliform	MPN/100 mL	TCVN 6187-2:1996	2500	5000	7500	10,000

Note: "-" is not available in the National Technical Regulation.

2.3. Data Processing

2.3.1. Evaluate Water Quality Characteristics

Surface water quality data were calculated on average and compared with National Technical Regulation QCVN 08-MT:2015/BTNMT on surface water quality [42]. Moreover, the Independent Sample T-Test method at the 5% significance level was used to compare the difference in surface water quality between the rainy and dry seasons. This analysis was processed using IBM SPSS 22 statistical software for Windows (IBM Corp., Armonk, NY, USA).

2.3.2. Calculate the Harmony Degree of Water Quality for Various Uses

In this study, the harmony degree equation (HDE) was applied to determine the harmony of water quality in the dry and rainy seasons for water use purposes specified in QCVN 08-MT:2015/BTNMT [42]. The harmony degree of each parameter with water quality levels is calculated based on Equation 1 [11].

$$HD = a_i - b_j \tag{1}$$

in which, HD is the harmony degree, a is the unity degree, b is the difference degree, and i and j are the harmony coefficient and disharmony coefficient, respectively.

(1) Establishment of limit values for each parameter according to different levels:

The limit values will be classified into levels s. Specifically, the limit values are graded according to QCVN 08-MT:2015/BTNMT (Table 1) [42], with four levels specified in descending order (s = I, II, III and IV).

(2) Establish a water quality level matrix for each parameter:

From the analytical data set, the study has input data with a set of parameters P (k = p₁, p₂, p₃, p₄,...p_n), in which n is the number of parameters. The value of the parameter belongs to one of the evaluation levels in Table 1. Particularly, if the value p_n corresponds to a level s, it would be encoded as 1 at this level. Simultaneously, the smaller s levels were also coded 1. On the contrary, if the value of p_n did not correspond to one of the s levels, it would be coded 0. The level matrix table of each parameter is shown as the matrix X.

$$X = \begin{bmatrix} X_{(p_1,I)} & X_{(p_1,II)} & X_{(p_1,III)} & X_{(p_1,IV)} \\ X_{(p_2,I)} & X_{(p_2,II)} & X_{(p_2,III)} & X_{(p_2,IV)} \\ X_{(p_3,I)} & X_{(p_3,II)} & X_{(p_3,III)} & X_{(p_3,IV)} \\ \dots & \dots & \dots & \dots \\ X_{(p_n,I)} & X_{(p_n,II)} & X_{(p_n,III)} & X_{(p_n,IV)} \end{bmatrix} \tag{2}$$

(3) Calculate the parameter weight using the Entropy method:

- Set up the normalized matrix of each parameter:

$$A_{pq} = \begin{bmatrix} A_{11} & A_{12} & A_{13} & \dots & A_{1n} \\ A_{21} & A_{22} & A_{23} & \dots & A_{2n} \\ A_{31} & A_{32} & A_{33} & \dots & A_{3n} \\ \dots & \dots & \dots & \dots & \dots \\ A_{t1} & A_{t2} & A_{t3} & \dots & A_{tn} \end{bmatrix} \tag{3}$$

After that, normalize the matrix A_{pq} by using Equation 4:

$$B_{pq} = \frac{C_{pq} - C_{pq \min}}{C_{pq \max} - C_{pq \min}} \tag{4}$$

where p is the water quality parameter, q is monitoring locations (q = 1, 2, 3,...t). C_{pq} is the concentration of parameter p at the monitoring location q.

- Calculate the information coefficient (H_p) by Equation 5:

$$H_p = -\frac{1}{\ln t} \sum_{q=1}^t \left(\frac{B_{pq}}{\sum_{q=1}^t B_{pq}} \ln \left(\frac{B_{pq}}{\sum_{q=1}^t B_{pq}} \right) \right) \tag{5}$$

In this case, if the A_{pq} = 0 or 1, the information coefficient is calculated according to Equation 6:

$$H_p = -\frac{1}{\ln t} \sum_{q=1}^t \left(\frac{1+B_{pq}}{\sum_{q=1}^t (1+B_{pq})} \ln \left(\frac{1+B_{pq}}{\sum_{q=1}^t (1+B_{pq})} \right) \right) \tag{6}$$

- Calculate the Entropy weight for each parameter:

$$\omega_p = \frac{1 - H_p}{n - \sum_{p=1}^n H_p} \tag{7}$$

(4) Calculate the harmony degree of different water quality levels

The harmony degree of each parameter is calculated using Equation (1). In which, the values i and j are selected depending on the specific characteristics of the region and other matrix iterations of $HD_{(pn, s)}$. According to Zou et al. [28], it could be set $i = 1$ and $j = 0$, so the unit degrees of $HD_{(pn, s)}$ is equal to the value in matrix X . The comprehensive degree of harmony is calculated using Equation 8.

$$HD_s = \sum_{p=1}^n \omega_{p_n} \times HD(p_n, s) \quad (8)$$

In which, HD_s is the comprehensive harmony degree of sampling location with level s and $HD_s \in [0, 1]$ and $HD_{(pn, s)}$ is the harmony degree of parameter p_n with level s .

(5) Determine the appropriate water quality level and purpose based on the harmony degree

Based on comprehensive harmonization degrees, water quality levels were determined according to Equation 9.

$$0 \leq HD(I) \leq HD(II) \leq HD(III) \leq HD(IV) \leq 1 \quad (9)$$

According to Zou et al. [28], the expected minimum harmony target (HD_0) value could be set as a criterion to evaluate water quality level. The larger the HD_0 value, the higher the water quality criterion. Normally, $HD_0 = 0.8$ will have a higher recognition ability for different levels, high reliability, and be more consistent with reality status [28]. In this study, HD_0 was set up at two levels ($HD_0 = 1$ and $HD_0 = 0.8$). This means that when $HD_0 = 1$, water quality is ranked at the lowest level. Similarly, when $HD_0 = 0.8$, it allows 20% of the parameters to be worse than the level s .

2.3.3. Calculate the Eutrophication Index

The eutrophication index (EI) was used to determine the eutrophication of water bodies based on three parameters (COD, DIN and DIP). The eutrophication index was calculated according to Equation 10 [43].

$$EI = \frac{COD \times DIP \times DIN}{4500} \times 10^6 \quad (10)$$

In which, COD is the concentration of COD; DIN is the total concentration of $N-NO_2^-$, $N-NO_3^-$, $N-NH_4^+$; DIP is the concentration of $P-PO_4^{3-}$. EI is classified into two types, including $EI < 0$ (not eutrophic) and $EI > 0$ (water is in a eutrophic state) [13, 43]. The eutrophication index (EI) results were presented visually in map form using QGIS 3.16 software (Open-Source Geospatial Foundation - OSGeo, Chicago, IL, USA).

2.3.4. Evaluate Treatment Priority using the Technique of Order Preference by Similarity to Ideal Solution (TOPSIS)

The technique of Order Preference by Similarity to Ideal Solution (TOPSIS) was used to rank water quality and water treatment priorities of monitoring locations [20, 44]. The steps in the method are performed and calculated from Equations 11 to 15.

(1) Setting up the initial matrix was done similarly to calculating the weights. Matrix normalization is then performed by Equation 11.

$$r_{pq} = \begin{cases} \frac{c_{pq}}{[\sum_{q=1}^t c_{qp}^2]^{\frac{1}{2}}} \\ \frac{-c_{pq}}{[\sum_{q=1}^t c_{pq}^2]^{\frac{1}{2}}} \end{cases} \quad (11)$$

(2) Determine the weighted normalized value using formula 12

$$f_{pq} = r_{pq} \times \omega_p \quad (12)$$

where f_{pq} is the weighted normalized value of parameter p at monitoring site q and ω_p is the weight of each parameter.

(3) Determine positive and negative ideal reference points, with positive and negative ideal reference points that can be determined using formula 13.

$$\begin{cases} f^+ = \max(f_{1p}, f_{2p}, f_{3p}, \dots) \\ f^- = \min(f_{1p}, f_{2p}, f_{3p}, \dots) \end{cases} \quad (13)$$

From the calculation results of Equation 13, the set of positive and negative ideal reference values of each parameter are recorded and shown at C and D, respectively.

$$C = \{f_1^+, f_2^+, \dots, f_n^+\} \quad (14)$$

$$D = \{f_1^-, f_2^-, \dots, f_n^-\} \quad (15)$$

(4) Calculate the distance to the positive and negative ideal reference points; they are calculated using Equation 16.

$$\begin{cases} d_q^+ = \sqrt{\sum_{p=1}^n [f_{pq} - (f_p)_C]^2} \\ d_q^- = \sqrt{\sum_{p=1}^n [f_{pq} - (f_p)_D]^2} \end{cases} \quad (16)$$

In which, $(f_{pq})_C$ and $(f_{pq})_D$ are the weighted standardized values in the positive and negative ideal reference points, respectively; d_q^+ and d_q^- are the distances to the positive and negative ideal reference points at the monitoring sites q , respectively.

(5) Calculation of the closeness coefficient (CC) of each site according to Equation 17.

$$CC = \frac{d_q^-}{d_q^+ + d_q^-}, \text{ with } CC \in [0, 1] \quad (17)$$

In this method, the closeness coefficient close to the positive ideal reference point is sorted in descending order to determine priority [24]. A more considerable CC value indicates better water quality. In contrast, the lower the CC value, the higher the treatment priority rank of the location [26].

A summary of the research methods is presented in Figure 2.

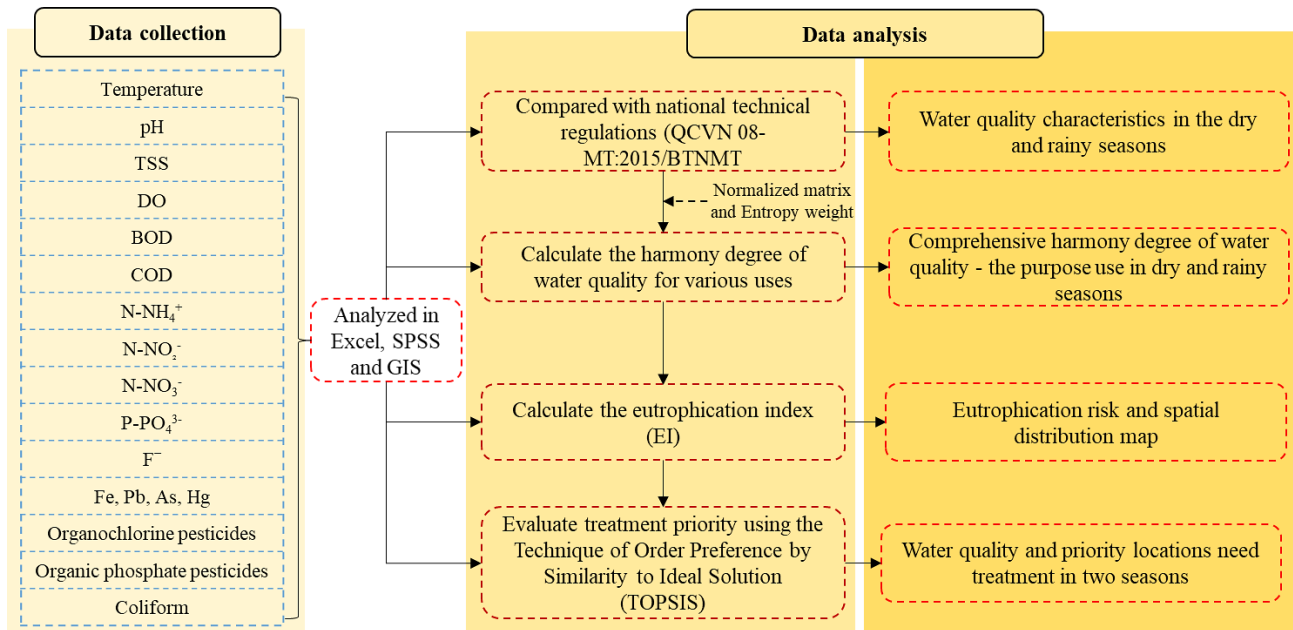


Figure 2. The summary flowchart of research methods

3. Results and Discussion

3.1. Overall Surface Water Quality in the Study Area

The results of the water quality analysis are presented in Table 2. The concentrations of As, Hg, chlorine-, and phosphorus-based pesticides in the dry and rainy seasons were all below the detection limits (Detection limits of As = 0.001 mg/L, Hg = 0.0003 mg/L, organochlorine pesticides = 0.0001 µg/L, and organophosphorus = 0.01 µg/L). Table 2 shows that the average water temperature and pH had no statistically significant differences at the 5% level between the dry and rainy seasons ($p > 0.05$). In particular, the average temperature and pH in the dry and rainy seasons varied from 29.47 ± 1.80 - 29.62 ± 1.84 °C and 7.19 ± 0.10 - 7.21 ± 0.08 , respectively. Generally, the pH range was insignificant and is within the allowable limit of QCVN 08-MT:2015/BTNMT, column A1 (6.0–8.5) [42].

The TSS values showed a statistically significant difference between the two seasons ($p < 0.05$). TSS concentrations in the dry season were 20.11 ± 2.76 mg/L and increased to 30.16 ± 5.52 mg/L in the rainy season. TSS exceeded the allowable limit of QCVN 08-MT:2015/BTNMT column A1 (20 mg/L) by 1.50 times [42]. Some previous studies indicated that TSS values in rivers in the Mekong Delta were relatively high and partly influenced by wastewater and waste from agricultural, industrial, and domestic activities [45, 46].

Table 2. Seasonal variations of surface water quality in the study area

Parameters	Unit	Dry season	Rainy season	Sig.
Temperature	°C	29.47±1.8	29.62±1.84	0.612
pH	-	7.19±0.1	7.21±0.08	0.241
DO	mg/L	4.24±0.39	4.24±0.22	0.986
BOD	mg/L	3.67±0.94	3.8±0.65	0.319
COD	mg/L	9.77±1.72	9.48±1.76	0.321
TSS	mg/L	20.11±2.76	30.16±5.52	0.000
N-NH ₄ ⁺	mg/L	0.11±0.06	0.06±0.05	0.000
N-NO ₂ ⁻	mg/L	0.02±0	0.02±0.01	0.284
N-NO ₃ ⁻	mg/L	0.15±0.09	0.23±0.13	0.000
P-PO ₄ ³⁻	mg/L	0.08±0.03	0.03±0.03	0.000
Fe _i	mg/L	0.01±0.03	BDL	0.000
F ⁻	mg/L	0.01±0.0	BDL	0.033
Pb	mg/L	BDL	0.0006±0.0	0.000
As	mg/L	BDL	BDL	-
Hg	mg/L	BDL	BDL	-
Organochloride pesticides	µg/L	BDL	-	-
Organophosphate pesticides	µg/L	BDL	-	-
Coliform	MPN/100 mL	2674±0	3094±0	0.514

Note: BDL: Below Detection Limit.

The average DO concentration was relatively low, while the BOD and COD concentrations were relatively high in the study area. All the content of the parameter, which indicated organic matter pollution, was below the allowable threshold compared to QCVN 08-MT:2015/BTNMT column A1 (DO \geq 6 mg/L, BOD \leq 4 mg/L, and COD \leq 10 mg/L) [42]. There was no statistically significant difference in DO, BOD, and COD content between the dry and rainy seasons ($p > 0.05$). This shows that water quality in the study area has improved compared to the previous report by Giao et al. [22], which documented organic pollution in water bodies. DO concentrations in the dry season (4.24±0.39 mg/L) were nearly similar to the rainy season (4.24±0.22 mg/L). The BOD in the dry season (3.67±0.94 mg/L) was lower than in the rainy season (3.8±0.65 mg/L), whereas the reverse was true for the COD (9.77±1.72 mg/L - in the dry season and 9.48±1.76 mg/L - in the rainy season). BOD and COD contents are affected and change significantly by seasons [47]. The variation of BOD and COD depends on human activities [48], the change in temperature, biological activity, and respiration of organisms, leading to an increased or decreased decomposition rate of organic matter in water bodies [49]. The concentrations of nutrients were significantly different between the dry and rainy seasons ($p < 0.05$), except for N-NO₂⁻. In addition, the content of N-NH₄⁺ and PO₄³⁻ in the dry season tended to be higher than in the rainy season; in contrast, N-NO₂⁻ and N-NO₃⁻ have tended to be higher in the rainy season. The concentrations of N-NH₄⁺, N-NO₂⁻, N-NO₃⁻ and P-PO₄³⁻ ranged from 0.06±0.05-0.11±0.06 mg/L, 0.02±0-0.02±0.05 mg/L, 0.15±0.09-0.23±0.13 mg/L, and 0.03±0.03-0.08±0.03 mg/L, respectively (Table 2). The concentration of nutrients was generally low compared to QCVN 08-MT:2015/BTNMT column A1 [42]. There were also low levels of nutrients found in the Mekong Delta water bodies in several previous studies [46, 50, 51].

Heavy metals (Fe, Pb) and F⁻ in water dramatically fluctuated between the dry and rainy seasons. Fe and F⁻ concentrations were only recorded in the dry season, with the values 0.01±0.03 mg/L and 0.001±0.0 mg/L, respectively. This was compatible with the previous study by Tam et al. [48], which reported that the Fe concentration in surface water in Can Tho city is usually low and focuses the highest content on agricultural production rather than industrial and residential areas. High Fe concentrations could strongly impact the growth and development of aquatic ecosystems [52]. On the other hand, F⁻ is also a vital substance that can be beneficial or harmful to organisms, depending on its concentration in water. F⁻ often originates in nature or is artificially produced by human and industrial activities [53]. Meanwhile, the concentration of Pb has a value of 0.0006±0.0 mg/L in the rainy season. Fe, Pb, and F⁻ were below the allowable thresholds of QCVN 08-MT:2015/BTNMT column A1 (Fe \leq 0.5 mg/L, F⁻ \leq 1 mg/L, and Pb \leq 0.02 mg/L). There were statistically significant differences between the dry and rainy seasons ($p < 0.05$). According to the former study of Pham et al. (2022) [54], they indicated that human activities can be the primary source of heavy metals in surface water.

The average coliform density was not significantly different between the dry and rainy seasons ($p > 0.05$). The coliform value was found in the dry season at 2674 ± 0 MPN/100mL and 3094 ± 0 MPN/100mL in the rainy season. Coliform density exceeded the allowable limit of QCVN 08-MT:2015/BTNMT column A1 (2500 MPN/100mL) by 1.06-1.23 times [42]. The coliform often originates from human or animal waste, and coliform concentrations in Mekong Delta water bodies are always relatively high [55, 56]. Generally, TSS and coliform exceeded the allowable thresholds of QCVN 08-MT:2015/BTNMT, column A1. Surface water quality in the study area was seasonally fluctuated. In particular, DO, COD, $N-NH_4^+$, $N-P-PO_4^{3-}$, Fe_t and F^- in the dry season were higher than in the rainy season. In contrast, TSS, BOD, $N-NO_2^-$, $N-NO_3^-$ and coliform in the rainy season were higher than in the dry season.

3.2. Harmony Degree of Water Quality with Various Purpose

The matrix of the harmony degree of each parameter and entropy weights is shown in Table 3. The input data of the method includes only 11 parameters, which have been removed from parameters below the detection limits and are not specific to national regulations. The weight of coliform, $N-NO_2^-$, Fe_t , and $N-NH_4^+$ was determined to be higher than the remaining parameters, with values of 0.190, 0.155, 0.140, and 0.130 (accounting for more than 60% of the importance level of the data set), respectively. The results showed that the matrix of harmony degree of each parameter in the study area reached level I, except for DO, TSS, and coliform.

Table 3. Matrix of harmony degree of each parameter in dry and rainy seasons

Parameters	Dry season				Rainy season				ω
	I	II	III	IV	I	II	III	IV	
pH	1	1	1	1	1	1	1	1	0.041
DO	0	0	1	1	0	0	1	1	0.078
BOD	1	1	1	1	1	1	1	1	0.073
COD	1	1	1	1	1	1	1	1	0.058
TSS	0	1	1	1	0	0	1	1	0.056
$N-NH_4^+$	1	1	1	1	1	1	1	1	0.130
$N-NO_2^-$	1	1	1	1	1	1	1	1	0.155
$N-NO_3^-$	1	1	1	1	1	1	1	1	0.003
$P-PO_4^{3-}$	1	1	1	1	1	1	1	1	0.077
Fe_t	1	1	1	1	1	1	1	1	0.140
Coliform	0	1	1	1	0	0	1	1	0.190

From the results of Table 3 combined with the entropy weights of each parameter, the comprehensive harmony degree of water quality for various uses in the dry and rainy seasons is shown in Table 4. The comprehensive harmony degree varied from 0.677-1.00, which was considered relatively uniform. Specifically, the degree of comprehensive harmony in the dry season with levels and uses at levels I, II, III, and IV was 0.677, 0.922, 1.00, and 1.00, respectively. Meanwhile, the harmony degree in the rainy season was recorded similarly at levels I and II ($HD_{I, II} = 0.677$) and III and IV ($HD_{III, IV} = 1.00$). Compared with the harmonized target value ($HD_0 = 1$), water quality in the dry and rainy seasons was consistent with level III, which was used for irrigation or other purposes with lower water quality requirements (level IV) [42]. However, when using $HD_0 = 0.8$, the comprehensive harmonization of water quality in the dry season was at a higher level (level II), suitable for domestic water supply purposes, but treatment technology must be applied suitable or for level III and IV uses [42]. Meanwhile, the degree of harmony in water quality and intended use was still determined at level III in the rainy season. This can be explained by the influence of TSS and coliform levels in water that have reduced the level of water quality in harmony with level II (Table 3), which is often reported to have higher concentrations in the rainy season [5, 57]. Therefore, TSS and coliform are the most influential parameters, requiring a solution to limit and handle their effects.

Table 4. The value of comprehensive harmony degree HD_s and water quality classification

Seasons	Comprehensive harmony degree (HD_s)				Judgement values (HD_0)	
	I	II	III	IV	$HD_0 = 1$	$HD_0 = 0.8$
Dry	0.677	0.922	1.000	1.000	III	II
Rainy	0.677	0.677	1.000	1.000	III	III

3.3. Eutrophic Risk in the Study Area

The results of the eutrophication index (EI) in the dry and rainy seasons in Can Tho city are shown in Figure 3. The results showed that the EI index in the study area ranged from 6.02–103.07 (dry season) and 0–82.30 (rainy season). It can be seen that all monitoring stations in the dry season had greater than 0, which showed that the rivers and canals in the study area were eutrophic. The value of EI in the rainy season was about 71.05% greater than 0, which means the sites were likely to be eutrophic. Meanwhile, 10 locations were recorded as not being eutrophic, namely SW4, SW7, SW8, SW9, SW10, SW13, SW14, SW15, SW31, and SW38. In addition, surface water eutrophication at SW25 (dry season) and SW28 (rainy season) was relatively serious, with the highest EI value. These monitoring locations belong to the areas of tourism, agricultural activities, and people's activities (markets). In particular, the excess use of fertilizers in agricultural activities has increased the amount of nutrients in water, affecting aquatic species [36, 58]. The lowest EI values were found at location SW20 in dry seasons, where fishing gear is mainly produced, with little impact on the area's water environment. The EI value in the dry season was higher than that of the rainy season, about 1.25–6 times. Some previous studies by Son et al. [13] and Youping et al. [59] also reported that the EI value in the dry season was always higher than that of the rainy season. The studies of Phung et al. [60] and Tuan et al. [51] pointed out that the study area is mainly polluted by organic substances and nutrients at relatively high levels by industrial, agricultural, and daily activities of people. This is consistent with the results of this study, and the study area is in a state of eutrophication.

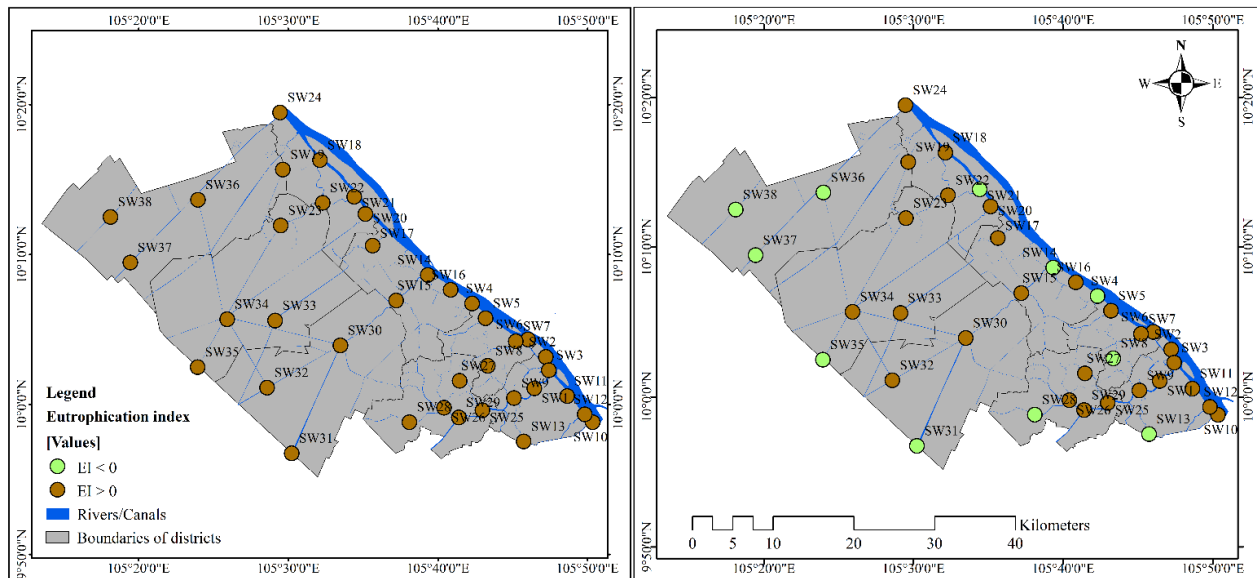


Figure 3. Spatial variation of eutrophication index in the study area

3.4. Rank the Treatment Priority Order of Locations Based on the TOPSIS Method

The overall ranking of the sampling locations given by the TOPSIS method is shown in Figure 4. In the study, several locations had relatively stable water quality, such as SW13, SW17, SW31, and SW32. In the dry season, the closeness coefficients of SW6, SW8, SW30, SW36, and SW19 were 0.9365, 0.7485, 0.7477, 0.6615, and 0.6520, respectively; these are the five locations with the best water quality. However, these locations have low closeness coefficients in the rainy season, which has bad water quality, typically SW36. In fact, SW36 is located in a market area with many people and agricultural cultivation activities. In the rainy season, the closeness coefficient of locations with positive ideal values was recorded to tend to decrease. The locations with the best water quality were arranged in descending order, including SW4 (0.8403) < SW8 (0.6820) < SW5 (0.6641) < SW7 (0.5954) < SW17 (0.5307). Similarly, SW4 has poor water quality in the dry season, which receives domestic wastewater as part of the industrial park. This indicates that if the parameters are considered as a whole, water quality at each location is significantly affected by seasonal changes in activity. According to the classification of Sonavane et al. [27], the closeness coefficient is divided into four groups to evaluate water quality, including very good ($CC \geq 0.8$), good ($0.6 \leq CC < 0.8$), bad ($0.3 \leq CC < 0.6$), and unsuitable ($CC < 0.3$). According to this classification, water quality in the dry season in the region has 8 locations unsuitable for use (accounting for 21.05%), 21 locations at a bad level (accounting for 55.26%), 8 locations at a good level (accounting for 21.05%), and 1 location with excellent quality (2.63%). In the rainy season, there were 15 unsuitable locations (39.47%), 20 locations at a bad level (52.63%), 2 locations at a good level (5.26%), and 1 location at an excellent level (2.63%).

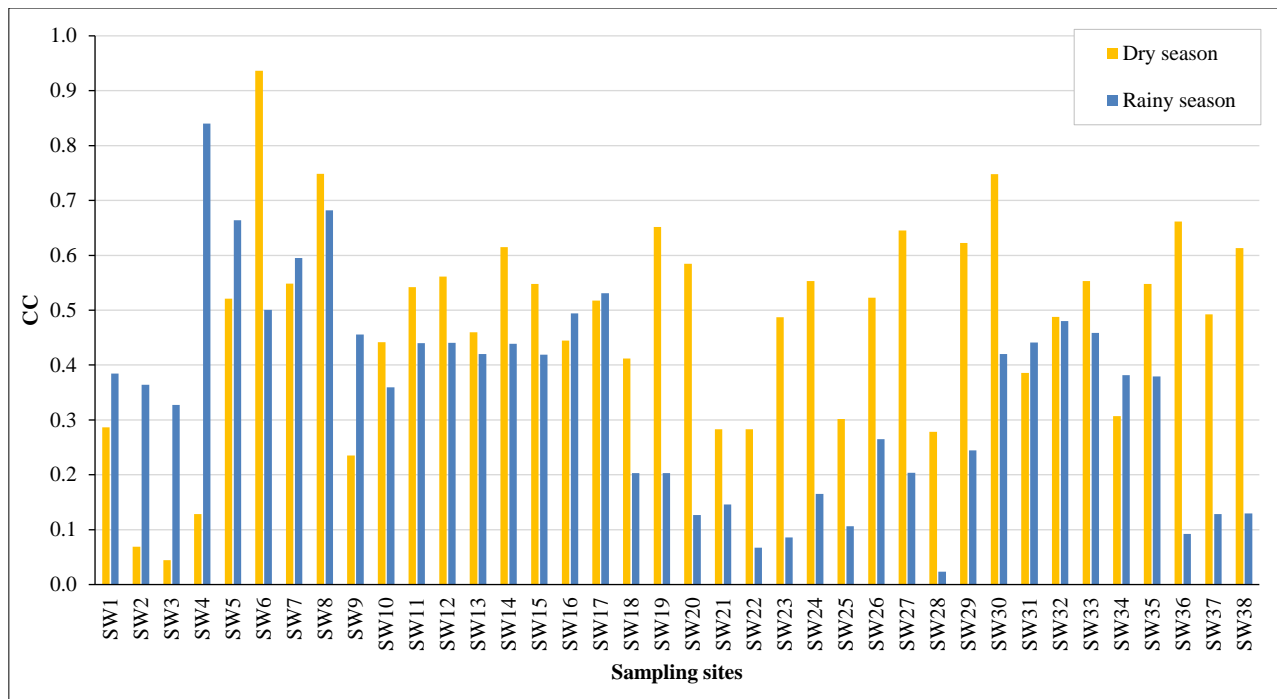


Figure 4. Closeness coefficient at the sampling sites in the dry and rainy season

Table 5 shows the ranking of monitoring locations (SW1 to SW38) in order of priority requiring treatment solutions. Based on the closeness coefficient (CC) at the locations, the treatment priority of the locations has significant fluctuations between the rainy and dry seasons; for instance, some locations have a reduced priority and vice versa. In the dry season, SW1-SW4, SW9, SW21, SW22, and SW28 were identified as having high treatment priority, indicating that the water quality at these locations has limited uses. The priority ranking results in the rainy season have changed. Specifically, the eight locations with high priority in descending order were SW28, SW22, SW23, SW36, SW25, SW20, SW37, and SW38, respectively. Combined with the results of eutrophication risk, water quality in the study area should be prioritized for treatment at SW2-SW4 in the dry season, SW23 in the rainy season, and SW22 and SW28 in both seasons.

Table 5. The positive and negative ideal points, closeness coefficient and ranking and priority ranking

Sites	Dry season				Rainy season			
	d ⁺	d ⁻	CC	Rank	d ⁺	d ⁻	CC	Rank
SW1	0.1865	0.0750	0.2868	8	0.4142	0.2591	0.3848	21
SW2	0.2444	0.0180	0.0687	2	0.4293	0.2458	0.3641	18
SW3	0.2611	0.0121	0.0445	1	0.4522	0.2203	0.3275	16
SW4	0.2308	0.0340	0.1285	3	0.1227	0.6458	0.8403	38
SW5	0.1252	0.1362	0.5212	20	0.2314	0.4576	0.6641	36
SW6	0.0174	0.2564	0.9365	38	0.3354	0.3365	0.5008	33
SW7	0.1172	0.1423	0.5483	25	0.2743	0.4036	0.5954	35
SW8	0.0659	0.1961	0.7485	37	0.2196	0.4709	0.6820	37
SW9	0.2014	0.0619	0.2351	4	0.3694	0.3094	0.4558	29
SW10	0.1456	0.1152	0.4418	13	0.4316	0.2422	0.3594	17
SW11	0.1198	0.1417	0.5418	22	0.3767	0.2960	0.4400	26
SW12	0.1160	0.1485	0.5615	28	0.3756	0.2960	0.4407	27
SW13	0.1425	0.1212	0.4596	15	0.3897	0.2825	0.4203	24
SW14	0.1030	0.1646	0.6151	31	0.3786	0.2960	0.4388	25
SW15	0.1202	0.1456	0.5478	23	0.3921	0.2826	0.4188	22
SW16	0.1467	0.1175	0.4446	14	0.3440	0.3363	0.4944	32
SW17	0.1275	0.1366	0.5173	19	0.3212	0.3633	0.5307	34
SW18	0.1544	0.1081	0.4120	12	0.5313	0.1352	0.2029	11

Sites	Dry season				Rainy season			
	d ⁺	d ⁻	CC	Rank	d ⁺	d ⁻	CC	Rank
SW19	0.0934	0.1751	0.6520	34	0.5306	0.1352	0.2031	12
SW20	0.1101	0.1548	0.5843	29	0.5822	0.0843	0.1264	6
SW21	0.1883	0.0744	0.2833	7	0.5693	0.0972	0.1459	9
SW22	0.1882	0.0742	0.2828	6	0.6217	0.0449	0.0674	2
SW23	0.1351	0.1283	0.4872	16	0.6084	0.0573	0.0861	3
SW24	0.1197	0.1481	0.5529	26	0.5561	0.1100	0.1652	10
SW25	0.1843	0.0797	0.3018	9	0.5932	0.0703	0.1060	5
SW26	0.1257	0.1377	0.5228	21	0.4886	0.1762	0.2651	15
SW27	0.0936	0.1705	0.6455	33	0.5296	0.1357	0.2039	13
SW28	0.1908	0.0736	0.2785	5	0.6471	0.0157	0.0236	1
SW29	0.0990	0.1635	0.6228	32	0.5007	0.1622	0.2447	14
SW30	0.0683	0.2024	0.7477	36	0.3918	0.2839	0.4201	23
SW31	0.1623	0.1018	0.3855	11	0.3765	0.2969	0.4409	28
SW32	0.1350	0.1286	0.4879	17	0.3513	0.3248	0.4804	31
SW33	0.1197	0.1481	0.5530	27	0.3663	0.3104	0.4586	30
SW34	0.1827	0.0810	0.3072	10	0.4156	0.2563	0.3814	20
SW35	0.1221	0.1481	0.5480	24	0.4192	0.2563	0.3794	19
SW36	0.0901	0.1760	0.6615	35	0.6080	0.0617	0.0921	4
SW37	0.1331	0.1292	0.4926	18	0.5837	0.0862	0.1286	7
SW38	0.1025	0.1624	0.6130	30	0.5837	0.0867	0.1293	8

4. Conclusion

The results showed that the surface water quality in Can Tho City was polluted with total suspended solids (TSS) and coliform. The parameters of DO, COD, N-NH₄⁺, and P-PO₄³⁻ were high in the dry season, whereas the reverse was true for pH, temperature, TSS, BOD, N-NO₂⁻, N-NO₃⁻, and Pb. The comprehensive harmony degree of water quality-purpose use has determined that water quality in the dry season was suitable for domestic purposes (Level II) but requires appropriate treatment measures; the rainy season was suitable for irrigation (Level III) and lower purposes. TSS and coliform are the most influential parameters for the purpose of use. The results showed that the EI index in the study area ranged from 6.02–103.07 (dry season) and 0–82.30 (rainy season), indicating that surface water was eutrophic, especially at SW25 and SW28. Based on the result of TOPSIS, the locations with decreasing priority are as follows: SW3 > SW2 > SW4 > SW9 > SW28 > SW22 > SW21 (dry season) and SW28 > SW22 > SW22 > SW36 > SW25 > SW20 > SW37 > SW38. Water quality at SW4 has significant potential source impacts by season. The research results can be a scientific basis for prioritizing decisions to implement mitigation or treatment measures based on priority order and recommended water use for the two seasons.

5. Declarations

5.1. Author Contributions

Conceptualization, N.T.G. and L.D.K.; methodology, N.T.G. and L.D.K.; software, N.T.G.; validation, L.D.K.; formal analysis, N.T.G. and L.D.K.; resources, N.T.G. and L.D.K.; data curation, N.T.G.; writing—original draft preparation, N.T.G. and L.D.K.; writing—review and editing, N.T.G. and L.D.K.; visualization, N.T.G. and L.D.K.; supervision, N.T.G. and L.D.K.; project administration, N.T.G. and L.D.K. All authors have read and agreed to the published version of the manuscript.

5.2. Data Availability Statement

The data presented in this study are available in the article.

5.3. Funding

The authors received no financial support for the research, authorship, and/or publication of this article.

5.4. Acknowledgements

We thank Huynh Thi Hong Nhien for her assistance during preparation of this manuscript.

5.5. Conflicts of Interest

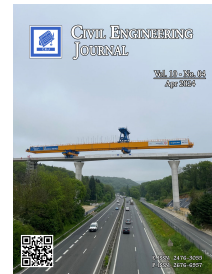
The authors declare no conflict of interest.

6. References





- [1] Li, Z. H., Li, Z. P., Tang, X., Hou, W. H., & Li, P. (2021). Distribution and risk assessment of toxic pollutants in surface water of the lower Yellow River, China. *Water*, 13(11). doi:10.3390/w13111582.
- [2] Luan, V. N., & Nam, N. D. (2022). The relationship between environment and economic development in Vietnam. *Journal of Pharmaceutical Negative Results*, 13(6), 99-102.
- [3] Liu, J., Liu, Y., Zhang, A., Liu, Y., Zhu, Y., Guo, M., & Zhang, R. (2019). Spatial distribution, source identification, and potential risk assessment of toxic contaminants in surface waters from Yulin, China. *Environmental Monitoring and Assessment*, 191(5), 293. doi:10.1007/s10661-019-7441-0.
- [4] Xi, H., Li, T., Yuan, Y., Chen, Q., & Wen, Z. (2023). River ecosystem health assessment based on fuzzy logic and harmony degree evaluation in a human-dominated river basin. *Ecosystem Health and Sustainability*, 9, 41. doi:10.34133/ehs.0041.
- [5] Wehrheim, C., Lübken, M., Stolpe, H., & Wichern, M. (2023). Identifying key influences on surface water quality in freshwater areas of the Vietnamese Mekong Delta from 2018 to 2020. *Water*, 15(7). doi:10.3390/w15071295.
- [6] Nguyen, T. T. N., Némery, J., Gratiot, N., Strady, E., Tran, V. Q., Nguyen, A. T., Aimé, J., & Peyne, A. (2019). Nutrient dynamics and eutrophication assessment in the tropical river system of Saigon – Dongnai (Southern Vietnam). *Science of the Total Environment*, 653, 370–383. doi:10.1016/j.scitotenv.2018.10.319.
- [7] Liu, J., Zhang, D., Tang, Q., Xu, H., Huang, S., Shang, D., & Liu, R. (2021). Water quality assessment and source identification of the Shuangji River (China) using multivariate statistical methods. *PLoS ONE*, 16(1 January), e245525. doi:10.1371/journal.pone.0245525.
- [8] Qin, G., Liu, J., Xu, S., & Wang, T. (2020). Water quality assessment and pollution source apportionment in a highly regulated river of Northeast China. *Environmental Monitoring and Assessment*, 192(7), 1–16. doi:10.1007/s10661-020-08404-0.
- [9] Singh, R., Majumder, C. B., & Vidyarthi, A. K. (2023). Assessing the impacts of industrial wastewater on the inland surface water quality: An application of analytic hierarchy process (AHP) model-based water quality index and GIS techniques. *Physics and Chemistry of the Earth, Parts A/B/C*, 129, 103314. doi:10.1016/j.pce.2022.103314.
- [10] Anwar Sadat, M., Guan, Y., Zhang, D., Shao, G., Cheng, X., & Yang, Y. (2020). The associations between river health and water resources management lead to the assessment of river state. *Ecological Indicators*, 109, 105814. doi:10.1016/j.ecolind.2019.105814.
- [11] Zuo, Q., Jin, R., Ma, J., & Cui, G. (2015). Description and application of a mathematical method for the analysis of harmony. *The Scientific World Journal*, 2015, 1–9. doi:10.1155/2015/831396.
- [12] Wu, Z., Lai, X., & Li, K. (2021). Water quality assessment of rivers in Lake Chaohu Basin (China) using water quality index. *Ecological Indicators*, 121, 107021. doi:10.1016/j.ecolind.2020.107021.
- [13] Son, C. T., Giang, N. T. H., Thao, T. P., Nui, N. H., Lam, N. T., & Cong, V. H. (2020). Assessment of Cau River water quality assessment using a combination of water quality and pollution indices. *Journal of Water Supply: Research and Technology - AQUA*, 69(2), 160–172. doi:10.2166/aqua.2020.122.
- [14] Varol, M., & Tokatlı, C. (2023). Evaluation of the water quality of a highly polluted stream with water quality indices and health risk assessment methods. *Chemosphere*, 311, 137096. doi:10.1016/j.chemosphere.2022.137096.
- [15] Nguyen, T. G., & Huynh, T. H. N. (2022). Assessment of surface water quality and monitoring in southern Vietnam using multicriteria statistical approaches. *Sustainable Environment Research*, 32(1), 1–12. doi:10.1186/s42834-022-00133-y.
- [16] Unigwe, C. O., & Egbueri, J. C. (2023). Drinking water quality assessment based on statistical analysis and three water quality indices (MWQI, IWQI and EWQI): a case study. *Environment, Development and Sustainability*, 25(1), 686–707. doi:10.1007/s10668-021-02076-7.
- [17] Giao, N. T., Nhien, H. T. H., Anh, P. K., & Van Ni, D. (2021). Classification of water quality in low-lying area in Vietnamese Mekong Delta using set pair analysis method and Vietnamese water quality index. *Environmental Monitoring and Assessment*, 193(6), 319. doi:10.1007/s10661-021-09102-1.
- [18] Tian, R., & Wu, J. (2019). Groundwater quality appraisal by improved set pair analysis with game theory weightage and health risk estimation of contaminants for Xuecha drinking water source in a loess area in Northwest China. *Human and Ecological Risk Assessment: An International Journal*, 25(1–2), 132–157. doi:10.1080/10807039.2019.1573035.
- [19] Singh, K. R., Dutta, R., Kalamdhad, A. S., & Kumar, B. (2018). Risk characterization and surface water quality assessment of Manas River, Assam (India) with an emphasis on the TOPSIS method of multi-objective decision making. *Environmental Earth Sciences*, 77(23), 1–10. doi:10.1007/s12665-018-7970-9.

- [20] Singh, K. R., Dutta, R., Kalamdhad, A. S., & Kumar, B. (2019). Information entropy as a tool in surface water quality assessment. *Environmental Earth Sciences*, 78(1), 1–12. doi:10.1007/s12665-018-7998-x.
- [21] Ewaid, S. H., Mhajej, K. G., Abed, S. A., & Al-Ansari, N. (2021). Groundwater Hydrochemistry Assessment of North Dhi-Qar Province, South of Iraq Using Multivariate Statistical Techniques. *IOP Conference Series: Earth and Environmental Science*, 790(1), 12075. doi:10.1088/1755-1315/790/1/012075.
- [22] Giao, N. T., Nhien, H. T. H., Anh, P. K., & Thuptimdang, P. (2022). Combination of water quality, pollution indices, and multivariate statistical techniques for evaluating the surface water quality variation in Can Tho City, Vietnam. *Environmental Monitoring and Assessment*, 194(11), 844. doi:10.1007/s10661-022-10474-1.
- [23] Xiao, J., Gao, D., Zhang, H., Shi, H., Chen, Q., Li, H., Ren, X., & Chen, Q. (2023). Water quality assessment and pollution source apportionment using multivariate statistical techniques: a case study of the Laixi River Basin, China. *Environmental Monitoring and Assessment*, 195(2), 287. doi:10.1007/s10661-022-10855-6.
- [24] Assari, A., Mahesh, T., & Assari, E. (2012). Role of public participation in sustainability of historical city: usage of TOPSIS method. *Indian Journal of Science and Technology*, 5(3), 2289–2294. doi:10.17485/ijst/2012/v5i3.2.
- [25] Li, Z., Yang, T., Huang, C. S., Xu, C. Y., Shao, Q., Shi, P., Wang, X., & Cui, T. (2018). An improved approach for water quality evaluation: TOPSIS-based informative weighting and ranking (TIWR) approach. *Ecological Indicators*, 89, 356–364. doi:10.1016/j.ecolind.2018.02.014.
- [26] Alvandi, E., Soleimani-Sardo, M., Meshram, S. G., Farid Giglou, B., & Dahmardeh Ghaleno, M. R. (2021). Using Improved TOPSIS and Best Worst Method in prioritizing management scenarios for the watershed management in arid and semi-arid environments. *Soft Computing*, 25(16), 11363–11375. doi:10.1007/s00500-021-05933-9.
- [27] Sonavane, A., Narkhede, D., Pawar, S., & Maktum, T. (2021). Assessment of water quality using Fuzzy-AHP and TOPSIS. *ITM Web of Conferences*, 40, 02002. doi:10.1051/itmconf/20214002002.
- [28] Zuo, Q., Han, C., Liu, J., & Ma, J. (2018). A new method for water quality assessment: by harmony degree equation. *Environmental Monitoring and Assessment*, 190(3), 1–12. doi:10.1007/s10661-018-6541-6.
- [29] Luo, Z., Zuo, Q., & Shao, Q. (2018). A new framework for assessing river ecosystem health with consideration of human service demand. *Science of the Total Environment*, 640–641, 442–453. doi:10.1016/j.scitotenv.2018.05.361.
- [30] Zuo, Q., Li, W., Zhao, H., Ma, J., Han, C., & Luo, Z. (2021). A harmony-based approach for assessing and regulating human-water relationships: A case study of Henan province in China. *Water (Switzerland)*, 13(1), 32. doi:10.3390/w13010032.
- [31] Zhang, J., Tang, D., Wang, M., Ahamd, I., Hu, J., Meng, Z., Liu, D., & Pan, S. (2023). A regional water resource allocation model based on the human–water harmony theory in the Yellow River Basin. *Water (Switzerland)*, 15(7), 1388. doi:10.3390/w15071388.
- [32] Shi, Y., Yang, S., Chen, W., Wang, X., & Feng, C. (2023). Research on the construction of a human-water harmony model in the Yellow River Basin. *Water Policy*, 25(7), 742–757. doi:10.2166/wp.2023.130.
- [33] Zhao, M., Li, J., Zhang, Y., Han, Y., & Wei, J. (2023). Water cycle health assessment based on combined weight and hook trapezoid fuzzy TOPSIS model: A case study of nine provinces in the Yellow River basin, China. *Ecological Indicators*, 147, 109977. doi:10.1016/j.ecolind.2023.109977.
- [34] Lv, B., Liu, C., Li, T., Meng, F., Fu, Q., Ji, Y., & Hou, R. (2023). Evaluation of the water resource carrying capacity in Heilongjiang, eastern China, based on the improved TOPSIS model. *Ecological Indicators*, 150, 110208. doi:10.1016/j.ecolind.2023.110208.
- [35] Siddiqua, A. (2019). Emergence of Water Urbanism for Water Born “Can Tho.” *Journal of Water Resource and Protection*, 11(2), 166–180. doi:10.4236/jwarp.2019.112010.
- [36] Nguyen, H. Q., Radhakrishnan, M., Huynh, T. T. N., Bains-Salingay, M. L., Ho, L. P., Van der Steen, P., & Pathirana, A. (2017). Water quality dynamics of urban water bodies during flooding in Can Tho City, Vietnam. *Water (Switzerland)*, 9(4), 260. doi:10.3390/w9040260.
- [37] Duc, N. H., Kumar, P., Lan, P. P., Kurniawan, T. A., Khedher, K. M., Kharrazi, A., Saito, O., & Avtar, R. (2023). Hydrochemical indices as a proxy for assessing land-use impacts on water resources: a sustainable management perspective and case study of Can Tho City, Vietnam. *Natural Hazards*, 117(3), 2573–2615. doi:10.1007/s11069-023-05957-4.
- [38] Thi, N. G. V., Thi, B. T. P., Nguyen, H. T., & Thanh, V. Q. (2021). Impact of climate change and socio-economic development on the water balance and water quality of the Can Tho River. *IOP Conference Series: Earth and Environmental Science*, 652(1), 12008. doi:10.1088/1755-1315/652/1/012008.
- [39] Department of Natural Resources and Environment (DoNRE). (2020). Report on the current state of the environment for 05 years, period 2015 – 2020. Department of Natural Resources and Environment of Can Tho City, Can Tho City, Vietnam. (In Vietnamese).

- [40] Center for Natural Resources and Environmental Monitoring (2022). Report summarizing the results of environmental quality monitoring in Can Tho City in 2022. Department of Natural Resources and Environment of Can Tho City, Can Tho city, Vietnam. (In Vietnamese).
- [41] APHA. (2017). Standard methods of for the examination of water and wastewater. American Public Health Association (APHA), Washington, United States.
- [42] MoNRE. (2015). National technical regulation on surface water quality (QCVN 08-MT:2015/BTNMT). Ministry of Natural Resources and Environment (MoNRE), Hanoi, Vietnam. (In Vietnamese).
- [43] Mishra, S., Sharma, M. P., & Kumar, A. (2016). Assessment of surface water quality in Surha Lake using pollution index, India. *Journal of Materials and Environmental Science*, 7, 713–719.
- [44] Yousefi, H., Zahedi, S., & Niksokhan, M. H. (2018). Modifying the analysis made by water quality index using multi-criteria decision making methods. *Journal of African Earth Sciences*, 138, 309–318. doi:10.1016/j.jafrearsci.2017.11.019.
- [45] Catherine, E. C., Danmama, A. A., Emeka, A., Emeka, N. K., & Michael, O. R. (2021). Assessment of surface water quality of Onuiyieke river in Imo State, Nigeria. *GSC Biological and Pharmaceutical Sciences*, 16(3), 071-084. doi:10.30574/gscbps.2021.16.3.0264.
- [46] Muoi, L. V., Srilert, C., Dang Tri, V. P., & Pham Van, T. (2022). Spatial and temporal variabilities of surface water and sediment pollution at the main tidal-influenced river in Ca Mau Peninsular, Vietnamese Mekong Delta. *Journal of Hydrology: Regional Studies*, 41, 101082. doi:10.1016/j.ejrh.2022.101082.
- [47] Nguyen, B. T., Vo, L. D., Nguyen, T. X., & Quang, N. X. (2020). The interactive effects of natural factor and pollution source on surface water quality in the Lower Mekong River Basin, Southwestern Vietnam. *Water Resources*, 47(5), 865-876. doi:10.1134/S0097807820050024.
- [48] Tam, N. T., Bao, T. Q., Minh, H. V. T., Thanh, N. T., Lien, B. T. B. & Minh, N. D. T. (2022). Evaluating the surface water quality affected by activities in Can Tho City. *Vietnam Journal of Hydro-Meteorology*, 733, 39–55. doi:10.36335/VNJHM.2022(733).39-55. (In Vietnamese).
- [49] Kamarudin, M. K. A., Wahab, N. A., Md Bati, S. N. A., Toriman, M. E., Saudi, A. S. M., Umar, R., & Sunardi. (2020). Seasonal variation on dissolved oxygen, biochemical oxygen demand and chemical oxygen demand in Terengganu River Basin, Malaysia. *Journal of Environmental Science and Management*, 23(2), 1–7. doi:10.47125/jesam/2020_2/01.
- [50] Lien, N. T. K., Huy, L. Q., Oanh, D. T. H., Phu, T. Q. & Ut, V. N. (2016). Water quality in mainstream and tributaries of Hau River. *Can Tho University Journal of Science*, 43, 68–79. doi:10.22144/ctu.jvn.2016.138. (In Vietnamese).
- [51] Tuan, D. D. A., Thu, B. A. & Trung, N. H. (2019). Assessing quality of surface water for urban water supply source for Soc Trang City. *Can Tho University Journal of Science*, 55, 61–70. doi:10.22144/ctu.jvn.2019.096. (In Vietnamese).
- [52] Edokpayi, J. N., Odiyo, J. O., Popoola, O. E., & Msagati, T. A. M. (2016). Assessment of trace metals contamination of surface water and sediment: A case study of Mvudi River, South Africa. *Sustainability*, 8(2), 135. doi:10.3390/su8020135.
- [53] Goyit, M. P., Solomon, O. A., & Kutshik, R. J. (2018). Distribution of fluoride in surface and groundwater: a case study of Langtang North, Plateau State, Nigeria. *International Journal of Biological and Chemical Sciences*, 12(2), 1057. doi:10.4314/ijbcs.v12i2.33.
- [54] Pham, A. D., Thieu, V. V. D., Nguyen, B. A., Dinh, T. T. H., Nguyen, T. T. T., & Nguyen, T. L. C. (2022). Assessment of heavy metal pollution in the surface water of the Doi Canal, the Cho Dem and Ben Luc Rivers, Vietnam. *GeoScience Engineering*, 68(1), 91–98. doi:10.35180/gse-2022-0072.
- [55] Hong, T. T. K., & Giao, N. T. (2022). Analysis of surface water quality in upstream province of Vietnamese Mekong Delta using multivariate statistics. *Water*, 14(12), 1975. doi:10.3390/w14121975.
- [56] Le, Q. T., Nguyen, K. V., & Nguyen, V. D. T. (2022). Assessment of surface water quality and some main rivers' capacity of receiving wastewater in Ca Mau province, Vietnam. *The Journal of Agriculture and Development*, 21(3), 53-66. doi:10.52997/jad.7.03.2022.
- [57] Nguyen, T. G., Phan, K. A., & Huynh, T. H. N. (2022). Major concerns of surface water quality in south-west coastal regions of Vietnamese Mekong Delta. *Sustainable Environment Research*, 32(1), 1–14. doi:10.1186/s42834-022-00156-5.
- [58] Huang, X., Luo, H., Wu, Q., Li, Z., Chen, X., & Hei, L. (2020). Study on eutrophication characteristics of rainy and dry season in Shenzhen Bay. *IOP Conference Series: Earth and Environmental Science*, 467(1), 12117. doi:10.1088/1755-1315/467/1/012117.
- [59] Youping, S., Junjie, Z., & Jianzhe, Q. (2020). Analysis of eutrophication trend of surface water in Tianjin coastal area. *E3S Web of Conferences*, 206, 03002. doi:10.1051/e3sconf/202020603002.
- [60] Phung, D., Huang, C., Rutherford, S., Dwirahmadi, F., Chu, C., Wang, X., Nguyen, M., Nguyen, N. H., Do, C. M., Nguyen, T. H., & Dinh, T. A. D. (2015). Temporal and spatial assessment of river surface water quality using multivariate statistical techniques: a study in Can Tho City, a Mekong Delta area, Vietnam. *Environmental Monitoring and Assessment*, 187(5), 1–13. doi:10.1007/s10661-015-4474-x.



Highlighting Traffic Accidents on Roundabouts Using MRSS-AHP Expert System

Ghassan Suleiman¹ , Mohammad K. Younes^{2*} , Murat Ergun³ ,
M. F. Abushammala⁴, Mohammad Aljaradin⁵ 

¹ Department of Civil Engineering, Aqaba University of Technology, Aqaba 77110, Jordan.

² Department of Civil Engineering, Applied Science Private University, Amman 11931, Jordan.

³ Division of Transportation, Department of Civil Engineering, Technical University of Istanbul, Istanbul 34469, Turkey.

⁴ Department of Civil and Mechanical Engineering, Middle East College, Knowledge Oasis Muscat, PB No 79, Al Rusayl 124, Sultanate of Oman.

⁵ School of Health and Environmental Studies, Hamdan Bin Mohammed Smart University, United Arab Emirates.

Received 01 December 2023; Revised 28 February 2024; Accepted 05 March 2024; Published 01 April 2024

Abstract

The frequency and severity of traffic accidents are causing growing concern. This study aims to develop a tool to improve the traffic safety level on roundabouts and identify the influence of traffic operations, geometric parameters, weather, and time of day on improving roundabout traffic safety. It is the first study to evaluate the performance of the integrated Median Ranked Set Sample (MRSS) and Analytic Hierarchy Process (AHP) with statistical analysis. A hierarchy tree of accident causes has been developed using data gathered from accident reports and relevant authorities. Then, the selected stakeholders' professionals prioritized the traffic accident causes using a MRSS and AHP. Moreover, traffic microsimulation software VISSIM was also used to extract traffic operation parameters for the analysis. Afterwards, Analysis of Variance (ANOVA) was used to validate the causes of traffic accidents. The results show that geometric design accounts for 36% of accidents at roundabouts, followed by traffic operation (22%). However, conflicting and queuing lengths are responsible for about 20% of traffic accidents. The tools developed, and the causes of accidents determined in this study will help geometric designers and city planners to take the necessary measures to minimize accidents and enhance traffic safety levels in urban areas.

Keywords: Traffic Accidents; Road Traffic Safety; Roundabout; AHP; Traffic Characteristics.

1. Introduction

Traffic accidents are caused by a complex interaction of three main factors: driver behavior, vehicles, and road conditions [1, 2]. Approximately, there are about 1.4 million human deaths reported annually as a result of traffic accidents worldwide. Thus, understanding the interactions between these factors and their combined influence is essential to reducing the negative impacts of accidents. Traditionally, roundabouts are introduced to facilitate traffic movement by eliminating or altering different conflicts and reducing the number and severity of accidents and vehicle speeds. However, increasing traffic has downgraded the safety and efficiency of roundabouts. Thus, it is urgent to investigate the traffic accidents at roundabouts in urban areas to improve the roundabouts' designs and operations to maintain their effectiveness. Traffic safety is a complex issue that requires a comprehensive evaluation of accident

* Corresponding author: m_younes@asu.edu.jo

 <http://dx.doi.org/10.28991/CEJ-2024-010-04-013>



© 2024 by the authors. Licensee C.E.J, Tehran, Iran. This article is an open access article distributed under the terms and conditions of the Creative Commons Attribution (CC-BY) license (<http://creativecommons.org/licenses/by/4.0/>).

causes to establish an optimal combination of appropriate measures to save lives and reduce social and economic costs [3, 4]. Moreover, there is a need to evaluate and analyze aspects with varying importance levels using different processing methods.

The reasons behind traffic accidents may be categorized as (i) geometric, (ii) road conditions, (iii) climate conditions, (iv) vehicle characteristics, and (v) traffic movement direction and operation parameters [5–9]. Yet, the integrated effect of these factors has not been extensively explored [10]; thus, it is necessary to investigate them using a suitable tool. Moreover, some researchers investigated the likelihood of traffic accidents on rural and urban roads based on trip makers' perceptions. They used partial least squares analysis to classify the causes as either human (fatigue) or high speed on urban and rural roads, respectively. However, intersections and roundabouts represent a small part of the overall traffic and transportation system, but the accidents that occur at these spots constitute a significant percentage of the total accidents anywhere in the world. For this reason, it is crucial that the roundabouts are designed and operated carefully to improve vehicle traffic and reduce road crashes and their severity. The determination of traffic crash contribution factors was based on site inspections by traffic engineers [11]. For a single-lane roundabout, about 54% of the investigated crashes were at the entry and about 20% at the exit, which indicates the importance of geometric design factors like excessive radius of deflection of the entering approach or the small deviation angle. However, there is a demand to consider the weather and accident conditions that are usually reported by traffic police, as well as their judgments as an official expert. Thus, the combination of professional stakeholders (police and traffic engineers) with statistical tools will improve traffic accident causes as well as traffic safety. Furthermore, Bayesian logistic regression and finite mixture logit models were implemented to evaluate the traffic accident likelihood and severity using weather and real-time traffic data [4]. However, in order to improve traffic safety and our knowledge of pre-accident conditions, there is still much to be analyzed.

Recent studies ranked Multi-Criteria Decision-Making (MCDM) as the most important tool that is capable of reshaping traffic safety, especially where there is a threat to human lives as well as potential economic loss. Moreover, MCDM techniques have received growing attention worldwide for solving complex real-time problems because of their capacity to gather, structure, and analyze problems and prioritize alternative decisions [12]. However, the AHP method is used to handle MCDM problems by conducting pairwise comparisons, ranking, rating, and trade-off analyses. It overcomes the drawbacks of traditional traffic analytical measures, which usually consider a single factor. It has the capacity to assess and analyze the significant causes of traffic accidents with careful consideration of people, vehicles, and roads, as well as environmental factors [13]. Moreover, the AHP relies on informed judgments by experts and stakeholders, allowing efficient and concurrent processing of qualitative and quantitative data [14]. Furthermore, it is relatively easy to use and understand. Consequently, it has been applied to solve complex real-life multi-attribute and multi-stakeholder issues like traffic accidents. For instance, the AHP tool was used to evaluate and prioritize the best methods to control and minimize traffic congestion in Iran [15]. However, integrating the decision-making tools with the traditional statistical tools is one step on the track for improving traffic safety precautions measures.

The traffic safety performances of 21 European cities have been assessed using eleven evaluation indicators to decrease the number of fatal accidents. Three MCDM methods, namely Simple Additive Weighting (SAW), AHP, and Fuzzy Technique for Order Performance by Similarity to Ideal Solution TOPSIS [16], have been used to investigate the reasons behind traffic accidents. Moreover, Ngoc & Thanh used a combination of AHP and customer satisfaction index tools to propose a traffic safety strategy [17]. In addition, the overall highway safety level has been determined by implementing an Analytic Network Process (ANP) integrated with statistical analysis [18]. Real-time data were integrated with social networking indicators to improve traffic accident analysis and forecasting [19]. On the other hand, the accident severity index was investigated using temporal statistical data incorporated with the Geographic Information System (GIS) to ascertain accident hotspots using kernel density estimation [20, 21].

Factors concerning road geometry consist of the road, shoulder, median, and lane widths; these are the most significant causes of traffic accidents at three-leg intersections in Taiwan [22]. Only a regression model was implemented, and the traffic accident number was considered the dependent variable [21]. In a study to investigate the nature and causes of unsafe driving behavior at roundabouts, the entry radius was reported as the most influential parameter. More entry lanes at roundabouts will increase the conflict. However, uncertainty in the decision-making process defines the quality of personal knowledge concerning risk evaluation and ambiguity avoidance [23]. Decisions are complex and involve a lack of initial information and quantitative and qualitative factors; therefore, a comprehensive decision-making model is required [14].

Furthermore, implementation of the MCDM involves ambiguity and uncertainty regarding expert preferences. Recent technological advances have facilitated real-time data collection regarding traffic and weather conditions [10]. Such data was used to analyze accident likelihood. Accurate data availability and special statistical techniques such as the maximum likelihood method, integrated MCDM, and expert judgment are usually applied to increase confidence levels. Moreover, any decision should be justified based on the knowledge available at the time. However, MRSS is a

modification of the Ranked Set Sample (RSS) technique. In MRSS, after the random selection of the strata, only the median observation is considered. Consequently, the ranking error is decreased, and the estimation efficiency will be improved [24]. Furthermore, it offers a representative tool to represent the research society without extensive observations.

The main goal of this article is to assess the criteria that influence traffic accidents and frequency at roundabouts in urban areas. This research will assist planning engineers and traffic authorities in implementing appropriate designs, decisions, and measures to save lives and reduce the number and severity of accidents. Moreover, it will provide a scientific instrument to rank the intersections based on their safety and efficiency using the AHP model. The rest of this study is organized as follows: Section 2 presents the collected data and its processing, stakeholder classification, and their preferences for processing techniques and tools. The results and discussion are shown in Section 3. It shows an example of stakeholders' preferences, the accident causes tree, as well as the results of the SPSS analysis of traffic accident causes. In addition, a summary of the key recommendations is also shown in this section. Section 5 presents the conclusion.

2. Research Methodology

2.1. Data Acquisition

Figure 1 schematically shows the data acquisition, classification, and analysis methods used in this research. The leading causes of accidents were selected based on literature reports and citations. The data were used to construct the accident cause tree; Figure 2 presents the main and sub-criteria of reported accident causes from literature as well as collected accident police reports. This research uses accident reports based on a two-year (2014–2015) average in three urban cities (Corum, Adana, and Konya) in Turkey. The selected intersections based on the available data are presented in Figure 3. The intersections (C_1 until C_{12}) were in Corum city, while (B_2 to B_6) and (K_1 to K_5) are in Adana and Konya, respectively. The digitally formatted reports included data about the time of day, weather conditions, speed, road geometry, number of fatalities and injuries, as well as the coordinates of accident locations. However, some accident reports have missing inputs. The proportion of such missing data for a particular variable was less than 1% of the total evaluated reports.

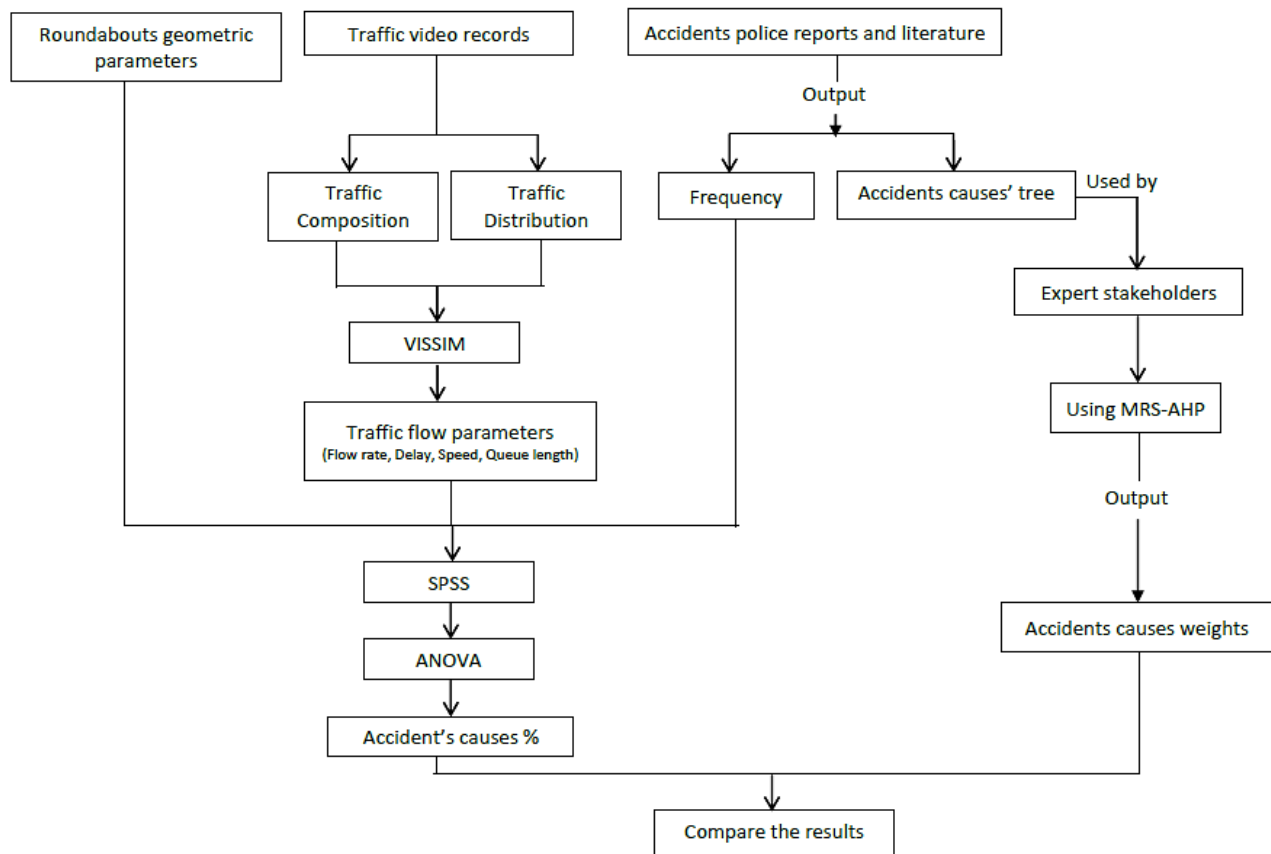


Figure 1. Schematic view of data collection, classification and analysis method

Accident causes at roundabout

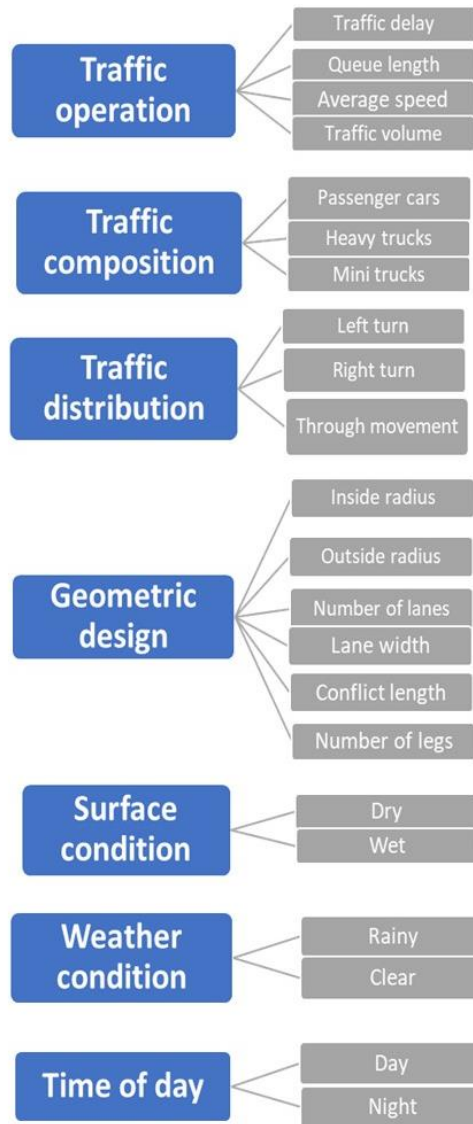


Figure 2. Main and Sub criteria of traffic accident causes from literature and police report



Figure 3. Satellite image of selected intersection

In addition, a classification of fatalities and injuries into three subgroups of drivers, pedestrians, and passengers is also available in the digitally formatted accident reports. Based on the above data on road crashes and the availability of actual traffic volume for the same period, twenty roundabouts most exposed to traffic accidents were selected for this study. Moreover, traffic volume data like vehicle composition (heavy, mini truck, and passenger car) and traffic distribution (right, left, and straight) were extracted from real-time video recordings. After determining the peak hour at each roundabout, the traffic counts were entered into the simulation software after the road characteristics were

determined (lane width, number of lanes, as well as other geometric design parameters of the roundabouts). Due to the availability of traffic counts every 15 minutes, counts of vehicles that change at every 15-minute measurement interval have been entered into the VISSIM simulation. This means that the data is dynamically assigned. The VISSIM software was used to find the traffic flow parameters [25]. These parameters, for example, included the average traffic flow speed on the roundabouts in km/hour, the average length of the traffic queue at the approach legs in meters, and finally the traffic delay in seconds/vehicle. Finally, geometric design parameters such as inside and outside radius, number of lanes, conflict length, and number of legs for each roundabout have been collected from relevant authorities.

2.2. Stakeholder Selection, Ranking the Traffic Accident Causes

Clustering the traffic accident causes at roundabout starts with a literature review and police reports to determine and classify the accident causes into main- and sub-groups. A clustering analysis gathers common data into meaningful groups that are associated with or share properties. Consequently, the traffic accident data has been classified into seven main groups, representing the potential causes of accidents. Under each of these groups, sub-criteria are added to form a hierarchy tree, as shown in Figure 1. This classification aims to investigate and analyze the causes and frequency of traffic accidents at roundabouts. Further, the expert stakeholders were classified into three groups; each group includes three experts (one from the government, one from the private sector, and an academician). This step aims to have the experts' feedback segmented into groups of significant common characteristics and to reflect the impact of varicose interests on the accident causes evaluation based on operation, economic, and scientific aspects. Additionally, clustering analysis minimizes the uncertainty and risk of regenerating symmetric decisions by involving and analyzing the feedback from stakeholders with various backgrounds as well as conflict of interest stakeholders [26].

A questionnaire was devised by asking experts to rank the causes of accidents at roundabouts and differentiate these based on the main and sub-criteria, including their impact on traffic accident causes, using pairwise comparisons. The odd-numbered rankings were used to determine the importance of the criteria, which range from 1 to 9. However, the stakeholder preferences were collected using pairwise comparisons, which are the fundamental blocks of the AHP tool. Then, the obtained expert's pairwise preferences were randomly grouped, as mentioned above, into three groups; Table 1 below shows an example of one of these preferences as well as the expert group. Each set of preferences consists of the responses of one academic, government, or private respondent. After that, these responses were ranked in increasing order, as shown in Table 2. Then, the MRSS technique is used to determine the represented preference or set of preferences [27]. The MRSS clustering and selecting technique may be summarized by the following equations:

- i. If the sample size (n) is odd, then the median number and/or set can be chosen by the following Equation 1:

$$\left(\frac{n+1}{2}\right)^{\text{th}} \tag{1}$$

- ii. However, this observation may be denoted as $X_{((n+1)/2: n)}$ and the general formula that express it is

$$X_{((n+1)/2 : n)_1}, X_{((n+1)/2 : n)_2}, \dots, X_{((n+1)/2: n)_n} \tag{2}$$

- iii. If the sample size, n, is even, then the median is selected by

$$\left(\frac{n}{2}\right)^{\text{th}} \tag{3}$$

This observation can be denoted as $X_{((n)/2: n)}$ and the general formula is:

$$X_{((n)/2 : n)_1}, X_{((n)/2 : n)_2}, \dots, X_{((n)/2: n)_n} \tag{4}$$

Table 1. Pairwise comparison of traffic operation with surface condition

Sector	Private sector	Government	Academic
Group No I	5	1	7
Group No I	7	3	5
Group No I	5	1	5

Table 2. Ranked stakeholders' preferences

	Ranked preferences		
Group No I	1	5	7
Group No I	3	5	7
Group No I	1	5	5

In stratified sampling method, if the population is consisting from N units and divided into L non overlapping subpopulations each of N_1, N_2, \dots, N_L units, respectively, such that $N_1 + N_2 + \dots + N_L = N$. Thus, these subunits are called strata. To maximize the benefit from stratification, the size of the h^{th} subunit, denoted by N_h for $h = 1, 2, \dots, L$, should be known. Then the sample drawn independently from each strata, producing samples sizes denoted by n_1, n_2, \dots, n_L , such that the total sample size is represented by Equation 5.

$$n = \sum_{h=1}^L N_h \quad (5)$$

The MRSS is an advanced tool derived originally from the RSS. The MRSS is advantageous (relative to the original RSS) because it minimizes ranking errors and enhances estimation efficiency [27]. After that, the preference sets obtained from the previous steps were subsequently applied in the AHP analysis for one more time to obtain the final weights of each main and sub-causes.

2.3. Analysis and Validation

The weights obtained by MRSS-AHP analysis for the main and sub-criteria were compared with the analysis of the causes of accidents using ANOVA to validate the results. However, in order to assess the goodness of the obtained MRSS-AHP results, the consistency ratio has been implemented. It can be calculated using the following equations:

$$CI = \frac{\lambda - n}{n - 1} \quad (6)$$

$$CR = \frac{CI}{RI} \quad (7)$$

where, CR, and RI are consistency index, consistency ratio, and random index, respectively. However, RI can be obtained from the tables available in the literature.

3. Results and Discussion

The questionnaire was analyzed to obtain the weights of each main and sub-criterion. This step aimed to determine the weights of all main and sub-criteria. Table 1 represents an example of one of these comparison groups. Each group includes one expert from private, government and academic that has been randomly selected. The preferences of each cluster are almost the same. For instance, the government officers believe that the traffic operation has almost the same importance in causing the traffic accident at a roundabout as the surface road condition. While Table 2 represents a ranked preference and selected set of a pairwise comparison of traffic operation with the road surface condition.

The selected preference set is (5, 5, 5), and again, from the resulted set, one more median rank is performed. Then a final weight can be selected; the weight in our case is 5. However, if the set is (7, 1, 3), then the selected weight based on the ranked median set (1, 3, 7) will be 3. However, the resulted final preference (5) means that traffic operations are moderately more effective in causing traffic accidents at the roundabout. Finally, an AHP procedure was performed to finalize the weights of each main and sub-criteria.

These steps have been repeated for each pair-wise comparison to obtain the weight of each main and sub-criteria. The resulting criteria weights are shown in Table 3. Moreover, the overall weight is equal to one. These weights reflect each criterion's relative importance (impact) in contributing to the causes of accidents. Additionally, knowing the main causes of traffic accidents helps the authorities focus, implement mitigation measures, and implement interventions to minimize traffic accidents and their consequences [28].

The geometric design is the most significant contributor to traffic accidents at roundabouts, with a weight of 36.65%, followed by traffic operations, with a weight of 22.6%. In comparison, the least significant contributory factors are time-of-day and traffic distribution, with weights equaling 5.8% and 6.8%, respectively. Also, many studies have reported geometric design as a significant contributor to accidents at roundabout intersections [11].

Building roundabouts than signal-free intersections in urban areas with conditions like (i) Speed limit (maximum speed of 50 km/h), (ii) Inscribed circle diameter ranging from 13 to 24 m, (iii) Circular roadway width of 4.5–6 m, and (iv) Only single-lane entries and exits are capable of reducing traffic accidents by 29%.

Final sub-factor scores are determined by multiplying major criteria weights with sub-criterion weights, as shown in Table 3. Conflicting length at roundabouts, queue length, and rain are other major contributory factors to traffic accidents, with weights of 12.6, 10.1%, and 10%, respectively. Although roundabouts reduce drivers' exposure to conflict time and the percentage of vehicles in conflict compared to signalized intersections [29]. The assessment of traffic collisions in the three selected cities indicated a remarkable reduction in fatal accidents. For instance, no accidents were classified as fatal. On the other hand, there was a very high percentage of accidents resulting in injuries. For example, 0.97% of accidents were classified as damage only, while 99.03% caused injuries. Regrettably, the total number of injuries reached 1,718. The percentages of injured drivers, pedestrians, and passengers were 38.82%, 4.71%,

and 56.46%, respectively. Furthermore, accidents were classified based on the number of vehicles: single-vehicle, two-vehicle, and more-than-two-vehicle collisions accounted for 24.6%, 68.4%, and 7.0% of overall accidents. Table 4 shows the primary statistics concerning the geometric designs of the assessed roundabouts. Conflicts at roundabouts are still a significant cause of accidents. This is due to roundabout geometric design [11], like radius, small deviation angle as well as large roundabout roadway width.

Table 3. Weights of main and sub-criteria concerning accidents at roundabouts

Main Criteria	Sub-Criteria and Weights	X _i	Final Weights
Geometric Design (36.6%)	Inside Radius (0.239)	X11	0.087
	Outside Radius (0.055)	X12	0.020
	No of lanes (0.046)	X13	0.017
	Lane width (0.076)	X14	0.028
	No of legs (0.241)	X15	0.088
	Conflicting Length (0.343)	X16	0.126
Traffic Operation (22.6%)	Queue Length (0.446)	X1	0.101
	Traffic Delay (0.094)	X2	0.021
	Traffic Volume (0.154)	X3	0.035
	Average speed (0.306)	X4	0.069
Weather Condition (11.4%)	Rainy (0.875)	X17	0.1
	Clear (0.125)	X18	0.014
Surface Condition (9.7%)	Wet (0.9)	X22	0.088
	Dry (0.1)	X21	0.009
Traffic Composition (7.1%)	Passenger car (0.07)	X9	0.005
	Heavy Truck (0.78)	X8	0.055
	Mini Truck (0.15)	X10	0.011
Traffic Distribution (6.8%)	Left Turn (0.751)	X6	0.051
	Right Turn (0.081)	X5	0.006
	Through movement (0.168)	X7	0.011
Time of day (5.8%)	Day (0.125)	X19	0.007
	Night (0.875)	X20	0.051
	Sum (SI)		1.00

Table 4. Geometric data statistics

Parameters	Average	Standard Deviation	Minimum	Maximum
Inside radius (m)	15.0	10.7	5.8	37.5
Outer Radius (m)	25.7	10.6	14.8	49.2
No of Lanes	2.0	0.3	2.0	3.0
Lane Width (m)	5.1	0.7	4.1	6.5
Conflicting Length (m)	32.0	16.6	16.3	68.1
Entry width (m)	8.6	1.3	6.8	10.7
Exit width (m)	10.6	4.1	7.7	22.1
Entry Angle (°)	70.7	8.1	48.5	82.8
Deviation Angle (°)	29.1	11.5	15.3	58.3

Table 5 presents the most frequent causes of accidents at the assessed roundabouts. An analysis of driver errors indicated that illegal parking, overturning, wrong merging, and diverging were the primary driver errors that caused accidents. Nonetheless, the most frequent types of accidents are side collisions and hits from behind, with shares of 49.6% and 17.7%, respectively. On the other hand, illegal parking on circulating roadways caused 6.2% of the total accidents, while collisions with pedestrians accounted for 9.7%. Finally, in addition to the previously cited errors, brake failure and other driver errors resulted in out-of-the-way movement and overturning, accounting for about 9.7% of all accidents. Most of these errors can be prevented by enforcing traffic laws and enhancing driver behavior. However, such results have been reported in a study performed by Alshannaq & Imam (2020) [30]. They reported the drivers' behaviors and/or absence of clear lane marking as the major causes of traffic accidents at roundabouts.

Table 5. Distribution of crash causes

Collision Type	% of Collision
Overtuning	6.2%
Getting out of the way	3.5%
Hit from behind	17.7%
Side collision	49.6%
Collision with a parked vehicle	6.2%
Collision with fixed object	7.1%
Pedestrian collision	9.7%

Figure 4-a presents the most dangerous roundabout (K1) regarding the number of accidents and injuries. The reported accidents varied between a side collision, a collision from behind, and a collision with a fixed object at a rate of 9 accidents and a total of 22 severe, medium, and light injuries. Moreover, Figure 4-b showed a new accident type, which included a vehicle getting out of the way and entering the central island (accident number 7).

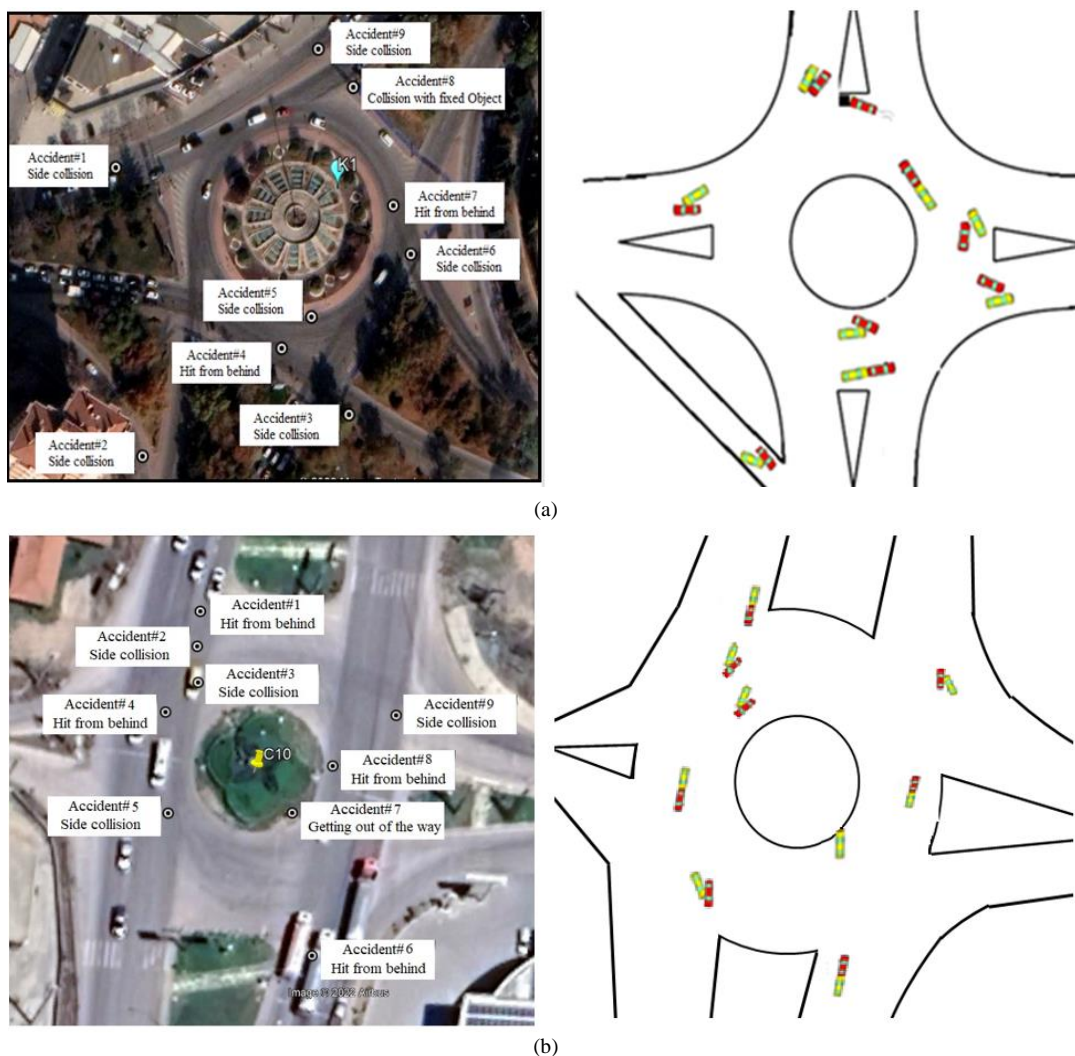


Figure 4. a) Types of crashes at the roundabout (K1), b) Types of crashes at the roundabout (C10)

Stepwise regression analysis was carried out to validate the results obtained from the AHP analytical method. Statistical analysis showed that all regression parameters were statistically significant at a 95% confidence level, with a coefficient of multiple determination of 0.91 ($R^2=0.83$, Adj. R-Sq=0.56, F-Value 2.9). The model summary is presented in Table 6. In this model, X_{11} , X_{13} , X_{14} and X_{16} are geometric parameters that explained about 39%, compared to 36.6% by the AHP method. On the other hand, X_1 , X_2 , X_3 and X_4 are traffic operation parameters that also explained around 24%, compared to 22.7% by the AHP. Finally, X_6 represented the traffic distribution (left turn), X_8 and X_{10} traffic composition (heavy truck and mini truck respectively), and X_{22} road surface condition. However, almost same results have been reported by various researches [4, 11, 16].

Table 6. Statistical model summary

R	R Square	Adjusted R Square	Std. Error of the Estimate	R Square Change	F Change	df1	df2	Sig. F Change
0.913 ^a	0.833	0.547	1.246	0.833	2.914	12	7	0.082

a. Predictors: (Constant), X16, X4, X22, X10, X14, X2, X8, X13, X6, X3, X1, X11

The last three independent parameters (X₆, X₈, and X₂₂) in the statistical analysis together explained about 32%, compared to 35% by the AHP method. In conclusion, the general model in the statistical analysis explains the issue of traffic accidents at the roundabouts by 91%, including all the parameters in the AHP except time of day, which is removed from the model. The analysis of variance and regression coefficients is presented in Table 6. Moreover, the ANOVA values of the model are presented in Table 7. Moreover, Figure 5 indicates that the implementation of the regression analysis in this study is not illogical since the observed and expected cumulative probabilities are almost identical. Minor result biases can be neglected. However, the ANOVA outcomes support the outcomes obtained from the integrated MRSS-AHP model that has been developed in this study.

Table 7. ANOVA table of the model

Model	Sum of Squares	df	Mean Square	F	Sig.
1 Regression	54.326	12	4.527	2.914	0.082 ^a
Residual	10.874	7	1.553		
Total	65.200	19			

a. Predictors: (Constant), X16, X4, X22, X10, X14, X2, X8, X13, X6, X3, X1, X11

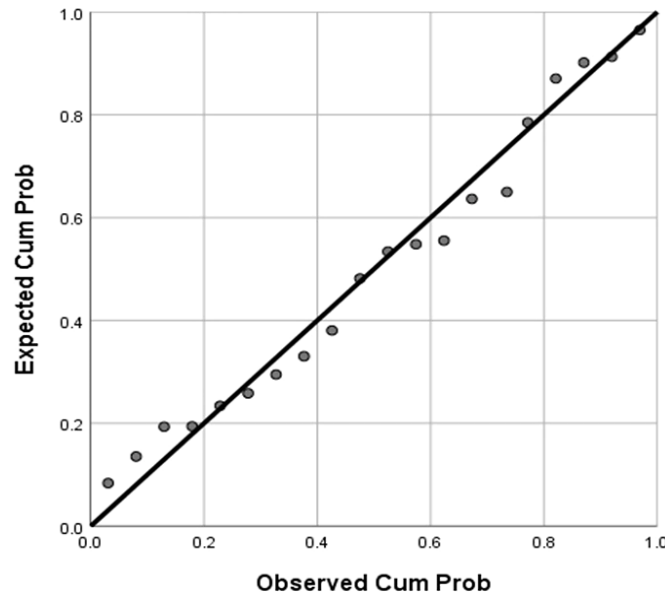


Figure 5. Normal P-P plots of regression standardized residual, (SPSS output)

4. Conclusion

Traffic accidents are a critical issue, especially considering the surge in vehicle numbers, accident victims, and related injuries. Though roundabouts reduce congestion at intersections, soaring traffic volumes cause them to become traffic accident hotspots. Most of the reported causes of traffic accidents were collected from the literature and categorized into primary groups. Each main group includes sub-criteria that share common linkages. AHP is the MCDM method capable of simultaneously handling quantitative and qualitative data. AHP was used in this study to determine most causes of accidents at roundabouts. The results were then validated using the ANOVA tool. Furthermore, the outcomes of MRSS and AHP are almost identical with the ANOVA analysis. The geometric design, represented mainly by the conflicting length and number of legs at the roundabout, is the leading cause of traffic accidents, followed by traffic operation, represented by queue length. Furthermore, the wet road surface also increases the accident potential at roundabouts. To reduce the number of accidents and resulting casualties at roundabouts, it is essential to determine the leading causes of accidents. Hence, this study will help decision-makers and local authorities design, manage, and control traffic appropriately at intersections and roundabouts. However, to improve traffic safety at the current roundabouts, it is recommended to reduce the allowable vehicle speed and apply traffic monitoring and inelegant management methods to segregate vehicles in time and space. While for future and under-construction roundabouts, special attention should be given to the geometric design, especially the lane width, entrance, and exit of the roundabout conflicting length.

5. Declarations

5.1. Author Contributions

Conceptualization, G.S., M.E., M.F.A.S., and M.A.; methodology, G.S. and M.K.Y.; software, G.S.; formal analysis, G.S. and M.K.Y.; data curation, G.S.; writing—original draft preparation, G.S., M.E., M.F.A.S., and M.A.; writing—review and editing, G.S., M.E., M.F.A.S., and M.A. All authors have read and agreed to the published version of the manuscript.

5.2. Data Availability Statement

The data presented in this study are available in the article.

5.3. Funding

The authors would like to express gratitude to their institutes for the financial support they provided to publish the article.

5.4. Institutional Review Board Statement

The study was conducted in accordance with the Declaration of Helsinki, and approved by the Institutional Review Board (or Ethics Committee) of Aqaba University of Technology (protocol code AUT-22-011-03 and date of approval 18 October 2022)

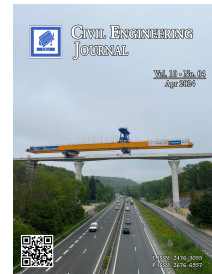
5.5. Conflicts of Interest

The authors declare no conflict of interest.

6. References

- [1] Čulík, K., Harantová, V., & Kalašová, A. (2019). Traffic Modelling of the Circular Junction in the City of Žilina. *Advances in Science and Technology Research Journal*, 13(4), 162–169. doi:10.12913/22998624/111476.
- [2] Ahmed, S. K., Mohammed, M. G., Abdulqadir, S. O., El-Kader, R. G. A., El-Shall, N. A., Chandran, D., Rehman, M. E. U., & Dhama, K. (2023). Road traffic accidental injuries and deaths: A neglected global health issue. *Health Science Reports*, 6(5), 1240. doi:10.1002/hsr2.1240.
- [3] Magableh, G. M., & Mumani, A. A. (2022). Simulation Based-MCDM Approach for Evaluating Traffic Solutions. *Promet - Traffic & Transportation*, 34(1), 117–133. doi:10.7307/ptt.v34i1.3842.
- [4] Theofilatos, A. (2017). Incorporating real-time traffic and weather data to explore road accident likelihood and severity in urban arterials. *Journal of Safety Research*, 61, 9–21. doi:10.1016/j.jsr.2017.02.003.
- [5] Suleiman, G. M., Younes, M. K., Ergun, M., & Al Omari, K. (2021). Effect of transportation parameters on traffic accident in urban areas comparison study of anfis with statistical analysis. *International Journal of Safety and Security Engineering*, 11(2), 129–134. doi:10.18280/ijssse.110201.
- [6] Bil, M., Andrášik, R., & Janoška, Z. (2013). Identification of hazardous road locations of traffic accidents by means of kernel density estimation and cluster significance evaluation. *Accident Analysis & Prevention*, 55, 265–273. doi:10.1016/j.aap.2013.03.003.
- [7] Ahmad, F., Shah, Z., & Al-Fagih, L. (2023). Applications of evolutionary game theory in urban road transport network: A state of the art review. *Sustainable Cities and Society*, 98, 104791. doi:10.1016/j.scs.2023.104791.
- [8] Han, Y., Wang, M., & Leclercq, L. (2023). Leveraging reinforcement learning for dynamic traffic control: A survey and challenges for field implementation. *Communications in Transportation Research*, 3, 100104. doi:10.1016/j.commtr.2023.100104.
- [9] Alkaabi, K. (2023). Identification of hotspot areas for traffic accidents and analyzing drivers' behaviors and road accidents. *Transportation Research Interdisciplinary Perspectives*, 22, 100929. doi:10.1016/j.trip.2023.100929.
- [10] Theofilatos, A., & Yannis, G. (2017). Investigation of powered 2-wheeler accident involvement in urban arterials by considering real-time traffic and weather data. *Traffic Injury Prevention*, 18(3), 293–298. doi:10.1080/15389588.2016.1198871.
- [11] Montella, A. (2011). Identifying crash contributory factors at urban roundabouts and using association rules to explore their relationships to different crash types. *Accident Analysis and Prevention*, 43(4), 1451–1463. doi:10.1016/j.aap.2011.02.023.
- [12] Silva, S., Alçada-Almeida, L., & Dias, L. C. (2014). Biogas plants site selection integrating Multicriteria Decision Aid methods and GIS techniques: A case study in a Portuguese region. *Biomass and Bioenergy*, 71, 58–68. doi:10.1016/j.biombioe.2014.10.025.
- [13] Cheng, C., Chen, Y., & Li, T. (2011). An AHP method for road traffic safety. *Proceedings - 4th International Joint Conference on Computational Sciences and Optimization, CSO 2011*, 305–308. doi:10.1109/CSO.2011.65.

- [14] Younes, M. K., Basri, N. E. A., Nopiah, Z. M., Basri, H., & Abushammala, M. F. M. (2015). Use of a Combination of MRSS-ANP for Making an Innovative Landfill Siting Decision Model. *Mathematical Problems in Engineering*, 2015. doi:10.1155/2015/381926.
- [15] Mirzahosseini, H., Sedghi, M., Motevalli Habibi, H., & Jalali, F. (2020). Site selection methodology for emergency centers in Silk Road based on compatibility with Asian Highway network using the AHP and ArcGIS (case study: IR Iran). *Innovative Infrastructure Solutions*, 5, 1-14. doi:10.1007/s41062-020-00362-3.
- [16] Khorasani, G., Mirmohammadi, F., Motamed, H., Fereidoon, M., & Tatari, A. (2013). Application of Multi Criteria Decision Making Tools in Road Safety Performance Indicators and Determine Appropriate Method with Average Concept. *International Journal of Innovative Technology and Exploring Engineering*, 3(5), 173–177.
- [17] Ngoc, A. M., & My Thanh, T. T. (2020). Towards the Development of Traffic Safety Strategies in Developing Countries: Analysis of Road Users' Perspective. *Transportation Research Procedia*, 48, 1278–1287. doi:10.1016/j.trpro.2020.08.149.
- [18] Yang, Y., Easa, S. M., Lin, Z., & Zheng, X. (2018). Evaluating Highway Traffic Safety: An Integrated Approach. *Journal of Advanced Transportation*, 4598985. doi:10.1155/2018/4598985.
- [19] Ali, F., Ali, A., Imran, M., Naqvi, R. A., Siddiqi, M. H., & Kwak, K. S. (2021). Traffic accident detection and condition analysis based on social networking data. *Accident Analysis and Prevention*, 151, 105973. doi:10.1016/j.aap.2021.105973.
- [20] Le, K. G., Liu, P., & Lin, L. T. (2020). Determining the road traffic accident hotspots using GIS-based temporal-spatial statistical analytic techniques in Hanoi, Vietnam. *Geo-Spatial Information Science*, 23(2), 153–164. doi:10.1080/10095020.2019.1683437.
- [21] Klaylee, J., Iamtrakul, P., & Sornlertlamvanich, V. (2022). Identification of Suburban Motorcycle Traffic Accident Hotspots Using GIS-Based Spatial Analysis. *2022 10th International Conference on Traffic and Logistic Engineering, ICTLE 2022*, 35–40. doi:10.1109/ICTLE55577.2022.9902103.
- [22] Lin, D. J., Yang, J. R., Liu, H. H., Chiang, H. Sen, & Wang, L. Y. (2022). Analysis of Environmental Factors on Intersection Accidents. *Sustainability (Switzerland)*, 14(3), 1764. doi:10.3390/su14031764.
- [23] Krueger, T., Page, T., Hubacek, K., Smith, L., & Hiscock, K. (2012). The role of expert opinion in environmental modelling. *Environmental Modelling and Software*, 36, 4–18. doi:10.1016/j.envsoft.2012.01.011.
- [24] Younes, M. K., Sulaiman, G., & Al-Mashni, A. (2020). Integration of Traffic Management and an Artificial Intelligence to Evaluate Urban Air Quality. *Asian Journal of Atmospheric Environment*, 14(3), 225–235. doi:10.5572/ajae.2020.14.3.225.
- [25] Abbood, A. N., & Fadel, L. S. (2023). Study of Basic Traffic Elements for Pedestrians Movement and their Impacted-on Level of Service Efficiency in Urban Area. *Journal of Ecological Engineering*, 24(8), 322–328. doi:10.12911/22998993/166453.
- [26] Hsiao, H., Chang, J., & Simeonov, P. (2018). Preventing Emergency Vehicle Crashes: Status and Challenges of Human Factors Issues. *Human Factors*, 60(7), 1048–1072. doi:10.1177/0018720818786132.
- [27] Younes, M. K. (2020). Integration of Mathematical Median Ranked Set Sample and Decision Making AHP Tools to Enhance Decentralized Wastewater Treatment System. *Journal of Water Chemistry and Technology*, 42(6), 472–479. doi:10.3103/s1063455x20060132.
- [28] Brilon, W. (2011). Studies on roundabouts in Germany: lessons learned. *3rd International TRB roundabout Conference*, 17-20 May, 2011, Carmel, Indiana.
- [29] Saccomanno, F. F., Cunto, F., Guido, G., & Vitale, A. (2008). Comparing safety at signalized intersections and roundabouts using simulated rear-end conflicts. *Transportation Research Record*, 2078(2078), 90–95. doi:10.3141/2078-12.
- [30] Alshannaq, M., & Imam, R. (2020). Evaluating the safety performance of roundabouts. *Transport Problems*, 15(1), 141–152. doi:10.21307/TP-2020-013.



Monitoring Physiological State of Drivers Using In-Vehicle Sensing of Non-Invasive Signal

Siti Fatimah Abdul Razak ^{1*}, Sharifah N. M. Sayed Ismail ¹, Bryan Hii Ben Bin ¹,
Sumendra Yogarayan ¹, Mohd Fikri Azli Abdullah ¹, Noor Hisham Kamis ¹

¹ Faculty of Information Science & Technology, Multimedia University, Melaka, Malaysia.

Received 27 October 2023; Revised 22 March 2024; Accepted 27 March 2024; Published 01 April 2024

Abstract

Eighty percent of traffic accidents are caused by human error, called hypo vigilance, stemming from drowsiness, stress, or distraction while driving. This poses a significant threat to road safety. An electrocardiogram (ECG) is often used to monitor drivers' health. Thus, enhancing vehicles with Internet of Things (IoT) sensors and local analytical databases becomes crucial for real-time detection and transmission of relevant health data to avoid things that compromise road traffic safety. This study introduces a cost-effective in-vehicle ECG sensing prototype using an AD8232 sensor integrated with an Arduino Uno and an AD8232 Wi-Fi module placed on the steering wheel to monitor the driver's heart signal while driving. Short-term heart rate variability (HRV) features were computed through Python from the acquired ECG data, and supervised machine learning techniques such as AdaBoost, Random Forest, Naïve Bayes, and Support Vector Machine (SVM) classified the features into normal and abnormal classes. Naive Bayes exhibited the highest accuracy (90.91%) and F1 score (85.71%), surpassing Random Forest's lower accuracy (63.64%) and F1 score (50.00%). These findings indicate the prototype's potential as a valuable tool for ensuring safe and efficient driving, proposing integration into standard vehicle safety systems for enhanced road traffic safety.

Keywords: ADAS; Driver Monitoring System; ECG; Vehicle Safety.

1. Introduction

Road accidents pose a significant threat to car drivers. Despite the various efforts made by the authorities to improve traffic and road safety, traffic accidents have increased in recent years. According to a study conducted by the Malaysian Institute of Road Safety Research (MIROS), one of the main causes of road accidents is human behavior, namely hypo-vigilance among drivers, a condition when individuals experience decreased sensory sensitivity and responsiveness due to factors such as drowsiness, fatigue, the influence of alcohol or drugs, stress, excessive cognitive demands, or distraction from the use of smartphones or GPS devices while driving [1–4]. In addition, the driver's health condition can also trigger a state of hypo-alertness. If an emergency occurs while driving, the driver only has 0.15 seconds to respond to the situation to prevent unwanted things from happening [2]. Thus, upgrading vehicles with Internet of Things (IoT) sensors connected to the Internet and local analytical databases to identify and address cognitive and physiological problems in real-time becomes an innovative approach that could revolutionize road safety by providing new perspectives on driver-related challenges [5].

* Corresponding author: fatimah.razak@mmu.edu.my

<http://dx.doi.org/10.28991/CEJ-2024-010-04-014>



© 2024 by the authors. Licensee C.E.J, Tehran, Iran. This article is an open access article distributed under the terms and conditions of the Creative Commons Attribution (CC-BY) license (<http://creativecommons.org/licenses/by/4.0/>).

The latest research and theoretical approach for monitoring the physiological state of drivers using in-vehicle sensing of non-invasive signals involves biometric sensors, artificial intelligence (AI), and virtual reality (VR) technologies. These approaches aim to detect and classify stress levels in drivers in real-time [6]. One study explores the neurophysiological effects of visual, auditory, and higher-order cognitive distraction on young drivers using electroencephalograms (EEG) [7]. Another study also utilized EEG to calculate the correlation between brain neural activity and driving behavior [8]. The proposed scheme in Yang et al.'s study accurately detects driver alertness using face landmarks, head poses, and gaze direction, offering high classification accuracy in actual road driving conditions [9].

While EEG and facial point features are the most studied physiologic measures of vigilance while driving, photoplethysmography (PPG) and other biometric sensors are integrated into the in-vehicle sensing of non-invasive signals for the driver's monitoring system. One study explores remote photoplethysmography (rPPG) to monitor drivers' cardio-respiratory functions, focusing on upgrading the single-wavelength NIR setup to multi-wavelength for more robust heart-rate monitoring [10]. Another study also employed rPPG with quality-guided spectrum peak screening that allowed tracking of the driver's heart rate under realistic driving conditions [11]. Besides, the study from Gharamohammadi et al. focuses on using Frequency Modulated Continuous Wave (FMCW) radars incorporated in a vehicle for breathing pattern monitoring to detect breathing abnormalities during driving [12]. Additionally, a proposed approach suggests using selected biosignals, such as EMG, GSR, and respiration rate, combined with machine learning models to classify stress levels in drivers [13].

The electrocardiogram (ECG) signal is also one of the methods often used to track a driver's health or attention. The ECG has several phases: the P signal, the QRS complex, and the T signal [5]. The driver's physical condition is commonly evaluated using the QRS complex because it has a higher amplitude and signal-to-noise ratio (SNR) than the P and T signals [14, 15]. Based on measurements of electrical properties, the ECG continuously records cardiac changes in heart rate, offers cardiac response information that describes cardiac activity, and measures the body's level of physical, psychological, and physical fatigue [16]. The signals have received increased attention and have been included in the in-vehicle sensing of advanced driver monitoring systems that detect, record, and transmit relevant health information to avoid things that could compromise traffic safety [5, 14].

Furthermore, the driver's physical condition can be evaluated non-invasively using parameters such as heart rate and heart rate variability (HRV), eliminating the need to put the driver at risk [17]. The HRV power spectrum analysis of the R-to-R time series (0.15–0.4 Hz) from two to five minutes of recording gives three frequency bands: the very low-frequency band (0.003-0.04 Hz), the low-frequency band (0.04-0.15 Hz), and the high-frequency band [18]. In a healthy state, the instantaneous heart rate fluctuates within a specific range of variation [19]. However, HRV data also fluctuates between individuals and over time within individuals, depending on internal and external conditions [20].

Several studies have used HR and HRV from the ECG as primary data to investigate the driver's condition. For example, Mathissen et al. [21] investigate tasks that could potentially induce stress in the driver to assess the driver's condition. These tasks included sequential memory tasks, sing-a-song stress tests, and noise exposure tests. Their study used Ag/AgCl (ECG) electrodes to obtain HR and HRV for further research. They found that sequential memory tasks strongly activated the sympathetic nervous system, resulting in increased HR and decreased HRV in response to stress-inducing secondary tasks. Aswathi et al. [22] developed a drowsiness detection system based on HRV. They compared several machine learning algorithms, including random forests, support vector machines, decision trees, Naive Bayes, and 1-dimensional convolutional neural networks. The algorithm was tested on the Physikalisch-Technische Bundesanstalt's (PTB) diagnostic ECG data set. The authors claim that the CNN 1D approach is superior to traditional machine learning, with an accuracy difference of 0.94 to 14 percent. They also noted that analyzing HRV could help reduce accidents caused by drowsy driving. A study by Arefnezhad et al. [23] used eleven features extracted from the HRV collected from the ECG using the g.Nautilus™ device classifies drowsiness into three different classes: alert, moderate drowsy, and extremely drowsy. HRV characteristics were classified using random forest and K-nearest neighbor techniques and obtained 62% and 64% accuracy, respectively. Ebrahimian et al. [24] propose a multi-level classification of drowsiness using two types of signals: ECG and respiratory signals. The signals were attached to the driver using several electrodes, and the experiment was performed in a controlled setup using a driving simulator by K. N. Toosi University of Technology. HRV, power spectral density, and respiration rate were considered for the classification using CNN-LSTM of a three-level classification (wakeful, moderately drowsy, and extremely drowsy) and a five-level classification (wakeful, slightly drowsy, moderately drowsy, very drowsy, and extremely drowsy). The accuracy obtained for three- and five-level classification is 91% and 67%, respectively.

Previous studies about driver performance have demonstrated a connection between these measurements and variations in drivers' attention [25, 26]. Consequently, in-vehicle gadgets and cameras are projected to dominate the detection process. At the same time future uses are expected to include equipment that can identify health issues and irregularities by driving as usual. For instance, a comparison study was conducted to compare the contact Biopac system with the non-contact Plessey Electric Potential Integrated Circuit (EPIC) system to understand levels of vehicle autonomy affecting human behavior and public perception. The study demonstrates that the inside-seat EPIC sensor can be used to accurately replicate autonomous driving scenarios with minimal movement artifacts [27].

Driver applications led to the development of non-invasive ECG recording techniques, such as the integration of sensors into the steering wheel [28]. To enable long-term electrocardiogram (ECG) monitoring and continuous in-vehicle heart rate monitoring while driving, thin, flexible polyurethane electrodes were developed [29]. Another study proposed a system that integrates a heart-rate sensor, Global Positioning System (GPS), and Global System for Mobile Communications (GSM) modules into the steering wheel to detect the driver's pulse rate and dynamically inform the rescue party about the driver's wellness to avert accidents [30]. Similarly, an unobtrusive monitoring approach was applied to track the vital signs of drivers, including heart-rate activities and breathing activities. Sensors were placed at the steering wheel and backseat of the vehicle [31].

Since the number of accidents worldwide keeps increasing yearly, knowing the driver's heart condition in advance may help avoid accidents on the road. However, equipment or hardware that can test heart conditions is very expensive. Therefore, many drivers are unaware of their heart conditions because they are unwilling to go to the clinic or hospital to check their heart condition due to time and cost constraints. Additionally, previous studies mostly focused on classifying hypo-vigilance states such as fatigue, drowsiness, or stress. In the current system, drivers are not equipped with an indicator to receive warnings if their heart rate is irregular. This caused the driver not to notice if they had heart problems like chest pains or, even worse, loss of consciousness, which makes them unable to contact a health provider for assistance [5]. Therefore, this study will build a low-cost in-vehicle sensing system for ECG signals and monitor the driver's heart rate variability. This study will collect the data while the driver is driving and gather information from HRV using built-in ECG sensors on a steering wheel to classify the driver's cardiac health as normal or abnormal. The system developed in this study hoped to enable users to monitor their heart condition regularly, even while driving.

This paper is organized as follows: Section 2 describes the related works, while Section 3 presents the research method applied in this study. Section 4 presents the results and analysis of this study. The discussion is elaborated in Section 5, and lastly, Section 6 provides the conclusion of this study.

2. Research Methodology

The project's primary goal is to develop an automatic heart rate variability monitoring device for passenger vehicle drivers that does not involve human interference to determine and alert the driver immediately with a light signal when the heart rate variability is abnormal. Hence, a prototype of the HRV monitoring device was developed to demonstrate the in-vehicle sensing of ECG signals and monitoring the driver's heart rate variability. Figure 1 shows a circuit diagram of the system for a clearer view of the prototype components. The hardware used to build this prototype consists of several IoT devices and microcontroller sensors, which are:

- Silver-colored woven conductive material
- Car steering wheel
- Steering cover
- ECG AD8232 sensor
- Arduino Uno
- ESP 8266 Wi-Fi Module
- USB 2.0 Cable Type A/B
- 8.5 × 5.5 cm mini breadboard
- 40pin Men to Men, 40pin Women to Women, Breadboard Jumper Wires, Ribbon Cables Kit
- Adafruit Neo Pixel LED Ring
- 12V Battery

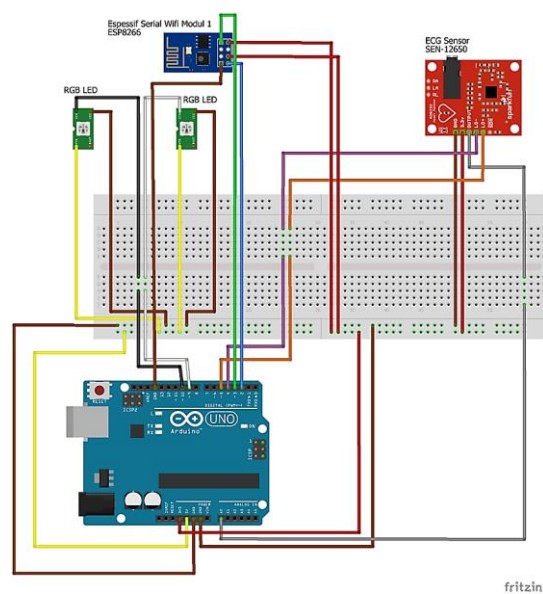


Figure 1. System Circuit Diagram

Two 7×7 pieces of silver-colored woven conductive material made of Copper and Nickel-plated nylon were placed at the 9-3 position of the steering wheel. The ECG AD8232 sensor was stuck together at the steering wheel to enable the transmission of the physiological signal from the conductive paper to the sensor when drivers are holding the steering wheel. The Arduino Uno Rev3 development board is utilized here to connect the ECG AD8232 sensor and AD8232 WiFi module via an 8.5×5.5cm mini breadboard packaged in a 4.8×3.2×1.5-inch enclosure. Once the AD8232 sensor begins to monitor the driver's ECG signals, the data is sensed and sent to the Arduino to process and analyze the variability of the heartbeat every 5 minutes before being saved to a database using the ESP8266 WiFi Module. In this stage, the R-R interval will be computed based on the difference between the second peak time (ms) and the first peak time (ms), and the HRV features will be calculated based on the R-R interval obtained. An Adafruit Neo Pixel LED Ring was placed at the center of the steering wheel to provide visual alerts to the driver regarding the current situation and to respond appropriately (refer to Figure 2). For example, if the result shows a heart rate lower than the normal rate of "60" or higher than "120", the light will turn yellow; if there are any severe heart problems detected, the light will turn red; if there are no problems with the heartbeat, the light will remain green. All lights will refresh every 20 seconds. The result and signal data will be sent to ThingSpeak and saved to a local Excel file.



Figure 2. LED ring placement on the steering wheel

In an actual driving situation, the prototype of the HRV monitoring device will technically start as soon as the vehicle begins the engine. The prototype device will detect the driver's heartbeat once it senses the driver's hand gripping the steering wheel. The signal collected is transmitted to the Arduino for data processing and analysis of the heart rate variability every five minutes. This will trigger the alert signal when any event or problem suddenly occurs to the driver while driving. The system will also classify, store, and provide real-time heart rate results to the driver. Figure 3 shows an overview of the system flow. In addition, before implementing this monitoring tool in real-life driving situations, an experiment is carried out in a controlled laboratory environment for the performance evaluation of the prototype. The following subsection will provide more details about the project and prototype.

2.1. Electrocardiogram (ECG) Signals Acquisition

A call for voluntary participants was made a week before the actual experiment took place. On the experimental day, the volunteers were briefed on the experimental setup and processes. The volunteers were asked to determine if they were unfit, which would make them unsuitable to participate. Ten of the volunteers had to be declined since they were feeling stressed and showed signs of not feeling well or tiredness, which would affect the data collection. Out of 35 volunteers, 25 of them (13 male and 12 female) agreed to participate and complete the experiment. The participants were asked to read and sign a consent form to indicate their agreement to take part in the experiment as approved by the organization's Ethical Committee. In addition, based on a brief preliminary questionnaire administered to the participants, they reported no history of heart-related problems, including shortness of breath, asthma, or experienced tight chest. The participants were asked about their food and beverage intake before data recording.

Each participant was asked to sit upright and hold the steering wheel for 5 minutes while listening to music or watching a short video that made them feel calm and peaceful. The average temperature of the experimental laboratory was set to 25 degrees Celsius and adjusted if necessary. During this period, their ECG signals were obtained, and the system's behavior was monitored by one of the research team members. The raw ECG data is available at the Zenodo repository (10.5281 / zenodo.7546094).

In addition, to prove the basic correctness and applicability of the prototype device with existing ECG devices, clinical ECG equipment (ADInstruments ML856 PowerLab 26t) was used for testing purposes and to compare the similarity of the collected data. A standard 3-electrode ECG signal is recorded for 5 minutes using a PowerLab with a positive electrode attached to the left wrist, a negative electrode to the right wrist, and a ground electrode to the right leg.

The acquired ECG signals were pre-processed to remove noise from the individuals' movement, respiration, and muscle electrical activity. In this study, 50 Hz notch filtering and a bandpass filter of 0.75 Hz to 35 Hz were applied to remove the noise and minimize the environmental noise or technological aberrations caused by analog and digital signal processing that might affect heart rate variability measurements as recommended by Hejjel [32]. Moreover, HRV values' accuracy for short-term recordings depends on robust digital infinite impulse response (IIR) filters, such as analog models, which can provide an NN-interval series adequate to reflect physiological signals [33].

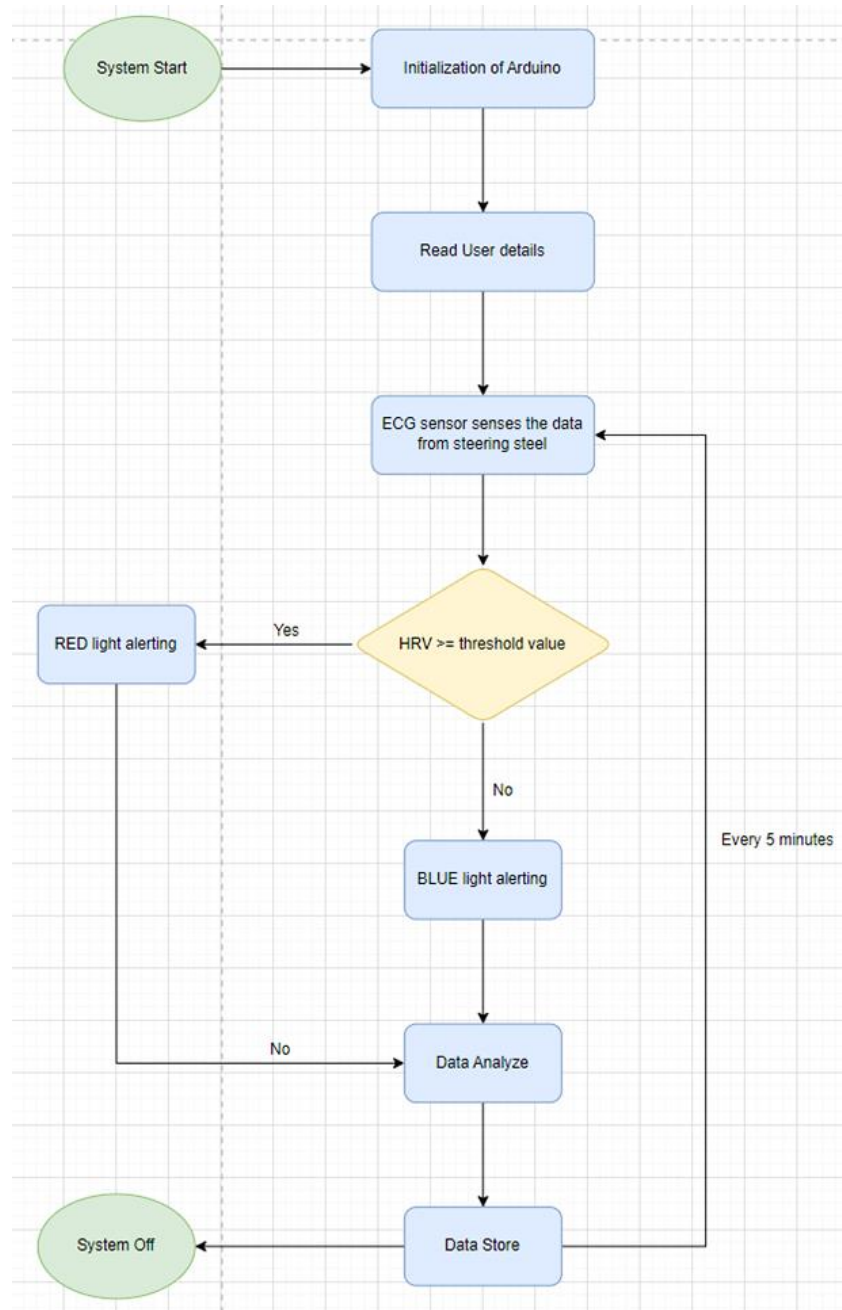
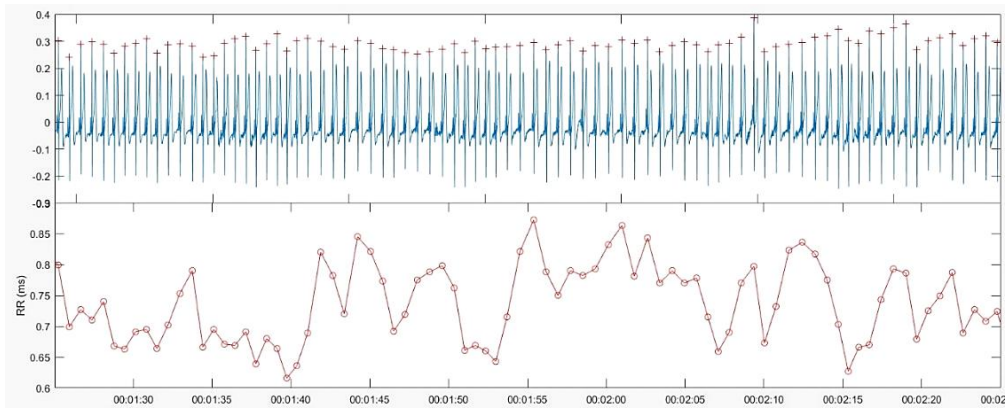


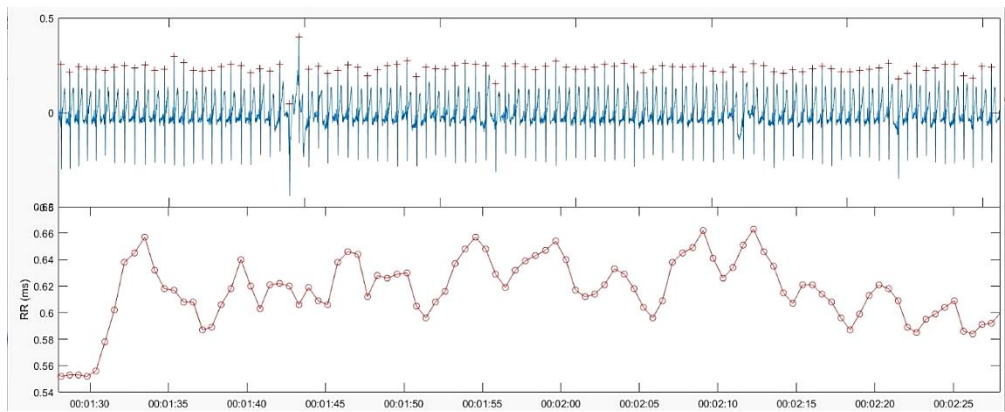
Figure 3. System flow chart

2.2. Computation of Heart Rate Variability (HRV)

The R-R interval, RR_i , is usually computed based on the difference between the peak, R_{i+n} , and the previous peak, R_i , where i is the order of the peaks ($i=1, 2, \dots, n$). This study used two settings to compute the RR_i : 1) a Python code, and 2) the HRVAnalysis Toolkit 1.2 [34]. In the first setting, Python code was written to automatically convert all the filtered ECG data and get the R-R interval values from the ECG data into an Excel file. For the second setting, the R-R interval was computed by feeding the raw ECG data into the toolkit, and it will automatically give the R-R interval as the output. LabChart Lightning software extracted and visualized the raw data from both settings. The ECG patterns and sample RR plots based on participants from PowerLab (refer to Figure 4) were compared with those from the prototype device (refer to Figure 5).

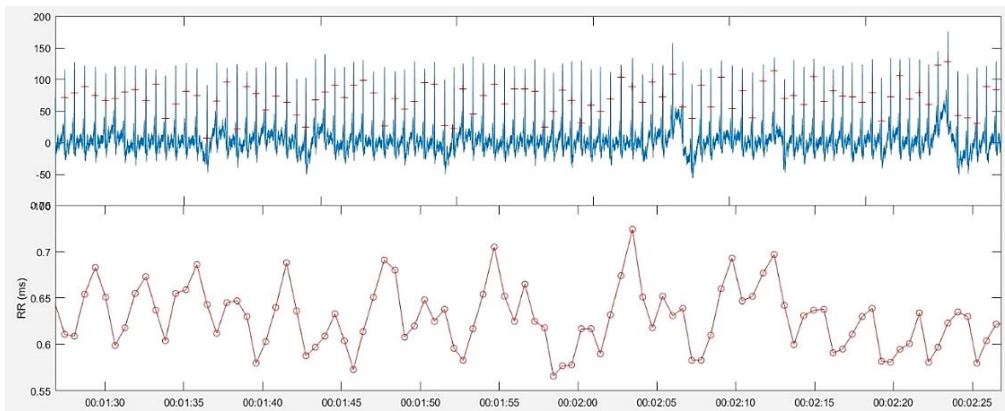


(a) Subject 1

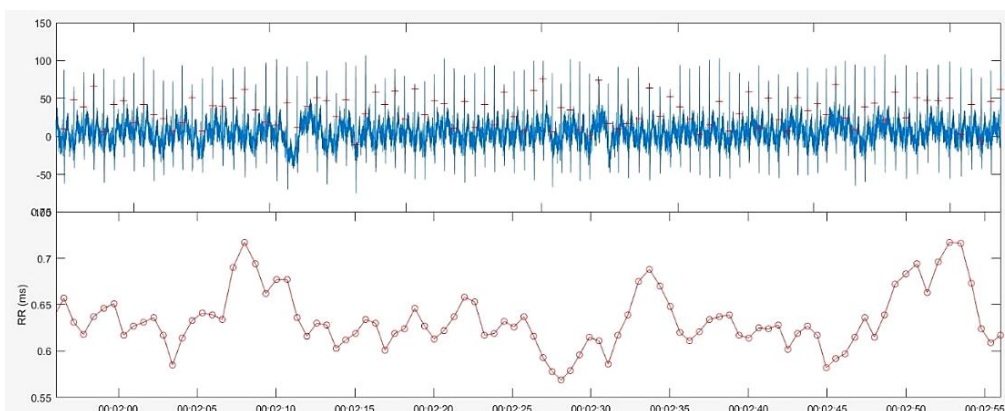


(b) Subject 2

Figure 4. Sample RR plots from PowerLab



(a) Subject 1



(b) Subject 2

Figure 5. Sample RR plots from the prototype device

In line with the ADInstruments ML856 PowerLab 26T, we observed a zero autocorrect RR value for all participants when utilizing our prototype system. Consequently, there is no requirement to identify and rectify abnormal RR intervals that deviate substantially from the expected pattern to enhance the accuracy and dependability of consequent HRV measures. The ECG sensors integrated into the prototype device effectively obtain ECG signals with minimal noise, artifacts, and other error types that may introduce spurious RR intervals.

HRV can be quantified in the time-domain, frequency-domain, and nonlinear analyses. In general, younger people have a higher HRV score than older people, and men frequently have a higher HRV score than women. Athletes have higher heart rate variability than non-athletes; within that category, endurance athletes have a higher HRV than strength athletes. The HRV score referred to in this study is based on the published age-gender-specific HRV range derived from the Elite HRV platform, accessible at <https://elitehrv.com/normal-heart-rate-variability-age-gender> and shown in Table 1. The normal range for males aged 18–25 is between 60.16 and 77.2, whereas the normal range for females is between 55.1 and 75.08.

Table 1. Age-gender specific HRV score

Age Range	Gender	Ln (RMSSD)	HRV Score
18-25	Male	4.46 ± 0.55	68.68 ± 8.52
	Female	4.23 ± 0.65	65.09 ± 9.99
26-35	Male	4.19 ± 0.63	64.48 ± 9.69
	Female	4.02 ± 0.69	61.83 ± 10.59
36-45	Male	3.92 ± 0.64	60.26 ± 9.92
	Female	3.82 ± 0.68	58.72 ± 10.45
46-55	Male	3.68 ± 0.65	56.65 ± 9.94
	Female	3.73 ± 0.69	57.35 ± 10.57
56-65	Male	3.46 ± 0.72	53.27 ± 11.07
	Female	3.48 ± 0.68	53.50 ± 10.44
65-75	Male	3.42 ± 0.83	52.66 ± 12.70
	Female	3.21 ± 0.72	49.35 ± 11.10
Above 75	Male	3.50 ± 0.98	53.88 ± 15.09
	Female	3.24 ± 1.09	49.85 ± 16.79

To further validate the effectiveness of the prototype device in obtaining ECG signals, the short-term HRV features proposed by Nunan et al. [35] were extracted using the open-source Python library and toolkit for analyzing HRV from ECG data, known as HeartPy [36]. Table 2 tabulates the extracted short-term HRV features using HeartPy, along with the associate description, mean value, standard deviation value, and normal range HRV features from Nunan et al. [35]. The class labeling process is done by marking the values within the normal range as zero, and values outside the normal range are scored 1 for all HRV features. If the total mark is below 4, the HRV is labeled normal; if the total mark is four or higher, the HRV is labeled abnormal.

Table 2. Short-term HRV features

Feature Name	Units	Description	Mean	Standard Deviation	Range
IBI	ms	Interbeat interval	926	90	785 - 1160
SDNN	ms	Standard deviation of NN intervals	50	16	32 - 93
RMSSD	ms	Root mean square of successive R-R intervals differences	42	15	19 - 75
LF	ms ²	Absolute power of the low-frequency band	519	291	193 - 1009
LF	nu	Relative power of the low-frequency band in normal units	52	10	30 - 65
HF	ms ²	Absolute power of the high-frequency band	657	777	83 - 3630
HF	nu	Relative power of the high-frequency band in normal units	40	10	16 - 60
LF/HF	ms ²	Ratio of LF-to-HF power	2.8	2.6	1.1 - 11.6

3. Results and Discussion

In this study, a range of supervised machine learning approaches, including AdaBoost, Random Forest, Naïve Bayes, and Support Vector Machine (SVM), were utilized to classify the HRV features. These four supervised machine learning approaches were chosen due to the excellent performance achieved in various monitoring systems, such as emotion, stress, and fatigue monitoring [13, 22]. AdaBoost is an ensemble learning method that combines multiple weak learners (usually decision trees) and assigns greater weight to misclassified data points in each repetition, allowing subsequent weak learners to focus on previously misclassified examples. The final prediction is a weighted combination of predictions from all weak students, with the more accurate weak students having a higher influence. Random forests are another ensemble learning algorithm that combines multiple decision trees for classification tasks. Models make predictions by following some rules or results, where the final prediction is obtained by aggregating the predictions of all individual trees by a majority vote.

Naive Bayes is a simple probability classification based on Bayes' Theorem and the assumption of independence between features. This theorem is a mathematical formula that can calculate the probability of an event occurring, given that another event has occurred. It works by calculating the probability of each data point belonging to each class and then assigning the data points to the class with the highest probability. SVM is a supervised learning algorithm that looks for hyperplanes in the data that best separate the data points between classes.

The performance of the models was evaluated using two widely used metrics in machine learning: accuracy and F1 score. Accuracy, being an intuitive measure of model performance, is commonly used in balanced datasets where false positives and false negatives are equally costly. The harmonic means of precision and recall, or the F1 score, provides a fair assessment of the two measurements. Given the small dataset, leave-one-out cross-validation was implemented. The accuracy and F1 score of the various techniques are summarized in Table 3.

Table 3. Classification results

Feature Name	Accuracy	F1 Score
AdaBoost	81.82	83.33
Random Forest	63.64	50.00
Naïve Bayes	90.91	85.71
Support Vector Machine	72.73	66.67

The Naïve Bayes method demonstrated strong performance with both high precision and recall, achieving the maximum accuracy and F1 score. In particular, the accuracy of 90.91% shows an almost 91% correct classification percentage for the entire dataset. This result implies that they are quite informative despite the small number of traits. The Naive Bayes technique can produce great generalization performance because it is based on a probabilistic model that represents the underlying data distribution. The Random Forest technique, in contrast, may show bias towards the dominant class, resulting in lower precision and F1 scores.

As a result of its ease of use and convenience, the prototype can acquire non-invasive signals from the steering wheel without disturbing the driver. The steering wheel is always within easy reach, and drivers do not have to wear additional devices, which can be uncomfortable or cumbersome. Thanks to its simplicity and convenience, the prototype can collect non-invasive signals from the steering wheel without upsetting the driver. Drivers do not have to wear extra equipment, which might be uncomfortable or heavy, and the steering wheel is always within easy reach. This enables continuous HRV monitoring without disrupting the driver's daily duties or making them uncomfortable.

4. Conclusion

Drivers' physiological states can be usefully gleaned via in-vehicle monitoring of non-invasive data from the drivers. In the present study, we suggest a prototype for detecting and monitoring heart rate variability (HRV), which is the fluctuation in the interval between heartbeats and regulates the body's response and relaxation response. A drop in HRV may occur when a motorist is stressed or exhausted. Therefore, tracking HRV can reveal details about the physiological state, amount of weariness, and general stress of the driver. Using this data, interventions can be created to support drivers in operating their vehicles safely and effectively. This technology can detect signs of driver impairment, such as drowsiness or distraction, allowing for timely alerts or interventions to prevent accidents. Additionally, monitoring non-invasive signals can help minimize distractions by enabling hands-free and voice-controlled interactions.

Additionally, as the use of autonomous vehicles spreads, it will be crucial to ensure that they are built with the utmost consideration for the security and comfort of their passengers. To achieve cost-effective goals, the ECG sensors in this investigation were mounted on the steering wheel. Data from the sensor and data from the lab instrument were compared. Machine learning techniques were also used to demonstrate the effectiveness of the approaches utilizing the prototype's obtained data because the use of non-invasive signals for HRV monitoring in driving scenarios is still relatively new.

The early results are encouraging, and this prototype has a great deal of promise to help promote safe and effective driving. This method might be included in the typical car safety systems as technology develops, giving drivers input in real-time, assisting in accident avoidance, and enhancing overall road safety. The prototype can also be improved by incorporating more sophisticated signal processing techniques, such as quality-guided spectrum peak screening (QSPS), to increase the precision and dependability of HRV measurements during the driving monitoring process. For instance, machine learning approaches could accomplish the automatic detection and elimination of noise, artifacts, and other defects that can skew HRV readings. Additionally, the temporal and frequency domains of HRV measurements might be modeled using sophisticated statistical techniques, which could increase the precision and dependability of subsequent analysis. Additional physiological sensors could be included to track physiological variables like skin conductance and pupil dilation, as well as other vital signs like blood pressure and oxygen saturation. This would provide a more thorough evaluation of the driver's physiological condition and could assist in spotting any health problems before they worsen.

5. Declarations

5.1. Author Contributions

Conceptualization, S.F.A.R. and S.Y.; methodology, S.F.A.R. and S.N.M.S.I.; software, B.H.B.B. and S.Y.; formal analysis, S.F.A.R., S.N.M.S.I., and B.H.B.B.; investigation, N.H.K.; resources, M.F.A.A.; writing—original draft preparation, S.F.A.R. and S.N.M.S.I.; writing—review and editing, S.F.A.R., S.N.M.S.I., and S.Y.; visualization, B.H.B.B.; supervision, S.F.A.R.; project administration, M.F.A.A.; funding acquisition, S.F.A.R. and S.Y. All authors have read and agreed to the published version of the manuscript.

5.2. Data Availability Statement

The data presented in this study are openly available in Zenodo: ECG datasets of young healthy adults at doi:10.5281/zenodo.7546094.

5.3. Funding

This research is funded by an external grant, TM R&D (RDTC/221046).

5.4. Acknowledgements

The authors would like to thank the Centre for Intelligent Cloud Computing (CICC) and Multimedia University (MMU) for their support and encouragement.

5.5. Conflicts of Interest

The authors declare no conflict of interest.

6. References

- [1] Lady, L., & Umyati, A. (2023). The Effects of Using Electronic Maps While Driving on The Driver Performance. *International Journal of Technology*, 14(5), 1029–1038. doi:10.14716/ijtech.v14i5.4778.
- [2] Hayawi, A. A., & Waleed, J. (2019). Driver's Drowsiness Monitoring and Alarming Auto-System Based on EOG Signals. 2019 2nd International Conference on Engineering Technology and Its Applications, IICETA 2019, 214–218. doi:10.1109/IICETA47481.2019.9013000.
- [3] Zainy, M. L. S., Pratama, G. B., Kurnianto, R. R., & Iridiastadi, H. (2023). Fatigue Among Indonesian Commercial Vehicle Drivers: A Study Examining Changes in Subjective Responses and Ocular Indicators. *International Journal of Technology*, 14(5), 1039–1048. doi:10.14716/ijtech.v14i5.4856.
- [4] Zuraida, R., & Abbas, B. S. (2020). The factors influencing fatigue related to the accident of intercity bus drivers in Indonesia. *International Journal of Technology*, 11(2), 342–352. doi:10.14716/ijtech.v11i2.3792.
- [5] Minea, M., Dumitrescu, C. M., & Costea, I. M. (2021). Advanced e-call support based on non-intrusive driver condition monitoring for connected and autonomous vehicles. *Sensors*, 21(24), 8272. doi:10.3390/s21248272.
- [6] Mateos-García, N., Gil-González, A. B., Luis-Reboredo, A., & Pérez-Lancho, B. (2023). Driver Stress Detection from Physiological Signals by Virtual Reality Simulator. *Electronics*, 12(10), 2179–2189. doi:10.3390/electronics12102179.
- [7] Goldsworthy, J., Watling, C. N., Rose, C., & Larue, G. (2024). The effects of distraction on younger drivers: A neurophysiological perspective. *Applied Ergonomics*, 114, 104–127. doi:10.1016/j.apergo.2023.104147.
- [8] Lan, Z., Zhao, J., Liu, P., Zhang, C., Lyu, N., & Guo, L. (2024). Driving fatigue detection based on fusion of EEG and vehicle motion information. *Biomedical Signal Processing and Control*, 92. doi:10.1016/j.bspc.2024.106031.

- [9] Yang, D., Wang, Y., Wei, R., Guan, J., Huang, X., Cai, W., & Jiang, Z. (2024). An efficient multi-task learning CNN for driver attention monitoring. *Journal of Systems Architecture*, 148, 103085. doi:10.1016/j.sysarc.2024.103085.
- [10] Wang, Z., Yang, X., Lu, H., Shan, C., & Wang, W. (2023). Benchmark of Physiological Model Based and Deep Learning Based Remote Photoplethysmography in Automotive Applications. *ICASSP 2023 - 2023 IEEE International Conference on Acoustics, Speech and Signal Processing (ICASSP)*, Rhodes Island, Greece. doi:10.1109/icassp49357.2023.10095078.
- [11] Gong, Z., Yang, X., Song, R., Han, X., Ren, C., Shi, H., Niu, J., & Li, W. (2024). Heart Rate Estimation in Driver Monitoring System Using Quality-Guided Spectrum Peak Screening. *IEEE Transactions on Instrumentation and Measurement*, 73. doi:10.1109/TIM.2024.3352710.
- [12] Gharamohammadi, A., Pirani, M., Khajepour, A., & Shaker, G. (2023). Multibin Breathing Pattern Estimation by Radar Fusion for Enhanced Driver Monitoring. *IEEE Transactions on Instrumentation and Measurement*, 73. doi:10.1109/TIM.2023.3345909.
- [13] Siam, A. I., Gamel, S. A., & Talaat, F. M. (2023). Automatic stress detection in car drivers based on non-invasive physiological signals using machine learning techniques. *Neural Computing and Applications*, 35(17), 12891–12904. doi:10.1007/s00521-023-08428-w.
- [14] Zeng, X., Wang, F., Wang, B., Wu, C., Liu, K. J. R., & Au, O. C. (2022). In-Vehicle Sensing for Smart Cars. *IEEE Open Journal of Vehicular Technology*, 3, 221–242. doi:10.1109/OJVT.2022.3174546.
- [15] Choi, Y., Han, S. I., Kong, S. H., & Ko, H. (2016). Driver status monitoring systems for smart vehicles using physiological sensors: A safety enhancement system from automobile manufacturers. *IEEE Signal Processing Magazine*, 33(6), 22–34. doi:10.1109/MSP.2016.2602095.
- [16] Murugan, S., Selvaraj, J., & Sahayadhas, A. (2020). Detection and analysis: driver state with electrocardiogram (ECG). *Physical and Engineering Sciences in Medicine*, 43(2), 525–537. doi:10.1007/s13246-020-00853-8.
- [17] Jung, S. J., Shin, H. S., & Chung, W. Y. (2014). Driver fatigue and drowsiness monitoring system with embedded electrocardiogram sensor on steering wheel. *IET Intelligent Transport Systems*, 8(1), 43–50. doi:10.1049/iet-its.2012.0032.
- [18] Meteier, Q., Capallera, M., Ruffieux, S., Angelini, L., Abou Khaled, O., Mugellini, E., Widmer, M., & Sonderegger, A. (2021). Classification of Drivers' Workload Using Physiological Signals in Conditional Automation. *Frontiers in Psychology*, 12, 1–18. doi:10.3389/fpsyg.2021.596038.
- [19] Arakawa, T. (2021). A review of heartbeat detection systems for automotive applications. *Sensors*, 21(18), 6112. doi:10.3390/s21186112.
- [20] Persson, A., Jonasson, H., Fredriksson, I., Wiklund, U., & Ahlstrom, C. (2021). Heart Rate Variability for Classification of Alert Versus Sleep Deprived Drivers in Real Road Driving Conditions. *IEEE Transactions on Intelligent Transportation Systems*, 22(6), 3316–3325. doi:10.1109/TITS.2020.2981941.
- [21] Mathissen, M., Hennes, N., Faller, F., Leonhardt, S., & Teichmann, D. (2022). Investigation of Three Potential Stress Inducement Tasks During On-Road Driving. *IEEE Transactions on Intelligent Transportation Systems*, 23(5), 4823–4832. doi:10.1109/TITS.2021.3112811.
- [22] Aswathi, C. D., Mathew, N. A., Riyas, K. S., & Jose, R. (2021). Comparison of Machine Learning Algorithms for Heart Rate Variability Based Driver Drowsiness Detection. *2021 2nd Global Conference for Advancement in Technology, GCAT 2021*, 1–7. doi:10.1109/GCAT52182.2021.9587733.
- [23] Arefnezhad, S., Eichberger, A., Frühwirth, M., Kaufmann, C., Moser, M., & Koglbauer, I. V. (2022). Driver Monitoring of Automated Vehicles by Classification of Driver Drowsiness Using a Deep Convolutional Neural Network Trained by Scalograms of ECG Signals. *Energies*, 15(2), 480. doi:10.3390/en15020480.
- [24] Ebrahimian, S., Nahvi, A., Tashakori, M., Salmanzadeh, H., Mohseni, O., & Leppänen, T. (2022). Multi-Level Classification of Driver Drowsiness by Simultaneous Analysis of ECG and Respiration Signals Using Deep Neural Networks. *International Journal of Environmental Research and Public Health*, 19(17), 10736. doi:10.3390/ijerph191710736.
- [25] Hu, X., & Lodewijks, G. (2020). Detecting fatigue in car drivers and aircraft pilots by using non-invasive measures: The value of differentiation of sleepiness and mental fatigue. *Journal of Safety Research*, 72(April), 173–187. doi:10.1016/j.jsr.2019.12.015.
- [26] Lemkaddem, A., Delgado-Gonzalo, R., Turetken, E., Dasen, S., Moser, V., Gressum, C., Sola, J., Ferrario, D., & Verjus, C. (2018). Multi-modal driver drowsiness detection: A feasibility study. *2018 IEEE EMBS International Conference on Biomedical & Health Informatics (BHI)*, Las Vegas, United States. doi:10.1109/bhi.2018.8333357.
- [27] Stephenson, A. C., Willis, R., & Alford, C. (2021). Using in-seat electrical potential sensors for non-contact monitoring of heart rate, heart rate variability, and heart rate recovery. *International Journal of Psychophysiology*, 169, 1–10. doi:10.1016/j.ijpsycho.2021.08.005.
- [28] Guettas, A., Ayad, S., & Kazar, O. (2019). Driver state monitoring system: A review. *ACM International Conference Proceeding Series*, 28, 1-7. doi:10.1145/3372938.3372966.

- [29] Warnecke, J. M., Ganapathy, N., Koch, E., Dietzel, A., Flormann, M., Henze, R., & Deserno, T. M. (2022). Printed and Flexible ECG Electrodes Attached to the Steering Wheel for Continuous Health Monitoring during Driving. *Sensors*, 22(11), 1–12. doi:10.3390/s22114198.
- [30] Priya, J., Reshmi, T. S., Gunasekaran, M. (2020). SSW: Smart Steering Wheel for Real-Time Heart Rate Monitoring of Drivers. *International Journal of Innovative Technology and Exploring Engineering*, 9(4), 3040–3043. doi:10.35940/ijitee.d1896.029420.
- [31] Leonhardt, S., Leicht, L., & Teichmann, D. (2018). Unobtrusive vital sign monitoring in automotive environments—A review. *Sensors*, 18(9), 1–38. doi:10.3390/s18093080.
- [32] Hejfel, L. (2004). Suppression of power-line interference by analog notch filtering in the ECG signal for heart rate variability analysis: To do or not to do? *Medical Science Monitor*, 10(1), 6–13.
- [33] Kim, J. K., & Ahn, J. M. (2019). Digital IIR filters for heart rate variability; a comparison between Butterworth and Elliptic filters. *International Journal of Scientific and Technology Research*, 8(12), 3509–3513.
- [34] Pichot, V., Roche, F., Celle, S., Barthélémy, J. C., & Chouchou, F. (2016). HRV analysis: A free software for analyzing cardiac autonomic activity. *Frontiers in Physiology*, 7(NOV), 1–15. doi:10.3389/fphys.2016.00557.
- [35] Nunan, D., Sandercock, G. R. H., & Brodie, D. A. (2010). A quantitative systematic review of normal values for short-term heart rate variability in healthy adults. *PACE - Pacing and Clinical Electrophysiology*, 33(11), 1407–1417. doi:10.1111/j.1540-8159.2010.02841.x.
- [36] van Gent, P., Farah, H., van Nes, N., & van Arem, B. (2019). HeartPy: A novel heart rate algorithm for the analysis of noisy signals. *Transportation Research Part F: Traffic Psychology and Behaviour*, 66, 368–378. doi:10.1016/j.trf.2019.09.015.



Investigating Barriers to the Adoption of Energy Management Practices for Sustainable Construction Projects: SEM and ANN Approaches

Yasir Alhammadi^{1*}, Ahmed Farouk Kineber¹ , Mohammad Alhusban² 

¹ Department of Civil Engineering, College of Engineering, Prince Sattam Bin Abdulaziz University, Alkharj 11942, Saudi Arabia.

² Department of Civil Engineering, Middle East University, Amman, Jordan.

Received 04 January 2024; Revised 21 March 2024; Accepted 26 March 2024; Published 01 April 2024

Abstract

This research addresses the critical challenges hindering the integration of Energy Management Practices (EMPs) within the construction industry, impeding its progress toward sustainability. Recognizing the pivotal role of EMPs in fostering sustainable practices, this study aims to fill a notable research gap by conducting a meticulous survey involving 100 industry professionals. Through the application of Partial Least Squares Structural Equation Modeling (PLS-SEM) and Artificial Neural Network (ANN) analyses, this study provides a comprehensive exploration of the intricate barriers and their interrelated dynamics within the construction sector. The findings reveal significant financial obstacles, including higher initial costs and limited financing options, underscoring the need for interventions to alleviate financial constraints. Additionally, policy and regulatory challenges, such as limited government incentives and shifting energy management rules, are identified, highlighting the necessity for stable and supportive regulatory environments to foster EMP adoptions. This research provides unique insights into the barriers hindering EMP adoption within the construction sector. The implications of this study extend beyond EMP adoption, offering a foundation for advancing sustainable practices in the construction industry. The insights gained can inform both academic research and practical decision-making, contributing to the ongoing discourse on sustainability in construction.

Keywords: Barriers; Energy Management Practices (EMP); Construction Industry; Overall Sustainable Success (OSS); Partial Least Squares Structural Equation Modeling (PLS-SEM); Artificial Neural Network (ANN).

1. Introduction

Stricter energy, environmental regulations, and sustainable infrastructure are needed to balance the environment, the economy, and society. For example, the International Energy Agency (2018) states that 36 percent of global energy consumption and 40 percent of carbon dioxide emissions are directly attributable to the building sector. Every construction project is different due to its complexity (such as project size, duration, and intricacy). Thus, these unique characteristics present new and unique obstacles for construction specialists to overcome, even with the application of cutting-edge technology [1, 2]. Identifying the barriers preventing the local construction industry from understanding and implementing energy-efficient solutions [3]. It is thought that the employment of cutting-edge technology to encourage energy conservation in various construction projects is severely limited by the absence of financial support, loans, and subsidies from financial institutions [4]. On the other hand, government incentives such as lower consumer energy bills may convince financiers to back profitable building projects (United Nations Industrial Development Organization).

* Corresponding author: y.alhammadi@psau.edu.sa

 <http://dx.doi.org/10.28991/CEJ-2024-010-04-015>



© 2024 by the authors. Licensee C.E.J, Tehran, Iran. This article is an open access article distributed under the terms and conditions of the Creative Commons Attribution (CC-BY) license (<http://creativecommons.org/licenses/by/4.0/>).

The rate and instances of successful energy management adoption in building projects can also be increased by government energy conservation policies, such as taxation, and financial support from financial institutions, such as loans and subsidies for energy conservation initiatives [5, 6]. Every phase of a construction project requires energy, and different natural resources are required from the beginning of work until the buildings are destroyed. Resources are required for raw material extraction, manufacture, usage, and transportation, which is the leading cause of this [7, 8]. Energy-intensive building projects require a significant amount of energy upfront. Furthermore, valuable environmental resources are also used when a structure is being demolished. These operations often generate large volumes of solid trash. As defined by Kangas et al. [9], life cycle energy is the total energy needed by a structure from the time of construction to its demolition. It is crucial to make this distinction.

Two forms of energy are used in buildings: operating energy and embedded energy [10–12]. The quantity of energy required to produce, prepare, manufacture, and deliver building supplies to the construction site is known as embodied energy. Manufacturing equipment and building materials requires fully exploiting resources [13]. Raw materials must be extracted, processed, and transported using embodied energy. Following that, this energy is used for building construction, transit, retrofitting, and, in the end, building demolition [14, 15]. Conversely, operating energy usually refers to the energy required to run machinery, utilize water, and maintain the interior environment of the structure [16]. The installed electrical appliances in our homes are often controlled by the HVAC system, which commonly uses operating energy [17].

Two primary energy sources are typically utilized in construction. One of these is electricity, and the other is fossil fuel. Similar to gasoline and diesel, the primary use of fossil fuels is in the production of automobiles and heavy machinery. Most construction projects require fuels like diesel, although certain projects usually use electricity. The specifics of the building project will determine the kind of energy source to be used; modifications could be made [18]. Diesel fuel is the primary energy source utilized in construction operations globally, accounting for 70–80% of the required and desired energy. The remaining twenty to twenty-five percent comes from electricity. Heavy machinery like loaders, diggers, dumpers, and mobile cranes needs much energy [19]. Nonetheless, just 5.968 million gallons of diesel, or 1.2% of all energy used in the country, are utilized for heavy construction machines each year in the United States (U.S. Environmental Protection Agency).

A contractor oversees the processes, equipment usage guidelines, and other duties prior to the start of the major construction project [20, 21]. Embodied energy is used at every stage of the project life cycle, from start to finish, and particularly from the contractor's perspective. A few of the numerous duties needed include purchasing the raw materials for the input, transporting necessary project resources (such as heavy equipment, building supplies, trucks, and operators), and building construction (including foundation, assembly, painting, and designing) [22]. Darko et al. [23] define energy management as calculating and monitoring a building's energy usage and efficiently and economically conserving energy. According to Fernando & Hor [24], energy management is the economical, environmentally conscious, and economical use of energy to maximize profit. Energy efficiency maximizes production while using the least energy resources possible [25]. Thus, the implementation of energy management programs (EMPs) is aided by energy monitoring systems, energy conservation, the appropriate use of energy-efficient equipment, and the identification of possible energy savings [26]. Notably, industrialized countries and the global community are closely monitoring electromagnetic pulses (EMPs) and trying to use them in energy-efficient construction projects. However, developing countries continue to depend on traditional energy sources.

The utilization of petroleum, diesel, and gasoline remains prevalent, particularly in countries such as Saudi Arabia, where societal responsibilities towards environmental preservation and natural resource conservation are often disregarded. This situation is exacerbated by low literacy rates, widespread ignorance, and a general reluctance to embrace innovative, eco-friendly technologies. Consequently, several driving forces underpin the adoption of Energy Management Practices (EMPs), including the implementation of new national regulations emphasizing energy efficiency in building projects, the rising costs associated with conventional energy sources, and efforts aimed at enhancing the efficiency of the construction process [27]. Various initiatives, such as the Energy Efficiency Management Project (EEMP), Energy Efficiency and Capacity (EEC), Energy Standards & Labelling Scheme (ESLS), and Energy Conservation Building Codes, have been established to promote EMPs. However, despite these initiatives, the construction sector has been slow to adopt EMPs due to numerous challenges. One significant issue is the lack of attention paid to EMPs in construction projects, particularly in developing countries like Saudi Arabia [28].

To fill this gap, this study aims to comprehensively investigate the barriers to EMP adoption within the construction industry. It employs a dual-method approach, utilizing Structural Equation Modeling (SEM) and Artificial Neural Network (ANN) analyses. The primary objectives include conducting an extensive literature review to identify gaps, quantifying and prioritizing barriers through a targeted survey of professionals engaged in Saudi Arabian construction maintenance projects, and utilizing SEM to unravel the interrelationships among these barriers. Additionally, the study aims to explore nonlinear dynamics using the ANN approach. The contribution of this research lies in providing a holistic understanding of the barriers to EMP adoption, offering quantitative insights through advanced analytics,

furnishing actionable recommendations for stakeholders, advancing methodological approaches, and ensuring contextual relevance by focusing on the specific nuances of the Saudi Arabian construction sector. Ultimately, this study aims to pave the way for strategic interventions that enhance EMP adoption and contribute to the sustainable success of construction projects.

2. Literature Review

2.1. EMPs and the Global Construction Sector

Using renewable energy in building projects has become a significant worldwide concern. The idea of using EMPs in building projects has come to light to address the serious issues surrounding the use of renewable energy sources. Numerous nations are addressing the problems of energy management and carbon emissions globally. Persson & Grönkvist [29] note that in this regard, Latin America developed strategic strategies for the application of electromagnetic pulses (EMPs) in residential and commercial building projects. Scholars from several nations have also developed original frameworks and models to assist energy-saving initiatives during the building process. Most prior international research has concentrated on aspects of EMPs, such as energy consumption [30], carbon reduction (Gopinath et al. 2020), and project cost minimization [31]. According to Zhang et al. [32], energy management and utilization frequently significantly impact how construction projects can evolve sustainably. When construction organizations make management decisions, energy management during the building process typically gets less attention [33–35]. The primary reasons are the clients' lack of interest and the government's lack of incentives. However, outside pressure from clients and other stakeholders about using EMPs has compelled the construction industry in several industrialized nations to adopt new sustainable practices [36]. Furthermore, contracting organizations' perspectives have shifted from traditional energy consumption ways to sustainable energy practices due to the strict rules in European nations targeted at putting EMPs into place [37]. According to Hesselink & Chappin [38], environmental protection awareness programs assist the construction industry in efficiently managing energy usage, potentially improving the status of the participating firms.

2.2. Barriers to Adopting EMPs

The various obstacles that prevent the use of EMPs in construction operations have been the subject of numerous studies. According to Liu et al. [39], the length and cost of a construction project are connected criteria, and both are necessary for a precise evaluation of the project's effectiveness and completion [40]. According to Davies et al. [41], project cost is one of the biggest obstacles to incorporating sustainable practices in building projects. Regarding this, Gupta et al. [42] discovered that a significant obstacle to adopting sustainable construction is the Chinese government's and important legislative agencies' poor policy execution. Furthermore, Moglia et al. [43] identified specific barriers to green building, especially in Asia. These include staff members' poor self-esteem regarding their ability to persuade customers to adopt sustainability, a lack of knowledge about sustainable technologies, and inadequate training or education for energy management and green building. Furthermore, Caputo & Pasetti [44] found that a lack of client demand is one of the biggest obstacles to implementing sustainable construction projects.

According to Azizi et al. [45], the lack of sustainable building regulations for labeling and registration is another obstacle inhibiting the use of green construction techniques. Furthermore, Li et al. [46] identified a number of difficulties that emerge from developing new business models that are mainly in favor of sustainability and the green transition, particularly in Northern Europe. They also provided a scientific solution to the issues that sustainable business models in the building industry, which is part of the industrial sector, encounter. A few of the issues mentioned are decreased customer demand, scarce investment resources, opposition to implementing sustainable practices, insufficient regulation, a lack of government participation, and a lack of knowledge about energy efficiency. Organizational impediments include mistrust between contractors and developers, a divide in stakeholder communication and knowledge sharing, a lack of coordination between management and staff, and a lack of enthusiasm for the research and development projects that organizations undertake [47].

According to Trinh et al. [48], financial restraints are one of the biggest obstacles to using green energy in building projects. These include increased expenses, a lack of government assistance, and a dearth of funding and financial institution subsidies. Furthermore, Žuk [49] discovered several essential factors seriously impede the building industry's ability to apply energy-saving measures. These include the absence of government and financial institution support, the general public's ignorance of sustainable building methods, the dearth of stakeholder conferences and training sessions, and the top leadership's indifference. Moreover, several barriers prevent the adoption of innovative and energy-saving solutions [50]. These include the knowledge gaps between clients and contractors, a lack of funding, and a lack of professional competency. Furthermore, inadequate governmental policies and directives significantly impede the successful and efficient adoption of eco-friendly technologies [51]. Despite these obstacles, bringing cutting-edge technology and ensuring they are integrated into construction projects related to energy management can give investors a competitive edge in the market [52].

From a business standpoint, a few adjustments are needed to overcome the obstacles to greater energy efficiency. Ikudayisi et al. [53] enumerate several of these obstacles, the most prevalent being ignorance, a lack of investment opportunities, energy expenses, decision-making processes, and the requirement for expensive, precise information. In addition, there are some obstacles that project contractors need to surmount to hinder the implementation of sustainable building practices in poor nations. According to Tafesse et al. [54], these problems include unethical government engagement, a lack of trained personnel, a lack of technology, and a lack of possibilities for employee training. Numerous prior studies conducted globally have impeded the adoption of green construction methodologies. Employees [55], consumers and market obstacles [54], stakeholder affiliation, awareness, and attitudes [53], and a lack of policies and procedures [44, 43] have identified numerous underlying explanations for the limited adoption of green construction. Gupta et al. [42] found that the cost of green construction techniques is a significant barrier to deployment. The study investigated the application of sustainable practices in Chinese building projects.

Funding for innovative sustainable technology is also seen as a financial obstacle when considering the client's purchasing power [41, 47, 48]. Various preferences or a lack of readiness to embrace change may prevent customers from choosing energy-efficient solutions [46]. Furthermore, social influence often leads people to adopt the superstitious beliefs of their peers. This makes it challenging for people to adapt to change effectively and efficiently, including utilizing energy-saving technologies in building projects [45]. Within this framework, Pietrosevoli & Rodríguez Monroy [36] noted barriers to energy management implementation in Italian building projects. The primary problems found were a lack of understanding of energy management concerns, challenges in establishing municipal objectives, the difficulty of gathering and analyzing data, and a shortage of experts in businesses to collect and evaluate data and create effective strategies. Fu et al. [35] state that relevant stakeholders adopt EMPs progressively. The progress of environmentally conscious buildings mainly depends on the availability of knowledge and information since modern green technologies are more sophisticated than those found in conventional buildings.

There are several significant challenges to be aware of when pursuing brownfield rehabilitation, controlling the initial cost of construction projects, and incorporating sustainability. These include financial institutions and quasi-governmental organizations that support government incentives and subsidies, high taxes, cash availability restrictions, energy conservation, and environmental deterioration [34]. According to Umar et al. [40], a significant obstacle to adopting energy-efficient construction practices is a lack of knowledge and awareness. According to Martek et al. [33], the ultimate goal of the stakeholders may be impacted by the top management's insensitivity and ignorance regarding adopting green techniques in building projects. Moreover, according to Liu et al. [39], a lack of cooperation and communication among stakeholders hinders the application of green practices in the building sector. The reluctance of clients to make demands is one of the main obstacles to the Saudi Arabia construction industry's adoption of energy conservation [38].

2.3. Overall Sustainable Success

Sustainable success in the construction industry encompasses a multifaceted approach, considering social, economic, and environmental dimensions. Achieving a harmonious balance between these elements is imperative for the long-term viability and positive impact of construction projects.

2.3.1. Social Sustainability

Social sustainability involves addressing the human aspects associated with construction projects. In the context of the discussed challenges, it becomes crucial to focus on education, awareness, and community engagement [27]. The text highlights that in certain regions, such as Saudi Arabia, low literacy rates and a lack of awareness contribute to the reliance on traditional energy sources. To promote social sustainability, initiatives should be undertaken to increase literacy rates, raise awareness about environmental responsibilities, and foster a willingness to embrace innovative, eco-friendly technologies. By incorporating social considerations, construction projects can become catalysts for positive societal change.

2.3.2. Economic Sustainability

Economic sustainability is central to the overall success of construction projects [4]. The text emphasizes the limitations posed by the absence of financial support, loans, and subsidies for energy-efficient solutions. To address this, financial institutions need to play a proactive role in supporting construction projects that prioritize energy efficiency [4]. Government incentives, such as tax benefits and financial support, can further encourage financiers to invest in economically viable and environmentally conscious building projects [5, 6]. Economic sustainability ensures that construction initiatives not only meet current financial needs but also contribute to long-term economic growth and stability.

2.3.3. Environmental Sustainability

The environmental dimension is a key focus in the pursuit of overall sustainability [1]. The text underscores the significant impact of the construction sector on global energy consumption and carbon dioxide emissions. Stricter energy and environmental regulations, along with sustainable infrastructure, are essential components of environmental sustainability [1]. Energy management programs (EMPs) and the adoption of electromagnetic pulses (EMPs) are identified as potential strategies to enhance energy efficiency in construction projects [26]. The life cycle approach,

considering embodied energy and operating energy, emphasizes the importance of minimizing environmental impacts from the extraction of raw materials to the demolition of buildings [14, 15]. Overall, achieving overall sustainable success in construction requires a holistic approach that addresses social, economic, and environmental dimensions [27]. By promoting social awareness, securing economic support, and implementing environmentally conscious practices, the construction industry can contribute positively to communities, economies, and the global environment.

2.4. Research Gaps

While prior research has delved into barriers to the adoption of EMPs in the construction industry, there exists a notable research gap concerning the holistic investigation of these barriers and their implications for the overall sustainable success of construction projects. Many studies have focused on individual aspects or specific barriers, often lacking a comprehensive approach that integrates various dimensions and their collective impact on project sustainability. Additionally, the use of advanced analytical methods, such as SEM and ANN, to understand the intricate relationships among identified barriers and their influence on sustainable outcomes is an underexplored area. The existing literature primarily lacks a robust and integrated framework that combines both qualitative and quantitative approaches to offer a nuanced understanding of the challenges hindering the widespread adoption of EMPs and their repercussions on the broader sustainability goals of construction projects. This research gap underscores the need for a more holistic and analytical exploration, which this study aims to address by employing a dual-method approach to unravel the complexities surrounding EMP adoption in the construction sector. Based on the above-mentioned literature this study assumed that: H1. The realization of OSS in building projects is significantly correlated with EMP barriers (Figure 1).

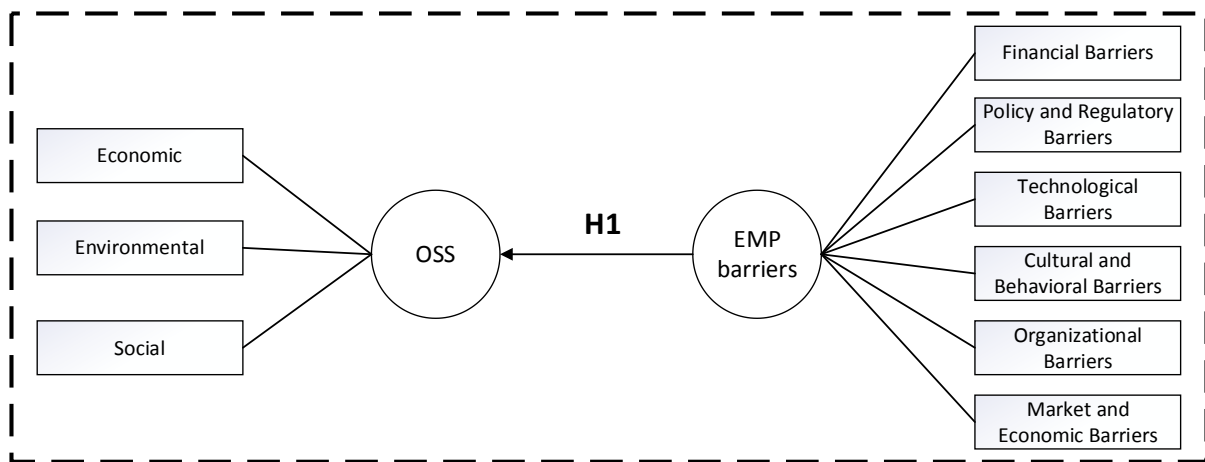


Figure 1. Hypothetical model

3. Research Methodology

The methodology of this study unfolds in three sequential steps, as shown in Figure 2. Firstly, it involves the identification of EMP barriers through an extensive literature review. Following this, the second step encompasses the development of survey questions and the collection of data from professionals engaged in construction projects in Saudi Arabia. Lastly, the study employs SEM and ANN analyses to discern crucial insights into the identified barriers and their underlying dimensions.

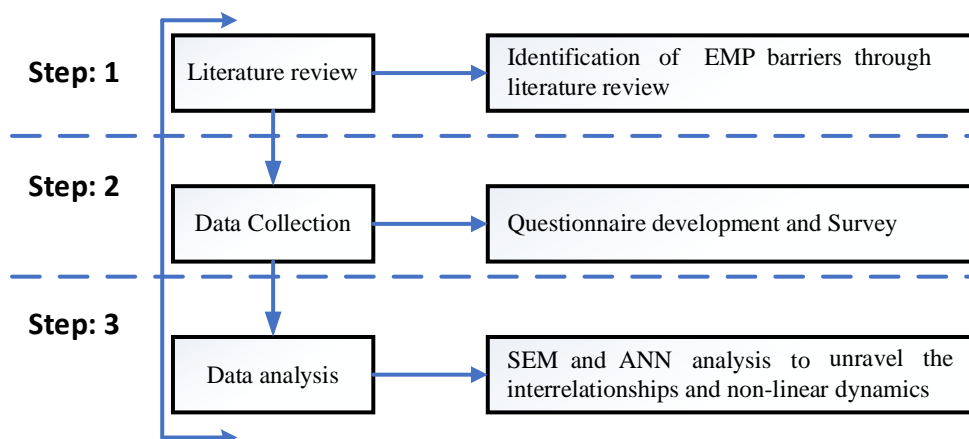


Figure 2. Research Framework

3.1. Identification of Barriers

The difficulties involved in implementing EMPs in the construction sector were thoroughly reviewed in this study. According to Ali et al. [56–58], the literature review thoroughly searched several databases, including ScienceDirect, Springer, Emerald Insight, Taylor & Francis, Google Scholar, JSTOR, and PubMed. Search terms including "barriers," "energy management," and "construction projects" were used in the beginning stages of the search to find more than two hundred publications. From a pool of 35 distinct publications, 85 pertinent papers were picked after a thorough screening procedure.

Following a thorough examination of the abstracts and content of these papers, some journals and publications that were judged unnecessary were removed from the final list. Thirty-nine papers from 23 sources, including one book and one conference, were included in the final edited collection. Among the esteemed journals that significantly influenced the research were *Procedia Manufacturing*, *International Journal of Sustainable Building Technology and Urban Development*, *Journal of Property Investment & Finance*, *Journal of Technology Management in China*, *Energy Policy*, *Journal of Energy*, *Procedia Engineering*, *Energy Conversion and Management*, and *Energy and Buildings*. Based on the literature review, Table 1 methodically outlines the barriers to EMP adoption in building projects.

Table 1. List of barriers to EMP in construction projects

Categories	Barriers	Code	References
Financial Barriers (FB)	The higher initial costs associated with adopting EMP.	Bar1	[27, 28, 37]
	Limited financing options, such as the absence of interest-free and long-term loans, for implementing energy management technology.	Bar2	[25, 26, 32, 59]
	Uncertain earnings and an extended payback period for EMP investments.	Bar3	[19, 20, 29, 31]
Policy and Regulatory Barriers (PRB)	Limited government incentives and support to encourage the adoption of EMP.	Bar4	[17, 18, 23, 24]
	Changes in energy management rules due to shifts in political governments.	Bar5	[13, 21, 22]
	The absence of EMP-based codes, rules, and regulations.	Bar6	[10-12]
Technological Barriers (TB)	Insufficient advancements in energy management technology, hindering innovation.	Bar7	[10, 11, 17]
	The absence of standardized metrics for measuring the performance of EMP initiatives.	Bar8	[10, 15, 16]
	Insufficient technical information and expertise related to EMP adoption.	Bar9	[4, 5, 14]
Cultural and Behavioral Barriers (CBB)	Resistance stemming from cultural, attitudinal, and behavioral factors impeding EMP adoption.	Bar10	[2, 3, 8, 9]
	Lack of awareness regarding the benefits and adoption of EMP.	Bar11	[1, 6, 7, 60]
	Limited interest from clients and a lack of market demand for EMP adoption.	Bar12	[61-64]
Organizational Barriers (OB)	A lack of interest from developers in implementing EMP.	Bar13	[65-68]
	A lack of interest and support from top management in addressing energy management issues.	Bar14	[52, 69, 70]
	Insufficient communication and collaboration among project stakeholders regarding EMP initiatives.	Bar15	[49-51, 71]
Market and Economic Barriers (MEB)	Delays in decision-making processes related to EMP initiatives.	Bar16	[44, 55, 72]
	Absence of specific conditions for implementing EMP on construction sites.	Bar17	[41-43, 48]
	Insufficient training and education on EMP and sustainable construction practices.	Bar18	[45-47]
OSS	Volatility in the prices of energy resources and carriers affecting EMP implementation.	Bar19	[35, 36, 40]
	Environmental	OSS1	
	Social	OSS2	
	Economic	OSS3	

3.2. Survey Design and Administration

We carefully designed a questionnaire to survey the obstacles to deploying EMPs in the construction industry. There were two main sections to the questionnaire: In Part 1, background data was gathered, and respondents' demographic profiles and jobs in the construction sector were examined. It sought to ascertain the frequency of exposure to incidents relevant to the deployment of EMPs. In Part 2, the adoption of EMPs in the construction industry was examined, and respondents were asked to rank these challenges on a Likert scale of 1 to 5. This scale included technical and soft skills evaluations, ranging from "not important" to "very important."

Senior people with research and industry experience in EMP thoroughly reviewed and revised the final sets of questionnaires before they were sent. The fundamental criterion for selecting appropriate respondents for this study was the inclusion of experts actively involved in maintenance projects within the Saudi Arabia construction sector. A combination of purposive and snowball sampling techniques—non-probability methods—was used to target this

audience. The study team used their contacts and industry experience to find participants affiliated with construction companies through purposeful sampling. Purposive sampling, as opposed to probability sampling procedures, adds some researcher bias, although it is justified without a sample frame [73]. Potential participants were emailed an online survey using the "Google Forms" tool. As an additional tactic, the "snowball technique" was employed to get respondents to share the survey link with acquaintances who would be beneficial sources of information for the study [74]. Email reminders were sent out regularly to encourage member participation. In the end, 106 replies were received; however, six were rejected because of too many missing data points. The remaining 100 responses were subjected to data analysis, which gave our investigation into the obstacles to EMP adoption in the Saudi Arabia construction industry a firm basis.

3.3. Data Analysis

3.3.1. SEM Analysis and Model Development

SEM is a multivariate analysis method that takes into account both econometric and psychometric points of view, according to Wong [75]. Numerous academic fields, including construction management [76], management, organizational behavior [77], construction management [78] and so on, have made extensive use of SEM. Factor analysis and multiple regression modeling are successfully combined in SEM. Using a straightforward method, researchers can replicate in a single analysis the links between latent variables (constructs) generated by visible variables (measurement items) [79]. SEM is frequently used to identify modeling and computational errors as well as to assess many interdependent connections. Therefore, the observed variables were computed, and a thorough assessment of data assumptions was carried out in accordance with substantive/theoretical and methodological issues. Scientists may develop a model, watch it work, and analyze all the relationships and correlations found in the data by using SEM [80]. PLS-SEM is another term for the component-based approach. In exploratory research, it is mostly utilized to develop concepts and theories [81]. PLS-SEM can help avoid making restrictive assumptions that are necessary for a thorough evaluation of the highest likelihood of theories [82]. The sustainability pillars have been the subject of additional research [83]. Project methodology and strategic sustainability goals could be hard to change [84]. Waqar et al. [85] assert that social sustainability, economic feasibility, and environmental concerns must all be balanced. Finding practical ways to integrate sustainability into contemporary workplaces has become more important as the building industry's interest in the concept has grown [86]. The expanded use of EMP in the early phases of planning may be motivated by the need for sustainable growth and the creative approach to corporate social responsibility that firms have adopted. The environmental, economic, and social pillars of sustainability are comparable to the function that EMP serves in the building process, claim Oke et al. [87]. However, through expert interviews, six major clusters of implementation-related hurdles were found, and these clusters matched the ideas and measurement systems outlined in (Perno et al., 2022) (see Figure 2). Furthermore, this study revealed that:

The SEM technique was employed to examine the impact of EMP barriers on OSS. The correlations between different elements are shown by the SEM approach [88]. This study used a SEM technique to investigate the relationship between OSS and lowering EMP barriers. The results show a link between each concept and the given indicators [89]. According to Zhang et al. (2019), the procedure is based on equations and has arbitrary factors and structural limitations [32]. According to Teng et al. [90], SEM is becoming more and more recognized as a methodology for non-experimental research, and hypothesis analysis approaches were not always adequately controlled. Using reflective and formative features of the Partial Least Square (PLS) model, the relationship between OSS and reducing barriers to EMP has been investigated. However, in order to do the PLS-SEM analysis in this work, three crucial evaluations were used: the measurement model, the structural model, and the common method variance. PLS-SEM is a popular route model that can connect independent and dependent components [91].

- Common Methods Variance (CMV)

From the Common Methods Variance (CMV) [87], the CMB was created. Clarification of the mistake examination's conclusions is a goal of CMB, as the data collection approach could lead to trigger difficulties [92]. It is essential to identify any CMV in order to comprehend these issues and challenges. Thus, a formal, methodical study of a single component was used, in line with Harman's conclusions [93].

- Measurement model

The relationship between the measurements and their construct is made clearer by the measurement model [94]. One may consider the analysis and assessment of the measurement model to be a validation process [94]. While evaluating the applicability of particular measurement sets, PLS keeps a running list of related ideas. Assessments of "(1) indicator reliability, (2) composite reliability (c_r), (3) average variance extracted (AVE), and (4) discriminant validity" are required in order to examine the reflective model (first order), according to Munianday et al. [95] Cronbach's alpha, sometimes called the consistency or dependability coefficient [95], is a measure of how well a collection of questions analyzes a single, one-dimensional idea. The expression for Cronbach's alpha (α) is as follows [96]:

$$\alpha = \frac{N - \bar{r}}{1 + (N - 1) - \bar{r}} \quad (1)$$

where r is the mean relationship between the items and N is the number of matters. Considering the documented variations in Cronbach alpha's performance, a confirmatory approach to reliability measurement must be taken into account [95]. Composite dependability (ρ_c) yields a more reliable statistic, claims [97]. According to Durdyev et al. [94], values of ρ_c more than 0.7 are required for all kinds of research, whereas 0.6 is a reasonable cutoff point for exploratory investigations. According to Durdyev et al. [94], the expression for composite reliability is as follows:

$$\rho_c = \frac{(\sum \lambda_i)^2}{(\sum \lambda_i)^2 + \sum \text{var}(\varepsilon_i)} \tag{2}$$

In this case, $\text{var}(\varepsilon_i) = 1 - \lambda_i^2$, i , ρ_c denotes the composite reliability score, and λ_i denotes each item's component loading to a latent construct. When calculating Cronbach's alpha, the factor loadings of each item are ignored. However, because the composite reliability makes use of the item loadings identified within the theoretical model, it performs better than Cronbach's alpha [98]. Furthermore, the average retrieved AVE was used to evaluate the latent variables' convergent validity [99]. The widely recognized AVE metric can be used to demonstrate the convergent validity of the model's component elements. The formula for AVE is as follows:

$$AVE = \frac{\sum \lambda_i^2}{\sum \lambda_i^2 + \sum \text{var}(\varepsilon_i)} \tag{3}$$

AVE stands for the average variance extracted, while $\text{var}(\varepsilon_i) = 1 - \lambda_i^2$, i indicates how each item is loaded onto a latent construct. Furthermore, research has been done to examine discriminant validity. Conceptually, each construct is evaluated [98]. The goal is to confirm that the studied notion is empirically distinct or unique [95].

- Model structural

One of the most important techniques for concurrently analyzing all intricate relationships between constructs was proposed: the structural model. In a similar vein, Durdyev et al. [94] employed it to create the structural model that evaluated the effect of EMP barriers on OSS. The two main approaches that form the basis of the structural model used in this study are as follows:

According to Durdyev et al. [94], the primary focus of a collinearity analysis is the extent to which other factors may predict or account for the effects of a variable. The main problem is that the informative measures of indicator weights may be misrepresented by collinearity [99]. Furthermore, bootstrap standard errors resulting from collinearity may raise and trigger mistakes dramatically. The variation Inflation Factor (VIF), which indicates how frequently more indicators of the same construct might address an indicator's variation, is used to measure collinearity. According to Awang et al. [98], in order to receive the PLS algorithm test report in the Smart PLS 4.0 software, VIF needs to be lower than the recommended threshold level 5.

Rather than using parametric assumptions, the bootstrapping methodology approximates the variance of data points among sub-samples. A resampling method for sampling analysis is called bootstrapping. One large data set is divided into multiple sample sizes, and a smaller number of related statistical data (expressed as structural or regression coefficients) are measured. This study proposed a causal relationship between (OSS) and £ (EMP barriers). As a result, "in this case, the internal relationship—the relationship between the £, μ , and €1 equation in the structural model—can be expressed as a linear equation as shown below" [95]:

$$\mu = \beta \text{ £} + \text{€1} \tag{4}$$

where residual variance (€1) and the path coefficient (β) are expressed. Consequently, the weight of a standardized regression analysis and a multiple regression analysis are comparable.

3.3.2. ANN Analysis

Artificial neural network analysis not only advances knowledge through learning mechanisms but also provides insight into how synapses and neurons function in the brain [78, 100]. By using machine learning approaches, ANN analysis enables researchers to forecast the significance of antecedents [101]. Furthermore, ANN makes it easier for researchers to validate and enhance PLS-SEM data. To address the problem of non-linearity and linearity between the constructs, Wong et al. [102] provide a hierarchy of constructs and a grading system based on sensitivity analyses [103]. The following are the formulas for activation functions:

$$\text{Distinctiveness (Linear)} (x) = x \tag{5}$$

$$\text{Hyperbolic Tangent } \tanh(x) f_x = \frac{2}{1+e^{-2x}} - 1 \tag{6}$$

$$\text{Sigmoid factor } f_x = \frac{2}{1+e^{-x}} \tag{7}$$

Additionally, studies have demonstrated that ANNs perform better in terms of accuracy and outcome reliability than SEMs or multi-step regressions. Thus, it is reasonable to conclude that studies employing PLS-SEM and ANN are complementary [78]. Furthermore, there have been suggestions that ANNs mimic the way that information travels through human brains. The three roles of artificial neural networks (ANNs) are the transfer function, network design, and learning rules [100]. Subcategories such as feed-forward multilayer perceptrons [78], recurrent networks [100] and radial basis networks [102] are also included in these functions. Researchers most often use three layers: inputs, outputs, and hidden neurons, in addition to feed-forward multilayer perceptrons (MLPs) [102]. Independent variables often represent the input layer. These parts gather unprocessed information and send it to buried neurons as synaptic weights. An output neuron represents the dependent variable in a model. Apart from the activation function, extensive research has been conducted on the sigmoid function [78]. Moreover, multilayer neural network models are widely recognized as substantial and dependable, and they can manage complex problems in higher-order models. Multilayer perceptron neural networks were utilized for both training and testing of the suggested model.

4. Results

This section of the paper presents the results of the demographic information of surveyed participants, barriers to EMP use in construction projects, and exploratory factor analysis on barriers to EMP use in construction projects amongst construction companies.

4.1. Demographic Details of the Survey Participants

Table 2 provides a comprehensive overview of the demographic characteristics of the 100 respondents in the study. The respondents were categorized based on several key variables. Regarding work experience, 19% of participants had less than five years, 27% had 5–10 years, 16% had 11–15 years, 22.7% had 16–25 years, and 15.3% had more than 25 years of experience. The professional field distribution included 26.7% architects, 30.7% civil engineers, 18.6% electrical engineers, 16% mechanical engineers, and 8% quantity surveyors. Current positions varied among the respondents, with 6% holding director positions, 9.3% being senior managers, 30% being managers, 18.7% being design engineers, and 36% being site engineers. Regarding educational attainment, 10% had diplomas, 15% had bachelor's degrees, 20% had M.Sc. degrees, 50% held Ph.D. degrees, and 5% had other educational qualifications. The respondents' organizational functions were distributed across client roles (40%), consultants (20%), and contractors (40%). This detailed breakdown provides a comprehensive snapshot of the diverse demographic characteristics within the respondent pool, offering valuable insights for the study's analysis and interpretation.

Table 2. Demographics details of the respondents

Variable	Characteristics	Percentage (%)
Work experience (Years)	Less than five	19
	5–10	27
	11–15	16
	16–25	22.7
	More than 25	15.3
Professional field	Architect	26.7
	Civil Engineer	30.7
	Electrical Engineer	18.7
	Mechanical Engineer	16
	Quantity surveying	8
Current position	Director	6
	Senior Manager	9.3
	Manager	30
	Design Engineer	18.7
	Site Engineer	36
Educational level	Diploma	10
	Bachelor's degree	15
	M.Sc.	20
	Ph.D.	50
	Others	5
Organization function	Client	40
	Consultant	20
	Contractor	40

4.2. SEM Results

4.2.1. Common Method Bias

To determine the variance of the conventional method, a single component analysis was conducted on the proposed model [92]. Research has shown that when the overall variation of the variables is less than fifty percent, the normal process bias does not affect the results that are obtained [95]. Because the common method variance is less than 50%, the study's conclusions—which showed that the first set of components accounted for 38.43% of the overall variance cannot be altered [104].

4.2.2. Measurement Model Assessment

4.2.2.1. Convergent Validity Analysis

The measurement model considers the degree of alignment and coherence between two or more measurements (barriers) of the same notion [105]. Construct validity is assessed using the measurement model. According to Munianday et al. [95], the following tests can be used with PLS-SEM to evaluate the convergent validity of the proposed constructs: "composite reliability scores (ρ_c), Cronbach's Alpha (α), and Average Variance Extracted (AVE)". Durdyev et al. [94] reported that Table 1 showed that every OSS and EMP barrier had a composite reliability greater than 0.60, suggesting acceptance. Table 1 indicates that the Cronbach Alpha was, nevertheless, 0.60.

Consequently, the evidence by Durdyev et al. [94] suggests a medium to high degree of reliability. The AVE was also used to evaluate the construct variables' convergent validity. A level of AVE larger than 0.5 is considered acceptable by Khan et al. [86], indicating that the measurement parameters account for at least 50% of the variation [106]. For every research construct, Table 3 shows the estimated AVE values, which are greater than 50%. These findings demonstrated the convergence and internal stability of the measurement model. It also meant that the measurement components did not quantify any other construct in the study model for any construct that was thoroughly measured. Chen et al. [107] note that while an external load score of 0.70 is optimal, scores of 0.50 or higher are nevertheless acceptable, provided the analysis explains. All measurements from the first model outdoor loads are shown in Table 4 and Figure 3. All outside loads are acceptable, with the exception of Bar14, which was removed from the original model because of a poor loading of less than 0.5 [108]. It demonstrated their minimal effect on linked structures. The evaluation of the modified model following the removal of these observations is shown in Table 4 and Figure 4.

Table 3. Measurement model of barriers to adopt EMP

Categories	Code	Outer loading	Cronbach's Alpha α	Composite Reliability ρ_c	AVE
Financial Barriers (FB)	Bar1	0.965	0.841	0.894	0.681
	Bar2	0.68			
	Bar3	0.915			
Policy and Regulatory Barriers (PRB)	Bar4	0.963	0.973	0.982	0.948
	Bar5	0.81			
	Bar6	0.97			
Technological Barriers (TB)	Bar7	0.837	0.917	0.948	0.859
	Bar8	0.804			
	Bar9	0.895			
Cultural and Behavioral Barriers (CBB)	Bar10	0.68	0.944	0.973	0.947
	Bar11	0.915			
	Bar12	0.846			
	Bar13	0.843			
Organizational Barriers (OB)	Bar15	0.877	0.902	0.933	0.823
	Bar16	0.905			
Market and Economic Barriers (MEB)	Bar17	0.957	0.905	0.941	0.841
	Bar18	0.864			
	Bar19	0.957			
OSS	OSS1	0.954	0.837	0.883	0.716
	OSS2	0.772			
	OSS3	0.982			

Table 4. Discriminant validity (HTMT)

Constructs	CBB	FB	MEB	OB	OSS	PRB	TB
CBB							
FB	0.371						
MEB	0.380	0.031					
OB	0.313	0.066	0.090				
OSS	0.414	0.019	0.075	0.073			
PRB	0.634	0.372	0.383	0.163	0.387		
TB	0.835	0.268	0.267	0.213	0.336	0.542	

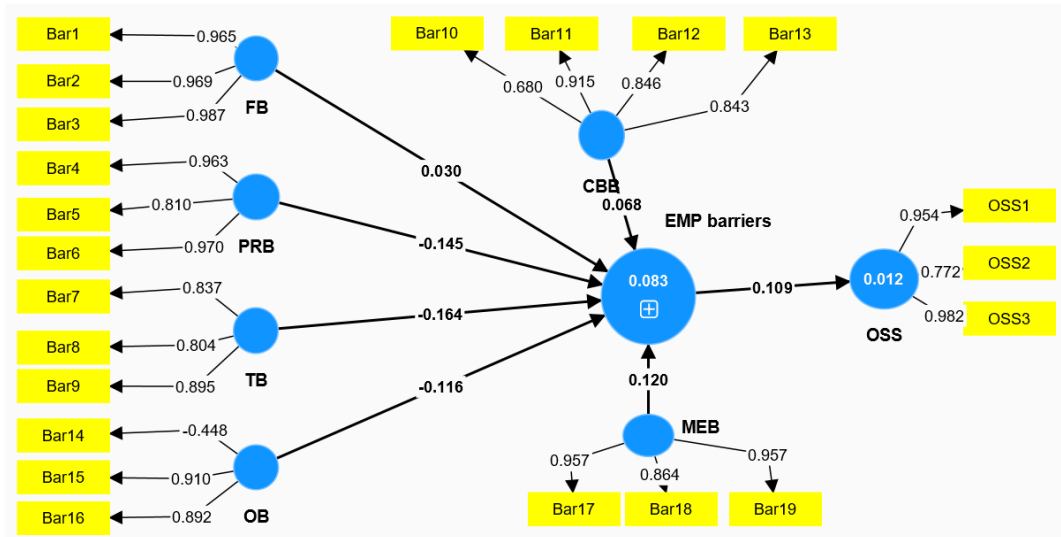


Figure 3. Initial Model

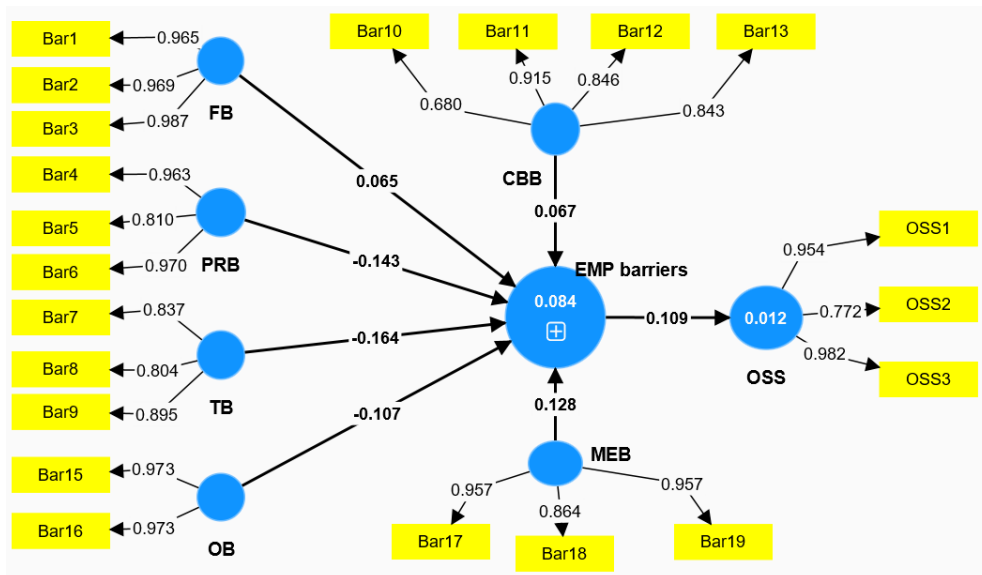


Figure 4. Final Model

4.2.3. Discriminant Validity Assessment

The application of discriminant validity evaluation in SEM research is growing [104]. It validates the concept's originality or empirical differentiation [105]. This study uses cross-loadings, the Heterotrait-Monotrait Criterion Ratio (HTMT), and the Fornell-Larcker criteria to evaluate discriminant validity. Table 4's statistics show that the Fornell and Larcker technique is used to recognize and approve the discriminant validity of the OSS components and EMP barriers, as per Wong et al. [102]. This is due to the fact that the correlation between the variables and construct indicators should be greater than the average variance extracted (AVE) square root. An additional technique for assessing discriminant validity in variance-based structural equation modeling (SEM) is the HeterotraitMonotrait (HTMT) criterion ratio.

The HTMT technique ascertains the precise correlation between two constructs, assuming accurate measurement. Using the HTMT technique, Kar and Jha [106] proposed variance-based structural equation modeling (SEM) to evaluate discriminant validity. When the score is between 0.85 and 0.90, there is a difference between the two constructs. If there are conceptual parallels between the conceptions, the score should be less than 0.90; if not, it should be less than 0.85. Table 3 displays the HTMT values for the components that are the subject of the inquiry. The results provide adequate evidence of discriminant validity. The cross-loading method was used to evaluate the discriminant validity of OSS components and EMP barriers, respectively. According to Wong et al. [102], it establishes if a variable has a higher cross-loading than any other on a latent construct (derived from other concepts). The loadings on the structures that are highlighted in Table 5 are greater than the loadings on the other constructs. (one after the other). Thus, it is possible to confirm that each build is one-dimensional.

Table 5. Cross loadings results

Items	CBB	FB	MEB	OB	OSS	PRB	TB
Bar1	0.303	0.965	0.908	-0.081	0.93	0.357	0.206
Bar2	0.68	0.112	0.046	0.101	0.118	0.379	0.464
Bar3	0.915	0.312	0.326	0.312	0.346	0.448	0.614
Bar4	0.846	0.33	0.327	0.15	0.353	0.561	0.558
Bar5	0.843	0.356	0.355	0.344	0.337	0.416	0.552
Bar6	0.271	-0.075	-0.105	0.973	-0.076	0.118	0.192
Bar7	0.255	-0.045	-0.057	0.973	-0.045	0.18	0.207
Bar8	0.315	0.982	0.957	-0.079	0.984	0.357	0.209
Bar9	0.26	0.686	0.864	-0.073	0.715	0.239	0.161
Bar10	0.315	0.982	0.957	-0.079	0.984	0.357	0.209
Bar11	0.363	0.969	0.903	-0.026	0.949	0.302	0.243
Bar12	0.299	0.987	0.956	-0.078	0.982	0.351	0.192
Bar13	0.535	0.3	0.297	0.151	0.314	0.963	0.467
Bar 15	0.506	0.296	0.315	0.102	0.299	0.81	0.415
Bar 16	0.478	0.36	0.34	0.162	0.336	0.97	0.417
Bar 17	0.723	0.262	0.258	0.158	0.309	0.449	0.837
Bar 18	0.611	0.231	0.225	0.13	0.247	0.375	0.804
Bar 19	0.497	0.141	0.125	0.205	0.164	0.401	0.895
OSS1	0.397	0.912	0.857	-0.026	0.954	0.293	0.297
OSS2	0.294	0.721	0.863	-0.081	0.772	0.301	0.249
OSS3	0.299	0.987	0.956	-0.078	0.982	0.351	0.192

4.2.4. Structural Model Assessment

4.2.4.1. Collinearity Analysis

Formative assessment models frequently show unexpectedly high correlations between measurements; in the meantime, the study's notions of the EMP barriers were formative. Every VIF result was less than 3.5. It implied that each of these concepts caused DT's challenges. Table 6 displays the significant route coefficient β for six first-order subscales related to EMP barriers: Financial, Policy and Regulatory, Technological, Cultural and Behavioral, Organizational, Market, and Economic.

Table 6. Formative constructs analysis

Paths	β	SD	P Values	VIF
CBB → EMP barriers	0.213	0.047	0	1.861
FB → EMP barriers	0.07	0.031	0	1.831
MEB → EMP barriers	0.178	0.048	0	1.149
OB → EMP barriers	0.821	0.027	0	1.133
PRB → EMP barriers	0.437	0.057	0	1.19
TB → EMP barriers	0.179	0.033	0	1.187

4.2.4.2. Bootstrap Analysis Evaluation

The investigation's validation of the proposed research hypothesis was a notable feature. The model hypothesis's significance was evaluated using the bootstrapping technique [109]. The route coefficient, which expresses the degree to which one path influences another, is represented by the value of each path [94]. The SmartPLS 4.0.9.9 software now includes a bootstrapping method for calculating the route coefficient errors for CFA. Therefore, to establish the t-statistics for proposition testing, 5000 subsamples were used to validate a suggestion by Cruz-Jesus et al. [110]. There is only one structural equation that explains the fundamental relationships between the constructs and Equation 1 in the PLS Model, and it also provides a workaround for EMP barriers.

Consequently, standardized p-values for the endogenous construct and route significance were scrutinized to construe the results of the bootstrapping investigation [106]. These results showed that OSS and getting past EMP hurdles had a significant and positive influence ($=0.109, p = 0.000$) (see Table 7). OSS and overcoming the EMP barriers are the two most important aspects of this study, and they both function similarly.

Table 7. Path analysis

Paths	β	SD	P Values	VIF
EMP barriers → OSS	0.109	0.078	0	1.128

4.2.4.3. The Structural Model's Explanatory Power (R2)

One of the most crucial assessments in PLSSEM is evaluating the R2 for the OSS [84]. In this study, the exogenous construct was found to be capable of explaining 19.6% of OSS, with OSS serving as the dependent variable. The R2 and adjusted R2 values of 0.012 demonstrated this. According to these results, the EMP barrier size is appropriate and has minimal impact [111].

4.3. ANN Results

This study used the major factors of the SEM-PLS path analysis as the input neurons in the ANN model, using a similar technique to that used by Arpaci et al. [112] (Figure 4). Large datasets with complicated nonlinear correlations can be efficiently captured by artificial neural networks (ANNs). Before using ANNs, linear approaches must be used to simplify the data and identify important variables. Artificial neural networks (ANNs) increase prediction and classification accuracy by identifying patterns that linear approaches can miss. Prior to utilizing ANNs, it was required to identify pertinent variables through the use of a linear technique in the earliest phases of data processing. Once key variables were found, artificial neural networks (ANNs) aided in the analysis of complex interactions. When there are nonlinear interactions between the exogenous and endogenous variables and the data are not regularly distributed, artificial neural networks (ANNs) can be used.

ANNs are also resistant to noise, outliers, and small sample sizes. The model can enable non-compensatory models, which are similar to compensatory models in that they don't need to raise one element to offset a decline in another [100]. An artificial neural network (ANN) was conducted using IBM's SPSS neural network module. A normal distribution is not necessary for the artificial neural network (ANN) method to capture both linear and nonlinear interactions. A feed-forward-backward-propagation (FFBP) algorithm uses training to estimate errors in the backward direction while feeding inputs in the forward direction to anticipate the result of an investigation [78]. Using a multilayer perceptron and the sigmoid activation function, the input and hidden layers were built. Prediction accuracy can be increased and mistakes reduced by employing multiple learning cycles. The remaining samples were used for training, and the remaining 90% of the samples were used for testing [113]. To prevent overfitting, the root means square error (RMSE) was calculated using ten-fold cross-validation [114]. To assess the model's prediction accuracy, the RMSE of the training data, the RMSE of the testing data, the mean, and the standard deviation were looked at (refer to Figure 5).

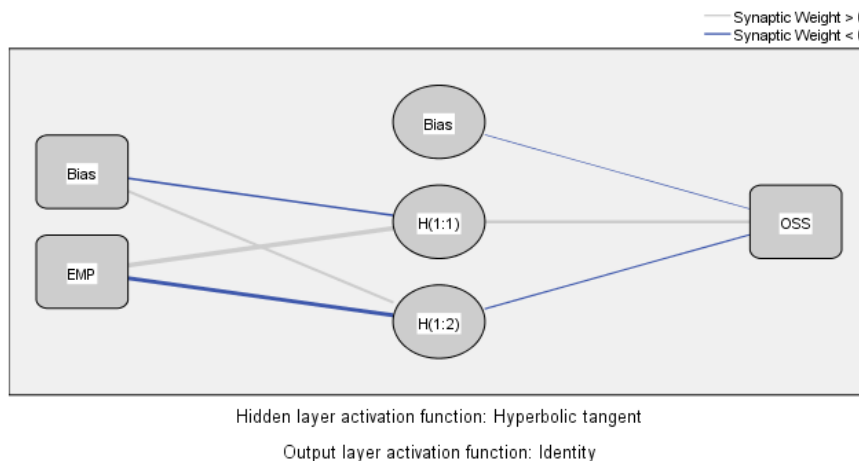


Figure 5. Model prediction

The training and testing procedures' RMSE values—0.698 and 0.663, respectively—are comparatively low, as Table 8 and Figure 6 demonstrate. We were able to verify that the model accurately reflected the data. We examined the R^2 value of the ANN model in accordance with the work of Loh et al. [115] and discovered that it predicted EMP barriers for OSS with an accuracy of 100%.

Table 8. RMSE values of the training and testing

Neural network	Model Input: EMP barriers; Output: OSS	
	Training	Testing
	RMSE	RMSE
ANN1	0.698	0.668
ANN2	0.710	0.658
ANN3	0.701	0.722
ANN4	0.704	0.716
ANN5	0.729	0.664
ANN6	0.698	0.734
ANN7	0.763	0.703
ANN8	0.704	0.663
ANN9	0.698	0.750
ANN10	0.702	0.695
Mean	0.710	0.697
SD	0.021	0.033

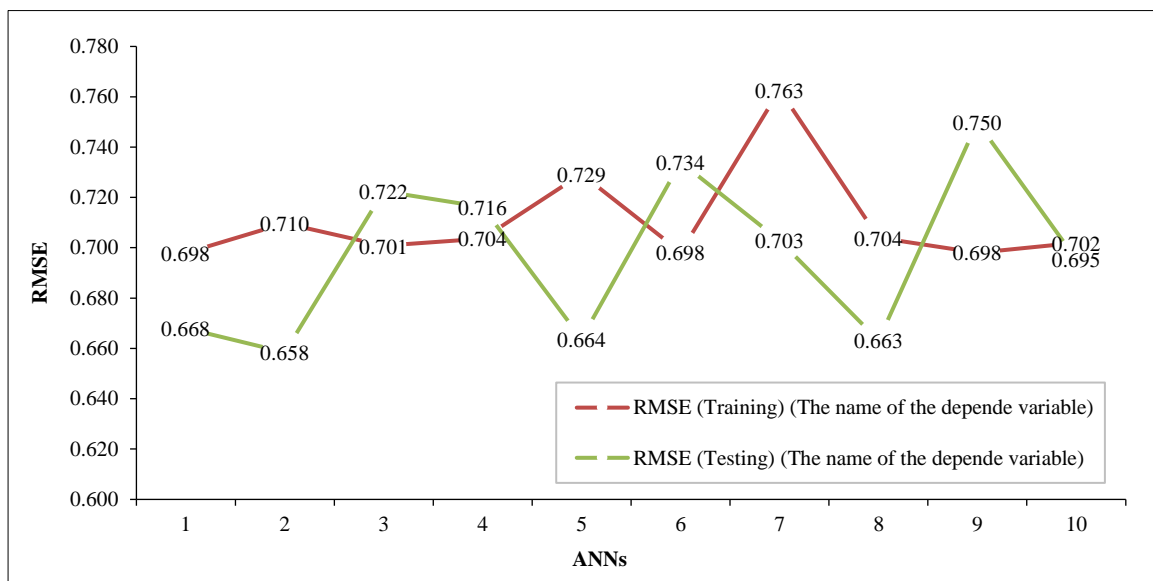


Figure 6. RMSE statistics

To ascertain how effectively each input neuron predicted events, a sensitivity analysis was performed. By dividing the relative importance of each input neuron by the greatest value, we were able to obtain its normalized importance, which we then displayed as a percentage [116]. The EMP barriers have a normalized relevance of 100% among the predictors.

5. Discussion

The investigation into barriers impeding the implementation of EMPs within the construction industry reveals a multifaceted landscape shaped by financial, policy and regulatory, technological, cultural and behavioral, and organizational constraints. Financial barriers, encompassing higher initial costs (Bar1: 0.965), limited financing options (Bar2: 0.68), and uncertain earnings (Bar3: 0.915), stand out as formidable obstacles, potentially impeding organizations from embracing sustainable practices [34, 36, 66, 71]. These financial hurdles underscore the challenges associated with funding sustainable initiatives and emphasize the need for innovative financial models and governmental support. Similarly, policy and regulatory challenges, such as limited government incentives (Bar4: 0.963), dynamic energy

management rules influenced by political shifts (Bar5: 0.81), and the absence of EMP-specific codes and regulations (Bar6: 0.97), contribute to an environment of uncertainty surrounding sustainable initiatives [38, 43, 50, 51, 55]. The high outer loadings indicate the significant impact of these challenges, highlighting the importance of advocating for consistent regulatory support and the development of dedicated codes for EMPs.

The technological dimension presents barriers rooted in insufficient advancements (Bar7: 0.837), the absence of standardized metrics (Bar8: 0.804), and a lack of technical expertise (Bar9: 0.895), collectively hindering innovation in energy management within the construction sector [61, 69, 70]. The high outer loadings suggest that technological barriers pose a substantial challenge, emphasizing the need for investments in research and development and capacity building. Cultural and behavioral factors manifest as resistance (Bar10: 0.68), lack of awareness (Bar11: 0.915), and limited interest from clients and developers (Bar12: 0.846, Bar13: 0.843), underscoring the importance of a cultural shift toward sustainable practices [36, 53, 60, 68, 72]. The substantial outer loadings indicate that addressing these cultural and behavioral challenges is pivotal for successful EMP implementation. Organizational barriers, including a lack of top management support (Bar14: 0.877), insufficient communication (Bar15: 0.905), and delays in decision-making (Bar16: 0.863), emphasize the need for comprehensive organizational strategies to drive sustainability initiatives [33, 51, 67]. The high outer loadings highlight the organizational challenges, requiring a concerted effort to foster commitment and streamline decision-making processes.

Addressing these barriers necessitates a multifaceted approach that integrates innovative financial strategies, advocacy for regulatory support, investments in technology and capacity building, cultural transformation programs, and organizational commitment. Drawing from insights gleaned from previous studies [3, 4, 35, 72], it is evident that a holistic response is essential to overcoming the challenges hindering the implementation of Energy Management Programs (EMPs) in the construction industry. By collaborating with industry stakeholders, policymakers, and organizations [28, 34, 59, 68], concerted efforts can be made to create an environment conducive to sustainable energy practices, facilitating a transformative shift in the sector. Furthermore, the specific values of the outer loadings obtained from empirical analyses provide a quantitative understanding of the relative impact of each barrier, thereby guiding targeted interventions for effective EMP implementation.

5.1. Implications

5.1.1 Theoretical Implications

The research presents a robust theoretical approach by introducing a comprehensive model that addresses various dimensions of barriers to Energy Management Practices (EMPs) adoption within the construction industry. This model encompasses financial, policy and regulatory, technological, cultural and behavioral, organizational, and market and economic dimensions, providing a holistic perspective on the challenges hindering EMP integration. By meticulously quantifying the impact of each barrier, the study offers a nuanced understanding of their relative importance, thereby contributing valuable insights for researchers.

This theoretical approach allows for a more informed view of the varying degrees of influence that different factors exert on the adoption of sustainable practices. Specifically, it validates existing theoretical frameworks related to the adoption of innovative technologies in construction. The study empirically supports factors such as economic considerations, regulatory support, technological readiness, cultural alignment, organizational dynamics, and market conditions, all of which are highlighted in innovation adoption theories. By substantiating these theoretical constructs within the context of EMP adoption, the research provides a solid foundation for understanding and addressing barriers to sustainability within the construction industry. Thus, this theoretical approach not only advances our understanding of EMP adoption but also offers insights that can inform future research in sustainable construction practices.

5.1.2 Practical Implications

The identification and quantification of barriers in this study provide invaluable insights for industry stakeholders, policymakers, and project managers, facilitating strategic planning to overcome specific challenges and successfully integrate Energy Management Practices (EMPs) into construction projects. Addressing financial constraints, enhancing regulatory support, fostering technological innovation, and promoting cultural awareness emerge as key components of strategic plans for EMP adoption. The study suggests that resource allocation should be guided by the most influential barriers identified, allowing organizations and policymakers to prioritize efforts and resources effectively, thus maximizing the impact of interventions.

Moreover, the study highlights the importance of addressing technological and informational gaps through targeted training programs aimed at enhancing technical expertise and awareness among construction professionals. Policy-makers can leverage these insights to develop effective policies tailored to address identified barriers, including designing financial incentives, ensuring regulatory stability, and promoting technological innovation to facilitate EMP adoption. The empirical support provided by the study emphasizes the significance of these policy dimensions in fostering sustainability within the construction industry.

Furthermore, the study underscores the necessity of industry-wide collaboration and awareness campaigns to address cultural and behavioral barriers effectively. By engaging with stakeholders such as clients and developers, interest and demand for EMP adoption in construction projects can be enhanced. Additionally, the study emphasizes the interconnected nature of environmental, social, and economic factors in achieving Overall Sustainable Success (OSS) in construction projects. Practitioners can utilize this insight to align projects with broader sustainability goals, emphasizing not only economic viability but also environmental and social responsibility. This aligns with the growing global emphasis on sustainable and responsible business practices.

6. Conclusions

This study investigates the barriers impeding the implementation of Energy Management Programs (EMPs) in the construction industry through a dual-method approach, combining an extensive literature review with a targeted survey. The identified barriers encompass financial, policy and regulatory, technological, cultural and behavioral, and organizational dimensions. It is found that financial constraints, limited governmental support, technological inadequacies, cultural resistance, and organizational challenges collectively hinder the widespread adoption of EMPs in construction projects. Empirical validation through SEM and ANN analyses reinforces the significance of these barriers, offering insights into their interrelationships and relative importance. The findings emphasize the necessity of a holistic approach involving financial innovation, regulatory advocacy, technological advancements, cultural transformation, and organizational commitment to address these challenges effectively.

However, it is important to acknowledge the study's limitations. Primarily focusing on the construction industry in Saudi Arabia may limit the generalizability of the findings to other geographical locations or industries with distinct contextual factors. Although efforts were made to mitigate the response bias inherent in self-reported data from professionals engaged in construction maintenance projects through rigorous analyses, the potential for bias remains. Future research should expand the geographical scope to capture diverse industry contexts and assess the generalizability of identified barriers. Additionally, conducting longitudinal studies could offer insights into the dynamic nature of these barriers over time, providing a more nuanced understanding of their evolution. Exploring potential interventions and strategies to overcome these barriers would offer valuable insights to practitioners and policymakers aiming to promote sustainable practices in the construction sector.

Regarding the conclusion's suggestion of a holistic approach to addressing EMP adoption barriers, practical examples could include implementing comprehensive training programs to enhance cultural awareness and technical expertise among construction professionals. Additionally, fostering collaborative partnerships between industry stakeholders, policymakers, and educational institutions could facilitate knowledge sharing and innovation adoption. Organizational-level initiatives such as creating incentives for sustainable practices and fostering a culture of environmental responsibility could also play a crucial role in overcoming cultural and organizational challenges.

7. Declarations

7.1. Author Contributions

Conceptualization, Y.A., A.F.K., and M.A.; methodology, Y.A., A.F.K., and M.A.; software, Y.A., A.F.K., and M.A.; formal analysis, Y.A., A.F.K., and M.A.; investigation, Y.A., A.F.K., and M.A.; resources, Y.A. and A.F.K.; writing—original draft preparation, Y.A., A.F.K., and M.A.; writing—review and editing, Y.A., A.F.K., and M.A.; visualization, A.F.K. and M.A.; supervision, Y.A., A.F.K., and M.A.; funding acquisition, Y.A., A.F.K., and M.A. All authors have read and agreed to the published version of the manuscript.

7.2. Data Availability Statement

The data presented in this study are available in the article.

7.3. Funding

The authors extend their appreciation to Prince Sattam bin Abdulaziz University for funding this research work through the project number (PSAU/2023/01/26586).

7.4. Conflicts of Interest

The authors declare no conflict of interest.

8. References

- [1] Jovanović, B., Filipović, J., & Bakić, V. (2015). Prioritization of manufacturing sectors in Serbia for energy management improvement - AHP method. *Energy Conversion and Management*, 98, 225–235. doi:10.1016/j.enconman.2015.03.107.
- [2] Cagno, E., Trianni, A., Abeelen, C., Worrell, E., & Miggiano, F. (2015). Barriers and drivers for energy efficiency: Different perspectives from an exploratory study in the Netherlands. *Energy Conversion and Management*, 102, 26–38. doi:10.1016/j.enconman.2015.04.018.

- [3] Shi, Q., Zuo, J., Huang, R., Huang, J., & Pullen, S. (2013). Identifying the critical factors for green construction - An empirical study in China. *Habitat International*, 40, 1–8. doi:10.1016/j.habitatint.2013.01.003.
- [4] Shen, L. Y., & Tam, V. W. Y. (2002). Implementation of environmental management in the Hong Kong construction industry. *International Journal of Project Management*, 20(7), 535–543. doi:10.1016/S0263-7863(01)00054-0.
- [5] Worrell, E., & Price, L. (2001). Policy scenarios for energy efficiency improvement in industry. *Energy Policy*, 29(14), 1223–1241. doi:10.1016/S0301-4215(01)00069-6.
- [6] Zhang, X., Shen, L., & Chan, S. Y. (2012). The diffusion of solar energy use in HK: What are the barriers? *Energy Policy*, 41, 241–249. doi:10.1016/j.enpol.2011.10.043.
- [7] Trianni, A., Cagno, E., & Worrell, E. (2013). Innovation and adoption of energy efficient technologies: An exploratory analysis of Italian primary metal manufacturing SMEs. *Energy Policy*, 61, 430–440. doi:10.1016/j.enpol.2013.06.034.
- [8] Schleich, J., Gassmann, X., Faure, C., & Meissner, T. (2016). Making the implicit explicit: A look inside the implicit discount rate. *Energy Policy*, 97, 321–331. doi:10.1016/j.enpol.2016.07.044.
- [9] Kangas, H. L., Lazarevic, D., & Kivimaa, P. (2018). Technical skills, disinterest and non-functional regulation: Barriers to building energy efficiency in Finland viewed by energy service companies. *Energy Policy*, 114, 63–76. doi:10.1016/j.enpol.2017.11.060.
- [10] Palm, J., & Thollander, P. (2010). An interdisciplinary perspective on industrial energy efficiency. *Applied Energy*, 87(10), 3255–3261. doi:10.1016/j.apenergy.2010.04.019.
- [11] Zhang, W., Wang, J., Liu, Y., Gao, G., Liang, S., & Ma, H. (2020). Reinforcement learning-based intelligent energy management architecture for hybrid construction machinery. *Applied Energy*, 275(5988), 115401. doi:10.1016/j.apenergy.2020.115401.
- [12] Morel, J. C., Mesbah, A., Oggero, M., & Walker, P. (2001). Building houses with local materials: Means to drastically reduce the environmental impact of construction. *Building and Environment*, 36(10), 1119–1126. doi:10.1016/S0360-1323(00)00054-8.
- [13] Verbeeck, G., & Hens, H. (2010). Life cycle inventory of buildings: A calculation method. *Building and Environment*, 45(4), 1037–1041. doi:10.1016/j.buildenv.2009.10.012.
- [14] Karimpour, M., Belusko, M., Xing, K., & Bruno, F. (2014). Minimising the life cycle energy of buildings: Review and analysis. *Building and Environment*, 73, 106–114. doi:10.1016/j.buildenv.2013.11.019.
- [15] Li, Y., Song, H., Sang, P., Chen, P. H., & Liu, X. (2019). Review of Critical Success Factors (CSFs) for green building projects. *Building and Environment*, 158(May), 182–191. doi:10.1016/j.buildenv.2019.05.020.
- [16] Kang, J., Wang, L., Wang, Z., Zhang, J., & Dai, H. (2023). Improving the emergency management of energy infrastructure using scenario construction. *International Journal of Hydrogen Energy*, 48(23), 8731–8742. doi:10.1016/j.ijhydene.2022.11.208.
- [17] Pelenur, M. J., & Cruickshank, H. J. (2012). Closing the Energy Efficiency Gap: A study linking demographics with barriers to adopting energy efficiency measures in the home. *Energy*, 47(1), 348–357. doi:10.1016/j.energy.2012.09.058.
- [18] Lu, Y., Chang, R., Shabunko, V., & Lay Yee, A. T. (2019). The implementation of building-integrated photovoltaics in Singapore: drivers versus barriers. *Energy*, 168, 400–408. doi:10.1016/j.energy.2018.11.099.
- [19] Golpîra, H., & Khan, S. A. R. (2019). A multi-objective risk-based robust optimization approach to energy management in smart residential buildings under combined demand and supply uncertainty. *Energy*, 170, 1113–1129. doi:10.1016/j.energy.2018.12.185.
- [20] Wang, Y., Li, K., Zeng, X., Gao, B., & Hong, J. (2022). Energy consumption characteristics based driving conditions construction and prediction for hybrid electric buses energy management. *Energy*, 245, 123189. doi:10.1016/j.energy.2022.123189.
- [21] Zhang, W., Wang, J., Xu, Z., Shen, Y., & Gao, G. (2022). A generalized energy management framework for hybrid construction vehicles via model-based reinforcement learning. *Energy*, 260(5988), 124849. doi:10.1016/j.energy.2022.124849.
- [22] Zhang, Q. (2004). Residential energy consumption in China and its comparison with Japan, Canada, and USA. *Energy and Buildings*, 36(12), 1217–1225. doi:10.1016/j.enbuild.2003.08.002.
- [23] Darko, A., Chan, A. P. C., Ameyaw, E. E., He, B. J., & Olanipekun, A. O. (2017). Examining issues influencing green building technologies adoption: The United States green building experts' perspectives. *Energy and Buildings*, 144, 320–332. doi:10.1016/j.enbuild.2017.03.060.
- [24] Fernando, Y., & Hor, W. L. (2017). Impacts of energy management practices on energy efficiency and carbon emissions reduction: A survey of Malaysian manufacturing firms. *Resources, Conservation and Recycling*, 126(July), 62–73. doi:10.1016/j.resconrec.2017.07.023.
- [25] Nazeer Ahamed, M. F., & Mariappan, M. (2023). A study to determine human-related errors at the level of top management, safety supervisors & workers during the implementation of safety practices in the construction industry. *Safety Science*, 162(February), 106081. doi:10.1016/j.ssci.2023.106081.

- [26] Ortiz, O., Castells, F., & Sonnemann, G. (2009). Sustainability in the construction industry: A review of recent developments based on LCA. *Construction and Building Materials*, 23(1), 28–39. doi:10.1016/j.conbuildmat.2007.11.012.
- [27] Brunke, J. C., Johansson, M., & Thollander, P. (2014). Empirical investigation of barriers and drivers to the adoption of energy conservation measures, energy management practices and energy services in the Swedish iron and steel industry. *Journal of Cleaner Production*, 84(1), 509–525. doi:10.1016/j.jclepro.2014.04.078.
- [28] Xue, X., Wu, H., Zhang, X., Dai, J., & Su, C. (2015). Measuring energy consumption efficiency of the construction industry: The case of China. *Journal of Cleaner Production*, 107, 509–515. doi:10.1016/j.jclepro.2014.04.082.
- [29] Persson, J., & Grönkvist, S. (2015). Drivers for and barriers to low-energy buildings in Sweden. *Journal of Cleaner Production*, 109, 296–304. doi:10.1016/j.jclepro.2014.09.094.
- [30] Chan, A. P. C., Darko, A., Olanipekun, A. O., & Ameyaw, E. E. (2018). Critical barriers to green building technologies adoption in developing countries: The case of Ghana. *Journal of Cleaner Production*, 172, 1067–1079. doi:10.1016/j.jclepro.2017.10.235.
- [31] Darko, A., Chan, A. P. C., Yang, Y., Shan, M., He, B. J., & Gou, Z. (2018). Influences of barriers, drivers, and promotion strategies on green building technologies adoption in developing countries: The Ghanaian case. *Journal of Cleaner Production*, 200, 687–703. doi:10.1016/j.jclepro.2018.07.318.
- [32] Zhang, Q., Oo, B. L., & Lim, B. T. H. (2019). Drivers, motivations, and barriers to the implementation of corporate social responsibility practices by construction enterprises : A review. *Journal of Cleaner Production*, 210, 563–584. doi:10.1016/j.jclepro.2018.11.050.
- [33] Martek, I., Hosseini, M. R., Shrestha, A., Edwards, D. J., & Durdyev, S. (2019). Barriers inhibiting the transition to sustainability within the Australian construction industry: An investigation of technical and social interactions. *Journal of Cleaner Production*, 211(2019), 281–292. doi:10.1016/j.jclepro.2018.11.166.
- [34] Maqbool, R., Arul, T., & Ashfaq, S. (2023). A mixed-methods study of sustainable construction practices in the UK. *Journal of Cleaner Production*, 430(August), 139087. doi:10.1016/j.jclepro.2023.139087.
- [35] Fu, C., Liu, Y. Q., & Shan, M. (2023). Drivers of low-carbon practices in green supply chain management in construction industry: An empirical study in China. *Journal of Cleaner Production*, 428(October), 139497. doi:10.1016/j.jclepro.2023.139497.
- [36] Pietrosemoli, L., & Rodríguez Monroy, C. (2013). The impact of sustainable construction and knowledge management on sustainability goals. A review of the Venezuelan renewable energy sector. *Renewable and Sustainable Energy Reviews*, 27, 683–691. doi:10.1016/j.rser.2013.07.056.
- [37] Karatayev, M., Hall, S., Kalyuzhnova, Y., & Clarke, M. L. (2016). Renewable energy technology uptake in Kazakhstan: Policy drivers and barriers in a transitional economy. *Renewable and Sustainable Energy Reviews*, 66, 120–136. doi:10.1016/j.rser.2016.07.057.
- [38] Hesselink, L. X. W., & Chappin, E. J. L. (2019). Adoption of energy efficient technologies by households – Barriers, policies and agent-based modelling studies. *Renewable and Sustainable Energy Reviews*, 99, 29–41. doi:10.1016/j.rser.2018.09.031.
- [39] Liu, H., Xing, X., Shang, W., & Li, T. (2021). NSGA-II Optimized Multiobjective Predictive Energy Management for Fuel Cell/Battery/Supercapacitor Hybrid Construction Vehicles. *International Journal of Electrochemical Science*, 16(4), 1–16. doi:10.20964/2021.04.24.
- [40] Umar, U. A., Shafiq, N., & Ahmad, F. A. (2021). A case study on the effective implementation of the reuse and recycling of construction & demolition waste management practices in Malaysia. *Ain Shams Engineering Journal*, 12(1), 283–291. doi:10.1016/j.asej.2020.07.005.
- [41] Davies, P. J., Emmitt, S., & Firth, S. K. (2015). Delivering improved initial embodied energy efficiency during construction. *Sustainable Cities and Society*, 14(1), 267–279. doi:10.1016/j.scs.2014.09.010.
- [42] Gupta, P., Anand, S., & Gupta, H. (2017). Developing a roadmap to overcome barriers to energy efficiency in buildings using best worst method. *Sustainable Cities and Society*, 31, 244–259. doi:10.1016/j.scs.2017.02.005.
- [43] Moglia, M., Cook, S., & McGregor, J. (2017). A review of Agent-Based Modelling of technology diffusion with special reference to residential energy efficiency. *Sustainable Cities and Society*, 31, 173–182. doi:10.1016/j.scs.2017.03.006.
- [44] Caputo, P., & Pasetti, G. (2017). Boosting the energy renovation rate of the private building stock in Italy: Policies and innovative GIS-based tools. *Sustainable Cities and Society*, 34(July), 394–404. doi:10.1016/j.scs.2017.07.002.
- [45] Azizi, E., Ahmadihangar, R., Rosin, A., Martins, J., Lopes, R. A., Beheshti, M. T., & Bolouki, S. (2021). Residential energy flexibility characterization using non-intrusive load monitoring. *Sustainable Cities and Society*, 75(May), 103321. doi:10.1016/j.scs.2021.103321.
- [46] Li, X., Luo, J., Li, Y., Wang, W., Hong, W., Liu, M., Li, X., & Lv, Z. (2022). Application of effective water-energy management based on digital twins technology in sustainable cities construction. *Sustainable Cities and Society*, 87(October), 104241. doi:10.1016/j.scs.2022.104241.

- [47] Surroop, D., Raghoo, P., Wolf, F., Shah, K. U., & Jeetah, P. (2018). Energy access in Small Island Developing States: Status, barriers and policy measures. *Environmental Development*, 27, 58–69. doi:10.1016/j.envdev.2018.07.003.
- [48] Trinh, H. A., Truong, H. V. A., Do, T. C., Nguyen, M. H., Phan, V. Du, & Ahn, K. K. (2022). Optimization-based energy management strategies for hybrid construction machinery: A review. *Energy Reports*, 8, 6035–6057. doi:10.1016/j.egy.2022.04.050.
- [49] Żuk, P. (2023). Soft power and the media management of energy transition: Analysis of the media narrative about the construction of nuclear power plants in Poland. *Energy Reports*, 9, 568–583. doi:10.1016/j.egy.2022.11.192.
- [50] Paulu, A., Vitvarová, M., & Kočí, V. (2022). Quantifying the industry-wide symbiotic potential: LCA of construction and energy waste management in the Czech Republic. *Sustainable Production and Consumption*, 34, 55–64. doi:10.1016/j.spc.2022.08.033.
- [51] Olawumi, T. O., Chan, D. W. M., Wong, J. K. W., & Chan, A. P. C. (2018). Barriers to the integration of BIM and sustainability practices in construction projects: A Delphi survey of international experts. *Journal of Building Engineering*, 20, 60–71. doi:10.1016/j.job.2018.06.017.
- [52] Che Ibrahim, C. K. I., Manu, P., Belayutham, S., Mahamadu, A. M., & Antwi-Afari, M. F. (2022). Design for safety (DfS) practice in construction engineering and management research: A review of current trends and future directions. *Journal of Building Engineering*, 52, 104352. doi:10.1016/j.job.2022.104352.
- [53] Ikudayisi, A. E., Chan, A. P. C., Darko, A., & Adedeji, Y. M. D. (2023). Integrated practices in the Architecture, Engineering, and Construction industry: Current scope and pathway towards Industry 5.0. *Journal of Building Engineering*, 73(May), 106788. doi:10.1016/j.job.2023.106788.
- [54] Tafesse, S., Girma, Y. E., & Dessalegn, E. (2022). Analysis of the socio-economic and environmental impacts of construction waste and management practices. *Heliyon*, 8(3), 9169. doi:10.1016/j.heliyon.2022.e09169.
- [55] Jia, J. J., Xu, J. H., Fan, Y., & Ji, Q. (2018). Willingness to accept energy-saving measures and adoption barriers in the residential sector: An empirical analysis in Beijing, China. *Renewable and Sustainable Energy Reviews*, 95, 56–73. doi:10.1016/j.rser.2018.07.015.
- [56] Ali, A. H., El-Mahdy, G. M., Ibrahim, A. H., & Daoud, A. O. (2023). Towards the Adoption of Modular Construction in Residential Projects in Egypt: Benefits, Barriers, and Enablers. *Towards a Sustainable Construction Industry: The Role of Innovation and Digitalisation*, 1, 72–81. doi:10.1007/978-3-031-22434-8_8.
- [57] Hassan Ali, A., Farouk Kineber, A., Elshaboury, N., Arashpour, M., & Osama Daoud, A. (2023). Analysing multifaceted barriers to modular construction in sustainable building projects: a comprehensive evaluation using multi-criteria decision making. *International Journal of Construction Management*, 0(0), 1–17. doi:10.1080/15623599.2023.2299557.
- [58] Ali, A. H., Kineber, A. F., Elyamany, A., Hussein Ibrahim, A., & Daoud, A. O. (2023). Exploring stationary and major modular construction challenges in developing countries: a case study of Egypt. *Journal of Engineering, Design and Technology*, 1–30. doi:10.1108/JEDT-03-2023-0099.
- [59] Somachandra, W. D. I. V., Sylva, K. K. K., Bandara, C. S., & Dissanayake, P. B. R. (2023). Corporate social responsibility (CSR) practices in the construction industry of Sri Lanka. *International Journal of Construction Management*, 23(13), 2230–2238. doi:10.1080/15623599.2022.2049489.
- [60] Williams, K., & Dair, C. (2006). What is stopping sustainable building in England? Barriers experienced by stakeholders in delivering sustainable developments. *Sustainable Development*, 15(3), 135–147. Portico. doi:10.1002/sd.308.
- [61] Iqbal, M., Ma, J., Ahmad, N., Hussain, K., & Usmani, M. S. (2021). Promoting sustainable construction through energy-efficient technologies: an analysis of promotional strategies using interpretive structural modeling. *International Journal of Environmental Science and Technology*, 18(11), 3479–3502. doi:10.1007/s13762-020-03082-4.
- [62] Sarkar, A., Qian, L., Peau, A. K., & Shahriar, S. (2021). Modeling drivers for successful adoption of green business: an interpretive structural modeling approach. *Environmental Science and Pollution Research*, 28(1), 1077–1096. doi:10.1007/s11356-020-10490-z.
- [63] Shahzad, U. (2020). Environmental taxes, energy consumption, and environmental quality: Theoretical survey with policy implications. *Environmental Science and Pollution Research*, 27(20), 24848–24862. doi:10.1007/s11356-020-08349-4.
- [64] Van Gorp, J. C. (2004). Maximizing energy savings with energy management systems. *Strategic Planning for Energy and the Environment*, 24(3), 57–69. doi:10.1080/10485230409509667.
- [65] Li, B., Akintoye, A., Edwards, P. J., & Hardcastle, C. (2005). Critical success factors for PPP/PFI projects in the UK construction industry. *Construction Management and Economics*, 23(5), 459–471. doi:10.1080/01446190500041537.
- [66] Serpell, A., Kort, J., & Vera, S. (2013). Awareness, actions, drivers and barriers of sustainable construction in Chile. *Technological and Economic Development of Economy*, 19(2), 272–288. doi:10.3846/20294913.2013.798597.



- [67] Love, P. E. D., Niedzweicki, M., Bullen, P. A., & Edwards, D. J. (2012). Achieving the Green Building Council of Australia's World Leadership Rating in an Office Building in Perth. *Journal of Construction Engineering and Management*, 138(5), 652–660. doi:10.1061/(asce)co.1943-7862.0000461.
- [68] Shan, M., Liu, W. Q., Hwang, B. G., & Lye, J. M. (2020). Critical success factors for small contractors to conduct green building construction projects in Singapore: identification and comparison with large contractors. *Environmental Science and Pollution Research*, 27(8), 8310–8322. doi:10.1007/s11356-019-06646-1.
- [69] Bruno, S., Dellino, G., La Scala, M., & Meloni, C. (2019). A microforecasting module for energy management in residential and tertiary buildings. *Energies*, 12(6). doi:10.3390/en12061006.
- [70] Laskurain, I., Ibarloza, A., Larrea, A., & Allur, E. (2017). Contribution to energy management of the main standards for environmental management systems: The case of ISO 14001 and EMAS. *Energies*, 10(11). doi:10.3390/en10111758.
- [71] Lipu, M. S. H. (2013). An Approach towards Sustainable Energy Performance by Green Building: A Review of Current Features, Benefits and Barriers. *International Journal of Renewable and Sustainable Energy*, 2(4), 180. doi:10.11648/j.ijrse.20130204.18.
- [72] Bhavsar, V., Sridharan, S. R., & Sudarsan, J. S. (2023). Barriers to circular economy practices during construction and demolition waste management in an emerging economy. *Resources, Conservation and Recycling Advances*, 20(November), 200198. doi:10.1016/j.rcradv.2023.200198.
- [73] Tan, T., Chen, K., Xue, F., & Lu, W. (2019). Barriers to Building Information Modeling (BIM) implementation in China's prefabricated construction: An interpretive structural modeling (ISM) approach. *Journal of Cleaner Production*, 219, 949-959. doi:10.1016/j.jclepro.2019.02.141.
- [74] Palinkas, L. A., Horwitz, S. M., Green, C. A., Wisdom, J. P., Duan, N., & Hoagwood, K. (2015). Purposeful Sampling for Qualitative Data Collection and Analysis in Mixed Method Implementation Research. *Administration and Policy in Mental Health and Mental Health Services Research*, 42(5), 533–544. doi:10.1007/s10488-013-0528-y.
- [75] Wong, K. K. K. (2013). Partial least squares structural equation modeling (PLS-SEM) techniques using SmartPLS. *Marketing bulletin*, 24(1), 1-32.
- [76] Talafubieke, M., Mai, S., & Xialifuhan, N. (2021). Evaluation of the Virtual Economic Effect of Tourism Product Emotional Marketing Based on Virtual Reality. *Frontiers in Psychology*, 12. doi:10.3389/fpsyg.2021.759268.
- [77] Roberts, N., Thatcher, J. B., & Grover, V. (2010). Advancing operations management theory using exploratory structural equation modelling techniques. *International Journal of Production Research*, 48(15), 4329–4353. doi:10.1080/00207540902991682.
- [78] Singh, A. K., Kumar, V. R. P., Shoaib, M., Adebayo, T. S., & Irfan, M. (2023). A strategic roadmap to overcome blockchain technology barriers for sustainable construction: A deep learning-based dual-stage SEM-ANN approach. *Technological Forecasting and Social Change*, 194, 122716. doi:10.1016/j.techfore.2023.122716.
- [79] Kineber, A. F., Singh, A. K., Fazeli, A., Mohandes, S. R., Cheung, C., Arashpour, M., Ejohwomu, O., & Zayed, T. (2023). Modelling the relationship between digital twins implementation barriers and sustainability pillars: Insights from building and construction sector. *Sustainable Cities and Society*, 99, 104930. doi:10.1016/j.scs.2023.104930.
- [80] Ali, A. H., Kineber, A. F., Elyamany, A., Ibrahim, A. H., & Daoud, A. O. (2023). Identifying and assessing modular construction implementation barriers in developing nations for sustainable building development. *Sustainable Development*, 31(5), 3346–3364. doi:10.1002/sd.2589.
- [81] Ali, A. H., Elyamany, A., Ibrahim, A. H., Kineber, A. F., & Daoud, A. O. (2023). Modelling the relationship between modular construction adoption and critical success factors for residential projects in developing countries. *International Journal of Construction Management*, 1–12. doi:10.1080/15623599.2023.2185940.
- [82] Kineber, A. F., Oke, A., Hamed, M. M., Alyanbaawi, A., Elmansoury, A., & Daoud, A. O. (2023). Decision Making Model for Identifying the Cyber Technology Implementation Benefits for Sustainable Residential Building: A Mathematical PLS-SEM Approach. *Sustainability (Switzerland)*, 15(3), 2458. doi:10.3390/su15032458.
- [83] Bello, A. O., Eje, D. O., Idris, A., Semiu, M. A., & Khan, A. A. (2023). Drivers for the implementation of modular construction systems in the AEC industry of developing countries. *Journal of Engineering, Design and Technology*, 2018. doi:10.1108/JEDT-11-2022-0571.
- [84] Nureen, N., Xin, Y., Irfan, M., & Fahad, S. (2023). Going green: how do green supply chain management and green training influence firm performance? Evidence from a developing country. *Environmental Science and Pollution Research*, 30(20), 57448–57459. doi:10.1007/s11356-023-26609-x.
- [85] Waqar, A., Othman, I., & Pomares, J. C. (2023). Impact of 3D Printing on the Overall Project Success of Residential Construction Projects Using Structural Equation Modelling. *International Journal of Environmental Research and Public Health*, 20(5), 3800. doi:10.3390/ijerph20053800.

- [86] Khan, S. A., Mubarik, M. S., Kusi-Sarpong, S., Gupta, H., Zaman, S. I., & Mubarik, M. (2022). Blockchain technologies as enablers of supply chain mapping for sustainable supply chains. *Business Strategy and the Environment*, 31(8), 3742–3756. doi:10.1002/bse.3029.
- [87] Oke, A. E., Farouk Kineber, A., Abdel-Tawab, M., Abubakar, A. S., Albukhari, I., & Kingsley, C. (2023). Barriers to the implementation of cloud computing for sustainable construction in a developing economy. *International Journal of Building Pathology and Adaptation*, 41(5), 988–1013. doi:10.1108/IJBPA-07-2021-0098.
- [88] Rajbhandari, S., Devkota, N., Khanal, G., Mahato, S., & Paudel, U. R. (2022). Assessing the industrial readiness for adoption of industry 4.0 in Nepal: A structural equation model analysis. *Heliyon*, 8(2), 8919. doi:10.1016/j.heliyon.2022.e08919.
- [89] Garg, R. K. (2021). Structural equation modeling of E-supplier selection criteria in mechanical manufacturing industries. *Journal of Cleaner Production*, 311(May), 127597. doi:10.1016/j.jclepro.2021.127597.
- [90] Teng, J., Mu, X., Wang, W., Xu, C., & Liu, W. (2019). Strategies for sustainable development of green buildings. *Sustainable Cities and Society*, 44, 215–226. doi:10.1016/j.scs.2018.09.038.
- [91] Gunduz, M., Birgonul, M. T., & Ozdemir, M. (2017). Fuzzy Structural Equation Model to Assess Construction Site Safety Performance. *Journal of Construction Engineering and Management*, 143(4), 4016112. doi:10.1061/(asce)co.1943-7862.0001259.
- [92] Podsakoff, P. M., & Organ, D. W. (1986). Self-Reports in Organizational Research: Problems and Prospects. *Journal of Management*, 12(4), 531–544. doi:10.1177/014920638601200408.
- [93] MacKenzie, S. B., & Podsakoff, P. M. (2012). Common Method Bias in Marketing: Causes, Mechanisms, and Procedural Remedies. *Journal of Retailing*, 88(4), 542–555. doi:10.1016/j.jretai.2012.08.001.
- [94] Durdyev, S., Ismail, S., Ihtiyar, A., Abu Bakar, N. F. S., & Darko, A. (2018). A partial least squares structural equation modeling (PLS-SEM) of barriers to sustainable construction in Malaysia. *Journal of Cleaner Production*, 204, 564–572. doi:10.1016/j.jclepro.2018.08.304.
- [95] Munianday, P., Radzi, A. R., Esa, M., & Rahman, R. A. (2022). Optimal Strategies for Improving Organizational BIM Capabilities: PLS-SEM Approach. *Journal of Management in Engineering*, 38(3). doi:10.1061/(asce)me.1943-5479.0001038.
- [96] Ali, A. H., Kineber, A. F., Elyamany, A., Ibrahim, A. H., & Daoud, A. O. (2023). Modelling the role of modular construction's critical success factors in the overall sustainable success of Egyptian housing projects. *Journal of Building Engineering*, 71(April), 1–18. doi:10.1016/j.job.2023.106467.
- [97] Abdel-Tawab, M., Kineber, A. F., Chileshe, N., Abanda, H., Ali, A. H., & Almkhtar, A. (2023). Building Information Modelling Implementation Model for Sustainable Building Projects in Developing Countries: A PLS-SEM Approach. *Sustainability (Switzerland)*, 15(12), 1–21. doi:10.3390/su15129242.
- [98] Awang, Z., Wan Afthanorhan, W. M. A., & Asri, M. A. M. (2015). Parametric and Non-Parametric Approach in Structural Equation Modeling (SEM): The Application of Bootstrapping. *Modern Applied Science*, 9(9), 58–67. doi:10.5539/mas.v9n9p58.
- [99] Li, C., Zhang, Y., & Xu, Y. (2022). Factors Influencing the Adoption of Blockchain in the Construction Industry: A Hybrid Approach Using PLS-SEM and fsQCA. *Buildings*, 12(9). doi:10.3390/buildings12091349.
- [100] Ashaari, M. A., Singh, K. S. D., Abbasi, G. A., Amran, A., & Liebana-Cabanillas, F. J. (2021). Big data analytics capability for improved performance of higher education institutions in the Era of IR 4.0: A multi-analytical SEM & ANN perspective. *Technological Forecasting and Social Change*, 173, 121119. doi:10.1016/j.techfore.2021.121119.
- [101] Lo, P. S., Dwivedi, Y. K., Wei-Han Tan, G., Ooi, K. B., Cheng-Xi Aw, E., & Metri, B. (2022). Why do consumers buy impulsively during live streaming? A deep learning-based dual-stage SEM-ANN analysis. *Journal of Business Research*, 147, 325–337. doi:10.1016/j.jbusres.2022.04.013.
- [102] Wong, L. W., Leong, L. Y., Hew, J. J., Tan, G. W. H., & Ooi, K. B. (2020). Time to seize the digital evolution: Adoption of blockchain in operations and supply chain management among Malaysian SMEs. *International Journal of Information Management*, 52, 101997. doi:10.1016/j.ijinfomgt.2019.08.005.
- [103] Leong, L. Y., Hew, T. S., Ooi, K. B., & Wei, J. (2020). Predicting mobile wallet resistance: A two-staged structural equation modeling-artificial neural network approach. *International Journal of Information Management*, 51(November), 102047. doi:10.1016/j.ijinfomgt.2019.102047.
- [104] Nicolas, C., Kim, J., & Chi, S. (2020). Quantifying the dynamic effects of smart city development enablers using structural equation modeling. *Sustainable Cities and Society*, 53, 101916. doi:10.1016/j.scs.2019.101916.
- [105] Tawalare, A., Laishram, B., & Thottathil, F. (2020). Relational Partnership in Public Construction Organizations: Front-Line Employee Perspective. *Journal of Construction Engineering and Management*, 146(1), 04019086. doi:10.1061/(asce)co.1943-7862.0001723.

- [106] Kar, S., & Jha, K. N. (2021). Exploring the Critical Barriers to and Enablers of Sustainable Material Management Practices in the Construction Industry. *Journal of Construction Engineering and Management*, 147(9), 04021102. doi:10.1061/(asce)co.1943-7862.0002125.
- [107] Chen, Y., Dib, H., Cox, R. F., Shaurette, M., & Vorvoreanu, M. (2016). Structural Equation Model of Building Information Modeling Maturity. *Journal of Construction Engineering and Management*, 142(9), 4016032. doi:10.1061/(asce)co.1943-7862.0001147.
- [108] Kursunoglu, N., Onder, S., & Onder, M. (2022). The Evaluation of Personal Protective Equipment Usage Habit of Mining Employees Using Structural Equation Modeling. *Safety and Health at Work*, 13(2), 180–186. doi:10.1016/j.shaw.2022.03.004.
- [109] Nwaogu, J. M., Chan, A. P. C., & Naslund, J. A. (2022). Measures to Improve the Mental Health of Construction Personnel Based on Expert Opinions. *Journal of Management in Engineering*, 38(4), 1–17. doi:10.1061/(asce)me.1943-5479.0001045.
- [110] Cruz-Jesus, F., Pinheiro, A., & Oliveira, T. (2019). Understanding CRM adoption stages: empirical analysis building on the TOE framework. *Computers in Industry*, 109, 1–13. doi:10.1016/j.compind.2019.03.007.
- [111] Rouhanizadeh, B., & Kermanshachi, S. (2022). Investigation of the Causal Relationships among Different Barrier Categories to Timely Posthurricane Recovery. *Natural Hazards Review*, 23(3). doi:10.1061/(asce)nh.1527-6996.0000565.
- [112] Arpacı, I., Karatas, K., Kusci, I., & Al-Emran, M. (2022). Understanding the social sustainability of the Metaverse by integrating UTAUT2 and big five personality traits: A hybrid SEM-ANN approach. *Technology in Society*, 71, 102120. doi:10.1016/j.techsoc.2022.102120.
- [113] Wang, G., Tan, G. W. H., Yuan, Y., Ooi, K. B., & Dwivedi, Y. K. (2022). Revisiting TAM2 in behavioral targeting advertising: A deep learning-based dual-stage SEM-ANN analysis. *Technological Forecasting and Social Change*, 175, 121345. doi:10.1016/j.techfore.2021.121345.
- [114] Prasad Das, C., Kumar Swain, B., Goswami, S., & Das, M. (2021). Prediction of traffic noise induced annoyance: A two-staged SEM-Artificial Neural Network approach. *Transportation Research Part D: Transport and Environment*, 100(September), 103055. doi:10.1016/j.trd.2021.103055.
- [115] Loh, X. M., Lee, V. H., & Leong, L. Y. (2022). Mobile-lizing continuance intention with the mobile expectation-confirmation model: An SEM-ANN-NCA approach. *Expert Systems with Applications*, 205, 117659. doi:10.1016/j.eswa.2022.117659.
- [116] Elseufy, S. M., Hussein, A., & Badawy, M. (2022). A hybrid SEM-ANN model for predicting overall rework impact on the performance of bridge construction projects. *Structures*, 46(June), 713–724. doi:10.1016/j.istruc.2022.10.100.



Concrete Strength and Aggregate Properties: In-Depth Analysis of Four Sources

Kamal Hosen ¹ , Md Abdulla Al Maruf ², Rayhan Howlader ³, Kripendra Chakma ^{4*} ,
Md Rezars Mia ⁵

¹ School of Civil Engineering, Southeast University, Nanjing, China.

² School of Civil Engineering, Nanjing Tech University, Nanjing, China.

³ School of Civil Engineering, Lamar University, Beaumont, TX 77705, United States.

⁴ School of Landscape Architecture, Beijing Forestry University, Beijing, China.

⁵ School of Civil Engineering, Tianjin University, Tianjin, China.

Received 23 August 2023; Revised 13 March 2024; Accepted 17 March 2024; Published 01 April 2024

Abstract

In the field of Reinforced Concrete Construction, concrete emerges as the predominant and extensively employed construction material. Concrete comprises a solid, chemically inert granular substance called coarse aggregate (CA) bonded with cement and water. Compared to fine aggregate or cement, CA has a larger volume of concrete. By examining the characteristics of the coarse aggregate using various laboratory testing processes, the coarse aggregate may be properly used in concrete. Bangladesh is experiencing significant growth in its infrastructure industry due to the construction of mega projects nationwide. For the building of RCC in Bangladesh, coarse aggregate is mainly procured from two sources in Bangladesh, and another is imported from China. This study aims to develop a clear understanding of aggregate and concrete strength quality for different coarse aggregates and track changes in the appearance of CA from multiple sources in China and Bangladesh. Coarse aggregates were collected from four prominent sources: Jaflong and Bholaganj (Bangladesh), Shandong, and Jiangsu (China). ACV (aggregate crushing value), gradation, voids, and unit weight; AIV (aggregate impact value), absorption, specific gravity, and resistance to abrasion-induced deterioration; and Los Angeles (LA) machines' impact tests have been conducted for all sources of CA. The concrete cylinder was made and tested for all sources of CA with the same ratio of cement, sand, and water to know the concrete strength for different CAs.

Keywords: Unit-Weight; Concrete Strength; Coarse Aggregate; Fineness Modulus; Abrasion; Specific Gravity.

1. Introduction

Concrete, characterized by its economic viability, constitutes the second most employed construction material globally, surpassed solely by water, with an annual consumption approaching nearly 30 billion tons [1]. The main elements of concrete are coarse aggregate, water, cement, and fine aggregate [2]. Even though concrete is used extensively, it might not be easy to anticipate its strength at different stages [3]. Naderi & Kaboudan [4] conducted an experimental study of the effect of aggregate type on concrete strength and permeability and observed that coarse aggregates comprise the majority of the concrete mix; they can significantly affect the permeability and strength of concrete. Barham et al. researched the effect of maximum coarse aggregate size on shear strengthening. Their experimental results showed that using full rough aggregate size positively impacts the ultimate shear strength,

* Corresponding author: kripendrachakma@bjfu.edu.cn

 <http://dx.doi.org/10.28991/CEJ-2024-010-04-016>



© 2024 by the authors. Licensee C.E.J, Tehran, Iran. This article is an open access article distributed under the terms and conditions of the Creative Commons Attribution (CC-BY) license (<http://creativecommons.org/licenses/by/4.0/>).

maximum deflections, toughness, and stiffness of strengthened RC members [5]. According to researchers, coarse aggregate changes may affect concrete strength failure characteristics [6]. According to Ezeldin & Aitcin [7], high-strength coarse aggregate typically results in higher compressive strength in high-strength concrete, whereas in standard-strength concrete, the strength of coarse aggregate has no bearing on compressive strength. Giaccio et al. directed research regarding different coarse aggregates and stated that most coarse aggregate particles in concrete containing limestone were shattered, but in concrete containing basalt, stress, mainly cracking, happened at the matrix-aggregate contact [8].

Lee et al. [9] and a team of ASCE researched on mechanical properties of concrete and concluded that the weakest point in low-strength concrete nearly always lies at the interface of matrix aggregate, and the mechanism of progressive micro cracking is that mortar cracks span adjacent joint cracks. High-strength concrete displayed fewer and smaller microcracks at all weights than normal-strength concrete. The observed behavior can be explained by treating high-strength concrete as a more homogeneous material. The compatibility of coarse aggregate with mortar strength and elastic characteristics is improved by matrix density and void content. The reduced stress at the matrix-aggregate interface also lowers the risk of interfacial failure, another benefit of the increased compatibility. As a result, microcracks are likely to spread through the aggregate, and their size gets smaller as the concrete's strength rises. Giaccio et al. conducted research on the fracture energy of high-strength concretes and observed that weak aggregates like limestone significantly lower the compressive strength of concrete since the strength of the concrete's aggregates determines how strong it may be [10]. Basalt mixes had a higher flexural strength in all eras than limestone combinations with the same mixing ratio. Up until a specific aggregate volume, the compressive strength of concrete improves with increasing coarse aggregate content and subsequently falls. Concrete compression is a complicated phenomenon. Several factors influence the behavior of concrete under such pressures. Sample size, shape, and friction are the main variables influencing concrete compaction [11]. Cordon et al. [12] observed that the variation in aggregate size significantly impacts concrete's compressive strength and split tensile strength. Concrete strength depends on the proportion of various aggregate sizes. Li & Song [13] developed a model to predict the compressive strength of rice husk ash concrete and observed that the two most significant factors affecting concrete's compressive strength are age and cement. A study on the effect of coarse aggregate quality on the mechanical properties of concrete has been done by Beshr et al. [14], who observed that it is essential to select suitable coarse aggregate to increase the compressive strength of concrete.

Although much research has been done on the impact of aggregate in concrete, there is little research based on the quality of different locations' coarse aggregates and their influence on concrete. In this study, several laboratory tests have been conducted to examine the properties of coarse aggregate and whether to use CA in the concrete mixture properly. From these tests, a holistic view of aggregate properties, such as size of aggregate, aggregate shape, and texture, has been gained. Four types of coarse aggregate were tested in the laboratory for different aggregate properties. Aggregate variation properties concerning sources have been recorded and compared. The main aim is to investigate changes in other material properties of gravel using various sources and their effects on the compressive strength of concrete.

2. Research Methodology

From four distinct sources in Bangladesh and China, four varieties of crushed stone coarse aggregate of 20mm grade were gathered. The CA sample gathered from four sources is shown in Figure 1.

All types of collected CA were tested for ACV-aggregate crushing value [15], gradation [16], absorption and specific gravity [17], voids and unit weight [18], AIV-aggregate impact value, resistance to abrasion-induced deterioration, and the Los Angeles (LA) machine's impact [19].



Jaflong (Bangladesh)



Bholaganj (Bangladesh)



Shandong (China)



Jiangsu (China)

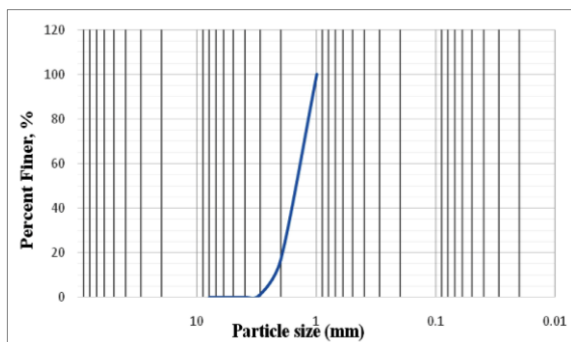
Figure 1. Location of coarse aggregate

2.1. Gradation

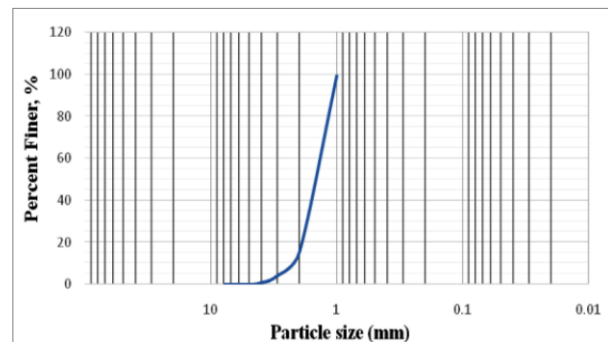
The determination of aggregate grade is a crucial stage in the development of concrete mixtures [20]. Local aggregate sources often produce concrete economically [21, 22]. Aggregation sources can have different aggregation properties, so blends are designed differently [23-25]. When defining the link between workability and the quantity of paste needed in concrete mixtures, the term "aggregate grading" has been applied [26-28]. In this work, sieve analysis was used to evaluate CA samples. The 20mm, 11mm, 4.80mm, 2.40mm, 1.20mm, 0.7mm, 0.4mm, and 0.20mm sieves were chosen for testing. The mechanical screen on which the CA sample was placed was used for grading. By multiplying the cumulative percentage of material retained on ASTM standard sieves by 100 and adding the result, the fineness modulus (FM) was determined. Table 1 displays the computed FM values for various CA sources. Figure 2 also shows the particle size distribution curves for each of the four types of CA.

Table 1. FM values of coarse aggregate

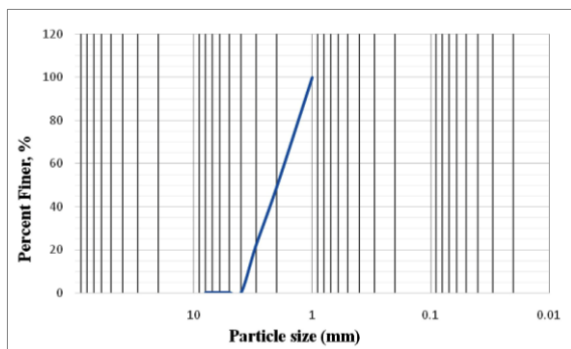
Location of CA	Jaflong	Bholaganj	Shandong	Jiangsu
FM	7.86	7.92	7.4	7.91



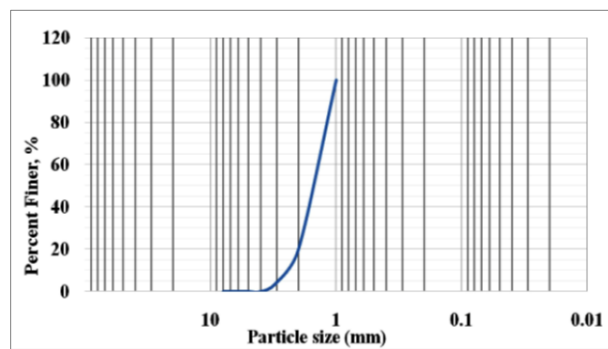
Jaflong



Bholaganj



Shandong



Jiangsu

Figure 2. Curve of gradation for coarse aggregate

2.2. Resistance to Abrasion-Induced Deterioration and Los Angles (LA) Machine's Impact

The most commonly used technique for assessing aggregates' abrasion resistance is the Los Angeles Abrasion Value Test (LAAV) [29]. This test evaluates an aggregate's resistance to wear brought on by abrasion between rock grains and impact and crushing by steel balls [30]. The Los Angeles Tester was used in this test to examine the resistance to deterioration of four coarse aggregate sources. For aggregates used in high-traffic roadways and floors, this test is crucial. Table 2 displays the abrasion values that the LA machine generated for various CA locations. Figure 3 shows some photographs captured during the laboratory testing phase.

Table 2. Coarse aggregate abrasion values

Location of CA	Jaflong	Bholaganj	Shandong	Jiangsu
Abrasion value	16.6%	17.1%	17.3%	18.6%



Figure 3. Photograph captured during the laboratory testing phase

2.3. Absorption and Specific Gravity

In the transportation sector, coarse aggregate specific gravity (Gs) and absorption capacity (Wa%) are crucial design factors [31]. In volumetric hot-mix asphalt construction, including super pave, the bulk-specific gravity of fine aggregate is used to calculate the quantity of asphalt binder absorbed by the aggregate and the porosity of the mineral aggregate [32]. Experiments for specific gravity and absorption were conducted on four distinct CA sources. Table 3 provides the derived values for the specific gravity, apparent specific gravity, and absorbance of oven dry basis (OD) and saturated surface dry basis (SSD).

Table 3. Absorption and specific gravity of coarse aggregate

Location of coarse aggregate	Jaflong	Bholaganj	Shandong	Jiangsu
Bulk-specific gravity (OD)	3.45	3.41	3.67	3.6
Bulk-specific gravity (SSD)	3.67	3.6	3.75	3.68
Apparent specific gravity	4.11	3.95	3.88	3.81
Absorption	9.07%	7.83%	3.01%	3.02%

2.4. Unit Weight and Voids

Vacuums within the aggregate are an essential parameter to ensure the durability of the concrete mixture [33]. The ideal grade must have the most miniature voids per unit weight and surface area [34]. Average unit weight (kg/m^3) and void percentages were calculated for four types of CA. Table 4 shows the results.

Table 4. Voids and unit weight of different coarse aggregates

Location of coarse aggregate	Jaflong	Bholaganj	Shandong	Jiangsu
Unit weight (kg/m^3)	1653	1684	1770	1711
Voids	11.63%	8.57%	5.23%	7.21%

2.5. Aggregate Impact Value (AIV)

The well-known AIV test is a British standard that provides a relative assessment of an aggregate's resistance to abrupt shock or impact, which can vary from the aggregate's resistance to a gradual compression load in some cases [35, 36]. Previous studies on lightweight aggregates have confirmed that lightweight aggregates produce higher values of AIV, and aggregates with greater coarseness may have lower values of AIV [37]. The total impact value, which compares resistance to abrupt shock or impact with resistance to progressively applied pressure, might differ. Table 5 displays the four CA kinds of AIV that were discovered.

Table 5. Aggregate impact value of coarse aggregate

Location of coarse aggregate	Jaflong	Bholaganj	Shandong	Jiangsu
AIV	25.5%	19.72%	12.26%	15.6%

2.6. Aggregate Crushing Value (ACV)

For asphalt mixes to remain stable, the crushing properties of the aggregates are crucial. Utilizing an aggregate crushing value test, crushing resistance is often measured statistically [38]. ACV is the famous British standard test for measuring resistance to AD when crushed by compressive loads [36, 39]. The aggregate crushing value test for coarse aggregates measures an aggregate's resistance to crushing under graded compressive loads. Table 6 displays the attained ACVs for four CA sources.

Table 6. ACV of different coarse aggregate

Location of coarse aggregate	Jaflong	Bholaganj	Shandong	Jiangsu
ACV	29.85%	21.35%	14.1%	29.6%

2.7. Compressive Strength of Concrete Cylinder

Concrete's compressive strength is one of its most crucial characteristics. In addition, it is frequently used as a benchmark for numerous other characteristics of concrete, including its elastic modulus and tensile strength. Additionally, compressive strength provides a decent general indication of concrete quality [25, 40]. The concrete cylinder was made and tested for all sources of CA with the same cement, sand, and water ratio to determine the concrete strength for different CAs. The concrete cylinders were made using a 1:1.5: 3 mixing ratio of cement, sand, and CA, respectively, and tested for 7 days, 14 days, and 28 days as per ASTM C39 [41]. Table 7 displays the concrete strength test data for different days, and Figure 4 shows the flowchart of the study.

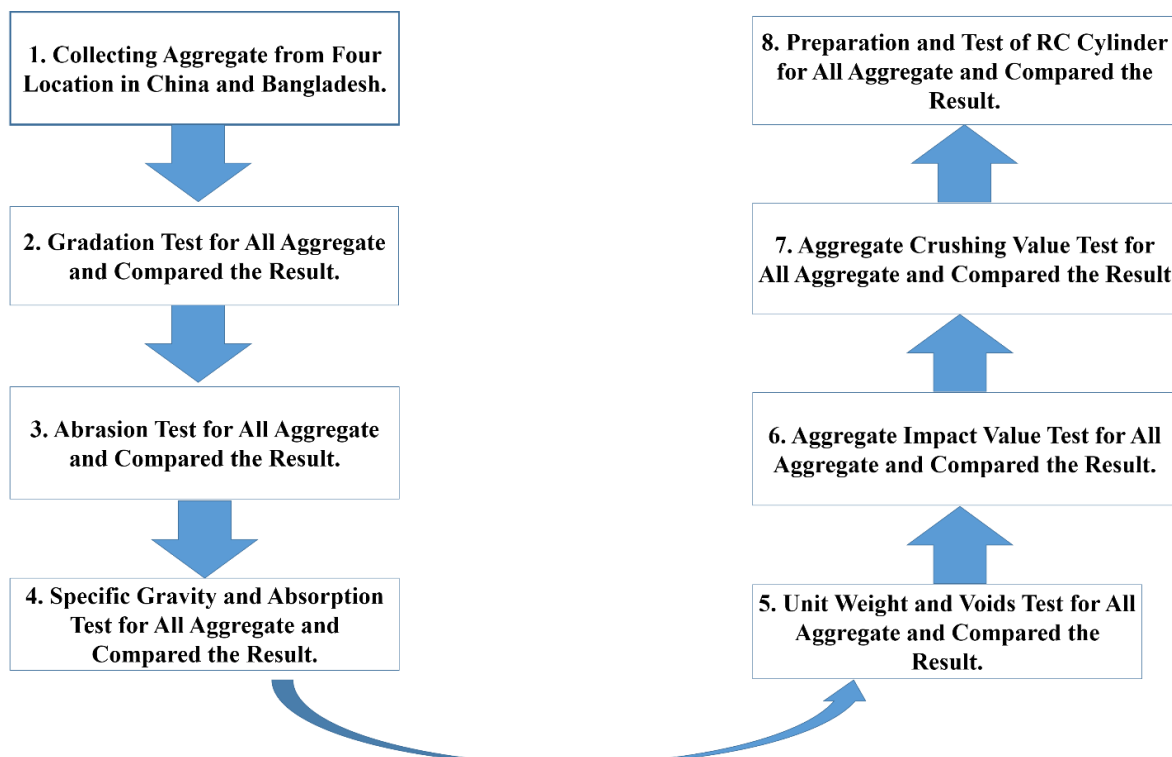


Figure 4. Flow chart of the study

Table 7. Concrete Compressive strength of different coarse aggregate

Location of CA	7 days Strength (psi)	14 days Strength (psi)	28 days Strength (psi)
Jaflong	2275	3150	3500
Bholaganj	2242	3105	3450
Shandong	2080	2880	3200
Jiangsu	2197	3042	3380

3. Result and Discussion

All results obtained from the various laboratory tests described above are displayed in bar graphs and compared concerning changes in the CA source. Figure 5 shows the FM values for different CA sources, from which it can be seen that CA Bholaganj has the highest FM value at 7.92, while CA Jiangsu and CA Shandong have similar values. The FM score was the lowest at 7.4.

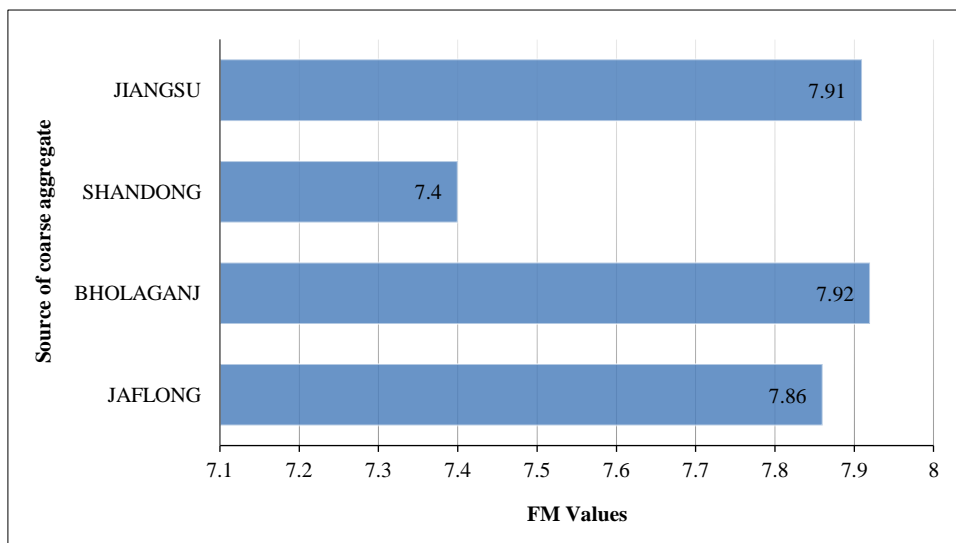


Figure 5. FM values of coarse aggregate

Figure 6 displays the abrasion values for four CA sources. With an 18.6% turnover rate, CA Jiangsu had the most significant turnover rate, followed by CA Jaflong and Bholaganj, with somewhat lower turnover rates, and CA Shandong, with the lowest.

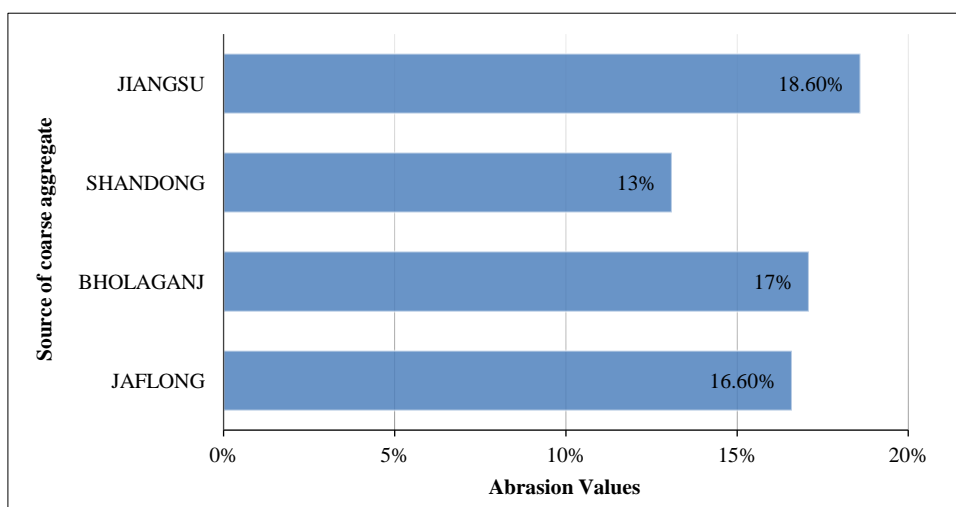


Figure 6. Abrasion values of coarse aggregate

Figure 7 shows bar graphs of apparent specific gravity and specific gravity (OD and SSD-based) about the CA source. With values of 3.67 and 3.75, respectively, the OD and SSD mass weights in Shandong, Jiangsu, were more significant than the others. Bholaganj CA had OD-specific and SSD mass values of 3.41 and 3.6, respectively. Once more, the apparent specific gravity was 4.11 in Jaflong’s coarse aggregate and 3.81 in Jiangsu’s coarse aggregate.

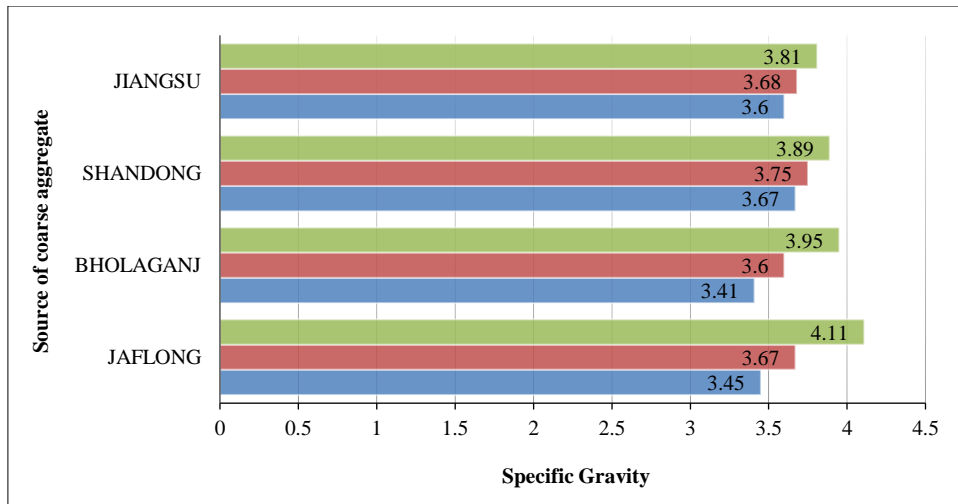


Figure 7. The specific gravity of coarse aggregate

Figure 8 shows the uptake of CA from various sources. Jaflong CA had the highest absorption rate of 10.47%, Jiangsu CA had the lowest absorption rate of 4.16%, and Shandong CA had similar values.

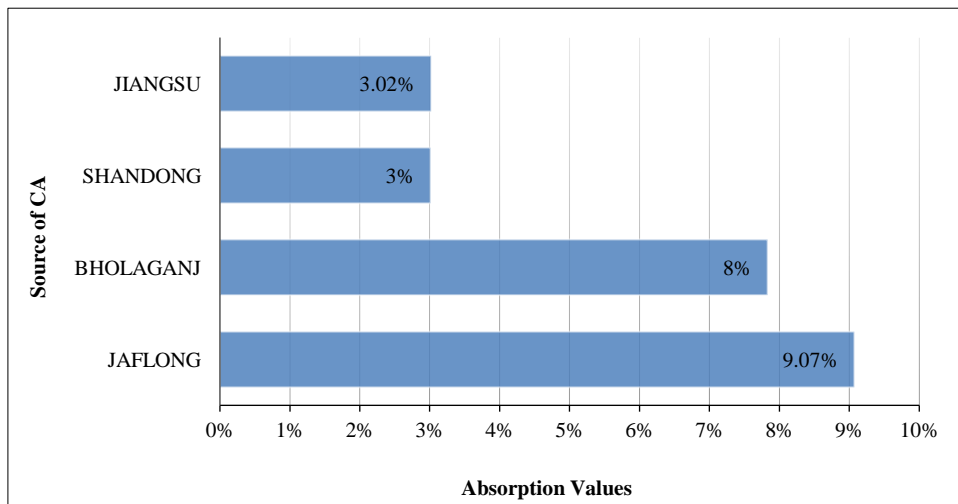


Figure 8. Absorption values of coarse aggregate

Figure 9 displays the unit weights of CA from various sources. In Shandong, CA, unit weight values were discovered to be 1769 kg/m³, while in Jaflong, CA, they were 1603 kg/m³. Figure 10 demonstrates that the void rate was highest in Jaflong, CA (11.63%) and lowest in Shandong, CA (5.23%).

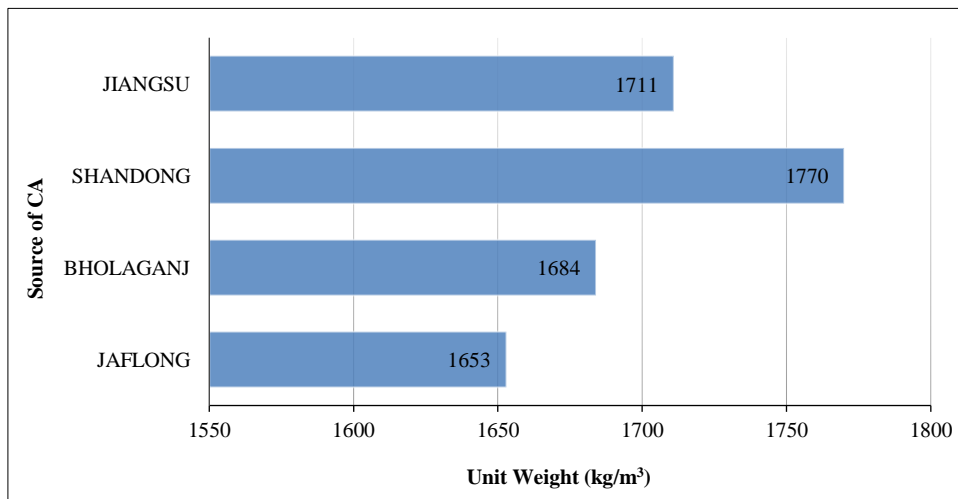


Figure 9. Unit weight of coarse aggregate

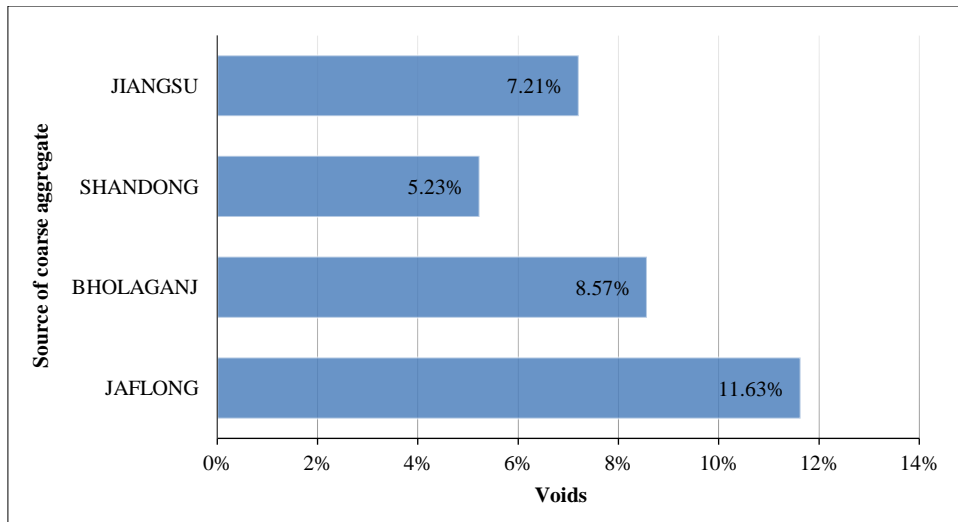


Figure 10. Void % of coarse aggregate

Figure 11 displays the AIV variation for several CA sources. AIV measured 25.5% in Jaflong, California, where it was most significant, and 12.1% in Shandong’s coarse aggregate, where it was lowest. ACV alterations for the four different forms of CA are shown in Figure 12. Compared to other CAs, the CA of Jaflong had the highest ACV, at 29.85%, virtually matching the CA of Jiangsu, while the CA of Shandong had the lowest, at 14.1%.

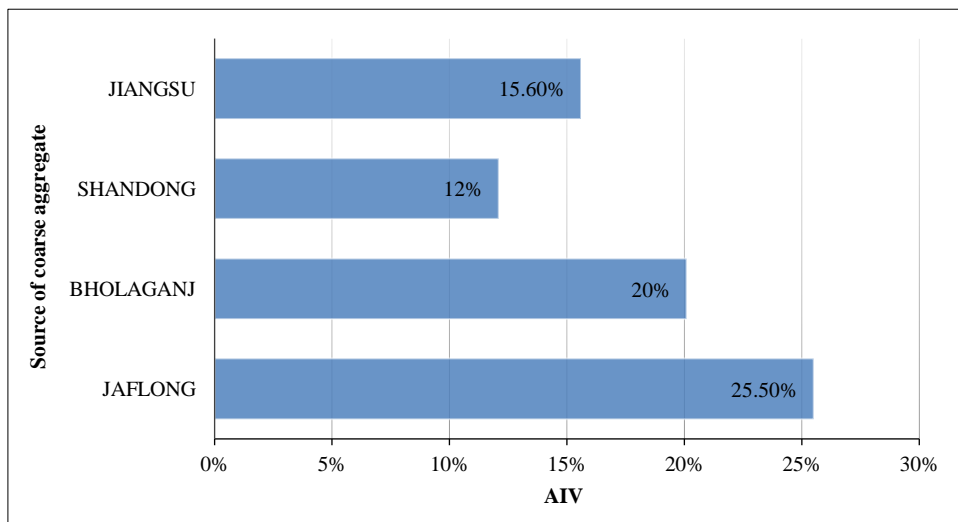


Figure 11. AIV of coarse aggregate

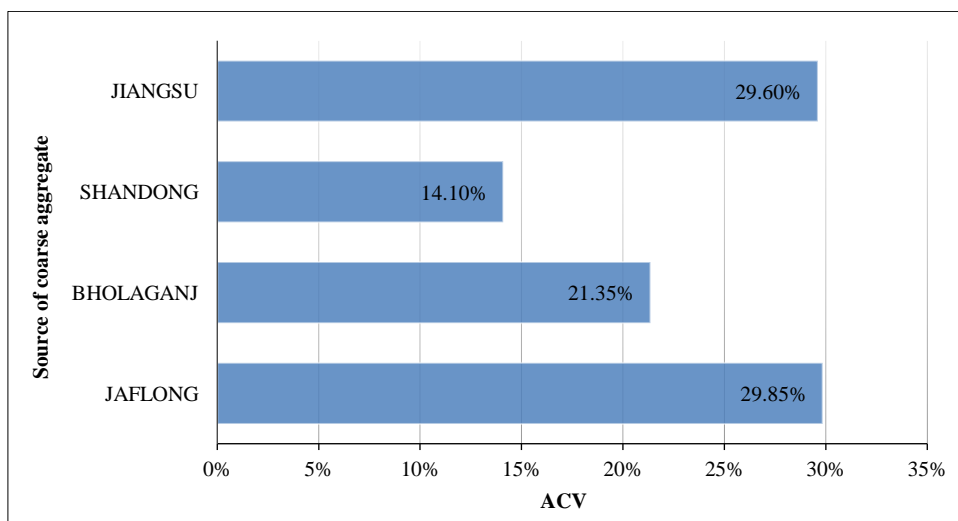


Figure 12. ACV of coarse aggregate

Figure 13 displays concrete compressive strength for different CA locations with test results of other days. Concrete cylinder made by Jaflong CA has the highest compressive strength while Shandong CA has the lowest compressive strength.

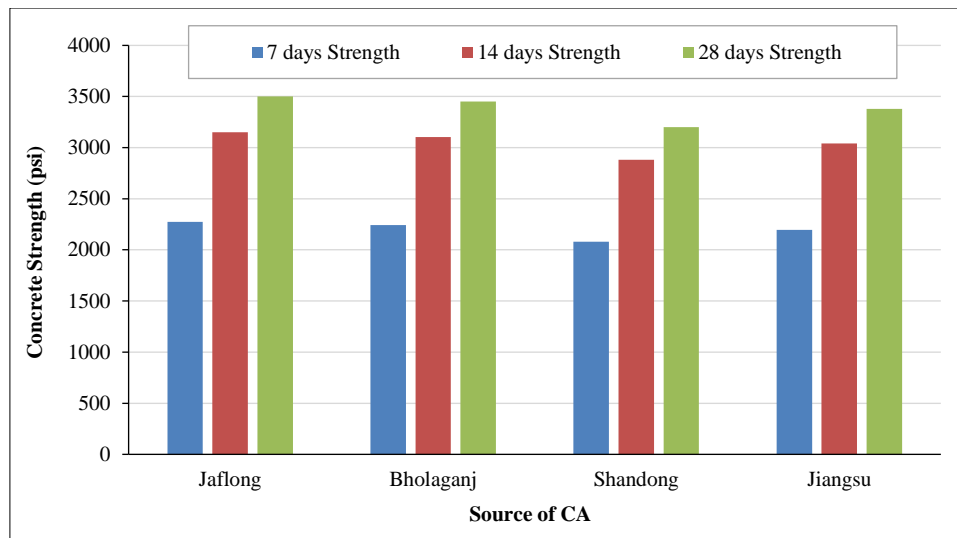


Figure 13. Concrete strength value

Concrete cylinder made by Jaflong CA has the highest compressive strength while Shandong CA has the lowest compressive strength.

4. Conclusion

This paper investigated the effect of aggregate type on the compressive strength of concrete and its permeability. For this purpose, different aggregates from other locations were used in the concrete mixtures. In addition, various properties of the aggregates, including ACV, AIV, gradation, absorption, abrasion, specific gravity, voids, and unit weight, were studied. Coarse aggregates were collected from four prominent sources: Jaflong and Bholaganj (Bangladesh), Shandong, and Jiangsu (China). The FM value of Shandong CA was observed to be less than that of others due to its being less coarse. Particle size was more significant than others and found the highest FM value for Bholaganj, CA. From this test, it's observed that the value of the coarse aggregate's fineness modulus is significantly influenced by particle size. The CA of Jiangsu has the highest abrasion value; it has higher toughness than other sources. The CA of Shandong absorbed less water than any other source; it has the highest specific gravity value. Less void space for water has been found for Shandong CA because it has less FM, and its absorption is lower than that of other sources. Aggregates became smaller voids between the particles when the value of FM was reduced. Because Shandong CA included fewer slums than other sources of CA, it had the most significant average unit weight. The lower FM content may account for the decreased voids compared to other CAs. Jaflong CA can absorb more impact load compared to other CA sources and showed the highest AIV value. It also revealed a significant value for abrasion and FM. A higher value of FM means that the aggregates are coarser and can withstand high loading. The abrasion value was reduced, resulting in a reduced AIV value. Compared to other CA sources, Jaflong CA can absorb compressive load better, and it's observed that it has the highest ACV value. According to this research, Jaflong CA can provide more compressive strength than other sources of CA.

4.1. Recommendation and Further Work

Recommendations for future work include optimizing aggregate mixtures, exploring alternative sources, and conducting long-term performance studies. Additionally, implementing advanced testing methods and validating findings in real-world applications, possibly through collaboration with industry experts, would enhance the practical implications of the research.

5. Declarations

5.1. Author Contributions

Conceptualization, K.H. and R.M.; methodology, K.C. and R.M.; software, K.H.; validation, A.A. and R.H.; formal analysis, K.H. and R.M.; investigation, K.C.; resources, R.H.; data curation, A.A.; writing—original draft preparation, K.C.; writing—review and editing, K.H.; visualization, A.A.; supervision, R.H.; project administration, K.H., R.M., and K.C. All authors have read and agreed to the published version of the manuscript.

5.2. Data Availability Statement

The data presented in this study are available in the article.

5.3. Funding

The authors received no financial support for the research, authorship, and/or publication of this article.

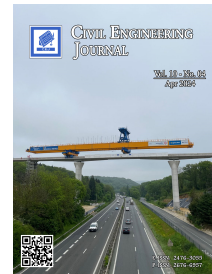
5.4. Conflicts of Interest

The authors declare no conflict of interest.

6. References

- [1] Nithurshan, M., & Elakneswaran, Y. (2023). A systematic review and assessment of concrete strength prediction models. *Case Studies in Construction Materials*, 18, 1830. doi:10.1016/j.cscm.2023.e01830.
- [2] Alghamdi, S. J. (2023). Determining the mix design method for normal strength concrete using machine learning. *Journal of Umm Al-Qura University for Engineering and Architecture*, 14(2), 95–104. doi:10.1007/s43995-023-00022-4.
- [3] Wang, L., Zhou, H., Zhang, J., Wang, Z., Zhang, L., & Nehdi, M. L. (2023). Prediction of concrete strength considering thermal damage using a modified strength-maturity model. *Construction and Building Materials*, 400, 132779. doi:10.1016/j.conbuildmat.2023.132779.
- [4] Naderi, M., & Kaboudan, A. (2021). Experimental study of the effect of aggregate type on concrete strength and permeability. *Journal of Building Engineering*, 37, 101928. doi:10.1016/j.jobbe.2020.101928.
- [5] Barham, W. S., Taleb Obaidat, Y., & Wael Qublan, A. (2023). Effect of maximum coarse aggregate size upon shear strengthening of RC beams using NSM-CFRP strips. *Structures*, 53, 652–663. doi:10.1016/j.istruc.2023.04.070.
- [6] Kozul, R., & Darwin, D. (1997). Effects of Aggregate Type, Size and Content on Concrete Strength and Fracture Energy. SM Report No. 43, University of Kansas, Kansas, United States.
- [7] Ezeldin, A. S., & Aitcin, P. C. (1991). Effect of coarse aggregate on the behavior of normal and high-strength concretes. *Cement, Concrete and Aggregates*, 13(2), 121–124. doi:10.1520/cca10128j.
- [8] Giaccio, G., Rocco, C., Violini, D., Zappitelli, J., & Zerbino, R. (1992). High-strength concretes incorporating different coarse aggregates. *ACI Materials Journal*, 89(3), 242–246. doi:10.14359/2568.
- [9] Lee, G. C., Shih, T. S., & Chang, K. C. (1988). Mechanical Properties of Concrete at Low Temperature. *Journal of Cold Regions Engineering*, 2(1), 13–24. doi:10.1061/(asce)0887-381x(1988)2:1(13).
- [10] Giaccio, G., Rocco, C., & Zerbino, R. (1993). The fracture energy (GF) of high-strength concretes. *Materials and Structures*, 26(7), 381–386. doi:10.1007/BF02472938.
- [11] Talaat, A., Emad, A., Tarek, A., Masbouba, M., Essam, A., & Kohail, M. (2021). Factors affecting the results of concrete compression testing: A review. *Ain Shams Engineering Journal*, 12(1), 205–221. doi:10.1016/j.asej.2020.07.015.
- [12] Cordon, W., & Gillespie, A. (1963). Variables in Concrete Aggregates and Portland Cement Paste which Influence the Strength of Concrete. *ACI Journal Proceedings*, 60(8), 1029–1052. doi:10.14359/7889.
- [13] Li, Q., & Song, Z. (2023). Prediction of compressive strength of rice husk ash concrete based on stacking ensemble learning model. *Journal of Cleaner Production*, 382, 135279. doi:10.1016/j.jclepro.2022.135279.
- [14] Beshr, H., Almusallam, A. A., & Maslehuddin, M. (2003). Effect of coarse aggregate quality on the mechanical properties of high strength concrete. *Construction and Building Materials*, 17(2), 97–103. doi:10.1016/S0950-0618(02)00097-1.
- [15] BS 812-1:1975. (1975). Testing aggregates. Methods for determination of particle size and shape. British Standard, London, United Kingdom.
- [16] ASTM C136/C136M-14. (2020). Standard Test Method for Sieve Analysis of Fine and Coarse Aggregates (2020). ASTM International, Pennsylvania, United States. doi:10.1520/C0136_C0136M-14.
- [17] ASTM C127-15. (2024). Standard Test Method for Relative Density (Specific Gravity) and Absorption of Coarse Aggregate (2024). ASTM International, Pennsylvania, United States. doi:10.1520/C0127-15
- [18] ASTM C29/C29M-97. (2017). Standard Test Method for Bulk Density (“Unit Weight”) and Voids in Aggregate. ASTM International, Pennsylvania, United States. doi:10.1520/C0029_C0029M-17A.
- [19] ASTM C131-06. (2010). Standard Test Method for Resistance to Degradation of Small-Size Coarse Aggregate by Abrasion and Impact in the Los Angeles Machine. ASTM International, Pennsylvania, United States. doi:10.1520/C0131_C0131M-20.

- [20] Cook, M. D., Ghaezadah, A., & Ley, M. T. (2018). Impacts of Coarse-Aggregate Gradation on the Workability of Slip-Formed Concrete. *Journal of Materials in Civil Engineering*, 30(2). doi:10.1061/(asce)mt.1943-5533.0002126.
- [21] Taylor, P. C., & Voigt, G. F. (2007). *Integrated materials and construction practices for concrete pavement: A state-of-the-practice manual*, No. FHWA HIF-07-004, Federal Highway Administration, Washington, United States.
- [22] Shilstone, J. M. (1991). Performance specifications for concrete pavements. *Concrete International*, 13(12), 28–34.
- [23] Richardson, D. N. (2005). *Aggregate Gradation Optimization--Literature Search*. Technical Report RDT 05-001, University of Missouri, Columbia, United States.
- [24] Abrams, D. A. (1922). Proportioning Concrete Mixtures. *ACI Journal Proceedings*, 18(2), 174-181. doi:10.14359/15683.
- [25] Neville, A. M. (2011). *Properties of concrete*. Prentice Hall, New Jersey, United States.
- [26] Fuller, W. B., & Thompson, S. E. (1907). The Laws of Proportioning Concrete. *Transactions of the American Society of Civil Engineers*, 59(2), 67–143. doi:10.1061/taceat.0001979.
- [27] Harrison, P. J. (2004). For the ideal slab on ground mixture. *Concrete international*, 26(3), 49-55.
- [28] Day, K. W. (2006). *Concrete Mix Design, Quality Control and Specification*. CRC Press, London, United Kingdom. doi:10.4324/9780203967874.
- [29] Palassi, M., & Danesh, A. (2016). Relationships Between Abrasion/Degradation of Aggregate Evaluated from Various Tests and the Effect of Saturation. *Rock Mechanics and Rock Engineering*, 49(7), 2937–2943. doi:10.1007/s00603-015-0869-9.
- [30] Kahraman, S., & Fener, M. (2007). Predicting the Los Angeles abrasion loss of rock aggregates from the uniaxial compressive strength. *Materials Letters*, 61(26), 4861–4865. doi:10.1016/j.matlet.2007.06.003.
- [31] Mills-Beale, J., You, Z., Williams, R. C., & Dai, Q. (2009). Determining the specific gravities of coarse aggregates utilizing vacuum saturation approach. *Construction and Building Materials*, 23(3), 1316–1322. doi:10.1016/j.conbuildmat.2008.07.025.
- [32] Kandhal, P. S., Mallick, R. B., & Huner, M. (2000). Measuring bulk-specific gravity of fine aggregates: Development of new test method. *Transportation Research Record*, 1721(1721), 81–90. doi:10.3141/1721-10.
- [33] Roquier, G. (2023). Estimation of voids in a multi-sized mineral aggregate for asphalt mixture using the Theoretical Packing Density Model. *Construction and Building Materials*, 367, 130302. doi:10.1016/j.conbuildmat.2023.130302.
- [34] Hu, J., & Wang, K. (2007). Effects of size and uncompacted voids of aggregate on mortar flow ability. *Journal of Advanced Concrete Technology*, 5(1), 75–85. doi:10.3151/jact.5.75.
- [35] BS 812-112. (1990). *Testing aggregates. Method for determination of aggregate impact value (AIV)*. British Standards Institution, 812-112.
- [36] Al-Harhi, A. A. (2001). A field index to determine the strength characteristics of crushed aggregate. *Bulletin of Engineering Geology and the Environment*, 60(3), 193–200. doi:10.1007/s100640100107.
- [37] Abdul Awal, A. S. M., Mohammadhosseini, H., & Hossain, M. Z. (2015). Strength, modulus of elasticity and shrinkage behaviour of concrete containing waste carpet fiber. *International Journal of Geomate*, 9(1), 1441–1446. doi:10.21660/2015.17.4345.
- [38] JTG E42-2005. (2005). *Test methods of aggregate for highway engineering*. Research Institute of Highway Ministry of Transport, Beijing, China.
- [39] BS 812-110. (1990). *Testing Aggregates. Methods for Determination of Aggregate Crushing Value (ACV)*. British Standards Institution, London, United Kingdom.
- [40] Lajčín, D., & Guzoňová, V. (2023). Identification of Knowledge Management Barriers in Scientific R&D Projects in Czech Academic Environment. *HighTech and Innovation Journal*, 4(1), 19-36. doi:10.28991/HIJ-2023-04-01-02.
- [41] ASTM C805/C805M-18. (2019). *Standard test method for Rebound Number of Hardened Concrete*. ASTM International, Pennsylvania, United States. doi:10.1520/C0805_C0805M-18.



Examining Soil Microplastics: Prevalence and Consequences Across Varied Land Use Contexts

Muhammad A. Walenna ^{1*}, Zarah A. Hanami ², Rachmat Hidayat ³, Annisa D. Damayanti ²,
Suprihanto Notodarmojo ⁴, Kurniaty ⁵, Lucky Caroles ¹

¹ Department of Infrastructure Planning Engineering, The Graduate School, Universitas Hasanuddin, Makassar 90245, Indonesia.

² Department of Environmental Engineering, Faculty of Engineering, Universitas Hasanuddin, Gowa 92171, Indonesia.

³ Department of Fisheries, Faculty of Marine Sciences and Fisheries, Universitas Hasanuddin, Makassar 90245, Indonesia.

⁴ Department of Environmental Engineering, Faculty of Civil and Environmental Engineering, Institut Teknologi Bandung, Bandung 40132, Indonesia.

⁵ Department of Regional Planning and Development, The Graduate School, Universitas Hasanuddin, Makassar 90245, Indonesia.

Received 21 November 2023; Revised 11 March 2024; Accepted 17 March 2024; Published 01 April 2024

Abstract

In an extensive exploration of microplastics within soil environments, our study aims to investigate the presence, spread, and ecological impact of microplastics in soil, focusing on Makassar City, Indonesia. Using a Sinher binocular digital microscope, we visually examined soil samples in Petri dishes, measuring microplastic sizes with Image-J software. Fourier-transform infrared (FTIR) spectroscopy was also employed for additional identification and analysis of polymer compositions. Our research uncovered a widespread presence of microplastics across diverse soil types and land uses, including residential, fishpond, agricultural, landfill, coastal, and bareland areas. The concentration of these microplastics was found to be between 16.6 to 21.9 particles/gram, showing consistency across most land uses, with some variations in coastal areas. We noted a significant variety in microplastic forms, predominantly fragments and films, across the different land uses. A wide range of colors was observed, including blue, green, red, and transparent. Polyethylene (PE) and polypropylene (PP) were identified as the predominant polymers. Our study highlights the non-uniform distribution of microplastics in soil, suggesting potential significant impacts on soil organisms and the wider ecosystem. These findings underscore the critical need for more comprehensive research on the ecological implications of microplastics in soil environments.

Keywords: Microplastics; Soil; Land Use; Polymer; Soil Environment; Pollution.

1. Introduction

The examination of microplastics in diverse land-use contexts assumes paramount importance in the contemporary era, primarily attributed to the far-reaching and profound ecological and human health implications associated with these diminutive plastic particles [1]. Microplastics, defined as plastic fragments measuring less than 5 mm in diameter [2], have pervaded terrestrial ecosystems on a global scale, bearing testament to the pervasive nature of plastic pollution. An intricate understanding of the presence and spatial distribution of microplastics is of paramount significance, as it serves as a foundational prerequisite for the formulation of efficacious mitigation strategies and policy interventions aimed at ameliorating the escalating global plastic pollution crisis [3]. Notably, urban areas have emerged as focal points of

* Corresponding author: mawalenna@unhas.ac.id

<http://dx.doi.org/10.28991/CEJ-2024-010-04-017>



© 2024 by the authors. Licensee C.E.J, Tehran, Iran. This article is an open access article distributed under the terms and conditions of the Creative Commons Attribution (CC-BY) license (<http://creativecommons.org/licenses/by/4.0/>).

microplastic pollution, manifesting elevated concentrations in locales characterized by high population density and industrial activity [4]. This underscores the pivotal role of urban planning and waste management strategies in abating the encroachment of microplastics into the environment. Extensive prior investigations have probed the prevalence of microplastics in agricultural soils, thereby illuminating the potential hazards attendant to their incorporation into these substrates, which can detrimentally impact soil health and potentially ingress the food chain [5, 6].

Microplastics have garnered notable scholarly attention in recent years, primarily due to their recognized potential for instigating adverse ecological consequences within terrestrial ecosystems. Within these terrestrial ecosystems, microplastics have been found to induce alterations in soil properties, disruptions in nutrient cycling dynamics, and deleterious effects on plant growth and microbial communities, as evidenced by recent studies [7, 8]. Such perturbations in terrestrial environments can precipitate cascading repercussions, ultimately impacting the structural and functional integrity of ecosystems, with consequential implications for the wildlife populations that depend on these ecosystems for habitat and sustenance. For instance, empirical investigations have unveiled that microplastics, upon ingestion by earthworms, give rise to physiological stress and provoke modifications in their feeding behaviors, thereby exemplifying the extent of the ecological perturbations attributable to microplastic contaminants [9]. Furthermore, it is imperative to underscore that the transport of microplastics from aquatic ecosystems to terrestrial environments is facilitated by diverse mechanisms, as elucidated in recent research endeavors [10]. This cross-environmental transfer highlights the necessity for rigorous and comprehensive examinations, encompassing diverse land use contexts, to thoroughly comprehend the prevalence and ramifications of microplastics.

The study of microplastics within a variety of contexts related to land use is crucially important when considering assessments of human health. This urgency is echoed by several scholarly investigations, which have emphasized the necessity of examining the subtle ways through which these microscopic plastic particles might enter our food chain, thereby posing potential risks to human health [11–13]. In a pivotal study conducted by Schwabl et al. [14], the presence of microplastics was identified in human stool samples, offering indisputable evidence that humans inadvertently ingest and possibly absorb these minute particles. Moreover, there is a well-documented correlation between microplastics and the attachment of harmful chemical substances to their surfaces. This connection stirs significant concern regarding the possibility that when humans consume contaminated food or water, they may also inadvertently ingest these dangerous compounds [15]. Therefore, undertaking a broad and meticulous exploration of microplastics within diverse land-use settings is not only vital for gaining a deeper understanding of the ecological impacts but is also indispensable for evaluating the hidden health risks that these particles might pose to the general population. Through such a comprehensive study, we will not only garner a nuanced understanding of microplastics' environmental impacts but will also be better positioned to navigate and mitigate the concealed health risks associated with them, ensuring a safer and more informed future for all.

A thorough examination of microplastics, covering both their prevalence and ensuing impacts, is vitally important, given their significant implications for sustainable development and their emergence as a prominent ecological issue intricately linked to sustainability [16]. Addressing the issue of microplastics aligns closely with several Sustainable Development Goals (SDGs), particularly SDG 14 (Life Below Water) and SDG 15 (Life on Land), by targeting marine and terrestrial ecosystems [17]. Furthermore, tackling microplastic pollution contributes to SDG 3 (Good Health and Well-being) by safeguarding human health from potential contaminants, as well as to SDG 12 (Responsible Consumption and Production) and SDG 13 (Climate Action) by promoting responsible consumption and mitigating climate impacts associated with plastic production [18]. To support these SDGs, concerted efforts are needed, including interdisciplinary research, policy interventions, public awareness campaigns, and innovative solutions for plastic waste management, emphasizing the interconnectedness of microplastic research with broader sustainability objectives. These initiatives highlight the crucial link between microplastics research and broader sustainability goals. Recognizing this vital focus, the primary objective of this research is to study the prevalence of microplastics in terrestrial ecosystems and their relationship with land use. Particularly, the study seeks to determine the extent of microplastic infiltration in these areas and identify the underlying causative factors.

A significant research gap exists in the study of microplastics in soil, necessitating focused investigation to address critical knowledge deficits in this domain. While earlier studies predominantly investigated the presence of microplastics in aquatic systems [19], recent studies have shifted their focus towards terrestrial soil, particularly with the fact that microplastic deposition in soil is estimated to be 4 to 23 times higher than in marine environments [20], causing a growing concern. This is substantiated by various studies identifying human activities as significant contributors to microplastic contamination in soil. Such activities encompass littering [21], the utilization of plastic mulching [22], soil amendment applications [23], irrigation with sewage water [24], waste disposal practices [25], and the application of fertilizer coatings [26]. Furthermore, environmental mediums like runoff and air transmission play a role in soil microplastic contamination as well [27]. Given the considerable uncertainty surrounding the composition, volume, and concentration of microplastic particles infiltrating terrestrial soil, there is corresponding ambiguity regarding their impact on the soil [28], particularly concerning different land uses. The variability in land use, from agricultural to industrial, further complicates the interaction between microplastics and soil, making it challenging to ascertain their

overall impact on soil health, structure, and function [29]. The intricate dynamics of land use, soil composition, and microplastic pollution necessitate comprehensive, site-specific investigations. This is imperative not only to delineate the scope and degree of soil contamination by microplastics but also to elucidate the nuanced relationship between soil use and the extent of contamination and impact. Conducting on-site, detailed investigations is essential to unveiling the complex interplay of these variables, thereby providing a foundation for effective strategies to mitigate the impact of microplastics on terrestrial environments.

According to the World Bank [30], Indonesia annually generates an alarming 7.8 million tons of plastic waste, out of which a substantial 4.9 million tons are mismanaged, leading to critical environmental and public health concerns. This mismanaged waste includes uncollected plastics, plastics disposed of in open dumpsites, and those leaking from inadequately managed landfills [30, 31]. Given the severity and scale of the problem, there is an urgent need to formulate effective waste management strategies and policies to mitigate the adverse impacts of mismanaged plastic waste in Indonesia.

In the context of Eastern Indonesia, South Sulawesi emerges as a paramount economic epicenter, evidenced by its substantial populace, totaling approximately 8.8 million, and its significant contribution to the region's economy [32]. The capital city of this province, Makassar, is particularly noteworthy, accounting for 47.2% of South Sulawesi's economic production. This economic prowess has predominantly been propelled by sectors such as agriculture, forestry, and fisheries, which collectively contribute 21.3% to the province's economy [33]. The confluence of escalated population growth and industrial advancement in Makassar presages an escalation in environmental challenges, particularly the intensification of microplastic pollution [3]. Prior research endeavors have primarily concentrated on the detection and distribution of microplastics within aquatic and coastal zones in Makassar [34-37]. A solitary investigation has addressed the contamination of terrestrial ecosystems by microplastics, with a specific focus on the potential transference from landfill sites to dug wells [38]. Nevertheless, there is a pronounced dearth of comprehensive studies examining the pervasiveness of microplastics across various land use categories within Makassar. The current understanding of the extent of microplastic pollution in this locale remains incomplete. Given this backdrop, our investigation aims to fill these critical knowledge gaps. Our study intends to systematically explore the prevalence and implications of microplastic pollution across diverse land use settings in Makassar. This research not only seeks to augment the existing body of knowledge within this specific urban context but also aspires to contribute significantly to the global discourse on microplastic pollution. Understanding the distribution and impact of microplastics across varying land use contexts is crucial, as it allows for a comprehensive assessment of the pathways and mechanisms through which these pollutants infiltrate different ecosystems, ranging from urban centers to agricultural lands, thereby informing targeted and effective mitigation strategies.

2. Literature Review

2.1. Plastic Pollution: The Current Global Landscape and Its Problem

Over recent years, the scientific community has acknowledged plastic pollution as a principal environmental threat [39]. Plastics have been increasingly identified as substantial environmental pollutants [40]. In 2021, the global production of plastics reached a staggering 390.7 million tons, growing annually at the rate of 5.8 percent since 2009, following a consistent upward production trend since the 1960s [41]. This increment in production inevitably results in an increasing amount of plastic ending up in the environment annually. Due to the durability and persistence of these materials, plastics continue to reside in the environment indefinitely [42]. Rochman & Hoellein [43] elucidated the interactions of plastics ranging from the lithosphere to the atmosphere and from the hydrosphere to the atmosphere. Analogous to other chemical elements, plastic waste undergoes a biogeochemical cycle. Depending on their degradation rates, plastics participate in cycles involving the atmosphere, terrestrial systems (lithosphere), and aquatic systems (hydrosphere), all of which are intricately interconnected.

2.2. Microplastic Pollution in The Soil Environment

Investigations into the presence of microplastics in soil are still in their initial stages worldwide. While the phenomenon of plastic pollution has been thoroughly examined since the early 1970s, such explorations have predominantly been confined to aquatic settings, primarily oceans. It was not until the recent decade that the scope of this research expanded to include terrestrial ecosystems, as highlighted by a study by Sun et al. [44]. Crucially, findings by researchers, including a significant study by Rodrigues et al. [45], have unveiled that plastics contaminating the environment do not remain in a fixed location. Instead, these materials are dynamic, moving, and circulating across various ecosystems. This implies a constant transfer of microplastics between different environmental segments, from water bodies to the land, and vice versa. The process through which microplastics find their way into terrestrial settings, or land-based environments, is depicted in Figure 1. This illustration serves as a visual representation to aid in understanding the movement and introduction of microplastics into the soil and broader land environments.

In accordance with Figure 1, Lu et al. [46] emphasized the intimate connection between the distribution and formation of soil aggregates and the surrounding ecological conditions. The development and dispersal of these

aggregates are invariably tethered to the local environmental context. Notably, human activities and the prevalent vegetation types exert considerable influence on this dynamic, subsequently molding the underlying biological processes and facilitating or impeding the movement and circulation within the soil. This interaction is crucial as it ultimately affects the soil's health and functionality [47].

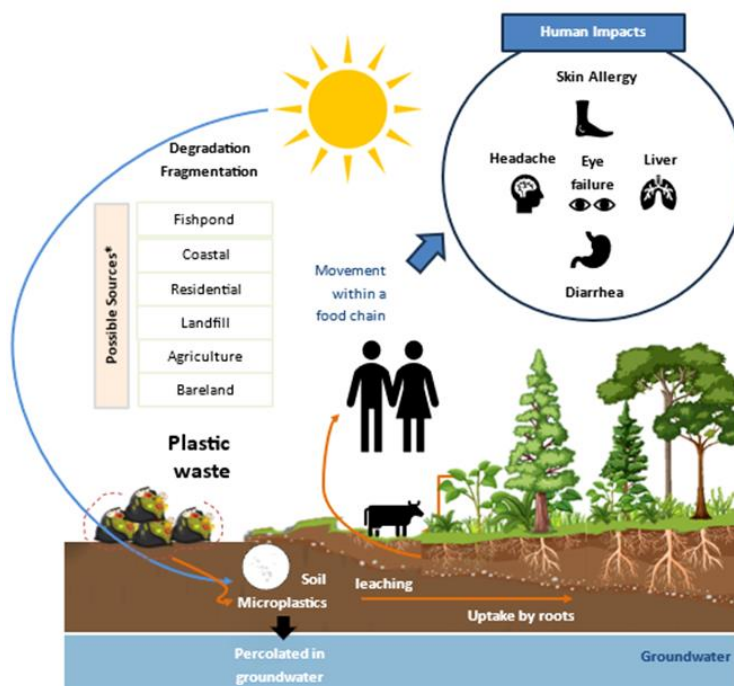


Figure 1. Microplastics Pathway to Soil Environment (Modified from [21, 48])

Further, Xu et al. [49] delineated how microplastics, upon entering the soil, become a quasi-permanent component of the environment. Once entrenched in the soil, these microplastics don't merely lie inert; they engage actively with the surroundings. They may accumulate over time, act as sponges absorbing various contaminants, or traverse through the soil matrix. This movement through the soil is not simplistic or unidirectional; it is a multistage process with several nuanced levels of transportation. For instance, at the cellular level, specific enzymes play a pivotal role in breaking down plastics into smaller, more manageable pieces [50, 51]. Simultaneously, at the organismal level, invertebrates inadvertently facilitate the exposure and perhaps even the redistribution of microplastics during their digestive processes [52]. These microplastics are not broken down completely and can be integrated into the food chain, increasing the potential for and degree of microplastic accumulation [53]. As these materials pass through the food chain, the probability of accumulation increases, posing potential risks to various organisms and the ecosystem at large [54].

Persistent presence of plastic waste leads to its accumulation in substantial concentrations, whereupon it undergoes degradation into minuscule pieces, a process expedited by UV radiation [55]. These microplastics once embedded in the soil, exert a tangible impact on the food chain dynamics. As elucidated by Gao et al. [56], plants are susceptible to absorbing microplastics, which infiltrate the soil and contaminate the groundwater. This absorption occurs as the contaminated water percolates through the soil and is subsequently taken up by the plants.

Once microplastics enter the vegetative components of the food chain, their presence becomes pervasive. Animals feeding on these contaminated plants inadvertently ingest microplastics [57]. Given that these animals, in turn, are consumed by humans, there is a consequent and inevitable transfer of microplastics to the human body. This accumulation within the human physiological system is not benign and has been linked to deleterious health effects, as documented by Issac & Kandasubramanian [48] and Zhang et al. [58]. These researchers have meticulously outlined the health risks associated with plastics, emphasizing that these risks are prevalent throughout various stages of plastics' life cycle.

Given the position of humans atop the food chain, and with food being significantly tainted by microplastics, the transfer of these tiny plastic particles to humans is not only plausible but highly likely. Moreover, other scholarly contributions have shed light on the negative implications microplastics pose to the vitality and growth of soil biota [59, 60]. Interestingly, research by Selonen et al. [61] underscored the vital role soil invertebrates play in the transportation of microplastics. According to their findings, these invertebrates can ingest microplastics, thereby incorporating them into the terrestrial food web. This cycle of ingestion and transfer eventually leads to the accumulation of microplastics, which, in turn, might precipitate detrimental effects on various facets of the environment, reverberating through the entire food chain and ecosystem.

Ajith et al. [62] put forth a significant assertion suggesting that microplastics discovered within marine ecosystems globally have their origins primarily linked to terrestrial sources. This perspective is not isolated, as it garners support from an array of other research endeavors in the field. A salient example can be observed in the work conducted by Zhang et al. [58], which throws light on the intricate relationships between surface soil aggregate composition, stability, and specific patterns of land use. According to their findings, distinct land-use patterns have a discernible impact on both the composition and stability of soil aggregates. These aggregates are not merely structural components of soil but serve a function vital to the ecosystem; they act as carriers of nutrients within the soil milieu, providing necessary sustenance to microorganisms thriving in this habitat. Such a role is indispensable, as it directly influences the soil structure, consequently affecting the availability and accessibility of nutrients within the soil environment [61, 63]. A study articulated by Yang et al. [21], alongside the insights provided by Kumar et al. [64], unveils the unsettling reality of persistent soil contamination caused by microplastics. These microplastics, derived from an array of different sources, continuously infiltrate the soil, emphasizing the urgency to comprehend the mechanisms underlying the dispersion of microplastics. Understanding these mechanisms is not merely an academic endeavor but a pressing environmental imperative as it significantly informs the efforts aimed at mitigating the extensive contamination and pollution propagated by microplastics. The collective findings underscore the need for increased awareness and intervention to address the widespread dispersion and consequential impacts of microplastics originating from diverse terrestrial sources.

Researchers in the field of soil science have meticulously compiled data, shedding light on the primary routes facilitating the ingress of microplastics into soil environments. There is compelling evidence pointing toward soil amendments, specifically compost [65] and sludge [66, 67], as vehicles transporting and dispersing microplastics. These amendments, commonly used in agricultural practices, inadvertently channel microplastics from urban waste disposal facilities to expansive tracts of agricultural land. In the scholarly landscape, there has been a discernible concentration of research efforts zeroing in on agricultural soils. This focus is attributed to the pervasive practice of over-fertilization, where phosphate fertilizers are used excessively in agricultural settings [66]. Intriguingly, there is a noticeable correlation unfolding between the increased presence of microplastics in soil and elevated phosphorus levels, drawing a direct link to the use of these phosphate fertilizers. Additionally, it is plausible that the farming community in certain regions may have consistently relied on compost for their agricultural needs. Empirical studies, one notably conducted by Cambier et al. [68], have brought to light that the practice of repeated compost application to soil does not come without repercussions. Continuous and repeated application cycles result in the gradual yet steady accumulation of microplastics in the soil, leading to heightened concentrations of these environmentally detrimental particles.

Drawing from an extensive review of prior research, a definitive presence of microplastics within various soil types has been unequivocally determined and established. Table 1 meticulously enumerates the data from different countries, each pinpointing the detection of microplastics in soils under assorted land use categorizations. The historical research has predominantly articulated findings regarding the concentration levels of these microplastics, the specific types of polymers identified, and the conjectured sources introducing microplastics into the soils. For soils associated with fishponds and aquaculture land uses, microplastic concentrations vary considerably, ranging from a minimal 0.46 to an excess of 112 particles per kilogram. Soils in landfill areas exhibit slightly elevated microplastic concentrations, with a range extending from 2.7 to a substantial 863 particles per kilogram.

Coastal regions also demonstrate diverse concentration levels, spanning from 12 to 590 particles per kilogram. Agricultural soils presented a wider range, with microplastic concentrations fluctuating between 5 and an alarming 1200 particles per kilogram. Notably, residential areas, which were the focus of a singular study in Turkey, displayed a surprising and unprecedented microplastic concentration of 3378 particles per kilogram. These findings collectively highlight the ubiquity and variability of microplastic concentrations in soils across different land-use types, each influenced by a distinct set of factors and sources contributing to the overall microplastic load in the environment. Understanding these variations is crucial for developing effective strategies for mitigating microplastic pollution and protecting soil health in these vulnerable areas. Despite the comprehensive data on microplastic presence in various soil types across different land uses, the research gap lies in the lack of a unified, comparative analysis of these findings. Specifically, there's a need to systematically compare and contrast microplastic concentrations and types across different land uses like fishponds, landfills, coastal regions, and agricultural soils. Additionally, the research predominantly focuses on quantifying microplastic levels and identifying polymer types, leaving a gap in understanding the direct and indirect ecological impacts of these microplastics on soil health and related ecosystems. Moreover, while the data shows significant variability in microplastic concentrations across land uses, there is a scarcity of research exploring the underlying reasons for these variations, such as specific local practices or environmental factors. Filling these gaps is essential for developing targeted and effective environmental management strategies to address microplastic pollution in soils.

Table 1. Microplastics Prevalence in Varying Land Use

Location	Land-Use Type	Concentration	Polymer Types	Potential Source	Reference
Hungary	Fishponds, Fresh Water	3.52-32.05 particles/m ³ (water) 0.46-1.62 particles/kg (sediment)	PP, PE (water) Polystyrene (sediment)	Uptake by organism	Bordos et al. (2019) [69]
Neijing River, China	Aquaculture Ponds	372 particles/m ³ (June) 429 particles/m ³ (December)	-	Water system	Xiong et a. (2022) [70]
Jakarta Bay, Indonesia	Aquaculture Ponds	111.7±13.2 particles/kg	PE, PP, PET, Polystyrene, Polyamide, PVC	Pipe, water system	Priscilla et al. (2020) [71]
North Carolina, USA	Landfill	382 particles/L (raw) 2.7 particles/L (treated)	LDPE, HDPE, Polystyrene, PVC, PET	Degradation and fragmentation of plastic waste	Kabir et al. (2023) [72]
Finland, Norway, Iceland, China	Landfill	291 particles/L	PE, PA, PVC, PET, PU, HDPE, LDPE	Waste, chemicals	Silva et al. (2021) [73]
Iran	Landfill (soil)	863 ± 681 particles/kg	LDPE, PP, PS	Degradation of plastic waste	Shirazi et al. (2023) [74]
Singapore	Coastal Areas	12-62.7 particles/kg	PA, PE, PP, PVC	-	Hazimah & Obbard (2014) [75]
Northern Coast, Taiwan	Coastal Areas	54.8 particles/kg	ABS, PE, PP, PS	Disposed Waste	Kunz et al. (2016) [76]
North Mississippi, USA	Beach	590±360 particles/kg	PE, Polyamide, PMMA, PET, PC, PP	Degradation of plastics	Gao et al. (2022) [77]
Chile	Agriculture	1200 particles/kg	-	Plastic mulching	Büks & Kaupenjohann (2020) [78]
Chile	Agriculture	306±360 particles/kg (cropland) 184±266 particles/kg (pastures)	Acrylates, PU, PE, EVA, PP, Nitrile Rubber, PS, CPE, PET, Polyamide, Polylactic Acid	Agriculture activities, mining, roadways, and urban environment	Corradini et al. (2021) [79]
Germany	Agriculture	30-50 mg/kg dry weight of agricultural area	-	Sewage sludge, compost	Henseler et al. (2022) [80]
China	Agriculture	263 – 571 particles/kg	PE, PP, PET, rayon, acrylic, polyamide	Agro-ecosystem	Zhou et al. (2020) [81]
China	Agriculture	4.94 – 252.70 particles/kg 37.32 particles/kg (average)	PP	Road Input	Cao et al. (2021) [82]
Turkey	Residential	3378 particles/kg	-	Anthropogenic activities	Tunali et al. (2022) [83]

ABS: Acrylonitrile Butadiene Styrene, **CPE:** Chlorinated Polyethylene, **EVA:** Ethylene-vinyl acetate, **HDPE:** High Density Polyethylene, **LDPE:** Low Density Polyethylene, **PA:** Polyacetylene, **PC:** Polycarbonate, **PE:** Polyethylene, **PET:** Polyethylene Terephthalate, **PMMA:** Poly(Methyl Methacrylate), **PP:** Polypropylene, **PS:** Polystyrene, **PU:** Polyurethane, **PVC:** Polyvinyl Chloride, **PVP:** Polyvinylpyrrolidone.

The polymers most commonly identified in these studies were Polyethylene (PE), Polystyrene (PS), and Polypropylene (PP), each contributing to the microplastic contamination within these diverse land use scenarios. The introduction and accumulation of microplastics in these soils are influenced by various sources according to Table 1, predominantly anthropogenic activities, which include but are not limited to, the gradual degradation of plastic materials and specific farming practices prevalent in these areas. In conclusion, the pervasive presence of microplastics across different land use types not only underscores the extensive environmental footprint of these particles but also calls for urgent and comprehensive strategies to mitigate their impact. The data gathered provides a compelling directive for future research and immediate intervention aimed at addressing this burgeoning environmental challenge.

Initiatives dedicated to uncovering the pathways through which microplastics infiltrate the soil are presently not as developed as those striving to gauge the prevalence of such contamination incidents. A significant portion of existing studies predominantly narrows their focus to identifying precise sources of pollution within isolated land use scenarios, with agriculture being the primary context under scrutiny. Such studies seldom venture into analyses conducted on a larger scale or explore different environmental settings. Although the information derived from Table 1 offers valuable insights regarding the pervasive existence of microplastics within terrestrial ecosystems, there has been a conspicuous absence of scholarly inquiries into this issue set against the backdrop of diverse or alternative environments. This conspicuous research void suggests an opportunity—and a need—for more ambitious scholarly endeavors that undertake assessments at the regional level, embracing a multitude of land use scenarios in the process. The current body of research is somewhat myopic, lacking in studies that take a holistic view of the issue by examining it across different land use paradigms. Consequently, the true scope and magnitude of the problem remain only partially understood and inadequately documented. Our work represents a preliminary attempt to bridge this significant knowledge chasm. Our work aims to expand the current understanding of microplastic pollution in soil by exploring its presence and impact across a diverse range of environmental settings, not just limited to agricultural lands. This broader approach addresses a notable gap in existing research, which often focuses on isolated land use scenarios. By integrating data from various land uses as presented in Table 1, our study will provide a more comprehensive and regional perspective on microplastic contamination. This will contribute to a more holistic understanding of the issue, shedding light on the scale and complexity of microplastic pollution in different terrestrial ecosystems, a crucial step towards developing effective environmental management strategies.

To fully grasp the extent of the microplastics issue, comprehensive research yielding crucial monitoring data on soil microplastics across diverse land-use types is indispensable. Such research should delve into the types of polymers involved, offering critical insights into the sources and nature of this pollution. This expansive approach is crucial for a nuanced understanding, allowing us to tailor effective mitigation strategies to the specific challenges posed by microplastic pollution in various environmental settings. Moreover, understanding the distribution and impact of microplastics in soil is not only essential for environmental health but also has significant implications for various aspects, such as agricultural productivity and food safety. By bridging these gaps, our research will not only contribute to environmental conservation but also to safeguarding public health and ensuring sustainable practices.

3. Research Methodology

In this section, we discuss the locations from which samples were retrieved, providing a detailed overview of the research methodology employed for this study. Moreover, the approach used for analyzing the obtained results is also explained. Each of these components is illustrated and clarified in Figure 2 for a better understanding.

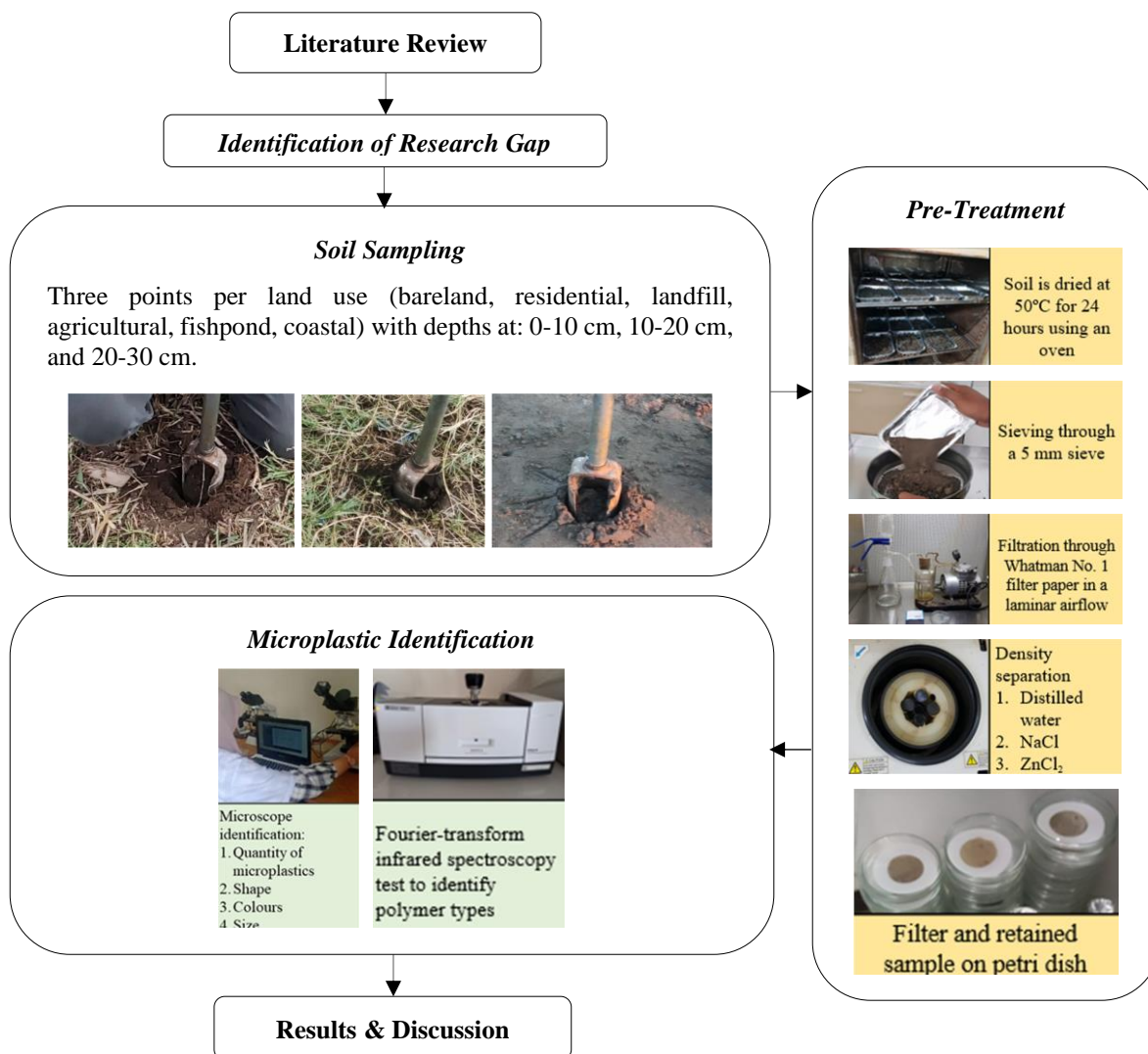


Figure 2. Research Flowchart

3.1. Location

The study took place in Makassar city, Indonesia, home to 1,432,189 individuals as of 2022, experiencing a population growth rate of 0.6% [84]. Arifin et al. [85] estimated that the city encompasses 9392.5 hectares of built-up areas, regions densely populated with houses and other structures, and 7682.4 hectares of unbuilt areas. Soil samples were collected in the dry months of May and June 2023, times characterized by negligible wet atmospheric deposition, with more weather details for these months depicted in Figure 3. Research sites were chosen and categorized based on various land use types within Makassar City, including residential, agricultural, bare land, fishpond/aquaculture, coastal, and landfill areas. For each type of land use, three specific sampling points were selected, as illustrated in the aerial map provided in Figure 4.

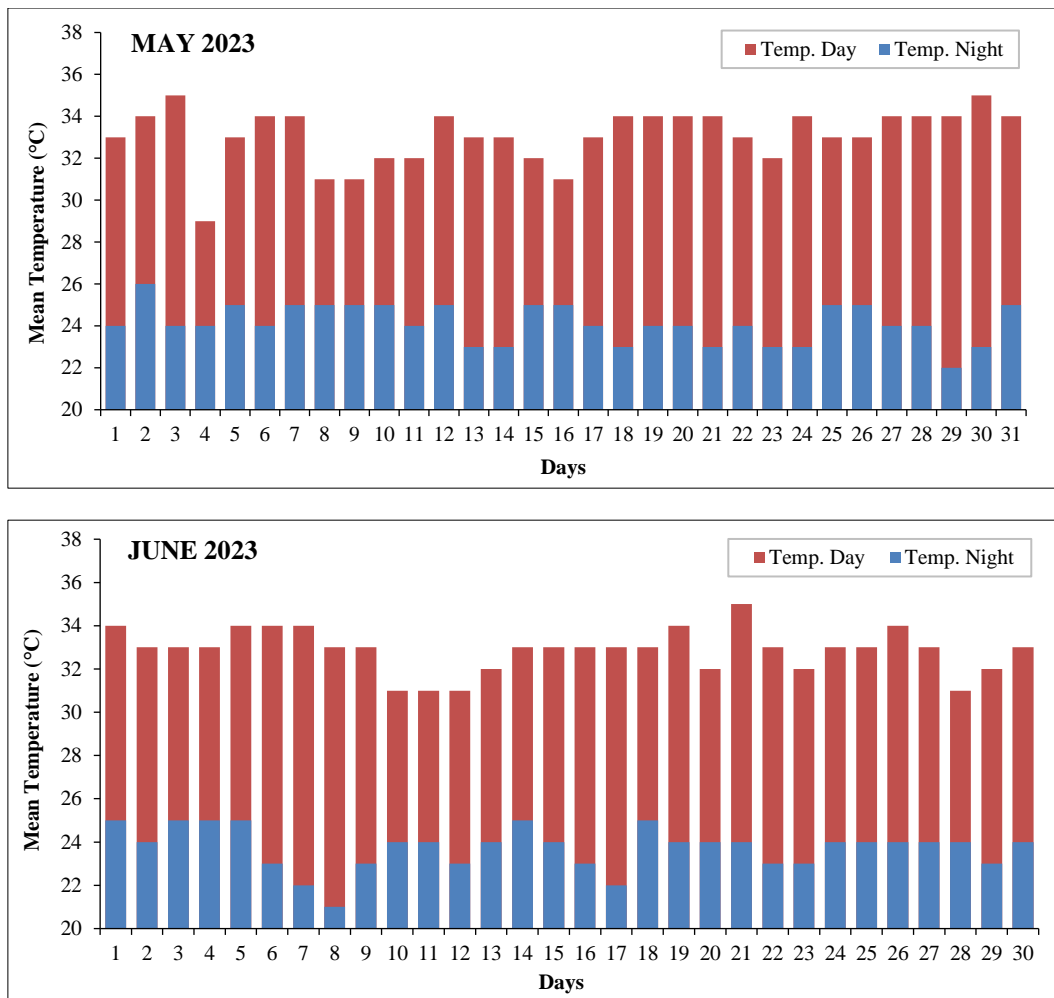


Figure 3. Makassar Weather in May and June 2023 (Samples were collected on May 25, 2023, and June 4, 2023)

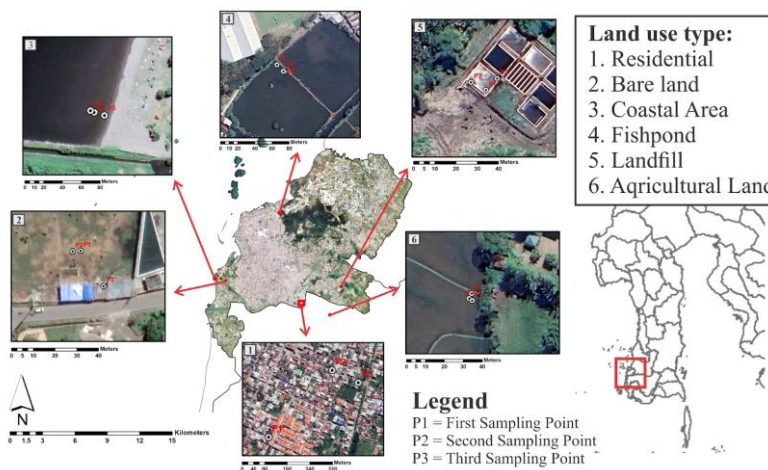


Figure 4. Aerial Map with Sampling Points

3.2. Sample Collection

A total of 54 soil samples were collected from six distinct types of land use, utilizing a borehole apparatus measuring 9.71 cm in length and 8.46 cm in width. For each land use type, soil was extracted from three separate points, with samples taken at three varied depths of topsoil: 0–10 cm, 10–20 cm, and 20–30 cm, in order to see the transport of microplastics in different depths following previous studies [86, 87]. The consideration of stratified soil was also chosen due to the higher levels of activity of soil organisms in those depths, and it is noteworthy that the average depths of rooting and ploughing activities do not surpass 30 cm [88, 89]. Every sample was then carefully placed in aluminium foil, securely stored in a labeled box, and transported to the laboratory for analysis. To minimize the risk of contamination, the sampling process employed little to no plastic materials, tools, or apparatus.

3.3. Pre-Treatment Procedure

Soil samples were initially collected, placed in laboratory storage, and subsequently oven-dried at a temperature of 50°C for a duration of 24 hours, a process aimed at moisture elimination [90, 91]. The application of low temperature during this drying phase is crucial, as it ensures that the concentration and characteristics of the microplastics within the samples remain unaltered [91]. Following the drying process, the samples were then sifted through a 5 mm stainless-steel sieve, a step implemented to isolate microplastics of specific sizes by removing any particles exceeding the 5 mm threshold.

The extraction process of microplastics from the soil samples was executed through a density-based separation method. This method involved the addition of salt to increase the density of the particles, which in turn facilitated the flotation of the lighter plastic materials. Detailed extraction steps were modeled after previous studies conducted by Corradini et al. [66] and Yang et al. [21]. In a summarized format, the process entailed placing 5 g of soil and 20 ml of water (with a density of 1.00 g cm⁻³) into a glass centrifuge tube, which was then centrifuged at 2000 rpm for 15 minutes. The resulting supernatant was carefully filtered using Whatman No.1 filter paper and a vacuum pump. In the following steps, the tube with the remaining sediment was filled with 20 ml of Sodium Chloride (NaCl 5 M, with a density of 1.20 g cm⁻³), serving as the chosen salt for the density separation process [92]. The sample was then centrifuged again for 2 minutes at 6,000 rpm, with the supernatant undergoing a second round of filtration. This process was repeated a third time using 20 ml of Zinc Chloride (ZnCl₂ 5 M, $\rho = 1.55$ g cm⁻³) and the sediment was stirred at 6,000 rpm for 2 minutes before a final round of filtration through the same filter paper.

The decision regarding the duration and speed of the second and third centrifugations was initially based on previous research by Corradini et al. [66], which recommended a rotation speed of 21,000 rpm. However, during the process, some tubes fractured at 7000 rpm while increasing the rotation speed. To navigate this limitation, the rotation speed was adjusted to 6000 rpm while simultaneously increasing the duration of the centrifugation process.

To mitigate the risk of external contamination, the filtration process was conducted within a laminar airflow, as suggested by Wesch et al. [93]. Post-extraction, the filters with the samples were securely stored in Petri dishes, ready for subsequent optical examinations.

3.4. Microplastics Identification

Samples in Petri dishes were visually identified using a Sinher binocular digital microscope, adhering to the guidelines set forth by the Marine and Environmental Research Institute [94] and Norén [95] for observing and quantifying microplastic properties. Microplastics are typically quantified as the number of particles per gram of dry soil. These particles were categorized based on morphological characteristics, including various forms like fibers, fragments, films, and pellets. The particles were also classified by color. Image-J software was utilized to measure the size of the microplastics.

For additional identification of potential microplastics, Fourier-transform infrared (FTIR) spectroscopy was employed due to its being a straightforward, reliable, and non-invasive technique with the ability to produce unique band patterns in the infrared spectra for various plastics [96]. The absorption and measurement of radiation—whether in reflection or transmission mode—are influenced by the chemical composition of the microplastics, and this occurs when they are exposed to an infrared sample (with a wave number range of 500–4000 cm⁻¹) [92, 97]. In this study, 108 particles were selected for FTIR analysis using Shimadzu equipment, with the goal of identifying the polymer type of each particle. Each selected particle represents different land uses.

3.5. Data Analysis

The application of descriptive analysis was utilised to evaluate the microplastics, whereby the data was organised based on concentration, type, colour, and size. The statistical software R was employed to perform data analyses, including the application of the Shapiro-Wilk normality test [98] and the T-test, to examine differences in microplastic concentrations across different land uses [99].

3.6. Quality Control and Detection Limit

To mitigate the risk of plastic contamination from external sources during the sampling procedure, sample preparation, and subsequent microplastics analysis, all equipment was rinsed and sterilized before use. Additionally, various non-plastic materials were employed, including aluminum foil, glass beakers, glass centrifuge tubes, and glass Petri dishes. Furthermore, it is important to note that the methodologies used to quantify and identify microplastic polymer types at a microscopic level may have limitations in terms of particle size. In this particular experiment, the minimum size observed was found to be 20 µm. Therefore, it is conceivable that microplastic particles of smaller sizes may have evaded detection.

4. Results

4.1. Microplastics Abundance across Varying Land Uses

Six distinct land uses were examined in this study, with each having varied concentrations of microplastics at different soil depths (as seen in Figure 5). These land uses include bareland, residential areas, landfills, agricultural land, fishponds, and coastal areas. In comparing the microplastics concentrations across these land uses, the landfill area exhibited the highest concentration at the 0-10 cm depth with 23.4 particles per gram. This concentration decreases slightly at deeper levels (20.1 particles per gram at both 10-20 cm and 20-30 cm depths). In contrast, residential areas displayed consistent microplastic concentrations across all depths, with the highest concentration observed at the 20-30 cm depth (21.8 particles per gram). Bareland and agricultural lands also showed similar consistency in microplastics concentrations, albeit with slight variations at different depths. Fishponds showed a reduction in concentration from 19.4 particles per gram at 0-10 cm to 18.9 at 10-20 cm, but then an increase at the 20-30 cm depth with 21.9 particles per gram. Coastal areas had the lowest concentrations at all depths, with an average of 17.1 particles per gram.

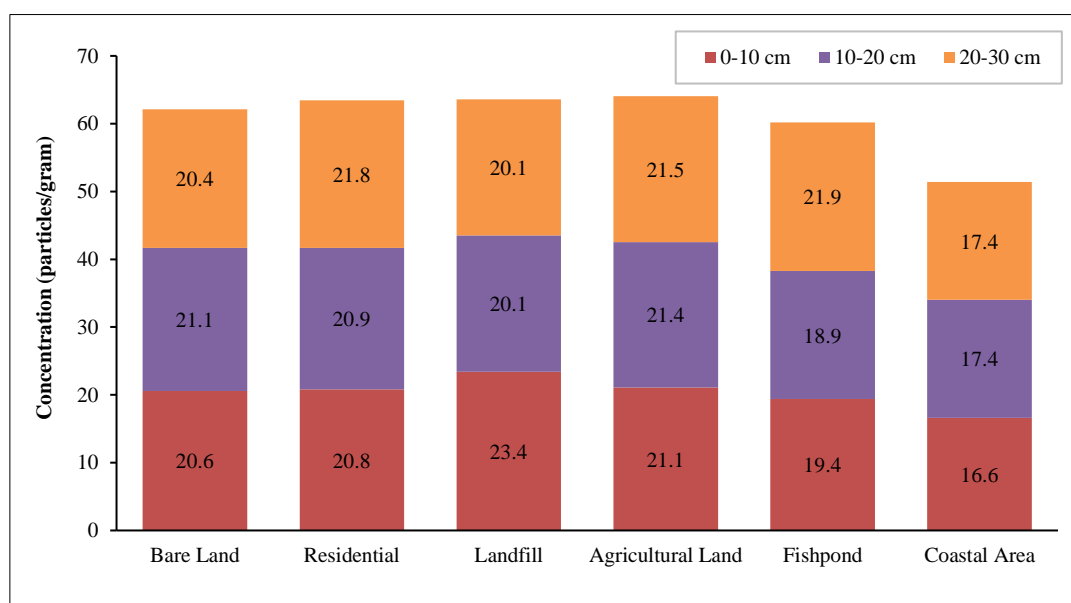


Figure 5. Microplastics Concentration Variations Across Different Land Uses

The observed distribution of microplastics at various soil depths revealed an unexpected pattern. While there is not a definitive trend documented in past studies regarding the prevalence of microplastics with depth, higher concentrations are generally anticipated at surface levels. This expectation is based on the presumption that surface levels are more exposed to microplastic sources and subject to sedimentation processes that trap these particles. However, the data from this study deviate from these expected patterns. Notably, the highest concentrations of microplastics in residential and fishpond areas were not discovered at the surface, but rather at depths of 20-30 cm. This irregular distribution suggests that other influential factors are at play, affecting the movement and deposition of microplastics within the soil strata. Such factors may include the texture and permeability of soil, as well as disturbances caused by human or animal activities.

4.2. Characteristics of Microplastics

The microplastics identified in this research were differentiated based on their shape, color, and size. These features are essential in understanding the complex nature of microplastic particles. Each attribute provides unique insights into the sources, dispersion, and potential environmental impacts of microplastics across various land uses. The findings concerning the shapes of microplastics across six distinct environments in Makassar City are presented in Figures 6 and 7.

Figure 6 presents the results of microplastic identification, highlighting four distinct shapes discovered in soil samples: fragment, film, fiber, and pellets (as further depicted in Figure 7). In bareland, agricultural land, and fishponds, fragments were the most prevalent, constituting over 60% of the identified microplastics. On the other hand, residential areas, landfills, and coastal zones predominantly contained films as the main type of microplastics. Fibers were scarcely observed across all six land uses, and pellets were the least frequent, accounting for 1% or even less.

Further details on the distribution of microplastic shapes across different soil depths can be found in the supplementary materials (Table S1). The prevalence of specific shapes varies with depth. For instance, the proportion

of fragments in bare land, landfills, and fishponds diminishes as depth increases. In contrast, residential and agricultural lands show an uptick in fragment percentages with increasing depth. However, in coastal areas, the fragment distribution is inconsistent, with fluctuations observed across the 0-10 cm, 10-20 cm, and 20-30 cm depth ranges.

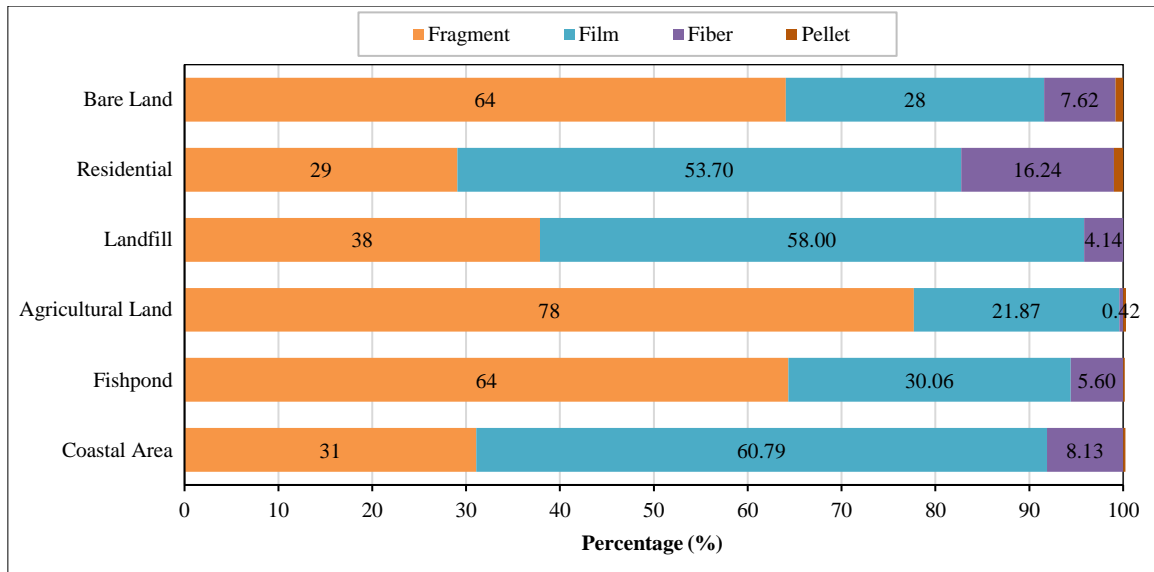


Figure 6. Percentage Distribution of Microplastic Shapes Across Different Land Uses

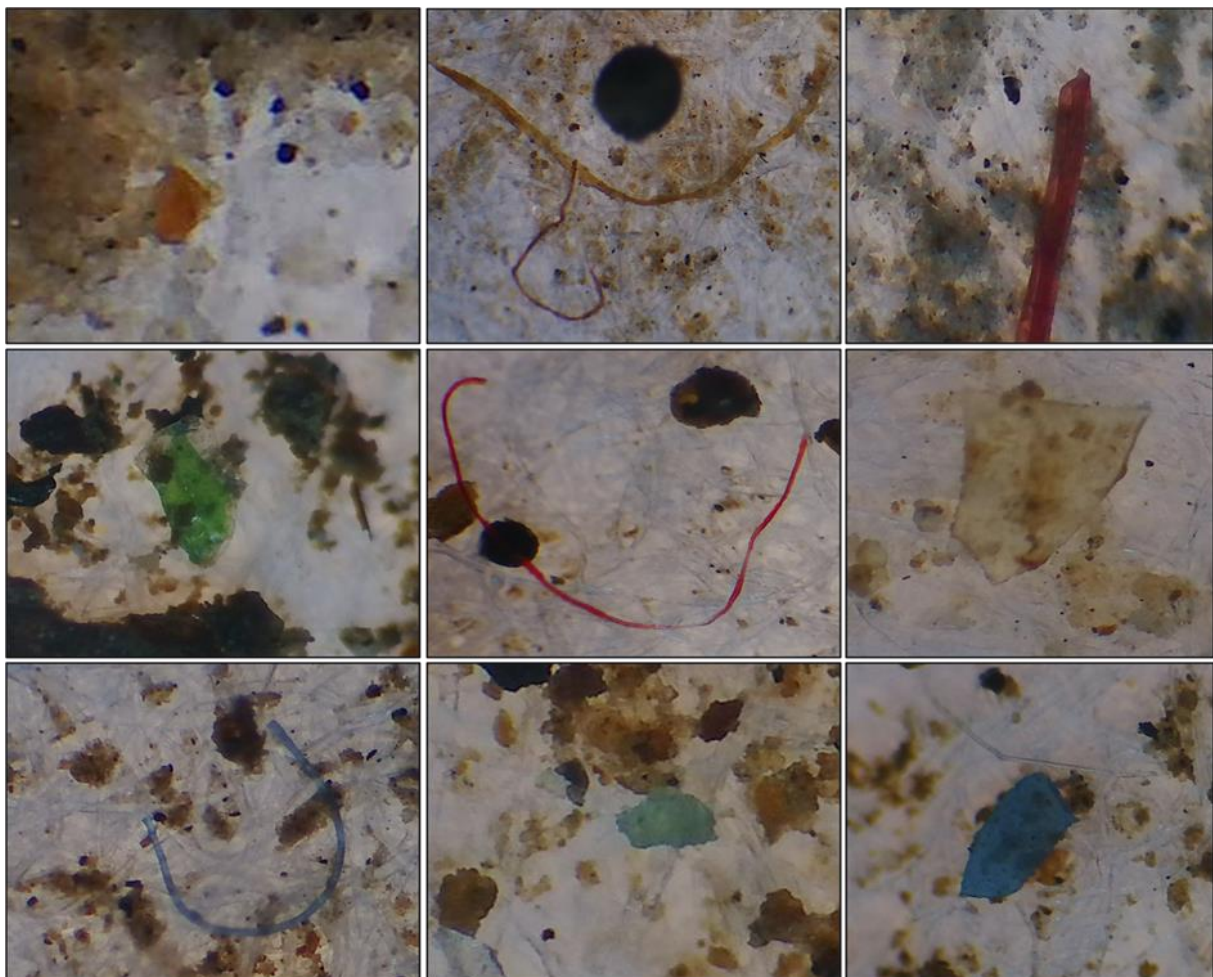


Figure 7. Visual Identification of Microplastic Shapes Using a Microscope

As depicted in Figure 7, microplastics come in a range of colors. The study has revealed intriguing patterns in the distribution of microplastics based on their color across various land uses (as elucidated in Figure 8). Agricultural lands predominantly contain Orange-colored microplastics, making up 36.9% of the samples, closely followed by Yellow at

25.58%, Transparent at 22.49%, and Blue at 14.67%. In contrast, the Coastal Area sees an overwhelming 60.78% of Transparent microplastics, the highest among all land uses. It is also noteworthy that Fishponds and Barelands have a similar distribution with Orange microplastics at 37.6% and 25.93%, respectively, and Transparent ones at 18.54% and 26.21%, respectively.

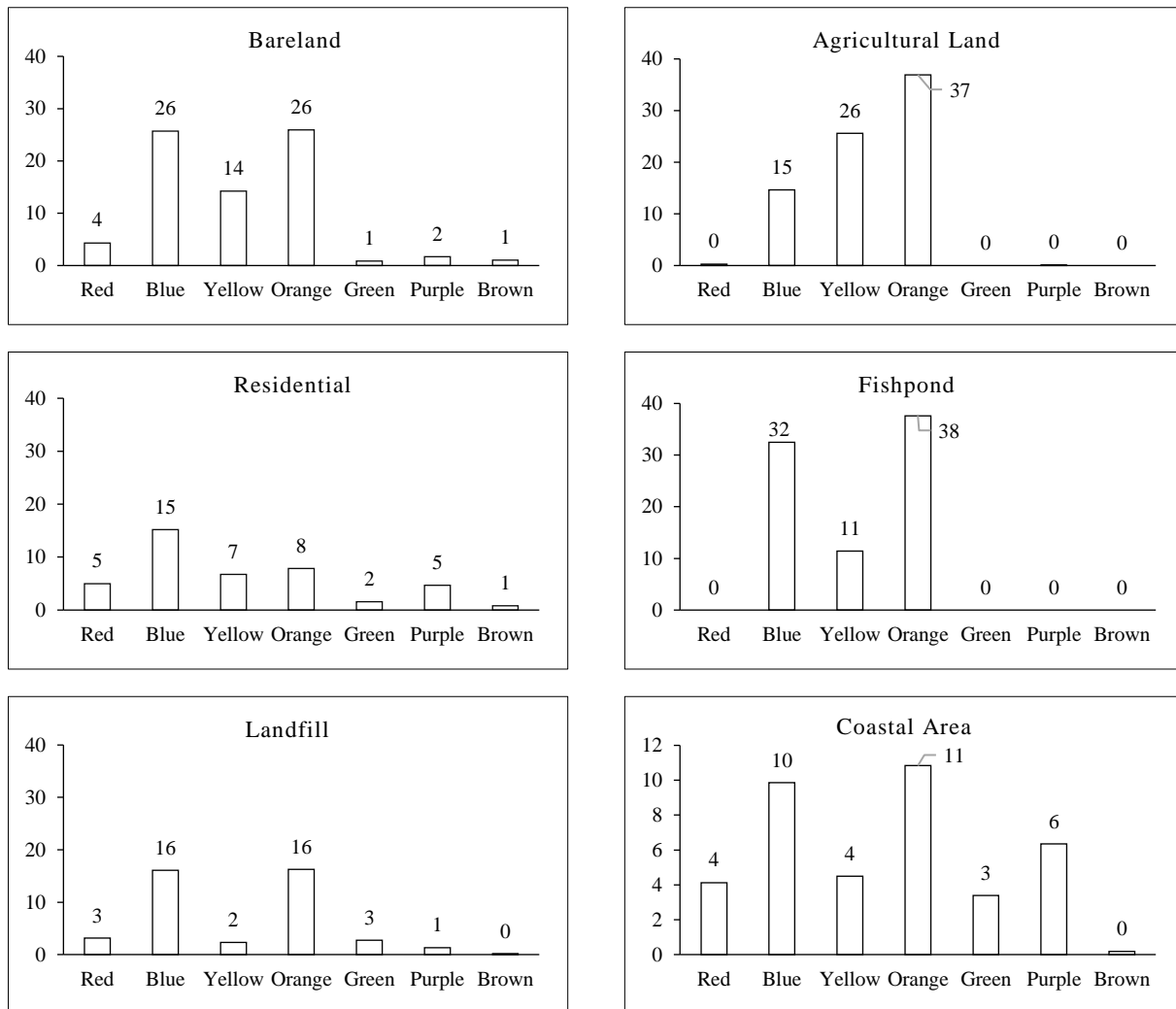


Figure 8. Percentage Distribution of Microplastic Colors Across Different Land Uses

When comparing these results against the land uses, some distinct patterns emerge. For instance, Transparent microplastics dominate in both Landfill and Residential areas, with 57.99% and 58.18% respectively. This could potentially indicate common sources or processes in these areas leading to such accumulation. Conversely, agricultural lands and fishponds have the least Transparent microplastics, hinting at different microplastic sources or the influence of particular activities in those areas. One unusual pattern that stands out is the near absence of Green microplastics in bareland, making up just 0.88%, a stark contrast to other regions. Overall, these findings emphasize the intricate relationship between land use and microplastic distribution. The marked variations in microplastic colors across different land uses suggest different sources, deposition processes, or both.

The distribution of microplastics by color across varying depths for each land use is detailed in Table 2, available in the supplementary materials. The relationship between color and soil depth does not present a consistent pattern. Some colors exhibit fluctuating percentages across the 0-30 cm range, while others, like blue in agricultural land, display a significant reduction from 50.87% to just 3.81% with increasing depth. In contrast, certain colors, such as red in bare land, amplify in prevalence with depth, peaking at 20-30 cm (compared to 7.59% at 0-10 cm). Notably, some colors are specific to particular depths, like the brown microplastics in landfill areas found exclusively at the 20-30 cm depth. In addition, Table 2 provides insights into the size distribution of microplastics across soil depths and the shape of microplastics for each land use.

Table 2. Microplastic Size and Shape Distribution Across Soil Depths for Each Land Use

Depth	Type	Min (μm)	Max (μm)	Size Interval (μm)
<i>Bareland</i>				
0-10 cm	fiber	162	2295	162-2295
	film	46	377	46-377
	fragment	36	306	36-306
	pellet	31	126	31-126
10-20 cm	fiber	128	4453	128-4453
	film	44	471	44-471
	fragment	41	219	41-219
	pellet	29	71	29-71
20-30 cm	fiber	77	1864	77-1864
	film	50	332	50-332
	fragment	39	294	39-294
	pellet	34	144	34-144
<i>Residential</i>				
0-10 cm	fiber	60	2603	60-2603
	film	42	399	42-399
	fragment	34	404	34-404
	pellet	29	70	29-70
10-20 cm	fiber	70	3130	70-3130
	film	46	2765	46-2765
	fragment	43	2316	43-2316
	pellet	54	63	54-63
20-30 cm	fiber	252	3163	252-3163
	film	40	399	40-399
	fragment	48	307	48-307
	pellet	48	62	48-62
<i>Landfill</i>				
0-10 cm	fiber	350	3135	350-3135
	film	41	1207	41-1207
	fragment	37	437	37-437
	pellet	0	0	0-0
10-20 cm	fiber	259	3478	259-3478
	film	33	827	33-827
	fragment	41	666	41-666
	pellet	0	0	0-0
20-30 cm	fiber	419	2562	419-2562
	film	42	499	42-499
	fragment	36	445	36-445
	pellet	0	0	0-0
<i>Agricultural Land</i>				
0-10 cm	fiber	59	862	59-862
	film	51	345	51-345
	fragment	45	305	45-305
	pellet	47	110	47-110
10-20 cm	fiber	148	148	148-148
	film	49	326	49-326
	fragment	37	545	37-545
	pellet	65	65	65-65

20-30 cm	fiber	0	0	0-0
	film	51	322	51-322
	fragment	38	288	38-288
	pellet	0	0	0-0
<i>Fishpond</i>				
0-10 cm	fiber	397	1449	397-1449
	film	51	1254	51-1254
	fragment	55	404	55-404
	pellet	54	56	54-56
10-20 cm	fiber	343	2411	343-2411
	film	61	374	61-374
	fragment	44	307	44-307
	pellet	0	0	0-0
20-30 cm	fiber	151	3163	151-3163
	film	41	625	41-625
	fragment	38	3163	38-3163
	pellet	0	0	0-0
<i>Coastal Area</i>				
0-10 cm	fiber	289	3478	289-3478
	film	33	697	33-697
	fragmen	36	377	36-377
	pelet	50	50	50-50
10-20 cm	fiber	350	3478	350-3478
	film	33	1207	33-1207
	fragmen	42	378	42-378
	pelet	0	0	0-0
20-30 cm	fiber	314	3135	314-3135
	film	33	851	33-851
	fragmen	29	404	29-404
	pelet	0	0	0-0

From the data on microplastic size identification across the six land uses - Bareland, Residential, Landfill, Agricultural Land, Fishpond, and Coastal area - the respective size ranges were determined as 29–4453 μm , 29–3163 μm , 33–3478 μm , 36–862 μm , 38–3263 μm , and 29–3478 μm . These ranges underscore the variability in microplastic sizes across different terrains. Notably, the Agricultural Land exhibits a relatively narrow size spectrum for its microplastics. An intriguing observation across all land uses is that the smallest microplastic sizes were typically found at depths of 20–30 cm, suggesting soil depth could influence the diminution of microplastic size.

The bulk of microplastics identified in this study predominantly fall within the size bracket of less than 100–300 μm , as elaborated in the supplementary materials. On bare land, most microplastics measure less than 100 μm . However, in Residential, Landfill, Agricultural Land, Fishpond, and Coastal areas, the majority of microplastics span a size range of 100–300 μm .

4.3. Identification of Polymers in Microplastic Samples Across Diverse Land Uses via FTIR Analysis

distinct microplastic polymer distribution, shedding light on the variety and dominance of microplastic types present (refer to Figures 9 and 10). Out of 108 samples, with 18 particles tested per land use via FTIR, two particles were identified as non-plastic: a soluble starch in Agricultural Land and a Microfibrillated Cellulose in ponds. These two particles were excluded from data analysis.

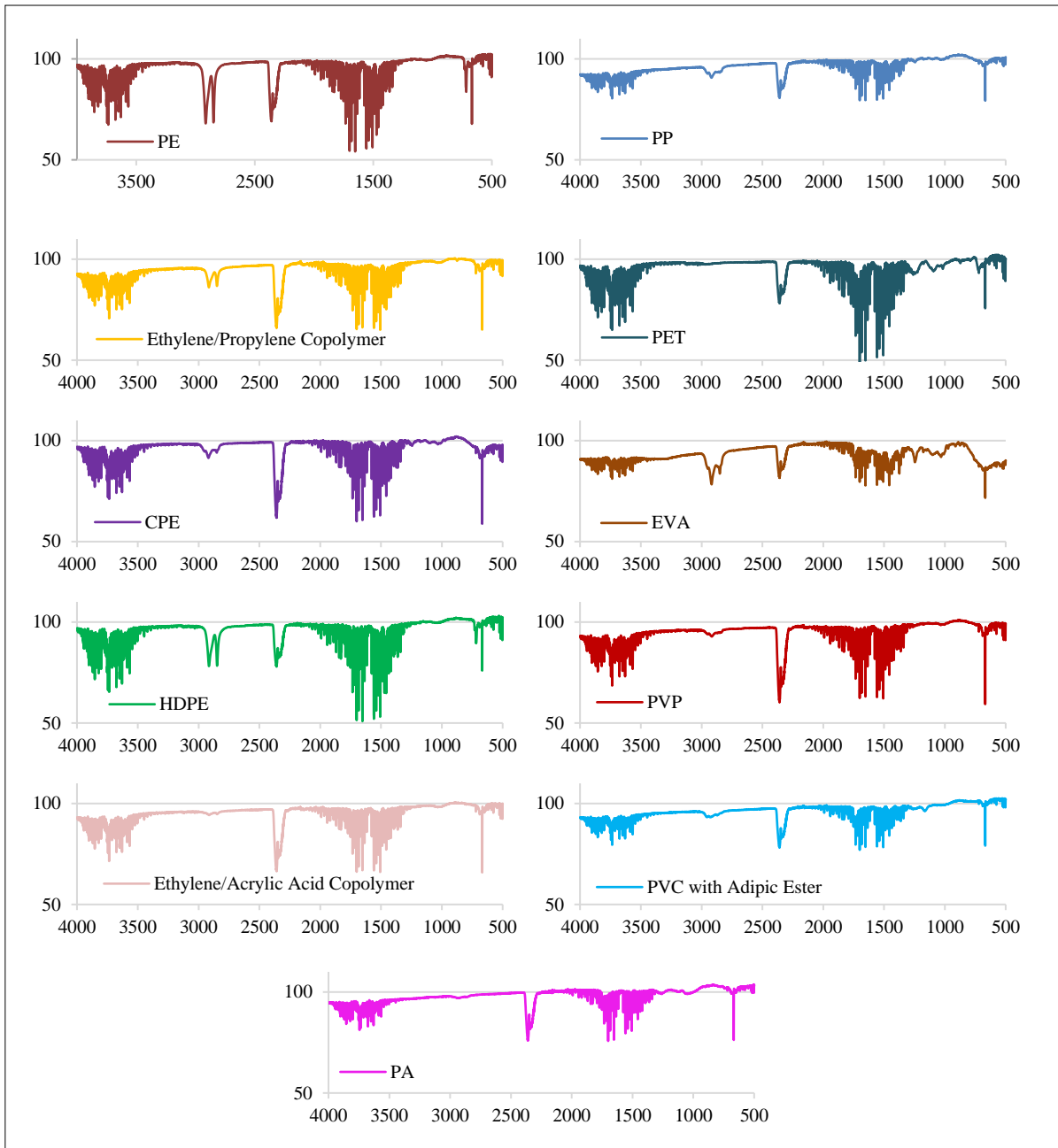
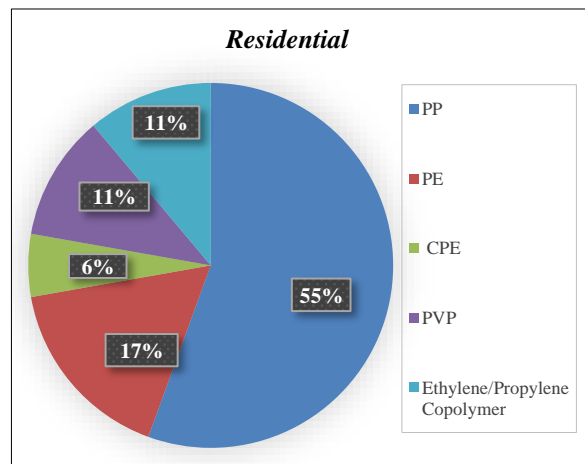
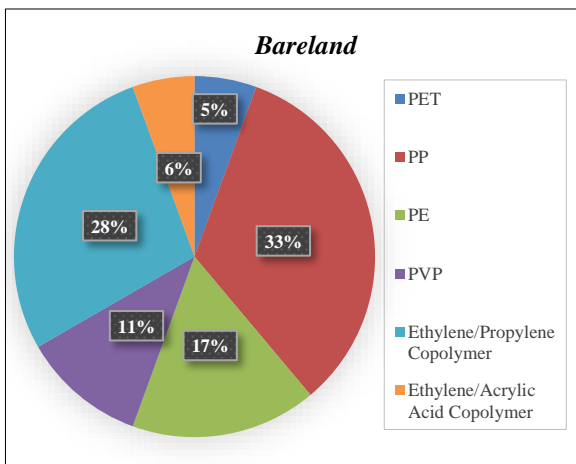


Figure 9. FTIR Spectral Analysis of Microplastics



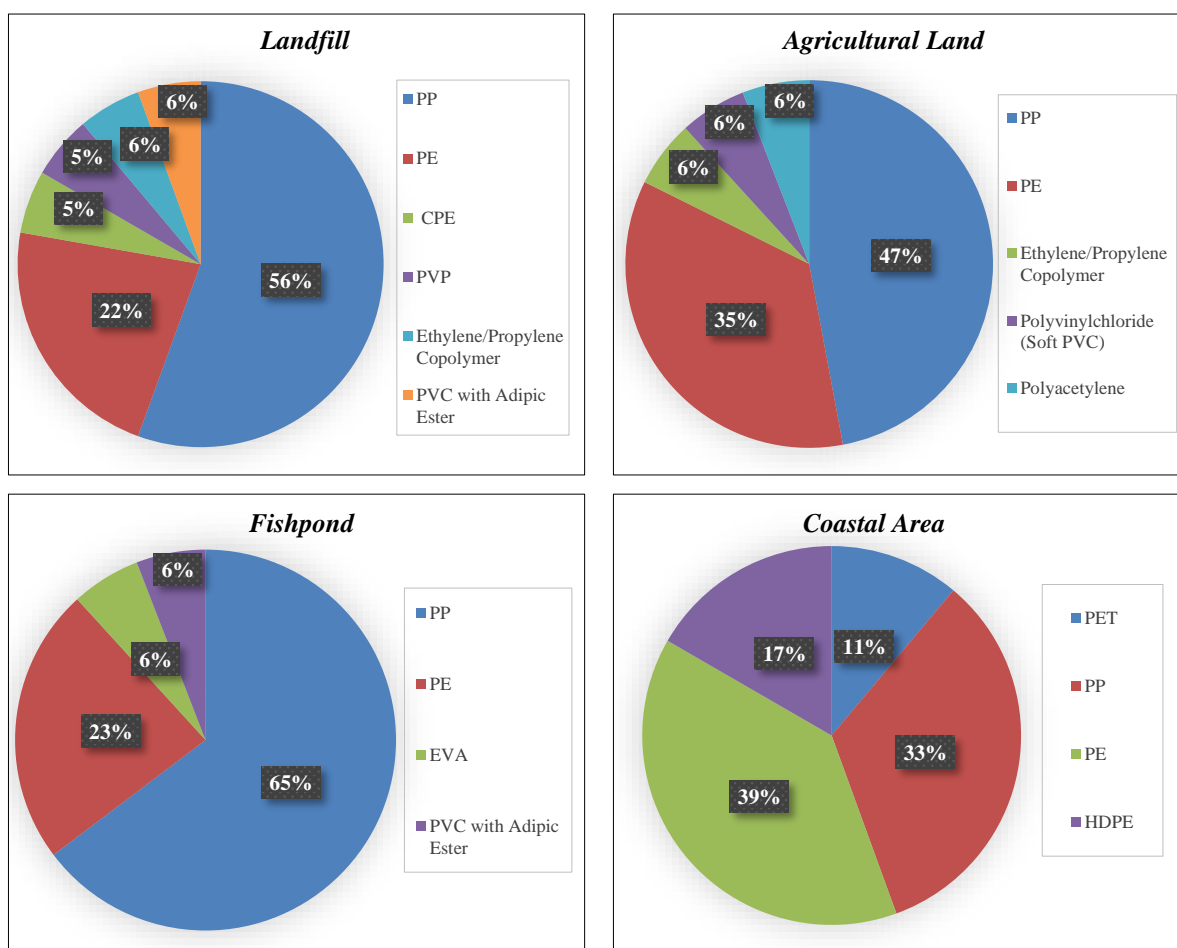


Figure 10. Distribution of Identified Polymers in Microplastic Samples from Various Land Uses

Through careful analysis of the results, a discernible pattern in the distribution of microplastic polymers emerges across the varied land uses. Polypropylene (PP) and Polyethylene (PE) are the two most frequently identified polymers in all land use types, signifying their widespread use and persistence in different environments. For instance, PP constitutes a significant percentage of the microplastics found, ranging from 33% in barelands to 65% in fishponds. Similarly, PE is present in noteworthy proportions, from 17% in barelands, residential areas, and landfills to 39% in coastal areas. Other recurrent polymers identified include Ethylene/Propylene Copolymer, Polyvinylpyrrolidone (PVP), and Chlorinated Polyethylene (CPE), albeit in varying and generally lower percentages.

Upon closer examination of the data, certain similarities and differences become evident in the polymer distribution among different land uses. While PP and PE are prevalent in all environments, their concentrations vary considerably, potentially reflecting the dominant types of plastic waste in each area. Barelands, for example, exhibit a diverse range of polymers, with Ethylene/Propylene Copolymer also featuring prominently at 28%. In contrast, fishponds predominantly contain PP (65%) and PE (23%), with minimal variation in other polymer types. Furthermore, certain polymers are exclusive to specific land uses; for instance, Polyvinyl Chloride with Adipic Ester is found only in landfills and fishponds, while Polyacetylene is unique to agricultural lands. These findings highlight the complex interplay between land use and microplastic pollution, with each environment reflecting a distinct profile of polymer types and concentrations. The observed patterns may be attributed to various factors, including the type of plastic products commonly used or disposed of in each area, the presence of waste management facilities, and the mechanisms of plastic degradation and transport unique to each land use type. Understanding these patterns is crucial for developing targeted interventions to mitigate microplastic pollution in different environments.

4.4. Statistical Analysis and Compatibility Testing of Microplastic Concentrations Across Various Land Uses

The normality test results for six different land uses reveal that five out of the six categories exhibit a normal distribution at a predetermined significance level ($\alpha = 0.05$). The land use associated with fishponds yields a p-value of 0.001117, which falls below the preset level of significance, thereby deviating from normal distribution. Consequently, in light of the derived data, the decision was taken to perform compatibility tests between various land uses utilizing two separate methodologies.

For data on microplastic concentrations demonstrating a normal distribution, statistical analysis was conducted through the application of the t-test method. It is imperative to acknowledge that the foundational assumption underpinning this test is the adherence of the examined data to a normal distribution. In cases involving fishpond land use, where the data diverges from normal distribution, all subsequent statistical tests were examined using the Mann-Whitney test method.

Table 3 elucidates that certain land uses under investigation do not exhibit significant differences in microplastic concentrations, as evidenced by the resultant p-values exceeding 0.05. However, this was not the case for coastal areas, which, when compared to other types of land use, produced p-values less than 0.05. This discrepancy was particularly evident when coastal areas were analyzed against Bare Land (p-value = 0.0188), Residential (p-value = 0.0184), Landfill (p-value = 0.0088), and Agricultural Land (p-value = 0.0043) through the t-test method. In essence, Table 3 substantiates that while microplastic concentrations are fairly consistent across various land uses, coastal areas represent a notable exception.

Table 3. Statistical Analysis of Microplastic Concentrations across Diverse Land Uses

Model	Land Use Type	Normality Test (p-value)	Vs		
			Land use type	T Test (p-value)	Mann-Whitney Test (p-value)
1	Bareland	0.1191	Residential	0.7044	-
2			Landfill	0.6208	-
3			Agricultural Land	0.4225	-
4			Fishpond	-	0.7908
5			Coastal Area	0.0188	-
6	Residential	0.5939	Landfill	0.974	-
7			Agricultural Land	0.8591	-
8			Fishpond	-	0.4795
9			Coastal Area	0.0184	-
10	Landfill	0.05463	Agricultural Land	0.8565	-
11			Fishpond	-	0.377
12			Coastal Area	0.0088	-
13	Agricultural Land	0.4527	Fishpond	-	0.6582
14			Coastal Area	0.0043	-
15	Fishpond	0.001117	Coastal Area	-	0.1329
16	Coastal Area	0.9465	-	-	-

5. Discussions

5.1. Microplastics Prevalence and Characterization across Diverse Land Use

In this study conducted at a regional scale, compelling evidence was discovered pertaining to the presence and abundance of soil microplastics across six distinct land-use categories: bareland, residential areas, landfills, agricultural land, fishponds, and coastal areas. The microplastic concentrations ranged between 16.6 to 21.9 particles/gram across all land uses, surpassing numbers reported in previous studies [71, 74-79, 80-83]. The elevated concentration of microplastics in Makassar city can be ascribed to its inefficient waste management system, societal behaviors, and the potential for microplastics to migrate across various locations and environments.

In this study, fragments and films predominantly represented the microplastics in various land-use types. This contrasts with Yang et al. [21], who found that fragments and fibers were the most common microplastic shapes; our study identified only a limited presence of fiber microplastics. The prevalent occurrence of fragment and film microplastics can be traced back to larger plastic debris breaking down into microplastic particles due to processes like mechanical wear, UV light exposure, and biodegradation [21, 100].

This research also revealed microplastics of diverse colors. Past observations indicate that disposable plastic items often degrade into clear microplastics, while long-lasting plastic items tend to yield colored microplastics [101]. Given these findings, it is inferred that the majority of microplastics in residential, landfill, and coastal areas likely originate from disposable plastics. In contrast, microplastics in bareland, fishponds, and agricultural land may predominantly arise from the breakdown of more durable plastic products.

Concerning the type of polymer in microplastics, studies have commonly reported PE and PP as the prevalent microplastic polymers in soil environments [79, 102]. Our findings, based on FTIR results, align with these reports. The

widespread presence of PE and PP is understandable, considering they rank among the most globally used plastics. They feature prominently in personal care and cosmetics, as well as in plastic bags and packaging [103].

Microplastic distributions were largely consistent across different land-use types, with the exception of coastal areas. The disparity in coastal regions is attributed to the diverse sources of contamination. Coastal areas not only receive microplastics from terrestrial sources but also directly from oceanic ones. As per [76], coastal microplastics might stem from discarded waste, and it is noteworthy that Indonesia ranks second in oceanic plastic waste contributions globally [104]. Asmal et al. [105, 106] emphasized the challenges of plastic waste and broader waste management in the coastal regions bordering the Makassar Strait. Wicaksono et al. [34] found microplastics in both water and sediment samples of the Tallo River, which flows into the Makassar Strait at Bosowa Beach. Díaz-Mendoza et al. [107] proposed that seawater microplastics can traverse laterally, potentially augmenting the microplastic levels on coasts. This study, examining the lower reaches of the Tallo River, similarly identified microplastics in the adjacent coastal soils. Interestingly, despite the microplastic presence, these coastal sampling sites showed no overt plastic debris, setting them apart from residential, agricultural, and pond areas. Water from the Tallo River, laden with microplastics, is influenced by a variety of sources, including laundry effluent, cosmetic granules, and other household waste. This claim is bolstered by the prevalent detection of PE and PP in our samples, the very polymers associated with these sources. These polymers have also been identified in recent coastal studies in Singapore [75] and Taiwan [76].

Landfills and waste disposal sites have traditionally been identified as major hotspots for microplastic accumulation. Interestingly, the concentration of microplastics detected in this study's landfill was somewhat lower than that in fishponds. This can be attributed to the sampling being conducted in the peripheral soil surrounding the landfill — an area with scattered rubbish — rather than its central section. Notably, Makassar city's landfill employs an open dumping system, leading to a towering pile of mixed waste, approximately 20 m high [108]. For detailed visual insights, refer to the supplementary materials provided. Various polymers, including PP, PE, CPE, PVP, Ethylene/Propylene Copolymer, and PVC with adipic ester, were detected in the Makassar landfill. Such findings align with other research on soil microplastics in landfills [72-74], where similar polymers were identified. The presence of these polymers is likely due to the degradation and fragmentation of plastic waste [72-74]. For instance, this study identified PVC with adipic ester in the form of a transparent film. This variant of PVC incorporates biodegradable plasticizer additives derived from adipic acid esters. These additives enhance the PVC's biodegradability, allowing it to break down in natural settings [109]. Consequently, the detected microplastics are likely remnants from microbial activity breaking down the PVC material.

Fishponds, among the various land uses examined, exhibited the highest average microplastic concentration. The dominant type in these areas was an orange-colored fragment associated with the PP polymer. Field observations, detailed in supplementary materials, indicate that these fishponds are in proximity to residential zones. Many floating PP-based trash items—like food containers, bottle caps, and assorted plastic packaging—were spotted in these ponds, suggesting them as potential microplastic sources. Notably, the polymer EVA was identified solely in fishponds. This polymer is widely used in the insulation and sheath layers of cables [110], hoses, tubes, and footwear [111]. Furthermore, as indicated by a study from Hungary [69], microplastics in fishponds could originate from organism uptake. Scheurer and Bigalke [112] also posited that microplastic pollution in floodplain zones might result from the dispersion of microplastics in water or their aeolian transportation.

In the case of agricultural land, microplastic characteristics largely mirror those observed in fishponds: the predominant shape is fragmented, the color is orange, and the associated polymer is PP. Past studies [78-82] suggest that microplastics in agricultural terrains might stem from farming practices such as plastic mulching, sewage sludge applications, nearby roadways, and urban influences.

In residential areas, it is noteworthy that fiber microplastics constitute approximately 16.24% of the total, a figure significantly higher than in other land uses where it is less than 10%. This can likely be attributed to the fact that most fiber particles stem from clothing or textiles, and residential areas naturally experience the highest human activity. The FTIR analysis revealed that the fiber microplastics found in residential areas are primarily composed of PE, a material extensively used in the textile industry [113]. In addition to PE, other polymers identified in this land use—much like in bare land—include PP, Ethylene-propylene copolymer, PVP, and CPE. Ethylene-propylene copolymer, a synthetic rubber, finds its applications in automotive components, building construction, and the cable sector [114]. Conversely, PVP is utilized broadly in food, pharmaceutical, and cosmetics industries [115], while CPE is popular in various applications such as piping, roofing, and a range of automotive and construction materials [116].

Potential microplastic sources in residential areas and bare lands might include road or vehicle emissions, given the proximity of sampling points to streets, as well as construction activities. Additionally, illegal waste practices, such as littering and inadequate waste disposal, can also contribute to the heightened microplastic concentrations [103]. This is especially true for barelands, which often bear the brunt of illegal dumping, including the discarding of single-use plastics. For a more comprehensive visual perspective, please refer to the supplementary materials provided.

Microplastics are generally defined as particles smaller than 5 mm in size. Notably, in this study, the predominant size of microplastics was found to be under 300 μm . This minute size can have significant implications for toxicity [117]. The heightened potential threat of these tiny microplastics to organisms is due to their expansive surface area, enhancing the absorption of harmful compounds. Furthermore, their diminutive size makes them easily ingestible by various species because they are less noticeable [21, 118].

Given that this research represents the inaugural study on soil microplastics across different land uses in Makassar City, Indonesia, there is a pressing need to delve deeper into the specific origins and pathways of microplastics within each land use. This study marks a significant advancement in understanding soil microplastic pollution, revealing higher concentrations of microplastics across various land uses than previously reported. It diverges from prior findings (e.g., Yang et al. [21]) by predominantly identifying fragments and films, rather than fibers, suggesting different sources and degradation processes. The research highlights the distinct microplastic contamination patterns in coastal areas, attributed to combined terrestrial and oceanic sources. Surprisingly, fishponds exhibited higher microplastic levels than landfills, challenging conventional assumptions and pointing to complex pollution sources. The study also confirms the dominance of polymers like PE and PP, aligning with global plastic usage trends. Notably, the significant presence of fiber microplastics in residential areas indicates the impact of human activities, particularly from textiles. The small size of these microplastics raises concerns about their potential toxicity and threat to organisms, underscoring the urgent need for comprehensive studies to explore the origins and pathways of microplastics in different environments.

5.2. Comparative Insights: Distribution and Pathways of Microplastics Across Land Uses and Depths

The findings of the current study on microplastics concentrations across various land uses unveil intriguing comparisons and contrasts with previously documented studies. Landfills in this study showed the highest concentration of microplastics at the surface depth (0-10 cm), aligning with general expectations that microplastics predominantly occur at surface levels due to the continual deposit of waste materials. Nevertheless, the observation of elevated concentrations at lower depths, especially in residential and fishpond areas, diverges from conventional anticipation, suggesting the presence of distinctive distribution mechanisms in these environments.

In the current study, the notable presence of plastic waste, observed visually at various soil depths in fishponds, bareland, landfills, and residential areas, underscored the pervasive existence of microplastics (available in supplementary materials). This presence is particularly pronounced in urban and agricultural soils, which are often considered hotspots for microplastic pollution due to their close proximity to human activities. Such activities invariably generate plastic waste externalities, contributing significantly to the microplastic content [119, 120]. This situation reflects the findings of Xu et al. [49] and Helmberger et al. [121], who explored the complex journey of microplastics within the soil environment. Upon entering the soil, microplastics undergo various interactions and transformations, neither remaining static nor inactive. A dynamic interplay exists between abiotic and biotic mechanisms [50-53], with each playing a crucial role in the dispersal and distribution of microplastics. The recorded presence of earthworm activity within the soil of residential, agricultural, and fishpond areas in the present study exemplifies this dynamic interaction. Such biological activities, especially those associated with earthworm burrowing, not only increase soil porosity but also enhance water infiltration rates, thereby actively influencing the movement and distribution of microplastics throughout different soil layers [122].

The distinct granular constitution of the soil in these coastal areas, which differs significantly in porosity from the predominantly fine-grained soils found in other land uses, facilitates easier penetration of microplastics. Given these observations, future studies should explore how soil characteristics may influence the rates of microplastic deposition and the pathways they traverse within the soil profile.

In reflecting on these insights, it is imperative to acknowledge that the movement and penetration of microplastics within the soil matrix are multifaceted processes influenced by both abiotic factors and biological activities. The observed variations in microplastic concentrations at different depths across diverse land uses, as evidenced in both the present and past studies, highlight the dynamic interactions within the environment that govern the behavior and distribution of microplastics. Understanding these nuances is crucial for devising effective strategies to mitigate the impact of microplastics on our ecosystems and public health. Hence, future research endeavors should continue to explore and elucidate the myriad factors influencing the pathways and fate of microplastics in various terrestrial environments.

5.3. Potential Impact of Microplastics Pollution

This study uncovers significant potential implications of microplastics across various land uses on the ecosystem. The dominant presence of small-sized microplastics (less than 300 μm) suggests an increased likelihood of accumulating and transferring contaminants, such as organic pollutants, human pathogens, and heavy metals [123]. This can jeopardize the balance of soil microbial populations and biological activities, resulting in ecological disruptions [124-126]. The physical structure of the soil may also be altered due to the integration of these microplastics, potentially compromising land fertility and integrity [127]. Predominantly, the identified microplastics were of PE and PP varieties. Notably, PE has been found to significantly reduce soil pH [128] and influence the soil's carbon and nutrient cycles [129]. In

agricultural settings, such plastic particles can adhere to plant root exteriors, potentially hampering plant productivity [130, 131]. The discovery of microplastics in residential areas amplifies health concerns, given the potential for airborne microplastics or their transition into water bodies. Such pathways can lead to human exposure through inhalation, ingestion, or skin absorption, raising alarms about health risks [132]. Moreover, once inhaled, denser particles could reside in the lungs, later entering the circulatory and lymphatic systems [133]. Considering this study pioneers the research on soil microplastics in Makassar City, Indonesia, there is an imperative need for further exploration. Specifically, assessing the nuanced impacts of microplastics across varied land uses is crucial, especially in the context of an expanding population and the anticipated rise in microplastic concentrations in these environments.

5.4. Recommended Mitigation Strategies

The elevated presence of microplastics in soil poses a significant environmental concern that demands immediate and effective intervention. As highlighted earlier, the repercussions of unchecked microplastic contamination can be detrimental, both ecologically and in terms of human health. This research suggests a suite of mitigation strategies tailored to specific land uses, emphasizing proactive prevention of further contamination. Each land use type necessitates a distinct approach for effective mitigation.

For agricultural terrains, bioremediation emerges as a viable solution. This technique leverages microorganisms to degrade plastic residues into benign substances [134]. Not only is this approach effective for farmlands, but coastal areas can also benefit from it to neutralize prevalent contaminants [135]. Additionally, reforestation areas surrounding agricultural land can significantly diminish the influx of microplastics into the soil [136]. Implementing vegetation like reeds and peanuts, known to assimilate byproducts from microplastic degradation [137], can further mitigate the spread and impact of these contaminants.

Coastal contamination is intricately linked to water flows from inland channels, especially rivers [34]. These river flows transport microplastics from diverse sources. To effectively combat the widespread problem of microplastic contamination in coastal regions, a comprehensive strategy is imperative due to the varied routes through which microplastics spread. While curtailing the use of plastic products and ensuring they do not end up in rivers is essential, other critical measures include improved waste management systems that effectively filter out plastics before they reach coastlines or oceans. Additionally, raising public awareness about the detrimental effects of microplastic pollution and enforcing strict regulations on microplastic discharge from industries and manufacturers are vital components of this holistic approach.

6. Conclusion

In our detailed study of the prevalence, distribution, and ecological implications of microplastics in soil environments, particularly within Makassar City, Indonesia, we have elucidated several significant findings. This research underscores the pervasive nature of microplastics across a variety of soil types and land uses, highlighting their widespread presence. The study yielded three primary insights: Firstly, microplastic concentrations were found to range between 16.6 to 21.9 particles per gram across all land uses, with a noted consistency in these levels except for coastal areas. Secondly, our research demonstrated a notable variance in the distribution of microplastics, with distinctions in shape, color, and size observed at varying soil depths. Furthermore, our analysis revealed diverse attributes of microplastics, such as the predominance of fragments and films across different land uses. We identified a spectrum of colors, including blue, green, orange, purple, red, transparent, and yellow, with polyethylene (PE) and polypropylene (PP) emerging as the principal polymers. Most microplastics were also found to be less than 300 μm in size.

Our findings regarding the movement and distribution of microplastics within soil indicate a non-uniform pattern, which could have substantial consequences for soil-dwelling organisms and the broader ecosystem. This underlines the critical need for more comprehensive studies on the ecological impacts of soil microplastic pollution. Nonetheless, our research acknowledges certain limitations, such as the essential requirement for standardized methodologies in the study of microplastics, the complex challenges in analyzing diverse particle sizes and compositions, and the evolving understanding of the chemical and physical properties of microplastics in soil. Therefore, future research endeavors should focus on addressing these challenges and building upon the foundational insights provided by our study. The significance of this research lies in its contribution to the broader understanding of microplastic pollution, offering vital information for the development of effective environmental management and conservation strategies. This is crucial for safeguarding soil health and ensuring the sustainability of ecosystems.

7. Declarations

7.1. Author Contributions

Conceptualization, M.A.W., Z.A.H., R.H., and A.D.D.; methodology, M.A.W., Z.A.H., R.H., and A.D.D.; laboratory administration, Z.A.H., R.H., and A.D.D.; investigation, M.A.W., Z.A.H., R.H., A.D.D., and S.N.; writing—original draft preparation, M.A.W., Z.A.H., and R.H.; writing—review and editing, M.A.W. and Z.A.H.; supervision, M.A.W., Z.A.H., R.H., S.N., K., and L.C.; funding acquisition, M.A.W. All authors have read and agreed to the published version of the manuscript.

7.2. Data Availability Statement

The data presented in this study are available in the article.

7.3. Funding and Acknowledgments

We extend our deepest appreciation to Lembaga Penelitian dan Pengabdian Kepada Masyarakat (LPPM) Universitas Hasanuddin for their unwavering support and the generous research grant, Grant Number 00323/UN4.22/PT.01.03/2023, which made this research feasible. We are immensely grateful to Noviyanti Pasolang, Buya Ibnu Fulqan, Muhammad Firmansyah, and Nurhaedah Azzahra, the dedicated undergraduate scholars from the Department of Environmental Engineering, Faculty of Engineering, Universitas Hasanuddin, for their invaluable assistance throughout the data collection and laboratory phases. Additionally, our heartfelt thanks go to the Laboratory of Water Quality, Faculty of Marine and Fisheries Sciences, Universitas Hasanuddin, for facilitating our laboratory experimentation.

7.4. Conflicts of Interest

The authors declare no conflict of interest.

8. References

- [1] Ghosh, S., Sinha, J. K., Ghosh, S., Vashisth, K., Han, S., & Bhaskar, R. (2023). Microplastics as an Emerging Threat to the Global Environment and Human Health. *Sustainability (Switzerland)*, 15(14), 10821. doi:10.3390/su151410821.
- [2] Crawford, C. B., & Quinn, B. (2017). Microplastic collection techniques. *Microplastic Pollutants*, 179–202, Elsevier Science, Amsterdam, Netherlands. doi:10.1016/b978-0-12-809406-8.00008-6.
- [3] Auta, H. S., Emenike, C. U., & Fauziah, S. H. (2017). Distribution and importance of microplastics in the marine environment review of the sources, fate, effects, and potential solutions. *Environment International*, 102, 165–176. doi:10.1016/j.envint.2017.02.013.
- [4] Zhang, Y., Kang, S., Allen, S., Allen, D., Gao, T., & Sillanpää, M. (2020). Atmospheric microplastics: A review on current status and perspectives. *Earth-Science Reviews*, 203, 103118. doi:10.1016/j.earscirev.2020.103118.
- [5] Li, W., Luo, Y., & Pan, X. (2020). Microplastics in Agricultural Soils. *Microplastics in Terrestrial Environments*, 63–76, Springer, Cham, Switzerland. doi:10.1007/978-3-030-39041-9_24.
- [6] Tian, L., Jinjin, C., Ji, R., Ma, Y., & Yu, X. (2022). Microplastics in agricultural soils: sources, effects, and their fate. *Current Opinion in Environmental Science and Health*, 25, 100311. doi:10.1016/j.coesh.2021.100311.
- [7] Dissanayake, P. D., Kim, S., Sarkar, B., Oleszczuk, P., Sang, M. K., Haque, M. N., Ahn, J. H., Bank, M. S., & Ok, Y. S. (2022). Effects of microplastics on the terrestrial environment: A critical review. *Environmental Research*, 209, 112734. doi:10.1016/j.envres.2022.112734.
- [8] Surendran, U., Jayakumar, M., Raja, P., Gopinath, G., & Chellam, P. V. (2023). Microplastics in terrestrial ecosystem: Sources and migration in soil environment. *Chemosphere*, 318, 137946. doi:10.1016/j.chemosphere.2023.137946.
- [9] Cui, W., Gao, P., Zhang, M., Wang, L., Sun, H., & Liu, C. (2022). Adverse effects of microplastics on earthworms: A critical review. *Science of the Total Environment*, 850, 158041. doi:10.1016/j.scitotenv.2022.158041.
- [10] Zhao, K., Wei, Y., Dong, J., Zhao, P., Wang, Y., Pan, X., & Wang, J. (2022). Separation and characterization of microplastic and nanoplastic particles in marine environment. *Environmental Pollution*, 297, 118773. doi:10.1016/j.envpol.2021.118773.
- [11] Akdogan, Z., & Guven, B. (2019). Microplastics in the environment: A critical review of current understanding and identification of future research needs. *Environmental Pollution*, 254, 113011. doi:10.1016/j.envpol.2019.113011.
- [12] Udovicki, B., Andjelkovic, M., Cirkovic-Velickovic, T., & Rajkovic, A. (2022). Microplastics in food: scoping review on health effects, occurrence, and human exposure. *International Journal of Food Contamination*, 9(1). doi:10.1186/s40550-022-00093-6.
- [13] Yuan, Z., Nag, R., & Cummins, E. (2022). Human health concerns regarding microplastics in the aquatic environment - From marine to food systems. *Science of the Total Environment*, 823, 153730. doi:10.1016/j.scitotenv.2022.153730.
- [14] Schwabl, P., Koppel, S., Konigshofer, P., Bucsics, T., Trauner, M., Reiberger, T., & Liebmann, B. (2019). Detection of various microplastics in human stool: A prospective case series. *Annals of Internal Medicine*, 171(7), 453–457. doi:10.7326/M19-0618.
- [15] Wright, S. L., & Kelly, F. J. (2017). Plastic and Human Health: A Micro Issue? *Environmental Science and Technology*, 51(12), 6634–6647. doi:10.1021/acs.est.7b00423.
- [16] Walker, T. R. (2021). (Micro)plastics and the UN Sustainable Development Goals. *Current Opinion in Green and Sustainable Chemistry*, 30, 100497. doi:10.1016/j.cogsc.2021.100497.
- [17] Elliff, C., Mansor, M.T.C., Feodrippe, R., & Turra, A. (2022). Microplastics and the UN Sustainable Development Goals. *Handbook of Microplastics in the Environment*. Springer, Cham, Switzerland. doi:10.1007/978-3-030-39041-9_24.

- [18] United Nations Development Programme. (2015) Sustainable Development Goals Booklet. United Nations Development Programme, New York, United States. Available online: <https://www.undp.org/publications/sustainable-development-goals-booklet> (accessed on March 2024).
- [19] Rillig, M. C. (2012). Microplastic in terrestrial ecosystems and the soil? *Environmental Science & Technology*, 46(12), 6453–6454. doi:10.1021/es302011r.
- [20] Nizzetto, L., Futter, M., & Langaas, S. (2016). Are Agricultural Soils Dumps for Microplastics of Urban Origin? *Environmental Science & Technology*, 50(20), 10777–10779. doi:10.1021/acs.est.6b04140.
- [21] Yang, L., Zhang, Y., Kang, S., Wang, Z., & Wu, C. (2021). Microplastics in soil: A review on methods, occurrence, sources, and potential risk. *Science of the Total Environment*, 780, 146546. doi:10.1016/j.scitotenv.2021.146546.
- [22] Huang, Y., Zhao, Y., Wang, J., Zhang, M., Jia, W., & Qin, X. (2019). LDPE microplastic films alter microbial community composition and enzymatic activities in soil. *Environmental Pollution*, 254, 112983. doi:10.1016/j.envpol.2019.112983.
- [23] Vithanage, M., Ramanayaka, S., Hasinthara, S., & Navaratne, A. (2021). Compost as a carrier for microplastics and plastic-bound toxic metals into agroecosystems. *Current Opinion in Environmental Science and Health*, 24, 100297. doi:10.1016/j.coesh.2021.100297.
- [24] Li, J., Zhang, K., & Zhang, H. (2018). Adsorption of antibiotics on microplastics. *Environmental Pollution*, 237, 460–467. doi:10.1016/j.envpol.2018.02.050.
- [25] Nizzetto, L., Bussi, G., Futter, M. N., Butterfield, D., & Whitehead, P. G. (2016). A theoretical assessment of microplastic transport in river catchments and their retention by soils and river sediments. *Environmental Science: Processes & Impacts*, 18(8), 1050–1059. doi:10.1039/c6em00206d.
- [26] Bian, W., An, L., Zhang, S., Feng, J., Sun, D., Yao, Y., Shen, T., Yang, Y., & Zhang, M. (2022). The long-term effects of microplastics on soil organomineral complexes and bacterial communities from controlled-release fertilizer residual coating. *Journal of Environmental Management*, 304, 114193. doi:10.1016/j.jenvman.2021.114193.
- [27] Dris, R., Gasperi, J., Saad, M., Mirande, C., & Tassin, B. (2016). Synthetic fibers in atmospheric fallout: A source of microplastics in the environment? *Marine Pollution Bulletin*, 104(1–2), 290–293. doi:10.1016/j.marpolbul.2016.01.006.
- [28] Kumar, A., Mishra, S., Pandey, R., Yu, Z. G., Kumar, M., Khoo, K. S., Thakur, T. K., & Show, P. L. (2023). Microplastics in terrestrial ecosystems: Un-ignorable impacts on soil characterizes, nutrient storage and its cycling. *TrAC Trends in Analytical Chemistry*, 158, 116869. doi:10.1016/j.trac.2022.116869.
- [29] Boots, B., Russell, C. W., & Green, D. S. (2019). Effects of Microplastics in Soil Ecosystems: Above and below Ground. *Environmental Science & Technology*, 53(19), 11496–11506. doi:10.1021/acs.est.9b03304.
- [30] The World Bank. (2021). Plastic Waste Discharges from Rivers and Coastlines in Indonesia. *Marine Plastics Series, East Asia and Pacific Region*. The World Bank, Washington, United States. Available online: <https://openknowledge.worldbank.org/bitstream/handle/10986/35607/Plastic%20Discharges%20Indonesia%20Study.pdf?sequence=4&isAllowed=y> (accessed on March 2024).
- [31] Curren, E., Kuwahara, V. S., Yoshida, T., & Leong, S. C. Y. (2021). Marine microplastics in the ASEAN region: A review of the current state of knowledge. *Environmental Pollution*, 288, 117776. doi:10.1016/j.envpol.2021.117776.
- [32] IBS. (2020) South Sulawesi Province in Numbers. Indonesian Bureau of Statistics, Jakarta, Indonesia. Available online: <https://sulsel.bps.go.id/publication/2020/04/27/4b655b65f433c8e7e452a45c/provinsi-sulawesi-selatan-dalam-angka-2020.html> (accessed on March 2024).
- [33] Evans, K., & Millott, M. (2020) Overview: South Sulawesi's economy. The Partnership for Australia-Indonesia Research (PAIR), Australia-Indonesia Centre, Caulfield East, Australia. Available online: https://pair.austriaindonesiacentre.org/wp-content/uploads/2020/05/PAIR-overview_SulSel-economy-2.pdf (accessed on March 2024).
- [34] Wicaksono, E. A., Werorilangi, S., Galloway, T. S., & Tahir, A. (2021). Distribution and seasonal variation of microplastics in Tallo River, Makassar, Eastern Indonesia. *Toxics*, 9(6), 129. doi:10.3390/toxics9060129.
- [35] Yuan, D., Corvianawatie, C., Cordova, M. R., Surinati, D., Li, Y., Wang, Z., Li, X., Li, R., Wang, J., He, L., Yuan, A. N., Dirhamsyah, D., Arifin, Z., Sun, X., & Isobe, A. (2023). Microplastics in the tropical Northwestern Pacific Ocean and the Indonesian seas. *Journal of Sea Research*, 194, 102406. doi:10.1016/j.seares.2023.102406.
- [36] Afdal, M., Werorilangi, S., Faizal, A., & Tahir, A. (2019). Studies on Microplastics Morphology Characteristics in the Coastal Water of Makassar City, South Sulawesi, Indonesia. *International Journal of Environment, Agriculture and Biotechnology*, 4(4), 1028–1033. doi:10.22161/ijeab.4421.
- [37] Sawalman, R., Putri Zamani, N., Werorilangi, S., & Samira Ismet, M. (2021). Spatial and temporal distribution of microplastics in the surface waters of Barranglombo Island, Makassar. *IOP Conference Series: Earth and Environmental Science*, 860(1), 12098. doi:10.1088/1755-1315/860/1/012098.

- [38] Fajaruddin Natsir, M., Selomo, M., Ibrahim, E., Arsin, A. A., & Alni, N. C. (2021). Analysis on microplastics in dug wells around Tamangapa Landfills, Makassar City, Indonesia. *Gaceta Sanitaria*, 35(1), S87–S89. doi:10.1016/j.gaceta.2020.12.024.
- [39] MacLeod, M., Arp, H. P. H., Tekman, M. B., & Jahnke, A. (2021). The global threat from plastic pollution. *Science*, 373(6550), 61–65. doi:10.1126/science.abg5433.
- [40] Dioses-Salinas, D. C., Pizarro-Ortega, C. I., & De-la-Torre, G. E. (2020). A methodological approach of the current literature on microplastic contamination in terrestrial environments: Current knowledge and baseline considerations. *Science of the Total Environment*, 730, 139164. doi:10.1016/j.scitotenv.2020.139164.
- [41] Statista. (2023) Global plastic production 1950–2020. Statista, Hamburg, Germany. Available online: <https://www.statista.com/statistics/282732/global-production-of-plastics-since-1950/> (accessed on March 2024).
- [42] Okoffo, E. D., O'Brien, S., Ribeiro, F., Burrows, S. D., Toapanta, T., Rauert, C., O'Brien, J. W., Tschärke, B. J., Wang, X., & Thomas, K. V. (2021). Plastic particles in soil: State of the knowledge on sources, occurrence and distribution, analytical methods and ecological impacts. *Environmental Science: Processes and Impacts*, 23(2), 240–274. doi:10.1039/d0em00312c.
- [43] Rochman, C. M., & Hoellein, T. (2020). The global odyssey of plastic pollution. *Science*, 368(6496), 1184–1185. doi:10.1126/science.abc4428.
- [44] Sun, Q., Li, J., Wang, C., Chen, A., You, Y., Yang, S., Liu, H., Jiang, G., Wu, Y., & Li, Y. (2022). Research progress on distribution, sources, identification, toxicity, and biodegradation of microplastics in the ocean, freshwater, and soil environment. *Frontiers of Environmental Science and Engineering*, 16(1), 1-14. doi:10.1007/s11783-021-1429-z.
- [45] Rodrigues, M. O., Abrantes, N., Gonçalves, F. J. M., Nogueira, H., Marques, J. C., & Gonçalves, A. M. M. (2018). Spatial and temporal distribution of microplastics in water and sediments of a freshwater system (Antuã River, Portugal). *Science of the Total Environment*, 633, 1549–1559. doi:10.1016/j.scitotenv.2018.03.233.
- [46] Lu, M., Yang, M., Yang, Y., Wang, D., & Sheng, L. (2019). Soil carbon and nutrient sequestration linking to soil aggregate in a temperate fen in Northeast China. *Ecological Indicators*, 98, 869–878. doi:10.1016/j.ecolind.2018.11.054.
- [47] de Souza Machado, A.A., Horton, A.A., Davis, T., & Maaß, S. (2020). Microplastics and Their Effects on Soil Function as a Life-Supporting System. *Microplastics in Terrestrial Environments. The Handbook of Environmental Chemistry*, 95, Springer, Cham, Switzerland. doi:10.1007/978-2020-450.
- [48] Issac, M. N., & Kandasubramanian, B. (2021). Effect of microplastics in water and aquatic systems. *Environmental Science and Pollution Research*, 28(16), 19544–19562. doi:10.1007/s11356-021-13184-2.
- [49] Xu, B., Liu, F., Cryder, Z., Huang, D., Lu, Z., He, Y., Wang, H., Lu, Z., Brookes, P. C., Tang, C., Gan, J., & Xu, J. (2020). Microplastics in the soil environment: Occurrence, risks, interactions and fate—A review. *Critical Reviews in Environmental Science and Technology*, 50(21), 2175–2222. doi:10.1080/10643389.2019.1694822.
- [50] Carmen, S. (2021). Microbial capability for the degradation of chemical additives present in petroleum-based plastic products: A review on current status and perspectives. *Journal of Hazardous Materials*, 402, 123534. doi:10.1016/j.jhazmat.2020.123534.
- [51] Boyle, K., & Örmeci, B. (2020). Microplastics and nanoplastics in the freshwater and terrestrial environment: A review. *Water (Switzerland)*, 12(9), 2633. doi:10.3390/w12092633.
- [52] Helmberger, M. S., Miesel, J. R., Tiemann, L. K., & Grieshop, M. J. (2022). Soil Invertebrates Generate Microplastics from Polystyrene Foam Debris. *Journal of Insect Science*, 22(1). doi:10.1093/jisesa/ieac005.
- [53] Sajjad, M., Huang, Q., Khan, S., Khan, M. A., Liu, Y., Wang, J., Lian, F., Wang, Q., & Guo, G. (2022). Microplastics in the soil environment: A critical review. *Environmental Technology and Innovation*, 27, 102408. doi:10.1016/j.eti.2022.102408.
- [54] Kaur, P., Singh, K., & Singh, B. (2022). Microplastics in soil: Impacts and microbial diversity and degradation. *Pedosphere*, 32(1), 49–60. doi:10.1016/S1002-0160(21)60060-7.
- [55] Chen, Y., Leng, Y., Liu, X., & Wang, J. (2020). Microplastic pollution in vegetable farmlands of suburb Wuhan, central China. *Environmental Pollution*, 257, 113449. doi:10.1016/j.envpol.2019.113449.
- [56] Gao, D., Li, X., & Liu, H. (2020). Source, occurrence, migration and potential environmental risk of microplastics in sewage sludge and during sludge amendment to soil. *Science of the Total Environment*, 742, 140355. doi:10.1016/j.scitotenv.2020.140355.
- [57] Cverenkárová, K., Valachovičová, M., Mackul'ak, T., Žemlička, L., & Bírošová, L. (2021). Microplastics in the food chain. *Life*, 11(12), 1349. doi:10.3390/life11121349.
- [58] Zhang, H., Huang, Y., An, S., Zhao, J., Xiao, L., Li, H., & Huang, Q. (2022). Microplastics trapped in soil aggregates of different land-use types: A case study of Loess Plateau terraces, China. *Environmental Pollution*, 310, 119880. doi:10.1016/j.envpol.2022.119880.
- [59] Jiang, X., Chang, Y., Zhang, T., Qiao, Y., Klobučar, G., & Li, M. (2020). Toxicological effects of polystyrene microplastics on earthworm (*Eisenia Fetida*). *Environmental Pollution*, 259. doi:10.1016/j.envpol.2019.113896.

- [60] Shafea, L., Yap, J., Beriot, N., Felde, V. J. M. N. L., Okoffo, E. D., Enyoh, C. E., & Peth, S. (2023). Microplastics in agroecosystems: A review of effects on soil biota and key soil functions. *Journal of Plant Nutrition and Soil Science*, 186(1), 5–22. doi:10.1002/jpln.202200136.
- [61] Selonen, S., Dolar, A., Jemec Kokalj, A., Skalar, T., Parramon Dolcet, L., Hurley, R., & van Gestel, C. A. M. (2020). Exploring the impacts of plastics in soil – The effects of polyester textile fibers on soil invertebrates. *Science of the Total Environment*, 700, 134451. doi:10.1016/j.scitotenv.2019.134451.
- [62] Ajith, N., Arumugam, S., Parthasarathy, S., Manupoori, S., & Janakiraman, S. (2020). Global distribution of microplastics and its impact on marine environment—a review. *Environmental Science and Pollution Research*, 27(21), 25970–25986. doi:10.1007/s11356-020-09015-5.
- [63] Kumar, A., Dorodnikov, M., Splettstößer, T., Kuzyakov, Y., & Pausch, J. (2017). Effects of maize roots on aggregate stability and enzyme activities in soil. *Geoderma*, 306, 50–57. doi:10.1016/j.geoderma.2017.07.007.
- [64] Kumar, M., Xiong, X., He, M., Tsang, D. C. W., Gupta, J., Khan, E., Harrad, S., Hou, D., Ok, Y. S., & Bolan, N. S. (2020). Microplastics as pollutants in agricultural soils. *Environmental Pollution*, 265, 114980. doi:10.1016/j.envpol.2020.114980.
- [65] Watteau, F., Dignac, M. F., Bouchard, A., Revallier, A., & Houot, S. (2018). Microplastic Detection in Soil Amended with Municipal Solid Waste Composts as Revealed by Transmission Electronic Microscopy and Pyrolysis/GC/MS. *Frontiers in Sustainable Food Systems*, 2(81). doi:10.3389/fsufs.2018.00081.
- [66] Corradini, F., Meza, P., Eguiluz, R., Casado, F., Huerta-Lwanga, E., & Geissen, V. (2019). Evidence of microplastic accumulation in agricultural soils from sewage sludge disposal. *Science of the Total Environment*, 671, 411–420. doi:10.1016/j.scitotenv.2019.03.368.
- [67] Edo, C., González-Pleiter, M., Leganés, F., Fernández-Piñas, F., & Rosal, R. (2020). Fate of microplastics in wastewater treatment plants and their environmental dispersion with effluent and sludge. *Environmental Pollution*, 259, 113837. doi:10.1016/j.envpol.2019.113837.
- [68] Cambier, P., Michaud, A., Paradelo, R., Germain, M., Mercier, V., Guérin-Lebourg, A., Revallier, A., & Houot, S. (2019). Trace metal availability in soil horizons amended with various urban waste composts during 17 years – Monitoring and modelling. *Science of the Total Environment*, 651, 2961–2974. doi:10.1016/j.scitotenv.2018.10.013.
- [69] Bordós, G., Urbányi, B., Micsinai, A., Kriszt, B., Palotai, Z., Szabó, I., Hantosi, Z., & Szoboszlai, S. (2019). Identification of microplastics in fish ponds and natural freshwater environments of the Carpathian basin, Europe. *Chemosphere*, 216, 110–116. doi:10.1016/j.chemosphere.2018.10.110.
- [70] Xiong, X., Xie, S., Feng, K., & Wang, Q. (2022). Occurrence of microplastics in a pond-river-lake connection water system: How does the aquaculture process affect microplastics in natural water bodies. *Journal of Cleaner Production*, 352, 131632. doi:10.1016/j.jclepro.2022.131632.
- [71] Priscilla, V., & Patria, M. P. (2019). Comparison of microplastic abundance in aquaculture ponds of milkfish *Chanos chanos* (Forsskal, 1775) at Muara Kamal and Marunda, Jakarta Bay. *IOP Conference Series: Earth and Environmental Science*, 404(1), 12027. doi:10.1088/1755-1315/404/1/012027.
- [72] Kabir, M. S., Wang, H., Luster-Teasley, S., Zhang, L., & Zhao, R. (2023). Microplastics in landfill leachate: Sources, detection, occurrence, and removal. *Environmental Science and Ecotechnology*, 16, 100256. doi:10.1016/j.ese.2023.100256.
- [73] Silva, A. L. P., Prata, J. C., Duarte, A. C., Soares, A. M. V. M., Barceló, D., & Rocha-Santos, T. (2021). Microplastics in Landfill Leachates: The Need for Reconnaissance Studies and Remediation Technologies. *Case Studies in Chemical and Environmental Engineering*, 3, 100072. doi:10.1016/j.cscee.2020.100072.
- [74] Ghorbaninejad Fard Shirazi, M. M., Shekoohiyan, S., Moussavi, G., & Heidari, M. (2023). Microplastics and mesoplastics as emerging contaminants in Tehran landfill soils: The distribution and induced-ecological risk. *Environmental Pollution*, 324, 121368. doi:10.1016/j.envpol.2023.121368.
- [75] Mohamed Nor, N. H., & Obbard, J. P. (2014). Microplastics in Singapore's coastal mangrove ecosystems. *Marine Pollution Bulletin*, 79(1–2), 278–283. doi:10.1016/j.marpolbul.2013.11.025.
- [76] Kunz, A., Walther, B. A., Löwemark, L., & Lee, Y. C. (2016). Distribution and quantity of microplastic on sandy beaches along the northern coast of Taiwan. *Marine Pollution Bulletin*, 111(1–2), 126–135. doi:10.1016/j.marpolbul.2016.07.022.
- [77] Gao, Z., Wontor, K., Cizdziel, J. V., & Lu, H. (2022). Distribution and characteristics of microplastics in beach sand near the outlet of a major reservoir in north Mississippi, USA. *Microplastics and Nanoplastics*, 2(1). doi:10.1186/s43591-022-00029-z.
- [78] Büks, F., & Kaupenjohann, M. (2020). Global concentrations of microplastics in soils - A review. *Soil*, 6(2), 649–662. doi:10.5194/soil-6-649-2020.
- [79] Corradini, F., Casado, F., Leiva, V., Huerta-Lwanga, E., & Geissen, V. (2021). Microplastics occurrence and frequency in soils under different land uses on a regional scale. *Science of the Total Environment*, 752, 141917. doi:10.1016/j.scitotenv.2020.141917.



- [80] Henseler, M., Gallagher, M. B., & Kreins, P. (2022). Microplastic Pollution in Agricultural Soils and Abatement Measures – a Model-Based Assessment for Germany. *Environmental Modeling and Assessment*, 27(4), 553–569. doi:10.1007/s10666-022-09826-5.
- [81] Zhou, B., Wang, J., Zhang, H., Shi, H., Fei, Y., Huang, S., Tong, Y., Wen, D., Luo, Y., & Barceló, D. (2020). Microplastics in agricultural soils on the coastal plain of Hangzhou Bay, east China: Multiple sources other than plastic mulching film. *Journal of Hazardous Materials*, 388, 121814. doi:10.1016/j.jhazmat.2019.121814.
- [82] Cao, L., Wu, D., Liu, P., Hu, W., Xu, L., Sun, Y., Wu, Q., Tian, K., Huang, B., Yoon, S. J., Kwon, B. O., & Khim, J. S. (2021). Occurrence, distribution and affecting factors of microplastics in agricultural soils along the lower reaches of Yangtze River, China. *Science of the Total Environment*, 794, 148694. doi:10.1016/j.scitotenv.2021.148694.
- [83] Tunali, M. M., Myronyuk, O., Tunali, M., & Yenigün, O. (2022). Microplastic Abundance in Human-Influenced Soils in Recreational, Residential, and Industrial Areas. *Water, Air, and Soil Pollution*, 233(11). doi:10.1007/s11270-022-05901-5.
- [84] BPS-Statistics of Makassar Municipality. (2023). Makassar Municipality in Figures. BPS-Statistics of Makassar Municipality. Makassar, Indonesia. Available online: <https://makassarkota.bps.go.id/> (accessed on March 2024).
- [85] Arifin, T., Nur Amri, S., Rahmania, R., Yulius, Ramdhan, M., Chandra, H., Adrianto, L., Geoffrey Bengen, D., Kurniawan, F., & Kurnia, R. (2023). Forecasting land-use changes due to coastal city development on the peri-urban area in Makassar City, Indonesia. *Egyptian Journal of Remote Sensing and Space Science*, 26(1), 197–206. doi:10.1016/j.ejrs.2023.02.002.
- [86] Zhang, J., Zou, G., Wang, X., Ding, W., Xu, L., Liu, B., Mu, Y., Zhu, X., Song, L., & Chen, Y. (2021). Exploring the Occurrence Characteristics of Microplastics in Typical Maize Farmland Soils with Long-Term Plastic Film Mulching in Northern China. *Frontiers in Marine Science*, 8. doi:10.3389/fmars.2021.800087.
- [87] Guo, S., Zhang, J., Liu, J., Guo, N., Zhang, L., Wang, S., Wang, X., Zhao, M., Zhang, B., & Chen, Y. (2023). Organic fertilizer and irrigation water are the primary sources of microplastics in the facility soil, Beijing. *Science of the Total Environment*, 895, 165005. doi:10.1016/j.scitotenv.2023.165005.
- [88] van den Berg, P., Huerta-Lwanga, E., Corradini, F., & Geissen, V. (2020). Sewage sludge application as a vehicle for microplastics in eastern Spanish agricultural soils. *Environmental Pollution*, 261, 114198. doi:10.1016/j.envpol.2020.114198.
- [89] Monkul, M. M., & Özhan, H. O. (2021). Microplastic contamination in soils: A review from geotechnical engineering view. *Polymers*, 13(23), 4129. doi:10.3390/polym13234129.
- [90] Sun, Y., Cao, L., Zhou, B., Wu, D., & Li, Q. (2021). Microplastic Distribution in Soils from the Typical Sparsely Populated Area, Northwest China. *IOP Conference Series: Earth and Environmental Science*, 668(1), 12026. doi:10.1088/1755-1315/668/1/012026.
- [91] Leitão, I. A., van Schaik, L., Ferreira, A. J. D., Alexandre, N., & Geissen, V. (2023). The spatial distribution of microplastics in topsoils of an urban environment - Coimbra city case-study. *Environmental Research*, 218, 114961. doi:10.1016/j.envres.2022.114961.
- [92] Tirkey, A., & Upadhyay, L. S. B. (2021). Microplastics: An overview on separation, identification and characterization of microplastics. *Marine Pollution Bulletin*, 170, 112604. doi:10.1016/j.marpolbul.2021.112604.
- [93] Wesch, C., Elert, A. M., Wörner, M., Braun, U., Klein, R., & Paulus, M. (2017). Assuring quality in microplastic monitoring: About the value of clean-air devices as essentials for verified data. *Scientific Reports*, 7(1). doi:10.1038/s41598-017-05838-4.
- [94] Marine & Environmental Research Institute. (2015) Guide to Microplastic Identification. Marine & Environmental Research Institute, Blue Hill, United States.
- [95] Norén, F. (2007) Small Plastic Particles in Coastal Swedish Waters. KIMO Report, Sweden.
- [96] Ojeda, J. J., Romero-González, M. E., & Banwart, S. A. (2009). Analysis of bacteria on steel surfaces using reflectance micro-Fourier transform infrared spectroscopy. *Analytical Chemistry*, 81(15), 6467–6473. doi:10.1021/ac900841c.
- [97] Käßler, A., Fischer, D., Oberbeckmann, S., Schernewski, G., Labrenz, M., Eichhorn, K. J., & Voit, B. (2016). Analysis of environmental microplastics by vibrational microspectroscopy: FTIR, Raman or both? *Analytical and Bioanalytical Chemistry*, 408(29), 8377–8391. doi:10.1007/s00216-016-9956-3.
- [98] Zhang, Q., Zhao, Y., Du, F., Cai, H., Wang, G., & Shi, H. (2020). Microplastic Fallout in Different Indoor Environments. *Environmental Science and Technology*, 54(11), 6530–6539. doi:10.1021/acs.est.0c00087.
- [99] Syafina, P. R., Yudison, A. P., Sembiring, E., Irsyad, M., & Tomo, H. S. (2022). Identification of fibrous suspended atmospheric microplastics in Bandung Metropolitan Area, Indonesia. *Chemosphere*, 308, 136194. doi:10.1016/j.chemosphere.2022.136194.
- [100] Raza, M., Lee, J. Y., & Cha, J. (2022). Microplastics in soil and freshwater: Understanding sources, distribution, potential impacts, and regulations for management. *Science Progress*, 105(3), 003685042211266. doi:10.1177/00368504221126676.

- [101] Zhang, G. S., & Liu, Y. F. (2018). The distribution of microplastics in soil aggregate fractions in southwestern China. *Science of the Total Environment*, 642, 12–20. doi:10.1016/j.scitotenv.2018.06.004.
- [102] Qi, R., Jones, D. L., Li, Z., Liu, Q., & Yan, C. (2020). Behavior of microplastics and plastic film residues in the soil environment: A critical review. *Science of the Total Environment*, 703, 134722. doi:10.1016/j.scitotenv.2019.134722.
- [103] Landeros Gonzalez, G. V., Dominguez Cortinas, G., Hudson, M., Shaw, P., & Williams, I. D. (2022). A Review of the Origins of Microplastics arriving at Wastewater Treatment Plants. Volume 20 - September 2022, 20, 41–55. doi:10.31025/2611-4135/2022.15224.
- [104] Sari, D. A. A., Suryanto, Sudarwanto, A. S., Nugraha, S., & Utomowati, R. (2021). Reduce marine debris policy in Indonesia. *IOP Conference Series: Earth and Environmental Science*, 724(1), 12118. doi:10.1088/1755-1315/724/1/012118.
- [105] Asmal, I., Walenna, M. A., Nas, W., & Ridwan. (2023). Application of local wisdom in handling waste in coastal settlements as an effort to minimize waste production. *Environmental and Sustainability Indicators*, 19, 100283. doi:10.1016/j.indic.2023.100283.
- [106] Asmal, I., Syarif, E., Amin, S., & Walenna, M. A. (2022). The Impact of the Environment and People's Attitudes on Greywater Management in Slum Coastal Settlements. *Civil Engineering Journal (Iran)*, 8(12), 2734–2748. doi:10.28991/CEJ-2022-08-12-05.
- [107] Díaz-Mendoza, C., Mouthon-Bello, J., Pérez-Herrera, N. L., & Escobar-Díaz, S. M. (2020). Plastics and microplastics, effects on marine coastal areas: a review. *Environmental Science and Pollution Research*, 27(32), 39913–39922. doi:10.1007/s11356-020-10394-y.
- [108] Lando, A. T., Rahim, I. R., Sari, K., Djamaluddin, I., Arifin, A. N., & Sari, A. M. (2021). Estimation of methane emissions from municipal solid waste landfill in Makassar city based on IPCC waste model. *IOP Conference Series: Earth and Environmental Science*, 841(1), 12002. doi:10.1088/1755-1315/841/1/012002.
- [109] Mazitova, A. K., Aminova, G. K., & Vikhareva, I. N. (2021). Designing of green plasticizers and assessment of the effectiveness of their use. *Polymers*, 13(11), 1761. doi:10.3390/polym13111761.
- [110] Jiang, P., Huanyan, X., Zhang, W., Dai, Y., & Liang, Y. (2022). Preparation and properties of ethylene-vinyl acetate grafted acrylonitrile. *Materials Research Express*, 9(5), 55304. doi:10.1088/2053-1591/ac7039.
- [111] Sessini, V., Arrieta, M. P., Raquez, J. M., Dubois, P., Kenny, J. M., & Peponi, L. (2019). Thermal and composting degradation of EVA/Thermoplastic starch blends and their nanocomposites. *Polymer Degradation and Stability*, 159, 184–198. doi:10.1016/j.polymdegradstab.2018.11.025.
- [112] Scheurer, M., & Bigalke, M. (2018). Microplastics in Swiss Floodplain Soils. *Environmental Science & Technology*, 52(6), 3591–3598. doi:10.1021/acs.est.7b06003.
- [113] Alberghini, M., Hong, S., Lozano, L. M., Korolovych, V., Huang, Y., Signorato, F., Zandavi, S. H., Fucetola, C., Uluturk, I., Tolstorukov, M. Y., Chen, G., Asinari, P., Osgood, R. M., Fasano, M., & Boriskina, S. V. (2021). Sustainable polyethylene fabrics with engineered moisture transport for passive cooling. *Nature Sustainability*, 4(8), 715–724. doi:10.1038/s41893-021-00688-5.
- [114] Noordermeer, J. W. M. (2002). Ethylene–Propylene Polymers. *Kirk-Othmer Encyclopedia of Chemical Technology*, John Wiley & Sons, Hoboken, United States. doi:10.1002/0471238961.0520082514151518.a01.pub2.
- [115] Awasthi, R., Manchanda, S., Das, P., Velu, V., Malipeddi, H., Pabreja, K., Pinto, T. D. J. A., Gupta, G., & Dua, K. (2018). Poly(vinylpyrrolidone). *Engineering of Biomaterials for Drug Delivery Systems*, 255–272, Woodhead Publishing, Sawston, United Kingdom. doi:10.1016/b978-0-08-101750-0.00009-x.
- [116] Akovali, G. (2012). Plastic materials: chlorinated polyethylene (CPE), chlorinated polyvinylchloride (CPVC), chlorosulfonated polyethylene (CSPE) and polychloroprene rubber (CR). *Toxicity of Building Materials*, 54–75. doi:10.1533/9780857096357.54.
- [117] Gray, A. D., & Weinstein, J. E. (2017). Size- and shape-dependent effects of microplastic particles on adult daggerblade grass shrimp (*Palaemonetes pugio*). *Environmental Toxicology and Chemistry*, 36(11), 3074–3080. doi:10.1002/etc.3881.
- [118] Xu, C., Zhang, B., Gu, C., Shen, C., Yin, S., Aamir, M., & Li, F. (2020). Are we underestimating the sources of microplastic pollution in terrestrial environment? *Journal of Hazardous Materials*, 400, 123228. doi:10.1016/j.jhazmat.2020.123228.
- [119] Möller, J. N., Löder, M. G. J., & Laforsch, C. (2020). Finding Microplastics in Soils: A Review of Analytical Methods. *Environmental Science and Technology*, 54(4), 2078–2090. doi:10.1021/acs.est.9b04618.
- [120] Li, Q., Wu, J., Zhao, X., Gu, X., & Ji, R. (2019). Separation and identification of microplastics from soil and sewage sludge. *Environmental Pollution*, 254, 113076. doi:10.1016/j.envpol.2019.113076.
- [121] Helmberger, M. S., Tiemann, L. K., & Grieshop, M. J. (2020). Towards an ecology of soil microplastics. *Functional Ecology*, 34(3), 550–560. doi:10.1111/1365-2435.13495.

- [122] Bottinelli, N., Jouquet, P., Capowiez, Y., Podwojewski, P., Grimaldi, M., & Peng, X. (2015). Why is the influence of soil macrofauna on soil structure only considered by soil ecologists? *Soil and Tillage Research*, 146(PA), 118–124. doi:10.1016/j.still.2014.01.007.
- [123] Zhou, Y., Liu, X., & Wang, J. (2019). Characterization of microplastics and the association of heavy metals with microplastics in suburban soil of central China. *Science of the Total Environment*, 694, 133798. doi:10.1016/j.scitotenv.2019.133798.
- [124] Huerta Lwanga, E., Gertsen, H., Gooren, H., Peters, P., Salánki, T., Van Der Ploeg, M., Besseling, E., Koelmans, A. A., & Geissen, V. (2016). Microplastics in the Terrestrial Ecosystem: Implications for *Lumbricus terrestris* (Oligochaeta, Lumbricidae). *Environmental Science and Technology*, 50(5), 2685–2691. doi:10.1021/acs.est.5b05478.
- [125] Lei, L., Liu, M., Song, Y., Lu, S., Hu, J., Cao, C., Xie, B., Shi, H., & He, D. (2018). Polystyrene (nano)microplastics cause size-dependent neurotoxicity, oxidative damage and other adverse effects in *Caenorhabditis elegans*. *Environmental Science: Nano*, 5(8), 2009–2020. doi:10.1039/c8en00412a.
- [126] Lei, L., Wu, S., Lu, S., Liu, M., Song, Y., Fu, Z., Shi, H., Raley-Susman, K. M., & He, D. (2018). Microplastic particles cause intestinal damage and other adverse effects in zebrafish *Danio rerio* and nematode *Caenorhabditis elegans*. *Science of the Total Environment*, 619–620, 1–8. doi:10.1016/j.scitotenv.2017.11.103.
- [127] Zhu, F., Zhu, C., Wang, C., & Gu, C. (2019). Occurrence and Ecological Impacts of Microplastics in Soil Systems: A Review. *Bulletin of Environmental Contamination and Toxicology*, 102(6), 741–749. doi:10.1007/s00128-019-02623-z.
- [128] Liu, S., Huang, K., Yuan, G., & Yang, C. (2022). Effects of Polyethylene Microplastics and Phenanthrene on Soil Properties, Enzyme Activities and Bacterial Communities. *Processes*, 10(10), 2128. doi:10.3390/pr10102128.
- [129] Liu, H., Yang, X., Liu, G., Liang, C., Xue, S., Chen, H., Ritsema, C. J., & Geissen, V. (2017). Response of soil dissolved organic matter to microplastic addition in Chinese loess soil. *Chemosphere*, 185, 907–917. doi:10.1016/j.chemosphere.2017.07.064.
- [130] Li, L., Zhou, Q., Yin, N., Tu, C., & Luo, Y. (2019). Uptake and accumulation of microplastics in an edible plant. *Kexue Tongbao/Chinese Science Bulletin*, 64(9), 928–934. doi:10.1360/N972018-00845.
- [131] De Souza MacHado, A. A., Lau, C. W., Till, J., Kloas, W., Lehmann, A., Becker, R., & Rillig, M. C. (2018). Impacts of Microplastics on the Soil Biophysical Environment. *Environmental Science and Technology*, 52(17), 9656–9665. doi:10.1021/acs.est.8b02212.
- [132] Chia, R. W., Lee, J. Y., Kim, H., & Jang, J. (2021). Microplastic pollution in soil and groundwater: a review. *Environmental Chemistry Letters*, 19(6), 4211–4224. doi:10.1007/s10311-021-01297-6.
- [133] Li, Z., Yang, Y., Chen, X., He, Y., Bolan, N., Rinklebe, J., Lam, S. S., Peng, W., & Sonne, C. (2023). A discussion of microplastics in soil and risks for ecosystems and food chains. *Chemosphere*, 313, 137637. doi:10.1016/j.chemosphere.2022.137637.
- [134] Wilkes, R. A., & Aristilde, L. (2017). Degradation and metabolism of synthetic plastics and associated products by *Pseudomonas* sp.: capabilities and challenges. *Journal of Applied Microbiology*, 123(3), 582–593. doi:10.1111/jam.13472.
- [135] Fachrul, M. F., Rinanti, A., Tazkiaturrizki, T., Agustria, A., & Naswadi, D. A. (2021). Degradation of Microplastics in Aquatic Ecosystems by Mixed Culture Bacteria *Clostridium* sp. AND *Thiobacillus* sp. *Journal of Research and Scientific Work, Trisakti University Research Institute*, 6(2), 304–316. doi:10.25105/pdk.v6i2.9935. (In Indonesian).
- [136] Dewi, N. M. N. B. S. (2022). Literature Study of the Impact of Microplastics on the Environment. *Sosial Sains Dan Teknologi*, 2(2), 239-250. (In Indonesian).
- [137] Tang, K. H. D. (2020). Effects of Microplastics on Agriculture: A Mini-review. *Asian Journal of Environment & Ecology*, 1–9. doi:10.9734/ajee/2020/v13i130170.



Mechanical and Microstructural Properties of Geopolymer Concrete Containing Fly Ash and Sugarcane Bagasse Ash

Mohammed Ali M. Rihan^{1, 2*} , Richard O. Onchiri³, Naftary Gathimba⁴ ,
Bernadette Sabuni⁵

¹ Pan African University Institute for Basic Sciences, Technology, and Innovation, hosted at the Jomo Kenyatta University of Agriculture and Technology, Nairobi, Kenya.

² Civil Engineering Department, Faculty of Engineering, University of Kordofan, El Obeid 51111, Sudan.

³ Department of Building and Civil Engineering, Technical University of Mombasa (TUM), Mombasa, Kenya.

⁴ Department of Civil, Construction and Environmental Engineering, Jomo Kenyatta University of Agriculture and Technology, Nairobi, Kenya.

⁵ Department of Civil and Structural Engineering, Masinde Muliro University of Science and Technology, Kakamega, Kenya.

Received 01 January 2024; Revised 18 March 2024; Accepted 22 March 2024; Published 01 April 2024

Abstract

Portland cement plays a vital role in construction and building projects. However, its manufacturing process releases detrimental pollutants and contributes to climate change. The environmental concerns linked to the manufacturing of conventional Portland cement, such as its high energy demands, raw material consumption, and significant CO₂ emissions, have prompted the need to look for alternatives such as geopolymer or green concrete. In addition, indiscriminate disposal of waste might have a detrimental effect on the environment. This paper investigates the mechanical and microstructural properties of geopolymer concrete incorporating fly ash and sugarcane bagasse ash as primary constituents. Sugarcane bagasse ash (SCBA) was employed as a partial substitute for Fly Ash (FA), with varying proportions ranging from 5% to 20% with increments of 5%. Alkaline activators utilized were NaOH (14M) and Na₂SiO₃, with a ratio of 1.5. Various tests, including the slump test, compressive strength test, splitting tensile strength test, and flexural strength test, were performed. The microstructural characteristics were assessed by scanning electron microscopy (SEM), energy dispersive analysis (EDS), and X-ray diffraction analysis (XRD). The results revealed that adding sugarcane bagasse ash influenced the workability of geopolymer concrete while enhancing its mechanical properties. The research findings have shown that the mixture comprising 5% SCBA has the greatest compressive strength of 64 MPa.

Keywords: Geopolymerization; Sugarcane Bagasse Ash; Fly Ash; Microstructure; Alkaline Activator; Building Projects.

1. Introduction

Global warming has become a crucial concern for the long-term survival and progress of human society, requiring an approach to development that is environmentally friendly and sustainable over a long time [1, 2]. Ordinary Portland cement (OPC) is among the building materials utilized in construction most of the time. OPC manufacturing is highly energy-intensive and produces CO₂ [3-5]. From an ecological perspective, it is necessary to establish a worldwide infrastructure utilizing industrial waste materials [6]. Substantial quantities of construction and related waste are created, and the inappropriate elimination of these waste products has led to notable environmental repercussions, including flooding and the devastation of natural areas. Substituting them for cement provides a viable solution for mitigating

* Corresponding author: moharihan20@gmail.com; rihan.mohammed@students.jkuat.ac.ke

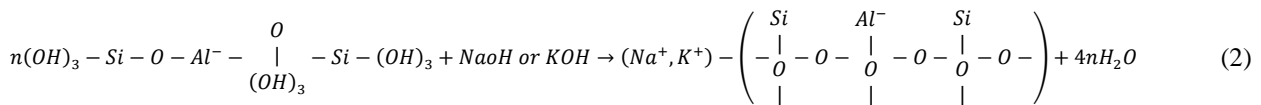
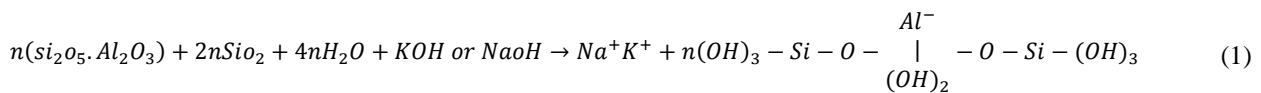
 <http://dx.doi.org/10.28991/CEJ-2024-010-04-018>



© 2024 by the authors. Licensee C.E.J, Tehran, Iran. This article is an open access article distributed under the terms and conditions of the Creative Commons Attribution (CC-BY) license (<http://creativecommons.org/licenses/by/4.0/>).

ecological concerns linked to waste disposal [7]. The usage of pozzolana ingredients obtained from agricultural and industrial waste materials, such as fly ash, blast furnace slag, metakaolin, corncob ash, rice husk ash, and sugarcane bagasse ash, decreases the amount used for energy and production expenses of concrete. Moreover, it addresses the problems associated with storage and disposal, thereby facilitating the creation of environmentally friendly concrete. Thus, the development of a suitable substitute for OPC is highly significant.

Recently, inorganic polymer concrete has become a promising option for environmentally friendly building materials, offering a viable solution to the need for alternative materials in the industry [8-10]. Geopolymers, which are cementitious materials, have been recently developed as a long-term substitute for OPC to alleviate the adverse environmental effects [11]. Davidovits first presented the concept of geopolymers as a novel type of binder that falls under the classification of inorganic polymers [12-14]. Geopolymers are formed of two main components: a raw material with a high amount of SiO₂ and Al₂O₃ and an alkaline activator solution. These materials are inorganic aluminosilicate compounds [15]. For civil engineering applications, GPC has superior chemical and mechanical characteristics over concrete based on Portland cement (PC), such as stronger mechanical strength and quick hardening [16-18], superior resilience to heat and fire [19-21], high impermeability, acid and salt resistance, and shallow chloride penetration depth [22, 23], and lower creep effects [24]. Geopolymerization is a series of steps that involve leaks and dispersals, polymerization, reorientation, and condensation [25]. The polymerization of GPC occurs due to the condensation process, resulting in heat release during the endothermic reaction [26]. An alkaline activator solution, which commonly consists of potassium hydroxide (KOH), sodium hydroxide (NaOH), potassium silicate (K₂SiO₃), or sodium silicate (Na₂SiO₃), plays a significant part in the development of Si and Al crystal structures [11]. However, a mixture of Na₂SiO₃ and NaOH is the most popular alkaline activator. At the time of geopolymerization, Si-O-Al bonds are formed through the polycondensation of aluminosilicate oxides (Si₂O₅, Al₂O₂) and alkali polysilicates (Na₂SiO₃) [27]. To produce geopolymer materials, OH ions and a collection of monomers undergo a chemical reaction that dissolves Al and Si from the waste product [26, 28]. The geopolymer can exist in various forms like -Si-O-Al-O- or -Si-O-Al-O-Si-O or -Si-O-Al-O-Si-O-Si-O-. Equations 1 and 2 can be used to depict the configuration of geopolymer material [13, 29, 30]:



FA remains a substance formed by coal combustion for energy generation, and it has been recognized as a detrimental agent to the environment. The annual production of FA is approximately 2.8 billion metric tons [31, 32]. The principal components of FA ash are Al₂O₃, SiO₂, CaO, and Fe₂O₃, which are found in both crystalline and amorphous oxides and a variety of minerals [33]. Minor elements, on the other hand, such as As, Pb, Cr, and Hg, may be toxic. Consequently, FA is extensively acknowledged as a detrimental by-product, and its inappropriate disposal negatively influences the environment and ecology. Additionally, the capacity of landfills will increase [34]. Recently, there have been efforts to utilize fly ash in more eco-friendly and practical applications. Instead of storing or disposing of FA, it could be used as a fundamental component in GPC to reduce waste and support sustainability. FA is categorized according to both physical and chemical characteristics. Class F is distinguished by having low silica and high calcium content and displays a lower reactivity than Class C, which contains a more significant proportion of silica [35]. The disparity in reactivity across components impacts the geopolymerization process and directly affects the geopolymer's strength [36]. On the other hand, SCBA is a globally accessible byproduct that converts bagasse into energy by combustion in boilers [37]. The yearly SCBA production is anticipated to reach 48-60 million tons based on yield [38], and if dumped recklessly will cause an environmental problem. In addition to becoming generally accessible, previous studies have shown that partially substituting cement weight with SCBA considerably enhances the mechanical characteristics and durability of the concrete mix [38-44]. High-quality SCBA can be produced by burning sugarcane bagasse at temperatures varying between 800 to 1000°C for 20 minutes [45, 46] or heating in the air at 600 °C for three hours [47]. The percentage of silica present in the ash changes depending on the temperature, the land used to cultivate sugarcane, and how it was burned [48-50].

The durability and mechanical properties of GPC utilizing GGBFs, or FA, have been researched recently. However, little research has been done on SCBA [51, 52]. Singh [53] examined the microstructure, mechanical properties, and durability of metakaolin and SCBA-based GPC. Metakaolin and SCBA were used to replace 10%, 20%, 30%, and 40% of FA in preparing FA-based GPC. Samples of geopolymer concrete were treated in an oven at 90°C for 24 hours before being permitted to cool to room temperature. Metakaolin-contained GPC has better mechanical and durability properties than SCBA-contained. Microstructure studies showed that metakaolin containing GPC has denser intermolecular bonding than bagasse ash. H.M. and Unnikrishnan [54], in their analysis of the microstructure and mechanical strength of GPC made from GGBS-SCBA, found that as molarity rose from 8M to 12M, the strength properties of the GPC also

raised. They concluded that with a Na_2SiO_3 to NaOH ratio 2.5 and an 8M NaOH solution, the geopolymer concrete composed of 80% GGBFs and 20% SCBA can achieve a desired strength of 30-35 MPa. Vanathi et al. [55] partially studied using FA to substitute SCBA in the presence of 50% GGBFs. The optimal mechanical performance is achieved when 20% of FA is replaced with SCBA. The compressive strength reaches 52.56 MPa after 28 days of curing, which is 22% higher than the control GPC. The findings showed that cylinder compressive and split tensile strengths and cube compressive and flexural strengths are all intimately related.

Researchers have demonstrated a rising interest and achieved successful results in utilizing industrial and agricultural byproducts, such as FA, GGBFs, metakaolin, rice husk ash, and corncob ash, as raw ingredients in making GPC. The efficacy of GPC derived from FA-SCBA has not been extensively studied. Therefore, synergistic use of fly ash and sugarcane bagasse ash as precursors to developing sustainable geopolymer concrete has been attempted in this study by involving partial replacement of FA with SCBA at various substitution levels ranging from 5% to 20%, with a 5% increment. Na_2SiO_3 gel and a 14M NaOH solution were the activators. Hence, in this current study, properties of newly developed sustainable geopolymer concrete have been studied in terms of workability, compressive strength, split tensile strength, and flexural strength and also in terms of microstructural characteristics based on Scanning electron microscope images, Energy dispersive X-ray analysis, and X-Ray diffraction analysis. The strength results were compared with the ordinary Portland cement concrete. The results revealed that the strength of the GPC performed better than ordinary Portland cement concrete.

2. Materials and Methods

2.1. Materials

2.1.1. SCBA and FA

Unprocessed SCBA was acquired from Western Kenya's Sukari Industries Ltd. To eliminate moisture, SCBA was dried in an oven for 24 hours at 105°C . The ash from sugarcane burning was passed using a $75\ \mu\text{m}$ filter to eliminate large clumps of ash substances and any remaining carbonaceous components to obtain the appropriate particle size for the SCBA. The next step involved testing the compositions of chemicals and loss of ignition (LOI). The unprocessed SCBA had a high LOI of 10.20%. As a result, it was burned again at 650° for four hours in a muffle furnace to decrease the LOI under 6% to conform to the ASTM C618 criteria. The LOI of re-burned SCBA was 0.97%. A chemical analysis was performed on the raw and processed SCBA using X-ray fluorescence (XRF), and the outcomes are displayed in Table 1. The FA that was employed in this investigation was obtained from India. As indicated in Table 1, it is classified as a Class F fly ash due to its calcium oxide level being below 10%, as per ASTM C-618.

Table 1. XRF and LOI results for SCBA and FA

Oxides	Raw SCBA	SCBA after burning	FA	Specification of ASTM C 618 for class F
SiO_2	81.32	76	54	
Al_2O_3	5.51	9	19.6	
Fe_2O_3	6.95	4.2	6.9	
$\text{SiO}_2 + \text{Al}_2\text{O}_3 + \text{Fe}_2\text{O}_3$	93.78	89.2	80.5	Min (70%)
CaO	1.71	3.1	7.9	Max (10%)
K_2O	2.68	3.83	2.2	
MgO	-	2.7	6.9	
P_2O_5	0.5	0.69	0.34	
TiO_2	0.65	0.46	0.88	
MnO	0.39	0.2	0.1	
LOI	10.20	0.97	1.87	Max (6%)

2.2.2. Aggregates

The crushed stone in coarse aggregate had a specific gravity and max aggregate size of 2.66 and 12.5 mm, respectively. The coarse aggregate was washed and dried in the sun. The fine aggregate is a mixture of 30% quarry dust and 70% river sand that has been cleaned through an ASTM 0.18 mm filter, followed by oven drying for 24 hours at 105°C . Table 2 displays the aggregates' properties. All testing was performed in compliance with ASTM recommendations. Figure 1 shows the distribution of particle sizes in the aggregate.

Table 2. Aggregate physical properties

Aggregates	Fineness modulus	Specific gravity	Water absorption (%)	Density (kg/m ³)	Voids ratio (%)	Crush value (%)	Impact value (%)
Coarse aggregates	-	2.66	3.6	1468	42	17.6	6.2
Fine aggregates	2.60	2.61	3.5	1677	28	-	-

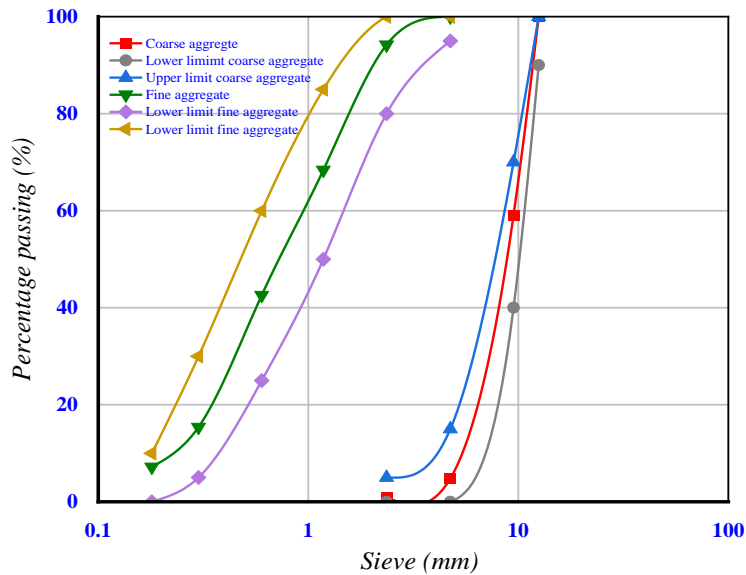


Figure 1. Aggregates' distribution of particle sizes

2.1.3. Activator Solution

Generally, three kinds of activators can be used to make GPC: Na₂SiO₃, NaOH, KOH, or a blend of both. The most commonly used activator to prepare GPC is a combination of Na₂SiO₃ and NaOH [56-58]. According to recent research and studies, using NaOH alone or in combination with Na₂SiO₃ improves the mechanics of strength and significantly accelerates geopolymer processing [59, 60]. The activators' concentration when producing geopolymer concrete or mortar influences the properties in the fresh and hardened stages [27, 61].

Alkaline activators, including Na₂SiO₃ and NaOH with a ratio of 1.5, were used to make FA-SCBA-based geopolymer concrete. They were acquired in Nairobi, Kenya, from Euro Industrial Chemicals. Sodium silicate was in solution form with a specific gravity of 1.530 at 20 ° C and a Na₂O: SiO₂ ratio of 1:2.10 (Na₂O of 13.76%, and SiO₂ of 28.9). The sodium hydroxide (NaOH) pearls used in the study had a purity of at least 99%. Figure 2 shows the Na₂SiO₃ solution and NaOH pearls.

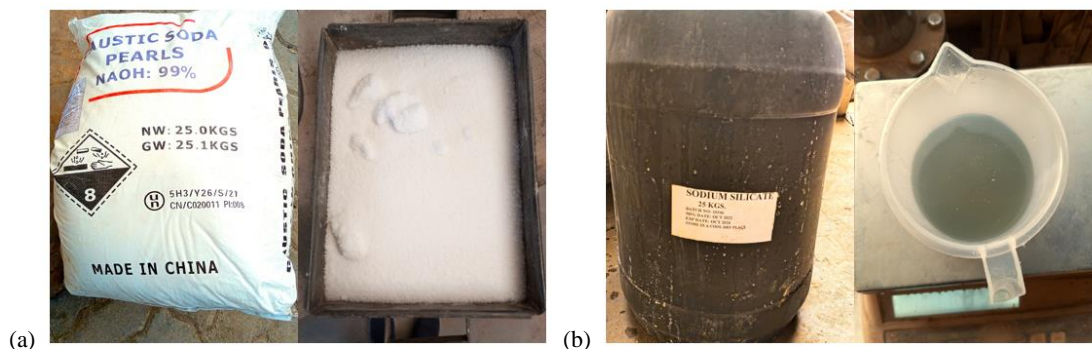


Figure 2. (a) Sodium hydroxide pearls and (b) sodium silicate solution

2.1.4. Water

Laboratory potable tap water was employed to prepare an alkaline solution.

2.1.5. Superplasticizer

A commercially available superplasticizer (SP) (ViscoCrete-20 HE KE) was utilized to increase the workability and flowability of fresh concrete. It satisfied the standards for SP as stated by ASTM-C-494 Type G and EN 934-2 with a specific gravity of 1.09 and clear color.

2.2. Mix proportions

This research employed different SCBA and fly ash variations in geopolymer concrete mixtures. The composition of the blended FA-SCBA geopolymer concrete is detailed in Table 3, in which SCBA took the place of FA at 5%, 10%, 15%, and 20% of the total binder.

Table 3. FA-SCBA-based geopolymer concrete proportions in kg/m³

Mix ID	Cement	FA	SCBA	Coarse agg	Fine agg	Na ₂ SiO ₃	NaOH	water	S. P
Control	500	-	-	1000	700	-	-	175	12.5
0% SCBA	-	500	0	1000	700	105	70	-	12.5
5% SCBA	-	475	25	1000	700	105	70	-	12.5
10% SCBA	-	450	50	1000	700	105	70	-	12.5
15% SCBA	-	425	75	1000	700	105	70	-	12.5
20% SCBA	-	400	100	1000	700	105	70	-	12.5

2.3. Methodology

2.3.1. Execution of the Study

The study was carried out according to the flow chart shown in Figure 3. The materials were collected, prepared, characterized, and then used to prepare the test samples. The samples were tested as described in the following sections.

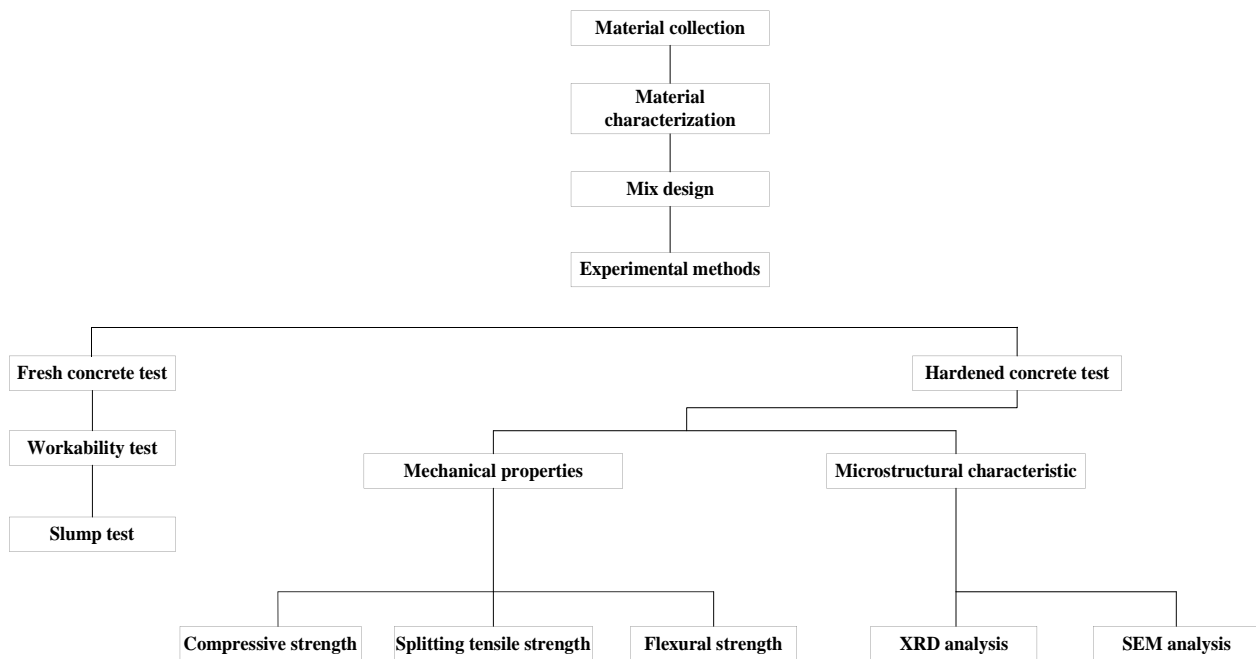


Figure 3. Flowchart of the study

2.3.2. Mixing Procedure

To make the NaOH solution, a suitable dose of NaOH pearls was dissolved in one liter of water to achieve the preferred NaOH concentration (14 M) 24 hours before casting. The mixing technique adopted in this study began by combining aggregates, FA, and SCBA with the Solution containing NaOH to break down the aluminum and silicon found in the unprocessed material. Then Na₂SiO₃ solution was added to increase the binding strength [32]. This mixing approach resulted in greater strength than alternative production methods [61]. A superplasticizer was added to compensate for the workability losses that occurred in the fresh condition. The superplasticizer was introduced progressively at a rate of 2.5%. The GPC mixture was blended for five minutes before being used. This was done to produce the needed flowability and workability of fresh concrete. Finally, the finished product was poured into several standard testing molds and cured at an oven temperature of 80°C for 24 hours.

2.3.3. Methods of Testing

2.3.3.1. Compressive Strength

After 7, 14, and 28 days, a total of 45 cubes, each measuring 100 100 100 mm, were evaluated. Following the British Standard EN 12390-03, a compressive strength test was performed. The cube samples were assessed using universal compression testing equipment with a capability of 1500 kN. Three cubes were utilized to determine the average compressive strength.

2.3.3.2. Splitting Tensile Strength

Fifteen cylinders were cast, each measuring 100 mm in diameter and 200 mm in height. ASTM C 496/C 496M 04 standards were employed to measure the split tensile strength at 28 days. The average of three-cylinder readings for each mixture was given.

2.3.3.3. Flexural Strength

In agreement with the ASTM C78 - 02 standard flexural strength, fifteen beams of 100x100x350 mm were evaluated after 28 days. Each mixture was examined with three prisms, and the average of the results was recorded after each examination.

3. Results and Discussions

3.1. Microstructure of Source Material

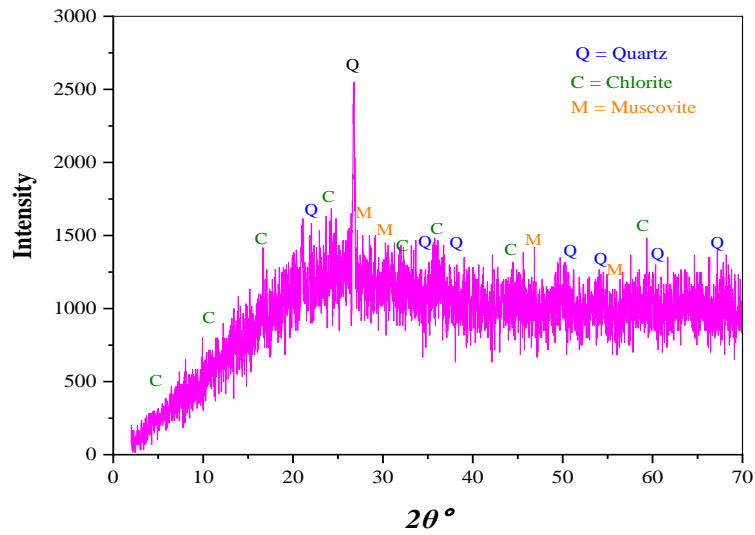
3.1.1. XRD Analysis

As illustrated in Figure 4-a, the primary FA's mineralogical phases were quartz, chlorite, and muscovite. The mineralogy properties of these cementitious materials were determined using XRD analysis on processed SCBA, as shown in Figure 4-b. Quartz was found to be present in the SCBA, as demonstrated by the results, which were also reported by Rukzon & Chindaprasirt [62], Andrade Neto et al. [63], and Abdalla et al. [64].

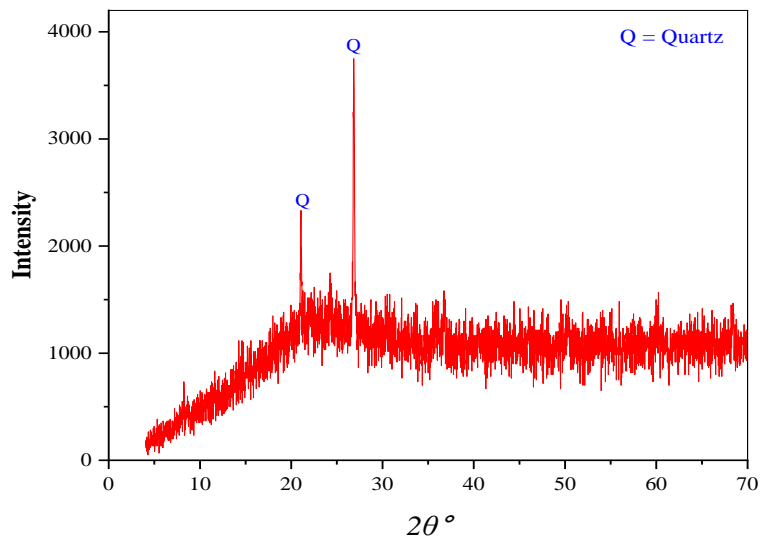
3.1.2. SEM and EDS Analysis

SEM pictures can aid in understanding the behavior of pozzolans and admixtures in geopolymer concrete. Pozzolans and admixtures were morphologically examined using SEM to assess the elements' shape, size, and surface structure. SEM was used in this investigation to capture images of the SCBA in microscopy, as Figure 5-a illustrates. The SCBA particles were found to be shaped like fibrous and irregular flakes and have round surface capillary pores. The particles are elongated, oval-shaped, and have several pores. SCBA requires more water than cement in concrete due to pores on the surface and the fibrous morphology of the particles, resulting in poorer workability. The porosity (sponginess) of these materials influences other concrete qualities. According to Yadav et al. [65], the consistency test revealed that SCBA needed 17-24% more water than cement. Additionally, it was noted that the configuration of SCBA resembles a cellulose sheet, suggesting that SCBA is organized into sub-microcrystalline aggregates, resulting in its inherent porosity. Combining SCBA into sub-microcrystalline clusters results from the imperfect crystallization of SCBA.

This permeable particle indicates that the SCBA particle combustion temperature has not yet reached the critical temperature in the boiler to convert it into a non-permeable state and enhance its ability to absorb water. Additionally, prismatic tetrahedral crystals were found in SCBA, which are just metastable cristobalite forms. SEM analysis of bagasse ash by Chusilp et al. [66] revealed that large surface areas, high porosity, and rough surfaces characterized the raw SCBA particles. The SCBA particles were small after grinding, but their surfaces were rough and porous. Jha et al. [45] used SEM to examine the SCBA, and it was discovered that the surface of the SCBA has a fibrous character, a tetrahedral shape (prismatic), and a crystalline character similar to that of the quartz mineral of silica. Abdalla et al. [64] observe that SCBA particles exhibit a fibrous structure characterized by elongated, irregular flakes with irregular shapes and circular capillary pores on the surface. The particles transform into a more spherical shape following the treatment. The SEM pictures in Figure 5-b reveal that the FA particles have a spherical morphology, characterized by spherical-shaped balls with fragmented Ceno spheres.

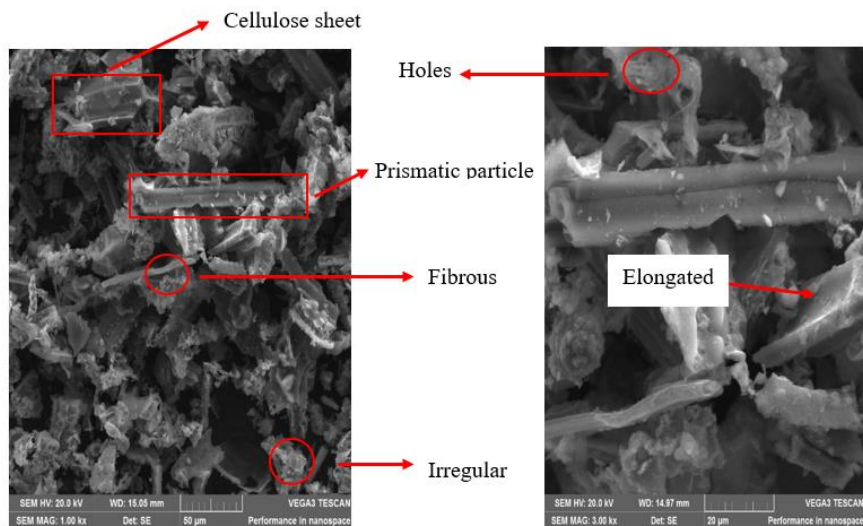


(a)

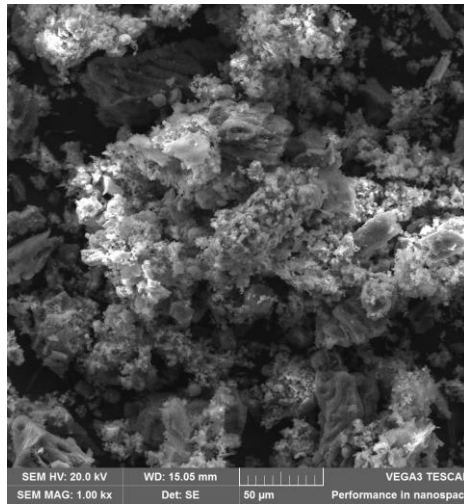


(b)

Figure 4. XRD of (a) FA and (b) processed SCBA



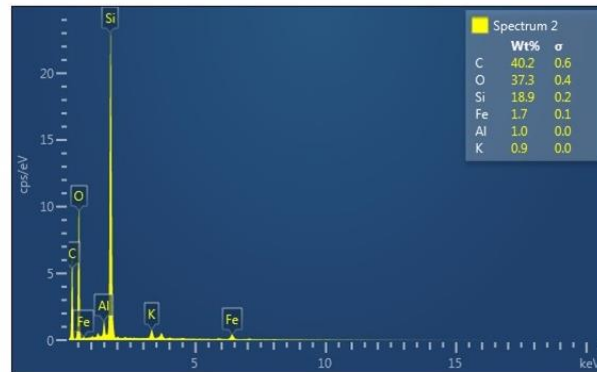
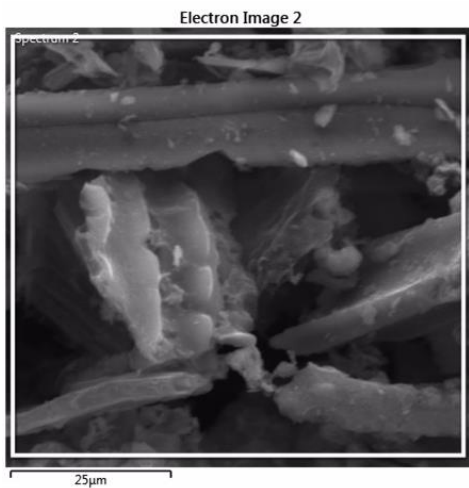
(a)



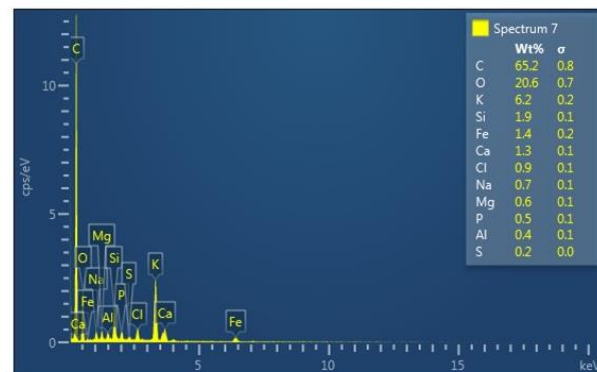
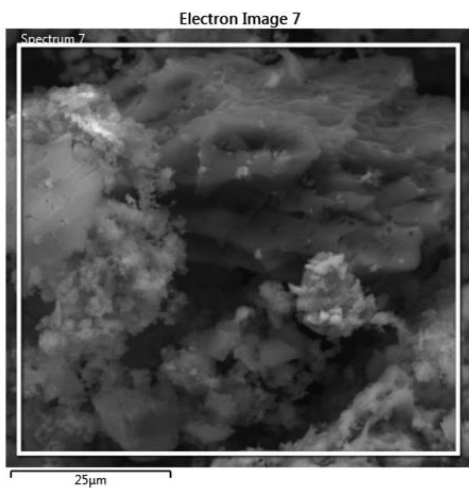
(b)

Figure 5. SEM picture of (a) Processed SCBA and (b) FA

The elemental composition can be ascertained using the analytical technique known as EDS. The system assumes that every voltage pulse's magnitude is directly proportional to the X-ray photons' energy being detected [67]. EDS was utilized to ascertain the elemental composition of each powder after samples were taken randomly from each powder. Figure 6 displays variations in the composition of elements between unprocessed SCBA and treated SCBA, as determined by SEM/EDS studies. The analysis reveals that every SCBA sample consists of oxygen, carbon, silica, aluminum, potassium, iron, and calcium as primary constituents, with variable proportions.



(a)



(b)

Figure 6. SEM/EDS analysis of (a) SCBA and (b) FA

3.2. Fresh Properties of FA-SCBA-based Geopolymer Concrete

3.2.1. Workability

Figure 7 displays the slump values for all geopolymer concrete mixes with various levels of SCBA replacement. The workability of the geopolymer mixes was discovered to diminish with an increase in the amount of SCBA. The slump values of mixes were 150, 210, 195, 185, 160, and 155 mm for cement concrete, 0%, 5%, 10%, 15% and 20% SCBA respectively. Prior research has demonstrated that the rise in the amount of SCBA causes a reduction in the workability of GPC [54, 68]. The values agree with the outcomes of Landa-Ruiz et al. [69] and Abdalla et al. [64], who discovered a decrease in workability with increasing SCBA volume. The decline in workability is explained by the lowered specific gravity of SCBA, which is 2.2, compared to FA, which is 2.5. Additionally, the presence of fibrous and uneven flakes on the surface of SCBA with spherical capillary holes, as observed in SEM images, increases water demand. There is a severe issue with activated alkali materials. Due to the materials' high viscosity and resulting inadequate workability parameters, it may be essential to employ superplasticizers to resolve the problem [70]. Furthermore, GPC is more workable than cement concrete. This is because the fine materials have smooth surfaces and hollow spherical shapes.

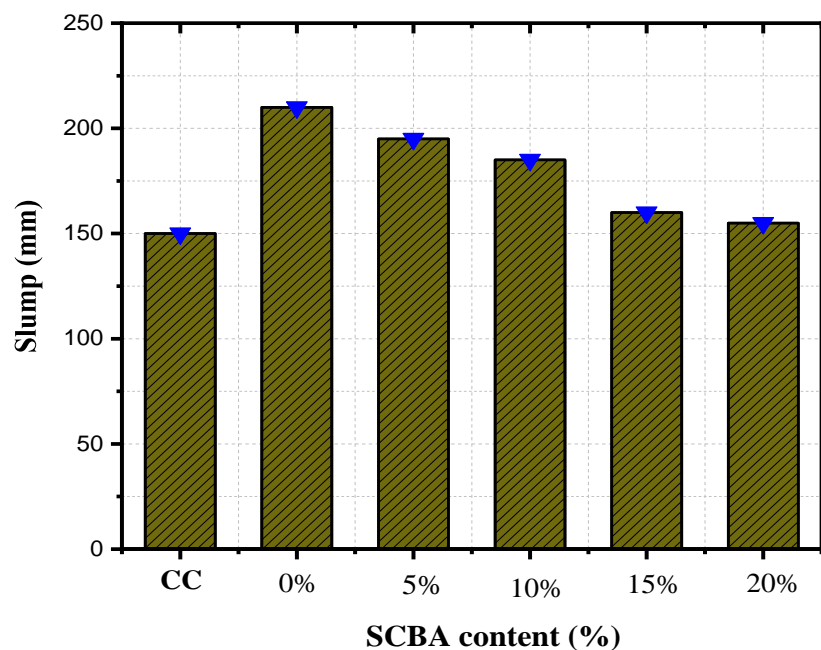


Figure 7. The impact of SCBA content on the GPC workability

3.3. Mechanical Properties

3.3.1. Compressive Strength

Figure 8 shows compressive strength outcomes for the five mixes of FA-SCBA-based geopolymer concrete (14M, SS/SH = 1.5) at different percentages of SCBA from 0 to 20%. The average compressive strength of mixes 0%, 5%, 10%, 15, and 20 of SCBA at 7 days were 55.3, 62.5, 53.8, 55.4, and 49.5 MPa respectively. And at 14 days was 57, 63.1, 57.7, 56.7, and 58.5 MPa, respectively. The average compressive strength of 28 days was 60.6, 64, 58.4, 57 and 59.2 respectively. A significant increase in strength over the cement concrete and 0% SCBA is observed in a mix containing 5% SCBA, with an increase of 28% and 6%, respectively. A comparison was made between the compressive strength of cement concrete mix and geopolymer concrete mixes. The compressive strength of the GPC demonstrated a higher level of performance than conventional Portland cement concrete. The enhanced strength can be ascribed to the small particle size of FA and SCBA, which is uniformly dispersed throughout the geopolymer concrete mixture and improves the density. There was a progressive increase in strength as the SCBA content increased up to 5%, after which there was a little decline. However, in all situations, the strength exceeded that of normal concrete. The 5% level of SCBA replacement exhibited maximal strength compared to the other mixtures. The drop in compressive strength that occurred with an increasing amount of SCBA can be assigned to the higher permeability of the materials (Figure 5). A comparable conclusion was reached by Chindaprasirt et al. [46].

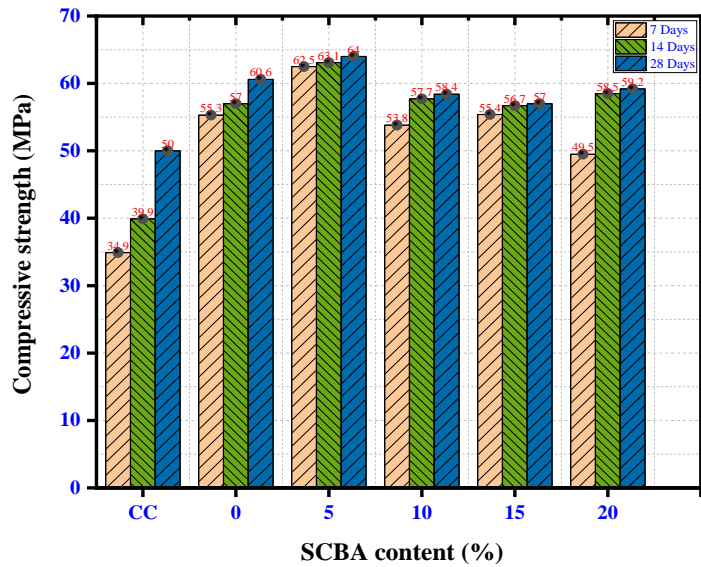


Figure 8. Compressive strength at different ratios of SCBA of FA-SCBA geopolymer concrete

3.3.2. Splitting Tensile Strength

The indirect tensile strength of the design mix for the GPC is ascertained using the splitting tensile strength test. Figure 9 displays the splitting tensile strength of geopolymer concrete after testing for 28 days. The splitting tensile strength of geopolymer concrete mixes has a comparable pattern to that of compressive strength. The mixtures of geopolymer concrete that contain 0%, 5%, 10%, 15%, and 20% have achieved split tensile strengths of 5.44, 6.2, 5.8, 3.21, and 4 MPa correspondingly after 28 days. Compared to a mixture consisting only of FA, the SCBA mixture containing 5% SCBA exhibited the highest tensile strength values, similar to the observation from the compressive strength results. Shafiq et al. [71] stated that a rise in the percentage of SCBA resulted in a corresponding decrease in splitting tensile strength, which exhibited a comparable trend to the decline in compressive strength.

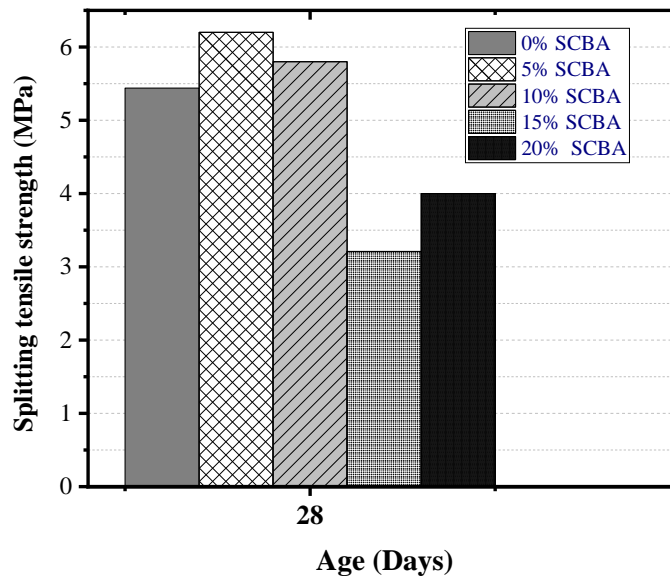


Figure 9. SCBA's Effect on the 28-day split tensile strength of GPC

3.3.3. Flexural Strength

The flexural strength of blends of geopolymers based on FA-SCBA is displayed in Figure 10 after 28 days, with varying amounts of SCBA. The specimens with fly ash only exhibited superior flexural strength compared to the others. The mean flexural strength values at 28 days for SCBA samples with 0%, 5%, 10%, 15%, and 20% content were 11.02, 9.1, 9.3, 8.61, and 8 MPa, respectively. The flexural strength of cement concrete was 7.7 Mpa. The GPC specimen exhibited superior flexural strengths compared to the PCC specimen. The reason for this could be the higher strength of Si-O-Al bonds (GPC) compared to C-H-S bonds (OPC) [72, 73], resulting in GPC having a stronger bond than PCC.

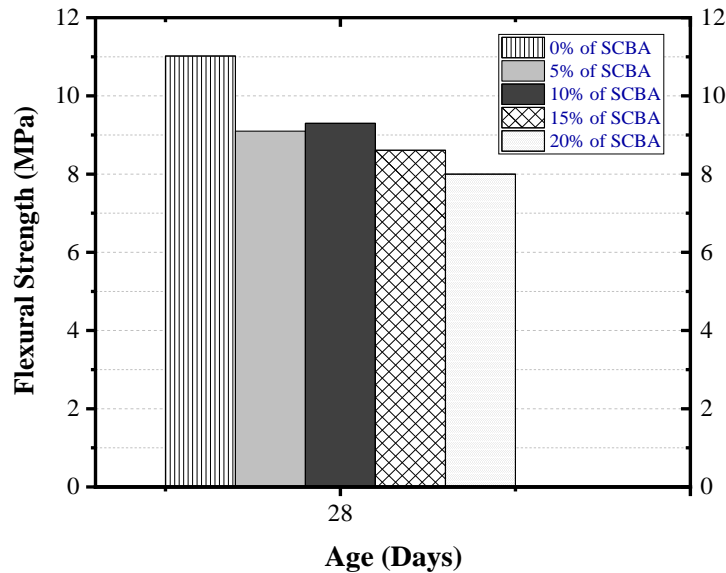
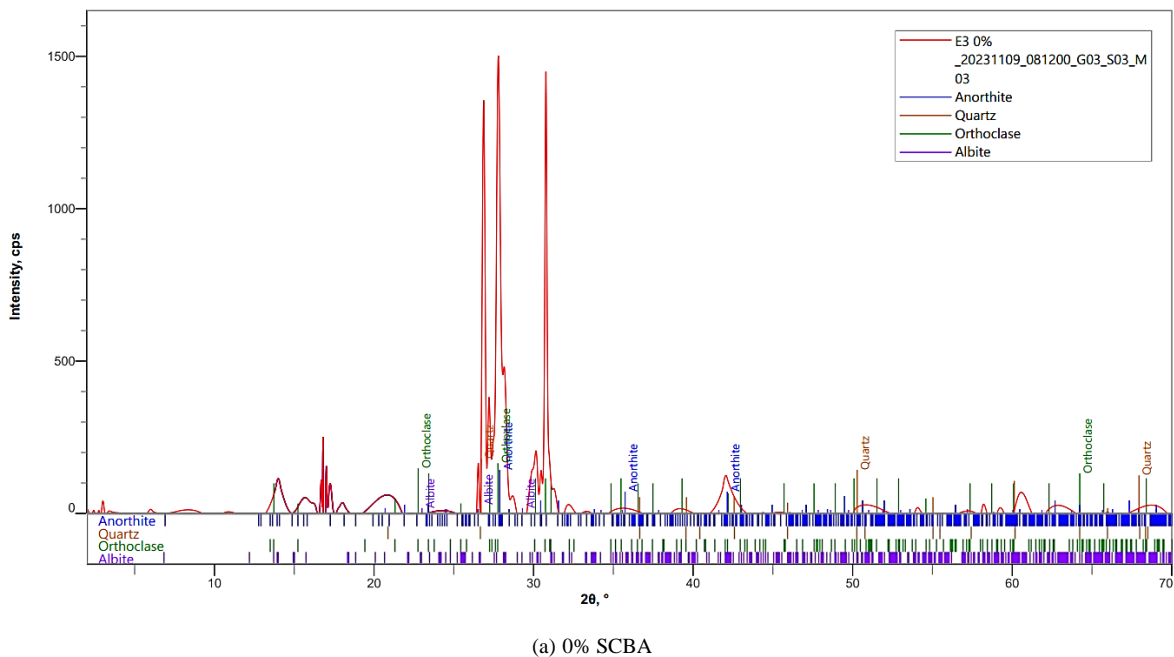


Figure 10. The Impact of SCBA on the 28-day flexural strength of GPC

3.4. Microstructure Characteristics of FA-SCBA Geopolymer Concrete

3.4.1. XRD Analysis

The X-ray diffraction (XRD) results of GPC at 28 days with 0, 5, and 10% SCBA are displayed in Figure 11. These mixes were selected based on their higher percentages of strength improvement. The broad peaks identified between 26.8° and 67.9° on the 2θ scale suggest a reaction of geopolymerisation, which results in the creation of the geopolymer product. Furthermore, prominent peaks in the geopolymer concrete signify a dominant crystal phase accompanied by a smaller amorphous phase. In addition, the mixtures indicated the existence of Partially crystallization phases that were previously described in the ash XRD investigation (Figure 4), as well as a new stage consisting of albite, orthoclase, and anorthite emerged as a result of the geopolymerization reaction. Mineral phases of quartz detected on the FA and SCBA diffractograms are still present following the geopolymerization reaction. This indicates that these minerals remained unaltered or did not undergo geopolymerization, allowing them to operate as aggregates and strengthen the geopolymer. Furthermore, quartz consists primarily of silica-based oxides, which significantly enhance GPC's strength and mechanical performance. Albite, which occurs in a partially crystalline form, belongs to the N-A-S-H gel family and is a polymeric material made of sodium-polysialate, as demonstrated by earlier studies [74, 75]. The anorthite phase that forms is categorized as a C-A-S-H gel and serves as a nucleation site, facilitating further geopolymer connections. This results in a more compact and tightly connected microstructure. The formation of CASH gels occurs through the reaction between alkalis in GPC and calcium, which assists in the hydration and strengthening of GPC [76].



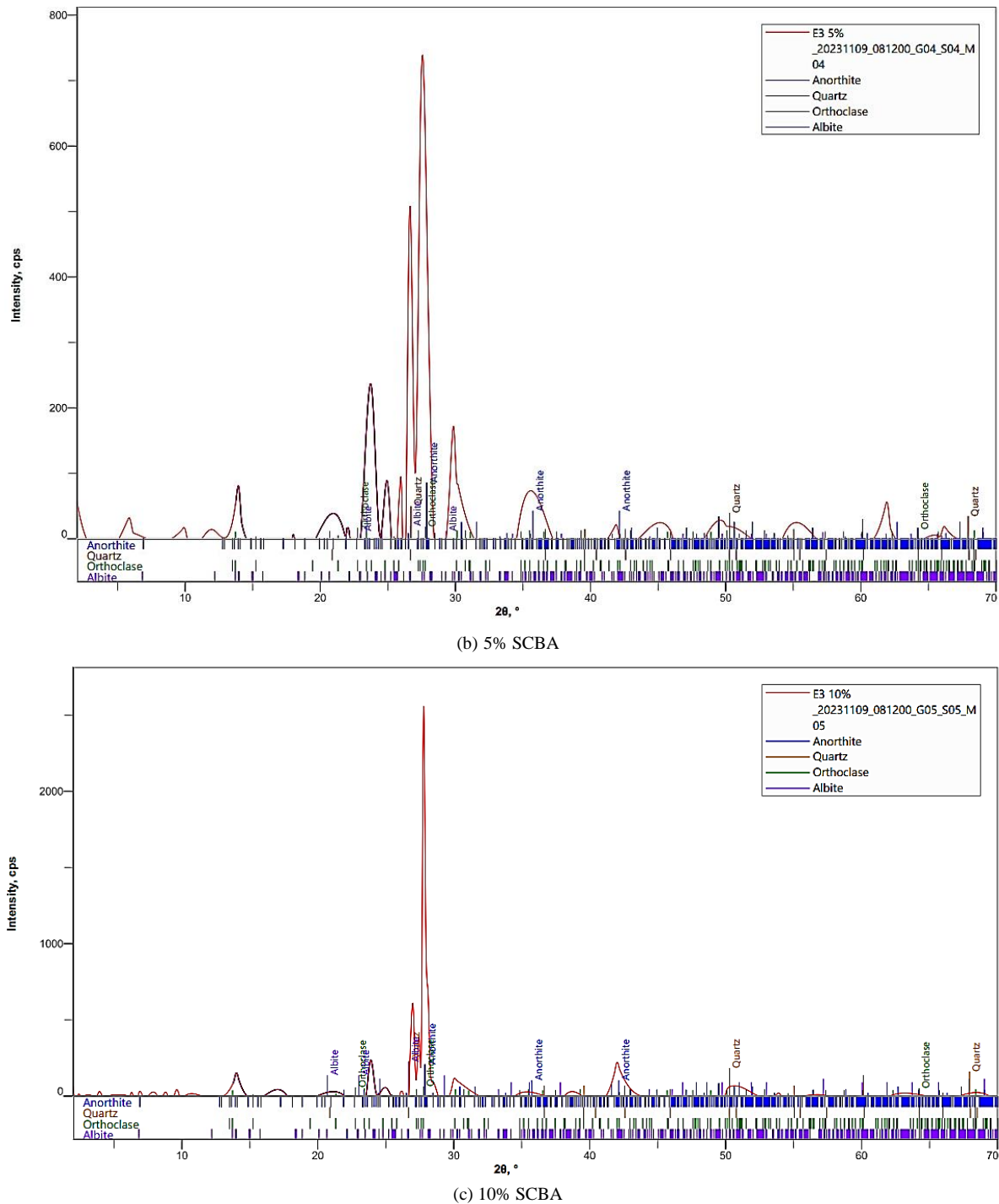
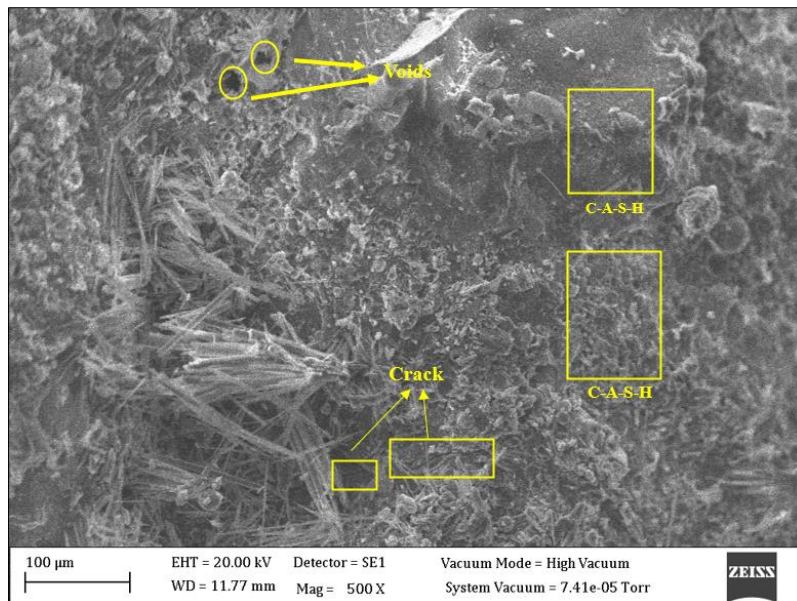


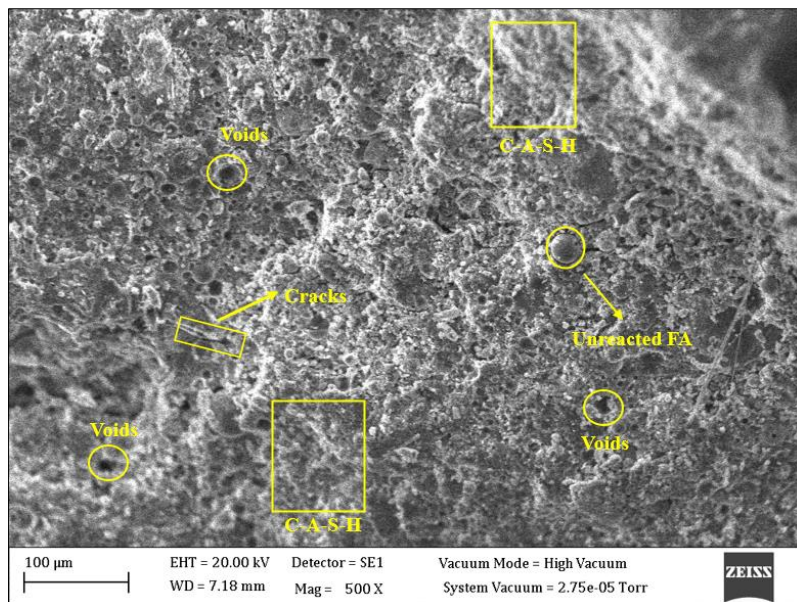
Figure 11. FA-SCBA based geopolymer concrete 28-day XRD patterns

3.4.2. SEM Analysis

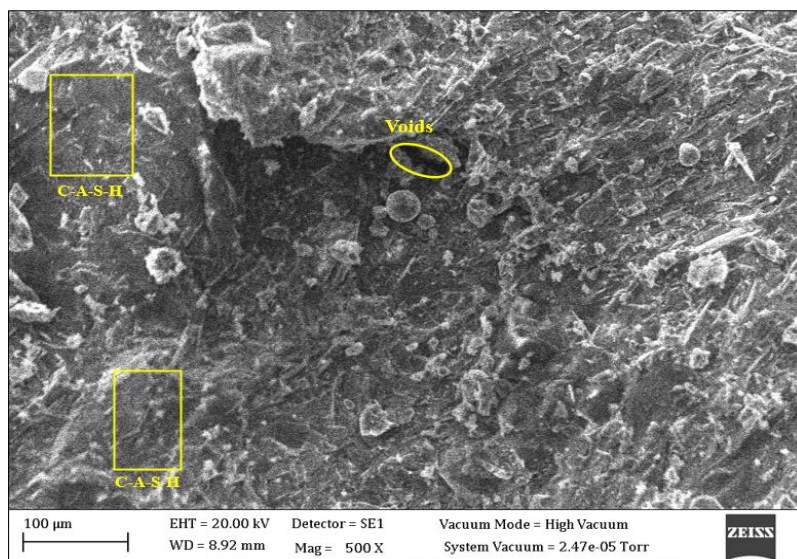
To test the rate of polymerization and the efficacy of the geopolymer gel within the matrix, specimens that had been aged for 28 days and tested for compressive strength were used to obtain samples of geopolymer concrete. Figure 12 shows SEM pictures of GPC mixes made with FA and SCBA. The sample findings showed that the geopolymer concrete had less density and void spaces because of large spheres of unreacted FA. The voids were formed due to the incomplete dissolving of FA during the initial mixing of GPC. Moreover, the presence of unreacted particles of FA and the free water evaporating throughout the aging-curing mechanisms likely contributed to the formation and spread of microcracks [74]. The inclusion of SCBA in the overall composition of the binder led to notable enhancements in the microstructure of geopolymer concrete. After 28 days, the microstructure of the 5 percent SCBA mixture showed a significant advancement in the density and consistency of the gel composition, outperforming that of the other mixtures. The geopolymerization process encompasses a chemical interaction between aluminosilicate minerals and an alkaline solution, which leads to the dissolving of FA and SCBA. This process creates geopolymeric gels that efficiently occupy the empty spaces and gaps in the geopolymer concrete [14].



(a) 0% SCBA



(b) 5% SCBA



(c) 10% SCBA

Figure 12. SEM micrograph of FA-SCBA-based geopolymer concrete

4. Conclusions

An investigation based on experiments was carried out to examine the effects of binary binders composed of FA and SCBA on the mechanical characteristics and microstructure of geopolymer concrete. Compressive strength, split tensile strength, flexural strength, X-ray diffraction, and scanning electron microscope were conducted. The results of the investigation allow for the drawing of the following conclusions:

- SEM pictures demonstrate that SCBA is made up of elongated, irregular forms with spaces between them, which negatively affected the workability of the paste while also increasing the need for water due to increased porosity.
- XRD analysis of the mineralogical phases confirmed the presence of albite, quartz, orthoclase, and anorthite phases in all geopolymer concrete mixtures.
- The combination containing 5% SCBA increased the density of the geopolymer matrix in the SEM image. This was confirmed by the presence of less unreacted or partially reacted FA particles compared to other mixtures.
- Concrete made of geopolymer has superior workability in comparison to ordinary Portland cement concrete.
- The compressive strength of the FA-SCBA-based GPC was discovered to be greater than that of ordinary Portland cement concrete. The combination with 5% SCBA provided the highest compressive strength, which is 64 MPa.
- The 5% mixture exhibited superior split tensile strength performance at 28 days, similar to compressive strength. Its split tensile strength was 6.2 MPa. However, the flexural strength reached the maximum at 100% of FA.

This study highlights the potential for producing geopolymer concrete using waste materials like fly ash and sugarcane bagasse ash, supporting resource conservation and green building techniques. Future studies should look at alternate waste resources, and geopolymer concrete's thermal performance and long-term durability should be investigated. Geopolymer concrete has the potential to be a viable substitute for conventional Portland cement-based concrete with more study and innovation, making the built environment more durable and environmentally friendly.

5. Declarations

5.1. Author Contributions

Conceptualization, M.A.M.R.; methodology, M.A.M.R.; validation, M.A.M.R.; formal analysis, M.A.M.R.; investigation, M.A.M.R.; resources, M.A.M.R.; writing—original draft preparation, M.A.M.R.; writing—review and editing, R.O.O., N.G., and B.S.; visualization, R.O.O.; supervision, R.O.O., N.G., and B.S. All authors have read and agreed to the published version of the manuscript.

5.2. Data Availability Statement

The data presented in this study are available on request from the corresponding author.

5.3. Funding and Acknowledgement

The authors appreciate and acknowledge the African Union for financial support for this work. Also, the authors appreciate Pan African University, Institute for Basic Science, Technology and Innovation, and Jomo Kenyatta University of Agriculture and Technology for their technical support of this research. The authors would also like to thank the University of Kordofan for their support

5.4. Conflicts of Interest

The authors declare no conflict of interest.

6. References

- [1] Gupta, A., Gupta, N., & Saxena, K. K. (2021). Mechanical and durability characteristics assessment of geopolymer composite (Gpc) at varying silica fume content. *Journal of Composites Science*, 5(9), 237. doi:10.3390/JCS5090237.
- [2] Farrant, W. E., Babafemi, A. J., Kolawole, J. T., & Panda, B. (2022). Influence of Sugarcane Bagasse Ash and Silica Fume on the Mechanical and Durability Properties of Concrete. *Materials*, 15(9), 3018. doi:10.3390/ma15093018.
- [3] H.M., T., & Unnikrishnan, S. (2022). Utilization of industrial and agricultural waste materials for the development of geopolymer concrete- A review. *Materials Today: Proceedings*, 65, 1290–1297. doi:10.1016/j.matpr.2022.04.192.
- [4] Tanu, H. M., & Unnikrishnan, S. (2023). Review on Durability of Geopolymer Concrete Developed with Industrial and Agricultural Byproducts. *Materials Today: Proceedings*, 1-7. doi:10.1016/j.matpr.2023.03.335.
- [5] Alahmari, T. S., Abdalla, T. A., & Rihan, M. A. M. (2023). Review of Recent Developments Regarding the Durability Performance of Eco-Friendly Geopolymer Concrete. *Buildings*, 13(12). doi:10.3390/buildings13123033.

- [6] Bellum, R. R., Venkatesh, C., & Madduru, S. R. C. (2021). Influence of red mud on performance enhancement of fly ash-based geopolymer concrete. *Innovative Infrastructure Solutions*, 6(4), 215. doi:10.1007/s41062-021-00578-x.
- [7] Zareei, S. A., Ameri, F., & Bahrami, N. (2018). Microstructure, strength, and durability of eco-friendly concretes containing sugarcane bagasse ash. *Construction and Building Materials*, 184, 258–268. doi:10.1016/j.conbuildmat.2018.06.153.
- [8] Shilar, F. A., Ganachari, S. V., Patil, V. B., Khan, T. M. Y., & Dawood Abdul Khadar, S. (2022). Molarity activity effect on mechanical and microstructure properties of geopolymer concrete: A review. *Case Studies in Construction Materials*, 16, 1014. doi:10.1016/j.cscm.2022.e01014.
- [9] Garcia-Lodeiro, I., Palomo, A., & Fernández-Jiménez, A. (2015). An overview of the chemistry of alkali-activated cement-based binders. *Handbook of Alkali-Activated Cements, Mortars and Concretes*, 19–47, Woodhead Publishing, Sawston, United Kingdom. doi:10.1533/9781782422884.1.19.
- [10] Mendes, B., Andrade, I. K., de Carvalho, J. M., Pedroti, L., & de Oliveira Júnior, A. (2021). Assessment of mechanical and microstructural properties of geopolymers produced from metakaolin, silica fume, and red mud. *International Journal of Applied Ceramic Technology*, 18(1), 262–274. doi:10.1111/ijac.13635.
- [11] Moradikhou, A. B., Safedian, M., & Golafshani, E. M. (2023). High-strength geopolymer concrete based on coal washing waste. *Construction and Building Materials*, 362, 129675. doi:10.1016/j.conbuildmat.2022.129675.
- [12] Ekinci, E., Türkmen, İ., Kantarci, F., & Karakoç, M. B. (2019). The improvement of mechanical, physical and durability characteristics of volcanic tuff based geopolymer concrete by using nano silica, micro silica and Styrene-Butadiene Latex additives at different ratios. *Construction and Building Materials*, 201, 257–267. doi:10.1016/j.conbuildmat.2018.12.204.
- [13] Aliabdo, A. A., Abd Elmoaty, A. E. M., & Salem, H. A. (2016). Effect of water addition, plasticizer and alkaline solution constitution on fly ash based geopolymer concrete performance. *Construction and Building Materials*, 121, 694–703. doi:10.1016/j.conbuildmat.2016.06.062.
- [14] Ng, C., Alengaram, U. J., Wong, L. S., Mo, K. H., Jumaat, M. Z., & Ramesh, S. (2018). A review on microstructural study and compressive strength of geopolymer mortar, paste and concrete. *Construction and Building Materials*, 186, 550–576. doi:10.1016/j.conbuildmat.2018.07.075.
- [15] Salas, D. A., Ramirez, A. D., Ulloa, N., Baykara, H., & Boero, A. J. (2018). Life cycle assessment of geopolymer concrete. *Construction and Building Materials*, 190, 170–177. doi:10.1016/j.conbuildmat.2018.09.123.
- [16] Karakoç, M. B., Türkmen, I., Maraş, M. M., Kantarci, F., Demirboğa, R., & Uğur Toprak, M. (2014). Mechanical properties and setting time of ferrochrome slag based geopolymer paste and mortar. *Construction and Building Materials*, 72, 283–292. doi:10.1016/j.conbuildmat.2014.09.021.
- [17] Karthik, A., Sudalaimani, K., & Vijaya Kumar, C. T. (2017). Investigation on mechanical properties of fly ash-ground granulated blast furnace slag based self-curing bio-geopolymer concrete. *Construction and Building Materials*, 149, 338–349. doi:10.1016/j.conbuildmat.2017.05.139.
- [18] Yaseri, S., Hajiaghahi, G., Mohammadi, F., Mahdikhani, M., & Farokhzad, R. (2017). The role of synthesis parameters on the workability, setting and strength properties of binary binder based geopolymer paste. *Construction and Building Materials*, 157, 534–545. doi:10.1016/j.conbuildmat.2017.09.102.
- [19] Sakkas, K., Papias, D., Nomikos, P. P., & Sofianos, A. I. (2014). Potassium based geopolymer for passive fire protection of concrete tunnels linings. *Tunnelling and Underground Space Technology*, 43, 148–156. doi:10.1016/j.tust.2014.05.003.
- [20] Sarker, P. K., Kelly, S., & Yao, Z. (2014). Effect of fire exposure on cracking, spalling and residual strength of fly ash geopolymer concrete. *Materials and Design*, 63, 584–592. doi:10.1016/j.matdes.2014.06.059.
- [21] Cheng, T. W., & Chiu, J. P. (2003). Fire-resistant geopolymer produce by granulated blast furnace slag. *Minerals Engineering*, 16(3), 205–210. doi:10.1016/S0892-6875(03)00008-6.
- [22] Ganesan, N., Abraham, R., & Deepa Raj, S. (2015). Durability characteristics of steel fibre reinforced geopolymer concrete. *Construction and Building Materials*, 93, 471–476. doi:10.1016/j.conbuildmat.2015.06.014.
- [23] Lee, W. K. W., & Van Deventer, J. S. J. (2002). The effects of inorganic salt contamination on the strength and durability of geopolymers. *Colloids and Surfaces A: Physicochemical and Engineering Aspects*, 211(2–3), 115–126. doi:10.1016/S0927-7757(02)00239-X.
- [24] Zhang, M., Guo, H., El-Korchi, T., Zhang, G., & Tao, M. (2013). Experimental feasibility study of geopolymer as the next-generation soil stabilizer. *Construction and Building Materials*, 47, 1468–1478. doi:10.1016/j.conbuildmat.2013.06.017.
- [25] Komnitsas, K., & Zaharaki, D. (2007). Geopolymerisation: A review and prospects for the minerals industry. *Minerals Engineering*, 20(14), 1261–1277. doi:10.1016/j.mineng.2007.07.011.
- [26] Bellum, R. R., Muniraj, K., & Madduru, S. R. C. (2020). Influence of activator solution on microstructural and mechanical properties of geopolymer concrete. *Materialia*, 10, 100659. doi:10.1016/j.mtla.2020.100659.


- [27] Hardjito, D., Wallah, S. E., Sumajouw, D. M. J., & Rangan, B. V. (2004). On the development of fly ash-based geopolymer concrete. *ACI Materials Journal*, 101(6), 467–472. doi:10.14359/13485.
- [28] Yip, C. K., Lukey, G. C., Provis, J. L., & van Deventer, J. S. J. (2008). Effect of calcium silicate sources on geopolymerisation. *Cement and Concrete Research*, 38(4), 554–564. doi:10.1016/j.cemconres.2007.11.001.
- [29] Amin, M., Elsakhawy, Y., Abu el-hassan, K., & Abdelsalam, B. A. (2022). Behavior evaluation of sustainable high strength geopolymer concrete based on fly ash, metakaolin, and slag. *Case Studies in Construction Materials*, 16. doi:10.1016/j.cscm.2022.e00976.
- [30] Zaid, O., Abdulwahid Hamah Sor, N., Martínez-García, R., de Prado-Gil, J., Mohamed Elhadi, K., & Yosri, A. M. (2024). Sustainability evaluation, engineering properties and challenges relevant to geopolymer concrete modified with different nanomaterials: A systematic review. *Ain Shams Engineering Journal*, 15(2), 102373. doi:10.1016/j.asej.2023.102373.
- [31] Tian, Z., Tang, X., Xiu, Z., Zhou, H., & Xue, Z. (2022). The mechanical properties improvement of environmentally friendly fly ash-based geopolymer mortar using bio-mineralization. *Journal of Cleaner Production*, 332, 130020. doi:10.1016/j.jclepro.2021.130020.
- [32] Bezabih, T., Kanali, C., & Thuo, J. (2023). Effects of teff straw ash on the mechanical and microstructural properties of ambient cured fly ash-based geopolymer mortar for onsite applications. *Results in Engineering*, 18, 101123. doi:10.1016/j.rineng.2023.101123.
- [33] Suraneni, P., Burris, L., Shearer, C. R., & Hooton, R. D. (2021). ASTM C618 fly ash specification: Comparison with other specifications, shortcomings, and solutions. *ACI Materials Journal*, 118(1), 157–167. doi:10.14359/51725994.
- [34] Zhuang, X. Y., Chen, L., Komarneni, S., Zhou, C. H., Tong, D. S., Yang, H. M., Yu, W. H., & Wang, H. (2016). Fly ash-based geopolymer: Clean production, properties and applications. *Journal of Cleaner Production*, 125, 253–267. doi:10.1016/j.jclepro.2016.03.019.
- [35] Kaya, M., Uysal, M., Yilmaz, K., Karahan, O., & Atis, C. D. (2020). Mechanical properties of class C and F fly ash geopolymer mortars. *Gradjevinar*, 72(4), 297–309. doi:10.14256/JCE.2421.2018.
- [36] Wattimena, O. K., Antoni, & Hardjito, D. (2017). A review on the effect of fly ash characteristics and their variations on the synthesis of fly ash based geopolymer. *AIP Conference Proceedings*, 1887, 020041. doi:10.1063/1.5003524.
- [37] El-said, A., Awad, A., Ahmad, M., Sabri, M. M. S., Deifalla, A. F., & Tawfik, M. (2022). The Mechanical Behavior of Sustainable Concrete Using Raw and Processed Sugarcane Bagasse Ash. *Sustainability (Switzerland)*, 14(18), 11181. doi:10.3390/su141811181.
- [38] Torres de Sande, V., Sadique, M., Pineda, P., Bras, A., Atherton, W., & Riley, M. (2021). Potential use of sugar cane bagasse ash as sand replacement for durable concrete. *Journal of Building Engineering*, 39, 102277. doi:10.1016/j.jobe.2021.102277.
- [39] Ganesan, K., Rajagopal, K., & Thangavel, K. (2007). Evaluation of bagasse ash as supplementary cementitious material. *Cement and Concrete Composites*, 29(6), 515–524. doi:10.1016/j.cemconcomp.2007.03.001.
- [40] Murugesan, T., Vidjeapriya, R., & Bahurudeen, A. (2020). Sugarcane Bagasse Ash-Blended Concrete for Effective Resource Utilization Between Sugar and Construction Industries. *Sugar Tech*, 22(5), 858–869. doi:10.1007/s12355-020-00794-2.
- [41] Memon, S. A., Javed, U., Shah, M. I., & Hanif, A. (2022). Use of Processed Sugarcane Bagasse Ash in Concrete as Partial Replacement of Cement: Mechanical and Durability Properties. *Buildings*, 12(10), 1769. doi:10.3390/buildings12101769.
- [42] Loganayagan, S., Mohan, N. C., & Dhivyabharathi, S. (2021). Sugarcane bagasse ash as alternate supplementary cementitious material in concrete. *Materials Today: Proceedings*, 45, 1004–1007. doi:10.1016/j.matpr.2020.03.060.
- [43] Jagadesh, P., Ramachandramurthy, A., & Murugesan, R. (2018). Evaluation of mechanical properties of Sugar Cane Bagasse Ash concrete. *Construction and Building Materials*, 176, 608–617. doi:10.1016/j.conbuildmat.2018.05.037.
- [44] Dineshkumar, R., & Balamurugan, P. (2021). Behavior of high-strength concrete with sugarcane bagasse ash as replacement for cement. *Innovative Infrastructure Solutions*, 6(2). doi:10.1007/s41062-020-00450-4.
- [45] Jha, P., Sachan, A. K., & Singh, R. P. (2021). Agro-waste sugarcane bagasse ash (ScBA) as partial replacement of binder material in concrete. *Materials Today: Proceedings*, 44, 419–427. doi:10.1016/j.matpr.2020.09.751.
- [46] Chindaprasirt, P., Sujumngtokul, P., & Posi, P. (2019). Durability and mechanical properties of pavement concrete containing bagasse ash. *Materials Today: Proceedings*, 17, 1612–1626. doi:10.1016/j.matpr.2019.06.191.
- [47] Sua-Iam, G., & Makul, N. (2013). Use of increasing amounts of bagasse ash waste to produce self-compacting concrete by adding limestone powder waste. *Journal of Cleaner Production*, 57, 308–319. doi:10.1016/j.jclepro.2013.06.009.
- [48] Wuttisombatjaroen, J., Hemnithi, N., & Chaturabong, P. (2023). Investigating the influence of rigid void of fillers on the moisture damage of asphalt mixtures. *Civil Engineering Journal*, 9(12), 3161–3173. doi:10.28991/CEJ-2023-09-12-014.

- [49] Atia, S. M., & Abbas, W. A. (2022). Effect of adding nano starch biopolymer on some properties of silica fume concrete. *Key Engineering Materials*, 911, 145-150. doi:10.4028/p-2i42va.
- [50] Ahmad, W., Ahmad, A., Ostrowski, K. A., Aslam, F., Joyklad, P., & Zajdel, P. (2021). Sustainable approach of using sugarcane bagasse ash in cement-based composites: A systematic review. *Case Studies in Construction Materials*, 15, 698. doi:10.1016/j.cscm.2021.e00698.
- [51] Kathirvel, P., Gunasekaran, M., Sreekumaran, S., & Krishna, A. (2020). Effect of partial replacement of ground granulated blast furnace slag with sugarcane bagasse ash as source material in the production of geopolymer concrete. *Medziagotyra*, 26(4), 477–481. doi:10.5755/j01.ms.26.4.23602.
- [52] Azad, N. M., & Samarakoon, S. M. S. M. K. (2021). Utilization of industrial by-products/waste to manufacture geopolymer cement/concrete. *Sustainability (Switzerland)*, 13(2), 1–22. doi:10.3390/su13020873.
- [53] Singh, K. (2020). Experimental study on metakolin and baggasse ash based geopolymer concrete. *Materials Today: Proceedings*, 37(Part 2), 3289–3295. doi:10.1016/j.matpr.2020.09.116.
- [54] H.M., T., & Unnikrishnan, S. (2023). Mechanical Strength and Microstructure of GGBS-SCBA based Geopolymer Concrete. *Journal of Materials Research and Technology*, 24, 7816–7831. doi:10.1016/j.jmrt.2023.05.051.
- [55] Vanathi, V., Nagarajan, V., & Jagadesh, P. (2023). Influence of sugarcane bagasse ash on mechanical properties of geopolymer concrete. *Journal of Building Engineering*, 79, 107836. doi:10.1016/j.jobe.2023.107836.
- [56] Alghannam, M., Albidah, A., Abbas, H., & Al-Salloum, Y. (2021). Influence of Critical Parameters of Mix Proportions on Properties of MK-Based Geopolymer Concrete. *Arabian Journal for Science and Engineering*, 46(5), 4399–4408. doi:10.1007/s13369-020-04970-0.
- [57] Sarkar, M., & Dana, K. (2021). Partial replacement of metakaolin with red ceramic waste in geopolymer. *Ceramics International*, 47(3), 3473–3483. doi:10.1016/j.ceramint.2020.09.191.
- [58] Upadhyay, D., Chanda, A., & Thakkar, S. (2023). Mixture Design of High-Strength Geopolymer Concrete. *Materials Today: Proceedings*, 93, 335–339. doi:10.1016/j.matpr.2023.07.265.
- [59] Shoaie, P., Musaei, H. R., Mirlohi, F., Narimani zamanabadi, S., Ameri, F., & Bahrami, N. (2019). Waste ceramic powder-based geopolymer mortars: Effect of curing temperature and alkaline solution-to-binder ratio. *Construction and Building Materials*, 227, 116686. doi:10.1016/j.conbuildmat.2019.116686.
- [60] Nematollahi, B., & Sanjayan, J. (2014). Effect of different superplasticizers and activator combinations on workability and strength of fly ash based geopolymer. *Materials and Design*, 57, 667–672. doi:10.1016/j.matdes.2014.01.064.
- [61] Hanjitsuwan, S., Hunpratub, S., Thongbai, P., Maensiri, S., Sata, V., & Chindaprasirt, P. (2014). Effects of NaOH concentrations on physical and electrical properties of high calcium fly ash geopolymer paste. *Cement and Concrete Composites*, 45, 9–14. doi:10.1016/j.cemconcomp.2013.09.012.
- [62] Rukzon, S., & Chindaprasirt, P. (2012). Utilization of bagasse ash in high-strength concrete. *Materials and Design*, 34, 45–50. doi:10.1016/j.matdes.2011.07.045.
- [63] Andrade Neto, J. da S., de França, M. J. S., Amorim Júnior, N. S. de, & Ribeiro, D. V. (2021). Effects of adding sugarcane bagasse ash on the properties and durability of concrete. *Construction and Building Materials*, 266, 120959. doi:10.1016/j.conbuildmat.2020.120959.
- [64] Abdalla, T. A., Koteng, D. O., Shitote, S. M., & Matallah, M. (2022). Mechanical and durability properties of concrete incorporating silica fume and a high volume of sugarcane bagasse ash. *Results in Engineering*, 16, 100666. doi:10.1016/j.rineng.2022.100666.
- [65] Yadav, A. L., Sairam, V., Muruganandam, L., & Srinivasan, K. (2020). An overview of the influences of mechanical and chemical processing on sugarcane bagasse ash characterisation as a supplementary cementitious material. *Journal of Cleaner Production*, 245. doi:10.1016/j.jclepro.2019.118854.
- [66] Chusilp, N., Jaturapitakkul, C., & Kiattikomol, K. (2009). Utilization of bagasse ash as a pozzolanic material in concrete. *Construction and Building Materials*, 23(11), 3352–3358. doi:10.1016/j.conbuildmat.2009.06.030.
- [67] Jha, P., Sachan, A.K., & Singh, R.P. (2021). Bagasse Ash (ScBa) and Its Utilization in Concrete as Pozzolanic Material: A Review. *Advances in Geotechnics and Structural Engineering. Lecture Notes in Civil Engineering*, 143. Springer, Singapore. doi:10.1007/978-981-33-6969-6_41.
- [68] Srinivas, D., Suresh, D., & Lakshmi, N. H. (2021). Experimental Investigation on Bagasse ash Based Geopolymer Concrete Subjected to Elevated Temperature. *IOP Conference Series: Earth and Environmental Science*, 796(1). doi:10.1088/1755-1315/796/1/012028.

- [69] Landa-Ruiz, L., Landa-Gómez, A., Mendoza-Rangel, J. M., Landa-Sánchez, A., Ariza-Figueroa, H., Méndez-Ramírez, C. T., Santiago-Hurtado, G., Moreno-Landeros, V. M., Croche, R., & Baltazar-Zamora, M. A. (2021). Physical, mechanical and durability properties of ecofriendly ternary concrete made with sugar cane bagasse ash and silica fume. *Crystals*, 11(9). doi:10.3390/cryst11091012.
- [70] Marvila, M. T., de Azevedo, A. R. G., de Matos, P. R., Monteiro, S. N., & Vieira, C. M. F. (2021). Rheological and the fresh state properties of alkali-activated mortars by blast furnace slag. *Materials*, 14(8). doi:10.3390/ma14082069.
- [71] Shafiq, N., Hussein, A. A. E., Nuruddin, M. F., & Al Mattarneh, H. (2018). Effects of sugarcane bagasse ash on the properties of concrete. *Proceedings of the Institution of Civil Engineers: Engineering Sustainability*, 171(3), 123–132. doi:10.1680/jensu.15.00014.
- [72] Moradikhou, A. B., Bahador Moradikhou, A., & Safehian, M. (n.d.). Comparison of Mechanical Strengths and Resistance to Acidic Conditions, Permeability and Resistance to Elevated Temperatures of Geopolymer Concrete and Conventional Concrete. *Advance Researches in Civil Engineering*, 3(2), 27–37. doi:10.30469/ARCE.2021.135124.
- [73] Silva, P. De, Sagoe-Crenstil, K., & Sirivivatnanon, V. (2007). Kinetics of geopolymerization: Role of Al₂O₃ and SiO₂. *Cement and Concrete Research*, 37(4), 512–518. doi:10.1016/j.cemconres.2007.01.003.
- [74] Ranjbar, N., Mehrali, M., Behnia, A., Alengaram, U. J., & Jumaat, M. Z. (2014). Compressive strength and microstructural analysis of fly ash/palm oil fuel ash based geopolymer mortar. *Materials & Design*, 59, 532–539. doi:10.1016/j.matdes.2014.03.037.
- [75] Davidovits, J. (2017). Geopolymers: Ceramic-like inorganic polymers. *Journal of Ceramic Science and Technology*, 8(3), 335–350. doi:10.4416/JCST2017-00038.
- [76] Saloni, Parveen, Yan Lim, Y., & Pham, T. M. (2021). Influence of Portland cement on performance of fine rice husk ash geopolymer concrete: Strength and permeability properties. *Construction and Building Materials*, 300, 124321. doi:10.1016/j.conbuildmat.2021.124321.



Seismic Resilience of Steel-Braced Frames Incorporating Steel Slit Dampers: A Review and Comparative Numerical Analysis

Zaid A. Al-Sadoon ^{1*} , M. Almohammad-albakkar ² 

¹ Department of Civil and Environmental Engineering, College of Engineering, University of Sharjah, P.O. Box. 27272, United Arab Emirates.

² Department of Civil Engineering, Isfahan University of Technology, Isfahan 84156-83111, Iran.

Received 08 December 2023; Revised 03 March 2024; Accepted 12 March 2024; Published 01 April 2024

Abstract

Steel dampers, specifically steel slit dampers (SSDs), are crucial for enhancing the seismic resilience of buildings by absorbing energy and mitigating damage. SSDs are celebrated for their ability to produce stable hysteretic behavior, owing to the inelastic deformation of their strips, alongside benefits such as lightness, ease of manufacture, and straightforward post-earthquake replacement. This research extensively examines SSD applications, design principles, and innovations in their modeling, optimization, and production processes. The literature highlights SSDs' consistent performance in resisting both compression and tension, their adaptability in strength, ductility, and energy dissipation through modifications in strip configurations and the superiority of non-prismatic and hourglass-shaped designs over traditional options. Numerical analyses have been conducted to assess the effectiveness of non-prismatic slit dampers in comparison to their prismatic counterparts within braced frames. Three distinct braced frame configurations have been analyzed: one with a diagonal brace without a damper, another featuring a uniform prismatic slit damper, and a third incorporating a non-prismatic slit damper with an hourglass shape. The analysis primarily compared these systems' hysteresis behavior, ductility, and energy dissipation capacities. Results indicate a significant enhancement in performance when utilizing non-prismatic slit dampers. Notably, these dampers exhibited a remarkable 69% increase in cumulative energy dissipation compared to prismatic ones. Furthermore, the study reveals that a steel slit damper-braced frame, when equipped with optimally designed slit geometries, can tolerate inter-story drifts in excess of 2% while simultaneously achieving a greater than 12% increase in energy dissipation efficiency.

Keywords: Steel Slit Damper; Braced Frames; Hysteresis Curves; Ductility; Energy Dissipation.

1. Introduction

The energy generated by large earthquakes must be mitigated using tools that enable structures to withstand intense ground motions. A significant portion of the transmitted energy can be absorbed, attenuated, and reflected by enhancing the damping capacity of the structure. As a result, the energy transfer to structural members decreases, reducing the energy consumption required for these elements [1–3]. Steel-yielding dampers are widely recognized as effective techniques for controlling structure vibrations [4–6]. Utilizing metallic dampers of this kind aims to concentrate inelastic deformations and prevent damage to other prominent frame members [7–9]. Among the steel-yielding dampers, steel slit dampers are the most commonly employed [10]. These dampers offer additional advantages such as lightweight construction, ease of fabrication, and convenient replacement following large earthquakes.

Structures may often suffer severe damage from wind, traffic, and earthquakes, among other dynamic and environmental loads [11]. Over 132 buildings were destroyed in the Mexico City earthquake, and over 200 were

* Corresponding author: zalsadoon@sharjah.ac.ae

 <http://dx.doi.org/10.28991/CEJ-2024-010-04-019>



© 2024 by the authors. Licensee C.E.J, Tehran, Iran. This article is an open access article distributed under the terms and conditions of the Creative Commons Attribution (CC-BY) license (<http://creativecommons.org/licenses/by/4.0/>).

damaged in the Loma Prieta earthquake in Northern California in 1989 [12, 13]. There are several ways in which structural vibration controls can be used to reduce or avoid such damage, and these techniques have been successfully implemented in several different civil structures for this purpose [14–16]. Control systems that manage structural vibration are crucial in various engineering applications [17–19]. These systems are classified into four main groups based on their method of operation: passive, active, semi-active, and hybrid types [20–22]. Passive control systems are designed to dissipate or absorb vibrational energy without requiring external power input [23, 24]. Common passive control devices include tuned mass dampers [25]. Active control systems utilize sensors, actuators, and controllers to monitor and counteract structural vibrations in real-time [26]. Semi-active control systems combine elements of both passive and active systems [26]. Hybrid control systems integrate multiple control strategies, combining the advantages of different approaches to optimize performance and efficiency [27].

Fundamentally, the utilization of energy-dissipation mechanisms has been extensively studied and applied in diverse fields [28]. Among these mechanisms, viscous fluid dampers, friction dampers, viscoelastic dampers, and metallic yielding dampers effectively absorb and dissipate energy [29–31]. Viscous dampers force a fluid [32–35], while friction dampers utilize the frictional force between surfaces to dissipate energy. These dampers typically comprise sliding interfaces with high-friction materials or devices such as friction plates [36]. Metallic yielding dampers employ yielding elements, such as steel plates or rods, designed to undergo controlled yielding or plastic deformation under load [6, 37–39]. Finally, viscoelastic materials exhibit viscous and elastic behavior, making them well-suited for energy dissipation applications [40, 41].

Over the past four decades, it has become common practice to install passive dampers to improve structures' hysterical behavior and dissipate energy with no external power source required [42, 43]. By using these systems, the main elements of the building suffer less damage, and energy is dissipated more efficiently [44–46]. As well as maintaining stability over a wide range of temperatures, these dampers have extremely high fatigue resistance due to their low cycle and displacement rates, bolted attachments, low fabrication costs, tolerances for large displacements, and long-term durability [47–49]. These advantages of steel-yielding dampers have made them a popular passive energy dissipation device among all kinds of dampers. Several passive vibration control devices have been developed and implemented in buildings, including steel plates with slits or openings susceptible to shear [50–52].

Generally, slit dampers are considered metallic-yielding dampers because the yielding of their steel strips determines their damping behavior [53]. A new device, the multi-slit damper, combines weak and strong slit dampers in series to retrofit soft-first story structures against earthquakes [54]. Its energy dissipation occurs in two stages: weak-slit damper yielding during minor earthquakes and activation of the strong slit damper through a gap mechanism during major earthquakes. Experimental and analysis results confirm the device's effectiveness in controlling seismic response [54]. In a subsequent investigation, SSDs were employed, revealing that they substantially enhanced the lateral load capacity by up to 40% and ductility by 1.88 [55]. Additionally, experimental and numerical testing has indicated the potential of single-plate SSDs to be incorporated as a component of seesaw brace systems, as an addition to conventional bracing, or as a beam-to-column connection [56]. These SSDs have effectively reduced the forces and displacements experienced by structures during seismic events.

SSDs have been the main focus of numerous studies, and various methods and devices have been proposed based on necessities. Due to some special characteristics, architectural aspects, and requirements, the design and retrofitting of building structures with SSDs have been of great interest. Therefore, it is crucial to evaluate existing designs and configurations and analyze the benefits, limitations, enhancements, and potential optimizations that can be implemented in the future. The research thoroughly reviews commonly used slit dampers in civil structures to ensure greater adaptability and reliability, focusing on improving performance.

This study embarks on a pioneering endeavor to conduct a comprehensive review of steel slit dampers, an area which, to the best of the authors' knowledge, has not been exhaustively explored in existing literature. This gap underscores the imperative to delve into the evolution and applications of these dampers within structural systems. The review meticulously scrutinizes the influence of slit dampers on structural performance, integrating insights from contemporary research. A methodical appraisal and citation of scholarly articles from 1998 to 2023 is undertaken. This approach ensures an extensive coverage of all pertinent facets of slit dampers, encompassing their diverse applications, design considerations, configurations, integration within steel-braced frame structures, and potential avenues for enhancement. Moreover, this paper assessed numerically the comparative efficacy of non-prismatic versus prismatic slit dampers in structural frames. This analysis is conducted across three distinct structural frame models: a diagonally braced frame, a frame equipped with a uniform prismatic slit damper, and another featuring an innovatively designed hourglass-shaped non-prismatic slit damper. Building on the insights gleaned from recent technological advancements, the review culminates in proffering strategic recommendations for future research trajectories in this field.

The research paper is organized into seven sections. Section one discusses the prior art and the research gap in the literature, while section two outlines the methodology employed in this research. Section three presents an overview of steel slit dampers, including their concept and basic theoretical analysis. Following this, section four comprehensively

reviews various types of SSDs and discusses their applications and performance in braced frames. Section five conducts a comparative numerical analysis on three test frames using the finite element software ABAQUS. Specifically, one of these frames represents a special braced frame without a damper (SBF), while the other two frames are equipped with slit dampers—one utilizing a slit prismatic damper. Section six summarizes the conclusions drawn from the conducted research. Lastly, section seven outlines recommendations and proposes future avenues for applying SSDs in steel-braced frames, emphasizing their significance as crucial seismic fuses.

2. Research Methodology

In the field of building construction, slit dampers are recognized for their effectiveness in seismic mitigation through energy absorption and dissipation. These devices, composed of slender metallic strips, are integrated into the structure, playing a critical role during seismic events by mitigating the energy. This study reviews existing literature on slit dampers, focusing on aspects such as structural configurations, energy dissipation, hysteresis behavior, failure mechanisms, and ductility. The methodology, illustrated in Figure 1, includes a stringent review and selection process to identify relevant studies that shed light on the optimal design and implementation of slit dampers.

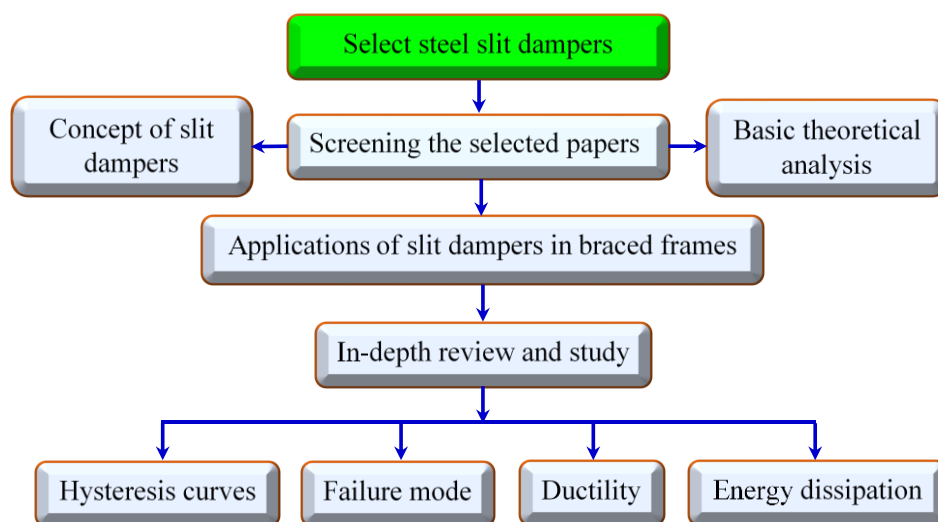


Figure 1. Flowchart depicting the methodology employed in this study

The aim is to assess the impact of slit dampers on the seismic resilience of buildings, leveraging data from prior research. Through a detailed analysis, this work synthesizes key findings and identifies best practices in the application of slit dampers for seismic protection. The outcome contributes to the body of knowledge by outlining strategies for enhancing building safety against seismic events.

3. Overview of Steel Slit Damper

3.1. The Concept of Slit Dampers

SSDs, or steel slit dampers, are widely recognized as one of the most prevalent passive dampers employed in structural engineering. These devices exhibit stable hysteretic behavior, highly resist temperature variations in the surrounding environment, demonstrate exceptional long-term reliability, and can be cheaply constructed [57]. Typically, SSDs are positioned between two structural elements or components, allowing for significant relative displacements. The energy generated during an earthquake can be effectively dissipated by subjecting to the cyclic movement of steel strips within the damper. Consequently, SSDs are extensively utilized in seismic design and earthquake retrofitting to ensure appropriate seismic response in structures. In the manufacturing process of SSDs, the damper plate can be perforated using various slits. Depending on the specific situation or element type, these slits can also be introduced in the web or flange of an I-section. In the manufacturing process of SSDs, the damper plate can be perforated using various slits. Depending on the specific situation or element type, these slits can also be introduced in the web or flange of an I-section. SSDs can be classified into two main categories based on their geometric characteristics: uniform prismatic and uniform non-prismatic slit dampers [58, 59]. Prismatic dampers maintain a consistent cross-sectional shape for all steel strips throughout the device's height, as their name implies. On the other hand, non-prismatic dampers exhibit varying cross-sectional shapes along their height (refer to Figure 2). A device in which all steel strips possess the same shape is considered uniform, whereas a device comprising different steel strip shapes is considered non-uniform, as depicted in Figure 3.

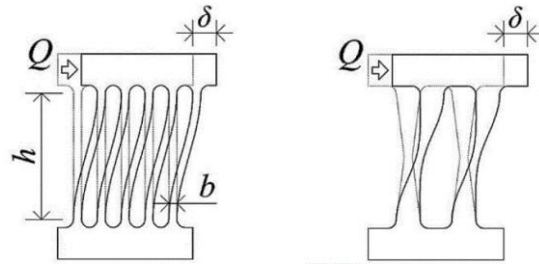


Figure 2. Traditional configurations of slit dampers and their lateral deformation; prismatic and non-prismatic [58]

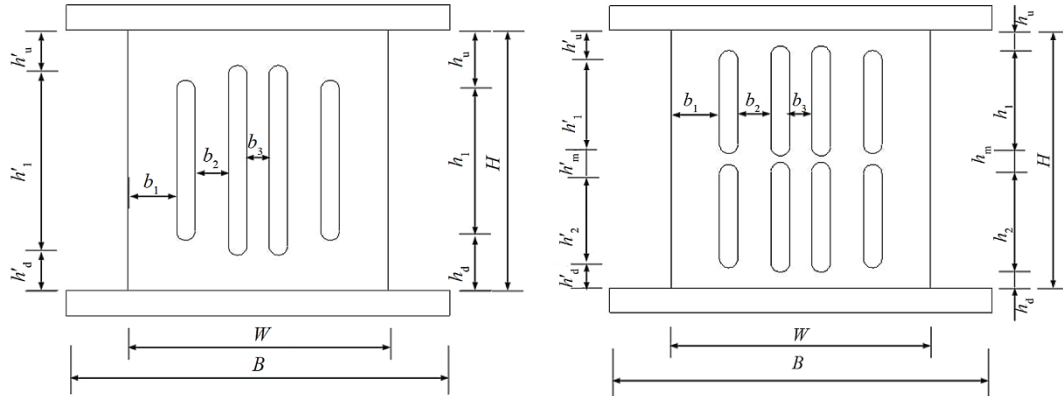


Figure 3. An example of a non-uniform slit damper configuration [59]

Oh (1998) [60] introduced SSDs in the literature, as depicted in Figure 4. A similar concept was further investigated and implemented experimentally by González-Sanz et al. [58]. Their study focused on steel slit plate dampers subjected to shear deformation. They derived analytical equations that predict these dampers' ultimate energy absorption capacity. Additionally, they observed that the resulting energy could be analytically estimated, with their experimental findings closely aligning with the analytical predictions. The energy dissipated by these dampers arises from the flexural yielding of their strips during inelastic cyclic deformation [61-63]. Each damper strip undergoes double curvature bending upon sufficient story drift, forming plastic hinges at both ends. Numerous studies have also focused on developing this type of damper [64, 65].

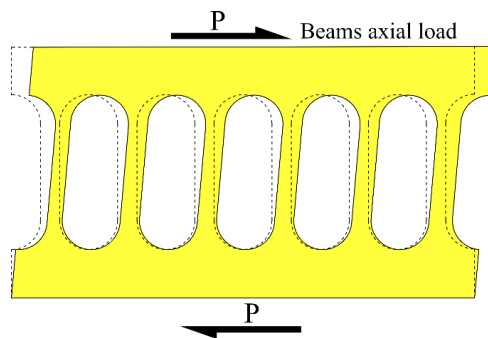


Figure 3. The configuration of steel slit damper and deformation under the lateral load [60]

Finally, SSDs can provide extensive design flexibility, permitting adjustments to parameters such as strip count, configurations (uniform prismatic or non-prismatic and non-uniform prismatic or non-prismatic), and dimensions (height, width, and thickness). This adaptability facilitates utilization across diverse load scenarios, drift conditions, and energy dissipation requirements. The performance of the SSDs can be modified by adjusting these parameters. This configurational flexibility empowers designers with a spectrum of design options. The analytical equations in the next section reveal that these parameters exert notable influence on the performance of slit dampers, impacting factors such as strength capacities, elastic stiffness, and yield displacement.

3.2. Basic Theoretical Analysis

The governing equations for SSDs can be rigorously deduced from the principles of strength of materials. Figure 5 illustrates how the strip ends of the damper were idealized to predict the yield strength and deformation when the round-shaped ends were replaced with straight ones [53].

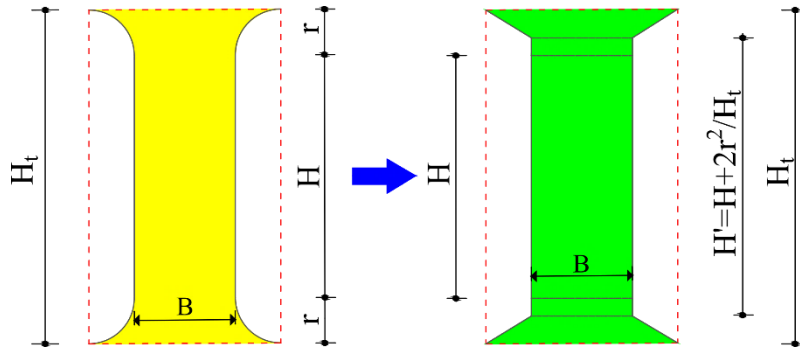


Figure 4. Idealization of strips

The flexural yielding loads at the ends of strips, denoted as $Q_{y,b}$, and the shear yielding loads of the strips, denoted as $Q_{y,s}$, represent the yield capacities of the slit plates. Additionally, the number of strips is represented by n . The total height of the strip is specified as H_t , the thickness of the slit gusset plate is denoted as t , the radius of the ends of the strips is indicated by r , and the strip width is denoted as B . The equivalent height, denoted as H' in Figure 5, is calculated using Equation 1.

$$H' = H + \frac{2r^2}{H_t} \tag{1}$$

Equation 2 is used to calculate the yielding displacement (δ_y) of the (SSDs) based on elasticity:

$$\delta_y = \delta_b + \delta_s = \frac{Q_y \cdot (H_t^3)}{nEtB^3} \left(1 + 3\ln \frac{H_t}{H}\right) + \frac{3Q_y \cdot (H_t)}{2ntBG} \left(1 + \ln \frac{H_t}{H}\right) \tag{2}$$

Where δ_b and δ_s represent the displacement components due to flexural and shear deformations. Q_y refers to the yielding strength of the SSDs, which is determined as the minimum between the flexural yielding ($Q_{y,b}$) and the shear yielding loads of the strips ($Q_{y,s}$), as described in Equation 3, E denotes Young's modulus, and G represents the shear modulus.

It can be observed that the strips exhibit behavior consistent with that of a series of partially fixed-ended beams and undergo double curvature under small relative displacement between both support ends. Consequently, it is possible to determine the yielding and ultimate strength of the slit damper analytically by employing the following simplification [63]:

$$\begin{cases} Q_y = \min\{Q_{y,b}, Q_{y,s}\} \rightarrow \\ Q_y = \min\left\{n \frac{tB^2}{2H'} \sigma_y, n \frac{2tB}{3\sqrt{3}} \sigma_y\right\} \end{cases} \tag{3}$$

Where n is the number of strips, and σ_y is the yield stress of the slit plate.

Plastic hinges are formed at the ends of each strip when a significant displacement occurs. As a result, the calculation of the ultimate strength of SSDs is performed according to the following procedure [63]:

$$\begin{cases} Q_B = \min\{Q_{B,b}, Q_{B,s}\} \rightarrow \\ Q_B = \min\left\{n \frac{tB^2}{2H'} \sigma_B, n \frac{2tB}{3\sqrt{3}} \sigma_B\right\} \end{cases} \tag{4}$$

Where Q_B refers to the ultimate strength, which is determined as the minimum between the flexural strength ($Q_{B,b}$) and the shear strength of the strips ($Q_{B,s}$). σ_B is the ultimate stress of the slit plate.

Certain observations can be emphasized based on the research conducted by Chan & Albermani [61] on the seismic behavior of slit dampers. The ends of the strips were rounded, and the overall length of the strips was considered during their derivations. Consequently, the equations for determining the yield strength (P_y) and stiffness (K_d) can be expressed as follows:

$$P_y = n \frac{\sigma_y t b^2}{3l_0} \tag{5}$$

$$K_d = cn \frac{E t b^3}{l_0^3} \tag{6}$$

The dimensions of the strips are denoted by the variables l_0 (length), t (thickness), and b (width). It is imperative to acknowledge that, to ascertain the elastic stiffness of the slit dampers (SSDs) via Equation 6, an underlying assumption is made regarding the strips' ends being partially fixed [61]. Moreover, the stiffness coefficient, c , was derived from

experimental data and utilized to calibrate the elastic stiffness. In this context, the radius of the fillet at the end of the strips can be considered another factor influencing the behavior of the SSDs. Previous research findings suggest that a minimum value for this parameter should be observed to mitigate the risk of premature fractures caused by stress concentration at the strip's end regions [66].

The analytical equations reveal that such as strip count and dimensions (height, width, and thickness) exert notable influence on the performance of slit dampers, impacting factors such as strength, elastic stiffness, and yield displacement. It becomes apparent from the analytical expressions that the structural attributes of the damper, encompassing yield strength (refer to Equations 3 and 5) and ultimate capacity (as depicted in Equation 4), exhibit a linear correlation with the thickness of the slit damper. Consequently, as the thickness of the slotted plate increases, both the yield strength and ultimate strength will also increase linearly. In contrast, according to Equations (3 to 5), an inverse correlation exists between the length of steel strips and strength capacities. As the length of the strip increases, the yield and ultimate strength of the damper decrease. Additionally, widening the slit damper, as indicated by Equation 3 and 4, results in an augmentation of both yield and ultimate strength.

On the other hand, SSDs are known to be thin slit plates. Therefore, to ensure SSDs exhibit stable hysteretic behavior and effectively resist both compression and tension, the slit plates, particularly the strips within these dampers, must avoid out-of-plane buckling. Therefore, it is crucial to carefully select the dimensions of the strips, including their length, width, and thickness. Specifically, the slenderness ratios of length to width and width to thickness must adhere to the criteria to prevent buckling under critical conditions.

3.3. Summary

The strips' thickness, height, and width are crucial factors that significantly influence the strength capacities, stiffness, and other key parameters of slit dampers. It should be emphasized that appropriately modifying these parameters can improve the seismic performance of slit dampers. Moreover, when the bending behavior governs, slit dampers generally exhibit stable performance levels that are deemed acceptable. Finally, these equations afford a computational avenue to discern pivotal mechanical parameters intrinsic to the SSD system, thereby preventing the prerequisite for exhaustive simulation and empirical testing.

4. Application of the Steel Slit Damper in Braced Frames

Numerous earthquakes have recently occurred worldwide, significantly damaging buildings and bridges. To withstand lateral loads, concentrically and eccentrically braced frames have been widely employed [67-69]. These frames have desirable stiffness and strength, making them suitable for earthquake-resistant structures [70, 71]. However, it should be noted that CBFs exhibit lower ductility compared to moment frames and eccentrically braced frames. This system dissipates energy through the inelastic deformation of braces, which can buckle, yield, and undergo inelastic deformation following a major earthquake [72-74]. Extensive research has been conducted to enhance the seismic performance of CBFs. For instance, investigations have focused on preventing brace buckling through restraining mechanisms, examining connection details of corner and middle gusset plates, evaluating the type and size of braces, and optimizing the arrangement of the braces [75-77]. For instance, a buckling-restrained brace (BRB) is engineered and employed to bolster strength, stiffness, and ductility against lateral loads. BRBs mitigate structural damage and augment the braced structures' seismic resilience [78, 79].

Recently, several studies have been conducted to address enhancing brace performance by incorporating energy dissipation devices. This approach aims to absorb the plastic action and prevent damage to other crucial components [80-84]. Significant advancements have been made in the system based on the "weak gusset plate-strong brace member" concept. Various techniques have been proposed to implement this concept, such as utilizing gusset plates with a low yield point. For instance, Chen & Chang [39] investigated the impact of gusset plates with low yield points. Their findings demonstrated a reduction in the pinching effect of braced frames resulting from corner gusset plate buckling.

Benavent-Climent [84] conducted experimental studies on slit plates subjected to shearing deformations to assess their ultimate energy absorption capacity. The study considered three parameters: strip width to plate height (B/H) ratio, material properties, and the loading pattern. Based on the assumptions made, the ultimate energy absorption capacity was determined by combining the energy dissipated by the structural skeleton and the Bauschinger component. In 2002, Lee et al. [83] proposed and developed an alternative device for efficient and cost-effective dissipation of seismically-induced energy. This device, known as a hysteric plate slit damper, could be easily installed in cross-braced frames and was primarily subjected to shear forces (see Figure 6). Subsequently, it became the first steel slit damper utilized in a V-braced system [60]. Another energy dissipation device, known as a tube-in-tube damper (TTD), was introduced by Benavent-Climent for braces [84]. TTDs involve cutting slits through the device's outer hollow section, generating strips attached to the inner section through welding. The strips dissipate energy through flexural/shear yielding when TTDs move toward the brace. A schematic view and detailed illustration of the TTD are presented in Figure 7.

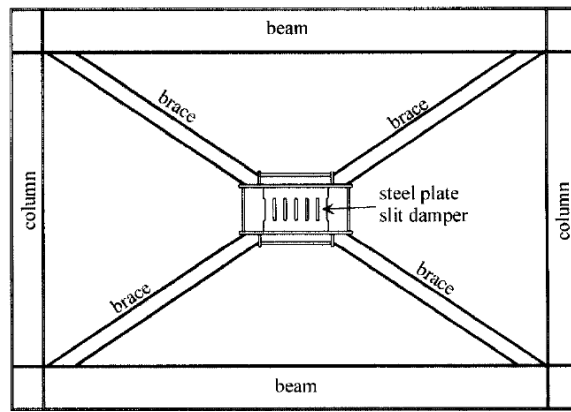


Figure 5. Slit plate damper in a cross-braced frame [83]

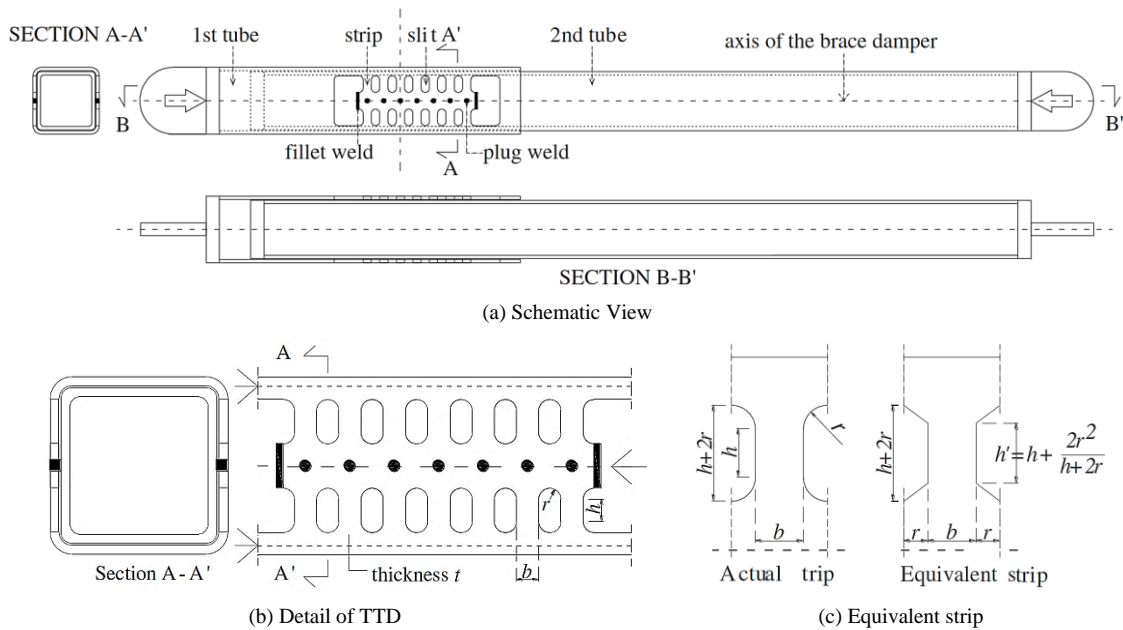


Figure 7. TTD as brace-type seismic damper [84]

To address the strain concentration at the ends of strips and determine the optimized shape of the slits, Ghabraie et al. [85], by utilizing the bidirectional evolutionary structural optimization technique, were able to optimize the shape of the slits and develop an effective configuration. The device's energy dissipation capacity and fatigue resistance under low cycling conditions were significantly enhanced by incorporating this configuration. In addition, A numerical model was used by Aminzadeh et al. [86] to obtain optimal boundary shapes for slit dampers. They employed the iso-geometric analysis method, allowing precise modeling of complex geometries for nonlinear damper analysis. Using B-splines with non-uniform rationality, an optimized shape was generated to simulate a conventional steel slit damper under a volume constraint. The newly proposed steel slit damper was compared with other shapes from the literature, and an optimization process was proposed and evaluated based on its performance. The optimal shape demonstrated a 12% increase in energy dissipation. The stress distribution in the proposed damper and the compared dampers can be seen in Figure 8.

González-Sanz et al. [58] investigated the development of a mild steel damper with non-uniform vertical slits. The study aimed to analyze the relationship between different forms of vertical slits on the core energy plate and their ability to dissipate energy and resist buckling. The researchers formulated theoretical equations to determine key damper parameters and validated numerical models using experimental data. By analyzing earthquake time-history data, they demonstrated the effectiveness of the dampers in reducing seismic responses of the prototype frame and achieving satisfactory energy dissipation. In another study, Tagawa et al. [87] utilized SSDs in a seesaw system, where the bracing members remain in tension during lateral movements (see Figure 9). The researchers conducted cyclic loading tests on the framed structure with this proposed system and found that it exhibited stable hysteretic behavior and had substantial energy dissipation capacity. Furthermore, all specimens showed yielding of the slit dampers at a story rotation angle of 0.001 rad.

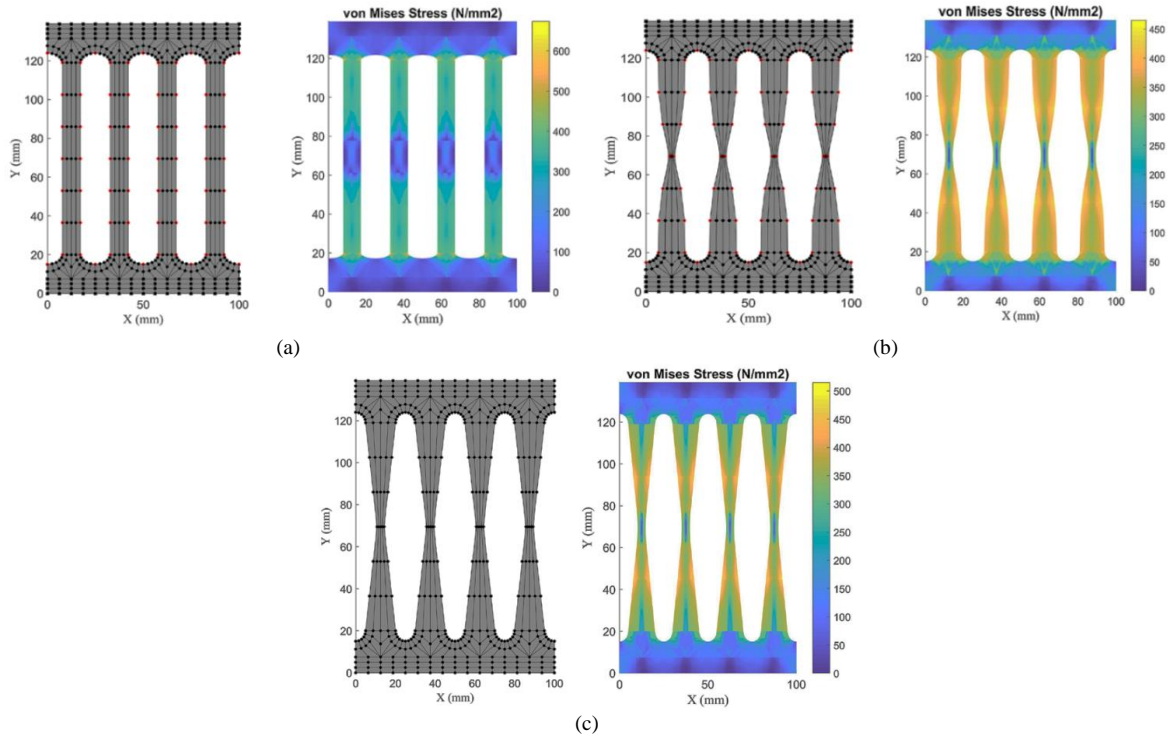


Figure 6. Stress distribution in slit dampers with various configurations; (a) conventional slit dampers [86], (b) optimal shape [86], and (c) proposed shape by Ghabraie et al. [85]

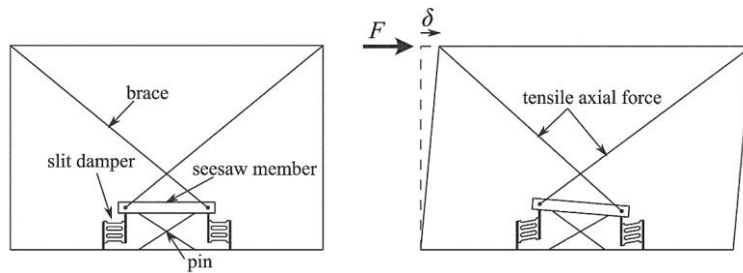


Figure 7. General and deformed configurations of a seesaw system equipped with SSDs [87]

Furthermore, Tagawa et al. [87] implemented slits as dampers in chevron-braced frames. A separate investigation by Ahmadie Amiri et al. [47] found that incorporating a block slit damper (BSD) can enhance chevron frames' performance. The BSD consists of a steel block with multiple slits, and it offers several desirable characteristics, such as high shear strength, energy absorption and dissipation capabilities, and favorable economic implications. The BSD can be integrated into a chevron frame, as Figure 10(a) illustrates. Building upon the previous study by Katal Mohseni et al. [88], further optimizations were made to steel BSDs to enhance their energy absorption capacity. Various geometric dimensions were examined, and the findings indicated that the frame equipped with BSDs exhibited significantly improved ductility and stiffness [88] compared to the earlier study [47]. Consequently, the energy absorption during hysteresis cycles experienced a substantial increase.

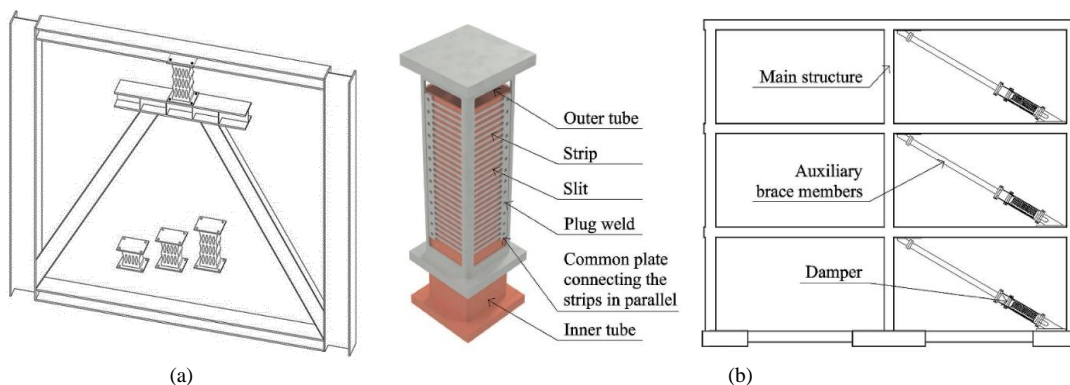


Figure 10. Braced frames equipped with BSD and SS-TTD dampers; (a) BSD device configuration [47] and (b) View of the SS-TTD in general and a typical building frame [58]

In a study by Kim [89], an investigation was carried out on a box-type SSD and a multi-SSD system. Gonzalez-Sanz et al. [58] explored a novel type of stainless-steel tube-in-tube damper (SS-TTD) composed of two telescopic tubes. The energy dissipation in the brace-type damper occurs through flexural plastic deformations of the strips when subjected to forced axial displacements. The exterior tube walls of the SS-TTD feature a series of slits that form the strips, which are connected to the interior tube (refer to Figure 10(b)). The seismic behavior of the SS-TTD was evaluated using quasi-static and dynamic shaking table tests. Comparative analysis revealed that the SS-TTD exhibits approximately four times higher cumulative ductility than slit-type plate dampers. Furthermore, its dissipation capacity is three times that of mild steel dampers and sixteen times that of high-strength steel dampers. Guo et al. [90] proposed an adjustable steel damper with replaceable steel strips, utilizing bolted connections for framed structures. Figure 11 illustrates this damper, along with potential installation locations in frames. To achieve maximum plasticity and fully use the load-bearing capacity of the steel strips, they must yield simultaneously and distribute energy uniformly across the entire section. The pumping hysteresis loops observed in the strips effectively dissipate potential energy. The bending moment strength primarily depends on the width of the central region.

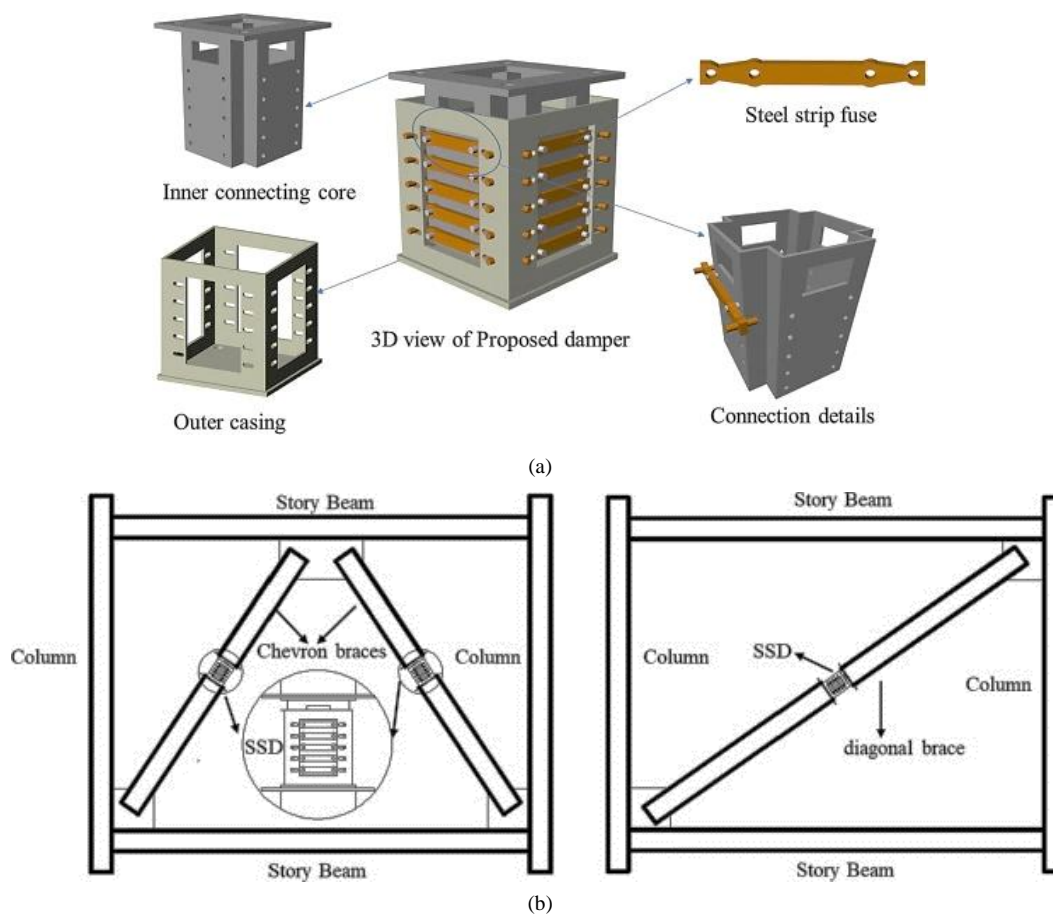


Figure 8. Illustration of the proposed damper and the location of potential installations in frames [90]

As an alternative to conventional link beams, Askariani et al. [66] introduced the concept of a slit link beam to enhance the structural performance of eccentrically braced frames (EBFs). Vertical strips can be formed by incorporating perforations in the web to create the link beam (refer to Figure 12(a)). The authors derived formulas to analyze the characteristics of the slit link beam and validated their findings using the ABAQUS software. Askariani also proposed a concept involving replaceable components [91]. Numerical simulations were conducted on a structure equipped with a novel brace-type slit damper (BSD), evaluating the influence of geometrical parameters on the frame's performance. The slit plate has two diagonals on each side, with links designed and arranged based on a specific geometry (see Figure 12(b)). A gusset plate is utilized to restrict the out-of-plane displacement of the diagonal members at one end, while a pin is employed at the other end. It was observed that all examined frames exhibited stable hysteresis curves under various loading conditions. Furthermore, upon completion of loading, no cracks were detected in the damper links. The results indicate that the proposed damper is an effective energy-dissipating device suitable for implementation in building structures. In subsequent research, Zhao et al. [92] developed a new type of damper known as the perforated web H-type brace damper (PWHBD). The H-profile brace used in their damper system features multiple slits along its length (see Figure 13), allowing for seismic energy dissipation through flexural yielding of the perforated webs under in-plane shear. The hysteretic curves exhibited stable and substantial behavior, further supporting the effectiveness of the damper in dissipating energy during seismic events.

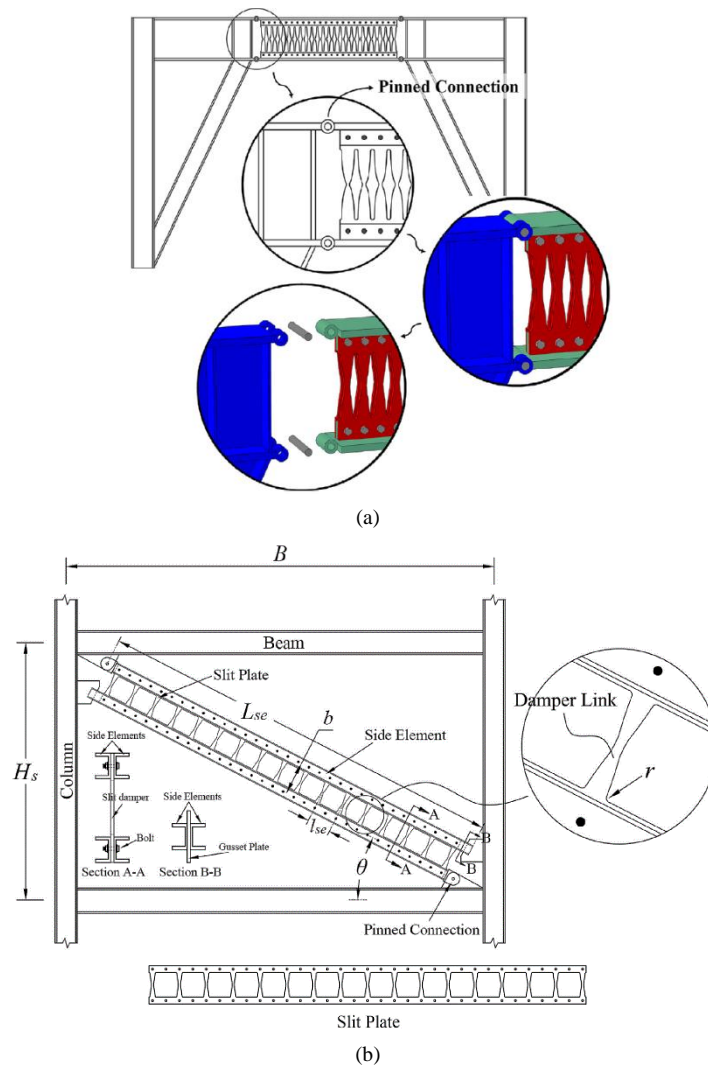


Figure 12. Eccentrically and concentrically braced frame equipped with slit dampers; (a) eccentrically braced frame with slit link beam [66] and (b) brace-type slit damper [91]

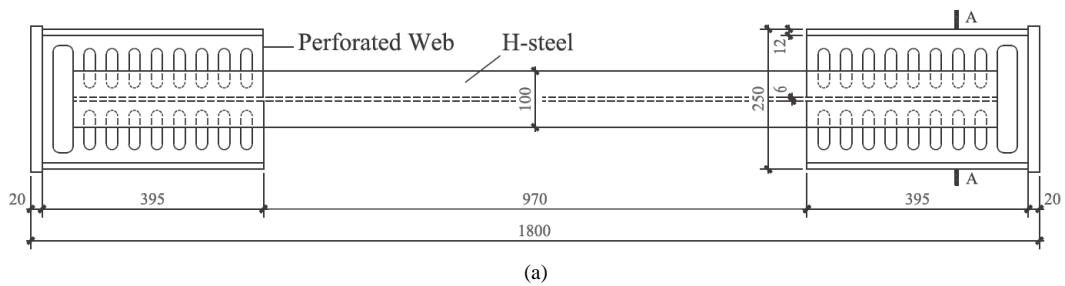


Figure 13. An example of a PWHBD test specimen [92]; (a) specimen dimensions and (b) view of the overall test setup

Based on a study by Javidan et al. [93], a steel multi-slit damper (MSD) has been proposed as a retrofit solution for partition walls. The study involved experiments on reinforced concrete frames comprising two stories, both with and without the suggested dampers. The study's findings indicate that implementing the MSD retrofit strategy enhances the hysteretic behavior of the structures. Similarly, Benavent-Climent et al. [94] have developed a novel metallic damper employing mild steel plastic deformation (refer to Figure 14). This damper is designed to dissipate energy during severe or extreme earthquakes. Including a gap mechanism in the damper helps prevent high-cycle fatigue damage. Additionally, the damper exhibits a remarkable energy dissipation capacity when subjected to large deformations caused by extreme ground motion. Dynamic shake-table tests were conducted on dampers installed in reinforced concrete structures alongside static cyclic tests of dampers isolated from the structure to evaluate their performance. The test results have enabled the development of a hysteresis model that accurately predicts the force-displacement curve of the damper under different cyclic loadings. The proposed hysteresis model can effectively capture increased stiffness and strength at large deformations. Furthermore, dampers' energy dissipation capacity is influenced by the phase in which they fail, suggesting new equations for predicting this behavior. The test results and a simple numerical model demonstrate that the damper exhibits a stable hysteresis response, predictable cyclic behavior, and a reliable ultimate energy dissipation capacity.

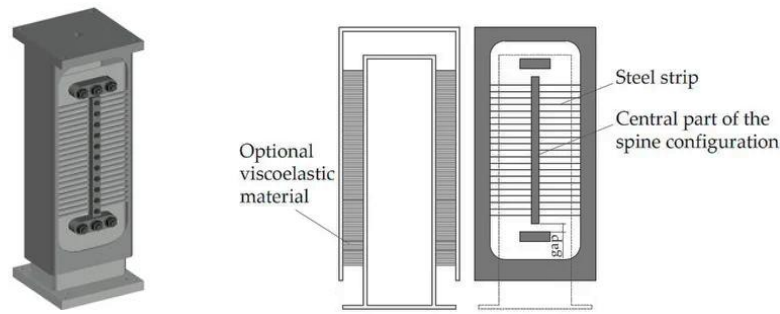


Figure 14. Details of the proposed damper by Benavent-Climent et al. [94]

According to a recent study by Almohammad-albakkar et al. [95-97], a novel damper that enhances the seismic performance of X-CBFs (Cross-Braced Frames) has been developed and tested numerically and experimentally. The proposed design consists of two cross braces with two segments each, where a grooved gusset plate damper (GGPD) was utilized to connect the four segments at the bay's midpoint. This connection prevents plastic action or buckling in the braces and other structural members. Figure 15 illustrates the addition of stiffener plates to the inner and outer edges of the GGPD, which effectively limits the occurrence of local instability in the grooved gusset plate. Specifically, it prevents early-stage out-of-plane buckling during story drift.

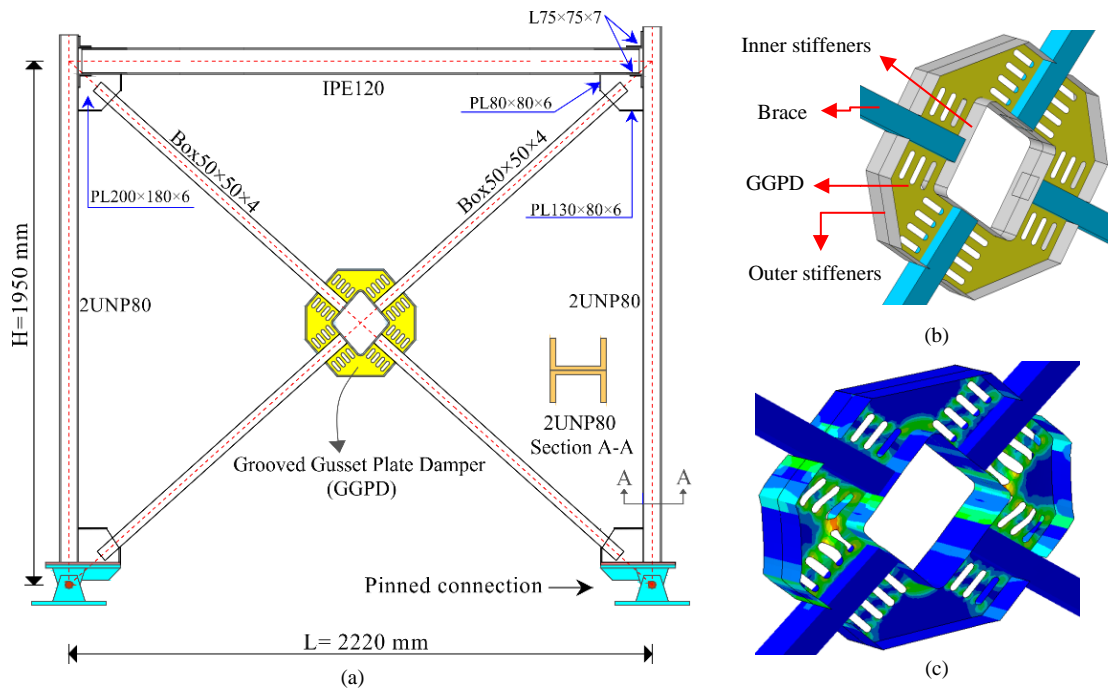


Figure 15. The grooved gusset plate damper (GGPD) [95]; (a) installation of GGPD in a cross-braced frame, (b) configuration of GGPD, and (c) the distribution of plastic strain

The working mechanism of the GGPD relies on the yielding of the gusset plate strips in in-plane bending, resulting in the dissipation of seismic energy. The experimental results indicate that the innovative system (GGPD) can tolerate a more than 3% relative drift. Additionally, a computational simulation was performed using the finite element software ABAQUS to assess the performance of this novel system. Additionally, the yield and ultimate capacities of the damper were analytically calculated using derived formulas. A comparison was made between the numerical outcomes and the results obtained from the analytical equations. The comparison results demonstrate a good agreement between the numerical and analytical findings.

In a recent study by Heyrani & Shooshtari [98], the hysteresis performance of new SSDs under cyclic loading. FEA was employed to simulate different slit sizes and the number of slits in single-column and dual-column SSDs. Sample SSDs with the highest ultimate strength were then subjected to testing. The findings indicate that dampers featuring steel strips of elliptical openings demonstrate enhanced energy dissipation compared to the tested specimens. Dual-column SSDs also show higher initial strength than single-column SSDs. In addition, single-column SSDs exhibit stable hysteresis performance, minimizing strength loss during displacement cycles. Roustaei et al. [3] introduced vertical steel panel flexural yielding dampers (VSPFYDs) to enhance the cyclic behavior and overall performance of SSDs (Figure 16). Numerical methods using ABAQUS software and extensive parametric studies were employed to validate and investigate their study. Comparison with traditional SSDs confirmed that VSPFYDs exhibited improved seismic parameters. Notably, VSPFYDs with a height of 15 cm demonstrated superior performance in various aspects. The plate connection construction was found to have a significant impact on the performance and hysteresis behavior of VSPFYDs compared to SSDs.

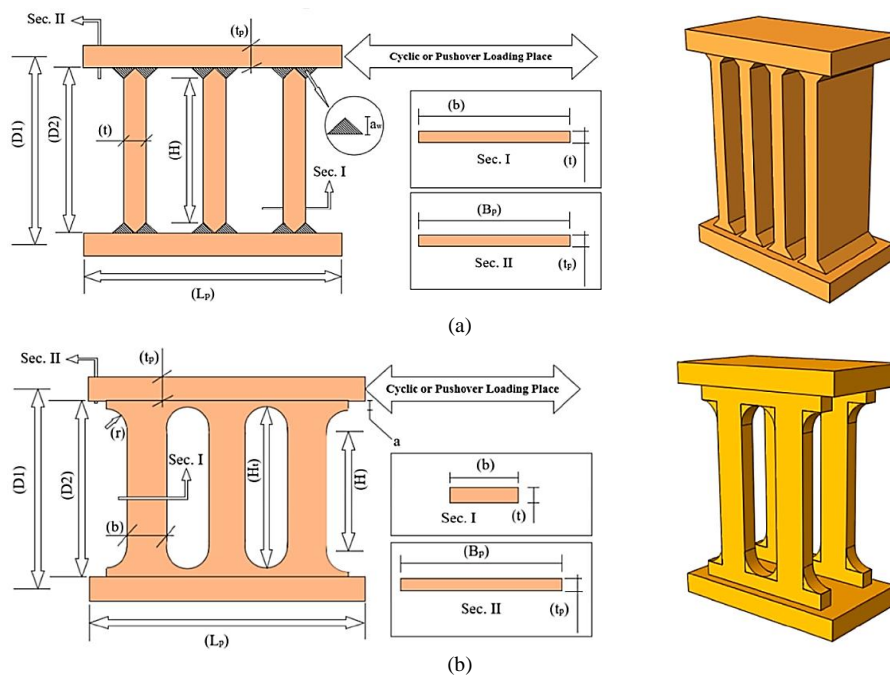


Figure 16. Schematic view and geometric parameters of the proposed system by Roustaei et al. [3]; (a) VSPFYD and (b) SSD

Hui et al. [99] introduced and conducted experimental assessments on an economical double-sided slotted steel tube shear damper (refer to Figure 17). This device leverages elastic-plastic deformation within the plane of the slotted steel plate on the steel tube's side to absorb seismic energy, effectively mitigating vibrations. Quasi-static tests were systematically conducted to investigate the influence of various design parameters on operational efficiency, energy dissipation capacity, and failure characteristics. The test results demonstrated the damper's robust plastic deformation capabilities, outstanding seismic performance, and substantial energy dissipation capacity. The hysteretic curve exhibited both symmetry and completeness, resembling a shuttle shape. Notably, increasing the bending element's width and the steel tube's wall thickness yielded significant improvements in energy dissipation.

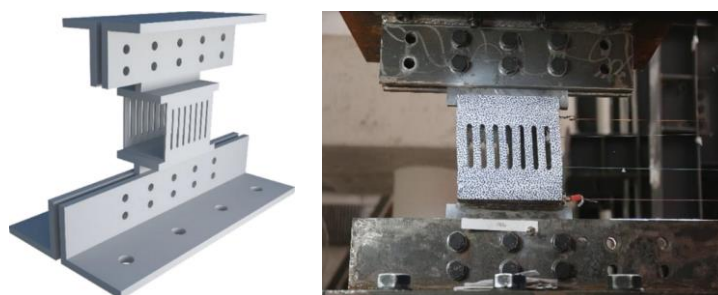


Figure 17. Double-sided slotted steel tube shear damper [99]

In the interest of comprehensiveness, Kang et al. [100] developed a seismic retrofit scheme using a combination of a steel moment frame and SSDs to mitigate earthquake damage in buildings. The hybrid system underwent a cyclic load test within an existing reinforced concrete frame. The device demonstrated energy dissipation capabilities similar to slit dampers, with a slight reduction in stiffness compared to traditional steel frame reinforcement methods. The results of a finite element analysis validated the test outcomes, showing a significant enhancement in structural strength and ductility when using slit dampers compared to bare structures. The model structure effectively reduced its seismic response below the target limit state by implementing slit dampers. The stress distribution in the test structures, obtained from the finite element analysis, is depicted in Figure 18.

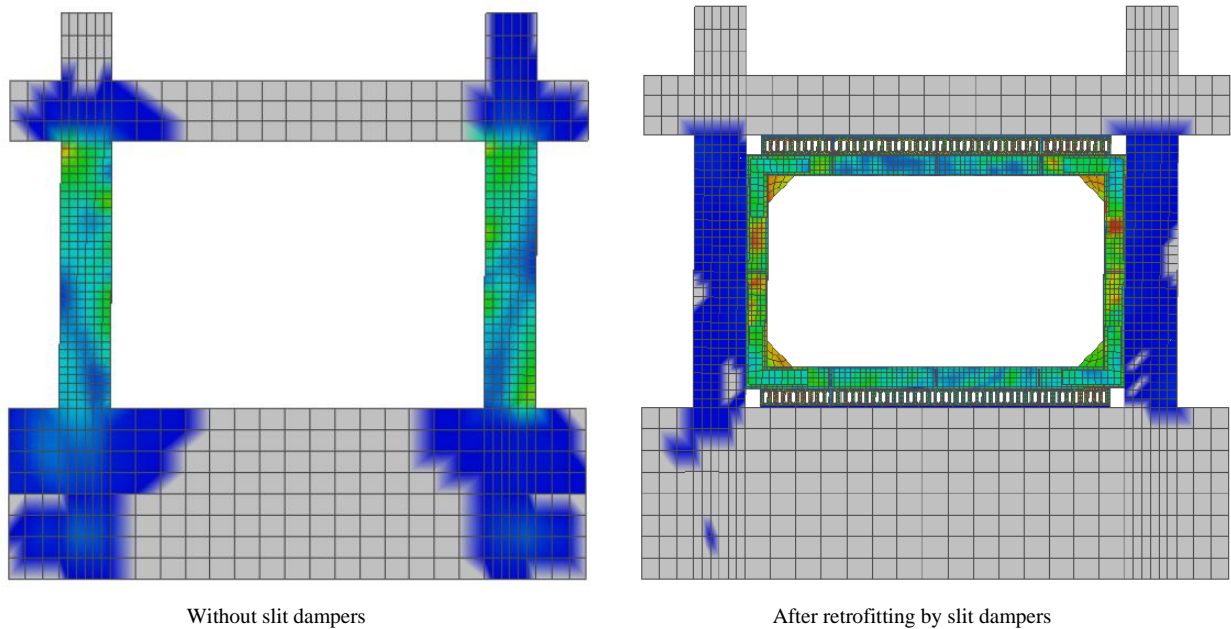


Figure 18. The stress distribution in the test structures resulting from the finite element analysis [100]

Traditionally used slit dampers are prone to cracking and breaking because of stress buildup at the ends of the strips when used for earthquake retrofitting. Bae et al. [101] proposed an improved damper design using radius-cut coke-shaped strips to address this issue and enhance ductility. Figure 19 illustrates the von Mises stress distributions for the three analysis models. By applying the reduced beam section method, the height-to-width ratio of the strip was increased to induce more bending deformation than shear deformation. Plastic hinges were intentionally created by focusing stress on the radius-cut section. This design specimen has higher inelastic deformation capacity and reduced fracture fragility. The experimental approach resulted in a finite element analysis demonstrating the coke-shaped damper's improved ductility. During cyclic loading, the radius-cut section was identified as the location of the final fracture, indicating sustained energy dissipation. The hysteresis curves of this damper are presented in Figure 20.

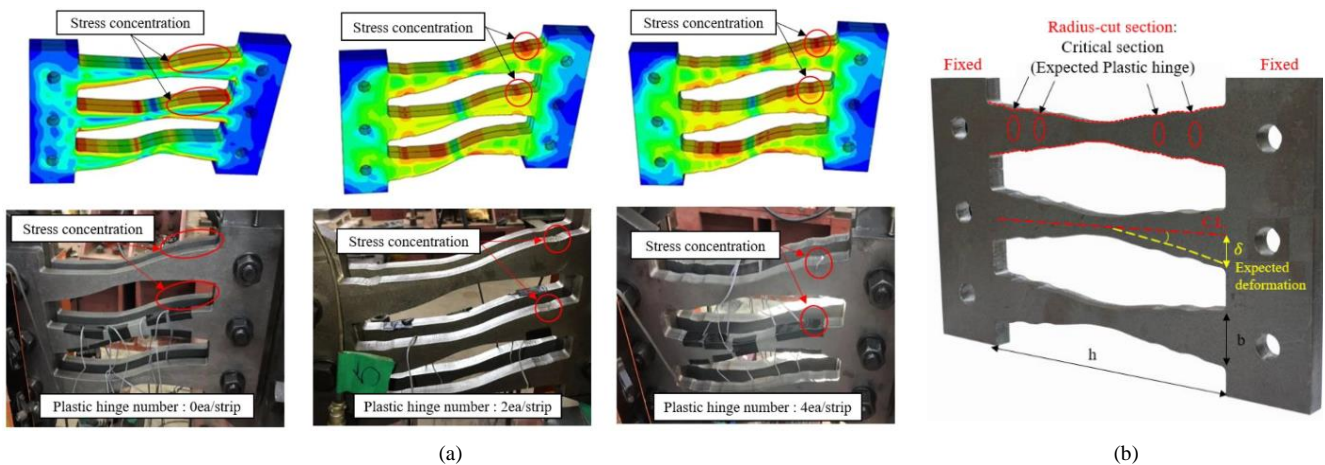


Figure 19. Radius-cut coke-shaped strip damper [101]; (a) Reduced beam section models (plastic hinges number: 0, 2, and 4ea/strip) and (d) An explanation of the strip with four plastic hinges

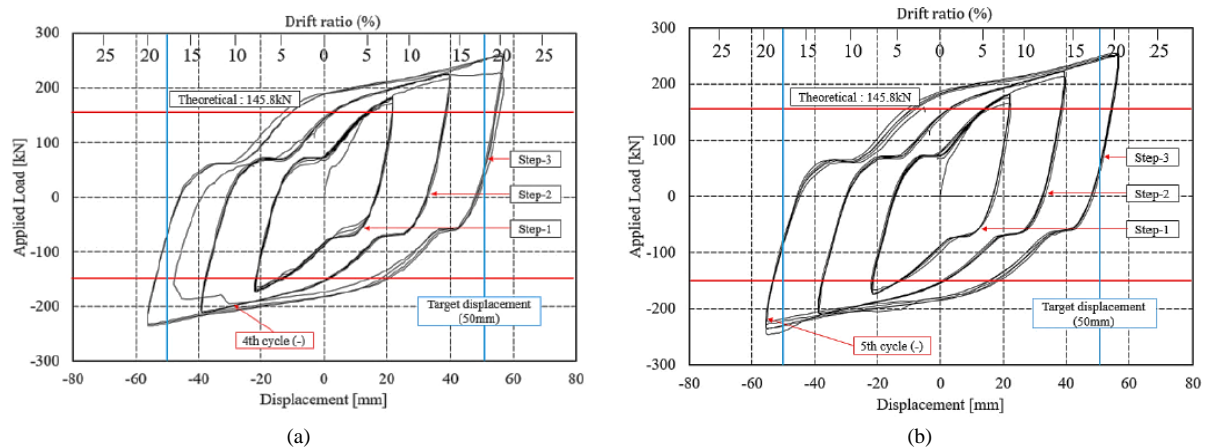


Figure 20. Hysteresis curves of radius-cut coke-shaped strip damper [101]; (a) first specimens (without reduced beam section) and (b) second specimen (with two plastic hinges)

A new double C-section steel slit damper (DCSSD) was introduced to examine the impact of strip aspect ratio, flange thickness, damper length, and steel grade on its resistance and hysteretic behavior [102]. Experimental results revealed that the DCSSD exhibited favorable structural characteristics. All DCSSD specimens displayed an equivalent damping ratio above 0.45, with Q160 exceeding this threshold and achieving a damping ratio exceeding 0.50. Moreover, the DCSSD utilizing Q160 demonstrated a cumulative displacement of approximately 1500 mm. Numerical models were subsequently developed for the test specimens, demonstrating excellent agreement with the experimental findings. He et al. [103] studied the structural performance of steel slit shear panels (SPs) in MRSF structures. The time-history analysis results indicated that installing SPs reduced floor displacement responses but increased floor acceleration responses. Among different SP types, the low-yield SP was the most effective in reducing maximum and residual inter-story drift.

In recent years, Block Slit Dampers (BSDs) have emerged as a promising solution for passive structural control, particularly in high seismicity regions where highly ductile systems like SMRFs are required [104]. BSD devices with secondary hardening in their hysteretic curves have demonstrated the ability to meet performance objectives for flexible steel SMRFs in such regions. Additionally, BSD devices effectively reduce inter-story drift ratios and regulate absolute floor accelerations (AFAs), minimizing damage to non-structural elements. Thus, BSD devices offer a suitable solution for designing and retrofitting flexible steel SMRFs, providing hysteretic behavior and enhanced performance. Two experimental boundary conditions were employed in another study by Oh and Park [105] to examine the performance of this particular damper: i) shear loading alone and ii) combined shear and tensile loading. The combined shear-tensile loading resulted in a butterfly-shaped hysteresis curve for the damper, while shear-only loading produced a parallelogram-shaped curve [105]. The damper's properties are influenced proportionally by adding additional tension, contingent upon the damper's aspect ratio and maximum deformation angle. According to the cyclic hysteresis analysis, the damper's plastic deformation capacity remains similar under both tensile and exclusive shear loading conditions. Furthermore, the energy absorbed up to failure is equal to that observed when the damper is only subjected to shear loading. However, when subjected to additional tensile loading, the damper dissipates a notable amount of unstable energy due to out-of-plane deformation. The damper exhibits lower hysteresis under additional tension than the predicted curve used for evaluating plastic energy based on test results.

Non-buckling slit dampers (NBSDs) integrated into a window-type seismic control system (WSCS) offer a viable solution for developing an effective seismic control system for existing reinforced concrete buildings [106]. Buildings retrofitted with NBSD-WSCS frames demonstrated minimal damage during seismic events, even under the highest recorded seismic intensity in Korea, reaching approximately 300 cm/s^2 , resulting in only minor or moderate damage. Lee et al. [106] successfully developed and validated NBSD-WSCS as an efficient method for seismic retrofitting.

4.1. Summary

According to existing research, the incorporation of steel slit dampers in braced frames has been found to enhance the overall ductility of structures. In particular, using SSDs has demonstrated the ability to achieve an inter-story drift ratio of over 2% when implemented in braced frames. The failure mechanism associated with these dampers typically involves the failure of the strips at their ends. Consequently, optimizing the configuration of these damper strips can enhance their performance and delay fracture. Significantly, the utilization of an optimized configuration not only increases the energy dissipation capacity but also improves fatigue resistance. Optimal-shaped SSDs have the potential to achieve an energy dissipation improvement of over 12%. Comparatively, non-prismatic and hourglass configurations have exhibited greater efficiency than conventional configurations. In terms of the hysteresis curve configuration, it is generally observed that this type of damper shows a parallelogram-shaped curve when subjected to shear loading.

5. Numerical Analyses and Discussion

5.1. Description of Frames and Dampers

The present study is dedicated to conducting a comparative analysis of three test frames. Specifically, one of these frames is a special braced frame without a damper (SBF), while the remaining two frames are equipped with slit dampers.

One of the frames is of slit prismatic damper (FSPD), while the other features a non-prismatic damper (FSNPD). In this study, the damper is affixed to the lower end of the brace, ensuring consistency across all three samples by maintaining meticulous dimensions and sections for the primary structural element within the braced frame. These dimensions include a height of 3.0 meters and a span of 3.5 meters. Subsequently, a comprehensive comparison is carried out, encompassing the evaluation of hysteresis curves, ductility, and dissipated energy among the results of the three numerical analyses. For visual reference, Figure 21 displays the frame used in this research. Additionally, Figure 22(a) and Figure 22(b) provide detailed illustrations of the uniform prismatic and non-prismatic slit dampers utilized in the other frames, respectively. The steel frame elements consist of an HSS steel section of 100×100×6 for the brace, an IPE220 for the beam, and an IPB140 for the column.

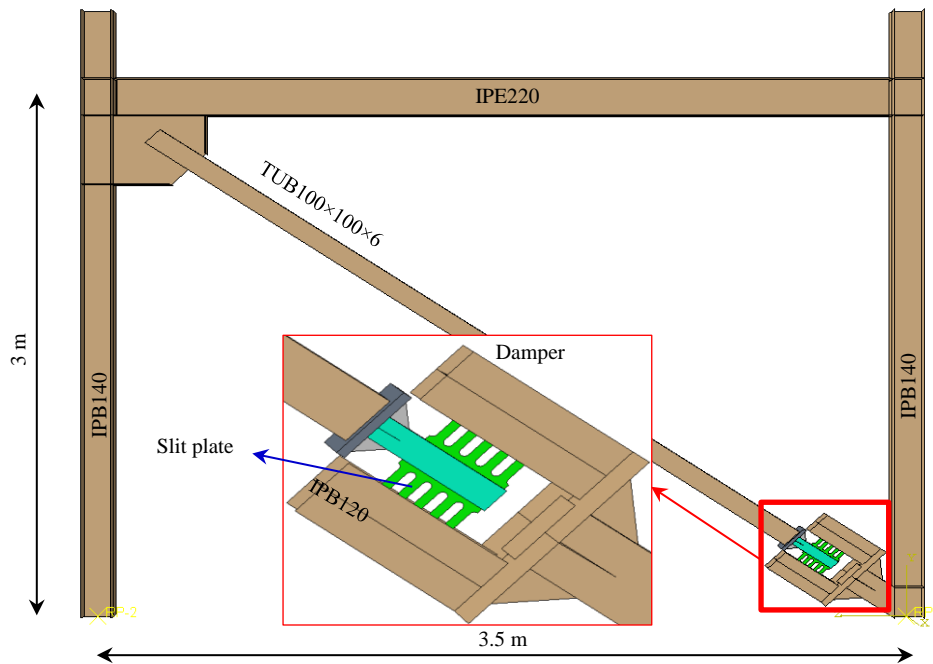


Figure 9. Details of the braced frame, along with the proposed damper

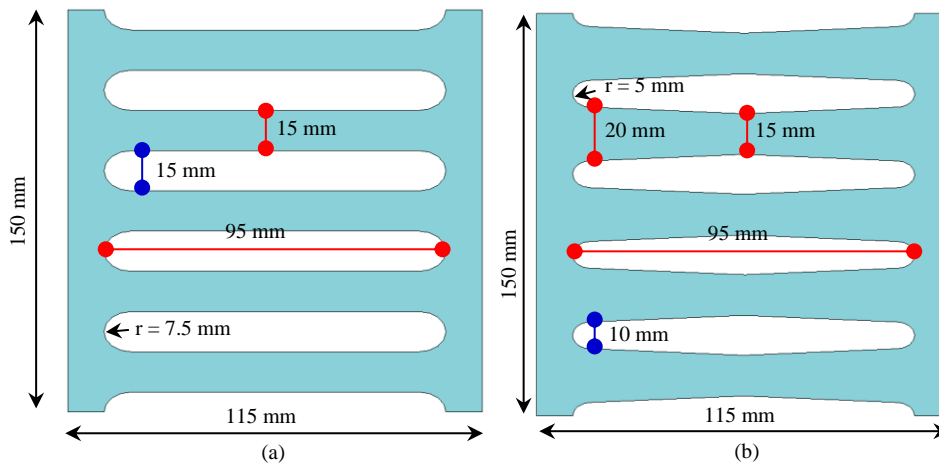


Figure 10. Comparative details of slit dampers: (a) uniform prismatic slit damper and (b) uniform non-prismatic slit damper

5.2. Modeling Techniques

The numerical investigations in this study, which encompassed the analysis of all specimens, accounting for both geometric and material non-linearities, were conducted using the nonlinear finite element (FE) software ABAQUS

[102]. A 4-node doubly curved thick shell element with reduced integration (S4R) was chosen to represent the test specimens accurately. This approach effectively captures the intricate structural behavior under examination.

A sophisticated combined cyclic model, which incorporates both kinematic and isotropic hardening components, was employed to simulate the cyclic response of the material, guided by the Von Mises yield criterion. It is worth noting that this material model has previously undergone validation for its efficacy in replicating the inelastic behavior of steel, as evidenced in references [55, 56]. The FE models were constructed using St37 steel, and the elastic-plastic response of this material was modeled through a comprehensive nonlinear approach that integrates isotropic and kinematic hardening properties. The mechanical properties of the material are systematically outlined in Table 1.

Table 1. Mechanical characteristics for FEA models

Material	F_y (MPa)	F_u (MPa)	E (GPa)	ν
St37	240	370	200	0.3

It is essential to emphasize that the FE modeling framework in this study intentionally excluded considerations of fracture evolution and material degradation. The bases of the specimens were modeled as pinned connections to effectively constrain any degrees of freedom that might result in unintended movements. Out-of-plane deformation was prevented at the upper column ends to mitigate out-of-plane buckling of the frame induced by lateral loads. The mesh size for the dampers was set at 5 mm, while other frame elements were adjusted to approximately 20 mm, as illustrated in Figure 23. The testing protocol for specimen examination adhered to the SAC guidelines [103], as shown in Figure 24. The testing regime was rigorously conducted up to a drift level of 3%.

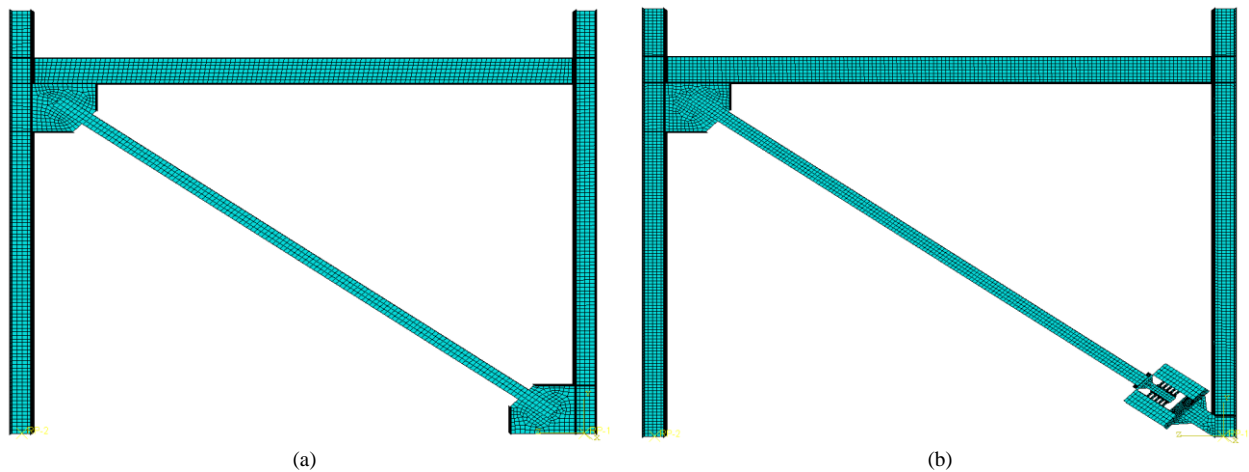


Figure 11. Mesh configuration of the test frames: (a) SBF and (b) FSPD and FSNPD

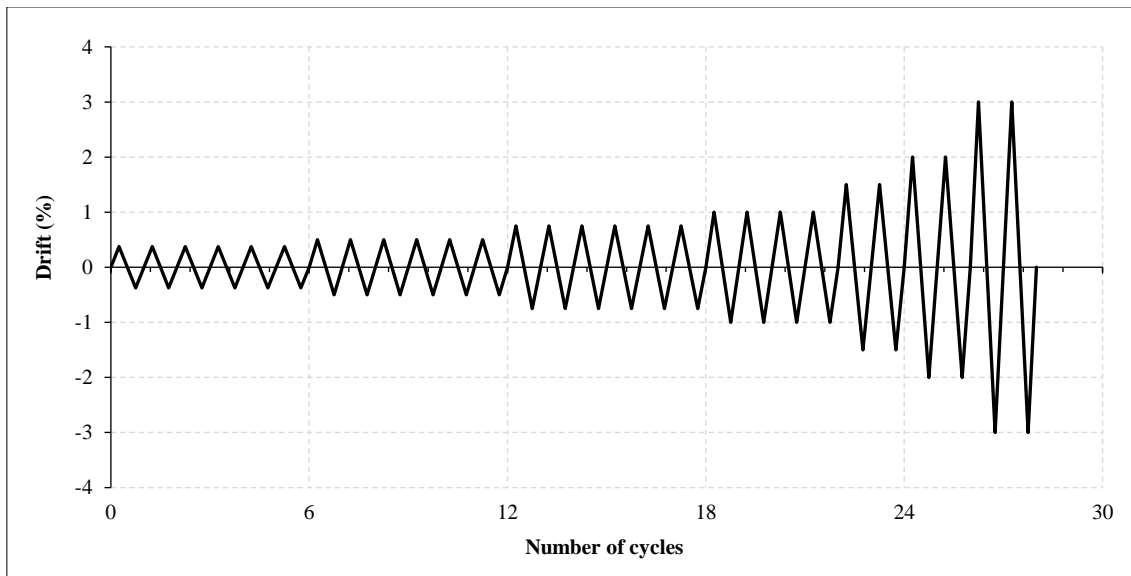


Figure 12. Protocol for cyclic loading

5.3. Results and Discussion

5.3.1. Force-Displacement Relationship

The force-displacement curves derived from finite element (FE) models are illustrated in Figure 25 for three configurations: a frame without steel slit dampers (SSD) and frames equipped with SSD dampers, one encompassing prismatic and the other non-prismatic slit dampers. The analysis indicates that the maximum positive and negative load capacities of the frames with SSDs are closely aligned with those without SSDs. However, a noteworthy distinction emerges in their hysteresis behavior. The frame with no SSD exhibited diminished strength under compressive loads. This reduction is primarily attributed to brace buckling at a peak displacement of 6.7 mm, corresponding to a relative drift of 0.22%. Conversely, frames integrated with SSD devices showcased enhanced hysteresis behavior without any signs of instability. Notably, these frames achieved up to a 3% drift (90 mm) without a concomitant decrease in strength, a significant improvement over the non-damper frames. This finding is consistent with the outcomes reported by Almohammad-albakkar et al. [95, 96], who observed that the cross-braced frames equipped with a steel slit damper achieved a relative drift exceeding 3%. A distinctive butterfly shape, indicative of improved energy dissipation capabilities, characterizes the hysteresis curves for damper-equipped frames. The butterfly-shaped hysteresis curves observed in the braced frame with SSDs closely resemble those documented in the literature for block slit dampers [47]. Further analysis reveals a marked difference between the frames equipped with different types of dampers. Frames with non-prismatic slit dampers exhibited a more pronounced hysteresis curve, especially in the initial cyclic loading phase, while maintaining comparable strength to those with prismatic slit dampers.

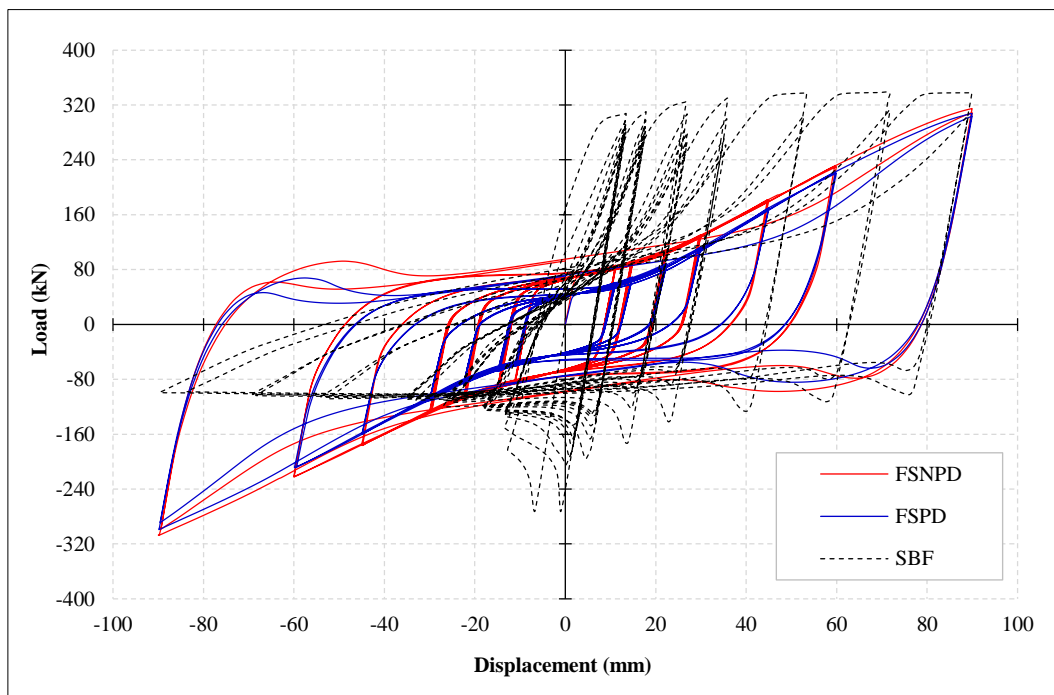


Figure 13. Force-displacement relationship

Table 2 presents a detailed comparative summary of these findings. It shows that the ultimate strength of the frame without a damper (SBF) marginally exceeds that of the frames with SSDs. In the positive phase, at a maximum displacement of 90 mm, the SBF attained a maximum load of 338.3 kN, compared to 307.6 kN and 314.7 kN for frames with prismatic and non-prismatic slit dampers, respectively. On the contrary, during the negative phase, the SBF achieved its highest load of 272.8 kN at a displacement of 6.72 mm, whereas frames FSPD and FSNPD exhibited peak loads around 299.1 kN and 307.2 kN at a displacement of 90 mm, respectively. The table also shows the comparable test results of frames' elastic stiffness and energy dissipation, discussed in the following sections. Furthermore, when comparing the outcomes derived from FSNPD with those of FSPD, it is evident that the non-prismatic shape boosts elastic stiffness by more than 25% compared to the prismatic configuration.

Table 2. Comparison of the ultimate strength, ductility, and energy dissipation of the test frames

Test frames	Ultimate strength (kN)		Elastic stiffness (kN/mm)	Energy dissipation	
	+Pu	-Pu		(kJ)	Ratio with (SBF)
Special braced frame (SBF)	338.27	-272.81	41.39	141.99	1
Frame with slit-prismatic damper (FSPD)	307.62	-299.07	26.55	178.46	1.26
Frame with slit-non-prismatic damper (FSNPD)	314.71	-307.22	33.73	240.17	1.69

In terms of hysteresis behavior, both prismatic and non-prismatic slit dampers exhibit a butterfly-shaped curve, albeit with noticeable differences. The hysteresis curves of non-prismatic slit dampers appear broader, particularly during the initial loading stages. Consequently, non-prismatic slit dampers dissipate energy more effectively compared to prismatic dampers, with the former exhibiting approximately 35% greater dissipation. Regarding ductility, both damper types boast a similar ductility level, around 3%, as per the obtained results. However, it should be noted that according to prior experimental research [85], the use of a non-prismatic slit damper can notably enhance the damper's performance under fatigue.

5.3.2. Distribution of Plastic Strain

Figures 26 and 27 show the distribution of Von Mises stress across the evaluated frames. A noticeable reduction in stress is observed in the frame outfitted with steel slit dampers (SSD) devices, particularly evident at panel zones and gusset plate junctions. In contrast, the frame without SSD devices exhibited stress intensities approaching the material yield threshold, predominantly at the panel zones and the base of columns. This disparity underscores the efficacy of the SSD intervention in mitigating stress concentrations in frame structures subjected to cyclical or dynamic loadings. Additionally, Figures 27 to 29 show that both FSPD and FSNPD exhibit significant strain and stress concentrations at the root of the strips. Specifically, the FSNPD strips exhibit a more uniform stress distribution at their root, contrasting with the variations observed in FSPD. This observation underscores the influence of the non-prismatic shape of the strips on their ability to enhance the damper's performance, particularly in absorbing and dissipating energy.

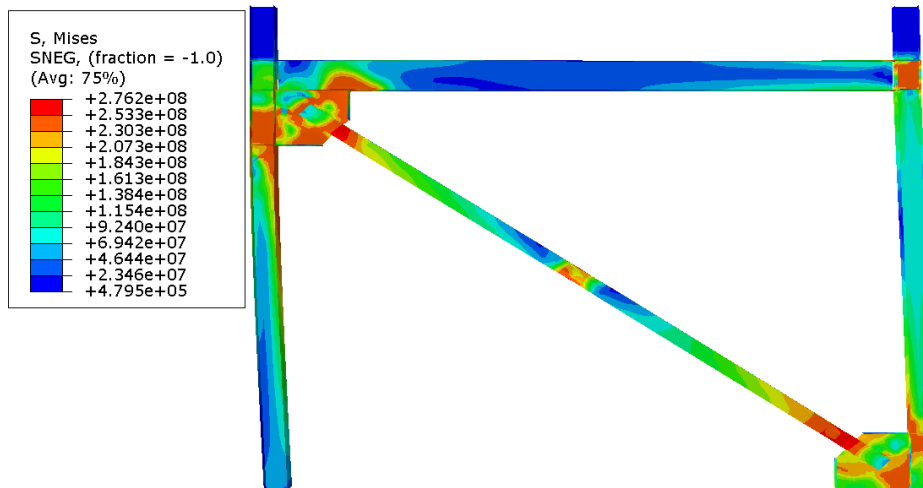


Figure 14. The Von Mises stress distribution for the frame without damper (SBF)

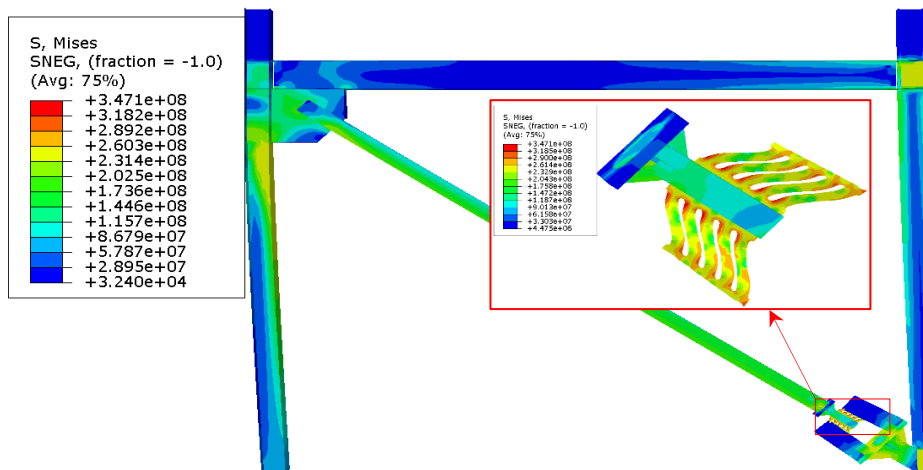


Figure 15. The Von Mises stress distribution for the frame equipped with non-prismatic slit damper (FSNPD)

Further explanation is provided in Figures 28 and 29, which compare the deformation shapes of frames equipped with and without SSD devices under lateral load conditions. The plastic strain is more uniformly distributed across the dampers in the frame incorporating SSD. This phenomenon can be attributed to the inherent design characteristics of the SSD devices, which ensures that the steel strips within the dampers yield preferentially. Consequently, this pre-emptive yielding predicts the emergence of pronounced stress concentrations at other critical junctures within the frame structure.

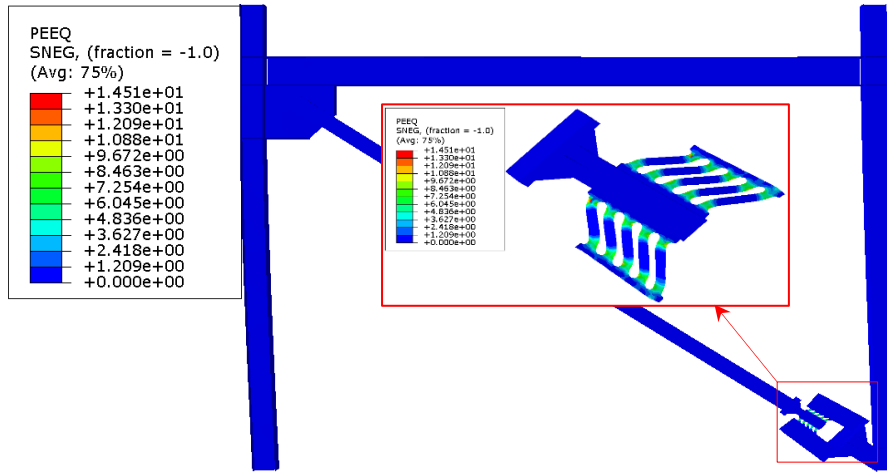


Figure 16. Distribution of equivalent plastic strain (PEEQ) within the slit damper of the prismatic damper (FSPD)

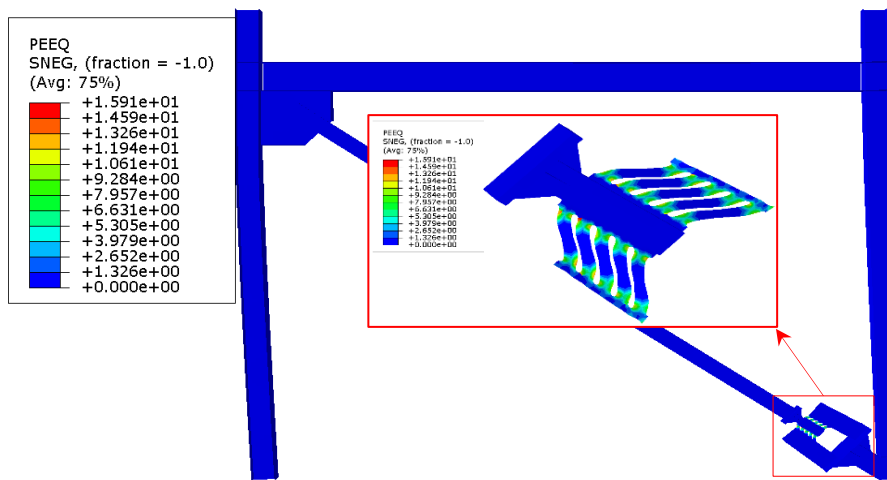


Figure 17. Distribution of equivalent plastic strain (PEEQ) within the slit damper of the non-prismatic damper (FSNPD)

5.3.3. Energy Dissipation Analysis

Figure 30 presents a detailed depiction of the cumulative energy dissipation in the frames. This figure distinctly highlights the enhanced energy dissipation capacity of frames when integrated with a non-prismatic slit damper. Specimen FSNPD demonstrates greater stability and superior energy dissipation capabilities than the other specimens. Complementing this graphical representation, Table 2 provides quantitative insights into the cyclic energy dissipation observed in these frames.

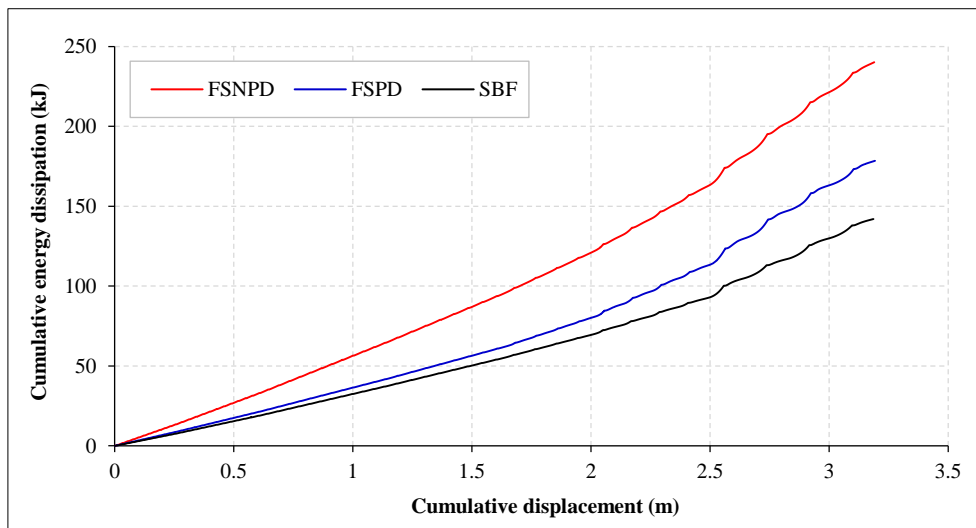


Figure 18. The cumulative energy dissipation of the frames

A notable observation from this data is the disparity in energy dissipation between the braced frame without the slit damper and those outfitted with prismatic and non-prismatic slit dampers. The quantitative analysis reveals an increase in energy dissipation by 26% and 69% for frames with prismatic and non-prismatic slit dampers, respectively. Such findings indicate the substantial impact that damper design can have on the energy dissipation characteristics of frames. Additionally, upon comparing the results obtained from FSNPD with those from FSPD, it becomes evident that the non-prismatic shape enhances energy dissipation by over 35% compared to the prismatic shape. These findings are consistent with those of previous studies on slit dampers in the literature. The previous research revealed that utilizing a tapered shape can enhance energy dissipation by approximately 37% compared to the conventional initial shape in literature [85] and around 12~50% in the literature [86].

5.4. Summary

The results derived from the finite element analysis provide compelling evidence for the efficiency of Steel Slit Damper (SSD) devices in enhancing the cyclic performance of frame structures under lateral loading conditions. These devices, notable for their simplicity, low mass, and cost-effectiveness, demonstrate a significant capacity to attenuate lateral loads. This is evidenced by the force-displacement hysteretic curves generated for the frame equipped with SSD devices, which markedly outperform the bare frame. Notably, the frame incorporating non-prismatic slit dampers exhibited a superior cumulative energy dissipation compared to its counterparts. Quantitatively, the integration of non-prismatic dampers resulted in a 69% increase in the cumulative energy dissipation of the frame, highlighting the potential of these devices in structural engineering applications.

6. Conclusions

This study comprehensively evaluates Steel Slit Dampers (SSDs) in steel-braced frames, focusing on their consistent hysteretic behavior, customizable configurations, and significant enhancement of seismic resilience. Comparative analysis has been conducted on a Special Braced Frame (SBF) without dampers and two other frames, one with prismatic and the other with non-prismatic SSDs dampers. The following can be concluded from the research conducted:

- Slit dampers used in braced steel frames provide significant strength, ductility, and dissipation capabilities, and they provide stable and predictable hysteretic behavior, displaying uniform force resistance in tension and compression.
- SSDs performance can be tailored by their geometry by adjusting the strips' number, dimensions, and configuration. Notably, SSDs with non-prismatic and hourglass shapes exhibit superior characteristics. Damper designs featuring steel strips as elliptical slits demonstrate the highest energy absorption.
- Optimal-shaped non-prismatic SSDs have the potential to achieve an energy dissipation improvement of over 12% compared with conventional non-prismatic dampers. Furthermore, optimized dampers exhibit significantly larger cumulative displacement than conventional SSDs, indicating a higher inelastic deformation capacity.
- The installation of SSDs in braced frames has demonstrated their ability to withstand an inter-story drift ratio of up to 2%. Through experiments and numerical analyses, a non-prismatic damper has been identified as exhibiting greater ductility.
- When subjected to combined shear and tensile loading, SSDs of prismatic and non-prismatic dampers exhibit a butterfly-shaped hysteresis curve, whereas shear-only loading results in a parallelogram-shaped curve.
- In the conducted numerical analysis, it was recognized that the frame outfitted with non-prismatic slit dampers exhibited an improved cumulative energy dissipation, surpassing that of the frame with prismatic configuration. Quantitatively, this enhancement in energy dissipation was calculated to be 69%, signifying a substantial increase attributable to the incorporation of the non-prismatic damper.
- The numerical results further demonstrate an enhancement in the strength during the negative phase of loadings for frames equipped with FSPD and FSNPD.

The findings of this study conclusively demonstrate that the integration of dampers into structural designs significantly improves their capability to withstand high levels of relative drift, thereby enhancing their ductility. This increased ductility significantly reduces the seismic forces exerted on the structure, promoting cost-effective design strategies. Buildings enhanced with damping systems can maintain critical performance standards necessary for immediate occupancy (IO) and life safety (LS) in the aftermath of seismic events.

A key insight from this research is the localization of damage to the dampers, which significantly reduces the economic impact associated with post-earthquake restoration efforts. Consequently, the strategic implementation of damping mechanisms in building design is highlighted as an effective measure for enhancing structural durability and safety in earthquake-prone areas while offering a cost-effective solution for initial construction and subsequent earthquake recovery processes.

6.1. Recommendation and Future Work

The research provides a comprehensive review and numerical analyses of the use of steel slit dampers (SSDs) in braced frames, identifying several critical avenues for future research. These recommendations are pivotal for advancing our understanding of SSDs in seismic-resistant design. However, to enhance the academic rigor and clarity of the recommendations, certain modifications and expansions are suggested:

- It is highly commendable to explore the advantages of using alternative SSD materials for SSDs, such as low mild yield and stainless steel.
- Investigate SSD behavior under low-cycle fatigue, as SSD failures can be attributed to concentrated stress at the strip ends.
- Investigating the use of hybrid systems that combine slit dampers with other types of dampers is an insightful approach.
- Conducting comprehensive research on the behavior of SSDs under various force combinations, including shear force with moment and/or axial force, is essential. Specifying force combinations or scenarios of significant interest, including extreme loading conditions or varying frequency and amplitude, would be advantageous.

The recommendations above would offer a more targeted direction for future investigations.

7. Declarations

7.1. Author Contributions

Conceptualization, Z.A. and M.A.; methodology, Z.A. and M.A.; software, M.A.; validation, Z.A. and M.A.; formal analysis, Z.A. and M.A.; investigation, Z.A. and M.A.; resources, Z.A. and M.A.; data curation, M.A.; writing—original draft preparation, Z.A. and M.A.; writing—review and editing, Z.A. and M.A.; visualization, Z.A. and M.A.; supervision, Z.A.; project administration, Z.A. and M.A.; funding acquisition, Z.A. All authors have read and agreed to the published version of the manuscript.

7.2. Data Availability Statement

The data presented in this study are available on request from the corresponding author.

7.3. Funding

The authors gratefully acknowledge the financial support from the Sustainable Construction Materials & Structural Systems Research Group of the Research Institute for Sciences and Engineering (RISE) at the University of Sharjah.

7.4. Acknowledgements

The authors express their gratitude to the University of Sharjah and the Isfahan University of Technology for granting access to their facilities and for the support provided throughout writing this manuscript.

7.5. Conflicts of Interest

The authors declare no conflict of interest.

8. References

- [1] Meshkat Rouhani, V. R., Zamani Ahar, G., & Saeed Monir, H. (2022). Experimental and numerical study on a new double-walled tuned liquid damper. *International Journal of Engineering*, 35(1), 29–44. doi:10.5829/IJE.2022.35.01A.04.
- [2] Jaisee, S., Yue, F., & Ooi, Y. H. (2021). A state-of-the-art review on passive friction dampers and their applications. *Engineering Structures*, 235, 112022. doi:10.1016/j.engstruct.2021.112022.
- [3] Roustaei, A. M., Gorji Azandariani, M., Safaei Ardakani, M. A., & Shoja, S. (2022). Cyclic behavior of an energy dissipation system with the vertical steel panel flexural-yielding dampers. *Structures*, 45, 629–644. doi:10.1016/j.istruc.2022.09.047.
- [4] Javidan, M.M., & Kim, J. (2020). Steel hysteretic column dampers for seismic retrofit of soft-first-story structures. *Steel and Composite Structures*, (37)3, 259-272. doi:10.12989/scs.2020.37.3.259.
- [5] Zahrai, S. M., & Froozanfar, M. (2019). Improving Seismic Behavior of MRFs by U-shaped Hysteretic Damper Along Diagonal Brace. *International Journal of Steel Structures*, 19(2), 543–558. doi:10.1007/s13296-018-0139-2.
- [6] Javanmardi, A., Ghaedi, K., Ibrahim, Z., Huang, F., & Xu, P. (2020). Development of a new hexagonal honeycomb steel damper. *Archives of Civil and Mechanical Engineering*, 20(2), 1–19. doi:10.1007/s43452-020-00063-9.
- [7] Sahoo, D. R., Singhal, T., Taraithia, S. S., & Saini, A. (2015). Cyclic behavior of shear-and-flexural yielding metallic dampers. *Journal of Constructional Steel Research*, 114, 247–257. doi:10.1016/j.jcsr.2015.08.006.

- [8] Najari Varzaneh, M., & Hosseini, M. (2019). Cyclic Performance and Mechanical Characteristics of the Oval-shaped Damper. *KSCE Journal of Civil Engineering*, 23(11), 4747–4757. doi:10.1007/s12205-019-1382-6.
- [9] Mousavi, H., Sabbagh-Yazdi, S.-R. & Almohammad-albakkar, M., (2021). New mathematical formula for design viscous dampers in Internal and external Scissor-Jack braces, 6th International Conference on Interdisciplinary Researches in Civil Engineering, Architecture and Urban Management in 21st Century; 17 August, 2021, Tehran, Iran.
- [10] Zahrai, S. M., & Cheraghi, A. (2017). Improving cyclic behavior of multi-level pipe damper using infill or slit diaphragm inside inner pipe. *Structural Engineering and Mechanics*, 64(2), 195–204. doi:10.12989/sem.2017.64.2.195.
- [11] Kassem, M. M., Mohamed Nazri, F., & Noroozinejad Farsangi, E. (2020). The seismic vulnerability assessment methodologies: A state-of-the-art review. *Ain Shams Engineering Journal*, 11(4), 849–864. doi:10.1016/j.asej.2020.04.001.
- [12] Ghaedi, K. (2017). *Earthquake Prediction. Earthquakes - Tectonics, Hazard and Risk Mitigation*, IntechOpen, London, United Kingdom. doi:10.5772/65511.
- [13] Javanmardi, A., Ibrahim, Z., Ghaedi, K., Benisi Ghadim, H., & Hanif, M. U. (2019). State-of-the-Art Review of Metallic Dampers: Testing, Development and Implementation. *Archives of Computational Methods in Engineering*, 27(2), 455–478. doi:10.1007/s11831-019-09329-9.
- [14] Boardman, P. R., Wood, B. J., & Carr, A. J. (1983). Union House - a Cross Braced Structure With Energy Dissipators. *Bulletin of the New Zealand National Society for Earthquake Engineering*, 16(2), 83–97.
- [15] Martinez-Romero, E. (1993). Experiences on the use of supplementary energy dissipators on building structures. *Earthquake Spectra*, 9(3), 581–625. doi:10.1193/1.1585731.
- [16] Perry, C. L., Fierro, E. A., Sedarat, H., & Scholl, R. E. (1993). Seismic upgrade in San Francisco using energy dissipation devices. *Earthquake Spectra*, 9(3), 559–579. doi:10.1193/1.1585730.
- [17] Housner, G. W., Bergman, L. A., Caughey, T. K., Chassiakos, A. G., Claus, R. O., Masri, S. F., Skelton, R. E., Soong, T. T., Spencer, B. F., & Yao, J. T. P. (1997). *Structural Control: Past, Present, and Future*. *Journal of Engineering Mechanics*, 123(9), 897–971. doi:10.1061/(asce)0733-9399(1997)123:9(897).
- [18] Soong, T. T., & Spencer, B. F. (2002). Supplemental energy dissipation: State-of-the-art and state-of-the-practice. *Engineering Structures*, 24(3), 243–259. doi:10.1016/S0141-0296(01)00092-X.
- [19] Symans, M. D., Charney, F. A., Whittaker, A. S., Constantinou, M. C., Kircher, C. A., Johnson, M. W., & McNamara, R. J. (2008). Energy Dissipation Systems for Seismic Applications: Current Practice and Recent Developments. *Journal of Structural Engineering*, 134(1), 3–21. doi:10.1061/(asce)0733-9445(2008)134:1(3).
- [20] Saaed, T. E., Nikolakopoulos, G., Jonasson, J. E., & Hedlund, H. (2015). A state-of-the-art review of structural control systems. *JVC/Journal of Vibration and Control*, 21(5), 919–937. doi:10.1177/1077546313478294.
- [21] Li, H., & Huo, L. (2010). Advances in Structural Control in Civil Engineering in China. *Mathematical Problems in Engineering*, 2010, 1–23. doi:10.1155/2010/936081.
- [22] Ghaedi, K., Ibrahim, Z., Adeli, H., & Javanmardi, A. (2017). Invited review: Recent developments in vibration control of building and bridge structures. *Journal of Vibroengineering*, 19(5), 3564–3580. doi:10.21595/jve.2017.18900.
- [23] Korkmaz, S. (2011). A review of active structural control: Challenges for engineering informatics. *Computers and Structures*, 89(23–24), 2113–2132. doi:10.1016/j.compstruc.2011.07.010.
- [24] Dargush, G. F., & Sant, R. S. (2005). Evolutionary aseismic design and retrofit of structures with passive energy dissipation. *Earthquake Engineering & Structural Dynamics*, 34(13), 1601–1626. doi:10.1002/eqe.497.
- [25] Rahimi, F., Aghayari, R., & Samali, B. (2020). Application of tuned mass dampers for structural vibration control: A state-of-the-art review. *Civil Engineering Journal*, 6(8), 1622–1651. doi:10.28991/cej-2020-03091571.
- [26] Fisco, N. R., & Adeli, H. (2011). Smart structures: Part I—Active and semi-active control. *Scientia Iranica*, 18(3), 275–284. doi:10.1016/j.scient.2011.05.034.
- [27] Fisco, N. R., & Adeli, H. (2011). Smart structures: Part II — Hybrid control systems and control strategies. *Scientia Iranica*, 18(3), 285–295. doi:10.1016/j.scient.2011.05.035.
- [28] Behnamfar, F., & Almohammad-albakkar, M. (2023). Development of Steel Yielding Seismic Dampers Used to Improve Seismic Performance of Structures: A Comprehensive Review. *International Journal of Engineering*, 36(4), 746–775. doi:10.5829/ije.2023.36.04a.13.
- [29] Bakhshinezhad, S., & Mohebbi, M. (2020). Multi-objective optimal design of semi-active fluid viscous dampers for nonlinear structures using NSGA-II. *Structures*, 24, 678–689. doi:10.1016/j.istruc.2020.02.004.

- [30] Ghabussi, A., Asgari Marnani, J., & Rohanimanesh, M. S. (2021). Seismic performance assessment of a novel ductile steel braced frame equipped with steel curved damper. *Structures*, 31, 87–97. doi:10.1016/j.istruc.2021.01.073.
- [31] Wang, W., Song, J. liang, Su, S. qing, Cai, H. li, & Zhang, R. fu. (2021). Experimental and numerical studies of an axial tension-compression corrugated steel plate damper. *Thin-Walled Structures*, 163, 107498. doi:10.1016/j.tws.2021.107498.
- [32] Lin, K., Zhou, A., Liu, H., Liu, Y., & Huang, C. (2020). Shear thickening fluid damper and its application to vibration mitigation of stay cable. *Structures*, 26, 214–223. doi:10.1016/j.istruc.2020.04.018.
- [33] Ghanbari, A., Mousavi, H., Almohammad-albakkar, M., & Habibi, M. R. (2022). Seismic Responses of Multi-Storey Structures Equipped with Linear and Nonlinear Viscous Dampers: A Comparison Study. *SSRN Electronic Journal*, 1-22. doi:10.2139/ssrn.4253077.
- [34] Setiawan, A. F., Santoso, A. K., Darmawan, M. F., Adi, A. D., & Ismanti, S. (2023). Nonlinear Analysis for Investigating Seismic Performance of a Spun Pile-Column of Viaduct Structure. *Civil Engineering Journal*, 9(7), 1561-1578. doi:10.28991/CEJ-2023-09-07-02.
- [35] Silwal, B., Michael, R. J., & Ozbulut, O. E. (2015). A superelastic viscous damper for enhanced seismic performance of steel moment frames. *Engineering Structures*, 105, 152-164. doi:10.1016/j.engstruct.2015.10.005.
- [36] Mousavi, H., Sabbagh Yazdi, S. R., & Almohammad-Albakkar, M. (2022). A novel method for efficient design of frame structures equipped with nonlinear viscous dampers by using computational results of cylindrical friction damper. *Australian Journal of Structural Engineering*, 24(1), 50–66. doi:10.1080/13287982.2022.2088055.
- [37] Gjukaj, A., Salihu, F., Muriqi, A., & Cvetanovski, P. (2023). Numerical Behavior of Extended End-Plate Bolted Connection under Monotonic Loading. *HighTech and Innovation Journal*, 4(2), 294-308. doi:10.28991/HIJ-2023-04-02-04.
- [38] Zheng, J., Zhang, C., & Li, A. (2019). Experimental investigation on the mechanical properties of curved metallic plate dampers. *Applied Sciences*, 10(1), 269. doi:10.3390/app10010269.
- [39] Chen, S. J., & Chang, C. C. (2012). Experimental study of low yield point steel gusset plate connections. *Thin-Walled Structures*, 57, 62–69. doi:10.1016/j.tws.2012.03.014.
- [40] Milanchian, R., & Hosseini, M. (2020). Torsional response reduction of plan-asymmetric vertical seismic isolation by appropriate distribution of viscous and viscoelastic dampers. *Structures*, 27, 962–974. doi:10.1016/j.istruc.2020.07.009.
- [41] Xiao, Y., Zhou, Y., & Huang, Z. (2021). Efficient direct displacement-based seismic design approach for structures with viscoelastic dampers. *Structures*, 29, 1699–1708. doi:10.1016/j.istruc.2020.12.067.
- [42] Abdul Aziz, M., Muhtasim, S., & Ahammed, R. (2022). State-of-the-art recent developments of large magnetorheological (MR) dampers: a review. *Korea Australia Rheology Journal*, 34(2), 105–136. doi:10.1007/s13367-022-00021-2.
- [43] Saravanan, M., Goswami, R., & Palani, G. S. (2018). Replaceable Fuses in Earthquake Resistant Steel Structures: A Review. *International Journal of Steel Structures*, 18(3), 868–879. doi:10.1007/s13296-018-0035-9.
- [44] Chen, S. J., & Jhang, C. (2006). Cyclic behavior of low yield point steel shear walls. *Thin-Walled Structures*, 44(7), 730–738. doi:10.1016/j.tws.2006.08.002.
- [45] Ayyash, A. jbury N. A., & Hejazi, F. (2023). Development of hybrid performance-based optimization algorithm for structures equipped with vibration damper devices. *Archives of Civil and Mechanical Engineering*, 23(2), 123. doi:10.1007/s43452-023-00665-z.
- [46] Ayyash, N., & Hejazi, F. (2022). Development of hybrid optimization algorithm for structures furnished with seismic damper devices using the particle swarm optimization method and gravitational search algorithm. *Earthquake Engineering and Engineering Vibration*, 21(2), 455–474. doi:10.1007/s11803-022-2088-1.
- [47] Ahmadi Amiri, H., Najafabadi, E. P., & Estekanchi, H. E. (2018). Experimental and analytical study of Block Slit Damper. *Journal of Constructional Steel Research*, 141, 167–178. doi:10.1016/j.jcsr.2017.11.006.
- [48] Dargush, G., & Soong, T. (1997). Passive Energy Dissipation and Active Control. *Handbook of Structural Engineering*, Second Edition, 1-28.
- [49] Christopoulos, C., & Filiatrault, A. (2006). Principles of passive supplemental damping and seismic. IUSS Press, Pavia, Italy.
- [50] Fukumoto, T. (1989). A Study on steel Damper with Honeycomb Shaped-Openings. Annual Meeting (Summaries of AIJ), Architectural Institute of Japan, Tokyo, Japan.
- [51] Naoki, T. (1991). A study on Steel Plate D. with Honeycomb-s. Openings s. to Low Cycle F. AIJ-37, Architectural Institute of Japan, Tokyo, Japan.
- [52] Wada, A., Huang, Y. H., Yamada, T., Ono, Y., Sugiyama, S., Baba, M., & Miyabara, T. (1997). Actual size and real time speed tests for hysteretic steel damper. *Proceedings of Stessa*, 97, 778–785.

- [53] Amadeo, B. C., OH, S. H., & Akiyama, H. (1998). Ultimate Energy Absorption Capacity of Slit-Type Steel Plates Subjected To Shear Deformations. *Journal of Structural and Construction Engineering (Transactions of AIJ)*, 63(503), 139–147. doi:10.3130/aijs.63.139_1.
- [54] Javidan, M. M., & Kim, J. (2024). An experimental study on a steel multi-slit damper for seismic retrofit of soft-first story structures. *Steel and Composite Structures*, 50(6), 721–734. doi:10.12989/scs.2024.50.6.721.
- [55] Srisuwan, T., & Yooprasertchai, E. (2024). Effects of unbonded prestressing steel tendons and slit dampers on the seismic behavior of precast concrete beam-column joints. *Structures*, 59. doi:10.1016/j.istruc.2023.105721.
- [56] Payawal, J. M. G., & Kim, D. K. (2023). Evaluation of the Seismic Performance of Single-Plate Metallic Slit Dampers Using Experimental and Numerical Data. *Buildings*, 13(9), 2188. doi:10.3390/buildings13092188.
- [57] Lee, C. H., Ju, Y. K., Min, J. K., Lho, S. H., & Kim, S. D. (2015). Non-uniform steel strip dampers subjected to cyclic loadings. *Engineering Structures*, 99, 192–204. doi:10.1016/j.engstruct.2015.04.052.
- [58] González-Sanz, G., Escolano-Margarit, D., & Benavent-Climent, A. (2020). A new stainless-steel tube-in-tube damper for seismic protection of structures. *Applied Sciences*, 10(4), 1410. doi:10.3390/app10041410.
- [59] Zheng, J., Li, A., & Guo, T. (2015). Analytical and experimental study on mild steel dampers with non-uniform vertical slits. *Earthquake Engineering and Engineering Vibration*, 14(1), 111–123. doi:10.1007/s11803-015-0010-9.
- [60] Oh, S. H. (1998). *Seismic Design of Energy Dissipating Multi-Story Frame with Flexible-Stiff Mixed Type Connection*, Ph.D. Thesis, Tokyo University, Japan.
- [61] Chan, R. W. K., & Albermani, F. (2008). Experimental study of steel slit damper for passive energy dissipation. *Engineering Structures*, 30(4), 1058–1066. doi:10.1016/j.engstruct.2007.07.005.
- [62] Saffari, H., Hedayat, A. A., & Nejad, M. P. (2013). Post-Northridge connections with slit dampers to enhance strength and ductility. *Journal of Constructional Steel Research*, 80, 138–152. doi:10.1016/j.jcsr.2012.09.023.
- [63] Oh, S. H., Kim, Y. J., & Ryu, H. S. (2009). Seismic performance of steel structures with slit dampers. *Engineering Structures*, 31(9), 1997–2008. doi:10.1016/j.engstruct.2009.03.003.
- [64] Karavasilis, T. L., Kerawala, S., & Hale, E. (2012). Hysteretic model for steel energy dissipation devices and evaluation of a minimal-damage seismic design approach for steel buildings. *Journal of Constructional Steel Research*, 70, 358–367. doi:10.1016/j.jcsr.2011.10.010.
- [65] Hedayat, A. A. (2015). Prediction of the force displacement capacity boundary of an unbuckled steel slit damper. *Journal of Constructional Steel Research*, 114, 30–50. doi:10.1016/j.jcsr.2015.07.003.
- [66] Askariani, S. S., Garivani, S., & Aghakouchak, A. A. (2020). Application of slit link beam in eccentrically braced frames. *Journal of Constructional Steel Research*, 170, 106094. doi:10.1016/j.jcsr.2020.106094.
- [67] Roeder, C. W., & Popov, E. P. (1978). Eccentrically Braced Steel Frames for Earthquakes. *Journal of the Structural Division (ASCE)*, 104(3), 391–412. doi:10.1061/jsdeag.0004875.
- [68] Bastami, M., & Ahmady Jazany, R. (2018). Development of Eccentrically Interconnected Braced Frame (EIC-BF) for seismic regions. *Thin-Walled Structures*, 131, 451–463. doi:10.1016/j.tws.2018.07.021.
- [69] Johnson S.M. (2005). *Improved seismic performance of special concentrically braced frames*. Master Thesis, University of Washington., Seattle, United States.
- [70] Metelli, G. (2013). Theoretical and experimental study on the cyclic behaviour of X braced steel frames. *Engineering Structures*, 46, 763–773. doi:10.1016/j.engstruct.2012.08.021.
- [71] Jazany, R. A., Hajirasouliha, I., & Farshchi, H. (2013). Influence of masonry infill on the seismic performance of concentrically braced frames. *Journal of Constructional Steel Research*, 88, 150–163. doi:10.1016/j.jcsr.2013.05.009.
- [72] Tremblay, R. (2001). Seismic behavior and design of concentrically braced steel frames. *Engineering Journal*, 38(3), 148–166. doi:10.62913/engj.v38i3.761.
- [73] Tremblay, R. (2002). Inelastic seismic response of steel bracing members. *Journal of Constructional Steel Research*, 58(5–8), 665–701. doi:10.1016/S0143-974X(01)00104-3.
- [74] Lumpkin, E. J., Hsiao, P. C., Roeder, C. W., Lehman, D. E., Tsai, C. Y., Wu, A. C., Wei, C. Y., & Tsai, K. C. (2012). Investigation of the seismic response of three-story special concentrically braced frames. *Journal of Constructional Steel Research*, 77, 131–144. doi:10.1016/j.jcsr.2012.04.003.
- [75] Karzad, A. S., Al-Sadoon, Z. A., Sagheer, A., & AlHamaydeh, M. (2022). Experimental and Nonlinear Finite Element Analysis Data for an Innovative Buckling Restrained Bracing System to Rehabilitate Seismically Deficient Structures. *Data*, 7(12), 171. doi:10.3390/data7120171.

- [76] Rafi, M. M., Lodi, S. H., Al-Sadoon, Z. A., Saatcioglu, M., & Palermo, D. (2022). Experimental Investigation of Dynamic Behavior of RC Frame Strengthened with Buckling-Restrained Bracing. *Journal of Structural Engineering*, 148(7), 4022076. doi:10.1061/(asce)st.1943-541x.0003371.
- [77] Rafi, M. M., Lodi, S. H., Al-Sadoon, Z. A., Saatcioglu, M., & Palermo, D. (2021). Shake-table testing of deficient reinforced concrete frame retrofitted with buckling restrained brace. *ACI Structural Journal*, 118(3), 161–173. doi:10.14359/51729351.
- [78] Al-Sadoon, Z. A., Saboor Karzad, A., Sagheer, A., & AlHamaydeh, M. (2022). Replaceable fuse buckling-restrained brace (BRB): Experimental cyclic qualification testing and NLFEA modeling. *Structures*, 39, 997–1015. doi:10.1016/j.istruc.2022.03.081.
- [79] Al-Sadoon, Z. A., Saatcioglu, M., & Palermo, D. (2020). New Buckling-Restrained Brace for Seismically Deficient Reinforced Concrete Frames. *Journal of Structural Engineering*, 146(6), 4020082. doi:10.1061/(asce)st.1943-541x.0002439.
- [80] Bastami, M., & Ahmady Jazany, R. (2019). Development of centrally fused braced frame (CFBF) for seismic regions. *Soil Dynamics and Earthquake Engineering*, 127, 105856. doi:10.1016/j.soildyn.2019.105856.
- [81] Yoo, J.-H., Roeder, C. W., & Lehman, D. E. (2008). Analytical Performance Simulation of Special Concentrically Braced Frames. *Journal of Structural Engineering*, 134(6), 881–889. doi:10.1061/(asce)0733-9445(2008)134:6(881).
- [82] Boostani, M., Rezaifar, O., & Gholhaki, M. (2018). Introduction and seismic performance investigation of the proposed lateral bracing system called “OGrid.” *Archives of Civil and Mechanical Engineering*, 18(4), 1024–1041. doi:10.1016/j.acme.2018.02.003.
- [83] Lee, H. M., Oh, H. S., Huh, C., Oh, S. Y., Yoon, H. M., & Moon, S. T. (2002). Ultimate Energy Absorption Capacity of Steel Plate Slit Dampers Subjected to Shear Force. *Steel Structures*, 12(2), 71–79.
- [84] Benavent-Climent, A. (2010). A brace-type seismic damper based on yielding the walls of hollow structural sections. *Engineering Structures*, 32(4), 1113–1122. doi:10.1016/j.engstruct.2009.12.037.
- [85] Ghabraie, K., Chan, R., Huang, X., & Xie, Y. M. (2010). Shape optimization of metallic yielding devices for passive mitigation of seismic energy. *Engineering Structures*, 32(8), 2258–2267. doi:10.1016/j.engstruct.2010.03.028.
- [86] Aminzadeh, M., Kazemi, H. S., & Tavakkoli, S. M. (2020). A numerical study on optimum shape of steel slit dampers. *Advances in Structural Engineering*, 23(14), 2967–2981. doi:10.1177/1369433220927281.
- [87] Tagawa, H., Yamanishi, T., Takaki, A., & Chan, R. W. K. (2016). Cyclic behavior of seesaw energy dissipation system with steel slit dampers. *Journal of Constructional Steel Research*, 117, 24–34. doi:10.1016/j.jcsr.2015.09.014.
- [88] Katal Mohseni, P., Zahedi-khameneh, A., & Naeemifar, O. (2020). Study of the Effect of Geometric Parameters of Steel Block Slit Dampers on Energy Absorption. *International Journal of Steel Structures*, 20(3), 1069–1079. doi:10.1007/s13296-020-00343-3.
- [89] Kim, J. (2019). Development of seismic retrofit devices for building structures. *International Journal of High-Rise Buildings*, 8(3), 221–227. doi:10.21022/IJHRB.2019.8.3.221.
- [90] Guo, W., Ma, C., Yu, Y., Bu, D., & Zeng, C. (2020). Performance and optimum design of replaceable steel strips in an innovative metallic damper. *Engineering Structures*, 205, 110118. doi:10.1016/j.engstruct.2019.110118.
- [91] Askariani, S. S., & Garivani, S. (2020). Introducing and numerical study of a new brace-type slit damper. *Structures*, 27, 702–717. doi:10.1016/j.istruc.2020.06.019.
- [92] Zhao, B., Lu, B., Zeng, X., & Gu, Q. (2021). Experimental and numerical study of hysteretic performance of new brace type damper. *Journal of Constructional Steel Research*, 183, 106717. doi:10.1016/j.jcsr.2021.106717.
- [93] Javidan, M. M., Nasab, M. S. E., & Kim, J. (2021). Full-scale tests of two-story RC frames retrofitted with steel plate multi-slit dampers. *Steel and Composite Structures*, 39(5), 645–664. doi:10.12989/scs.2021.39.5.645.
- [94] Benavent-Climent, A., Escolano-Margarit, D., Arcos-Espada, J., & Ponce-Parra, H. (2021). New metallic damper with multiphase behavior for seismic protection of structures. *Metals*, 11(2), 1–30. doi:10.3390/met11020183.
- [95] Almohammad-Albakkar, M., & Behnamfar, F. (2022). Numerical investigation of grooved gusset plate damper for using in cross-braced frames. *Journal of Constructional Steel Research*, 196, 107434. doi:10.1016/j.jcsr.2022.107434.
- [96] Almohammad-albakkar, M., Behnamfar, F., & Ataei, A. (2024). Experimental and numerical study of grooved gusset plate damper for cross-braced frames. *Journal of Constructional Steel Research*, 216, 108611. doi:10.1016/j.jcsr.2024.108611.
- [97] Almohammad-albakkar M. and Behnamfar F., (2023). Seismic Performance Assessment of Cross-Braced Steel Frame Equipped with New Damper, 13th International Congress on Civil Engineering, 9-11 May, 2023, Tehran, Iran.
- [98] Heyrani Moghaddam, S., & Shoostari, A. (2023). Numerical and experimental investigation on seismic performance of proposed steel slit dampers. *Journal of Constructional Steel Research*, 200, 107646. doi:10.1016/j.jcsr.2022.107646.

- [99] Hui, C., Zhou, Z., Li, Y., Jiao, Y., & Hai, R. (2022). Quasi-static cyclic loading experiment and analysis of double-side slotted steel tube shear damper. *Archives of Civil and Mechanical Engineering*, 23(1), 45. doi:10.1007/s43452-022-00581-8.
- [100] Kang, H., Adane, M., Chun, S., & Kim, J. (2022). Development of a seismic retrofit system made of steel frame with vertical slits Development of a seismic retrofit system made of steel frame with vertical slits. *Steel and Composite Structures*, 44(2), 269–280.
- [101] Bae, J., Lee, C. H., Park, M., Alemayehu, R. W., Ryu, J., Kim, Y., & Ju, Y. K. (2020). Cyclic loading performance of radius-cut double coke-shaped strip dampers. *Materials*, 13(18), 3920. doi:10.3390/MA13183920.
- [102] Zhou, X., Tan, Y., Ke, K., Yam, M. C. H., Zhang, H., & Xu, J. (2023). An experimental and numerical study of brace-type long double C-section steel slit dampers. *Journal of Building Engineering*, 64, 105555. doi:10.1016/j.job.2022.105555.
- [103] He, L., Sun, X., Bu, H., & Tang, Z. (2022). Seismic Performance of MRSF Structures Damped with Steel Slit Shear Panels. *International Journal of Structural Stability and Dynamics*, 22(03n04), 2240013. doi:10.1142/s0219455422400132.
- [104] Ahmadie Amiri, H., Pournamazian Najafabadi, E., Esmailpur Estekanchi, H., & Ozbakkaloglu, T. (2020). Performance-based seismic design and assessment of low-rise steel special moment resisting frames with block slit dampers using endurance time method. *Engineering Structures*, 224, 110955. doi:10.1016/j.engstruct.2020.110955.
- [105] Oh, S. H., & Park, H. Y. (2022). Experimental study on seismic performance of steel slit damper under additional tensile load. *Journal of Building Engineering*, 50, 104110. doi:10.1016/j.job.2022.104110.
- [106] Lee, K. S., Lee, B. G., & Jung, J. S. (2022). Seismic Strengthening of R/C Buildings Retrofitted by New Window-Type System Using Non-Buckling Slit Dampers Examined via Pseudo-Dynamic Testing and Nonlinear Dynamic Analysis. *Applied Sciences*, 12(3), 1220. doi:10.3390/app12031220.



Evaluating Recycled PET as an Alternative Material for the Construction Sector Towards Sustainability

Omar Albatayneh ¹, Mohammad Nadeem Akhtar ^{2*}

¹ Civil and Environmental Engineering Department, School of Natural Resources Engineering and Management (SNREM), German Jordanian University (GJU), Amman 11180, Jordan.

² Department of Civil Engineering, Fahad Bin Sultan University, Tabuk, Saudi Arabia.

Received 31 December 2023; Revised 10 March 2024; Accepted 16 March 2024; Published 01 April 2024

Abstract

Addressing the environmental threat of Polyethylene Terephthalate (PET) waste is critical for sustainable development. Despite PET's prevalence in everyday products, its improper disposal endangers environmental health. This study targets a pivotal gap in current research. PET waste's potential as a sustainable building material will be thoroughly evaluated, focusing on whether recycling PET waste is feasible. In the construction industry, it can be a substitute for natural sand and an additive in cement. This study contributes to a dual-purpose solution: mitigating environmental pollution and innovating in construction material science. The systematic literature review (SLR) delves into existing studies, focusing on PET's impact on concrete properties when substituting natural sand at ratios of 5% to 20% and as a cement additive at 0.5% to 2% by weight. The findings revealed that up to a 10% PET replacement enhances compressive strength, highlighting a sustainable pathway for construction practices. However, replacements above 10% show a reduction in strength, indicating an optimal substitution threshold. Moreover, incorporating PET additives at 1% by cement weight optimizes flexural strength, underscoring the material's viability in enhancing structural integrity. This study sheds light on PET waste's application in reducing environmental impact and proposes a viable, eco-friendly alternative for construction materials. The recommendation for further research underscores the necessity to refine PET's application in construction, aiming to bridge the knowledge gap and encourage sustainable future innovations.

Keywords: PET Waste Utilization; Eco-friendly Building Materials; PET in Civil Engineering; Recycled Plastic Aggregate Innovation.

1. Introduction

For more than ten decades, rapid growth in the world population can be seen, leading to a very intense need for natural resources being utilized by industrial enterprises and the urban expansion of developing countries. For this reason, a massive burden on natural materials causes natural disasters. Recycling waste products has a lot of benefits for the sustainable development introduced by the Rio Earth Summit [1–3]. It helps reduce pollution, which can be induced in water, air, and soil. It helps save electricity and minimizes solid waste and greenhouse gases. Therefore, it is imperative to comprehend the factors that could positively impact the construction industry, particularly in relation to the utilization of waste and recycled materials [4–7]. This field has become an essential subject of study and has been explored by researchers. It primarily focuses on strategies for effectively utilizing suitable waste materials to enhance sustainability and the economy by emphasizing recycling and reutilization [8–11]. Within the construction industry, materials frequently recycled comprise crumb rubber, silica fumes, roofing shingles, palm fruit husks, citrus rinds, kiln dust cement, asphalt, flyash, foundry sand, glass, slag, and recycled aggregates derived from dismantled concrete infrastructures [12–15]. For this review article, PET waste as a substitute for natural construction material is selected for systematic review.

* Corresponding author: nakhtar@fbsu.edu.sa

 <http://dx.doi.org/10.28991/CEJ-2024-010-04-020>



© 2024 by the authors. Licensee C.E.J, Tehran, Iran. This article is an open access article distributed under the terms and conditions of the Creative Commons Attribution (CC-BY) license (<http://creativecommons.org/licenses/by/4.0/>).

Only the European Union (EU) recorded the data on plastic waste production and allowed access to the public, excluding Asian countries. The unprecedented worldwide rise of plastic output indicates its excessive usage and manhandling. If improperly handled, the end product of plastic waste is consumed in landfills, oceans, and seas. Estimations suggest that approximately 30% of total solid waste disposal could be reduced upon achieving an optimal solution for plastic waste management. Consequently, there is an urgent requirement for a sustainable strategy for the consumption and processing of plastic waste. The plastic material in concrete will significantly contribute towards more sustainable and holistic building materials for the construction industry. The long-term processing and environmental consequences of plastic residues in concrete are recommended for further study after their service life [16–19]. As presented in the overview by Padgelwar et al. [20], India ranks 5th globally for plastic product consumption. About 38 kg/person, followed by Brazil, China, Europe, and the USA, which have the highest, 109 kg/person. Some studies have shown plastic is used to replace aggregates in concrete, replace plastic fiber aggregate in concrete, and use plastic materials to construct flexible pavement. Furthermore, a comprehensive analysis concluded that polyethylene and PET are the most prevalent among the diverse forms of plastic waste [21–23].

The recyclability and potential of PET waste as a sustainable construction material are attracting significant research interest. PET waste's massive availability is estimated to be nearly 400 metric tons annually [21]. Due to its massive demand in the packaging industry and mineral water bottles, its disposal has become a serious matter of concern. As its consumption has grown faster, the waste landfill area required for PET products' disposal is also increasing rapidly [20, 21]. The production and disposal of plastic in large amounts have created a colossal level. Hence, recycling is a critical matter that must be resolved shortly. In the past few years, we have come across many recycling techniques that are financially and technically feasible while keeping ecological health under consideration [24, 25]. Many research studies studying lightweight concrete have successfully examined PET waste products' impact as aggregate particles [26–28].

The consideration of recycled plastic as input for the construction and plastic recycling industries has become significant. Considering the numerous benefits of recycling plastic, the most substantial one is maintaining ecological balance, which blesses nature with immense relief. As a researcher, it becomes a huge responsibility to emerge with such techniques and ideas for recycling that are cost-effective, reliable, practically feasible, and durable for a longer period of time.

While there is considerable research on PET recycling methods, such as mechanical recycling and chemical depolymerization, less attention has been devoted to the integration of PET waste in construction materials. Studies have focused on the potential of various waste materials in construction to promote sustainability; however, the utilization of PET waste, particularly in concrete, remains underexplored. This gap highlights a critical area for investigation, given the dual benefits of reducing environmental pollution and addressing the construction industry's demand for sustainable materials.

In light of the identified gaps, this study explores the feasibility of using recycled PET waste as an alternative construction material. Specifically, it investigates the mechanical properties of concrete integrated with PET aggregates, offering insights into the potential of PET waste to replace conventional materials. This research contributes to the body of knowledge by comprehensively evaluating PET's viability in construction applications by conducting a systematic review coupled with experimental analysis. Moreover, it proposes a sustainable pathway for managing PET waste, aligning with global sustainability goals.

2. Research Methodology

This research was meticulously planned to explore the potential of PET waste as an alternative to natural construction materials. The study began with a comprehensive literature review to identify gaps in the current understanding and opportunities for innovation in using PET waste in construction. The objective was to assess PET waste's environmental impact and utility as a sustainable construction resource. Following this, a systematic methodology was set to evaluate the performance of PET waste when used as a substitute for natural sand and as an additive in cement in various proportions. This approach allowed for a controlled investigation into the effects of PET waste on concrete properties, enabling us to draw comparisons and identify optimal configurations for its use in the construction industry.

The method employed for this critical article is the Systematic Literature Review (SLR) approach, formulated by Moher et al. [29]. This methodological approach is depicted in Figure 1, which outlines the data selection procedure. The research methodology involved an extensive search across multiple databases (e.g., Web of Science, Science Direct, Google Scholar, and Scopus) alongside various published online technical reports. This search was broad-ranging, encompassing a wide array of relevant references, all of which were considered for inclusion in this study. Key subject terms such as "polyethylene terephthalate (PET)," "recycled plastic waste," "PET waste in concrete," "PET waste as construction material," and "replacement of PET in concrete as sand" were systematically employed in the SLR to ensure a thorough investigation of relevant literature.

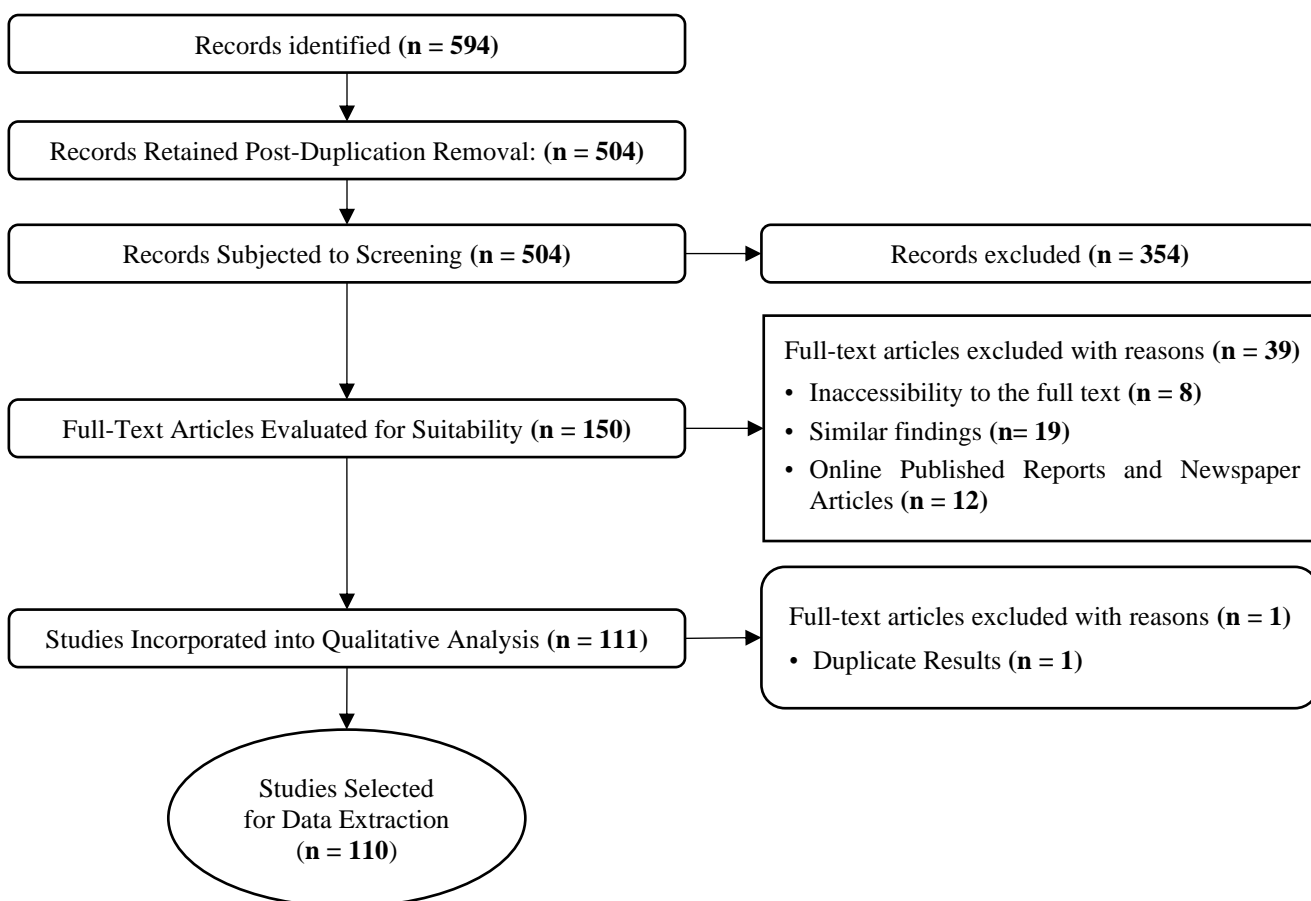


Figure 1. Methodology for the data selection

The search focused on construction materials based on PET, particularly those replacing natural substances. Any articles from irrelevant sources were excluded from consideration, leading to the removal of 354 items. For this review, 110 publications were carefully chosen for an in-depth subject matter analysis. This study incorporates data from various sources, including research papers, reports (practical and theoretical), comprehensive reviews, and proceedings from relevant conferences.

The data collected from the literature review was systematically analyzed to draw meaningful insights into using recycled PET waste in construction. Additionally, a meta-analysis of the gathered literature was performed to contextualize our experimental results within the broader scope of existing research.

3. PET as a Non-Bio-Degradable Waste

The escalation in global population, pervasive urbanization, and enhanced living standards, accompanied by the extensive utilization of polymers, have led to the generation of non-biodegradable polymeric waste. This phenomenon poses a persistent global environmental challenge. Concurrently, the escalating energy demands of modern society represent a significant concern. In contemporary times, polymeric materials are integral to everyday life, attributed to their broad spectrum of applications across diverse sectors. Consequently, the management of polymer waste and its global production have witnessed a substantial increase in recent decades. Notably, these polymeric wastes are more voluminous than other organic residues and are characterized by their non-degradable nature. Therefore, the accumulation of debris in landfills contributes to environmental hazards, and massive space consumption may lead to the continuous demand for this non-biodegradable waste [30-33]. Polymeric waste materials predominantly consist of a composite of various polymers, including but not limited to Polyethylene Terephthalate (PET), High-Density Polyethylene (HDPE), Low-Density Polyethylene (LDPE), Polypropylene (PP), Polystyrene (PS), Polyvinyl Chloride (PVC), and Polyamide (PA) [34-37].

In academic literature, Polyethylene Terephthalate (PET) is recognized by commercial trade names such as Decron, Mylar, Recron, and Terylene. It is characterized by a notable crystalline melting point of approximately 260°C. The molecular structure of PET contributes to its increased mechanical strength, fatigue resistance, particularly efficacious till 150-170°C, and substantial toughness. Additionally, PET exhibits commendable resistance to chemicals, solvents, and hydrolysis. Their exceptional crease and abrasion resistance distinguish the fibers derived from PET.

Furthermore, these fibers can undergo treatment with specific cross-linking resins, enhancing their durability with permanent wear and wash characteristics [38–40]. These fibers can be blended with cellulosic fibers and other cotton

materials to give moisture permeation. Thus, these fibers find diverse applications, including in upholstery, wearing apparel, thread, curtains, industrial fibers, tire cord filaments, and fabrics used for industrial filtration. PET finds extensive application in engineering plastics, where it serves as a substitute for metals such as aluminum and steel. Precision moldings that involve substitution are commonly used in various applications, including but not limited to electronics, appliances, and automotive components. The semi-crystalline polymer Polyethylene Terephthalate (PET) has garnered significant attention for its remarkable versatility and potential for sustainable applications across diverse industries. This thermoplastic polymer is highly favored for its exceptional chemical resistance, spinnability, and mobility.

PET is produced through a multi-step process that involves melt phase polymerization, which results in resins with an inherent viscosity varying from 0.5 to 0.7 dL/g. The synthesized PET is then subjected to a solid-state polymerization process to create high-molecular-weight polymers. During this process, a low-molecular-weight melt phase polymer solid is heated to a temperature exceeding its Glass Transition Temperature (T_g) yet below its boiling point. The outstanding mechanical properties imparted by this process establish PET as a preferred material for various applications, including manufacturing robust bottles, flexible films, and durable fibers [41–43]. The repeating units of the PET polymer, each ~1.09 nm in length and with a molecular weight of approximately 200, covalently connect to form its extended chain structure. These polymers are formed through the interaction between terephthalic acid and ethane 1, 2 diol, resulting in a structure capped with -OH on the right side and H on the left, as depicted in Figure 2. The polymerization process is marked by the creation of water, which is subsequently eliminated under vacuum conditions and at elevated temperatures. It is crucial to note that the presence of water can rapidly depolymerize the structure in its molten state. Therefore, it is essential to thoroughly dry the polymer before the melt-spinning process for fiber production. The molecule's rigidity can be attributed to incorporating an aromatic ring conjoined with a short aliphatic chain.

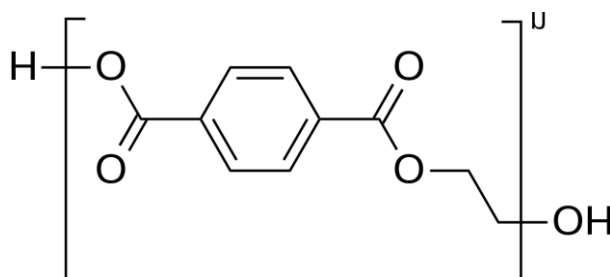


Figure 2. Structure of PET

Non-biodegradable polymers do not break down in environmental and naturally safe conditions by biological processes. Most plastics are non-biodegradable because they are widely used for their low cost, durability, and versatility. This durability is based on the benign, uncommon plastic target of bacteria, making it non-biodegradable. However, some chemical plastics can be biodegradable by breaking the polymer structure. PET has the properties of strength, toughness, heat resistance, and moisture and gas barriers. It has applications in soft drink bottles, beer bottles, water bottles, dressing containers, ovenable film, and trays. Plastics are used because they have many long-lasting applications, but unfortunately, they create a huge pollution problem. Plastic is very cheap, so it gets easily discarded, and its persistence can harm the environment significantly over decades [44].

3.1. Recycling Methods

Polymer plastics have become increasingly popular over the last decade due to their exceptional properties, including corrosion resistance, user-friendly design, low density, and many other unique characteristics. Consequently, recycling has become a critical process to mitigate environmental effects and illustrates one of the most critical sectors in the contemporary plastics industry. The degradation of polymer plastics occurs through four primary environmental mechanisms: photodegradation, hydrolytic degradation, biodegradation (facilitated by microorganisms), and thermo-oxidative degradation. With photodegradation, polymer plastic's natural degradation process begins due to the sunlight, giving the activation energy required to incorporate oxygen atoms into the plastic polymer. After the natural degradation, the thermo-oxidative degradation begins with incorporating oxygen atoms into a polymer, where the plastic converts into a brittle form and starts breaking into smaller pieces. Microorganisms now convert carbon from the polymer chain into carbon dioxide or incorporate it into bio-molecules. It will take considerable time, as discussed by Francis [45]. Therefore, recycling is one of the solutions to these problems. Here are some recycling methods that have been used to solve these problems.

3.1.1. Primary Recycling

The recycling approach is a method known for its simplicity and cost-effectiveness. It involves repurposing products in their original form, which means the materials are used again without significant processing or alteration.

This approach has advantages, such as being inexpensive to implement compared to more complex recycling methods. A key sustainability challenge associated with these materials lies in their finite reusability. Their performance deteriorates after a specific number of cycles, ultimately rendering them unsuitable for further use. Therefore, it is essential to consider alternative recycling methods to ensure that we can maximize the use of our resources while minimizing waste [46-48].

3.1.2. Mechanical Recycling (Secondary Recycling)

This technique applies exclusively to thermoplastic polymers, which can be remelted and reshaped into final products. It is a physical process where waste plastic is transformed into granulated pellets or flakes through shredding and cutting, which is suitable for manufacturing. These prepared samples are then melted and extruded to create new products. Tailoring the final material's properties might involve incorporating virgin material alongside the reprocessed component, following established blending protocols. Plastic waste will be reduced dramatically after all these processes, as shown in Figure 3. A drawback of this recycling technique is the multifariousness of solid waste and the deterioration of product property in each cycle [45, 46].



Figure 3. Mechanical recycling process

3.1.3. Chemical Recycling (Feedstock Recycling)

Beyond mechanical recycling, a distinct avenue for polymer valorization lies in chemical reactions that induce their chemical depolymerization, yielding either reconstituted monomers or lower-molecular-weight oligomers. This approach deconstructs the original polymer chains at the molecular level. Subsequently, these monomers can be repurposed in new polymerization reactions to fabricate the original or related polymeric products [49]. The main chemical reactions used to decompose polymers into monomers are shown in Figure 4 [50-52].

There are various methods to break down Polyethylene terephthalate (PET), including water, acids, alcohols, or glycols. Each method utilizes different reagents and generates different products. Hydrolysis, for instance, involves the reaction of PET with water in acidic, alkaline, or neutral environments to break it down entirely into monomers. On the other hand, glycolysis involves inserting ethylene glycol into PET chains to produce (hydroxyethyl) terephthalate (BHET) [53, 54]. While methanolysis employs methanol at elevated temperatures and pressures (180-280°C, 2-4 MPa) to depolymerize PET into primary products like ethylene glycol (EG) and dimethyl terephthalate (DMT), pyrolysis offers an alternative route by thermally decomposing polymeric materials in the absence of oxygen [55].

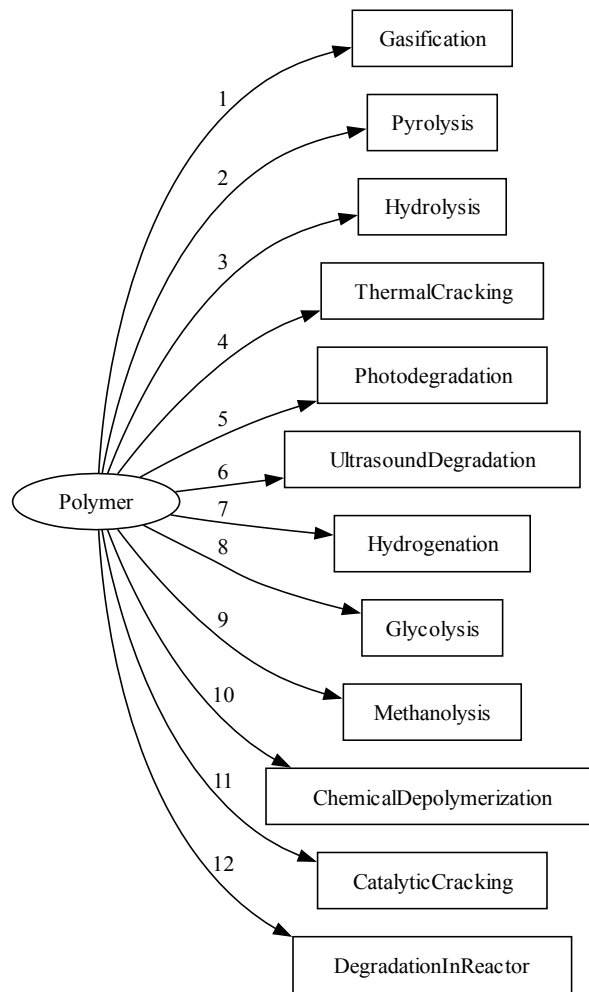


Figure 4. Various chemical reactions that decompose polymers [51]

3.1.4. Quaternary Recycling (Energy Recovery)

This method focuses on harnessing the energy content inherent in plastics. Incineration is recognized as an efficient approach for reducing the volume of organic materials. Chemical recycling presents a promising avenue for advancing sustainable development due to its ability to deconstruct polymers and recover valuable feedstocks for reuse, potentially complementing and enhancing existing mechanical recycling methods. This method gives rise to monomer formation from which the polymeric material is made [46, 56-58]. The challenges and advantages of recycling methods are represented in Table 1.

Table 1. Overview of recycling methods discussed

Techniques	Limitations	Benefits	Sources
Mechanical Recycling	Property deterioration, the necessity for pre-treatment	Cost-effectiveness, established familiarity, high efficiency	[49, 59]
Chemical Recycling	Primarily suitable for condensation polymers	Simplified process, effectively applicable to PET	[49, 52, 60]
Energy Recovery	Ecological acceptability concerns	Significant energy generation from polymers	[45, 61]

3.2. Characterization of PET Waste-Based Concrete

The analysis of concrete microstructure often employs a Scanning Electron Microscope (SEM). It has been observed that concrete containing Polyethylene Terephthalate (PET) exhibits a relatively asymmetrical morphology, which is conducive to the formation of pores ranging in size from 2 to 4 μm. The connection between PET fibers and the matrix is strengthened by many brilliant inclusions (cement formations) ringed by hydrating chemicals on the surface. The contact between the cement matrix and PET particles in concrete containing PET is significantly denser. A further benefit of PET fiber is reducing micro-cracks [46].

Fourier Transform Infrared (FTIR) studies can be conducted to identify the functional group characterization of PET waste. The obtained peaks at 1740 and 750 cm⁻¹ indicate the presence of C=O—O stretching, and at 1250 cm⁻¹, indicate C—O—C stretching. The phthalate ester group present in PET makes it flexible, enhancing PET-based concrete's flexural property [62]. Pereira et al. (2017) presented a study on a composite from PET waste with geopolymer concrete waste

(GCW) in the varied ratio (PET/GCW) 80/20, 60/40, and 50/50 (wt %). They characterized the composite by FTIR, FEG-SEM, X-ray fluorescence, and thermogravimetric analysis (TGA). Geopolymer concrete waste was used to create composites in its untreated state (U-GCW) and after oleic acid (T-GCW) treatment. To verify the composition of these materials, an analytical assessment was performed on both the geopolymer concrete waste and Polyethylene Terephthalate (PET) using techniques like X-ray Fluorescence and Fourier Transform Infrared (FT-IR) Spectroscopy, which established the geopolymer structure.

The thermal stability of the polymer composites was thoroughly investigated using Thermogravimetric analysis (TGA). This technique revealed a trend of increasing stability with higher filler content. Field Emission Gun Scanning Electron Microscopy (FEG-SEM) was employed to elucidate the observed behavior further and delve into the adhesion characteristics between the fillers and polymer matrix in the treated composites. The findings suggested that oleic acid on the surfaces of geopolymer concrete waste played a crucial role in promoting strong adhesion. Mechanical testing demonstrated the robust performance was consistent across all composite samples, with further improvement achieved through compatibilization [63].

Further bolstering the case for utilizing PET waste in construction, a meticulous study on the stability and morphological characteristics of high-strength PWBs was conducted, offering valuable data on their structural integrity and microstructural features. These were created by combining foundry sand (FS) with PET waste (PW) in varying ratios (PW: FS) of 20%, 30%, and 40% relative to the dry mass of FS. In this study, when compared to burnt clay bricks, the developed PWBs were tested for tensile and compressive strength, durability, and load-bearing capability. Scanning electron microscopy (SEM) examinations were used to further examine the morphological structure of the bricks. This study shows that utilizing plastic waste and different amounts of foundry sand can be an innovative solution for brick masonry. This approach can improve the load-bearing capacity and the tensile and compressive strength of the resulting product compared to the traditional burned clay brick.

The SEM study confirmed the formation of a stable foundry sand matrix framework within the PET waste bricks, evidenced by its thorough integration with the surface and interior sections. Additionally, the presence of viscous floccules suggests further strengthening mechanisms. The PWB morphology had stronger inter-cluster bonds on the surface than clay bricks. The SEM demonstrated that the microstructure of PWB developed with lesser porosity; thus, the plastic waste bricks do not require wetting before masonry building. The results showed a practical methodological strategy for producing high-strength masonry bricks from a blend of PET waste and used foundry sands [64]. Lee et al. [65] presented a study on chemically treated PET and PP concrete at 10%, 20%, and 30% incorporation of PET and PP waste by weight of cement. This work examines the impact of treating PET wastes with calcium hypochlorite and hydrogen peroxide solutions before using them as replacements for coarse aggregate in concrete.

Analysis of SEM provided revealing insights into the interfacial bonding between the cementitious matrix and PET aggregates. The control mix exhibited suboptimal adhesion, characterized by sizable gaps visible in the SEM images. However, a significant improvement was observed in concrete mixes containing $\text{Ca}(\text{ClO})_2$ -modified PET aggregates and H_2O_2 -treated PE aggregates. These treated mixes displayed markedly reduced gaps between the matrix and aggregates, signifying enhanced bonding. The chemical treatments applied to the plastic aggregates were found to augment the binding strength and diminish the gap at the interfacial transition zone (ITZ). Such improvements in the microstructure contributed to a decrease in permeability and porosity, simultaneously enhancing the compressive strength of the material [65]. Expanding upon understanding of recycled PET waste in concrete, Kangavar et al. [66] investigated its performance as a partial replacement for fine aggregate (0%, 10%, 30%, and 50%). This work evaluated some properties of PET-containing concrete, such as compressive strength, workability (slump), elastic modulus, density, tensile strength, crack mouth opening displacement, and flexural strength. The SEM analysis characterized the microstructure study of the PET-contained concrete. PET waste granules improved the durability and mechanical properties of the PET-modified concrete in this study. SEM imaging demonstrated an even dispersion of PET granules within the concrete mix at replacement levels of up to 10%. However, increasing the substitution ratio to 30% and 50% led to a more uneven distribution and pronounced demarcation between the PET granules and the cement matrix, attributed to increased porosity. These studies' compressive, tensile, and flexural strength tests revealed significantly enhanced performance, especially in concrete samples containing 10% PET particles [66].

3.3. Applications of PET Waste

After the recycling and recovery methods of plastics, various applications of recycled plastics are summarized in Table 2. The PET production rate is projected to increase by 30 million tonnes by 2020. In India, nearly 900 kilo-tonnes of PET were utilized during 2015-2016 [67]. Over the past sixteen years, there has been a significant increase in the usage of PET for manufacturing drinking bottles. In 2000, the global consumption rate stood at 300 billion, which soared to 480 billion by 2016. This growth trend is expected to continue, and the consumption rate is forecasted to reach a staggering 583 billion by 2021 [68]. The National Chemical Laboratory (NCL) and the PET Packaging Association for Clean Environment (PACE) [67] indicate that India achieves a PET recycling rate of 90%, exceeding those of Japan at 72.1%, Europe at 48.3%, and the United States at 31%. Within India, PET waste recycling is segmented across various sectors, with the organized sector responsible for 65% of recycling activities, the unorganized sector contributing 15%, and the remaining 10% repurposed domestically, forming a substantial part of the overall recycling process [67].

Table 2. Utilization of recycled plastics applications

Product Identification Code	Plastic	Applications	References
PETE	PET	Detergent bottles, drinking bottles, carpet fiber, clear film for packaging	[69]
HDPE	HDPE	Mobile components, detergent bottles, agricultural pipes, pallets, toys	[69, 70]
V	PVC	Textile, drinking bottles, packaging for food, medical materials	[71]
PP	PP	Kerb side recycling crates, compost bins	[46]
PS	PS	Disposable cutlery	[72]
LDPE	LDPE	Plastic tubes, bottles, food packaging	
OTHER	Other materials, such as Polylactic Acid, Nylon, Acrylonitrile Butadiene Styrene, and Polycarbonate	Containers	[73]

4. PET Waste in the Construction Industry

PET recycling research was undertaken for construction materials over the past decade (2010 to 2020). The present section aims to investigate research articles that have been reviewed for using PET in different sustainable construction materials. This has been an activity of interest for a considerable period, from the early decade [74, 75]. 2012, global plastic production was estimated to be approximately 280 million tonnes. Of this, around 130 million tonnes were either landfilled or recycled. On an annual basis, the worldwide processing of plastics reaches nearly 300 million metric tonnes, serving various industries [48]. Within this context, India specifically recovers about 6.5 to 8.5 million tonnes of plastic annually as waste, predominantly collected from municipal sources [76]. A sustainable solution suggested by Padgelwar et al. [20] is recycling plastic waste to reduce environmental haggard. Recycling plastic waste as a value-added component in concrete presents a promising avenue for alternative use of plastic waste [77]. After carefully reviewing the available research articles in the mentioned period, it is noticed that not much research has been done on this topic. It was observed that this area of research has fascinated researchers for the last decade. This waste material gives new research opportunities for civil engineering construction industry researchers [75, 78-82]. Table 3 provides the construction sector's critical findings on waste PET recycling.

Table 3. Wastes PET recycling for construction sectors

References	LWM	OMM	MI	Significant Remarks
[83]	PET	Portland cement	Cementitious mortar	Incorporating PET plastic aggregates into cement-based materials has opened new doors for creating robust and energy-absorbing substances. These materials have displayed exceptional characteristics for engineering purposes, especially for structures that require resistance to dynamic or impact events. Research has yielded promising results, showing PET-based cementitious materials can withstand high-stress loads without cracking or breaking. This discovery presents a significant breakthrough in the construction field and provides a sustainable solution for recycling PET waste.
[84]	PET	blasting sand	Thermoplastic composites	The study prepared composite materials to be used as floor tiles, paving slabs, or bricks in the construction industry, with good structural performance.
[85]	PET	Aggregate, bitumen, and Portland cement	Stone mastic asphalt (SMA)	The study results indicate that integrating PET waste into mixtures (e.g., Stone Mastic Asphalt) significantly impacts the resulting mixture's properties. This inclusion has the potential to improve the sustainability of road construction by promoting the reuse and recycling of waste materials. Moreover, it can enhance the mixture's ability to resist permanent deformations and increase its stiffness while reducing binder drainage. Roads constructed with SMA mixtures containing waste PET can potentially last longer and require less maintenance, leading to cost savings and environmental benefits.
[86]	PET	Natural river sand and limestone powder	Cementitious Mortar	This study used recycled PET bottles to produce plastic mortar. Critical parameters such as compressive strength, gradation, the ratio of sand to PET, curing conditions, and temperature exposure were methodically examined. It was observed that the plastic sand mortar exhibited superior compressive strength at specific gradation levels. The ideal proportion of sand to PET was identified as 3:1; remarkably, the mortar accomplished over 90% of the projected seven-day strength by a mere 3 hours. Furthermore, when subjected to higher curing temperatures, the mortar displayed enhanced compressive strength.
[87]	PET	Crushed basalt aggregate and asphalt	Roadway pavement	This study explored the potential of incorporating reclaimed PET bottle waste into asphalt and asphalt mixtures. The results demonstrated that newly developed additive products derived from PET waste enhanced the performance of these materials and provided a sustainable and advantageous option for diverting this ecologically harmful waste stream. This approach offers a promising avenue for promoting environmental responsibility and improved infrastructure performance.

[88]	PET	Portland-limestone blended cement, lime, and hydraulic lime	Lightweight Plaster	The research demonstrated that environmentally sustainable plasters can be formulated by substituting virgin materials with 100% PET waste components. These plasters, characterized by their low thermal conductivity and notable lightness, have exhibited energy efficiency. Based on the outcomes of sensitivity tests concerning sulfate reactions in hydraulic binders, these plasters show potential applicability in restoring ancient masonry.
[89]	PET	Asphalt cement 60/70, sand, granite chippings, and stone dust	Bituminous asphaltic concrete	This study stands out in developing a sustainable method tailored for the 21st century, focusing on recycling PET waste plastic bottles into bituminous asphaltic concrete (BAC) in North Central Nigeria. This approach is primarily driven by the dual benefits of environmental conservation, through the diversion of multiple million tons of PET waste from landfills, and economic advantages, including extended service life of highways, efficient management of natural resources, and potential revenue generation from handling such waste.
[90]	PET	Portland cement and water	Plastic cement	Polyethylene packages, including bottles and food crates in the 10 to 80% range, were used experimentally in the temporary reinforcement structure. The study results show positive findings for producing plastic cement from polyethylene waste. Results emphasize that their density has decreased, flexibility has increased, and workability has improved, resulting in light materials.
[91]	PET	Fine & coarse aggregate and cement	Structural concrete	In India, a significant portion of waste plastic, approximately 40%, is not reused. This research involved testing eleven concrete mixtures, where plastic was utilized as a partial substitution for sand. The utilization of sand-graded PET fragments was capped at a 10% substitution ratio. The findings of this study suggest that replacing waste plastic with sand could potentially conserve 820 million tons of sand annually.
[92]	PET	Recycled concrete aggregate (RCA), crushed brick (CB.)	Construction materials	When combined with Recycled Concrete Aggregate (RCA) and Crushed Brick (CB), the PET mixture underwent testing to evaluate its crucial geotechnical properties. This assessment also included the geo-environmental parameters of PET, RCA, and CB following specified standards. It was found that all blends met the California Bearing Ratio (CBR) requirement of 80%, rendering them suitable for use in pavement applications.
[93]	PET	Asphalt cement, crushed aggregates, hot mix asphalt (HMA)	Fiber-Modified Asphalt	The cost-advantage analysis has shown that fibers can be a dependable way of improving typical asphalt mixtures' efficiency at a reasonable cost for transportation agencies. The next step of this research is a microscopic study to ensure that fiber is well spread into the asphalt mix. The fiber length impacts the mixing characteristics and the fatigue life determination for fiber-modified asphalt mixes.
[64]	PET	Waste and Foundry Sand	PET waste-based bricks	PET waste bricks were fabricated using varying ratios of PET waste to foundry sand, specifically 20%, 30%, and 40% of the total dry weight of the foundry sand. The study evaluated these PET waste bricks' durability, compressive, and tensile strength. Additionally, their load-bearing capacities under tension and compression were analyzed and compared with those of traditional heated clay bricks.
[87]	PET	Asphalt and hot mix asphalt (HMA)	PET-Modified Asphalt	This research explores the effectiveness of two PET waste-derived additives, Viscous Polyol PET (VPP) and Thin Liquid Polyol PET (TLPP), in modifying asphalt and HMA mixtures. The results demonstrated that TLPP and VPP effectively improve the asphalt's cold weather flexibility, resistance to fatigue cracking, and HMA's resistance to moisture damage and mechanical deformation.

LWM = leading waste materials, OMM = Other mixing materials, MI = Materials invented

4.1. Engineering Properties

The engineering properties of any material are a prime concern for practical utilization in any construction industry. Any recycled material can be replaced as a filling or supplementary cementitious materials (SCM) because its compressive and flexural strength are the two most essential parameters for the approval of any construction material [94, 95]. The comparative strengths were determined by calculating the materials' design strength ratio in comparison to the reference design strength of the concrete. Documentation of the incorporation ratio of PET in sustainable construction materials is extensively reported in the literature, as referenced in surveys [96, 97].

4.1.1. Comparative Analysis of Compressive Strength

The following Figure 5 compares the relative compressive strength and the percentages of PET as reported in various published studies. The compressive strength variation of construction material by incorporating 1-20% PET is presented by SLR for this review article.

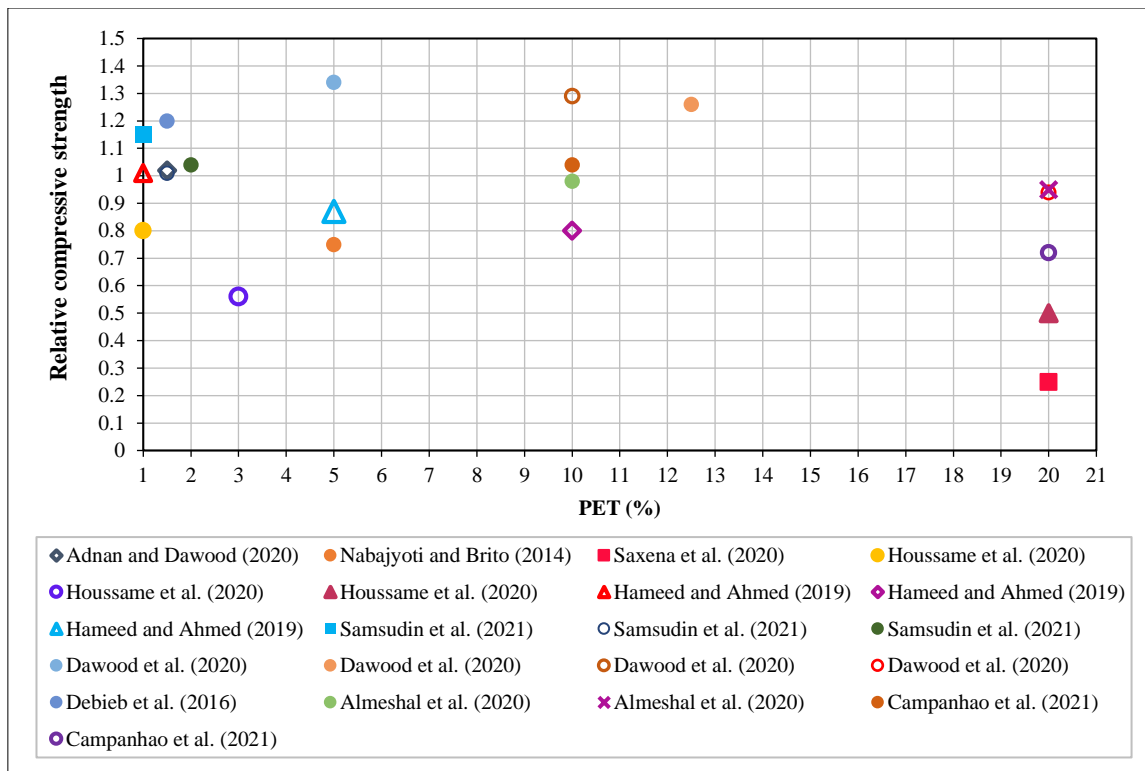


Figure 5. Relative compressive strength variation with PET percentage

Limami et al. [98] examined the efficacy of clay bricks enhanced with PET additives, focusing on their potential practical applications within the building industry. As seen in Figure 5, the relative strength is calculated from the ratio of material design strength to concrete design strength. An inverse correlation was seen between the strength and the increasing percentages of PET additives. Specifically, at PET additive levels of 1%, 3%, and 20%, there were corresponding reductions in compressive strength of approximately 20%, 40%, and 50%, respectively. The reason for reduced strength at higher PET replacement with clay is the incorporation of porosity in the sample due to PET additives compared to reference samples without PET. The more significant proportion and finer grain size in polymeric additives PET is the main reason for producing porous brick samples, ultimately reducing the compressive strength. Hameed & Ahmed [99] disclosed compressive strength results at 1%, 5%, and 10% of PET incorporation. The study observed a nuanced trend in compressive strength relative to PET percentages. A marginal increase of approximately 1% in compressive strength was noted at a 1% PET concentration, while PET levels at 5% and 10% resulted in compressive strength reductions of about 13% and 20%, respectively. This pattern indicates a clear correlation where PET percentage increases are associated with compressive strength decreases. Further, Samsudin et al. [100] evaluated the compressive strength of concrete with 1%, 1.5%, and 2% PET. Figure 7 illustrates the increase in compressive strength values by 15%, 1%, and 4% by adding 1%, 1.5%, and 2% PET to the concrete mixture. The study shows that 1% of PET fiber concrete mixture shows better fiber distribution than others. Therefore, the highest compressive strength was obtained at 1% PET fiber content. Dawood et al. [101] explored the efficacy of concrete made using PET waste, replacing natural river sand with 5%, 10%, 12.5%, and 20% PET waste. The findings revealed an increase in compressive strength between 5% and 12.5% PET incorporation, with noted enhancements of 34%, 29%, and 26% at 5%, 10%, and 12.5%, respectively. However, at a 20% substitution level, a notable decline in compressive strength was recorded, showing a 6% reduction compared to natural river sand. These results suggest that compressive strength improves with PET waste replacement up to 12.5%, but it diminishes at higher replacement ratios, especially at 20%. It leads to the conclusion that replacing natural river sand with PET waste up to a threshold of 12.5% benefits compressive strength.

The studies done by previous studies at 20% replacement of natural river sand with PET waste revealed a 75%, 5%, and 28% reduction in compressive strength [102-104]. However, the variation in strength was seen in different studies, and trends show precise observation of declining strength at a higher replacement ratio of up to 20%. Different design mixes and using numerous SCMs in the same concrete mix are the leading causes of strength differences at the same replacement ratio. The reduction in compressive strength is demonstrated by a replacement ratio of 20% PET waste. Studies have revealed that the results are more positive when the replacement ratios are between 1 and 12.5%. At a 10% replacement ratio, a threshold and ideal results were observed. The microstructure is demonstrated to become denser with smaller quantities of PET waste, increasing the material's compressive strength. Because it is so fine, PET trash will have a large surface area and establish a strong binding with the cement and sand. The right amount of PET trash will also offer compaction.

4.1.2. Flexural Strength (Relative)

The relative flexural strength and PET proportions from published research are shown in Figure 6. The flexural strength variation of construction material by incorporating 0.5-20% PET is presented by SLR for this review article.

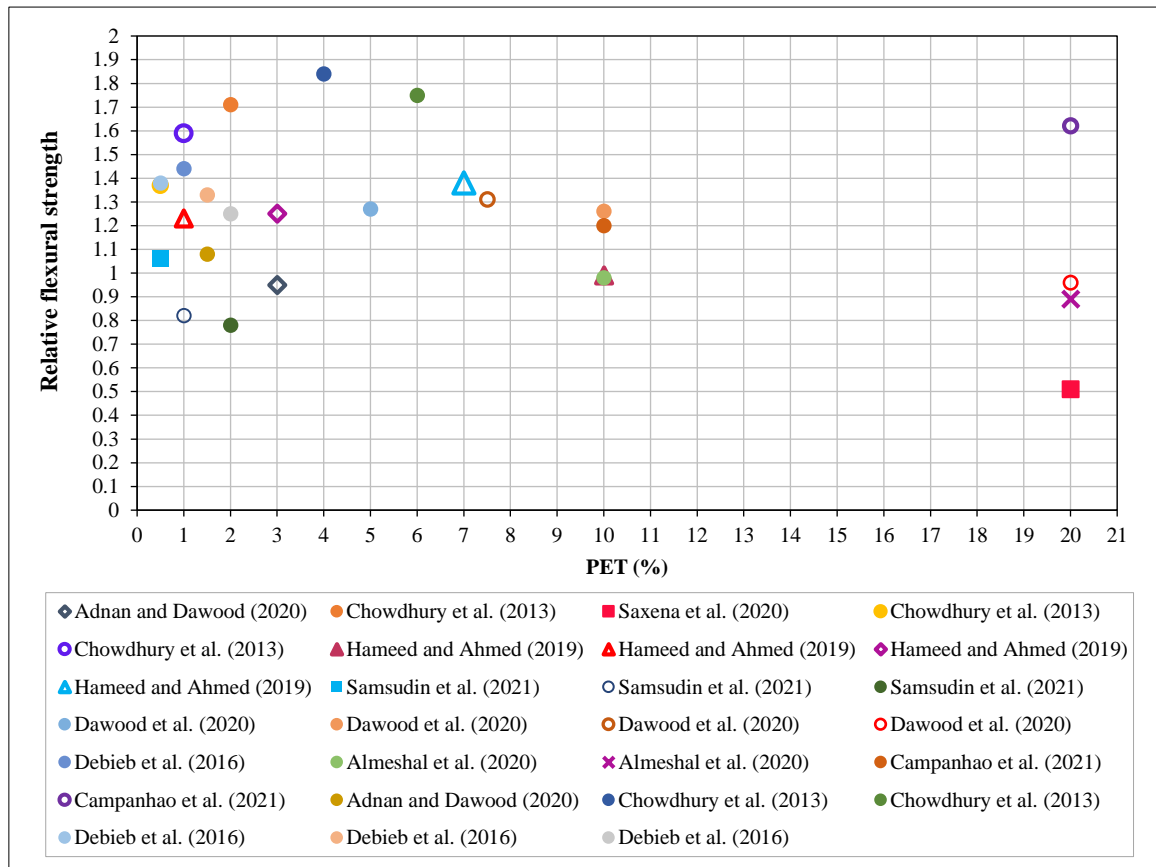


Figure 6. Relative flexural strength variation with PET percentage

Hameed & Ahmed [99] studied the performance of recycled plastic aggregate concrete by replacing 1%, 3%, 7%, and 10% PET waste with natural fine aggregate. Figure 6 shows flexural strength increased by 23%, 25%, and 38% at 1%, 3%, and 7% incorporation of PET aggregate. When the replacement ratio reached 10%, the strength was decreased by about 1% approximately. The interfacial shear strength of the inner layers and the compressive and tensile strengths of the top and bottom surface determine how resistant the material is to bending if it consists of layers of matrix and filler material. Incorporating PET aggregate in concrete structures slows growth and halts the propagation of fractures at particular percentages [105]. As a result, the ratings for flexural strength are improved when a small quantity of aggregate is added; nevertheless, this can also result in flaws in the concrete (such as voids), which lower the strength of the material when it reaches the optimum.

Dawood et al. [101] investigated PET waste concrete's strength (flexural) performance when incorporating 5%, 7.5%, 10%, and 20% PET waste aggregate in place of natural river sand. The study results show an increment in flexural strength from 5-10% PET waste aggregate. The increments in flexural strength of 27%, 31%, and 26% at 5%, 7.5%, and 10% incorporation of PET waste have been observed. At a 20% substitution ratio, a sudden fall in flexural strength was noted. A 4% decline in strength (compressive) at 20% replacement of PET waste with natural river sand was seen. The results showed that the flexural strength parameter declined at a higher replacement ratio of up to 20%. This study concluded that up to 10% of the replacement of natural river sand with PET waste positively affects flexural strength.

Guendouz et al. [106] have researched incorporating 0.5%, 1%, 1.5%, and 2% PET waste fiber in new concrete. Experimental results revealed the enhancement in flexural strength value by 38%, 44%, 33%, and 25% at 0.5%, 1%, 1.5%, and 2% addition of PET waste fiber by weight of cement. The ability to use leftover PET fiber to create concrete that behaves more ductility is a desirable consequence. Pereira De Oliveira & Castro-Gomes [107] found that 1.5% of PET fibers at 28 days increased the flexural strength of mortar by around 30%. In their study, Ochi et al. [108] explored various techniques for reinforcing fibers extracted from recycled PET waste bottles. They also evaluated the flexibility of concrete specimens subjected to these reinforced fibers. The findings of their study were comparable to previously reported results.

Samsudin et al. [100] presented a study on PET fiber concrete at 0.5%, 1%, and 2% incorporation of PET fiber by weight of cement. The study proved that flexural strength value increased by 6% at 0.5% of PET fiber. Further increasing the PET fiber percentage revealed a reduction in flexural strength. It has been noticed that flexural strength was reduced at 1% and 2% PET fiber, approximately 18% and 22% compared to reference concrete. It has been proven that PET fibers perform effectively with other components in concrete at an optimum 0.5% compared to regular concrete.

In previous studies [109, 110], the replacement of natural sand by PET fiber incorporation at 0.5%, 1%, 2%, 4%, and 6% in new concrete. The study showed that replacing waste PET fiber in new concrete significantly improved flexural strength. The results showed a continuous increment of about 37%, 59%, 71%, and 84% at 0.5%, 1%, 2%, and 4% waste PET fiber content addition. With an increase in replacement percentage, the flexural strength of samples containing PET fiber as fine aggregate gradually rises; however, as it is already between 4 and 6%, it may fall for further replacement percentage.

5. Conclusions

This critical review has systematically explored the innovative application of PET waste as a sustainable alternative in the construction industry, particularly as a replacement for natural sand and an additive in cement. Through a comprehensive analysis of over 110 peer-reviewed publications, this study has illuminated the significant theoretical and practical contributions of incorporating recycled PET waste into construction materials. The study's investigation reveals that optimal utilization of PET waste enhances construction materials' compressive and flexural strengths and alleviates environmental pollution attributed to PET waste accumulation.

Additionally, this study underscores the imperative for a paradigm shift towards sustainable construction methodologies, advocating for a transition that encompasses the academic and research communities, policymakers, industry stakeholders, and civil engineering practitioners. The conclusions drawn are based on data extracted from 110 peer-reviewed articles.

- Past experimental studies disclosed that PET waste can be recycled using chemical and mechanical methods to form precursor material for sustainable development.
- Past experimental studies disclosed that recycled PET waste-based concrete can be characterized by the SEM, TGA, FTIR, and EDX, which could examine the microstructure of the concrete, thermal stability, and chemical composition.
- Past experimental studies disclosed that PET waste could be successfully replaced as a leading waste material to replace natural materials in the construction industry.
- Based on previous experimental studies, it has been observed that replacing natural sand with PET waste is in the range of 5-20%. Most studies' compressive strength threshold reached a 10% replacement ratio. If 10% of natural river sand is replaced with PET waste, it can positively affect compressive strength. However, it is essential to note that beyond this point, a reduction in compressive strength is observed, and a significant drop in strength is noted at 20% replacement. These findings suggest that while PET waste can be a valuable substitute for natural sand, there are limitations to the amount that can be used to maintain the desired level of compressive strength.
- For flexural strength, adding 0.5%, 1%, 1.5%, and 2% PET waste powder in new concrete was studied by the weight of the cement. Experimental results revealed the enhancement in flexural strength value by 38%, 44%, 33%, and 25% at 0.5%, 1%, 1.5%, and 2% addition of PET waste powder. However, all replacement ratios show an increment in flexural strength, its optimum value observed at 1% addition. Furthermore, it also affected the concrete specimens' flexibility and bending.

In light of the findings and the potential impact on sustainable development, this conclusion serves as a catalyst, urging the academic community to engage in further research that bridges the gap between theoretical exploration and practical application. It is incumbent upon the collective expertise of researchers, engineers, and industry professionals to innovate.

5.1. Recommendation for Future Research

The SLR on PET waste-based construction materials is discussed in this review study. As demonstrated by the SLR, numerous researchers have successfully produced fresh concrete using recycled PET waste. There isn't much research on substituting recycled PET waste for natural sand. It has also been emphasized that little is known about the resilience of PET waste-derived concrete. Uncertainty exists over the effects of PET waste; recycled fine aggregate and desert sand can be added to PET waste in new concrete to make it more sustainable. An in-depth study was done on the selected studies for this review article. Prior studies have shown that using up to 12.5% recycled PET waste as sand and 1% recycled PET waste powder by weight of cement is the best option for maintaining engineering properties. The implications of substituting natural sand in new concrete with recycled PET waste and other sustainable fine aggregate alternatives remain uncertain. Given the findings and current research, further investigations are warranted. Based on these insights, the following recommendations are proposed:

- It is advisable to experiment with incorporating recycled PET waste into the concrete design mix, particularly at an elevated replacement ratio of 20%. It should be done in conjunction with completely substituting river sand with recycled fine aggregate and desert sand.
- A thorough understanding of the strength and durability parameters of the concrete mixture is essential, especially after observing the collective effects of adding recycled fine aggregate and desert sand in higher proportions.

Developing a sustainability measurement model using AI and machine learning tools is also suggested. This model would specifically evaluate scenarios where recycled PET waste is amalgamated with 100% alternative sustainable sources of fine aggregates to replace natural sand.

6. Declarations

6.1. Author Contributions

Conceptualization, M.N.A. and O.A.; methodology, M.N.A.; validation, O.A. and M.N.A.; formal analysis, M.N.A.; investigation, O.A.; resources, O.A.; data curation, M.N.A.; writing—original draft preparation, M.N.A.; writing—review and editing, O.A.; visualization, O.A.; supervision, M.N.A.; funding acquisition, O.A. All authors have read and agreed to the published version of the manuscript.

6.2. Data Availability Statement

Data presented in this study is available in the article.

6.3. Funding

The article processing charge for the presented article is funded by Fahad Bin Sultan University, Saudi Arabia.

6.4. Conflicts of Interest

The authors declare no conflict of interest.

7. References

- [1] United Nations. (1992). Report of The United Nations Conference on Environment and Development. A/CONF.151/26, Vol. I), 1-5.
- [2] Akhtar, M. N., Jameel, M., Ibrahim, Z., & Bunnori, N. M. (2022). Incorporation of recycled aggregates and silica fume in concrete: an environmental savior—a systematic review. *Journal of Materials Research and Technology*, 20, 4525–4544. doi:10.1016/j.jmrt.2022.09.021.
- [3] Akhtar, M. N., & Tarannum, N. (2018). Flyash as a resource material in construction industry: a clean approach to environment management. *Sustainable Construction and Building Materials*, Springer, Singapore. doi:10.5772/intechopen.82078.
- [4] Lajčín, D., & Guzoňová, V. (2023). Identification of Knowledge Management Barriers in Scientific R&D Projects in Czech Academic Environment. *HighTech and Innovation Journal*, 4(1), 19-36. doi:10.28991/HIJ-2023-04-01-02.
- [5] Prasad Bhatta, D., Singla, S., & Garg, R. (2022). Experimental investigation on the effect of Nano-silica on the silica fume-based cement composites. *Materials Today: Proceedings*, 57, 2338–2343. doi:10.1016/j.matpr.2022.01.190.
- [6] Akhtar, M. N., Ibrahim, Z., Bunnori, N. M., Jameel, M., Tarannum, N., & Akhtar, J. N. (2021). Performance of sustainable sand concrete at ambient and elevated temperature. *Construction and Building Materials*, 280, 122404. doi:10.1016/j.conbuildmat.2021.122404.
- [7] Akhtar, M. N., Jameel, M., Ibrahim, Z., Muhamad Bunnori, N., & Bani-Hani, K. A. (2024). Development of sustainable modified sand concrete: An experimental study. *Ain Shams Engineering Journal*, 15(1), 102331. doi:10.1016/j.asej.2023.102331.
- [8] Akhtar, M. N., Bani-Hani, K. A., Akhtar, J. N., Khan, R. A., Nejem, J. K., & Zaidi, K. (2022). Flyash-based bricks: an environmental savior—a critical review. *Journal of Material Cycles and Waste Management*, 24(5), 1663–1678. doi:10.1007/s10163-022-01436-3.
- [9] Alhajiri, A. M., & Akhtar, M. N. (2023). Enhancing Sustainability and Economics of Concrete Production through Silica Fume: A Systematic Review. *Civil Engineering Journal*, 9(10), 2612–2629. doi:10.28991/CEJ-2023-09-10-017.
- [10] Ahmad Khan, R., Nisar Akhtar, J., Ahmad Khan, R., & Nadeem Akhtar, M. (2023). Experimental study on fine-crushed stone dust a solid waste as a partial replacement of cement. *Materials Today: Proceedings*. doi:10.1016/j.matpr.2023.03.222.
- [11] Akhtar, M. N., Bani-Hani, K. A., Malkawi, D. A. H., & Malkawi, A. I. H. (2023). Porous Asphalt Mix Design Pavement by Incorporating a Precise Proportion of Recycled Coarse Aggregate. *International Journal of Pavement Research and Technology*, 1–12. doi:10.1007/s42947-023-00406-8.

- [12] Akhtar, M. N., Husein Malkawi, D. A., Bani-Hani, K. A., & Husein Malkawi, A. I. (2023). Durability Assessment of Sustainable Mortar by Incorporating the Combination of Solid Wastes: An Experimental Study. *Civil Engineering Journal*, 9(11), 2770–2786. doi:10.28991/CEJ-2023-09-11-09.
- [13] Kaniraj, S. R., & Gayathri, V. (2003). Geotechnical behavior of fly ash mixed with randomly oriented fiber inclusions. *Geotextiles and Geomembranes*, 21(3), 123-149. doi:10.1016/S0266-1144(03)00005-0.
- [14] Akhtar, M. N. (2012). Role of soil mechanics in civil engineering. *International Journal of Emerging trends in Engineering and Development*, 2(6), 104-111.
- [15] Akhtar, M. N., Hattamleh, O., & Akhtar, J. N. (2017). Feasibility of coal fly ash based bricks and roof tiles as construction materials: A review. *MATEC Web of Conferences*, 120, 3008. doi:10.1051/mateconf/201712003008.
- [16] Kamaruddin, M. A., Abdullah, M. M. A., Zawawi, M. H., & Zainol, M. R. R. A. (2017). Potential use of plastic waste as construction materials: Recent progress and future prospect. *IOP Conference Series: Materials Science and Engineering*, 267(1), 12011. doi:10.1088/1757-899X/267/1/012011.
- [17] Kryeziu, D., Selmani, F., Mujaj, A., & Kondi, I. (2023). Recycled concrete aggregates: a promising and sustainable option for the construction industry. *Journal of Human, Earth, and Future*, 4(2), 166-180. doi:10.28991/HEF-2023-04-02-03.
- [18] Akhtar, M., Khan, M., & Akhtar, J. (2014). Use of the Falling-head Method to Assess Permeability of Fly Ash Based Roof Tiles with Waste Polythene Fibre. *International Journal of Scientific & Engineering Research*, 5(12), 476–483.
- [19] Akhtar, M. N., Akhtar, J., Hattamleh, O. H. Al, & Halahla, A. M. (2016). Sustainable Fly Ash Based Roof Tiles with Waste Polythene Fibre: An Experimental Study. *Open Journal of Civil Engineering*, 6(2), 314–327. doi:10.4236/ojce.2016.62026.
- [20] Padgelwar, S., Nandan, A., & Mishra, A. K. (2021). Plastic waste management and current scenario in India: a review. *International Journal of Environmental Analytical Chemistry*, 101(13), 1894–1906. doi:10.1080/03067319.2019.1686496.
- [21] Hossain, R., Islam, M. T., Shanker, R., Khan, D., Locock, K. E. S., Ghose, A., Schandl, H., Dhodapkar, R., & Sahajwalla, V. (2022). Plastic Waste Management in India: Challenges, Opportunities, and Roadmap for Circular Economy. *Sustainability*, 14(8), 4425. doi:10.3390/su14084425.
- [22] Faraca, G., & Astrup, T. (2019). Plastic waste from recycling centres: Characterisation and evaluation of plastic recyclability. *Waste Management*, 95, 388–398. doi:10.1016/j.wasman.2019.06.038.
- [23] Awoyera, P. O., & Adesina, A. (2020). Plastic wastes to construction products: Status, limitations and future perspective. *Case Studies in Construction Materials*, 12, 330. doi:10.1016/j.cscm.2020.e00330.
- [24] Choi, Y. W., Moon, D. J., Chung, J. S., & Cho, S. K. (2005). Effects of waste PET bottles aggregate on the properties of concrete. *Cement and Concrete Research*, 35(4), 776–781. doi:10.1016/j.cemconres.2004.05.014.
- [25] Akhtar, M., Halahla, A., & Almasri, A. (2021). Experimental study on compressive strength of recycled aggregate concrete under high temperature. *SDHM Structural Durability and Health Monitoring*, 15(4), 335–348. doi:10.32604/sdhm.2021.015988.
- [26] Akçaözöğlü, S., Atiş, C. D., & Akçaözöğlü, K. (2010). An investigation on the use of shredded waste PET bottles as aggregate in lightweight concrete. *Waste Management*, 30(2), 285–290. doi:10.1016/j.wasman.2009.09.033.
- [27] Rahmani, E., Dehestani, M., Beygi, M. H. A., Allahyari, H., & Nikbin, I. M. (2013). On the mechanical properties of concrete containing waste PET particles. *Construction and Building Materials*, 47, 1302–1308. doi:10.1016/j.conbuildmat.2013.06.041.
- [28] Saikia, N., & De Brito, J. (2014). Mechanical properties and abrasion behaviour of concrete containing shredded PET bottle waste as a partial substitution of natural aggregate. *Construction and Building Materials*, 52, 236–244. doi:10.1016/j.conbuildmat.2013.11.049.
- [29] Moher, D., Liberati, A., Tetzlaff, J., Altman, D. G., and Prisma Group, (2009). Preferred reporting items for systematic reviews and meta-analyses: the PRISMA statement. *Annals of internal medicine*, 151(4), 264-269. doi:10.7326/0003-4819-151-4-200908180-00135.
- [30] Félix, M., Martín-Alfonso, J. E., Romero, A., & Guerrero, A. (2014). Development of albumen/soy biobased plastic materials processed by injection molding. *Journal of Food Engineering*, 125, 7-16. doi:10.1016/j.jfoodeng.2013.10.018.
- [31] PlasticsEurope. (2016). *Plastics—The Facts 2016: An Analysis of European Plastics Production, Demand and Waste Data*. PlasticsEurope, Brussels, Belgium.
- [32] Wu, C., Nahil, M. A., Miskolczi, N., Huang, J., & Williams, P. T. (2014). Processing real-world waste plastics by pyrolysis-reforming for hydrogen and high-value carbon nanotubes. *Environmental Science and Technology*, 48(1), 819–826. doi:10.1021/es402488b.
- [33] Anuar Sharuddin, S. D., Abnisa, F., Wan Daud, W. M. A., & Aroua, M. K. (2016). A review on pyrolysis of plastic wastes. *Energy Conversion and Management*, 115, 308–326. doi:10.1016/j.enconman.2016.02.037.

- [34] Govindan, S., Ramos, M., & Al Jumaily, A. M. (2023). A Review of Biodegradable Polymer Blends and Polymer Composite for Flexible Food Packaging Application. *Materials Science Forum*, 1094, 51–60. doi:10.4028/p-DC7WkH.
- [35] Benítez, A., Sánchez, J. J., Arnal, M. L., Müller, A. J., Rodríguez, O., & Morales, G. (2013). Abiotic degradation of LDPE and LLDPE formulated with a pro-oxidant additive. *Polymer Degradation and Stability*, 98(2), 490–501. doi:10.1016/j.polymdegradstab.2012.12.011.
- [36] Nomadolo, N., Mtibe, A., Ofosu, O., Mekoa, C., Letwaba, J., & Muniyasamy, S. (2024). The Effect of Mechanical Recycling on the Thermal, Mechanical, and Chemical Properties of Poly (Butylene Adipate-Co-Terephthalate) (PBAT), Poly (Butylene Succinate) (PBS), Poly (Lactic Acid) (PLA), PBAT-PBS Blend and PBAT-TPS Biocomposite. *Journal of Polymers and the Environment*, 1–16. doi:10.1007/s10924-023-03151-y.
- [37] Popović, K., Živanović, S., & Jevtić, I. (2024). Biopolymer Packaging Materials in the Pharmaceutical Industry. *AIDASCO Reviews*, 2(1), 46–56. doi:10.59783/aire.2024.43.
- [38] Perez Bravo, J. J., Gerbehaye, C., Raquez, J. M., & Mincheva, R. (2024). Recent Advances in Solid-State Modification for Thermoplastic Polymers: A Comprehensive Review. *Molecules*, 29(3), 667. doi:10.3390/molecules29030667.
- [39] Chaudhari, U. S., Lin, Y., Thompson, V. S., Handler, R. M., Pearce, J. M., Caneba, G., Muhuri, P., Watkins, D., & Shonnard, D. R. (2021). Systems Analysis Approach to Polyethylene Terephthalate and Olefin Plastics Supply Chains in the Circular Economy: A Review of Data Sets and Models. *ACS Sustainable Chemistry and Engineering*, 9(22), 7403–7421. doi:10.1021/acssuschemeng.0c08622.
- [40] Trejo-Carbajal, N., Ambriz-Luna, K. I., & Herrera-González, A. M. (2022). Efficient method and mechanism of depolymerization of PET under conventional heating and microwave radiation using t-BuNH₂/Lewis acids. *European Polymer Journal*, 175, 111388. doi:10.1016/j.eurpolymj.2022.111388.
- [41] Martínez-García, R., Sánchez de Rojas, M. I., Jagadesh, P., López-Gayarre, F., Morán-del-Pozo, J. M., & Juan-Valdes, A. (2022). Effect of pores on the mechanical and durability properties on high strength recycled fine aggregate mortar. *Case Studies in Construction Materials*, 16, 1050. doi:10.1016/j.cscm.2022.e01050.
- [42] Smith, A. (2020). Ultraviolet Photo-Chemical Degradation of Polyethylene Terephthalate for Use as an Alternative Recycling Method. Ph.D. Thesis, Illinois Institute of Technology, Chicago, United States.
- [43] Ferreira, M. M., da Silva, E. A., Cotting, F., & Lins, V. de F. C. (2021). UV weathering and performance of a novel corrosion protective coating on steel made from recycled polyethylene terephthalate (PET). *Corrosion Engineering Science and Technology*, 56(3), 199–209. doi:10.1080/1478422X.2020.1836880.
- [44] Bharadwaj, A., Yadav, D., & Varshney, S. (2015). Non-biodegradable waste—its impact & safe disposal. *International Journal on Advanced Science, Engineering and Information Technology*, 3(1), 184–191.
- [45] Francis, R. (2016). Recycling of polymers: Methods, characterization and applications. In *Recycling of Polymers: Methods, Characterization and Applications*. John Wiley & Sons, Hoboken, United States. doi:10.1002/9783527689002.
- [46] Askar, M. K., Al-Kamaki, Y. S. S., & Hassan, A. (2023). Utilizing Polyethylene Terephthalate PET in Concrete: A Review. *Polymers*, 15(15), 3320. doi:10.3390/polym15153320.
- [47] Bovea, M. D., Ibáñez-Forés, V., Gallardo, A., & Colomer-Mendoza, F. J. (2010). Environmental assessment of alternative municipal solid waste management strategies. A Spanish case study. *Waste Management*, 30(11), 2383–2395. doi:10.1016/j.wasman.2010.03.001.
- [48] Singh, N., Hui, D., Singh, R., Ahuja, I. P. S., Feo, L., & Fraternali, F. (2017). Recycling of plastic solid waste: A state of art review and future applications. *Composites Part B: Engineering*, 115, 409–422. doi:10.1016/j.compositesb.2016.09.013.
- [49] Ragaert, K., Delva, L., & Van Geem, K. (2017). Mechanical and chemical recycling of solid plastic waste. *Waste Management*, 69, 24–58. doi:10.1016/j.wasman.2017.07.044.
- [50] Achilias, D. S., Roupakias, C., Megalokononimos, P., Lappas, A. A., & Antonakou, V. (2007). Chemical recycling of plastic wastes made from polyethylene (LDPE and HDPE) and polypropylene (PP). *Journal of Hazardous Materials*, 149(3), 536–542. doi:10.1016/j.jhazmat.2007.06.076.
- [51] Matsumura, S. (2002). Enzyme-catalyzed synthesis and chemical recycling of polyesters. *Macromolecular Bioscience*, 2(3), 105–126. doi:10.1002/1616-5195(20020401)2:3<105::AID-MABI105>3.0.CO;2-K.
- [52] Karayannidis, G. P., & Achilias, D. S. (2007). Chemical Recycling of Poly(ethylene terephthalate). *Macromolecular Materials and Engineering*, 292(2), 128–146. Portico. doi:10.1002/mame.200600341.
- [53] Kosmidis, V. A., Achilias, D. S., & Karayannidis, G. P. (2001). Poly(ethylene terephthalate) recycling and recovery of pure terephthalic acid. Kinetics of a phase transfer catalyzed alkaline hydrolysis. *Macromolecular Materials and Engineering*, 286(10), 640–647. doi:10.1002/1439-2054(20011001)286:10<640::AID-MAME640>3.0.CO;2-1.

- [54] López-Fonseca, R., Duque-Ingunza, I., de Rivas, B., Flores-Giraldo, L., & Gutiérrez-Ortiz, J. I. (2011). Kinetics of catalytic glycolysis of PET wastes with sodium carbonate. *Chemical Engineering Journal*, 168(1), 312–320. doi:10.1016/j.cej.2011.01.031.
- [55] Yang, Y., Lu, Y., Xiang, H., Xu, Y., & Li, Y. (2002). Study on methanolytic depolymerization of PET with supercritical methanol for chemical recycling. *Polymer Degradation and Stability*, 75(1), 185–191. doi:10.1016/S0141-3910(01)00217-8.
- [56] Al-Salem, S. M., Lettieri, P., & Baeyens, J. (2009). Recycling and recovery routes of plastic solid waste (PSW): A review. *Waste Management*, 29(10), 2625–2643. doi:10.1016/j.wasman.2009.06.004.
- [57] Fisher, M. M., Mark, F. E., Kingsbury, T., Vehlow, J., & Yamawaki, T. (2005). Energy recovery in the sustainable recycling of plastics from end-of-life electrical and electronic products. *Proceedings of the 2005 IEEE International Symposium on Electronics and the Environment*, 2005. doi:10.1109/isee.2005.1436999.
- [58] Andrady, A. L. (2003). *Plastics and the Environment*. John Wiley & Sons, Hoboken, New Jersey. doi:10.1002/0471721557.
- [59] Bernat, K. (2023). Post-Consumer Plastic Waste Management: From Collection and Sortation to Mechanical Recycling. *Energies*, 16(8), 3504. doi:10.3390/en16083504.
- [60] Ghosal, K., & Nayak, C. (2022). Recent advances in chemical recycling of polyethylene terephthalate waste into value added products for sustainable coating solutions—hope vs. hype. *Materials Advances*, 3(4), 1974–1992. doi:10.1039/d1ma01112j.
- [61] Liu, Y., Fu, W., Liu, T., Zhang, Y., & Li, B. (2022). Microwave pyrolysis of polyethylene terephthalate (PET) plastic bottle sheets for energy recovery. *Journal of Analytical and Applied Pyrolysis*, 161, 105414. doi:10.1016/j.jaap.2021.105414.
- [62] Negi, A., Hariwal, R. V., Semwal, A., Kanjilal, D., Rana, J. M. S., & Ramola, R. C. (2011). The role of electronic energy loss in PET polymer. *Radiation Effects and Defects in Solids*, 166(8–9), 621–627. doi:10.1080/10420150.2011.578630.
- [63] Dos Santos Pereira, A. P., Da Silva, M. H. P., Lima, É. P., Dos Santos Paula, A., & Tommasini, F. J. (2017). Processing and characterization of PET composites reinforced with geopolymer concrete waste. *Materials Research*, 20, 411–420. doi:10.1590/1980-5373-MR-2017-0734.
- [64] Aneke, F. I., Awuzie, B. O., Mostafa, M. M. H., & Okorafor, C. (2021). Durability assessment and microstructure of high-strength performance bricks produced from pet waste and foundry sand. *Materials*, 14(19), 5635. doi:10.3390/ma14195635.
- [65] Lee, Z. H., Paul, S. C., Kong, S. Y., Susilawati, S., & Yang, X. (2019). Modification of Waste Aggregate PET for Improving the Concrete Properties. *Advances in Civil Engineering*, 2019, 1–10. doi:10.1155/2019/6942052.
- [66] Kangavar, M. E., Lokuge, W., Manalo, A., Karunasena, W., & Frigione, M. (2022). Investigation on the properties of concrete with recycled polyethylene terephthalate (PET) granules as fine aggregate replacement. *Case Studies in Construction Materials*, 16, 934. doi:10.1016/j.cscm.2022.e00934.
- [67] Choudhary, K., Sangwan, K. S., & Goyal, D. (2019). Environment and economic impacts assessment of PET waste recycling with conventional and renewable sources of energy. *Procedia CIRP*, 80, 422–427. doi:10.1016/j.procir.2019.01.096.
- [68] Benavides, P. T., Dunn, J. B., Han, J., Bidy, M., & Markham, J. (2018). Exploring Comparative Energy and Environmental Benefits of Virgin, Recycled, and Bio-Derived PET Bottles. *ACS Sustainable Chemistry and Engineering*, 6(8), 9725–9733. doi:10.1021/acssuschemeng.8b00750.
- [69] Siddique, R., Khatib, J., & Kaur, I. (2008). Use of recycled plastic in concrete: A review. *Waste Management*, 28(10), 1835–1852. doi:10.1016/j.wasman.2007.09.011.
- [70] Rahimi, A. R., & García, J. M. (2017). Chemical recycling of waste plastics for new materials production. *Nature Reviews Chemistry*, 1(6), 46. doi:10.1038/s41570-017-0046.
- [71] Zare, Y. (2015). 3Recycled Polymers: Properties and Applications. *Recycled Polymers: Properties and Applications*, Volume 2, 2, 27.
- [72] Gallop, W. A., Evans, M. G., & Mithal, A. K. (2009). U.S. Patent Application No. 12/455,322. The United States Patent and Trademark Office (USPTO), Alexandria, United States.
- [73] Grigore, M. E. (2017). Methods of recycling, properties and applications of recycled thermoplastic polymers. *Recycling*, 2(4), 24. doi:10.3390/recycling2040024.
- [74] Rochman, C. M., Browne, M. A., Halpern, B. S., Hentschel, B. T., Hoh, E., Karapanagioti, H. K., Rios-Mendoza, L. M., Takada, H., Teh, S., & Thompson, R. C. (2013). Classify plastic waste as hazardous. *Nature*, 494(7436), 169–171. doi:10.1038/494169a.
- [75] Lazorenko, G., Kasprzhitskii, A., & Fini, E. H. (2022). Polyethylene terephthalate (PET) waste plastic as natural aggregate replacement in geopolymer mortar production. *Journal of Cleaner Production*, 375, 134083. doi:10.1016/j.jclepro.2022.134083.
- [76] Nandy, B., Sharma, G., Garg, S., Kumari, S., George, T., Sunanda, Y., & Sinha, B. (2015). Recovery of consumer waste in India - A mass flow analysis for paper, plastic and glass and the contribution of households and the informal sector. *Resources, Conservation and Recycling*, 101, 167–181. doi:10.1016/j.resconrec.2015.05.012.

- [77] Pan, D., Su, F., Liu, C., & Guo, Z. (2020). Research progress for plastic waste management and manufacture of value-added products. *Advanced Composites and Hybrid Materials*, 3(4), 443–461. doi:10.1007/s42114-020-00190-0.
- [78] Reis, J. M. L., & Carneiro, E. P. (2012). Evaluation of PET waste aggregates in polymer mortars. *Construction and Building Materials*, 27(1), 107–111. doi:10.1016/j.conbuildmat.2011.08.020.
- [79] Spósito, F. A., Higuti, R. T., Tashima, M. M., Akasaki, J. L., Melges, J. L. P., Assunção, C. C., Bortoletto, M., Silva, R. G., & Fioriti, C. F. (2020). Incorporation of PET wastes in rendering mortars based on Portland cement/hydrated lime. *Journal of Building Engineering*, 32, 101506. doi:10.1016/j.jobe.2020.101506.
- [80] da Luz Garcia, M., Oliveira, M. R., Silva, T. N., & Castro, A. C. M. (2021). Performance of mortars with PET. *Journal of Material Cycles and Waste Management*, 23(2), 699–706. doi:10.1007/s10163-020-01160-w.
- [81] Abed, J. M., Khaleel, B. A., Aldabagh, I. S., & Sor, N. H. (2021). The effect of recycled plastic waste polyethylene terephthalate (PET) on characteristics of cement mortar. *Journal of Physics: Conference Series*, 1973(1), 12121. doi:10.1088/1742-6596/1973/1/012121.
- [82] da Luz Garcia, M., Oliveira, M. R., Silva, T. N., & Castro, A. C. M. (2021). Performance of mortars with PET. *Journal of Material Cycles and Waste Management*, 23(2), 699–706. doi:10.1007/s10163-020-01160-w.
- [83] Hannawi, K., Kamali-Bernard, S., & Prince, W. (2010). Physical and mechanical properties of mortars containing PET and PC waste aggregates. *Waste Management*, 30(11), 2312–2320. doi:10.1016/j.wasman.2010.03.028.
- [84] Dumitrescu, O., Ropotă, I., Bratu, M., & Muntean, M. (2011). Reuse of pet waste as thermoplastic composites. *Environmental Engineering and Management Journal*, 10(8), 1179–1181. doi:10.30638/eemj.2011.169.
- [85] Ahmadiania, E., Zargar, M., Karim, M. R., Abdelaziz, M., & Ahmadiania, E. (2012). Performance evaluation of utilization of waste Polyethylene Terephthalate (PET) in stone mastic asphalt. *Construction and Building Materials*, 36, 984–989. doi:10.1016/j.conbuildmat.2012.06.015.
- [86] Ge, Z., Sun, R., Zhang, K., Gao, Z., & Li, P. (2013). Physical and mechanical properties of mortar using waste Polyethylene Terephthalate bottles. *Construction and Building Materials*, 44, 81–86. doi:10.1016/j.conbuildmat.2013.02.073.
- [87] Gürü, M., Çubuk, M. K., Arslan, D., Farzarian, S. A., & Bilici, I. (2014). An approach to the usage of polyethylene terephthalate (PET) waste as roadway pavement material. *Journal of Hazardous Materials*, 279, 302–310. doi:10.1016/j.jhazmat.2014.07.018.
- [88] Corinaldesi, V., Donnini, J., & Nardinocchi, A. (2015). Lightweight plasters containing plastic waste for sustainable and energy-efficient building. *Construction and Building Materials*, 94, 337–345. doi:10.1016/j.conbuildmat.2015.07.069.
- [89] Sojobi, A. O., Nwobodo, S. E., & Aladegboye, O. J. (2016). Recycling of polyethylene terephthalate (PET) plastic bottle wastes in bituminous asphaltic concrete. *Cogent Engineering*, 3(1), 1133480. doi:10.1080/23311916.2015.1133480.
- [90] Jassim, A. K. (2017). Recycling of Polyethylene Waste to Produce Plastic Cement. *Procedia Manufacturing*, 8, 635–642. doi:10.1016/j.promfg.2017.02.081.
- [91] Thorneycroft, J., Orr, J., Savoikar, P., & Ball, R. J. (2018). Performance of structural concrete with recycled plastic waste as a partial replacement for sand. *Construction and Building Materials*, 161, 63–69. doi:10.1016/j.conbuildmat.2017.11.127.
- [92] Perera, S., Arulrajah, A., Wong, Y. C., Horpibulsuk, S., & Maghool, F. (2019). Utilizing recycled PET blends with demolition wastes as construction materials. *Construction and Building Materials*, 221, 200–209. doi:10.1016/j.conbuildmat.2019.06.047.
- [93] Perca Callomamani, L. A., Hashemian, L., & Sha, K. (2020). Laboratory Investigation of the Performance Evaluation of Fiber-Modified Asphalt Mixes in Cold Regions. *Transportation Research Record*, 2674(7), 323–335. doi:10.1177/0361198120922213.
- [94] Muralidharan, R., Park, T., Yang, H. M., Lee, S. Y., Subbiah, K., & Lee, H. S. (2021). Review of the effects of supplementary cementitious materials and chemical additives on the physical, mechanical and durability properties of hydraulic concrete. *Materials*, 14(23), 7270. doi:10.3390/ma14237270.
- [95] Ramzi, S., & Hajiloo, H. (2022). The effects of supplementary cementitious materials (SCMs) on the residual mechanical properties of concrete after exposure to high temperatures. *Buildings*, 13(1), 103. doi:10.3390/buildings13010103.
- [96] Qaidi, S., Al-Kamaki, Y., Hakeem, I., Dulaimi, A. F., Özkılıç, Y., Sabri, M., & Sergeev, V. (2023). Investigation of the physical-mechanical properties and durability of high-strength concrete with recycled PET as a partial replacement for fine aggregates. *Frontiers in Materials*, 10, 1101146. doi:10.3389/fmats.2023.1101146.
- [97] Mohammed, A. A. (2017). Modelling the mechanical properties of concrete containing PET waste aggregate. *Construction and Building Materials*, 150, 595–605. doi:10.1016/j.conbuildmat.2017.05.154.
- [98] Limami, H., Manssouri, I., Cherkaoui, K., & Khaldoun, A. (2020). Study of the suitability of unfired clay bricks with polymeric HDPE & PET wastes additives as a construction material. *Journal of Building Engineering*, 27, 100956. doi:10.1016/j.jobe.2019.100956.

- [99] Hameed, A. M., & Ahmed, B. A. F. (2019). Employment the plastic waste to produce the light weight concrete. *Energy Procedia*, 157, 30–38. doi:10.1016/j.egypro.2018.11.160.
- [100] Samsudin, M. A., Manaf, A. F. A., Aznan, M. F. F., Zuki, S. S. M., Ramasamy, S., Azmi, M. A. M., & others. (2021). Investigation on Polyethylene Terephthalate (PET) Waste Fiber Performances in Concrete Material. *Recent Trends in Civil Engineering and Built Environment*, 2(1), 682–690.
- [101] Dawood, A. O., AL-Khazraji, H., & Falih, R. S. (2021). Physical and mechanical properties of concrete containing PET wastes as a partial replacement for fine aggregates. *Case Studies in Construction Materials*, 14, 482. doi:10.1016/j.cscm.2020.e00482.
- [102] Saxena, R., Gupta, T., Sharma, R. K., Chaudhary, S., & Jain, A. (2020). Assessment of mechanical and durability properties of concrete containing PET waste. *Scientia Iranica*, 27(1), 1–9. doi:10.24200/sci.2018.20334.
- [103] Almehsal, I., Tayeh, B. A., Alyousef, R., Alabduljabbar, H., & Mohamed, A. M. (2020). Eco-friendly concrete containing recycled plastic as partial replacement for sand. *Journal of Materials Research and Technology*, 9(3), 4631–4643. doi:10.1016/j.jmrt.2020.02.090.
- [104] Campanhão, A. F., Marvila, M. T., de Azevedo, A. R. G., da Silva, T. R., Fediuk, R., & Vatin, N. (2022). Recycled pet sand for cementitious mortar. *Materials*, 15(1), 273. doi:10.3390/ma15010273.
- [105] Kozul, R., & Darwin, D. (1997). Effects of Aggregate Type, Size and Content on Concrete Strength and Fracture Energy. SM Report No. 43, University of Kansas Center for Research, Kansas, United States.
- [106] Guendouz, M., Debieb, F., Boukendakdji, O., Kadri, E. H., Bentchikou, M., & Soualhi, H. (2016). Use of plastic waste in sand concrete. *Journal of Materials and Environmental Science*, 7(2), 382–389.
- [107] Pereira De Oliveira, L. A., & Castro-Gomes, J. P. (2011). Physical and mechanical behaviour of recycled PET fibre reinforced mortar. *Construction and Building Materials*, 25(4), 1712–1717. doi:10.1016/j.conbuildmat.2010.11.044.
- [108] Ochi, T., Okubo, S., & Fukui, K. (2007). Development of recycled PET fiber and its application as concrete-reinforcing fiber. *Cement and Concrete Composites*, 29(6), 448–455. doi:10.1016/j.cemconcomp.2007.02.002.
- [109] Chowdhury, S., Maniar, A. T., & Suganya, O. (2013). Polyethylene Terephthalate (PET) Waste as Building Solution. *International Journal of Chemical, Environmental & Biological Sciences*, 1(5), 2320–4087.
- [110] Tang, R., Wei, Q., Zhang, K., Jiang, S., Shen, Z., Zhang, Y., & Chow, C. W. K. (2022). Preparation and performance analysis of recycled PET fiber reinforced recycled foamed concrete. *Journal of Building Engineering*, 57, 104948. doi:10.1016/j.job.2022.104948.